Under the influence: Understanding the thermodynamic and optical properties of stimuli-responsive complex organic systems

---

Inaugural-Dissertation

to obtain the academic degree
Doctor rerum naturalium (Dr. rer. nat.)

submitted to
The Department of Biology, Chemistry, Pharmacy
of Freie Universität Berlin

by
Jan Felix Witte
from Berlin, Germany
2021

This work was conducted under the supervision of
Prof. Dr. Beate Paulus (Freie Universität Berlin)
from January 2018 until January 2021

1. Reviewer:	Prof. Dr. Beate Paulus
2. Reviewer:	Prof. Dr. Christoph A. Schalley
Date of defense:	March 24, 2021

Statutory Declaration

I, Jan Felix Witte, declare that I have authored my thesis with the subject

Under the influence: Understanding the thermodynamic and optical properties of stimuli-responsive complex organic systems

independently, that I have not used other than the declared sources, and that I have explicitly marked all material which has been quoted either literally or by content from the used sources.

Berlin, February 1, 2021

All good stories deserve embellishment.

– Gandalf in "*The Hobbit: An Unexpected Journey*"

Danksagung

Ich möchte damit beginnen, zu sagen, dass die letzten drei Jahre eine tolle Zeit für mich waren. Die Entscheidung, in die Theoretische Chemie zu gehen, habe ich kein einziges Mal bereut. Das lag vor allem auch daran, dass ich durch meine großartigen Kooperationspartner immer so nahe am Laborgeschehen wie nur möglich sein konnte.
Allen voran gilt mein Dank Prof. Dr. Beate Paulus, die mir die Möglichkeit gegeben hat, als Teil ihrer Arbeitsgruppe in der Theoretischen Chemie zu promovieren. Ohne ihren Einfluss wäre ich nicht dort, wo ich bin, und diese Arbeit wäre nicht zustandegekommen.
Desweiteren gilt mein Dank meinem Zweitgutachter Prof. Dr. Christoph Schalley, der mir bereits im Laufe meines Studium die Welt der supramolekularen Chemie näher gebracht hat, um die es nun auch in meiner Dissertation geht.
Ich hatte das große Glück, in einer fantastischen Arbeitsatmosphäre mit überaus motivierten und gleichzeitig so entspannten Kollegen arbeiten zu können. Meinen langjährigen Bürokollegen Jan, Tim, Christian und Hannah gilt mein ganz besonderer Dank! Außerdem bedanke ich mich recht herzlich für die vielen Ideen und anregenden Diskussionen mit Dr. Jan Götze, der ebenfalls einen großen Einfluss auf mich und meine Arbeit in den letzten Jahren hatte. Ich möchte auch allen weiteren derzeitigen und ehemaligen Mitgliedern der AGs Paulus, Keller und Tremblay für eine tolle Zeit Danke sagen. Andi, Jenni, Marius, Marco, Steffi, Olli, Jingjing, Kai, Simon, Kangli, Christian und ich werde gar nicht erst versuchen, diese Liste zu vervollständigen. Ich entschuldige mich aufrichtig bei allen, die ich jetzt nicht namentlich erwähnt habe! Vielen Dank außerdem an meine Forschungspraktikanten Lauren Finn, Julian Hille und Yuan-Wei Pi, an denen ich meine didaktischen Fähigkeiten erproben durfte.
Wie bereits erwähnt, hätte diese Arbeit ohne meine wundervollen Kooperationspartner nicht entstehen können. Ich bedanke mich bei allen Mitgliedern der AG Schalley und AG Eigler für eine tolle Zusammenarbeit und das ein oder andere Feierabendbier. Danke vor allem an Hendrik Schröder, Henrik Hupatz, Marius Gaedke, Fei Jia, Siegfried Eigler und Philipp Rietsch!
Ich möchte mich darüber hinaus bei der ZEDAT und dem HLRN für ihre Rechenressourcen und technischen Hilfestellungen bedanken. Danke auch an die DFG für finanzielle Unterstützung im Rahmen des SFB 765 und des Forschungsprojekts PA 1360/16-1.
Zu guter Letzt möchte ich mich bei allen meinen Freunden und bei meiner Familie bedanken für alles, was ihr für mich tut und getan habt. Ihr wisst, wer ihr seid. Danke, dass es euch gibt!
Marvin, so häufig kommt man ja nicht dazu, seinem besten Freund zu sagen, was er einem bedeutet. Du bist der beste. Ich freue mich schon auf unsere Silberhochzeit und darauf, dass wir uns zusammen in unseren Schaukelstühlen Zigarre rauchend und Whisky trinkend auf der Veranda den Sonnenuntergang anschauen!

Ich widme diese Doktorarbeit meinem Opa, Dr. Eberhard Witte.

Abstract

A solid understanding of the optical and thermodynamic features of a chemical system is indispensable for the development and optimisation of new materials. Stimuli-responsive substances may be incorporated into optoelectronic devices, such as organic light-emitting diodes or sensory systems. Especially in recent years, photo-sensitive molecular aggregates and redox-switchable supramolecular architectures have proven their merit. Due to their flexible components, these noncovalently bound systems often exhibit perplexing behaviour when submitted to external stimuli, such as light or electric potential. Examples addressed in this thesis include substitution-pattern controlled fluorescence quantum yields and redox-induced switchable spectroscopic responses. While there are plenty of powerful experimental techniques around to examine the underlying mechanisms, high-level quantum-chemical approaches are often crucial for a final and conclusive interpretation of one's experimental results.

The aim of this thesis is to examine the broad scope of stimuli-responsive molecular aggregates and demonstrate the versatility of quantum-chemical methods to study their optical and thermodynamic properties. To this end, I will present six different publications separated into two parts, **A** and **B**, each contributing three papers. Due to the variety of the molecules studied in this work, computational protocols effectively tailored for each project had to be developed. The applied methods are used to study electronic as well as molecular structures and include solvent and finite-temperature effects for comparison to experiment. A major emphasis is put on the evaluation of excited states. In addition to the valuable knowledge we could gain about the underlying chemistry of the investigated systems, these protocols serve as a potent tool for the examination of similar problems. All papers include combined approaches of theory and experiment and, hence, showcase the efficient collaboration of experimental and theoretical groups.

In part **A**, I will present a new class of fluorescent dyes: Diaminodicyanoquinones (DADQs). Owing to a large dipole moment, redox-activity, and tailorable fluorescence, DADQs are promising candidates for a variety of applications in the context of molecular electronics. Papers **A1**–**A3** effectively follow a bottom-up approach examining monomers, aggregates in solution, and the solid state with a focus on their absorption and emission features. In all three publications, remarkable experimental observations are made including notably high quantum yields and counterintuitive concentration-dependent absorption peaks. In each case, a combination of multiple high-level state-of-the-art quantum-chemical approaches including DFT/MRCI (density functional theory/multi-reference configuration interaction) is utilised to thoroughly investigate the chemical systems and find explanations for the often unexpected experimental results.

Part **B** presents three different redox-responsive supramolecular systems, each displaying intriguing thermodynamic or optical properties, which could only be fully unravelled by rigorous theoretical studies. Redox-responsiveness is induced either by incorporation of the organosulfur compound tetrathiafulvalene (TTF) or by complexation with a redox-active molecule such as cobaltocene. A variety of different quantum-chemical methods based on DFT and time-dependent DFT (TD-DFT) is employed in the course of part **B** to study switching mechanisms and rationalise thermodynamic features. In this way, the examined supramolecular structures are now equipped with an in-depth understanding of their often non-trivial chemical behaviour which paves the way towards applications in novel optoelectronic technologies.

Kurzzusammenfassung

Ein klares Verständnis der optischen und thermodynamischen Eigenschaften chemischer Systeme ist unabdingbar für die Entwicklung und Optimierung neuer Materialien. Substanzen, die sich von äußeren Einflüssen steuern lassen, können in optoelektronische Geräte wie organische Leuchtdioden oder Sensorsysteme eingebaut werden. Besonders in den vergangenen Jahren haben photo-sensitive molekulare Aggregate und redox-schaltbare supramolekulare Architekturen ihren Wert unter Beweis gestellt. Aufgrund ihrer flexiblen Einzelkomponenten zeigen diese nichtkovalent gebundenen Systeme oftmals ein verblüffendes Verhalten, wenn sie durch äußere Reize wie Licht oder ein elektrisches Potenzial beeinflusst werden. Beispiele, die in dieser Dissertation adressiert werden, sind Substitutionsmuster-kontrollierte Fluoreszenzquantenausbeuten und redox-induzierte schaltbare spektroskopische Signale. Während es eine große Anzahl an vielseitigen experimentellen Methoden gibt, um die zugrundeliegenden Mechanismen zu studieren, ist oftmals die Verwendung anspruchsvoller quantenchemischer Ansätze vonnöten, um eine endgültige und schlüssige Interpretation der experimentellen Ergebnisse zu erhalten.

Diese Arbeit ist darauf ausgerichtet, die Vielseitigkeit von durch äußere Reize steuerbare (eng. *stimuli-responsive*) molekulare Aggregate zu analysieren und die Flexibilität von quantenchemischen Methoden aufzuzeigen, die zur Untersuchung ihrer optischen und thermodynamischen Eigenschaften genutzt werden. Zu diesem Zweck werde ich sechs Publikationen vorstellen, aufgeteilt in zwei Teile, **A** und **B**, die jeweils drei Arbeiten beitragen. Aufgrund der Vielfältigkeit der untersuchten Moleküle wurden Berechnungsverfahren entwickelt, die im wesentlichen für jedes Projekt aufs Neue maßgeschneidert werden mussten. Die angewandten Methoden sind darauf ausgelegt, sowohl elektronische als auch molekulare Strukturen zu beschreiben und Solvatations- und Temperatureinflüsse für den Vergleich zu Experimenten mit einzubeziehen. Ein großes Augenmerk liegt auf der Analyse von angeregten Zuständen. Abgesehen von den wertvollen Erkenntnissen, die wir über die zugrundeliegende Chemie der untersuchten Systeme erhalten konnten, dienen die entwickelten Berechnungsansätze als leistungsfähiges Werkzeug für das Herangehen an ähnliche Probleme. Alle Publikationen beinhalten aus Theorie und Experiment kombinierte Ansätze und illustrieren damit die effiziente Zusammenarbeit von theoretisch und experimentell arbeitenden Forschungsgruppen.

In Teil **A** werde ich eine neuartige Klasse von fluoreszierenden Farbstoffen vorstellen: Diaminodicyanochinone (DADQs). Aufgrund ihrer hohen Dipolmomente, Redoxaktivität und einstellbaren Fluoreszenz sind DADQs vielversprechende Kandidaten für eine Vielzahl von Anwendungen im Kontext der molekularen Elektronik. Publikationen **A1**–**A3** folgen im wesentlichen einem Bottom-up-Ansatz, bei dem es um die Untersuchung von Monomeren, Aggregaten in Lösung und Festkörperstoffen geht, wobei ein Fokus auf deren Absorptions- und Emissionseigenschaften liegt. In allen drei Arbeiten sind erstaunliche experimentelle Beobachtungen gemacht worden wie beispielsweise extrem hohe Fluoreszenzquantenausbeuten oder kontraintuitive konzentrationsabhängige Absorptionsbanden. In jeder Untersuchung wurde eine Vielzahl an hochmodernen quantenchemischen Methoden inklusive des DFT/MRCI (Dichtefunktionaltheorie/Multireferenz-Konfigurationswechselwirkung) Ansatzes genutzt, um eine ausführliche Analyse der chemischen Systeme zu gewährleisten und Erklärungen für die unerwarteten experimentellen Beobachtungen zu finden.

In Teil **B** werden drei verschiedene redox-stimulierbare supramolekulare Systeme präsentiert, die alle interessante thermodynamische und optische Eigenschaften aufzeigen, welche nur durch den sorgfältigen Einsatz von theoretischen Methoden vollkommen verstanden werden konnten. Redox-Stimulierbarkeit wurde entweder durch die Eingliederung der schwefelorganischen Verbindung Tetrathiafulvalen (TTF) oder durch Komplexierung mit einem redox-aktiven Molekül wie Cobaltocen induziert. Verschiedene quantenchemische auf DFT und zeitabhängiger DFT (TD-DFT) basierende Ansätze wurden in Teil **B** benutzt, um Schaltmechanismen zu untersuchen und thermodynamische Eigenschaften zu rationalisieren. Dadurch erhielten wir ein tiefes Verständnis der oftmals alles andere als trivialen chemischen Verhaltensweisen der supramolekularen Strukturen, was den Weg zur Anwendung in neuartigen, optoelektronischen Technologien ebnet.

Contents

1 List of publications

Part A: Photoexcited diaminodicyanoquinones

A1: "Diaminodicyanoquinones: Fluorescent Dyes with High Dipole Moments and Electron-Acceptor Properties"
P. Rietsch,* F. Witte,* S. Sobottka, G. Germer, A. Becker, A. Güttler, B. Sarkar, B. Paulus, U. Resch-Genger, S. Eigler
Angew. Chem. Int. Ed. **2019**, 58, 8235–8239.
DOI: 10.1002/anie.201903204
* Co-first authors

A2: "Fluorescence quenching in J-aggregates through the formation of unusual metastable dimers"
F. Witte, P. Rietsch, S. Sinha, A. Krappe, J.-O. Joswig, J. P. Götze, N. Nirmalananthan-Budau, U. Resch-Genger, S. Eigler, B. Paulus
submitted

A3: "Aggregation-induced emission leading to two distinct emissive species in the solid-state structure of high-dipole organic chromophores"
F. Witte, P. Rietsch, N. Nirmalananthan-Budau, J. P. Götze, S. Eigler, B. Paulus
submitted

Part B: Redox-responsive supramolecular frameworks

B1: "Switchable synchronisation of pirouetting motions in a redox-active [3]rotaxane"
H. V. Schröder, A. Mekic, H. Hupatz, S. Sobottka, F. Witte, L. H. Urner, M. Gaedke, K. Pagel, B. Sarkar, B. Paulus, C. A. Schalley
Nanoscale **2018**, 10, 21425–21433.
DOI: 10.1039/c8nr05534c

B2: "Chiroptical inversion of a planar chiral redox-switchable rotaxane"
M. Gaedke, F. Witte, J. Anhäuser, H. Hupatz, H. V. Schröder, A. Valkonen, K. Rissanen, A. Lützen, B. Paulus, C. A. Schalley
Chem. Sci. **2019**, 10, 10003–10009.
DOI: 10.1039/C9SC03694F

B3: "Naphthocage: A Flexible yet Extremely Strong Binder for Singly Charged Organic Cations"
F. Jia, H. Hupatz, L.-P. Yang, H. V. Schröder, D.-H. Li, S. Xin, D. Lentz, F. Witte, X. Xie, B. Paulus, C. A. Schalley, W. Jiang
J. Am. Chem. Soc. **2019**, 141, 10, 4468–4473.
DOI: 10.1021/jacs.9b00445

Other publications

1. "An aryl-fused redox-active tetrathiafulvalene with enhanced mixed-valence and radical-cation dimer stabilities"
H. V. Schröder, F. Witte, M. Gaedke, S. Sobottka, L. Suntrup, H. Hupatz, A. Valkonen, B. Paulus, K. Rissanen, B. Sarkar, C. A. Schalley
Org. Biomol. Chem. **2018**, 16, 2741–2747.
DOI: 10.1039/C8OB00415C

2. "To Anion–π or not to Anion–π: The Case of Anion-Binding to Divalent Fluorinated Pyridines in the Gas Phase"
M. Göth, F. Witte, M. Quennet, P. Jungk, G. Podolan, D. Lentz, W. Hoffmann, K. Pagel, H.-U. Reissig, B. Paulus, C. A. Schalley
Chem. Eur. J. **2018**, 24, 12879–12889.
DOI: 10.1002/chem.201800893

3. "Scalable Production of Nanographene and Doping via Nondestructive Covalent Functionalization"
G. Guday, I. S. Donskyi, M. F. Gholami, G. Algara-Siller, F. Witte, A. Lippitz, W. E. S. Unger, B. Paulus, J. P. Rabe, M. Adeli, R. Haag
Small **2019**, 15, 1805430.
DOI: 10.1002/smll.201805430

4. "A user-friendly, Python-based quantum mechanics/Gromacs interface: gmx2qmmm"
J. P. Götze, Y.-W. Pi, S. Petry, S, F. Langkabel, F. Witte, O. Lemke
Int. J. Quantum Chem. **2020**, e26486.
DOI: 10.1002/qua.26486

5. "Unexpected substituent effects in aryl-aryl Negishi cross-coupling reactions rationalized by DFT and natural population analysis"
F. Witte, S. P. Zucker, B. Paulus, C. C. Tzschucke
in revision

2 Introduction

Noncovalent interactions are ubiquitous in nature. Their ever-growing importance is perhaps best summarised by a quote from Mark Ratner:[1]

> *Chemistry of the 20th century was about intramolecular interactions,*
> *chemistry of the 21st century will be about intermolecular interactions.*

Indeed, there is a plethora of concepts lying beyond the covalent bond, waiting to be uncovered. Ranging from π-π-stacking in supramolecular aggregates and hydrogen bonds in DNA base pairs to geckos attaching to walls[2,3] and the cohesive forces holding together rubble-pile asteroids,[4] noncovalent interactions are of multi-disciplinary relevance.

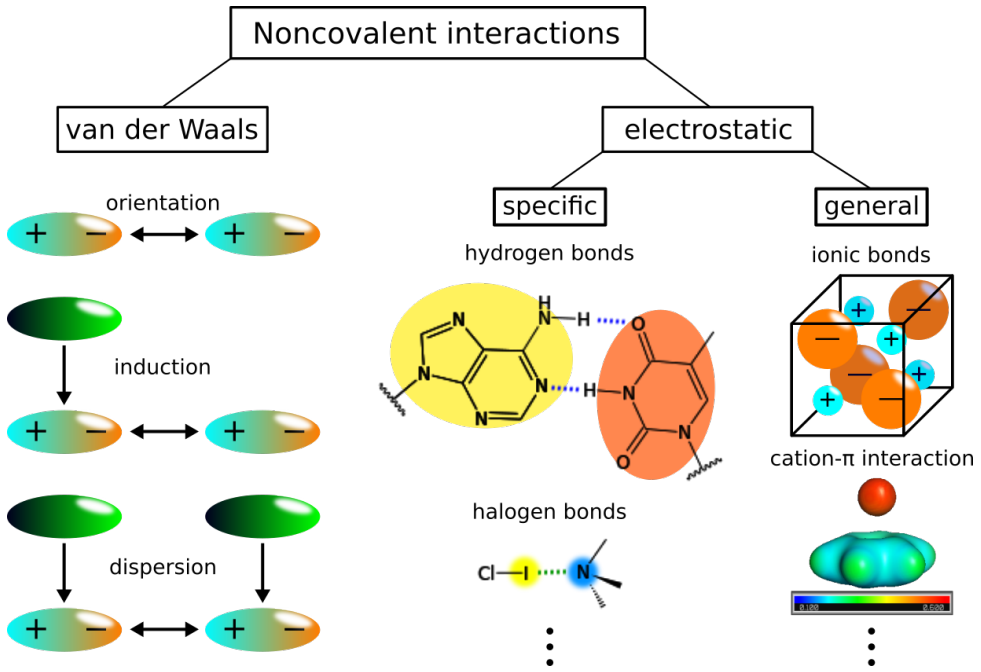

Figure 2.1: Classification of noncovalent interactions into van-der-Waals and electrostatic interactions: Ellipsoids on the left correspond to neutral charge distributions (green) and induced or permanent dipoles (cyan-orange mix). See text for details.

Within this framework, it is useful to differentiate two subordinate terms: van-der-Waals (vdW) interactions and electrostatics (**Fig. 2.1**). While this differentiation might be somewhat arbitrary and not entirely unambiguous, it provides a didactic basis to discuss some of the results of this thesis. vdW-interactions describe all types of multipole-interactions and can be divided into three categories according to the nature of the involved molecular species.[5] First, *orientation* refers to dipole-dipole interactions caused by mutual repulsion or attraction of two permanent dipoles (or multipoles in general). *Induction* describes dipole-induced dipole interactions, and London *dispersion* is associated with two induced dipoles. The latter are in fact so prominent that the term "dispersive interactions" is often erroneously used interchangeably with the general vdW term. Thermal averaging in the liquid phase yields a short-range R^{-6} dependence on distance for all vdW-interactions.[6]

In contrast, electrostatic interactions usually exhibit a much larger range of action. For instance, the attractive potential between two opposite charges is well known to be linear in $1/R$. We may consider electrostatics to encompass all permanent Coulomb-type interactions usually, but not exclusively, involving charges. This includes ion-dipole and ion-induced dipole interactions which may be somewhat debatable due to their intermediate area of effect depending on R^{-4}. We may furthermore distinguish general system-independent phenomena, e.g., ionic bonding and cation-π interactions, from element- or system-specific interactions, such as hydrogen bonds or σ-holes. The latter classification is subtle but important. For example, without analysing the corresponding molecular wavefunction – a cornerstone of theoretical chemistry – the geometry-dependent features of hydrogen or halogen bonds could not be explained.
Noncovalent interactions are the sole foundation of molecular aggregation processes. Consider as an extreme example the condensation of rare gas atoms, which would not be possible without the existence of London dispersion forces. While the general concept of molecular aggregation is as old as chemistry itself, it was not until the late 1930s that Günter Scheibe and Edwin Jelley provided the first experimental evidence for a dye aggregate in solution.[7–9] They both independently observed that pseudoisocyanine displayed unusual optical effects. Comparing an alcoholic and an aqueous solution, a sharp, red-shifted absorption band emerges in the latter, which is in addition highly fluorescent with a very small Stokes shift. Scheibe originally proposed polymerisation as the origin of this behaviour.[10]

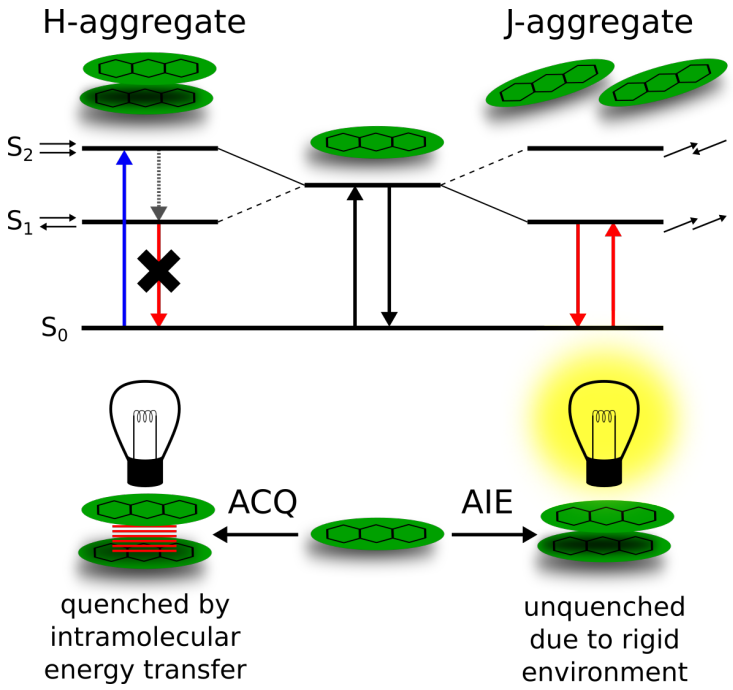

Figure 2.2: Top: Exciton splitting according to Kasha in H- and J-aggregates, chromophores are represented by green ellipses. Small double arrows indicate transition dipole moment coupling, solid arrows refer to absorption and emission, and the dashed arrow on the left represents fluorescence quenching through internal conversion; bottom: aggregation-caused quenching (ACQ) and aggregation-induced emission (AIE), especially important for the photophysical properties of organic solids.

Nowadays, pseudoisocyanines in water are referred to as J-aggregates named after Jelley. In general, these types of aggregates are defined by a red-shifted absorption signal with respect to the

spectral position of the isolated monomer and display only slightly mitigated or even enhanced fluorescence.[11] Its counterpart, H-aggregates, show blue-shifted (**H**ypsochromic) nonfluorescent absorption bands. This classification scheme is based on the seminal works of Michael Kasha[12,13] who proposed in 1958 that dye aggregates can be categorised on the basis of Coulomb-coupled transition dipole moments invoking Davydov's exciton theory (**Fig. 2.2**). Exciton splitting in aggregates is associated with the two monomers generating two non-degenerate excited states accessible through photoexcitation. The blue-shift encountered in H-aggregates relates to a bright high-energy S_2 and dark low-energy S_1 state. In J-aggregates the lower-lying S_1 is populated, while the high-lying S_2 remains dark. According to Kasha's rule,[14] fluorescence usually progresses from the lowest excited state of the molecule, which explains the behaviour of the aggregates with respect to emission. H-aggregates are barely or non-emissive due to the dark S_1, while emission in J-aggregates can be practically unquenched.

An extension of Kasha's work is the expanded H- and J-aggregate theory due to Francis Spano and co-workers who realised that Coulomb-coupled transition dipoles are insufficient to describe a large number of photophysical phenomena especially discovered in the last decade. Examples of non-Kasha aggregates include fluorescent H-aggregated phthalocyanines,[15] "red-shifted H-aggregates",[16,17] or "null-aggregates", in which the aggregate absorption band resembles that of the monomer.[18] To account for these unusual observations, Spano and co-workers identified short-range wave-function overlap as a key concept in addition to Kasha's long-range Coulomb coupling. Within this framework "HJ-aggregates" are possible owing to a subtle interplay of both coupling mechanisms.[19,20] The intricacies of this approach are further discussed in the theoretical part of this thesis.

Having addressed a few general concepts, let us discuss some more practical examples. Numerous advances in the context of optoelectronic devices based on the vast research of molecular aggregates could be achieved in recent years. Especially anthracenes and members of the rylene families have been the centre of attention including applications in solar cells[21–23] and other solid-state optoelectronic devices.[24–28] However, frequently aggregation is viewed as an undesired side effect when studying optoelectronic materials. This is often associated with the emergence of H-aggregates which have a deteriorating influence on emission features. The general term for this behaviour is aggregation-caused quenching (ACQ). Especially in solids, close molecular packing can lead to severe reduction of fluorescence quantum yields. Probably the most prominent quenching mechanism in organic crystals involves energy transfer mediated through π-π-stacking in excimers. Quenching mechanisms include Förster resonance energy transfer (FRET) and the short-range Dexter process.[29,30] While the former depends on the potentially far-reaching (> 10 Å) interaction of molecular (transition) dipoles, decaying with an R^{-6} dependence, the latter is determined by wavefunction overlap which decays much quicker with an exponential dependence on distance. Note that there is a conceptual similarity between Förster and Dexter processes usually important for quenching in the solid state and Kasha's Coulomb coupling and Spano's wavefunction overlap for aggregates in solution.

In contrast to ACQ, solid-state materials may also experience emission enhancement due to close molecular packing. In 2001, Daoben Zhu and co-workers introduced the concept of aggregation-induced emission (AIE) by presenting a silole compound which for the first time showed improved emission upon aggregation in solution.[31,32] This sparked a rapid increase in interest in the topic and many systems were introduced exploiting the AIE idea.[33–35] Approaches to enhance emission

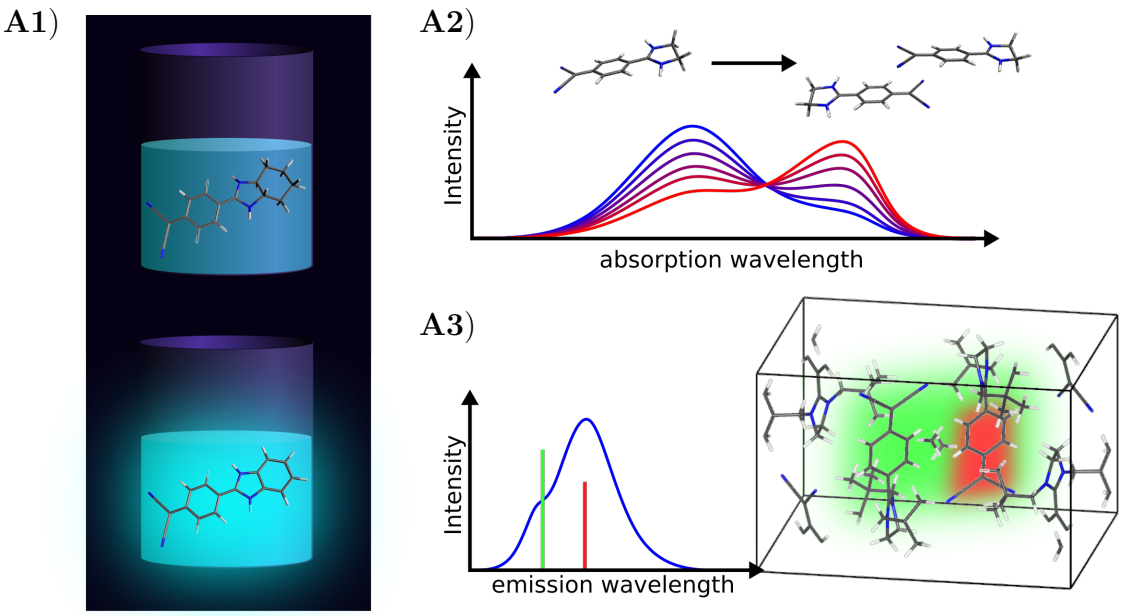

Figure 2.3: Optical properties of diaminodicyanoquinones: paper **A1** investigates monomers with an emphasis on differences in fluorescence among various derivatives, paper **A2** studies DADQ aggregates in solution and proposes a mechanism to explain an aggregation-induced red-shift observed in steady-state absorption experiments, paper **A3** examines DADQ derivatives in the crystal showing that monomer and dimer attributes can be used to rationalise solid-state optical properties.

in the solid state include the design of materials based on J-aggregates[36] and embedded or structurally isolated dimers, which disfavour non-radiative decay pathways due to the rigidity of their microscopic environment.

In search of efficient materials for potential application in optoelectronic devices, part **A** of this thesis revolves around a new class of high-dipole fluorescent dyes: Diaminodicyanoquinones (DADQs). As we will see, DADQs are remarkably versatile compounds with lots of desirable and intriguing attributes ranging from redox-active, highly fluorescent monomers to nonfluorescent J-aggregates in solution and enhanced emission in the solid state (**Fig. 2.3**). Paper **A1** represents a fundamental study of the basic properties of a variety of DADQ derivatives, including absorption and fluorescence measurements and cyclic voltammetry (CV) experiments with the major focus of this thesis being on the theoretical analysis of the optical features. Paper **A2** extends this work and examines the photophysical behaviour of aggregates up to hexamers in solution with a particular emphasis on dimers, which are computationally most feasible. An unprecedented mechanism is presented involving nonfluorescent J-aggregates to account for the unusual optical properties observed in absorption and emission experiments. Finally, in the third paper (**A3**) solid-state DADQs are investigated. A reverse trend between emission in solution and in the crystal is observed related to ACQ and AIE effects depending on the derivative under study. We complete the circle by showing that most of the solid-state photophysical features of DADQs originate from monomers and dimers merely polarised by the crystal environment. In this way, papers **A1**–**A3** essentially follow a bottom-up approach of DADQs as optoelectronic building blocks.

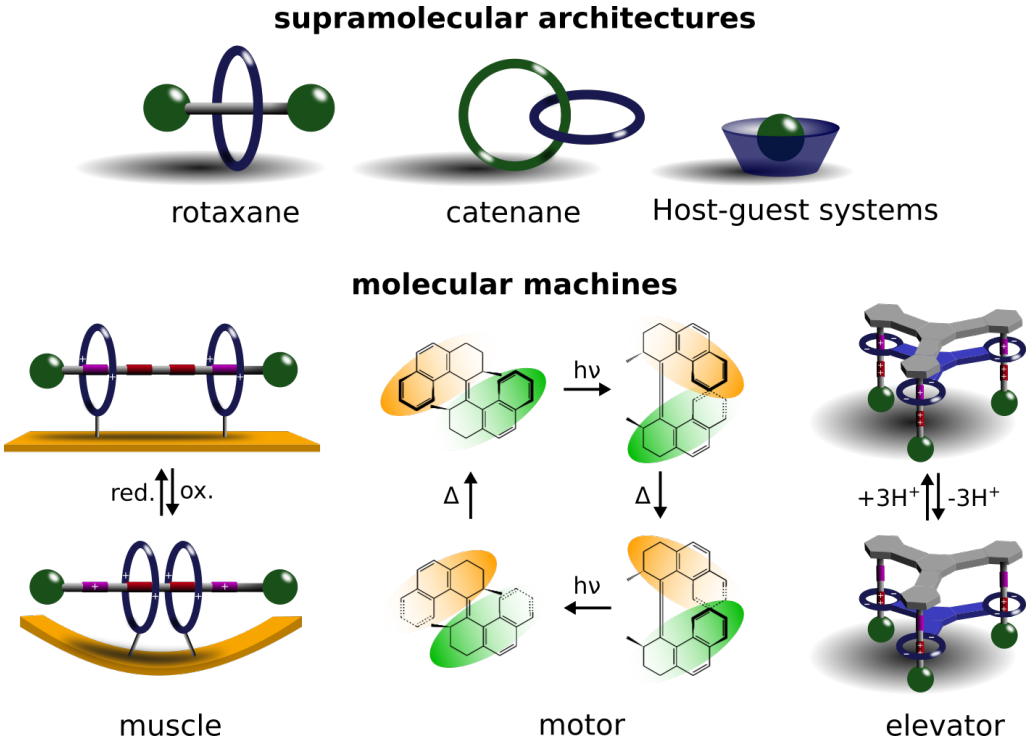

Figure 2.4: Schematic representation of common supramolecular frameworks used for potential application in so-called "molecular machines", defined by their ability to convert a specific form of energy into mechanical motion.

A fascinating field of research directly intertwined with the concept of molecular aggregates is the vast realm of supramolecular chemistry. The "chemistry beyond the molecule", as Jean-Marie Lehn phrased it in his Nobel lecture in 1987,[37] is an intriguing subject bearing manifold possibilities for studies ranging from selective host-guest complexes to stimuli-responsive molecular switches. Most recently, this has been underlined by the 2016 Nobel Prize in Chemistry awarded to Jean-Pierre Sauvage, James Fraser Stoddart, and Bernard Feringa "for the design and synthesis of molecular machines"[38–40] – a bewildering application of chemistry at the nanoscale level. Arguably at the heart of supramolecular chemistry are so-called mechanically interlocked molecules (MIMs, **Fig. 2.4**). Examples include rotaxanes, consisting of one or more macrocycles and a long linear chain ("axle") equipped with two large terminal groups ("stopper") at the end to prevent the macrocycle from slipping, and catenanes defined by two interlocked macrocycles. The mechanical bond, first realised experimentally by Edel Wassermann in 1960 through the formation of a catenane,[41] is a most curious phenomenon in the context of chemical bonding, since one cannot separate the components of, e.g., a rotaxane without cutting a covalent bond even though no such bond exists between them. Moreover, supramolecular hosts such as cucurbiturils, calixarenes, or cyclodextrins are important systems in their own right with applications spanning all subdisciplines in chemistry.[42–44]

Rotaxanes, catenanes, and host-guest complexation build the foundation of stimuli-responsive, switchable molecular machines. Sauvage[45–47] and Stoddart[48–52] among others[53,54] could show off the versatility of the mechanical bond providing an entire library of building blocks to potentially implement in molecular machines, while Feringa[55–57] was the first to actually create working

molecular machines. Examples of these complex structures include a redox-switchable molecular muscle,[51] a pH-sensitive nanoelevator,[52] and a molecular motor driven by UV light and heat (**Fig. 2.4** bottom).[55]

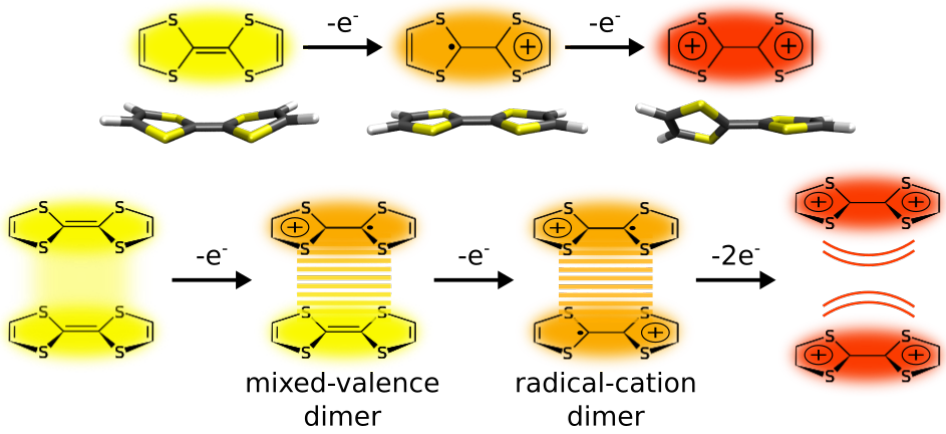

Figure 2.5: Top: Charge-dependent structural changes in TTF, bottom: charge-dependent intermolecular interactions in TTF_2. Neutral TTF monomers are bound due to dispersive interactions, while electrostatic repulsion drifts the TTF units apart in the fully oxidised ${TTF_2}^{4+}$.

A prerequisite to the proper functioning of most of these constructs is the existence of a stimuli-responsive component. Redox-active supramolecular switches most often feature components like viologens, naphthalene diimide (NDI), or tetrathiafulvalene (TTF).[58–62] Especially the latter is a major focus of this thesis, which makes it useful to discuss some of its properties here. TTF is readily oxidisable, easily incorporated into other building blocks, and displays intriguing and rather unique structural properties depending on its charge (**Fig. 2.5**). In its neutral form, TTF is a 14-π electron pro-aromatic system in C_{2v} symmetry. Upon oxidation, the structure flattens out yielding a D_{2h} point group which twists into a D_2 structure after a second oxidation. This startling behaviour is related to the induced aromaticity in $TTF^{+\cdot}$ and TTF^{2+}. While the aromatic character of $TTF^{+\cdot}$ is delocalised over the entire molecule with an unpaired electron fluctuating between the two rings, TTF^{2+} contains two separate aromatic systems twisting due to the repulsive electrostatic interaction of the charge densities localised at the sulfur atoms.
Apart from investigations about single TTF units incorporated in supramolecular compounds,[63–65] a remarkably large amount of research has been dedicated to the study of noncovalently bound TTF dimers.[66–72] TTF_2 displays compelling electronic properties as a direct result of the redox-active features of TTF. TTF_2 can be reversibly oxidised three times to yield a total of four electronically unique complexes. Neutral TTF_2 is moderately bound mostly by dispersive interactions between the two electron-rich subunits. Upon oxidation, the dimer contracts while the monomers each become planar, yielding ${TTF_2}^{+\cdot}$ as a so-called mixed-valence system. Originating from the increasing repulsive electrostatic interactions, ${TTF_2}^{2+}$ is actually a metastable structure.[73] However, in solution the dissolved state is significantly favoured over that of two separated $TTF^{+\cdot}$ radicals. In its final charge state, ${TTF_2}^{4+}$ is unstable with respect to dissociation owing to the large degree of electrostatic repulsion between the highly charged monomers. The charge-dependent properties of TTF and TTF_2 have stimulated a multitude of investigations and are also the focus of papers **B1** and **B2**.

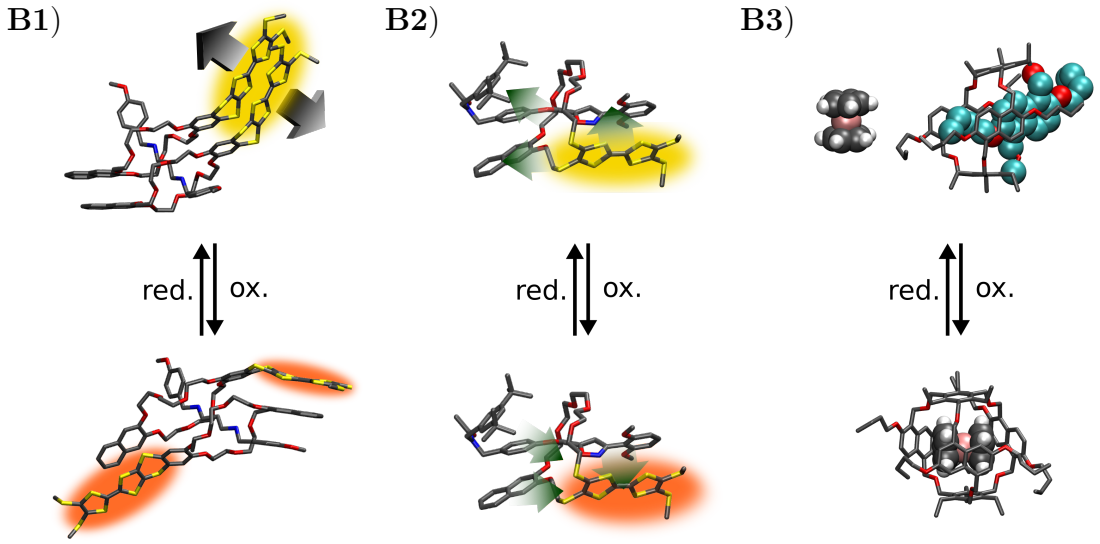

Figure 2.6: Supramolecular systems examined in this thesis: paper **B1** focuses on a [3]rotaxane able to perform a redox-switchable pirouetting motion of its macrocycles, paper **B2** rationalises the optical properties of a chiral [2]rotaxane which shows a redox-switchable ECD response, green arrows schematically represent the electron-flow in the system upon electronic excitations depending on the charge of the complex, paper **B3** investigates an extremely strong binder for singly charged organic and organometallic cations, the guestless host folds itself to yield a self-included complex with one of its naphthalene moieties (indicated by differently coloured van-der-Waals spheres).

While the first part of this thesis is concerned with the systematic investigation of organic compounds starting from single molecules *at the bottom* and working its way up to large clusters, the second part of this thesis aims at unravelling the intricacies of the thermodynamic and optical properties of large supramolecular aggregates *at the top*. To this end, three projects are presented featuring two redox-active rotaxanes and a molecular cage showcasing the versatility of supramolecular systems when implemented in photophysical or electrochemical experiments (**Fig. 2.6**). Paper **B1** is concerned with the redox-responsive intramolecular motion of two macrocycles in a [3]rotaxane ("[X]" referring to the number of interlocked components) containing the aforementioned TTF_2 motif. It is shown both experimentally and theoretically that co-conformational changes are induced by oxidation of the supramolecule which results in a switchable synchronised or counter-rotatory motion of the macrocycles depending on the charge state. In paper **B2** a chiral [2]rotaxane likewise equipped with a TTF unit is investigated. The supramolecular complex displays an intriguing chiroptical inversion of its main electronic circular dichroism (ECD) signal upon oxidation. This property is rationalised theoretically by reproducing the spectrum and analysing the nature of the involved electronic excitations. Finally, paper **B3** describes a molecular cage ("naphthocage") with an extremely high binding affinity towards singly charged organic and organometallic cations. The host-guest complex is switchable in CV measurements which is studied both experimentally and theoretically. Especially the nature of the interaction is addressed in theoretical terms.

3 Theory

The following pages describe the basic theories that constitute the foundation of this doctoral thesis. While it attempts to be as comprehensive as possible and serves as a solid basis to understand the implications of this work, this section is in no way meant to be exhaustive. For more thorough illustrations, derivations, and discussions please consult the literature that will be referenced at any appropriate point.

This part is divided into two major subsections. First, we will outline and discuss aspects of the electronic ground state. This involves building up a foundation starting from the time-dependent Schrödinger equation and discussing the most important features of Hartree-Fock (HF) and density functional theory (DFT). General concepts, such as the Born-Oppenheimer approximation (BOA) and the variational principle will be addressed. The DFT part focusses on density functional approximations (DFAs) and dispersive interactions.

A major aspect of this thesis related to electronic ground states of molecular aggregates is the evaluation of thermodynamic properties. Principle equations for association enthalpies, including thermal corrections and solvation effects, will be outlined and the calculation of redox potentials will be discussed.

Second, we will examine theories related to excited electronic states. The most important approach in this context is the time-dependent extension of DFT, TD-DFT. Most calculations make use of the linear-response formalism of TD-DFT also addressed in this part. A more involved theory concerned with the accurate treatment of excited electronic states is DFT/MRCI which combines the computational efficiency of DFT with the flexibility of the multi-reference configuration interaction approach. DFT/MRCI represents a means of accurately accounting for multi-excitation processes, which pose a severe challenge for linear-response single-reference TD-DFT methods. A few notes on the characterisation of excited states will be outlined.

Finally, a few practical aspects of calculating excited states are addressed, especially with regards to comparing experiment and theory. This involves discussion of the Franck-Condon principle, line broadening and the influence of solvent models on excited-state potential energy surfaces. Theoretical aspects concerning the interpretation of UV/Vis, electronic circular dichroism (ECD), and fluorescence spectra are given attention to. The final paragraphs of the theoretical section are about the concept of H- and J-aggregation which is extremely important in the context of studying supramolecular aggregates.

3.1 The electronic ground state

3.1.1 From Erwin Schrödinger to Clemens Roothaan

> Where did we get that from? It's not possible to derive it from anything you know. It came out of the mind of Schrödinger.
>
> – Richard Feynman about the Schrödinger equation[74]

Schrödinger's equation (SE)[75] undisputably represents one of the most fundamental relations in quantum mechanics,

$$\hat{H}\Phi(t) = i\hbar\frac{\partial}{\partial t}\Phi(t) \tag{3.1.1}$$

with $\hat{H}$ being a system's Hamiltonian and Φ its time-dependent many-body wavefunction, respectively. In quantum chemistry, we usually drop the time-dependence of the wavefunction and assume the Hamiltonian operator to only consist of time-independent terms. In this case, the time-dependent part of the SE is reduced to a simple phase factor and we are left with the time-independent SE

$$\hat{H}\Psi = E\Psi \tag{3.1.2}$$

with eigenvalue E being the system's energy associated with electronic state Ψ. For a molecular system containing M nuclei (n) and N electrons (e) we can write the electronic structure Hamiltonian in atomic units as

$$\begin{aligned}\hat{H} &= \hat{T}_\mathrm{e} + \hat{T}_\mathrm{n} + \hat{V}_\mathrm{ee} + \hat{V}_\mathrm{nn} + \hat{V}_\mathrm{en} \\ &= -\frac{1}{2}\sum_{i=1}^{N}\nabla_i^2 - \sum_{\alpha=1}^{M}\frac{1}{2m_\alpha}\nabla_\alpha^2 + \sum_{i=1}^{N}\sum_{j>i}^{N}\frac{1}{r_{ij}} + \sum_{\alpha=1}^{M}\sum_{\beta>\alpha}^{M}\frac{Z_\alpha Z_\beta}{R_{\alpha\beta}} - \sum_{i=1}^{N}\sum_{\alpha=1}^{M}\frac{Z_\alpha}{r_{i\alpha}}\end{aligned} \tag{3.1.3}$$

where we have used a short-hand notation for particle distances $r_{ij} = |\mathbf{r}_i - \mathbf{r}_j|$ and introduced expressions for the kinetic energies ($\hat{T}_\mathrm{e}$, $\hat{T}_\mathrm{n}$) and attractive ($\hat{V}_\mathrm{en}$) and repulsive ($\hat{V}_\mathrm{ee}$, $\hat{V}_\mathrm{nn}$) Coulomb interactions. Roman letters $i, j, ...$ refer to electrons, Greek letters $\alpha, \beta, ...$ to nuclei. m_α and Z_α are mass and charge of nucleus α. ∇_i^2 is the Laplacian of particle i. Throughout this section we will use atomic units if not stated otherwise.

Schrödinger's equation – even in its time-independent form – is notoriously difficult to solve. Exact solutions can only be found for extremely simple systems, such as the particle in a box, the harmonic oscillator, or the hydrogen atom. For the evaluation of large chemical systems, **Eq. (3.1.2)** is much too complicated and in desperate need of simplifications. A powerful concept is the Born-Oppenheimer approximation (BOA) which is based on the fact that nuclei are much heavier than electrons ($\approx 10^4 : 1$).[76] Within the first step of the BOA, nuclei are assumed to be static, which enables the decoupling of nuclear and electronic motion as $\hat{T}_\mathrm{n}$ is set to zero and $\hat{V}_\mathrm{nn}$

is simply treated as a constant. As a result, the electronic SE,

$$\hat{H}_{\mathrm{el}}\Psi_{\mathrm{el}}(\mathbf{r};\mathbf{R}) = E_{\mathrm{el}}\Psi_{\mathrm{el}}(\mathbf{r};\mathbf{R}) \tag{3.1.4}$$

contains the electronic wavefunction Ψ_{el} which treats the nuclear coordinates $\mathbf{R}$ only as parameters. In general, the BOA introduces extremely small errors. However, there are problematic situations, for example at conical intersections where the decoupling of electronic and nuclear motion can result in larger inaccuracies.[77] It should be noted that the BOA is the basis for the concept of potential energy surfaces (PESs), which may be obtained from static solutions of **Eq. (3.1.4)** by varying $\mathbf{R}$. Analysing PESs is essential in estimating thermodynamic properties of molecular systems which will be addressed in a later section.

Despite the simplifications made thus far, we are still far from being able to compute chemically relevant systems. A powerful tool in quantum chemistry is the mean-field approach which reduces a complicated n-particle problem to n much simpler 1-particle problems. This method hinges on the assumption that the many-body wavefunction Ψ_{el} can be expressed as a product of single-particle wavefunctions,

$$\Psi^{\mathrm{HP}} = \prod_i \psi_i. \tag{3.1.5}$$

Ψ^{HP} is the so-called Hartree product and ψ_i are eigenfunctions of a one-particle Hamiltonian,

$$\hat{h}_i\psi_i = \left(-\frac{1}{2}\nabla_i^2 - \sum_{\alpha=1}^{M}\frac{Z_\alpha}{r_{i\alpha}}\right)\phi_i = \varepsilon_i\psi_i \tag{3.1.6}$$

commonly referred to as *orbitals* with orbital energy ε_i as eigenvalue. Let us examine Ψ^{HP} a little closer. The product ansatz in **Eq. (3.1.5)** suggests that the orbitals are all uncorrelated. This is obviously not the case as they represent the motion of negatively charged electrons in a chemical system. Until now we have neglected a fundamental property of the electron – its spin. Since electrons are fermions, we need to impose Pauli's exclusion principle[78] on Ψ_{el} to obtain a physically meaningful quantity. This requires the wavefunction to be antisymmetric with respect to the exchange of two electrons, also known as Fermi correlation. While this is not the case for Ψ^{HP}, a mathematical object that fulfills this condition is a so-called Slater determinant,[79,80]

$$\begin{aligned}\Psi_{\mathrm{el}} = \Psi^{\mathrm{SD}}(\mathbf{x}_1,\mathbf{x}_2,...,\mathbf{x}_N) &= \frac{1}{\sqrt{N!}}\begin{vmatrix}\chi_1(\mathbf{x}_1) & \chi_1(\mathbf{x}_2) & \cdots & \chi_1(\mathbf{x}_N)\\ \chi_2(\mathbf{x}_1) & \chi_2(\mathbf{x}_2) & \cdots & \chi_2(\mathbf{x}_N)\\ \vdots & \vdots & \ddots & \vdots\\ \chi_N(\mathbf{x}_1) & \chi_N(\mathbf{x}_2) & \cdots & \chi_N(\mathbf{x}_N)\end{vmatrix}\\ &= |\chi_1\chi_2\cdots\chi_N\rangle\end{aligned} \tag{3.1.7}$$

where we have introduced the spin-orbitals χ comprised of a spatial function and a spin part and the collective variable $\mathbf{x}$ containing both the electron's spatial and spin coordinates,

$$\chi(\mathbf{x}) = \psi(\mathbf{r})\sigma(\mathbf{s}). \tag{3.1.8}$$

In calculations, $\chi_i(\mathbf{x}_i)$ are usually constructed to be orthonormal. A common way to abbreviate Ψ^{SD} is by its representation in Dirac ket-notation.

Before we can finally come up with a solution to **Eq. (3.1.4)**, we need to introduce another basic concept in quantum mechanics: the variational principle. If the eigenfunctions of a system's Hamiltonian span a complete orthonormal set, it states that any trial wavefunction Ψ_{tr} provides an upper bound to the true electronic ground-state energy E_0,

$$E_{\mathrm{tr}} = \frac{\left\langle \Psi_{\mathrm{tr}} \middle| \hat{H} \middle| \Psi_{\mathrm{tr}} \right\rangle}{\langle \Psi_{\mathrm{tr}} | \Psi_{\mathrm{tr}} \rangle} \geq E_0, \tag{3.1.9}$$

written in bra-ket notation to represent the integrals. In order to arrive at an optimal solution, we may thus vary Ψ_{tr}, e.g., by changing the orbitals, until the energy is minimised. By inserting Ψ^{SD} into **Eq. (3.1.4)** and applying the variational principle according to the Rayleigh-Ritz method, one arrives at the Hartree-Fock equations,[79,81,82]

$$f(\mathbf{x}_1)\chi_p(\mathbf{x}_1) = \left(\hat{h}_1 + v^{\mathrm{HF}}(\mathbf{x}_1)\right)\chi_p(\mathbf{x}_1) = \varepsilon_p \chi_p(\mathbf{x}_1), \tag{3.1.10}$$

with $p, q, \ldots$ counting the orbitals, Fock operator f containing the one-particle Hamiltonian $\hat{h}$, and an effective potential v^{HF} which can be written as

$$v^{\mathrm{HF}}(\mathbf{x}_1)\chi_p(\mathbf{x}_1) = \sum_{q=1}^{N} \left(\hat{J}_q(\mathbf{x}_1) - \hat{K}_q(\mathbf{x}_1)\right)\chi_p(\mathbf{x}_1). \tag{3.1.11}$$

$\hat{J}$ and $\hat{K}$ are the Coulomb and exchange operators, respectively. In matrix form, they are defined as

$$J_{pq} = \iint \chi_p^*(\mathbf{x}_1)\chi_q^*(\mathbf{x}_2)\frac{1}{r_{12}}\chi_p(\mathbf{x}_1)\chi_q(\mathbf{x}_2)\,\mathrm{d}\mathbf{x}_1\,\mathrm{d}\mathbf{x}_2 = \langle pq|pq\rangle \tag{3.1.12}$$

$$K_{pq} = \iint \chi_p^*(\mathbf{x}_1)\chi_q^*(\mathbf{x}_2)\frac{1}{r_{12}}\chi_q(\mathbf{x}_1)\chi_p(\mathbf{x}_2)\,\mathrm{d}\mathbf{x}_1\,\mathrm{d}\mathbf{x}_2 = \langle pq|qp\rangle\,, \tag{3.1.13}$$

where we have used another short-hand notation for two-electron integrals. $\hat{J}$ is a local operator whose matrix elements J_{pq} can be classically interpreted as the Coulomb interaction between an electron in orbital p with an electron in orbital q. On the other hand, $\hat{K}$ is a non-local operator without a classical analogue and basically originates from the antisymmetry property of the wavefunction. An advantage of Hartree-Fock theory is that unphysical self-interaction ($p = q$) cancels in **Eq. (3.1.11)**, which poses a severe problem in density functional theory methods. Each spin orbital in **Eq. (3.1.10)** occupied with an electron is thus constructed by considering the average field of the other $N - 1$ electrons. This has an interesting consequence for the virtual orbitals. Since the sum in **Eq. (3.1.11)** runs over all occupied spin orbitals, all unoccupied orbitals are constructed using the average field of all N electrons. One might thus argue that in Hartree-Fock theory, virtual orbitals formally correspond to an $N + 1$-wavefunction. We will make use of this idea later on.

The total energy at the Hartree-Fock level can be expressed as

$$E^{\mathrm{HF}} = \sum_{p=1}^{N} \varepsilon_p - \frac{1}{2} \sum_{p,q=1}^{N} \left(J_{pq} - K_{pq} \right). \tag{3.1.14}$$

The factor 1/2 is introduced to avoid double counting of electron-electron interaction. Note that the Hartree-Fock energy is *not* simply the sum of the eigenvalues of the Fock operator. Furthermore, **Eq. (3.1.12)** and **Eq. (3.1.13)** require integration over spin components ($\mathrm{d}\mathbf{x} = \mathrm{d}\mathbf{r}\mathrm{d}\mathbf{s}$). As can be easily shown, this results in vanishing matrix elements for $\hat{K}$ with electrons of different spin. As a consequence, every other exchange contribution can be omitted in **Eq. (3.1.14)** yielding a spin-free total energy,

$$E^{\mathrm{HF}} = 2 \sum_{p=1}^{N/2} \varepsilon_p - \sum_{p,q=1}^{N/2} \left(J_{pq} - \frac{1}{2} K_{pq} \right). \tag{3.1.15}$$

A major disadvantage of the Hartree-Fock approach, however, is that as an integro-differential equation it is rather difficult to solve and its implementation in quantum-chemical computer programmes is quite involved.[83,84] It is, hence, much more useful to reformulate **Eq. (3.1.10)** using an expansion of the spatial orbitals in a finite set of L basis functions. Within the MO-LCAO (molecular orbital – linear combination of atomic orbitals) framework, the spatial orbitals ψ are referred to as MOs, while basis functions τ are atom-centred hydrogen-like orbitals, or AOs for short,

$$\psi_p(\mathbf{r}) = \sum_{\mu=1}^{L} c_{\mu p} \tau_\mu(\mathbf{r}) \tag{3.1.16}$$

with AO coefficients $c_{\mu p}$. Recasting **Eq. (3.1.10)** into matrix form using **Eq. (3.1.16)** yields the Roothaan-Hall equations,[85,86]

$$\mathbf{FC} = \mathbf{SC}\boldsymbol{\varepsilon} \tag{3.1.17}$$

with an element of the Fock matrix $\mathbf{F}$ defined as $F_{\mu\nu} = \langle \tau_\mu | \hat{f} | \tau_\nu \rangle$, AO coefficient matrix $\mathbf{C}$, and diagonal matrix $\boldsymbol{\varepsilon}$ containing the MO eigenvalues. Since atom-centred orbitals in a system with more than one atom are not orthogonal anymore, an overlap matrix $\mathbf{S}$ with elements $S_{\mu\nu} = \langle \tau_\mu | \tau_\nu \rangle$ emerges. Consequently, **Eq. (3.1.17)** is evaluated by employing a unitary transformation $\mathbf{U}$ to obtain an orthonormal subset within the space of the original basis functions $\boldsymbol{\tau}$, which yields

$$\mathbf{S}' = \mathbf{U}^\dagger \mathbf{S} \mathbf{U} = \mathbf{1} \tag{3.1.18}$$

$$\Rightarrow \mathbf{F}'\mathbf{C}' = \mathbf{C}'\boldsymbol{\varepsilon}. \tag{3.1.19}$$

An important thing to note is that both $\mathbf{F}$' and $\mathbf{C}$' depend on the expansion coefficients of the orbitals. Solving **Eq. (3.1.19)** thus requires an initial guess of start orbitals and an iterative procedure which is referred to as the self-consistent field (SCF) method.
In practice, the HF method does not provide very accurate results.[87] This is in part due to the fact that it is based on a single Slater determinant, which neglects electron correlation derived

from instantaneous electron-electron Coulomb interaction. However, due to its straight-forward derivation from first principles, Hartree-Fock theory represents the foundation for a plethora of much more sophisticated approaches collectively termed post-HF methods. Examples include other single-reference methods such as second-order Møller-Plesset perturbation theory (MP2)[88] or coupled-cluster (CC) theory[89] or multi-reference approaches like the multi-configurational self-consistent field (MCSCF) method[90] or multi-reference configuration-interaction (MRCI).[91] The latter will be discussed in a little more detail in a later section. In this way, the shortcoming of the HF equations to capture electron correlation, can be systematically compensated for. A major disadvantage of all wavefunction-based methods, however, is their unfavourable scaling with respect to system size. MP2, for example, has a formal scaling of $O(N^5)$,[92] where N is the number of basis functions, which quickly exceeds the limits of most computational clusters for large chemical systems.

3.1.1.1 Basis sets and periodic calculations

Basis sets are a fundamental concept and especially relevant for the implementation of quantum-chemical computer programmes. Within the aforementioned LCAO framework, MOs are represented by a sum over AOs. An accurate description of an AO would be a Slater-type orbital (STO, $\tau \propto \mathrm{e}^{-r}$), as directly obtained from the time-independent Schrödinger equation by solving the problem of the hydrogen atom. For actual molecular calculations, however, Gaussian-type orbitals (GTOs, $\tau \propto \mathrm{e}^{-r^2}$) are employed to approximate STOs. This has the massive advantage that the ensuing integrals can be solved analytically. Furthermore, Gaussian functions possess the fortunate property that two Gaussians $g_\mathrm{A}(\mathbf{r})$ and $g_\mathrm{B}(\mathbf{r})$ centred on $\mathbf{A}$ and $\mathbf{B}$, respectively, can always be expressed by a single Gaussian owing to the Gaussian product rule.[93] Using $r_\mathrm{A} = |\mathbf{r} - \mathbf{A}|$ and $r_\mathrm{B} = |\mathbf{r} - \mathbf{B}|$, it is

$$g_\mathrm{A}(\mathbf{r})g_\mathrm{B}(\mathbf{r}) \equiv \exp(-\alpha r_\mathrm{A}^2)\exp(-\beta r_\mathrm{B}^2) = \exp\left[-\frac{\alpha\beta}{\alpha+\beta}(\mathbf{B}-\mathbf{A})^2\right]\exp\left[-(\alpha+\beta)r_C^2\right], \qquad (3.1.20)$$

with $r_\mathrm{C} \equiv |\mathbf{r} - \mathbf{C}|$ and $\mathbf{C} = (\alpha\mathbf{A} + \beta\mathbf{B})/(\alpha + \beta)$. The systematic improvability of GTO basis sets is based on the amount of functions that are included in a quantum-chemical calculation. A minimal basis set, such as STO-3G, requires only the minimal amount of AOs to be included. A carbon atom calculated in a minimal basis, for example, is only described by a 1s-, a 2s-, and the three 2p-orbitals using five so-called contracted Gaussians in total. Obviously, minimal basis sets offer to little variational flexibility during the optimisation of the basis set coefficients, so that larger basis sets usually employing a split-valence approach are used in practice. These are conventionally categorised by the number ζ of contracted Gaussians used to treat the valence shell of an atom. Structure optimisations are often performed using a smaller double-ζ basis set, while energy and property calculations are frequently conducted employing a high-level triple-, quadruple, or even quintuple-ζ basis set. Especially, wavefunction-based approaches require larger basis sets until convergence is reached. Smaller basis sets are more susceptible to the so-called basis set superposition error (BSSE) which causes an artificial lowering of the total energy of a molecular complex (e.g., a dimer) with respect to its components (e.g., two monomers). In density functional theory based methods, however, BSSE is often negligible as convergence is usually reached already at the triple-ζ level.

Importantly, GTOs are not the only type of basis functions used in computational chemistry. In periodic systems, GTOs are less frequently applied since they are rather prone to numerical instabilities due to their non-orthogonal set-up.[94] Instead, the spatial part u_j of periodic orbital $\psi_{j\mathbf{k}}$ is expressed by plane waves according to[95]

$$u_j(\mathbf{r}) = \sum_{\mathbf{G}} c_{j\mathbf{G}} \mathrm{e}^{i\mathbf{G}\mathbf{r}}, \tag{3.1.21}$$

with reciprocal lattice vectors $\mathbf{G}$ and expansion coefficients $c_{j\mathbf{G}}$. The basis set size is determined by an energy cut-off. Note that **Eq. (3.1.21)** is nothing else than a Fourier series expansion of u_j in reciprocal (or k-) space. By Bloch's theorem,[96] which states that the eigenstates of a periodic system must be invariant under translation along the lattice vectors, single-particle wavefunctions $\psi_{j\mathbf{k}}$ can be written as the product of u_j and a plane wave,

$$\psi_{j\mathbf{k}}(\mathbf{r}) = \mathrm{e}^{i\mathbf{k}\mathbf{r}} u_j(\mathbf{r}). \tag{3.1.22}$$

Combining **Eq. (3.1.21)** and **Eq. (3.1.22)** yields

$$\psi_{j\mathbf{k}}(\mathbf{r}) = \sum_{\mathbf{G}} c_{j\mathbf{G}} \mathrm{e}^{i(\mathbf{k}+\mathbf{G})\mathbf{r}}, \tag{3.1.23}$$

which can be used in the construction of bandstructures by sampling over all k-points. Solid-state DADQ compounds in paper **A3** required an initial assessment of their crystal structures using the plane-wave approach as implemented in VASP.[97–99]

3.1.2 Density functional theory

From a quantum-chemical point of view, a chemical system's molecular wavefunction Ψ is its most valuable feature, although it does not have a physical interpretation. Moreover, mathematically it is a fairly complicated quantity consisting of $4N$ electronic (Cartesian and spin) and $3M$ nuclear coordinates. This had already been realised at the end of the 1920s, when Llewellyn Thomas[100] and Enrico Fermi[101] proposed models to calculate atomic properties based on a (spin-free) electron density ρ, which can be derived from Ψ using

$$\rho(\mathbf{r}) = N \int \mathrm{d}\mathbf{r}_2 \cdots \int \mathrm{d}\mathbf{r}_N \Psi^*(\mathbf{r}_1, \mathbf{r}_2, ..., \mathbf{r}_N)\Psi(\mathbf{r}_1, \mathbf{r}_2, ..., \mathbf{r}_N) \tag{3.1.24}$$

Depending only on its three Cartesian coordinates, ρ is by far a much simpler quantity than Ψ. However, satisfactory results cannot be obtained from the Thomas-Fermi model. In fact, it can be shown, that it cannot account for chemical bonding in a molecule[1] the major problem being an inadequate description of the kinetic energy. 40 years passed before Pierre Hohenberg and Walter Kohn (HK) finally presented their famous theorems[102] and set the stage for density functional theory (DFT). The first HK theorem states that a quantum-mechanical system's ground state electron density ρ_0 uniquely determines its external potential v_{ext}, which in turn defines its Hamilton operator from which any ground-state property of interest can be derived,

$$\rho_0 \rightarrow v_{ext} \rightarrow \hat{H} \rightarrow ... \tag{3.1.25}$$

The validity of the first HK theorem can be rationalised by two surprisingly simple facts: To set up a Hamiltonian, we need to know the number of electrons in the system and the positions of the nuclei. Integration of the density precisely returns the number of electrons,

$$\int \rho(\mathbf{r})\mathrm{d}\mathbf{r} = N \tag{3.1.26}$$

while the nuclear cusp condition[103] directly yields the positions of the nuclei,

$$\frac{\partial}{\partial r_\alpha}\,\bar{\rho}(r_\alpha)|_{r_\alpha=0} = -2Z_\alpha\bar{\rho}(0), \tag{3.1.27}$$

where $\bar{\rho}(r_\alpha)$ is the spherical average of $\rho(\mathbf{r})$. As a result of the first HK theorem, we can write down the ground-state energy of a system as a functional of ρ_0,

$$E_0[\rho_0] = T_\mathrm{e}[\rho_0] + V_\mathrm{ee}[\rho_0] + \int v_\mathrm{ext}\rho_0(\mathbf{r})\mathrm{d}\mathbf{r} + V_\mathrm{nn} \tag{3.1.28}$$

v_ext is the external potential containing the electron-nuclei attraction term and other possible system-specific terms. Within the BOA, V_{nn} is not a functional of ρ as it is still treated as a constant. The second HK theorem proves the existence of a variational principle for DFT in accordance with **Eq. (3.1.9)**. Still, adequately describing kinetic energies remained a challenge. To circumvent this problem, Walter Kohn and Lu Jeu Sham (KS) introduced a fictitious system of non-interacting particles moving in an effective potential v_KS constructed in such a way that its electron density ρ_S mimics that of the true system,[104]

$$\rho_S = \sum_{i\,\in\,\mathrm{occ}} |\varphi_i|^2 = \rho_0. \tag{3.1.29}$$

The KS orbitals φ and energies ε are eigenfunctions and eigenvalues of the KS operator $\hat{f}^\mathrm{KS}$, which bares a striking resemblance to the HF operator $\hat{f}^\mathrm{HF}$ of **Eq. (3.1.10)**,

$$\hat{f}^\mathrm{KS}(\mathbf{r}_i)\varphi_p(\mathbf{r}_i) = \left[-\frac{1}{2}\nabla_i^2 + v_\mathrm{KS}(\mathbf{r}_i)\right]\varphi_p(\mathbf{r}_i) = \varepsilon_p\varphi_p(\mathbf{r}_i), \tag{3.1.30}$$

with the important difference being that **Eq. (3.1.30)** is, in principle, an exact representation of the many-body problem. Within KS-DFT, the energy of a system can be expressed as a functional of the electron density according to

$$E_0[\rho] = T_\mathrm{S}[\rho] + J[\rho] + v_\mathrm{ext}[\rho] + E_\mathrm{XC}[\rho]. \tag{3.1.31}$$

The kinetic energy of the non-interacting system $T_\mathrm{S}[\rho_0]$ is readily obtained from the KS orbitals,

$$T_\mathrm{S}[\rho] = -\frac{1}{2}\sum_{i\,\epsilon\,\mathrm{occ}} \left\langle \varphi_i \left| \nabla_i^2 \right| \varphi_i \right\rangle \tag{3.1.32}$$

and $J[\rho]$ is the classical Coulomb repulsion integral, also known as Hartree potential, defined as

$$J[\rho] = \frac{1}{2}\iint \frac{\rho(\mathbf{r}_1)\rho(\mathbf{r}_2)}{r_{12}}\mathrm{d}\mathbf{r}_1\mathrm{d}\mathbf{r}_2. \tag{3.1.33}$$

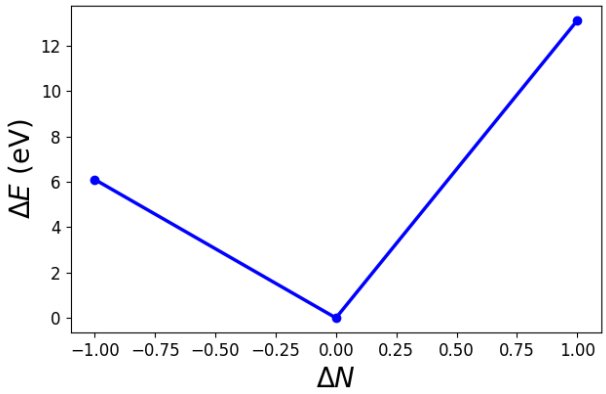

Figure 3.1: Change in total energy of an infinitely separated Li + H pair, with ΔN being the number of electrons transferred from H to Li, calculated at the PBE/def2-SVP[105,106] level of DFT.

The most important part, however, is the exchange-correlation (XC) energy functional $E_{\mathrm{XC}}[\rho]$ which basically absorbs all aspects of the electronic structure problem not covered by the other terms. $E_{\mathrm{XC}}[\rho]$ can be written as

$$E_{\mathrm{XC}}[\rho] = (T_{\mathrm{e}}[\rho] - T_{\mathrm{S}}[\rho]) + (V_{\mathrm{ee}}[\rho] - J[\rho]) = T_{\mathrm{e,corr}} + V_{\mathrm{ee,corr}}, \tag{3.1.34}$$

where the correction terms $T_{\mathrm{e,corr}}$ and $V_{\mathrm{ee,corr}}$ correspond to the differences between the non-interacting KS system and the real system. $E_{\mathrm{XC}}[\rho]$ is implicitly contained in the effective potential v_{KS} of **Eq. (3.1.30)**,

$$v_{\mathrm{KS}}(\mathbf{r}_i) = \int \frac{\rho(\mathbf{r}_j)}{r_{ij}} \mathrm{d}\mathbf{r}_j + v_{\mathrm{ext}}(\mathbf{r}_i) + \frac{\delta E_{\mathrm{XC}}[\rho]}{\delta \rho(\mathbf{r}_i)} \tag{3.1.35}$$

$$= \int \frac{\rho(\mathbf{r}_j)}{r_{ij}} \mathrm{d}\mathbf{r}_j + v_{\mathrm{ext}}(\mathbf{r}_i) + v_{\mathrm{XC}}[\rho](\mathbf{r}_i), \tag{3.1.36}$$

where we have introduced the XC potential v_{XC}.
As an interesting side note, John Perdew et al.[107] showed that, if KS-DFT is extended to fractional occupation numbers $N \pm f$ with $0 < f < 1$, the total energy of a molecular system plotted against the number of electrons displays derivative discontinuities at integral values. The slopes of the lines connecting each integer define the ionisation potential IP and electron affinity EA, (**Fig. 3.1**)

$$\left.\frac{\partial E}{\partial N}\right|_{N-f} = IP \qquad \left.\frac{\partial E}{\partial N}\right|_{N+f} = EA. \tag{3.1.37}$$

This observation is also known as integer discontinuity. An XC functional that satisfies these conditions for $N > 1$ is called N-electron self-interaction free.[108]

3.1.2.1 Density functional approximations

$E_{\mathrm{XC}}[\rho]$ is the key ingredient to obtaining an accurate description of the electronic structure of a chemical system in KS-DFT. Unfortunately, finding an exact expression for $E_{\mathrm{XC}}[\rho]$ is close to impossible as inserting the exact XC functional into the KS equations is equivalent to exactly solving the Schrödinger equation.[103] In spite of this, the last decades have seen a tremendous amount of

research conducted to examine E_{XC} and a myriad of density functional approximations (DFAs) have been proposed.[1,103,109,110] A lot of DFAs are specifically tailored to accurately reproduce molecular properties obtained from experiment or high-level wavefunction-based calculations.
The functional one chooses to calculate properties of a specific system is crucial. Conventionally, DFAs are categorised according to "Jacob's ladder", a biblical simile proposed by John Perdew to illustrate how involved a certain functional is.[111] The first three rungs of Jacob's ladder effectively correspond to a Taylor expansion of ρ,

$$E_{\mathrm{XC}}[\rho] = \int f(\rho, \nabla\rho, \nabla^2\rho)\mathrm{d}\mathbf{r}, \tag{3.1.38}$$

where $E_{\mathrm{XC}}[\rho]$ is usually approximated by treating the system as a homogeneous electron gas. Spin dependence is omitted for simplicity. Methods that only take into account ρ itself are called local density approximations (LDAs). Since typical molecular systems are far from homogeneous, LDAs often perform very poorly for them, usually resulting in overbinding.[112] On the other hand, for periodic systems such as metals, LDAs may show satisfactory results. Adding the gradient of the density $\nabla\rho$ yields the generalised gradient approximation (GGA) which is in general a significant improvement over LDAs. The most popular GGA-based DFA is called PBE due to John Perdew, Kieron Burke, and Matthias Ernzerhof.[105] PBE is the most widely used functional for periodic calculations, but also yields accurate molecular properties for inhomogeneous organic systems.[113]
For the next rung, the meta-GGA (mGGA) functionals, the laplacian of the density $\nabla^2\rho$ is usually replaced by the kinetic energy density,

$$\tau(\mathbf{r}) = \sum_{i \in \mathrm{occ}} \frac{1}{2}|\nabla\varphi_i(\mathbf{r})|^2. \tag{3.1.39}$$

TPSS[114] (Tao, Perdew, Staroverov, and Scuseria) is an example for a mGGA functional yielding satisfactory results for structures and energies while being computationally feasible.[115,116] Probably the most popular third-rung DFAs, however, are the Minnesota family of functionals devised by Donald Truhlar and co-workers.[117] Their algebraic forms are quite involved and consist of a range of parameters fitted to large physico-chemical databases. Most Minnesota functionals are constructed in a way to reproduce very specific properties, e.g., reaction barriers, non-covalent interactions, or even excitation energies. Thorough reviews of their performance can be found in the literature.[118–120] One major advantage of the Minnesota functionals is their inherent treatment of dispersive interactions due to specific parametrisation.[120] The lack of a proper description of dispersion forces poses a serious problem to most DFAs when non-covalently bound complexes are concerned. The topic of dispersion forces in DFT deserves some more attention and will be addressed further down below.
A problem with DFAs up until here is that the Coulomb term (**Eq. (3.1.33)**) does not have an exchange counterpart that compensates for double-counting of electron-electron interaction and, thus, introduces self-interaction error. As a countermeasure, at the fourth rung of Jacob's ladder

we introduce non-local Hartree-Fock exchange (*cf.* **Eq. (3.1.13)**) in E_{XC} through

$$E_{\mathrm{X}}^{\mathrm{HF}} = -\frac{1}{2}\sum_{p,q}\iint \varphi_p^*(\mathbf{r}_1)\varphi_q(\mathbf{r}_1)\frac{1}{r_{12}}\varphi_q^*(\mathbf{r}_2)\varphi_p(\mathbf{r}_2)\mathrm{d}\mathbf{r}_1\mathrm{d}\mathbf{r}_2. \tag{3.1.40}$$

$$= -\frac{1}{2}\sum_{p,q}(pq|qp) \tag{3.1.41}$$

which reduces self-interaction in the calculations. In **Eq. (3.1.41)** we have used Mulliken's notation for two-electron integrals, in general defined as

$$\iint \varphi_p^*(\mathbf{r}_1)\varphi_q(\mathbf{r}_1)\frac{1}{r_{12}}\varphi_r^*(\mathbf{r}_2)\varphi_s(\mathbf{r}_2)\mathrm{d}\mathbf{r}_1\mathrm{d}\mathbf{r}_2 = (pq|rs)\,. \tag{3.1.42}$$

In this way, so-called hybrid functionals (hGGA) are constructed. Typically, some amount a_{X} of $E_{\mathrm{X}}^{\mathrm{HF}}$ is incorporated into GGAs or mGGAs through mixing of the exchange parts,

$$E_{\mathrm{XC}}^{\mathrm{hGGA}} = a_{\mathrm{X}}E_{\mathrm{X}}^{\mathrm{HF}} + (1-a_{\mathrm{X}})E_{\mathrm{X}}^{\mathrm{GGA}} + E_{\mathrm{C}}^{\mathrm{GGA}}. \tag{3.1.43}$$

It is noteworthy that in standard implementations of hybrid DFT, the energy is minimised with respect to orbitals. Strictly speaking, this is not KS theory, which requires the energy to be minimised with respect to the density. Optimised effective potentials can be used to surround this.[121,122] Originally, hGGAs were derived in an adiabatic-connection formalism interpolating between the non-interacting KS system and the real one.[1] The first DFA obtained in this way was Becke's "half-and-half" functional, BHLYP, that incorporates exactly 50% HF exchange.[123] While we could technically set a_{X} to 100% and get rid of self-interaction entirely, mixing HF exchange into a DFA has also drawbacks. Obviously, HF exchange introduces static electron correlation error for systems with multi-referential character.[124] More importantly, however, calculating $E_{\mathrm{X}}^{\mathrm{HF}}$ is quite resource-demanding. For GGAs and mGGAs, the computational bottleneck is usually the evaluation of the Coulomb integral (**Eq. (3.1.33)**), which can be efficiently approximated in a straight-forward manner by density-fitting approaches.[125] For hybrid DFAs, on the other hand, calculating $E_{\mathrm{X}}^{\mathrm{HF}}$ becomes the new bottleneck while **Eq. (3.1.41)** cannot be approximated in a straight-forward manner. More sophisticated approximations such as RIJCOSX[126] proposed by Frank Neese and co-workers are necessary if one wants to reduce computing time.

Note that the separation of E_{XC} in **Eq. (3.1.43)** into an exchange part X and a correlation part C is purely artificial. While in wavefunction-based theories a clear distinction can be made between electron exchange and correlation, in DFT the two are deeply intertwined. Most often, the amount of HF exchange is deduced from fitting to experimental values. Examples include most Minnesota functionals[127] or the popular B3LYP functional.[128] However, it is also possible to algebraically rationalise the parameter a_{X}. Perdew *et al.* proposed a perturbation theoretical ansatz for PBE0[129] and argued that 1/4 of HF exchange mixed into PBE should yield an accurate hGGA functional. Indeed, PBE0 performs decently in many cases, especially for organic molecules.[130–132]

While hybrid DFAs are a notable improvement over most GGAs and mGGAs, there are still deficiencies that arise from the overall local description of the density (even though some non-locality is introduced by $E_{\mathrm{X}}^{\mathrm{HF}}$). Because of the exponential decay of ρ, long-range interactions cannot be well reproduced with local DFAs. The most prominent two examples are charge-transfer (CT) states

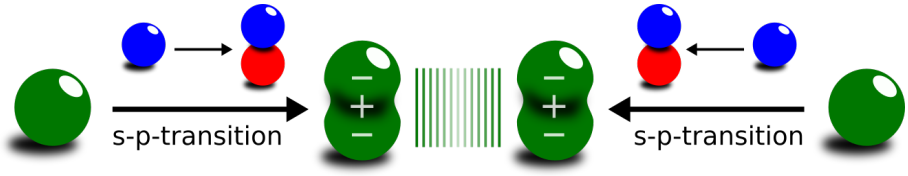

Figure 3.2: Schematic visualisation of two interacting charge distributions in an otherwise non-interacting spherically-shaped molecular system induced by a spontaneous fluctuation in the electronic structure (here, an s-p-transition).

and London dispersion forces.[1] Both show a polynomial dependence on interfragment distance with r^{-1} for pure CT states and r^{-6} for dispersion in the long-range limit. While treating CT states is a topic that is better addressed when talking about excited states, dispersive interactions will be discussed in the following.

3.1.2.2 Dispersive interactions

The terms "Dispersion" and "van-der-Waals" (vdW) interactions are commonly used interchangeably in the literature, although dispersion, or London dispersion forces, only refers to the mutual coupling of two temporary multipoles, while vdW interactions are more general.[133,134] In its simplest form, dispersion can be described by interacting transition dipoles. Picture, for example, two rare gas atoms with a spherical distribution of their electronic charge clouds (**Fig. 3.2**). Obviously neutral monopoles in and of themselves do not show any kind of electrostatic interaction. However, a spontaneous electronic transition of an electron, e.g., from an s- into a p-orbital, immediately distorts the spherical charge distribution inducing a temporary dipole moment, which results in brief electrostatic interactions between the atoms. Mathematically, London dispersion forces can be obtained from the asymptotic limit of the MP2 correlation energy,[133]

$$E_{\text{corr}}^{\text{MP2}} = -\frac{1}{4}\sum_{i,j}^{N_{\text{occ}}}\sum_{a,b}^{N_{\text{virt}}}\frac{[(ia|jb)-(ib|ja)]^2}{\omega_{ai}+\omega_{bj}} \tag{3.1.44}$$

$$\lim_{R_{\text{AB}}\to\infty} E_{\text{corr}}^{\text{PT2}} = E_{\text{disp}}^{\text{AB}} = -\sum_{i,a\in A}\sum_{j,b\in B}\frac{(ia|jb)^2}{\omega_{ai}+\omega_{bj}} \tag{3.1.45}$$

where $i,j,...$ run over all occupied and $a,b,...$ over all virtual orbitals and $\omega_{ai} = \varepsilon_a - \varepsilon_i$. AB may for instance be a simple dimer. In the limit ($R_{\text{AB}} \to \infty$) the exchange integral $(ib|ja)$ vanishes as transitions become localised on each fragment. As a result, the Coulomb term $(ia|jb)$ remains, which can be expanded into multipoles, where the third expansion term (the dipole-dipole interaction) is the first one that contributes, as both the monopole-monopole and the monopole-dipole interaction vanish for neutral atoms. If higher-order contributions are neglected, it can be shown that[133]

$$E_{\text{disp}}^{\text{AB}} \approx -\sum_{i,a\in A}\sum_{j,b\in B}\frac{1}{\omega_{ai}+\omega_{bj}}\left(\frac{\boldsymbol{\mu}_{ia}\boldsymbol{\mu}_{jb}-3(\boldsymbol{\mu}_{ia}\mathbf{e}_R)(\boldsymbol{\mu}_{jb}\mathbf{e}_R)}{R^3}\right)^2 \tag{3.1.46}$$

$$E_{\text{disp}}^{(6)} = -\frac{3}{2}\sum_{i,a\in A}\sum_{j,b\in B}\frac{1}{\omega_{ai}+\omega_{bj}}\frac{|\mu_{ia}|^2|\mu_{jb}|^2}{R^6} \tag{3.1.47}$$

with transition dipoles $\boldsymbol{\mu}$ and vector $\mathbf{e}_R$ connecting the two fragments. The last equation is obtained by spherically averaging over all possible orientations of $\boldsymbol{\mu}$ and reveals the well-known R^{-6} long-range behaviour of London dispersion interactions. In a next step, we use the following integral identity to rewrite **Eq. (3.1.47)**,[135]

$$\frac{1}{\omega_{ai}+\omega_{bj}} = \frac{2}{\pi}\int_0^\infty \frac{\omega_{ai}\omega_{bj}}{[\omega_{ai}^2+\omega^2][\omega_{bj}^2+\omega^2]}\mathrm{d}\omega \tag{3.1.48}$$

from which follows

$$E_{\mathrm{disp}}^{(6)} = -\frac{3}{\pi R^6}\int_0^\infty \left[\sum_{i,a\in A}\frac{\omega_{ai}|\mu_{ia}|^2}{\omega_{ai}^2+\omega^2}\right]\left[\sum_{j,b\in B}\frac{\omega_{bj}|\mu_{bj}|^2}{\omega_{bj}^2+\omega^2}\right]\mathrm{d}\omega. \tag{3.1.49}$$

The expressions in square brackets are exactly linked to dynamic polarisabilities $\alpha(i\omega)$ at imaginary frequency ω, which results in the Casimir-Polder equation for the C_6 dispersion coefficients when setting $\omega^2 = -(i\omega)^2$,

$$E_{\mathrm{disp}}^{(6)} = -\frac{3}{\pi R^6}\int_0^\infty \alpha_A(i\omega)\alpha_B(i\omega)\mathrm{d}\omega = -\frac{C_6^{\mathrm{AB}}}{R^6}. \tag{3.1.50}$$

A common way to improve upon the shortcoming of conventional DFAs to describe dispersion forces is to find an accurate approximation to the C_6 coefficients of **Eq. (3.1.50)**.[133,134] Due to its algebraic form which allows for an easy implementation, the most widely applied dispersion correction scheme is Stefan Grimme's DFT-D approach.[136] The third generation, DFT-D3, incorporates two- ($E^{(2)}$) and three-body terms ($E^{(3)}$) to correct the KS energy,[137]

$$\begin{aligned} E^{\mathrm{D3}} &= E^{\mathrm{KS}} - E^{\mathrm{disp}} \\ &= E^{\mathrm{KS}} - (E^{(2)} + E^{(3)}). \end{aligned} \tag{3.1.51}$$

Notably, the current flavour, DFT-D4, does not improve upon DFT-D3 for organic molecules as it was created to enhance the description of transition metal complexes and provide a balanced overall scheme.[138] $E^{(2)}$ is given by

$$E^{(2)} = \frac{1}{2}\sum_{\mathrm{A}\neq\mathrm{B}}\sum_{n=6,8,\ldots} s_n \frac{C_n^{\mathrm{AB}}}{R_{\mathrm{AB}}^n} f_{\mathrm{damp}}(R_{\mathrm{AB}}) \tag{3.1.52}$$

and covers all pairwise interactions. s_n is a global scaling factor. Coefficients beyond C_8 are usually not included as they prove to be quite difficult to assess and contribute rather insignificantly.[137] In DFT-D3, C_6 coefficients are obtained from time-dependent DFT (TD-DFT) calculations of atomic polarisabilities inserted in a modified version of **Eq. (3.1.50)**. $E^{(3)}$ may be obtained from third-order perturbation theory and summing over so-called Axilrod-Teller-Muto dispersion terms.[139,140] Its implementation is somewhat more involved, but it is said to improve thermochemical calculations.[137] The damping function f_{damp} compensates for the short-range singularity of R_{AB}^{-6},

$$f_{\mathrm{damp},n}(R_{\mathrm{AB}}) = \frac{1}{1+6\left[R_{\mathrm{AB}}/(s_{r,n}R_{\mathrm{AB}}^0)\right]^{-\gamma}}. \tag{3.1.53}$$

$s_{r,n}$ is another global scaling factor, γ is an adjustable parameter, and R^0_{AB} is a cut-off radius for atoms A and B. Note that f_{damp} vanishes at small internuclear distances, which is somewhat unphysical as pointed out by Koide.[141] He argued that the dispersion energy should approach some finite, constant value in the short-range limit. Without the need for an actual damping function, **Eq. (3.1.52)** can be adjusted in the following way[142]

$$E^{(2)} = \frac{1}{2} \sum_{\mathrm{A} \neq \mathrm{B}} \sum_{n=6,8,\ldots} \frac{C_n^{\mathrm{AB}}}{R_{\mathrm{AB}}^n + \mathrm{const.}}. \tag{3.1.54}$$

This ansatz is known as Becke-Johnson (BJ) or rational damping. In combination with DFT-D3, it yields the relation

$$E_{\mathrm{disp}}^{\mathrm{D3(BJ)}} = \frac{1}{2} \sum_{\mathrm{A} \neq \mathrm{B}} \left(s_6 \frac{C_6^{\mathrm{AB}}}{R_{\mathrm{AB}}^6 + f^6(R^0_{\mathrm{AB}})} + s_8 \frac{C_8^{\mathrm{AB}}}{R_{\mathrm{AB}}^8 + f^8(R^0_{\mathrm{AB}})} \right), \tag{3.1.55}$$

with $f(R^0_{\mathrm{AB}}) = a_1 \sqrt{C_8^{\mathrm{AB}}/C_6^{\mathrm{AB}}} + a_2$. The scaling factor s_6 is set to unity and a_1 and a_2 are atom-independent fit parameters individually adjusted depending on the DFA. The usual notation to indicate the use of DFT-D3 with BJ-damping is to suffix the DFA by 'D3(BJ)', e.g., PBE0-D3(BJ) or TPSS-D3(BJ).

Apart from Grimme's DFT-D scheme, there are many other methods around to account for dispersion forces in DFT. Examples include the VV10 functional by Vydrov and van Voorhis[143] based on the vdW-DF approach due to Dion, Langreth, and Lundqvist[144] or Tkatchenko and Scheffler's correction scheme,[145] which is formally identical to Grimme's DFT-D method with the key difference that the correction terms are density-dependent. For an exhaustive overview the reader is referred to the literature.[133,134]

3.2 Thermodynamic properties

> One of the principal objects of theoretical research is to find the point of view from which the subject appears in the greatest simplicity.
>
> – Josiah Willard Gibbs[146]

A significant part of this thesis is concerned with the accurate analysis of molecular aggregation in solution. A fundamental thermodynamic property to describe this process is the Gibbs free energy of association,

$$\Delta G_{\mathrm{a}} = \Delta E + \Delta G_{\mathrm{therm}} + \Delta G_{\mathrm{solv}}, \tag{3.2.1}$$

where ΔE is the difference in the electronic energies of reactants and products, which may be computed using an accurate DFA *in vacuo*, $\Delta G_{\mathrm{therm}}$ summarises the thermal corrections due to effects of the PES, and ΔG_{solv} represents the change in solvent effects. In the following, we will recapitulate a few fundamental aspects of statistical thermodynamics and discuss how to arrive at an accurate description of $\Delta G_{\mathrm{therm}}$ before analysing solvent effects in the next section. Before that, however, in order to properly understand the physical implications associated with aggregation processes, we need to address a few basic principles regarding PESs and address the problem of conformational sampling.

As discussed earlier, the BOA introduces the concept of molecular structure and PES. Physicochemical terms like reaction barrier, equilibrium constant, or conformational landscape would be meaningless without it from a theoretical point of view. As a consequence of the decoupled treatment of electrons and nuclei, two types of algorithms have found application in most quantum-chemical programme packages. On the one hand, there are techniques such as the direct inversion in iterative subspace (DIIS)[147] or the supermatrix formalism[148] concerned with optimising electronic structure, i.e., optimising the SCF procedure. On the other hand, there are approaches like the steepest-descent or conjugate gradient algorithm frequently applied to optimise a molecular structure.[149] "Optimising" a molecular structure, in this context, means finding either a local or a global minimum $\mathbf{R}_0$ on the PES,

$$\frac{\partial}{\partial \mathbf{R}} E[F(\mathbf{R})] \equiv \boldsymbol{\nabla}(\mathbf{R}) \xrightarrow{\mathbf{R}\to\mathbf{R}_0} \boldsymbol{\nabla}(\mathbf{R}_0) = 0 \tag{3.2.2}$$

$$\frac{\partial^2}{\partial \mathbf{R}^2} E[F(\mathbf{R})] \equiv \mathbf{H}(\mathbf{R}) \xrightarrow{\mathbf{R}\to\mathbf{R}_0} \mathbf{x}^T\mathbf{H}\mathbf{x} > 0 \;\forall\, \mathbf{x} \in \mathbb{R}^n \setminus \{\mathbf{0}\}. \tag{3.2.3}$$

The function F may for example be a wavefunction or a density as in DFT. The condition in **Eq. (3.2.3)** demands the Hessian matrix $\mathbf{H}$ to be positive-definite. This is the same as imposing that all eigenvalues of $\mathbf{H}$ be positive. The first condition, the vanishing gradient $\boldsymbol{\nabla}$, is usually met with a stopping criterium such as an energy threshold. Evaluating $\mathbf{H}$, however, is much more troublesome due to the resource-demanding calculation of the second derivatives, especially for large molecular systems. In practice, $\mathbf{H}$ is computed within the harmonic approximation, which

is the assumption that small geometrical perturbations at local minima can be described by a harmonic potential. Diagonalisation of **H** yields the normal modes and vibrational frequencies of the molecule. Conveniently, the latter correspond to the experimental signals measured in an IR-spectrum. Furthermore, vibrational frequencies are necessary for the estimation of enthalpies and entropies as we will see in the following.
An important thing to note is that most optimisation techniques converge structures to the nearest local minimum. Obtaining the global minimum is somewhat more involved as the conformational landscape has to be analysed. Furthermore, one may be interested in several conformations that are close in energy, since all experiments are performed at finite temperature. An efficient conformational sampling strategy involves meta-dynamics[150] (MTD) simulations using a density-functional tight-binding (DFTB) approach.[151] Grimme's GFN2-xTB[152,153] programme is currently one of the most popular methods to access the conformational landscape of large systems.
DFTB schemes belong to the family of semi-empirical quantum-chemical methods that bridge the gap between high-level quantum-mechanical approaches and force fields. Valence-only minimal basis sets are usually employed in semi-empirical methods and computational scaling is reduced by two orders of magnitude compared to HF or DFT due to the significant parametrisation and approximation of two-electron integrals.[151,154] In DFTB the KS energy $E[\rho]$ is expanded in terms of density fluctuations $\delta\rho$ around a superposition of neutral atomic reference densities $\rho_0 = \sum_A \rho_A$,[154]

$$E[\rho] = E^{(0)}[\rho_0] + E^{(1)}[\rho_0, \delta\rho] + E^{(2)}[\rho_0, (\delta\rho)^2] + E^{(3)}[\rho_0, (\delta\rho)^3] + \cdots \tag{3.2.4}$$

Depending on the implementation the series is truncated at some point.[155,156]
As most formalisms do, the GFN2-xTB scheme includes expansion terms up to third order. In contrast to most DFTB methods however, GFN2-xTB does not employ element pair-specific parameters. The total GFN2-xTB energy can be expressed as

$$E_{\mathrm{GFN2-xTB}} = E_{\mathrm{rep}} + E_{\mathrm{disp}} + E_{\mathrm{EHT}} + E_{\mathrm{ES,XC}} + G_{\mathrm{Fermi}}, \tag{3.2.5}$$

where E_{rep} is the classical repulsion energy related to Lennard-Jones-type potentials, E_{disp} is the dispersion correction based on the most recent DFT-D4 scheme, E_{EHT} is the covalent bonding term derived from extended Hückel theory, and $E_{\mathrm{ES,XC}}$ summarises all contributions based on electrostatics and the exchange-correlation contribution. G_{Fermi} is an entropic term arising from the application of the Fermi smearing method[157] necessary to obtain a variational solution for fractional occupation numbers, which for example facilitates a proper description of covalent bond breaking. For a more thorough overview and formulas for each term, the reader is referred to the paper by Christoph Bannwarth et al.[153]
For an extensive conformer search, it is convenient to separate the total energy of a system E_{tot} into an electronic part E_{el} and a bias potential E_{bias},

$$E_{\mathrm{tot}} = E_{\mathrm{el}} + E_{\mathrm{bias}}, \tag{3.2.6}$$

where the electronic part may be derived from a tight-binding approach as the one presented above. In the GFN2-xTB programme, the bias potential is evaluated in a MTD framework. That is, the chemical system at hand is described using a set of so-called collective variables $\mathbf{\Delta}_i$ and a history-dependent potential that fills up the minima of the PES, so that large reaction barriers can

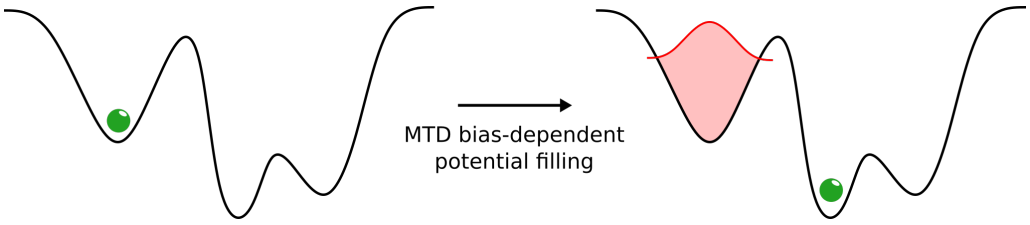

Figure 3.3: Bias-dependent potential filling of minima during a meta-dynamics (MTD) simulation run. Green spheres indicate the current structure of the run. The red area represents a filled zone the system is not going to access anymore.

be surpassed over the run time of the simulation. Grimme proposed to use the root-mean-square deviation (RMSD) as a collective variable. The bias potential can then be written as

$$E_{\text{bias}} \equiv E_{\text{bias}}^{\text{RMSD}} = \sum_{i=1}^{n} k_i \exp(-\alpha \mathbf{\Delta}_i^2), \tag{3.2.7}$$

with positive "pushing strengths" k_i and potential width parameter α. During the run, more and more Gaussian potentials are accumulated preventing the system to return to previous structures (**Fig. 3.3**). Grimme and co-workers could show that this approach performs well for conformer and rotamer sampling of large organic and organometallic systems.

Let us now discuss a few fundamental aspects of (statistical) thermodynamics. The Gibbs free energy (or free enthalpy) G is associated with an isothermal (constant temperature T) and isobaric (constant pressure p) process and is defined by the enthalpy H and entropy S,

$$G = H - TS. \tag{3.2.8}$$

Importantly, despite its misleading name G is actually not an independent form of energy such as the inner energy U. G is rather a physical quantity to describe the thermodynamic properties of a reaction. If the total derivative dG associated with a chemical process is negative, the reaction proceeds spontaneously, that is, without the need of an external source of energy. Note that this says nothing about reaction rates. If dG is equal to zero, the system is in its thermodynamic equilibrium. Evaluating dG in an isothermal framework yields for finite variations the Gibbs-Helmholtz equation[158]

$$\Delta G = \Delta H - T\Delta S. \tag{3.2.9}$$

Enthalpic and entropic terms can be split up in translational, rotational, and vibrational contributions,

$$H = U_{\text{trans}} + U_{\text{rot}} + U_{\text{vib}} + RT \tag{3.2.10}$$

$$S = S_{\text{trans}} + S_{\text{rot}} + S_{\text{vib}}, \tag{3.2.11}$$

with ideal gas constant R. RT accounts for the difference between H and U. Note that we are using molar quantities, otherwise the difference in H and U is $k_{\text{B}}T$ with Boltzmann constant k_{B}. In the context of molecular association processes, mathematical expressions for H and S are obtained

from the partition function of an ideal gas,

$$q = \sum_{\kappa=1}^{\infty} \mathrm{e}^{-\varepsilon_\kappa / k_\mathrm{B} T} \tag{3.2.12}$$

with eigenvalues ε_κ corresponding to the respective degree of freedom. It turns out that the eigenvalues for translation and rotation for a non-linear ideal gas are sufficiently narrow so that the sum in **Eq. (3.2.12)** can be replaced by an integral which yields surprisingly simple expressions for U,

$$U_\mathrm{trans} = \frac{3}{2} RT \tag{3.2.13}$$

$$U_\mathrm{rot} = \frac{3}{2} RT, \tag{3.2.14}$$

and slightly more intricate equations for S,

$$S_\mathrm{trans} = \frac{5}{2} R + R \ln \left[\frac{V_m}{N_\mathrm{A}} \left(\frac{2\pi m k_\mathrm{B} T}{h^2} \right)^{3/2} \right] \tag{3.2.15}$$

$$S_\mathrm{rot} = \frac{3}{2} R + R \ln \left[\frac{\sqrt{\pi}}{\sigma} \left(\frac{8\pi^2 k_\mathrm{B} T}{h^2} \right)^{3/2} \sqrt{I_1 I_2 I_3} \right]. \tag{3.2.16}$$

N_A is Avogadro's constant, σ is a symmetry dependent constant, I_X refers to the moments of inertia, m is the molecular mass, and V_m the molar volume at T. **Eq. (3.2.15)** is also known as the Sackur-Tetrode equation and corresponds to the total entropy of a monoatomic gas. Calculating U_vib and S_vib is somewhat more involved as the sum in **Eq. (3.2.12)** cannot be replaced by an integral for the vibrational degrees of freedom. U_vib and S_vib are derived from the partition function of the harmonic oscillator

$$U_\mathrm{vib} = R \sum_i \left[\frac{h\nu_i}{2k_\mathrm{B}} \coth \left(\frac{h\nu_i}{2k_\mathrm{B}} \right) \right] \tag{3.2.17}$$

$$S_\mathrm{vib} = R \sum_i \left\{ \frac{h\nu_i}{k_\mathrm{B} T} \left[\exp \left(\frac{h\nu_i}{k_\mathrm{B} T} \right) - 1 \right]^{-1} - \ln \left[1 - \exp \left(-\frac{h\nu_i}{k_\mathrm{B} T} \right) \right] \right\}, \tag{3.2.18}$$

where ν_i refers to the vibrational frequencies derived from a normal mode analysis of the chemical system. Note that S_vib is susceptible to numerical instabilities for small ν_i. Grimme proposed to use a modified rotational entropy S_R instead of the vibrational term for low-lying frequencies to remedy this problem.[159] Within the so-called rigid-rotor harmonic-oscillator (RRHO) approximation, a corrected entropy S_corr is introduced which smoothly interpolates between S_vib and S_R,

$$S_\mathrm{corr} = \alpha S_\mathrm{vib} + (1 - \alpha) S_\mathrm{R}, \tag{3.2.19}$$

where α is a parameter derived from some damping function,[160] and

$$S_\mathrm{R} = \frac{1}{2} R \left[1 + \ln \left(\frac{8\pi^3 k_\mathrm{B} T}{h^2} \cdot \frac{\mu B_\mathrm{av}}{\mu + B_\mathrm{av}} \right) \right]. \tag{3.2.20}$$

μ corresponds to the moment of inertia for a free rotor with the same frequency as the vibration that it replaces,

$$\mu = \frac{h}{8\pi^2\nu}, \tag{3.2.21}$$

and B_{av} is a limiting average molecular moment of inertia to prevent the logarithmic expression from diverging. Typically, **Eq. (3.2.19)** is applied to frequencies below 100–500 cm^{-1}. Using this approximation, we can rewrite **Eq. (3.2.1)**,

$$\Delta G_{\mathrm{a}} = \Delta E + \Delta H - T\Delta S^{\mathrm{RRHO}} + \Delta G_{\mathrm{solv}}. \tag{3.2.22}$$

Note that the way in which H is presented here, it does not contain the electronic energy E. This form of representation of ΔG_{a} is useful as electronic energies and thermal corrections are usually obtained in separate calculations. Furthermore, it should be pointed out that the zero-point energy E_{ZPE} is included in H or, more precisely, in U_{vib}. We can immediately see this, if we rewrite the hyperbolic cotangent in **Eq. (3.2.17)** with $\gamma_i = h\nu_i/2k_{\mathrm{B}}$,

$$U_{\mathrm{vib}} = R\sum_i [\gamma_i \coth(\gamma_i)] \tag{3.2.23}$$

$$= R\sum_i \left[\gamma_i \left(1 + \frac{2}{\mathrm{e}^{2\gamma_i} - 1}\right)\right] \tag{3.2.24}$$

$$= R\sum_i (\gamma_i) + 2R\sum_i (\mathrm{e}^{2\gamma_i} - 1)^{-1}, \tag{3.2.25}$$

where the first term on the right-hand side yields

$$R\sum_i (\gamma_i) = \frac{R}{2k_{\mathrm{B}}}\sum_i (h\nu_i) = N_{\mathrm{A}}E_{\mathrm{ZPE}}, \tag{3.2.26}$$

where we have used $R = N_{\mathrm{A}}k_{\mathrm{B}}$ with N_{A} being Avogadro's constant. The solvent term in **Eq. (3.2.22)** needs some more attention and will be discussed in the next section.

3.2.1 Continuum solvation models

As a quick Google picture search of the word "chemical" will tell you, most of chemistry takes place in solution. This poses, however, something of a conceptual problem for a computational scientist, because quantum-mechanical calculations by default treat chemical systems *in vacuo* at zero Kelvin. Simulating environmental effects is not at all a trivial task. Fortunately, research in this area has been very fruitful culminating in the Nobel Prize in Chemistry 2013 awarded to Martin Karplus, Michael Levitt, and Arieh Warshel "for the development of multiscale models for complex chemical systems".[161]

To introduce environmental effects in the system, we define an effective Hamiltonian incorporating a perturbation in the form of

$$\hat{H}_{\mathrm{eff}} = \hat{H}_0 + \hat{V}_{\mathrm{env}}. \tag{3.2.27}$$

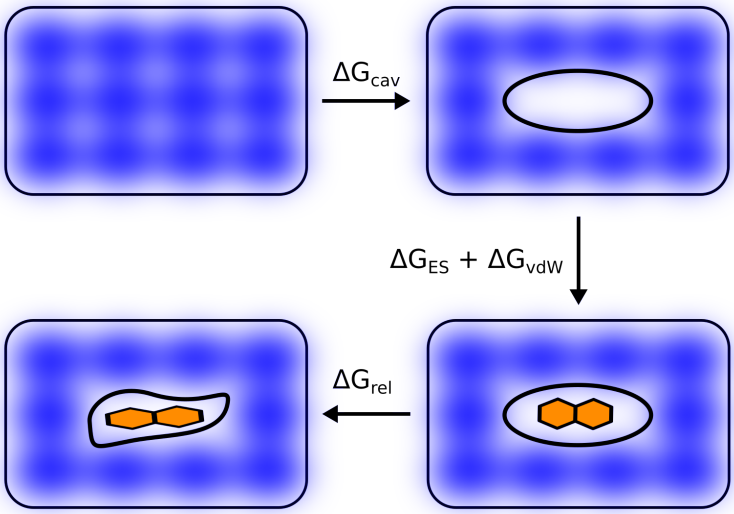

Figure 3.4: Schematic representation of the contributions involved in the set-up of a continuum solvation model. Blue background represents an even distribution of solvent molecules, the black ellipsis corresponds to the molecular cavity. Interaction is switched on in the second step represented by the insertion of a generic solute coloured in orange.

In principle, $\hat{V}_{\text{env}}$ may originate from a QM/MM (quantum-mechanics/molecular-mechanics) or a QM/CSM (continuum solvation model) partitioning of the system. The former is usually employed to simulate complex chemical reactions in inhomogeneous environments such as proteins or enzymes,[162–164] while the latter is the standard approach for the QM description of solutes in solvents. QM/CSM approaches, or simply "solvent models", focus on the free energy change ΔG_{solv} associated with transferring a molecule from the gas phase to an infinitely diluted solution treated as a homogeneous dielectric medium (**Fig. 3.4**)

$$\Delta G_{\text{solv}} = \Delta G_{\text{cav}} + \Delta G_{\text{ES}} + \Delta G_{\text{vdW}} + \Delta G_{\text{rel}}. \tag{3.2.28}$$

ΔG_{cav} corresponds to the formation of a cavity to accommodate the solute, ΔG_{ES} and ΔG_{vdW} are electrostatic and vdW-interactions between solute and solvent, and ΔG_{rel} refers to the free energy difference with respect to structural relaxation in solution. The electrostatic component ΔG_{ES} is the key ingredient of all CSMs. Due to the mutual polarisation of solute and solvent, the interaction has to be solved iteratively, which is usually referred to as the self-consistent reaction field (SCRF). ΔG_{ES} can be written as[165,166]

$$\Delta G_{\text{ES}} = \left\langle \Psi_{\text{S}} \middle| \hat{H}_{\text{eff}} - \frac{1}{2}\hat{V}_{\text{cont}} \middle| \Psi_{\text{S}} \right\rangle - \left\langle \Psi_0 | \hat{H}_0 | \Psi_0 \right\rangle \tag{3.2.29}$$

where we have replaced $\hat{V}_{\text{env}}$ by $\hat{V}_{\text{cont}}$ in **Eq. (3.2.27)**. Ψ_0 and Ψ_{S} correspond to vacuum and solvated wavefunction. The factor 1/2 indicates that the solvation free energy was corrected by the work required to polarise the solvent, which amounts to half of the solute-solvent interaction energy. Solvent models based on the CSM scheme differ in the way they treat $\hat{V}_{\text{cont}}$. Most popular approaches as e.g. the polarisable continuum model (PCM) use the apparent surface charge (ASC)

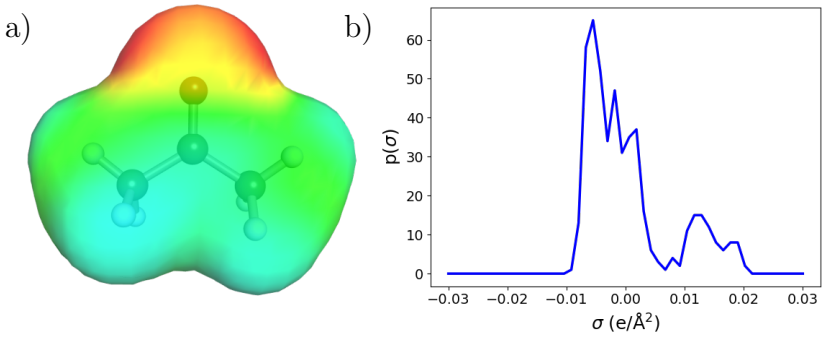

Figure 3.5: a) σ-surface of acetone, colours represent screening charge densities with red as positive, green as neutral, and blue as negative. Note that "positive" means that the surface has a certain affinity towards positive charges, b) σ-profile of acetone summing over all screening charge densities, the bulk around zero can be attributed to the non-polar methyl groups, while the elevation in the positive region corresponds to the carbonyl functional group.

strategy which incorporates an induced charge density $q(\mathbf{s})$ at the surface of the solute cavity Γ,

$$V_q(\mathbf{r}) = \int_\Gamma \frac{q(\mathbf{s})}{|\mathbf{r}-\mathbf{s}|} \mathrm{d}^2\mathbf{s}. \tag{3.2.30}$$

An ingenious way of deriving an expression for $\mathbf{q}$ was proposed by Andreas Klamt[167] who suggested to use the boundary condition of an ideal conductor, i.e., a medium with dielectric constant $\varepsilon = \infty$, to describe solvation phenomena. The potential $\Phi(\mathbf{s})$ at the surface of the solute cavity Γ vanishes for a perfectly conducting material,

$$\Phi(\mathbf{s}) = \mathbf{A}\mathbf{q} + \mathbf{B}\mathbf{Q} = 0 \tag{3.2.31}$$

$$\Rightarrow \mathbf{q} = -\mathbf{A}^{-1}\mathbf{B}\mathbf{Q} \tag{3.2.32}$$

with solute charges $\mathbf{Q}$ and electronic interaction matrices $\mathbf{A}$ and $\mathbf{B}$ coupling the solute to Γ. Lastly, the screening charges are scaled according to,

$$\mathbf{q}_{\mathrm{solv}} = \frac{\varepsilon - 1}{\varepsilon + \frac{1}{2}} \cdot \mathbf{q}, \tag{3.2.33}$$

for solvents with finite dielectric constants. This method is called conductor-like screening model (COSMO) and is one of the most widely applied solvent models in computational chemistry.
Perhaps unsurprisingly, a major disadvantage of implicit models like COSMO is the missing treatment of explicit effects such as hydrogen-bonding. An extension of COSMO that attempts to improve upon this shortcoming is COSMO-RS (real solvents).[168,169] Here, the incorporation of explicit solvent effects is achieved through reference calculations of the solute and a solvent molecule both embedded in an ideal conductor. Hence, all compounds can be interpreted as ideally screened solvent cavities which interact through their surface charge densities. Various correction terms are introduced to counterbalance the deviation of the ideally screened, homogeneous charge densities to the real molecules. At the core of COSMO-RS theory, however, is the so-called σ-profile $p^i(\sigma)$ of component i which is a measure of its relative amount of surface with some specific polarity σ (**Fig. 3.5**). The σ-profile of the entire solvent S is defined as the sum over all individual σ-profiles

weighted by their respective mole fractions x^i,

$$p_{\mathrm{S}}(\sigma) = \sum_{i \in S} x^i p^i(\sigma). \tag{3.2.34}$$

The crucial point is that $p_{\mathrm{S}}(\sigma)$ can be used to define a chemical potential $\mu_{\mathrm{S}}(\sigma)$ of the solution called σ-potential,

$$\mu_{\mathrm{S}}(\sigma) \propto -\ln\left[\int p_{\mathrm{S}}(\sigma')F[\mu_{\mathrm{S}}(\sigma')]\mathrm{d}\sigma'\right]. \tag{3.2.35}$$

$F[\mu_{\mathrm{S}}(\sigma')]$ contains the correction terms mentioned earlier. The specific σ-potential of some compound i is obtained by integrating over all polarities,

$$\mu_{\mathrm{S}}^i = \mu_{\mathrm{C,S}}^i + \int p^i(\sigma)\mu_{\mathrm{S}}(\sigma)\mathrm{d}\sigma, \tag{3.2.36}$$

with combinatorial correction term $\mu_{\mathrm{C,S}}^i$. If μ_{gas}^i is the chemical gas-phase potential of compound i obtained from a vacuum and a COSMO calculation, the free energy of solvation can then be written as

$$G_{\mathrm{solv}}^i = G_{\mathrm{S}}^i - G_{\mathrm{gas}}^i \tag{3.2.37}$$

$$= (\mu_{\mathrm{S}}^i - \mu_{gas}^i) + RT\ln\left(\frac{\rho_{\mathrm{S}}V_{\mathrm{gas}}}{M_{\mathrm{S}}}\right), \tag{3.2.38}$$

with $G_{\mathrm{X}}^i = \mu_{\mathrm{X}}^i + RT\ln(V^\circ/V_{\mathrm{X}})$, ρ_{S} and M_{S} as the solvent's density and molecular mass, V_{gas} as the molecular volume of the molecule in the gas phase, and V° as the molar volume under normal conditions. **Eq. (3.2.38)** is evaluated within the COSMOthermX[170] programme employing a specific parametrisation scheme.

Apart from solvent models based on the ASC formalism, there are other strokes based on different strategies. The multipole expansion method (MPE) is based on the description of solute-solvent interactions in terms of solid spherical harmonics and multipole moments,[171,172]

$$V_{\mathrm{cont}} \rightarrow V_{mult} = \sum_{lm}\sum_{l'm'} M_l^m f_{ll'}^{mm'} S_{l'}^{m'} \tag{3.2.39}$$

with reaction field factors f. Depending on the shape of the solute cavity, calculating f may become somewhat cumbersome. Another common approach is the generalised Born (GB) method which is similar to the multipole expansion, if the series is truncated after the first term, i.e., the monopoles, represented by partial atomic charges q_j,

$$V_{\mathrm{cont}} \rightarrow V_{\mathrm{GB}}(r_i) = \left(1 - \frac{1}{\varepsilon}\right)\sum_j q_j\eta_{ij}, \tag{3.2.40}$$

with effective Coulomb integral η_{ij}. The SMx (e.g. SM8) solvent models[173] due to Christopher Cramer and Donald Truhlar use this ansatz with optimised values for q_j. Based on this approach is the somewhat more sophisticated SMD[174] (solvent model based on density) method which includes the quantum-mechanical density of the solute as an input parameter. Although, this

renders computations slightly more involved, SMD has been shown to yield satisfactory results for solvation free energies.[175,176]

3.2.2 Calculating redox potentials

The concept of redox potentials is a fundamental aspect of physical chemistry. All supramolecular complexes examined as part of this thesis were either utilised in cyclic voltammetry (CV) experiments or redox reactions. As evident from our investigations, depending on its charge, the same chemical system may have significantly differing photophysical or thermodynamic properties. It is, therefore, worthwhile to outline typical theoretical approaches to estimate redox potentials.
In 1933, Tjalling Koopmans showed that for the HF treatment of a molecular system, the negative eigenvalue of the highest occupied molecular orbital ($\varepsilon_{\mathrm{HOMO}}$) coincides with the ionisation energy,[177]

$$IP = -\varepsilon_{\mathrm{HOMO}}. \tag{3.2.41}$$

This is known as Koopmans' theorem which can in principle be extended to electron affinities, since the virtual HF orbitals are formally evaluated from an $N+1$-wavefunction,

$$EA = -\varepsilon_{\mathrm{LUMO}}. \tag{3.2.42}$$

with LUMO being the lowest unoccupied molecular orbital. Electron affinities calculated from orbital energies are however somewhat dubious as virtual orbitals are much less well-defined than occupied ones.[149]
Interestingly, there is an equivalent of Koopmans' theorem in DFT. Using the integer discontinuity (**Eq. (3.1.37)**) and Janak's theorem,[178]

$$\frac{\partial E}{\partial n_i} = \varepsilon_i \tag{3.2.43}$$

with occupation number n_i of KS orbital i, it follows that

$$\varepsilon_N|_{N-f} = -IP \tag{3.2.44}$$

$$\varepsilon_{N+1}|_{N+f} = -EA. \tag{3.2.45}$$

Taking the limit $f \to 0$ then yields

$$IP = -\lim_{f\to 0} \varepsilon_N|_{N-f} = -\varepsilon_{\mathrm{HOMO}} \tag{3.2.46}$$

$$EA = -\lim_{f\to 0} \varepsilon_{N+1}|_{N+f} = -\varepsilon_{\mathrm{LUMO}}. \tag{3.2.47}$$

Note that these equations only hold for the exact XC functional. Koopmans' approach may be referred to as "frozen orbital approximation", which points out a serious problem when estimating redox potentials in this way. The electronic structure of a cation or anion may significantly differ from its neutral state. A more rigorous approach is to explicitly calculate all desired charge states and subtract total energies, which is sometimes referred to as ΔSCF method.[92] An advantage over Koopmans' theorem is that no orbitals from a single-reference method are required. Arguably

the most accurate procedure however is to take into account structural relaxation of the molecules as well. We may call this method adiabatic Δ_{ad}SCF, since it is in contrast to the vertical (meaning no structure relaxation allowed) ΔSCF method. The latter is naturally more efficient, if structural relaxation effects are negligible. Δ_{ad}SCF was successfully applied in papers **B1**, **B2**, and **B3**.

3.3 Excited electronic states

3.3.1 Time-dependent DFT

Explain time? Not without explaining existence.
Explain existence? Not without explaining time.

– John A. Wheeler[179]

The first part of this theoretical section was dedicated to calculating ground states of molecules and deriving related properties with an emphasis on thermodynamic aspects. While the ground state of a quantum-mechanical system is associated with the lowest-energy solution of the time-independent Schrödinger equation, all other solutions are called excited states. Paradoxically, although the experimental study of excited-state properties is always related to some time-dependent quantity, such as an electric field, as we will see in the following, it is still entirely sufficient to solve time-independent equations for most practical applications.
Time-dependent density functional theory (TD-DFT) is a popular approach to access excited states of molecules in computational chemistry. It is based on the Runge-Gross[180] and the van-Leeuwen[181] theorems. While the latter represents the time-dependent analogue of KS theory, the former is an extension of the first Hohenberg-Kohn theorem for time-dependent densities $\rho(\mathbf{r},t)$. Its proof is quite involved and will not be covered in full here, but we will outline a few key steps. First, a one-to-one mapping is established between time-dependent external potentials $v_{\text{ext}}(\mathbf{r},t)$ and current densities $j(\mathbf{r},t)$ given in operator form as

$$\hat{j}(\mathbf{r},t) = \frac{i}{2}\Big[[\nabla\Psi^*(\mathbf{r},t)]\Psi(\mathbf{r},t) - \Psi^*(\mathbf{r},t)\nabla\Psi(\mathbf{r},t)\Big]. \tag{3.3.1}$$

Using the time evolution of $j(\mathbf{r},t)$, it can be shown that two different current densities must originate from two external potentials, v^{A} and v^{B}, differing by more than an exclusively time-dependent function ($v^{\text{A}} - v^{\text{B}} \neq f(t)$),[182]

$$j(\mathbf{r},t) \leftrightarrow v_{\text{ext}}(\mathbf{r},t). \tag{3.3.2}$$

The connection between time-dependent densities and external potentials is established through the continuity equation,[183]

$$\frac{\partial}{\partial t}\rho(\mathbf{r},t) = -\nabla j(\mathbf{r},t). \tag{3.3.3}$$

which states that the density variation in a certain volume with respect to time must equal the spatial change of the current density flux in that volume. Application of **Eq. (3.3.3)** yields after some algebra a relation of the form

$$\frac{\partial^2}{\partial t^2}[\rho^{\text{A}} - \rho^{\text{B}}] = \nabla[\rho_0\nabla(v^{\text{A}} - v^{\text{B}})]. \tag{3.3.4}$$

In a final step, Green's theorem is utilised to show that the right-hand side of **Eq. (3.3.4)** cannot vanish for physically sound external potentials,[184] which yields a one-to-one mapping of $\rho(\mathbf{r},t)$ and $v_{\text{ext}}(\mathbf{r},t)$.
For time-dependent systems, the action A takes the place of the energy in quantum mechanics,

$$A = \int_{t_0}^{t_1} \left\langle \Psi(\mathbf{r},t) | i\frac{\partial}{\partial t} - \hat{H}(\mathbf{r},t) | \Psi(\mathbf{r},t) \right\rangle \mathrm{d}t. \tag{3.3.5}$$

Solutions of the time-dependent Schrödinger equation correspond to stationary points of A. A derivation of this is given by Löwdin and Mukherjee.[185] The variational condition $\delta A = 0$ yields

$$\delta A = 0 = \int_{t_0}^{t_1} \mathrm{d}t \left\langle \delta\Psi | i\frac{\partial}{\partial t} - \hat{H} | \Psi \right\rangle + \int_{t_0}^{t_1} \mathrm{d}t \left\langle \Psi | i\frac{\partial}{\partial t} - \hat{H} | \delta\Psi \right\rangle. \tag{3.3.6}$$

If we permit arbitrary variations $\delta\Psi = \delta\Psi'$ and $\delta\Psi = i\delta\Psi'$, which is equivalent to demanding that the real and imaginary part of $\delta\Psi$ can be varied independently, we obtain two conditions

$$0 = \int_{t_0}^{t_1} \mathrm{d}t \left\langle \delta\Psi' | i\frac{\partial}{\partial t} - \hat{H} | \Psi \right\rangle + \int_{t_0}^{t_1} \mathrm{d}t \left\langle \Psi | i\frac{\partial}{\partial t} - \hat{H} | \delta\Psi' \right\rangle \tag{3.3.7}$$

$$0 = -i\int_{t_0}^{t_1} \mathrm{d}t \left\langle \delta\Psi' | i\frac{\partial}{\partial t} - \hat{H} | \Psi \right\rangle + \int_{t_0}^{t_1} \mathrm{d}t \left\langle \Psi | i\frac{\partial}{\partial t} - \hat{H} | \delta\Psi' \right\rangle. \tag{3.3.8}$$

Combining **Eq. (3.3.7)** and **Eq. (3.3.8)** yields

$$0 = \int_{t_0}^{t_1} \mathrm{d}t \left\langle \delta\Psi' | i\frac{\partial}{\partial t} - \hat{H} | \Psi \right\rangle, \tag{3.3.9}$$

which recovers the time-dependent Schrödinger equation, since $\delta\Psi'$ is arbitrary,

$$0 = \left(i\frac{\partial}{\partial t} - \hat{H} \right) |\Psi\rangle. \tag{3.3.10}$$

Within the framework of TD-DFT, the action is represented as a functional of the density,

$$A[\rho] = \int_{t_0}^{t_1} \left\langle \Psi[\rho](\mathbf{r},t) | i\frac{\partial}{\partial t} - \hat{H}(\mathbf{r},t) | \Psi[\rho](\mathbf{r},t) \right\rangle \mathrm{d}t, \tag{3.3.11}$$

where its functional derivative with respect to the exact density must vanish in accordance with the stationary action principle,

$$\frac{\delta A[\rho]}{\delta\rho(\mathbf{r},t)} = 0. \tag{3.3.12}$$

Technically, **Eq. (3.3.12)** can be used to extract the exact density. However, since we are still dealing with a many-body system at this point, it is not immediately clear how solutions can be found.
In 1999, Robert van Leeuwen[181] showed that, in analogy to KS theory, the time-dependent density $\rho_0(\mathbf{r},t)$ of a many-body system can be reproduced by a non-interacting external potential $v_{\text{KS}}(\mathbf{r},t)$ associated with a single Slater determinant comprised of time-dependent one-particle orbitals $\phi(\mathbf{r},t)$

given as the solutions of the time-dependent KS equations,

$$i\frac{\partial}{\partial t}\phi_i(\mathbf{r},t) = \left(-\frac{1}{2}\nabla_i^2 + v_{\mathrm{KS}}(\mathbf{r},t)\right)\phi_i(\mathbf{r},t). \tag{3.3.13}$$

Similar to **Eq. (3.1.29)** the density of the non-interacting system is then given as

$$\rho_{\mathrm{S}}(\mathbf{r},t) = \sum_{i\,\in\,\mathrm{occ}} |\phi_i(\mathbf{r},t)|^2 = \rho_0(\mathbf{r},t). \tag{3.3.14}$$

Note that **Eq. (3.3.14)** and **Eq. (3.3.12)** are directly related as both formally represent prescriptions on how to obtain the exact time-dependent density of the many-body system. Within the framework of the van Leeuwen theorem, $A[\rho]$ can be expressed in terms of the non-interacting system,

$$A_{\mathrm{S}}[\rho] = B_{\mathrm{S}}[\rho] - \int_{t_0}^{t_1} \mathrm{d}t \int \mathrm{d}\mathbf{r}\rho(\mathbf{r},t)v_{\mathrm{KS}}(\mathbf{r},t), \tag{3.3.15}$$

where we have defined the potential-independent functional $B_{\mathrm{S}}[\rho]$ as

$$B_{\mathrm{S}}[\rho] = \int_{t_0}^{t_1} \mathrm{d}t \left\langle \Psi[\rho](\mathbf{r},t)|i\frac{\partial}{\partial t} - \hat{T}|\Psi[\rho](\mathbf{r},t)\right\rangle. \tag{3.3.16}$$

$B_{\mathrm{S}}[\rho]$ only contains the time derivative and the kinetic energy operator in the non-interacting particles picture. Once again, the functional derivative with respect to $\rho(\mathbf{r},t)$ must vanish for the exact density, so we can write

$$\frac{\delta A_{\mathrm{S}}[\rho]}{\delta\rho(\mathbf{r},t)} = 0 = \frac{B_{\mathrm{S}}[\rho]}{\delta\rho(\mathbf{r},t)} - v_{\mathrm{KS}}(\mathbf{r},t) \leftrightarrow v_{\mathrm{KS}}(\mathbf{r},t) = \frac{B_{\mathrm{S}}[\rho]}{\delta\rho(\mathbf{r},t)}. \tag{3.3.17}$$

This relationship is useful for the evaluation of the time-dependent KS equations (**Eq. (3.3.13)**). In a next step, let us analyse the action functional $A[\rho]$ of the interacting system. Using $B_{\mathrm{S}}[\rho]$, $A[\rho]$ can be rewritten with the external potential of the real system v_{ext} as

$$A[\rho] = B_{\mathrm{S}}[\rho] - \int_{t_0}^{t_1} \mathrm{d}t \int \mathrm{d}\mathbf{r}\rho(\mathbf{r},t)v_{\mathrm{ext}}(\mathbf{r},t) - \frac{1}{2}\int_{t_0}^{t_1} \mathrm{d}t \int \mathrm{d}\mathbf{r} \int \mathrm{d}\mathbf{r}' \frac{\rho(\mathbf{r},t)\rho(\mathbf{r}',t)}{|\mathbf{r}-\mathbf{r}'|} - A_{\mathrm{XC}}[\rho], \tag{3.3.18}$$

where $A_{\mathrm{XC}}[\rho]$ is the exchange-correlation action defined as

$$A_{\mathrm{XC}}[\rho] = B_{\mathrm{S}}[\rho] - \frac{1}{2}\int_{t_0}^{t_1} \mathrm{d}t \int \mathrm{d}\mathbf{r} \int \mathrm{d}\mathbf{r}' \frac{\rho(\mathbf{r},t)\rho(\mathbf{r}',t)}{|\mathbf{r}-\mathbf{r}'|} - B[\rho]. \tag{3.3.19}$$

and the universal functional of the interacting system is simply

$$B[\rho] = B_{\mathrm{S}}[\rho] - \int_{t_0}^{t_1} \mathrm{d}t\langle V_{\mathrm{ee}}(\mathbf{r},t)\rangle. \tag{3.3.20}$$

Invoking for the third time the stationary action principle **Eq. (3.3.12)** and **Eq. (3.3.17)** yield

$$\frac{B_{\mathrm{S}}[\rho]}{\delta\rho(\mathbf{r},t)} = v_{\mathrm{KS}}(\mathbf{r},t) = v_{\mathrm{ext}}(\mathbf{r},t) + \int \mathrm{d}\mathbf{r}' \frac{\rho(\mathbf{r}',t)}{|\mathbf{r}-\mathbf{r}'|} + \frac{\delta A_{\mathrm{XC}}[\rho]}{\delta\rho(\mathbf{r}',t)}, \tag{3.3.21}$$

where the second term on the right is the time-dependent Hartree potential. Inserting **Eq. (3.3.21)** into **Eq. (3.3.13)** finally yields an expression comparable to the time-independent KS equations,

$$i\frac{\partial}{\partial t}\phi_i(\mathbf{r},t) = \left(-\frac{1}{2}\nabla_i^2 + v_{\text{ext}}(\mathbf{r},t) + \int \mathrm{d}\mathbf{r}'\,\frac{\rho(\mathbf{r}',t)}{|\mathbf{r}-\mathbf{r}'|} + \frac{\delta A_{\text{XC}}[\rho]}{\delta\rho(\mathbf{r}',t)}\right)\phi_i(\mathbf{r},t) = f_t^{\text{KS}}\phi_i(\mathbf{r},t). \tag{3.3.22}$$

Although just like in the time-independent case **Eq. (3.3.22)** is formally exact, in practice, approximations have to be employed to represent $A_{\text{XC}}[\rho]$. For most experimental setups, where comparably weak fields are applied, we can make the very reasonable assumption, that our density varies only slowly in time. Under this assumption, we can replace the time-dependent XC action with the time-independent XC energy functional examined earlier,

$$\frac{\delta A_{\text{XC}}[\rho]}{\delta\rho(\mathbf{r},t)} \approxeq \left.\frac{\delta E_{\text{XC}}[\rho]}{\delta\rho(\mathbf{r},t)}\right|_{t=t_0} = v_{\text{XC}}[\rho] \tag{3.3.23}$$

This is extremely helpful, since it enables the use of DFAs from DFT in TD-DFT. This approach is known as the adiabatic approximation and is commonly applied in quantum-chemical computer codes.

3.3.1.1 Linear-response TD-DFT

By far the most frequently used strategy in the framework of TD-DFT to derive its working equations is to analyse the linear response of the time-independent density to a small external time-dependent perturbation $\delta v_{\text{ext}}(\mathbf{r},t)$. The response of the electron density can be expressed as a power series with respect to $\delta v_{\text{ext}}(\mathbf{r},t)$,

$$\rho(\mathbf{r},t) = \rho_0(\mathbf{r}) + \rho_1(\mathbf{r},t) + \rho_2(\mathbf{r},t) + \ldots \tag{3.3.24}$$

Higher-order terms, e.g., the quadratic response, are concerned with non-linear effects such as frequency doubling (also known as second-harmonic generation).[186,187] The linear response term $\rho_1(\mathbf{r},t)$ is evaluated using the density-density response function χ as

$$\rho_1(\mathbf{r},t) = \iint \mathrm{d}t'\mathrm{d}\mathbf{r}'\chi(\mathbf{r},t,\mathbf{r}',t')v_{\text{ext},1}(\mathbf{r}',t'), \tag{3.3.25}$$

Since the non-interacting external potential of the KS system by construction yields the exact time-dependent density of the interacting system, the first-order density-response can also be expressed in the KS formalism as

$$\rho_1(\mathbf{r},t) = \iint \mathrm{d}t'\mathrm{d}\mathbf{r}'\chi_{\text{KS}}(\mathbf{r},t,\mathbf{r}',t')v_{\text{KS},1}(\mathbf{r}',t'), \tag{3.3.26}$$

where χ_{KS} is the functional derivative of the density with respect to the external potential evaluated at the KS level, i.e., the density-density response function of the non-interacting system,

$$\chi_{\text{KS}}(\mathbf{r},t,\mathbf{r}',t') = \left.\frac{\delta\rho(\mathbf{r},t)}{\delta v(\mathbf{r}',t')}\right|_{v=v_{\text{KS},0}}. \tag{3.3.27}$$

The first-order response of the non-interacting KS potential $v_{\mathrm{KS},1}$ can be obtained from the functional variation of v_{KS} in **Eq. (3.3.21)** which yields

$$v_{\mathrm{KS},1}(\mathbf{r},t) = v_{\mathrm{ext},1}(\mathbf{r},t) + \int \mathrm{d}\mathbf{r}' \frac{\rho_1(\mathbf{r}',t)}{|r-r'|} + \iint \mathrm{d}t'\mathrm{d}\mathbf{r}' f_{\mathrm{XC}}(\mathbf{r},t,\mathbf{r}',t')\rho_1(\mathbf{r}',t') \tag{3.3.28}$$

$$= v_{\mathrm{ext},1}(\mathbf{r},t) + \iint \mathrm{d}\mathbf{r}'\mathrm{d}t' \left(\frac{\delta(t-t')}{|r-r'|} + f_{\mathrm{XC}}[\rho](\mathbf{r},t,\mathbf{r}',t') \right) \rho_1(\mathbf{r}',t') \tag{3.3.29}$$

with the XC kernel $f_{\mathrm{XC}}[\rho]$ defined as

$$f_{\mathrm{XC}}[\rho](\mathbf{r},t,\mathbf{r}',t') = \left. \frac{\delta v_{\mathrm{ext}}[\rho](\mathbf{r},t)}{\delta\rho(\mathbf{r}',t')} \right|_{\rho=\rho_0}. \tag{3.3.30}$$

It can be shown,[188] that the non-interacting density-density response function may be expressed as a sum-over-states (SOS) representation depending on the KS orbitals,

$$\chi_{\mathrm{KS}}(\mathbf{r},\mathbf{r}',\omega) = \lim_{\eta\to 0^+} \sum_{i,a} \left[\frac{\phi_i^*(\mathbf{r})\phi_a(\mathbf{r})\phi_i(\mathbf{r}')\phi_a^*(\mathbf{r}')}{\omega - \omega_{ai} + \imath\eta} - \frac{\phi_i(\mathbf{r})\phi_a^*(\mathbf{r})\phi_a(\mathbf{r}')\phi_i^*(\mathbf{r}')}{\omega + \omega_{ai} + \imath\eta} \right], \tag{3.3.31}$$

where i,j and a,b run over all occupied and, notably, also virtual orbitals, respectively. The complex number $\imath\eta$ ensures that the expression remains well-defined for all values of ω. For the interacting response function, the poles of the first and second term in the square brackets yield the excitation and de-excitation energies of the system. However, $\omega_{ai} = \varepsilon_a - \varepsilon_i$ are simply the orbital energy differences of KS theory. To obtain the excitation energies of the interacting system, we need to obtain a relationship between χ_{KS} and χ. Note that, for practical purposes and because it serves our cause much better, **Eq. (3.3.31)** is written in frequency space (ω) derived from a Fourier transformation of $\chi_{\mathrm{KS}}(\mathbf{r},t,\mathbf{r}',t')$. Inserting **Eq. (3.3.29)** into **Eq. (3.3.26)** and equating it with **Eq. (3.3.25)**, yields after some algebra a Dyson-like equation for the interacting density-density response function in terms of the non-interacting one,

$$\chi(\mathbf{r},\mathbf{r}',\omega) = \chi_{\mathrm{KS}}(\mathbf{r},\mathbf{r}',\omega) + \iint \mathrm{d}\mathbf{r}_1\mathrm{d}\mathbf{r}_2\, \chi_{\mathrm{KS}}(\mathbf{r},\mathbf{r}_1,\omega)\times$$
$$\times \left[\frac{1}{|r_1 - r_2|} + f_{\mathrm{XC}}[\rho_0](\mathbf{r}_1,\mathbf{r}_2,\omega) \right] \chi(\mathbf{r}',\mathbf{r}_2,\omega), \tag{3.3.32}$$

which may be solved iteratively. While it is usually rewritten for a more feasible implementation in quantum-chemical programmes, **Eq. (3.3.32)** represents the central component of linear-response TD-DFT.

A possible way of recasting **Eq. (3.3.32)** into a matrix equation is based on a parametrisation of the linear density response in Fourier space,[189]

$$\rho_1(\mathbf{r},\omega) = \sum_{i,a} \left[P_{ia}(\omega)\phi_i(\mathbf{r})\phi_a^*(\mathbf{r}) + P_{ai}(\omega)\phi_a(\mathbf{r})\phi_i^*(\mathbf{r}) \right] \tag{3.3.33}$$

with excitation and de-excitation density matrix elements P_{ia} and P_{ai}. By invoking **Eq. (3.3.31)** it can be shown that the parametrisation leads to two coupled eigenvalue problems with $P_{ia} = X_{ia}$

and $P_{ai} = Y_{ia}$ usually summarised as the so-called Casida equations,[188]

$$\begin{pmatrix} \mathbf{A} & \mathbf{B} \\ \mathbf{B}^* & \mathbf{A}^* \end{pmatrix} \begin{pmatrix} \mathbf{X} \\ \mathbf{Y} \end{pmatrix} = \begin{pmatrix} \boldsymbol{\omega} & 0 \\ 0 & -\boldsymbol{\omega} \end{pmatrix} \begin{pmatrix} \mathbf{X} \\ \mathbf{Y} \end{pmatrix}. \tag{3.3.34}$$

$\mathbf{A}$ and $\mathbf{B}$ are often referred to as orbital rotation Hessians[182] with

$$A_{ia,jb} = \delta_{ij}\delta_{ab}(\varepsilon_a - \varepsilon_i) + (ia|jb) - a_\mathrm{X}(ij|ab) + (1 - a_\mathrm{X})(ia|f_\mathrm{XC}|jb) \tag{3.3.35}$$

$$B_{ia,jb}, = (ia|jb) - a_\mathrm{X}(ib|aj) + (1 - a_\mathrm{X})(ia|f_\mathrm{XC}|bj) \tag{3.3.36}$$

with HF exchange portion a_X in case of hybrid DFAs and two-electron integrals written in Mulliken notation. Note that the frequency dependences were dropped for simplicity. Since the orbitals are usually real, the non-Hermitian eigenvalue problem **Eq. (3.3.34)** can be simplified by defining matrices $\mathbf{C}$ and $\mathbf{Z}$ with

$$\mathbf{C} = (\mathbf{A} - \mathbf{B})^{1/2}(\mathbf{A} + \mathbf{B})(\mathbf{A} - \mathbf{B})^{1/2} \tag{3.3.37}$$

$$\mathbf{Z} = (\mathbf{A} - \mathbf{B})^{-1/2}(\mathbf{X} + \mathbf{Y}). \tag{3.3.38}$$

It follows the Hermitian eigenvalue problem

$$\mathbf{CZ} = \omega^2\mathbf{Z}, \tag{3.3.39}$$

which in the case of non-hybrid functionals ($a_\mathrm{X} = 0$) saves some computational resources as $(\mathbf{A} - \mathbf{B})$ is diagonal. Coincidentally, if the exchange-correlation kernel f_XC is neglected in the foregoing equations, the Casida equations correspond to the time-dependent HF (TDHF) method or random-phase-approximation (RPA) as it is better known in theoretical physics. Note that we have not quite yet determined a way to calculate oscillator strengths, which is essential for the description of excited states.

As an alternative route to the density response formalism, we may make use of the fact, that the density-density response function, formally also known as the susceptibility, is directly linked to the polarisability of a chemical system $\alpha = \alpha[\chi(\omega)]$. Employing **Eq. (3.3.31)**, it can be shown that this leads to an SOS formula,[188]

$$\bar{\alpha}(\omega) = \frac{1}{3}tr(\boldsymbol{\alpha}) = \sum_i \frac{f_i}{\omega_i^2 - \omega^2} \tag{3.3.40}$$

where $\bar{\alpha}(\omega)$ is the mean polarisability. The poles and residues of $\bar{\alpha}(\omega)$ correspond to excitation energies ω_i and oscillator strengths f_i, respectively, with

$$\begin{aligned} f_i &= \frac{2}{3}\omega_i|\langle\Psi_0|\boldsymbol{\mu}|\Psi_1\rangle|^2 \\ &= \frac{2}{3}\omega_i|\mathbf{M}_{01}|^2. \end{aligned} \tag{3.3.41}$$

Hence, oscillator strengths couple the stationary states Ψ of the unperturbed Hamiltonian using the dipole moment operator $\boldsymbol{\mu}$. $\mathbf{M}_{01}$ corresponds to the transition dipole moment between ground state Ψ_0 and excited state Ψ_1. Note that **Eq. (3.3.41)** is directly related to Fermi's golden rule[190,191]

which is a more general formula for the transition probability between two states after a weak perturbation. All selection criteria are based on this rule. Laporte's rule, for example, states that transitions are only allowed between states of different inversion symmetry. This becomes immediately clear when evaluating **Eq. (3.3.41)** for two inversion symmetric wavefunctions and realising that $\boldsymbol{\mu}$ is an antisymmetric operator ($\boldsymbol{\mu} = \mathbf{r}$ in atomic units). If Ψ_0 and Ψ_1 are of the same symmetry, then $\mathbf{M}_{01}$ vanishes identically because the integration is over an antisymmetric (*ungerade*) function.
In a next step, the polarisability is expressed in terms of matrices **A**, **B**, and **C**. Using the (x,z)-component as an example, it can be shown, that

$$\alpha_{xz}(\omega) = 2\mathbf{x}^{\dagger}(\mathbf{A}-\mathbf{B})^{-1/2}[\mathbf{C}-\omega^2\mathbf{1}]^{-1}(\mathbf{A}-\mathbf{B})^{-1/2}\mathbf{z}. \tag{3.3.42}$$

Comparing this result with the SOS formula for the polarisability (**Eq. (3.3.40)**) enables the determination of excitation energies and oscillator strengths in terms of orbital rotation Hessians **A** and **B**. The expression in square brackets approaches zero for the excitation energies, since these correspond to the poles of the polarisability. This yields a pseudo eigenvalue problem of the form

$$\mathbf{C}\mathbf{g}_i = \omega_i^2\mathbf{g}_i. \tag{3.3.43}$$

Using a spectral expansion and renormalisation of the pseudo eigenvectors $\mathbf{g}_i$ gives after some algebra an equation for the oscillator strengths,

$$f_i = \frac{2}{3}|\mathbf{r}^{\dagger}(\mathbf{A}-\mathbf{B})^{-1/2}\mathbf{g}_i|^2. \tag{3.3.44}$$

Furthermore, the oscillator strengths evaluated in the linear-response TD-DFT framework obey the Thomas-Reich-Kuhne sum rule,[192] which is useful in assessing the quality of the basis set employed in quantum-chemical calculations.
A popular ansatz to further simplify the Casida equations is the so-called Tamm-Dancoff approximation (TDA), where the **B** matrix is neglected and with it all de-excitation contributions,[193]

$$\mathbf{A}\mathbf{X} = \omega\mathbf{X}. \tag{3.3.45}$$

This is comparable to the configuration-interaction singles (CIS) approach obtained from TDHF. The TDA can speed up calculations with hybrid functionals by a factor of roughly two due to the exchange contributions which renders $(\mathbf{A}-\mathbf{B})$ non-diagonal in full TD-DFT.[182] Otherwise, for non-hybrid DFAs no significant speed-up is to be expected. While the TDA is frequently applied in computational chemistry, the underlying approximation may sometimes become too severe. Systems with a certain multi-reference character, for instance, are not well described within the TDA as electron-correlation in the ground-state plays a major role for which de-excitation contributions may be crucial.[182,193]
If one deals with extremely large, say, supramolecular structures and needs to compute a lot of electronic states, neither full TD-DFT nor TDA may be feasible. In 2013, Grimme[194] published a simplified variant of the TDA approach, called sTDA. It introduces three simplifications on top of the TDA. First, the response of the XC kernel (f_{XC}) is neglected so that expensive numerical integration is avoided. Second, two-electron integrals are replaced by short-range damped interactions

of Löwdin charges q_{ij}^{A} of atom A and molecular orbitals i and j,

$$(ij|kl) \approx \sum_{\mathrm{A,B}} q_{ij}^{\mathrm{A}} q_{kl}^{\mathrm{B}} \gamma_{\mathrm{AB}}, \tag{3.3.46}$$

where γ_{AB} is the Mataga-Nishimoto-Ohno-Klopman damped Coulomb operator.[195–197] Different sets of parameters are defined for γ_{AB} for Coulomb and exchange terms. Reformulation of **A** in **Eq. (3.3.34)** leads to

$$A'_{ia,jb} = \delta_{ij}\delta_{ab}(\epsilon_a - \epsilon_i) + \sum_{\mathrm{A,B}} \left(2q_{ia}^{\mathrm{A}} \gamma_{\mathrm{AB}}^{K} q_{jb}^{\mathrm{B}} - q_{ij}^{\mathrm{A}} \gamma_{\mathrm{AB}}^{J} q_{ab}^{\mathrm{B}}\right). \tag{3.3.47}$$

where superscripts J and K refer to Coulomb and exchange terms, respectively. Since Löwdin charges are expressed in terms of basis functions, we may consider this approach a form of resolution-of-the-identity approximation. As a last simplification the configuration space is truncated depending on an energetic threshold. The basis for this approach is that, in practice, only a small number of configuration state functions (CSF) contribute significantly to the excitations. The extension of simplified TDA to simplified TD-DFT (sTD-DFT) is straight-forward.[198] The same approximations as discussed above are applied for the full evaluation of the Casida equations. Analogously, we obtain

$$\mathbf{B'}_{ia,jb} = \sum_{\mathrm{A,B}} \left(2q_{ia}^{\mathrm{A}} \gamma_{\mathrm{AB}}^{K} q_{jb}^{\mathrm{B}} - a_{\mathrm{X}} q_{ib}^{\mathrm{A}} \gamma_{\mathrm{AB}}^{K} q_{aj}^{\mathrm{B}}\right). \tag{3.3.48}$$

Instead of parametrising the Coulomb operator anew, the same parameter set as in sTDA is used scaled by the amount of HF exchange a_{X} used in the (hybrid) functional.

3.3.1.2 Challenges in TD-DFT

As alluded to earlier, there are a few issues when using standard TD-DFT approaches one has to be aware of. For one thing, charge-transfer (CT) states are notoriously difficult to assess with standard DFAs. A famous example is the zincbacteriochlorin-bacteriochlorin complex (**Fig. 3.6**) investigated by Andreas Dreuw and Martin Head-Gordon.[199] The molecule's HOMO and LUMO are localised on the two different moieties giving rise to excited states with typical CT character. According to TD-DFT calculations at the B3LYP level, the first two excited singlet states can be described by intramolecular electron transfer. However, CT states are usually underestimated when calculated in this way, which can be rationalised from the definition of the **A** and **B** matrices in **Eq. (3.3.34)**. If i and j correspond to occupied orbitals on one moiety, and a and b to virtual orbitals localised on another, the matrix elements of **A** and **B** reduce to

$$A_{ia,jb} = \delta_{ij}\delta_{ab}(\epsilon_a - \epsilon_i) - a_{\mathrm{X}}(ij|ab) \tag{3.3.49}$$

$$B_{ia,jb} = 0 \tag{3.3.50}$$

in the asymptotic limit. While the **B** term completely vanishes, **A** depends on KS orbital energy differences and a Coulomb integral scaled by the amount of HF exchange. The latter in fact recovers the $1/r$ distance dependence of CT states which is expected for the electrostatic interaction of two point charges. As a consequence, purely local DFAs ($a_{\mathrm{X}} = 0$) cannot recover the correct

asymptotic behaviour of CT states and hybrid functionals with low amounts of HF exchange will at least show significant deficits. It is interesting to note that **Eq. (3.3.50)** is exactly equivalent to omitting **B** in the TDA. In other words, the TDA can be used as a diagnostic of a CT state. If excitation energies obtained from full TD-DFT and the TDA differ, then the state at hand cannot involve significant CT due to the contribution of the **B** matrix.

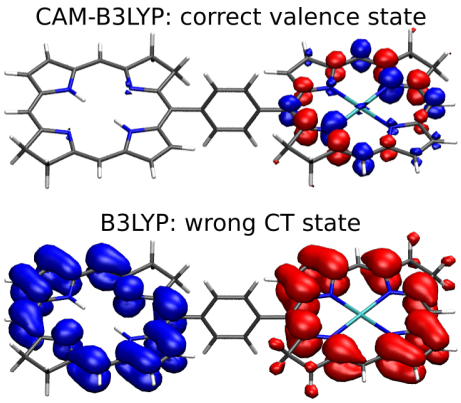

Figure 3.6: Difference density (*cf.* section 3.3.3) of the lowest singlet excited state of a zincbacteriochlorin-bacteriochlorin complex obtained at the CAM-B3LYP[200] (top) and B3LYP[128] (bottom) levels of TD-DFT using a def2-SVP basis set and the ORCA programme package,[201] the correct valence excited-state nature is reproduced only by employing a long-range corrected functional. Orbital isosurfaces were calculated with ORBKIT,[202] isovalue = 0.001 a_0^{-3}. Red and blue zones correspond to areas of electron depletion and electron enhancement, respectively.

A possible remedy is to employ TDHF or include 100% HF exchange in **Eq. (3.3.49)** fully recovering the correct $1/r$ dependence. However, this significantly degrades the functional performance for short-range properties. Furthermore, TDHF or CIS excitation energies are usually much too large as the virtual orbitals are formally evaluated with an $N+1$-wavefunction. Consequences of these shortcomings are a wrong state-ordering in the zincbacteriochlorin-bacteriochlorin compound and false asymptotic behaviour for CT-dominated systems such as the ethylene-tetrafluoroethylene complex.[203]

A solution to this problem is known as Coulomb-attenuation or range-separation where the two-electron operator $1/r_{12}$ is partitioned into a short-range and a long-range part using the Gaussian error function,

$$\frac{1}{r_{12}} = \underbrace{\frac{\mathrm{erf}(\mu r_{12})}{r_{12}}}_{\mathrm{long-range}} + \underbrace{\frac{1-\mathrm{erf}(\mu r_{12})}{r_{12}}}_{\mathrm{short-range}}, \tag{3.3.51}$$

with $\mathrm{erf}(x) = \frac{2}{\sqrt{\pi}} \int_0^x \mathrm{e}^{-\tau^2} \mathrm{d}\tau$. μ is a functional-dependent parameter. Since the HF exchange portion approaches zero in the short-range limit in **Eq. (3.3.51)**, these range-separated hybrid functionals yield rather poor results for properties such as atomisation energies. Yanai et al.[200] proposed an alternative formulation of **Eq. (3.3.51)**,

$$\frac{1}{r_{12}} = \frac{[\alpha + \beta \mathrm{erf}(\mu r_{12})]}{r_{12}} + \frac{1-[\alpha + \beta \mathrm{erf}(\mu r_{12})]}{r_{12}}, \tag{3.3.52}$$

which converges to a HF exchange of α associated with the underlying hybrid functional. In this way, for example, the popular CAM-B3LYP functional was constructed with $\mu = 0.33$ a.u., $\alpha = 0.19$, and $\beta = 0.46$. CAM-B3LYP successfully increases the energy of the CT states of the bacteriochlorin complex, so that the lowest state is correctly predicted as a local Q state (**Fig. 3.6**). Another example of a range-separated hybrid functional was suggested by Martin Head-Gordon and co-workers termed ωB97X,[204] a variant of which has found successful application in this thesis on several occasions (papers **A2**, **A3**, and **B2**). ωB97X contains a parametrised short-range modified version of Axel Becke's original B97 hybrid functional and a long-range part smoothly increasing the amount of HF exchange from roughly 16% to 100%. Both CAM-B3LYP and ωB97X (and its variants ωB97X-D[160] and ωB97X-D3[205]) yield much better results for Rydberg and CT states and reaction barriers than their standard hybrid functional counterparts.[206,207]
In a way, range-separated DFAs can still be assumed to belong to the fourth rung of Jacob's ladder as no unique new component has been included in the functional description. The fifth and currently final step of Jacob's ladder are so-called double-hybrid (dh) functionals proposed by Stefan Grimme.[208] While hybrid GGAs introduce a global parameter a_X to denote inclusion of HF exchange, dhGGAs contain, in addition, a parameter a_C to furthermore include MP2 correlation,

$$E_\mathrm{XC}^\mathrm{dhGGA} = a_\mathrm{X} E_\mathrm{X}^\mathrm{HF} + (1 - a_\mathrm{X}) E_\mathrm{X}^\mathrm{GGA} + a_\mathrm{C} E_\mathrm{C}^\mathrm{MP2} + (1 - a_\mathrm{C}) E_\mathrm{C}^\mathrm{GGA}. \tag{3.3.53}$$

Double-hybrid functionals such as B2GP-PLYP[209] perform admirably across various benchmark sets.[209–211] However, usage of MP2 correlation energy comes with a prohibitive computational scaling of $O(N^5)$, which renders large molecules out of reach and arguably defeats the purpose of employing DFT-based methods.
Another severe problem for all DFAs when calculating electronic transitions are states with significant multi-excitation character. Polyenes such as typical carotenoids represent important examples. This shortcoming is very simply explained by the fact that DFT, just like HF, is a single-reference approach, i.e., based on a single Slater determinant or CSF. A natural remedy to this problem is, hence, the inclusion of double and higher excited reference configurations into the DFT scheme. A successful method employing this idea is DFT/MRCI,[212,213] (multi-reference configuration interaction) which will be outlined in the following section.

3.3.2 DFT/MRCI

Proposed in 1998 by Stefan Grimme and Mirko Waletzke, DFT/MRCI is a multi-referential approach to accurately describe excited states including a significant contribution from multi-excitations. Grimme and Waletzke opted to combine the flexibility of MRCI with the efficiency of DFT for a more general purpose electronic-structure theory. MRCI is an extremely powerful method to describe electronic excited states, which usually possess a certain degree of multi-referential character. Static electron correlation is recovered by expressing the reference state in terms of multiple reference configurations spanning a so-called reference space, while dynamic correlation is introduced by including excited configurations into the CI wavefunction. As a consequence, however, MRCI has the unfortunate drawback that it can become absurdly expensive from a computational point of view, since both basis set coefficients as well as CI expansion coefficients are optimised simultaneously. Large molecules with reference spaces containing more than a few CSFs are pretty much out of reach.

Moreover, Hartree-Fock orbitals provide a poor basis for the description of excited states, since the virtual HF orbitals are formally calculated using an N-electron mean-field instead of an $N-1$-electron one. KS orbitals are a much better basis, since both occupied and virtual orbitals are evaluated using the same potential. KS orbital energy differences are often already a good approximation to transition energies.[214] Furthermore, a large portion of the dynamical electron correlation is usually recovered in KS-DFT rendering long CI expansions unnecessary.[212,213] This has the computational advantage that the CI space can be truncated quite significantly. In DFT/MRCI, the reference space is refined in an iterative procedure instead of hand-picking configurations as in a complete active-space SCF (CASSCF) calculation.

To discuss the general outline of the method, it is useful to briefly introduce the language of second quantisation. While in the standard formulation of quantum mechanics, "first quantisation" so to speak, observables are represented by operators and states by functions, in second quantisation wavefunctions are also expressed by operators. These are the creation $a^\dagger$ and annihilation operator a acting on a reference state, which may, for example, correspond to a ground-state Slater determinant $|\Psi_0\rangle$. A singly excited determinant $|\Psi_i^a\rangle$, where an electron has been moved from occupied orbital i to virtual orbital a, may hence be written as

$$|\Psi_i^a\rangle = a_a^\dagger a_i |\Psi_0\rangle = \hat{E}_i^a |\Psi_0\rangle, \tag{3.3.54}$$

where we have introduced the one-electron excitation operator $\hat{E}$. Operators in second quantisation consist of annihilation and creation operators weighted by the matrix element corresponding to the expectation value of the first-quantisation operator evaluated between two states. While this may sound somewhat confusing, the result is a compact notation expedient for the derivation of mathematical expressions. A molecular electronic Hamiltonian can then be written as

$$\hat{H} = \sum_{pq} h_{pq} a_p^\dagger a_q + \frac{1}{2} \sum_{pqrs} g_{pqrs} a_p^\dagger a_r^\dagger a_s a_q \tag{3.3.55}$$

$$= \sum_{pq} h_{pq} \hat{E}_q^p + \frac{1}{2} \sum_{pqrs} g_{pqrs} (\hat{E}_q^p \hat{E}_s^r - \delta_{qr} \hat{E}_s^p), \tag{3.3.56}$$

where we have made use of the anticommutation relations of the annihilation and creation operators.[92] The one- and two-electron matrix elements are defined as

$$h_{pq} = \langle \chi_p | -\frac{1}{2}\nabla^2 - \sum_\alpha \frac{Z_\alpha}{r_\alpha} | \chi_q \rangle \tag{3.3.57}$$

$$g_{pqrs} = \langle \chi_p \chi_r | \chi_q \chi_s \rangle = (pq|rs), \tag{3.3.58}$$

with spin orbitals χ and electron-nuclear separation r_α. Note that the nuclear-nuclear potential is not included in the expression for brevity. The creation and annihilation operators in **Eq. (3.3.56)** make sure that at most two-electron contributions arise.

We recall the expressions for the Fock matrix elements (*cf.* **Eq. (3.1.10)**) and the total SCF

energy (*cf.* **Eq. (3.1.15)**), which can be rewritten as

$$f_{pq} = h_{pq} + \sum_r w_r[g_{pqrr} - \frac{1}{2}g_{prqr}], \tag{3.3.59}$$

$$E^{\mathrm{SCF}} = \sum_p w_p f_{pp} - \frac{1}{2}\sum_{pq} w_p w_q[g_{ppqq} - \frac{1}{2}g_{pqpq}], \tag{3.3.60}$$

where w_p is the occupation number of orbital p. In second quantisation, the CI Hamiltonian can then be rewritten in terms of f and E^{SCF} as[215]

$$H^{\mathrm{CI}} = E^{\mathrm{SCF}} - \sum_p \bar{w}_p f_{pp} + \frac{1}{2}\sum_{pq} \bar{w}_p \bar{w}_q[g_{ppqq} - \frac{1}{2}g_{pqpq}] \tag{3.3.61}$$

$$+ \sum_{pq} f_{pq}\hat{E}^q_p - \sum_{pqr} \bar{w}_r[g_{pqrr} - \frac{1}{2}g_{prqr}]\hat{E}^q_p \tag{3.3.62}$$

$$+ \frac{1}{2}\sum_{pqrs} g_{pqrs}(\hat{E}^q_p\hat{E}^s_r - \delta_{qr}\hat{E}^s_p), \tag{3.3.63}$$

with $\bar{w}_p$ as the occupation number of orbital p of reference CSF $|mw\rangle$ with spin-coupling pattern m and spatial occupation number vector w. Three cases of non-vanishing matrix elements can be distinguished for the spatial part: diagonal, off-diagonal differing in one-electron, and off-diagonal differing in two electrons. In the DFT/MRCI scheme, these three cases are examined individually for semi-empirical parametrisation. Using the short-hand notation $\Delta w_p = w_p - \bar{w}_p$, after some algebra it follows:

1. diagonal elements:

$$\begin{aligned} H^{\mathrm{CI}}_{mm} &= \langle mw|H^{\mathrm{CI}}|mw\rangle \\ &= E^{\mathrm{SCF}} + \sum_p f_{pp}\Delta w_p + \frac{1}{2}\sum_{p\neq q} g_{ppqq}\Delta w_p \Delta w_q \\ &\quad + \frac{1}{2}\sum_{p\neq q} g_{pqpq}\left(-\frac{1}{2}\Delta w_p \Delta w_q + \frac{1}{2}w_p w_q - w_p + \eta^{qp}_{pq}\right) \\ &\quad + \frac{1}{2}\sum_p g_{pppp}\left(\frac{1}{2}\Delta w_p \Delta w_q + \frac{1}{2}w_p w_q - w_p\right) \end{aligned} \tag{3.3.64}$$

2. off-diagonal elements with one-electron difference:

$$\begin{aligned} H^{\mathrm{CI}}_{mm'} &= \langle mw|H^{\mathrm{CI}}|m'w'\rangle \\ &= f_{pq}\eta^q_p + \frac{1}{2}\sum_{r\neq p,q} g_{pqrr}\Delta w'_r \eta^q_p \\ &\quad + \sum_{r\neq p,q} g_{prrq}\left(-\frac{1}{2}\Delta w'_r \eta^q_p + \frac{1}{2}w'_r\eta^q_p - \eta^q_p + \eta^{rq}_{pr}\right) \\ &\quad + g_{pppq}\left(\frac{1}{2}\Delta w'_p + w'_p\right)\eta^q_p - g_{pqqq}\left(\frac{1}{2}\Delta w'_q + \frac{1}{2}w'_q - 1\right) \end{aligned} \tag{3.3.65}$$

3. off-diagonal elements with two-electron difference:

$$\begin{aligned} H^{\mathrm{CI}}_{mm''} =& \langle mw|H^{\mathrm{CI}}|m''w''\rangle \\ =& \frac{g_{pqrs}\eta^{qs}_{pr} + g_{psrq}\eta^{sq}_{pr}}{(1+\delta_{pr})(1+\delta_{qs})} \end{aligned} \tag{3.3.66}$$

The coefficients $n^{qs}_{pr} = \langle E^q_p E^s_r\rangle$ are simply weights of the respective one- and two-electron integrals. Since they do not need to be optimised in any way, they can be computed in advance and stored. An advantage of the equations presented above is that all excitations depend on the same closed-shell reference state. In the DFT/MRCI approach, this is exploited by expressing all matrix elements with respect to an optimised one-electron basis of KS orbitals obtained from a BHLYP calculation. The space that spans all reference CSFs is referred to as reference space. For diagonal elements of the effective DFT/MRCI Hamiltonian H^{DFT}, this results in

$$\begin{aligned} \langle mw|H^{\mathrm{DFT}} - E^{\mathrm{DFT}}|mw\rangle = \langle mw|H^{\mathrm{CI}} - E^{\mathrm{HF}}|mw\rangle \\ - \sum_{p\in c}^{n_{\mathrm{exc}}}(f^{\mathrm{HF}}_{pp} - f^{\mathrm{KS}}_{pp}) + \sum_{p\in a}^{n_{\mathrm{exc}}}(f^{\mathrm{HF}}_{pp} - f^{\mathrm{KS}}_{pp}) + \Delta E_J - \Delta E_K, \end{aligned} \tag{3.3.67}$$

with total KS energy E^{DFT} of the reference configuration. The sums over a and c correspond to all configurations obtained by annihilating and creating electrons within a certain excitation class n_{exc} (1 for single excitations, 2 for double excitations, etc.). Importantly, E^{HF} and f^{HF} are only HF-*like*. Both are evaluated in a KS orbital basis using an operator constructed similarly to the Fock operator of **Eq. (3.1.10)**. ΔE_J and ΔE_K are the Coulomb and exchange energy differences arising from KS and HF theory.

In the original construction of the diagonal elements different parameter sets for singlet and triplet CSFs were employed for the particle-hole Coulomb and exchange interactions. However, for loosely coupled photoexcited chromophores this approach results in inaccuracies due to artificially low-lying singlet-coupled triplet pairs, also referred to as intruder states.[216] Prompted by this, Igor Lyskov et al. refined the DFT/MRCI Hamiltonian by introducing a spin-independent parameter set.[217] The result is the redesigned Hamiltonian denoted by R2016, which was successfully applied in papers **A1**, **A2**, and **A3**.

The off-diagonal terms are separated into matrix elements between CSF with the same and with different spatial occupation w. In the original scheme, matrix elements between different CSF with coinciding spatial occupation part were chosen to be equal to the unmodified CI matrix elements. The modified R2016 Hamiltonian employs a scaling factor $(1 - p_{\mathrm{X}})$, where p_{X} is the parameter used in correcting the exchange term in **Eq. (3.3.67)**,

$$\langle mw|H^{\mathrm{DFT}}|m'w\rangle = \langle mw|(1-p_{\mathrm{X}})H^{\mathrm{CI}}|m'w\rangle. \tag{3.3.68}$$

As pointed out earlier, dynamical correlation is already incorporated at the ground-state DFT level to some extent. To avoid double-counting of dynamical correlation effects at the CI level, contributions from off-diagonal terms have to be scaled appropriately. Fortunately, static and dynamic electron correlation are usually well-separated in practice. While the former is mainly represented by a fairly small number of energetically low-lying states, the latter depends on a rather large number of high-lying configurations. This has a conceptual consequence for the off-

diagonal terms of the DFT/MRCI Hamiltonian between states differing in their spatial occupation calculated in the R2016 variant according to

$$\langle mw|H^{\mathrm{DFT}}|m'w'\rangle = \langle mw|H^{\mathrm{CI}}|m'w'\rangle \frac{p_1}{1+[(p_2\Delta E_{ww'})\arctan(p_2\Delta E_{ww'})]^5}, \tag{3.3.69}$$

which introduces a damping function with two more parameters p_1 and p_2. In this way, CSFs with an energy difference of up to roughly 0.4 Hartree can couple strongly, while CSFs beyond that are scaled down smoothly to zero.

Apart from the R2016 Hamiltonian, the R2017 and R2018 flavours are available.[218,219] The R2017 is an extension of the method to systems with uneven multiplicities and the R2018 Hamiltonian is equipped with an exponential damping function instead of the one proposed in **Eq. (3.3.69)** and was parametrised for a more accurate description of transition metal complexes. In general, DFT/MRCI performs very well across a multitude of chemical systems. It is one of the few methods that can correctly predict the energy of the $2^1\mathrm{A_g}$ state in polyenes such as butadiene. One significant disadvantage of DFT/MRCI (and methods constructed in a similar manner) is the fact that no analytical gradients are available for it. In contrast to approaches like CASSCF, where the reference space is fixed, the energy obtained from a DFT/MRCI run is not invariant with respect to orbital rotations, because the reference space needs to be iteratively refined until convergence is reached. Structure optimisations and even more so normal mode analyses are unfeasible at the DFT/MRCI level for molecules with more than a few tens of atoms as only numerical gradients may be programmed.

3.3.3 Characterising excited states

Apart from acquiring knowledge about excitation energies and oscillator strengths, it is most often useful to analyse excited electronic states by visualising them. Especially in the context of molecular electronics, it is essential to find a way to distinguish valence from charge-transfer states, for instance.

A straight-forward way to characterise an excited state is by examining the molecular orbitals involved in the transition. All modern TD-DFT codes, for example, print the contribution of the dominating orbitals to the electronic transition in the output. A visualisation programme can then be used to look at the orbitals. In this way, excited states in most organic molecules can be readily classified, even including more subtle n–π^* transitions. However, two major drawbacks have to be addressed. For one, molecular orbitals alone rarely yield any significant insight for larger molecules, especially if extended π-systems with heteroatoms are involved. By construction, molecular orbitals are in general highly delocalised. Identifying n- or π^*-type orbitals is much more ambiguous in this case. While there are localisation schemes around,[220,221] localised molecular orbitals are not associated with an orbital energy anymore, on top of the fact that the significance of localised virtual orbitals is arguably rather dubious.

Moreover, and perhaps more importantly, analysing excited states in terms of molecular orbitals is only convenient as long as just one or a few determinants contribute to the excited state. If this is not the case, molecular orbital analysis is certain to become rather tedious and n–π^* or similar transitions associated with a one-particle picture can only be vaguely discerned.

A more sophisticated way of studying electronic transitions is by examining the transition density

$$T(\mathbf{x}_1) = N \int \mathrm{d}\mathbf{x}_2 \cdots \int \mathrm{d}\mathbf{x}_N \Psi_1(\mathbf{x}_1, \mathbf{x}_2, ..., \mathbf{r}_N)\Psi_0^*(\mathbf{x}_1, \mathbf{x}_2, ..., \mathbf{x}_N) \tag{3.3.70}$$

coupling the ground state Ψ_0 to an excited state of interest, here Ψ_1. T can be expressed in matrix form in the basis of the molecular orbitals as

$$T_{ia} = \langle \phi_i | T(\mathbf{x}) | \phi_a \rangle. \tag{3.3.71}$$

Associated with the transition density matrix are the so-called natural transition orbitals (NTOs), which give valuable insight into the nature of electronic transitions. However, NTOs cannot be directly obtained from $\mathbf{T}$, since it is a rectangular matrix of dimension $N_{\mathrm{occ}} \times N_{\mathrm{virt}}$. Instead, an orbital transformation scheme based on a singular value decomposition of $\mathbf{T}$ according to Amos and Hall[222] is proposed,

$$\mathbf{T} = \mathbf{U}\mathbf{W}\mathbf{V}^\dagger, \tag{3.3.72}$$

where $\mathbf{U}$ and $\mathbf{V}$ are unitary matrices with dimensions $N_{\mathrm{occ}} \times N_{\mathrm{occ}}$ and $N_{\mathrm{virt}} \times N_{\mathrm{virt}}$, respectively. It is furthermore easy to show that,

$$\mathbf{W}^2 = \mathbf{U}^\dagger \mathbf{T}\mathbf{T}^\dagger \mathbf{U}, \tag{3.3.73}$$

which in turn means that $\mathbf{U}$ and the singular matrix $\mathbf{W}$ can be determined by solving the eigenvalue problem associated with $\mathbf{T}\mathbf{T}^\dagger$. Analogously, $\mathbf{V}$ is obtained from the eigenvalues of $\mathbf{T}^\dagger\mathbf{T}$,

$$\mathbf{T}\mathbf{T}^\dagger \mathbf{u}_i = \lambda_i \mathbf{u}_i \tag{3.3.74}$$

$$\mathbf{T}^\dagger\mathbf{T} \mathbf{v}_i = \lambda_i \mathbf{v}_i. \tag{3.3.75}$$

It follows that the occupied and virtual NTOs can be defined as

$$\phi_i^{\mathrm{NTO}} = \phi_i \mathbf{U} \qquad i = 1, \ldots, N_{\mathrm{occ}} \tag{3.3.76}$$

$$\phi_a^{\mathrm{NTO}} = \phi_a \mathbf{V} \qquad a = 1, \ldots, N_{\mathrm{occ}}. \tag{3.3.77}$$

Note that both indices stop at N_{occ} due to the mismatch of the dimensions of $\mathbf{T}\mathbf{T}^\dagger$ and $\mathbf{T}^\dagger\mathbf{T}$. Their first N_{occ} eigenvalues λ_i are identical, while $N_{\mathrm{virt}} - N_{\mathrm{occ}}$ virtual orbitals are mapped onto the null vector.

Next to transition density and molecular orbital analysis, probably the most frequently applied method to obtain insight into the nature of electronic excitations is to plot the one-particle electron difference density, simply defined as

$$\mathbf{\Delta} = \mathbf{P}_1 - \mathbf{P}_0 \tag{3.3.78}$$

for ground-state and excited-state electron densities $\mathbf{P}_0$ and $\mathbf{P}_1$, respectively. While the nodal shape of $\mathbf{\Delta}$ is often somewhat complicated, charge-transfer states are easily distinguished from localised valence excited states. Furthermore, difference densities are extremely simple to implement and are

readily available from most quantum-chemistry programme packages. The analysis of difference densities has found successful application in papers **A1**, **A2**, **A3**, and **B2**.

3.4 Optical properties

> Experiment is the only means of knowledge at our disposal. Everything else is poetry, imagination.
>
> – Max Planck[223]

In this final section of the theoretical part we will outline a few practical aspects when predicting optical properties of single molecules or molecular aggregates. Throughout we will stay in the linear regime and focus on absorption in the visible region (UV/Vis), electronic circular dichroism, which is important in the description of chiral compounds, and fluorescence emission spectroscopy. While the experimental results of all of these methods may be readily analysed employing linear-response TD-DFT or DFT/MRCI, there are a few critical aspects that should be addressed for each kind of measurement. Furthermore, a few issues arise when calculating excited states in solution due to the change in the mutual polarisation of the solute and the solvent.

3.4.1 Absorption

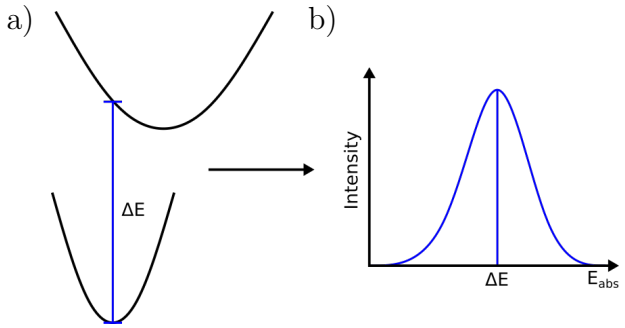

Figure 3.7: a) Franck-Condon principle: molecular electronic excitations are treated as vertical, b) line broadening: Calculations provide single line excitation spectra which can be artificially broadened for a better comparison to experimental spectra.

Molecular vibrations are typically encountered on a time scale of femtoseconds (10^{-15} s), whereas electrons usually operate on an attosecond time scale (10^{-18} s). This observation is crucial in the consideration of excited states in quantum chemistry. A photon carrying the correct amount of energy may raise a molecular system up to an excited state. After photoexcitation, the electronic structure is equilibrated much faster than the nuclei can react. As a result, electronic transitions proceed vertically, i.e., structural changes due to the shape of the excited PES can be assumed to occur *after* the excited state has been reached (**Fig. 3.7**a). This is known as the Franck-Condon (FC) principle and represents a fundamental tool in describing photophysical phenomena. A similar line of argumentation has been used in the Born-Oppenheimer approximation. The two approaches are directly linked since the FC principle depends on the existence of PESs.
In practice, absorption energies are typically overestimated for several reasons. The first is somewhat obvious and usually least significant. Electronic excitations, e.g., in the form of UV/Vis responses are certainly not exactly vertical in experiment but adiabatic, especially for molecules

with large structural reorganisation. The energy difference between the excited states is, hence, slightly reduced. A more severe effect is the fact that excited states are by nature more multi-referential than the ground state. As has been addressed earlier, single-reference approaches such as TD-DFT do not account for static electron correlation. The true excited state is therefore usually a little lower in energy as the calculated one. A remedy to this problem is to use multi-reference methods, e.g., DFT/MRCI. Lastly, since excited states are often associated with weakened bonding interactions, the PES of an excited state is usually much more shallow than that of the ground state. As a result, the zero-point energy (*cf.* **Eq. (3.2.26)**) of the ground state is notably larger than that of the excited state, decreasing the excitation energy in the measurement.
Absorption spectra obtained from the excitation energies of a theoretical calculation are line spectra. For a proper comparison of experiment and theory, often artificial line broadening is used, employing for example Gaussian functions (**Fig. 3.7**b). Natural line broadening is related to a number of effects,[224] one of which is Heisenberg's uncertainty principle,

$$\Delta E \Delta t \geq \frac{\hbar}{2}. \tag{3.4.1}$$

The necessarily finite time of measurement causes an uncertainty in energy ΔE, which is nothing else than a broadened spectroscopic signal. Therefore, a perfect line spectrum can in practice not be achieved. Moreover, absorption spectra can be influenced by electron-vibration (vibronic) coupling, which originates from the interaction of vibrational modes with electronic motion and introduces a well-defined fine structure into the absorption bands.
Another crucial aspect concerning the calculation of excited states is the influence of solvent effects.[225] The electronic changes induced in the solute polarise the environment and provoke a response of the surrounding solvent molecules. In accordance with the FC principle, electronic and nuclear motion can be decoupled in the solvent response. This leads to a separation into so-called fast and slow terms. The fast part of the polarisability response is associated with the electronic degrees of freedom of the solvent molecules, while the slow term corresponds to the structural response of the nuclei. The total polarisability $\mathbf{P}$ can hence be expressed as

$$\mathbf{P} = \mathbf{P}^{\text{fast}} + \mathbf{P}^{\text{slow}}. \tag{3.4.2}$$

The properties of $\mathbf{P}^{\text{fast}}$ and $\mathbf{P}^{\text{slow}}$ can be described within the two complementary partitioning theories of Marcus[226,227] and Pekar.[228]

3.4.1.1 Electronic circular dichroism

Chirality is a fundamental concept in chemistry and nature itself. Important examples are nearly all of the amino acids that make up the proteins and enzymes keeping us alive. Due to their three-dimensional dissymmetry chiral molecules interact differently with circularly polarised light than achiral compounds. In fact, this also applies to linearly polarised light, which is just a linear combination of equally contributing right and left circularly polarised light. Upon passing through a chiral medium, molar circular dichroism is measured as the difference between the extinction coefficients of the two circularly polarised lights,

$$\text{CD} = \Delta\varepsilon_{\text{LR}} = \varepsilon_{\text{L}} - \varepsilon_{\text{R}}, \tag{3.4.3}$$

although in practice for historical reasons the molar ellipticity $[\theta]$ is plotted, which is related to $\Delta\varepsilon_{\mathrm{LR}}$ simply by a factor, $[\theta] = 3298\Delta\varepsilon_{\mathrm{LR}}$. The CD spectra of two enantiomers are always mirror images of each other, since the sign of $\Delta\varepsilon_{\mathrm{LR}}$ will simply change. CD spectra obtained in the UV/Vis region are referred to as ECD spectra, because electronic excitations are measured. As has been well established, excitation energies can be obtained computationally with various methods. However, plain absorption spectra of two enantiomers look exactly the same, since oscillator strengths only depend on the magnitude of the electric transition dipole moment. The key quantity in optical activity measurements, on the other hand, is the rotational strength R, which depends not only on the electric but also on the magnetic transition dipole moment,

$$R_{0i} = \Im[\langle\Psi_0|\boldsymbol{\mu}_{\mathrm{el}}|\Psi_i\rangle\langle\Psi_0|\boldsymbol{\mu}_{\mathrm{mag}}|\Psi_i\rangle], \tag{3.4.4}$$

where the coupling is between ground state Ψ_0 and excited state Ψ_i. $\Im$ denotes the imaginary part of the product. The rotational strength can have positive and negative signs and is defined as the residue of the optical activity tensor $\mathbf{G}$ calculated from the Rosenfeld equation for a given excited state,[229]

$$\mathbf{G}(\omega) = -2\omega \sum_{i\neq 0} \frac{R_{0i}}{\omega_{0i}^2 - \omega^2}. \tag{3.4.5}$$

Apart from ECD, vibrational CD spectra can be measured in the IR region where molecular vibrations are stimulated. Standard DFAs usually perform well for the prediction of ECD spectra, although they are frequently outperformed by post-HF coupled-cluster methods.[230]

3.4.2 Emission

Various aspects determine the behaviour of a chemical system after photoexcitation into an excited state. These are usually summarised in a Jablonski diagram (**Fig. 3.8**). All excited systems will eventually lose their energy and drop down to the ground state again. It is convenient to differentiate radiative from non-radiative decay mechanisms. Perhaps the simplest form of a non-radiative decay pathway is vibrational relaxation (VR) where a vibrationally excited state transforms its energy into heat while the molecule falls into the minimum of the respective PES. VR alone is however never enough to completely dissipate the energy after an electronic excitation. Two other important non-radiative decay mechanisms are internal conversion (IC) and intersystem-crossing (ISC). Both describe the change in electronic state without the loss of energy. While IC conserves spin multiplicity (e.g., $S_2 \rightarrow S_1$), ISC changes it (e.g., $S_1 \rightarrow T_1$). The quantum-mechanical operators that describe IC and ISC are the non-adiabatic coupling (NAC), $d_{pq} = \langle\Psi_p|\nabla|\Psi_q\rangle$, and the spin-orbit coupling (SOC) interaction, $j_{pq} = a\langle\Psi_p|\hat{\mathbf{l}}\cdot\hat{\mathbf{s}}|\Psi_q\rangle$, respectively. SOC matrix elements are determined by the angular momentum operator $\hat{\mathbf{l}}$, spin operator $\hat{\mathbf{s}}$, and SOC constant a. ISC events with time scales ranging from 10^{-8} to 10^{-3} s are significantly slower than IC (10^{-14} to 10^{-11} s) since spin-flip transitions are spin-forbidden.[231]

Radiative decay or luminescence is the general term that summarises fluorescence and phosphorescence. Luminescence is the result of an excited system relaxing back to the ground state while dissipating energy through the release of photons. Fluorescence is associated with spin conservation, while phosphorescence involves two states with different spin multiplicities. As a result,

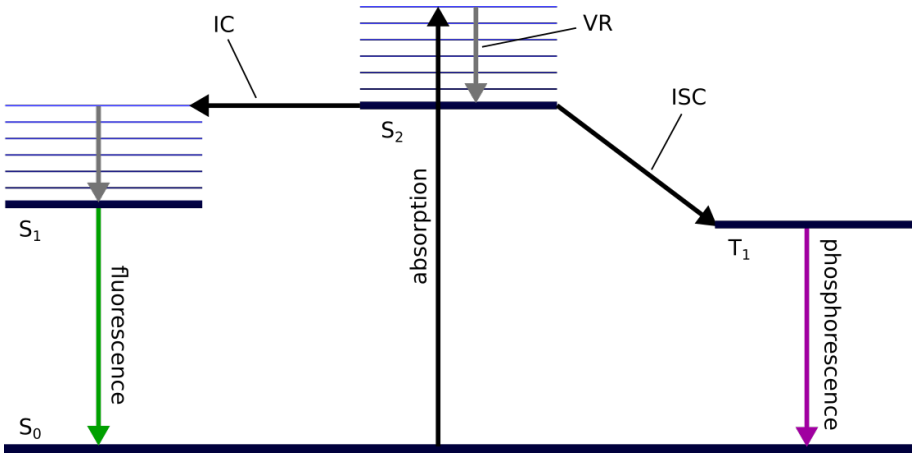

Figure 3.8: Jablonski diagram: internal conversion (IC) and intersystem-crossing link states of the same and of different multiplicity, respectively. Vibrational relaxation (VR) relaxes a molecule from its vibrationally excited state to the vibrational ground state of the respective electronic state.

fluorescence is quite fast (10^{-9} to 10^{-7} s) in comparison to the much slower phosphorescence observed on time scales from 10^{-3} to 1 s. In general, radiative decay mechanisms are slower than their non-radiative counterparts. Consequently, IC events lead to population of the lowest state accessible through NAC, before a radiative decay process can occur. Especially for organic molecules, this means that fluorescence is pretty much exclusively associated with an $S_1 \rightarrow S_0$ transition, if the electronic ground state is inaccessible through IC events. This observation is known as Kasha's rule[14] which is a useful concept in interpreting optical features of chemical systems.
From a computational point of view, emission is much harder to examine than absorption, simply because of the vastly different time scales involved in the processes. Absorption spectra are readily obtained from a linear-response TD-DFT calculation or DFT/MRCI using a single ground-state optimised structure of the molecule under investigation. Calculating fluorescence bands is, however, much less straight-forward as it necessitates excited-state structure optimisation. Excited PESs are usually somewhat more shallow, which means that the criteria involving the step size of the optimisation run have to be carefully assessed. Furthermore, solvation effects may lead to inconsistencies when studying excited states. The polarisation partitioning as outlined in **Eq. (3.4.2)** is a little more intricate, since the slow term has to be adjusted for an accurate optimisation of the solute. This is not easy to implement, which is why only few quantum-chemistry programme packages have done so.
Moreover, it is rarely the case that excited-state PESs are completely separated from all other states. Conical intersections involving multiple state crossings can be the result. These situations often require a resource-demanding quantum-dynamics treatment as the Born-Oppenheimer approximation breaks down. Especially charge-transfer states pose a tedious problem, if these are not well described within the excited-state calculation.

3.4.2.1 H- and J-aggregates

As addressed in the introduction, H- and J-aggregates are part of a classification scheme for molecular aggregates initially proposed by Eion McRae and Michael Kasha[12,13] in the late 1950s. In general, aggregates showing a hypsochromically (blue) shifted absorption band with respect

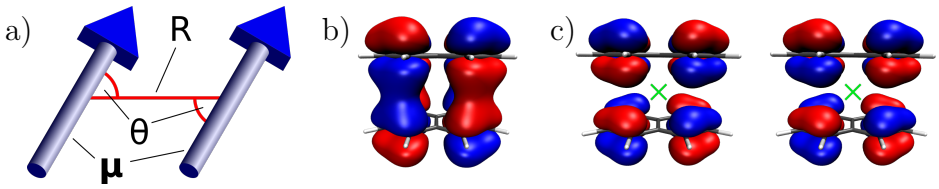

Figure 3.9: a) Coulomb coupling of two parallel transition dipole moments, b) short-range wavefunction overlap illustrated by the delocalisation of the second highest occupied orbital of a naphthalene dimer (isovalue = 0.02 a_0^{-3}), c) in-phase (left) and out-of-phase (right) combination of two monomer HOMOs (isovalue = 0.04 a_0^{-3}), centres of inversion are represented by a green cross. Orbitals were obtained at the PBE0/def2-SVP[105,106] level, isosurfaces were calculated with ORBKIT.[202]

to that of the isolated monomer are known as H-aggregates, while chromophores exhibiting a bathochromic (red) shift are referred to as J-aggregates due to Edwin Jelley.[7,8] Put in more theoretical terms, H-aggregates favour population of a high-energy state (usually S_2), while in J-aggregates the low-energy state (usually S_1) consumes all of the oscillator strength. According to Kasha's rule, this implies that H-aggregates are barely or even non-emissive, since the S_1 is a dark state. On the other hand, emission in J-aggregates may even be enhanced.[11]
Kasha's model is based on Coulomb-coupled transition dipole moments based on Davydov's exciton theory,[232]

$$J_{\text{Coul}} = \frac{\mu^2(1 - 3\cos^2(\theta))}{4\pi\varepsilon R^3}. \tag{3.4.6}$$

Fig. 3.9a illustrates the coupling of two monomers represented by their transition dipoles. R is the intermolecular distance between the centres of mass of the monomers, θ is the angle between $\boldsymbol{\mu}$ and $\mathbf{R}$, and ε refers to the permittivity of the medium. In this framework, H- and J-aggregates are defined by positive and negative values of J_{Coul}, respectively.
While Kasha's ideas have been successfully applied to a number of systems,[233–237] in recent years, several non-Kasha aggregates were found. Examples include fluorescent H-aggregated phthalocyanines,[15] "red-shifted H-aggregates",[16,17] or "null-aggregates", in which the aggregate absorption band resembles the monomer signal.[18] To account for these unusual observations, Spano and coworkers[238] have identified charge-transfer mediated short-range wavefunction overlap (**Fig. 3.9**b),

$$J_{\text{CT}} \propto -t_{\text{e}}t_{\text{h}}, \tag{3.4.7}$$

as another key concept in addition to Kasha's long-range Coulomb coupling. J_{CT} exhibits a significantly different spatial behaviour in comparison to J_{Coul} since the electron- and hole-transfer integrals, t_{e} and t_{h}, depend on the nodal structures of the molecular orbitals (MOs) involved. t_{e} is related to the splitting of the two monomer LUMOs, $\phi^{\text{L}}_{\text{M}_1}$ and $\phi^{\text{L}}_{\text{M}_2}$, and t_{h} to the splitting of the two monomer HOMOs, $\phi^{\text{H}}_{\text{M}_1}$ and $\phi^{\text{H}}_{\text{M}_2}$, upon dimer formation.[239] The sign of the integrals is essential in determining H- or J-like behaviour and depends on the symmetry and phase of the MOs. For inversion symmetric systems, we may define the phase using the inversion operator $\hat{i}$ (**Fig. 3.9**c),

$$\hat{i}\phi_{\text{M}_1} = +\phi_{\text{M}_2} \text{ (in-phase)}$$
$$\hat{i}\phi_{\text{M}_1} = -\phi_{\text{M}_2} \text{ (out-of-phase)}$$

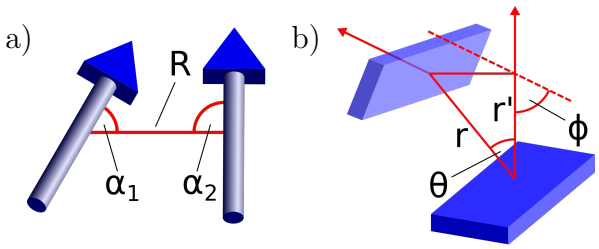

Figure 3.10: a) Förster transfer mode mediated through Coulomb coupling of two transition dipole moments, b) Dexter mode mediated orbital overlap of two close molecular planes represented by blue planes.

As usual, we define

$$\psi^{\mathrm{H}} = \frac{1}{\sqrt{2}}(\phi^{\mathrm{H}}_{\mathrm{M}_1} - \phi^{\mathrm{H}}_{\mathrm{M}_2}) \qquad \psi^{\mathrm{L+1}} = \frac{1}{\sqrt{2}}(\phi^{\mathrm{L}}_{\mathrm{M}_1} - \phi^{\mathrm{L}}_{\mathrm{M}_2}) \tag{3.4.8}$$

$$\psi^{\mathrm{H-1}} = \frac{1}{\sqrt{2}}(\phi^{\mathrm{H}}_{\mathrm{M}_1} + \phi^{\mathrm{H}}_{\mathrm{M}_2}) \qquad \psi^{\mathrm{L}} = \frac{1}{\sqrt{2}}(\phi^{\mathrm{L}}_{\mathrm{M}_1} + \phi^{\mathrm{L}}_{\mathrm{M}_2}) \tag{3.4.9}$$

If ψ^{L} corresponds to an in-phase (symmetric or *gerade*) and $\psi^{\mathrm{L+1}}$ to an out-of-phase (antisymmetric or *ungerade*) linearly combined dimer MO, t_{e} has a negative sign because the interaction is stabilising. The same argument applies to the phases of $\psi^{\mathrm{H-1}}$ and ψ^{H} for t_{h}.[238]
Within this framework "HJ-aggregates" are possible owing to a subtle interplay of both coupling mechanisms.[19,20] If long-range and short-range coupling originates from different sets of molecules, the assembly is called *segregated*.[240] If both interactions arise from the same set of molecules, e.g., from a single dimer, the aggregate is referred to as *integrated*. Conjugated π-stacked perylene polymers fall into the segregated HJ category,[241] while nanopillars of 7,8,15,16-tetraazaterrylene (TAT) are an example for integrated HJ-aggregates.[242] The diaminodicyanoquinone (DADQ) aggregates examined in paper **A2** can partly be identified as integrated HJ-aggregates.

3.4.2.2 Emission quenching in solids

Especially in the solid state, the formation of H-type aggregates is often quite undesirable due to their non-emissive properties. Probably the most prominent emission quenching mechanisms in organic crystals are Förster resonance energy transfer (FRET), effective over comparably long ranges (> 10 Å), and the short-range Dexter process. While FRET is mediated through (transition) dipole coupling, Dexter transfer is caused by short-range wavefunction overlap and is, hence, most frequently encountered in π-π-stacked chromophores. Radhakrishnan and co-workers have developed a model to estimate relative Förster and Dexter energy transfer rates for DADQs using simple geometric arguments.[243,244] **Fig. 3.10** illustrates both mechanisms corresponding to the following relations,

$$k_{\mathrm{F}} \propto \frac{[3\cos(\alpha_1)\cos(\alpha_2) + \cos(\alpha_1 + \alpha_2)]^2}{R^6} \tag{3.4.10}$$

$$k_{\mathrm{D}} \propto \cos(\theta)\cos(\phi)\mathrm{e}{-r'} = \cos(\theta)\cos(\phi)\mathrm{e}^{-r\cos(\theta)}. \tag{3.4.11}$$

R connects the centres of mass of the molecules and α_1 and α_2 are the angles between R and the respective transition dipole in **Eq. (3.4.10)**. r and r' in **Eq. (3.4.11)** refer to the centre of plane

distance and the perpendicular distance between the π-planes, respectively. θ defines the angle between the normal vector of the first plane and $\mathbf{r}$, while ϕ describes the interplanar angle between the two π-systems.
Radhakrishnan and co-workers employed this approach to a series of similar DADQs to rationalise fluorescence quantum yield trends in the solid state. Their methods have found successful application in paper **A3**.

4 Publications

4.1 Paper A1

"Diaminodicyanoquinones: Fluorescent Dyes with High Dipole Moments and Electron-Acceptor Properties"

P. Rietsch,* F. Witte,* S. Sobottka, G. Germer, A. Becker, A. Güttler, B. Sarkar, B. Paulus, U. Resch-Genger, S. Eigler
Angew. Chem. Int. Ed. **2019**, 58, 8235–8239.
DOI: 10.1002/anie.201903204
URL: https://doi.org/10.1002/anie.201903204
* Co-first authors

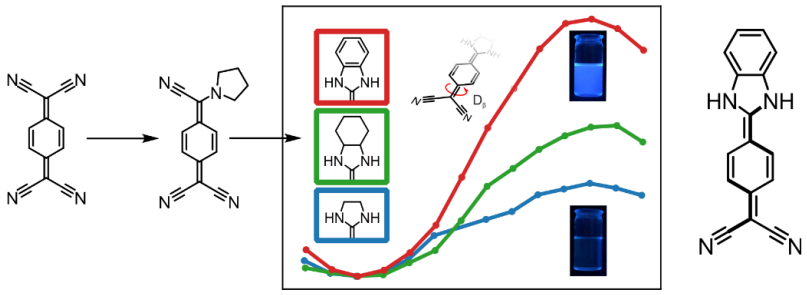

Figure 4.1: Graphical abstract of paper **A1**.

Contributions

Philipp Rietsch and Felix Witte are co-first authors of this publication. The general concept was conceived by P.R., F.W., and Siegfried Eigler. All computational work was conducted by F.W. Gregor Germer synthesised and characterised compounds 5 and 6. Alexander Becker synthesised and characterised compound 7. The remaining experimental work was performed by P.R. Cooling experiments were conducted with help from A.B. Sebastian Sobottka performed cyclic voltammetry (CV) measurements and analyses. The manuscript was mainly written by P.R., F.W., and S.E. All authors contributed to the final version of the manuscript.

4.2 Paper A2

"Fluorescence quenching in J-aggregates through the formation of unusual metastable dimers"

F. Witte, P. Rietsch, S. Sinha, A. Krappe, J.-O. Joswig, J. P. Götze, N. Nirmalananthan-Budau, U. Resch-Genger, S. Eigler, B. Paulus
Reproduced with permission from *The Journal of Physical Chemistry B*, submitted for publication. Unpublished work copyright 2021 American Chemical Society."

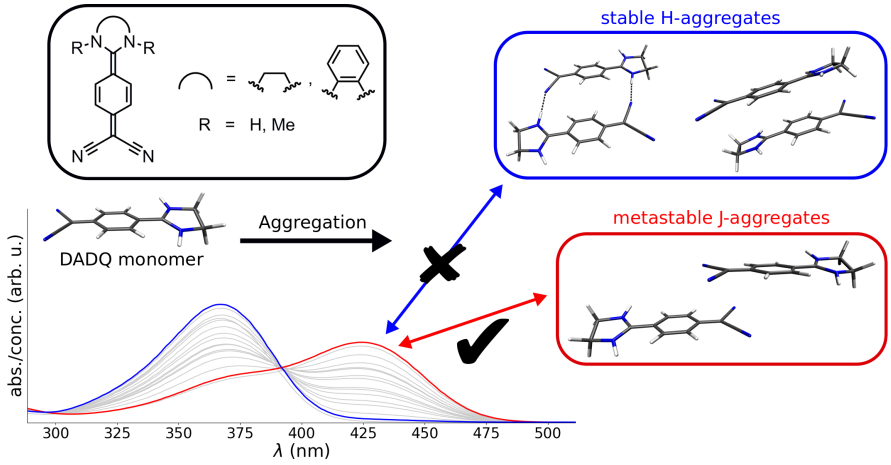

Figure 4.2: Graphical abstract of paper **A2**.

Contributions

The project was conceived by Felix Witte and Philipp Rietsch. F.W. designed and performed all quantum-chemical calculations and wrote the manuscript. J. Joswig aided in analysing ab-initio MD simulations. Alexander Krappe synthesised and characterised compounds $1Me_2$, 2Me, and $2Me_2$. Shreya Sinha performed viscosity measurements and helped with the photophysical characterisation of all compounds. P.R. prepared and conducted all remaining experimental work. All authors contributed to the final version of the manuscript.

Fluorescence quenching in J-aggregates through the formation of unusual metastable dimers

Felix Witte,[1]* Philipp Rietsch,[2] Shreya Sinha,[3] Alexander Krappe,[2] Jan-O. Joswig,[1] Jan P. Götze,[1] Nithiya Nirmalananthan-Budau,[3] Ute Resch-Genger,[3] Siegfried Eigler,[2] and Beate Paulus[1]

Abstract: Molecular aggregation alters the optical properties of a system as fluorescence may be activated or quenched. This is usually described within the well-established framework of H- and J-aggregates. While H-aggregates show nonfluorescent blue-shifted absorption bands with respect to the isolated monomer, J-aggregates are fluorescent displaying a red-shifted peak. In this publication, we employ a combined approach of experiment and theory to study the complex aggregation features and photophysical properties of diaminodicyanoquinone (DADQ) derivatives, which show unusual and puzzling nonfluorescent red-shifted absorption bands upon aggregation. Our theoretical analysis demonstrates that stable aggregates do not account for the experimental observations. Instead, we propose an unprecedented mechanism involving metastable dimeric species forming from stable dimers to generate nonfluorescent J-aggregates. These results represent a novel kind of aggregation-induced optical effect and will have broad implications for the photophysics of dye aggregates.

Introduction

Understanding molecular aggregation processes[1,2] is fundamental for various fields of research including organic semiconductors[3–7] and light emitting diodes (OLEDs),[8–11] non-linear optics,[12–15] and the vast realm of supramolecular chemistry.[16–18] In 1958 Michael Kasha proposed that chromophore aggregates may be categorized on the basis of Coulomb-coupled transition dipole moments using Davydov's exciton theory.[19–21] Compounds which showed a hypsochromic shift (blue-shift) at their absorption band with respect to the monomer signal upon aggregation are meanwhile known as H-aggregates, while chromophores exhibiting a bathochromic shift (red-shift) are termed J-aggregates.[22] According to Kasha's rule,[23] fluorescence progresses from the lowest singlet excited state. Hence, H-aggregates are commonly barely or even non-emissive as excitation into a high-energy state favors intersystem-crossing or related events leading to strong fluorescence quenching. Emission in J-aggregates, on the other hand, may even be enhanced since the low-energy state consumes all of the oscillator strength.[24]

[1] *F. Witte, J.-O. Joswig, J. P. Götze, Prof. Dr. B. Paulus*
Institute of Chemistry and Biochemistry
Freie Universität Berlin
Arnimallee 22, 14195 Berlin, Germany
E-mail: jf.witte@fu-berlin.de

[2] *P. Rietsch, A. Krappe, Prof. Dr. S. Eigler*
Institute of Chemistry and Biochemistry
Freie Universität Berlin
Takustr. 3, 14195 Berlin, Germany

[3] *S. Sinha, N. Nirmalananthan-Budau, U. Resch-Genger*
Division Biophotonics
Federal Institute for Material Research and Testing (BAM)
Richard-Willstätter-Straße 11, 12489 Berlin, Germany

While Kasha's ideas have been successfully applied to a number of systems,[25–29] in recent years, several non-Kasha aggregates were found. Examples include fluorescent H-aggregated phthalocyanines,[30] "red-shifted H-aggregates",[31,32] or "null-aggregates", in which the aggregate absorption band resembles the monomer signal.[33] To account for these unusual observations, Spano and coworkers[34] have identified short-range wave-function overlap as a key concept in addition to Kasha's long-range Coulomb coupling. Within this framework "HJ-aggregates" are possible owing to a subtle interplay of both coupling mechanisms.[35,36] If long-range and short-range coupling originates from different sets of molecules, the assembly is called *segregated*.[37] If both interactions arise from the same set of molecules, e.g., from a single dimer, the aggregate is referred to as *integrated*. Conjugated π-stacked perylene polymers fall into the segregated HJ category,[38] while nanopillars of 7,8,15,16-tetraazaterrylene (TAT) are an example for integrated HJ-aggregates.[39]

Here, we present results on the complex aggregation behavior and unusual photophysical properties of diaminodicyanoquinone (DADQ) compounds in solution. DADQs are a class of redox-active organic molecules derived from 7,7,8,8-tetracyanoquinodimethane (TCNQ) displaying notably high dipole moments of up to 30 Debye, which may additionally exhibit large fluorescence quantum yields (QYs) exceeding 90%.[40,41] In this study, we examine concentration-dependent absorption spectra and study the emission properties of a series of non-, singly-, and doubly-methylated DADQ compounds. This reveals red-shifted absorption bands upon aggregation which did not show any relevant fluorescence in excitation-emission matrices.

Using a combination of experimental and quantum-chemical

approaches, we demonstrate that DADQs cannot be classified as typical H- or J-aggregates according to Kasha, as they behave similarly to integrated HJ-aggregates according to Spano and co-workers. However, neither the red-shifted absorption bands nor the insignificant emission can be explained by these models. To unravel the extremely vast conformational landscape of DADQ aggregates, we employ dispersion-corrected DFT (density functional theory) based methods with an emphasis on dimers. Finally, inspired by studies in the literature involving H- to J-aggregation,[42,43] we propose a dynamic mechanism based on high-level DFT/MRCI[44,45] (multi-reference configuration interaction) calculations and Spano's extended HJ-aggregate theory that includes short-lived, metastable dimers. These systems can be interpreted as nonfluorescent J-aggregates.

Results and Discussion

Synthesis. All substances were prepared according to literature by coupling 7-pyrrolidino-7,8,8-tricyanoquinomethane (PTCNQ) and the respective diamine (Scheme 1).[41,46] We differentiate DADQs **1**, **1Me**, and **1Me$_2$** possessing an ethylene-bridged diamino moiety from their benzene-functionalized counterparts **2**, **2Me**, and **2Me$_2$** (Figure 1).

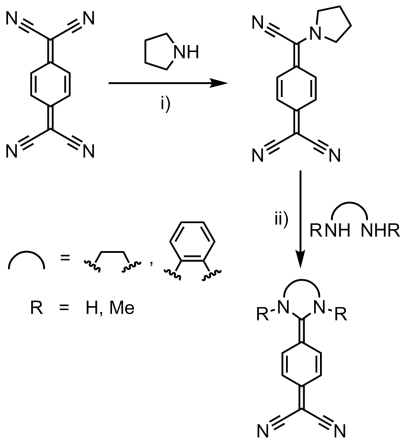

Scheme 1: Synthetic route to DADQ derivatives starting from TCNQ by reaction with pyrrolidine and subsequent reaction with the respective primary or secondary diamine. i) 0.8 eq. pyrrolidine, 70 °C, 4 hours. ii) 1 eq. of the respective diamine, 70 °C, 2–20 hours. Detailed protocols, yields and the characterization of the compounds can be found in the Supporting Information.

Concentration-dependent absorption spectra. Figure 1 shows the concentration-dependent UV/Vis absorption spectra of all compounds. Molecule **2Me**, featuring a single tertiary amine, yields a yellow solution in ACN (insets in Figure 1) with an absorption maximum at 425 nm, which loses its color after dilution to 10^{-5} M yielding an absorption maximum at 367 nm. Its isosbestic point at 398 nm indicates a straightforward transformation without side products. We observe an analogous behavior for compound **1Me** and, with

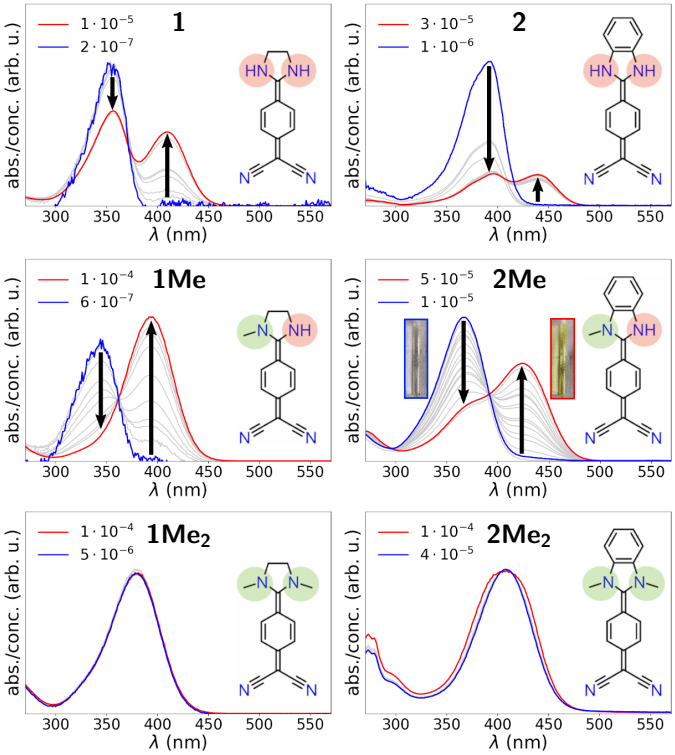

Figure 1: Concentration dependent UV/Vis absorption spectra and Lewis structures of **1**–**2Me$_2$**. The different amine substitution patterns are highlighted. Depicted is the absorbance divided by the concentration of each respective curve. Compound **2** was recorded in DMSO, all other molecules in ACN. Arrows point in the direction of increasing concentration. Minimum and maximum concentrations are given in mol·L^{-1} in the figure.

slightly less clear isosbestic points, for **1** and **2**. **1Me$_2$** and **2Me$_2$**, both equipped with two tertiary amines, only show one absorption maximum at 380 nm and 409 nm, respectively.

To gain insight into the nature of the aggregates and to probe their stability, we recorded absorption spectra at varying temperatures, solvent polarities (DMSO and H_2O), and viscosities as external stimuli. Temperature-dependent spectra measured in ACN varying from 25 °C to 75 °C (Figure S3) revealed that, if two absorption maxima are present, the high-energy band is intensified and the red-shifted absorption peak is weakened upon increasing temperatures. Theoretical analyses show that a dimer formation of **1** is accompanied by a gain in free enthalpy of around –18 kJ/mol, which is reduced to roughly –7 kJ/mol at 75 °C.

Addition of 10 μL of polar additives DMSO (1760 eq.) and H_2O (7000 eq.) to 1 mL of a $8{\cdot}10^{-5}$ M ACN solution of **2Me** leads to a strong reduction of the absorption band at longer wavelengths and an increase of the band at shorter wavelengths (Figure S4). The red-shifted band vanishes after an addition of 14000 eq. H_2O or 8800 eq. DMSO. Increasing the viscosity, polarity, and proticity by adding polyethylene glycol to an ACN solution of **2Me** has a comparable effect (Figure S5). This illustrates the reduction of hydrogen-bonding

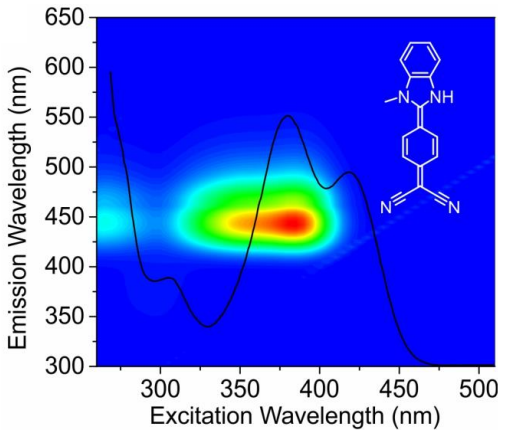

Figure 2: Excitation-emission-matrix of **2Me** in ACN at $2{\cdot}10^{-5}$ M. Overlayed in black is the respective absorption spectrum at the same concentration.

Table 1: Free enthalpies of association in kJ/mol for the formation of a dimer conformation from two monomers in ACN at 298.15 K and average amount of electrostatic interaction (⌀ ES) in per cent contributing to the stabilizing part of the electronic energy in each conformation.

	A_{HB}	A_{ST}	A_{SD}	S_{HT}	S_{ST}
1	–17.7	–16.4	–7.9	+22.8	+39.7
1Me	–16.2	–7.8	–9.2	+21.1	+51.4
1Me$_2$	+12.3	—	+3.6	—	—
2	–20.1	–14.9	–5.2	+17.3	+24.1
2Me	–21.5	+3.8	–11.4	+15.7	+37.0
2Me$_2$	+14.7	—	+15.2	—	—
⌀ ES	73.6	52.7	59.9	40.3	7.8

and dipole-dipole interactions by polar molecules. As will be shown later on, energy decomposition analyses (EDA) confirm that the stabilizing interaction between two monomers is mostly due to electrostatic effects.

Emission properties. **1Me$_2$** and **2Me$_2$** are nonfluorescent and the non-benzene functionalized derivatives **1**, **1Me**, and **1Me$_2$** possess much lower QYs (1–10%) showing a similar trend with respect to methylation as **2**, **2Me**, and **2Me$_2$** (Table S1).[41] **2Me** shows large QYs comparable to those of **2** with two notable exceptions in THF (3%) and DMSO (4%). Fluorescence quenching is likely facilitated through intersecting states (intersystem crossing or internal conversion) on the potential energy surface (PES) depending on the solvent.[41] Fluorescence lifetimes do not show a coherent trend with respect to substance, solvent, or QY.
Red-shifted absorption peaks with respect to the monomer band are indicative of J-aggregates. According to Kasha's rule,[23] J-aggregates should not show significantly diminished fluorescence quantum yields. However, excitation emission matrices (EEM) of **1Me**, **2** and **2Me** display no or only very weak emission for the red-shifted peak compared to the monomer absorption band. Figure 2 shows this exemplarily for **2Me** in ACN. Similar results are found for **1Me** in ACN and **2** and **2Me** in MeOH (Figure S7 and S8). Thus, DADQs represent a counterexample to Kasha's exciton model.[19] As will be discussed in more detail later, the low emission rates are likely explained by the lowest singlet excited state, S_1, losing its oscillator strength upon relaxation. In the following, we will perform a thorough analysis of the thermodynamic and optical properties of DADQ aggregates employing state-of-the-art quantum-chemical methods.

Thermodynamic properties of DADQ aggregates. To obtain insight into the conformational landscape of our DADQs, we performed metadynamics simulations based on Grimme's GFN2-xTB program[47] and extracted the most relevant structures upon visual inspection. Association free enthalpies for all aggregated complexes were obtained using the PBEh-3c composite method[48] for optimization and normal mode analysis, the ωB97X-D3[49] functional for single point energies, and the COSMO-RS[50] approach for solvation effects (see section 5 in the Supporting Information for computational details). Figure 3 compares different DADQ dimer structures in solution using the example of **1**. Other dimer conformations can be found in Figure S9. We differentiate *anti*- (A_{HB}, A_{ST}, A_{SD}) from *syn*-dimers (S_{HT}, S_{ST}) owing to the alignment of the monomers. Conformation A_{HB} is characterized by a nearly planar structure with hydrogen bonds connecting the amines and the cyano moieties in an almost linear fashion ($\measuredangle$ H$\cdots$N$\equiv$C $\approx$ 153 °). While in A_{ST} monomers are stacked directly on top of each other, the monomers in A_{SD} are slightly displaced enabling tilted hydrogen bonds. S_{HT} is a slightly bent head-to-tail-like structure and S_{ST} is the *syn* analogue of conformation A_{ST}, which is somewhat displaced due to repeling charge densities of the monomers.
Table 1 summarizes the free association enthalpies (ΔG_a) of all dimers in ACN at 298.15 K with additional indication of the average amount of electrostatic interaction contributing to the total electronic stabilization. A summary of the individual contributions to ΔG_a can be found in Table S4. All *anti*-dimers are found to be more stable than their *syn* counterparts due to the stabilizing Coulomb interaction of canceling monomer dipole moments. Both *syn*-dimers are unstable with respect to dissociation into monomers.
Energy decomposition analysis (EDA) based on the fragment molecular orbital (FMO) scheme[51,52] illustrates and confirms that most of the stabilization ($\approx$ 50–75%, Table 1) between the monomers in the *anti*-dimers is due to electrostatic interaction, i.e., the canceling of dipole moments and hydrogen bonding. Other contributions originate from charge transfer (orbital interaction) and dispersive interactions (electron correlation). In contrast, *syn*-dimers are mainly stabilized through dispersive interactions, amounting to roughly 90% in **1**-S_{ST} (i.e., compound **1** in conformation S_{ST}) and **1Me**-S_{ST}.

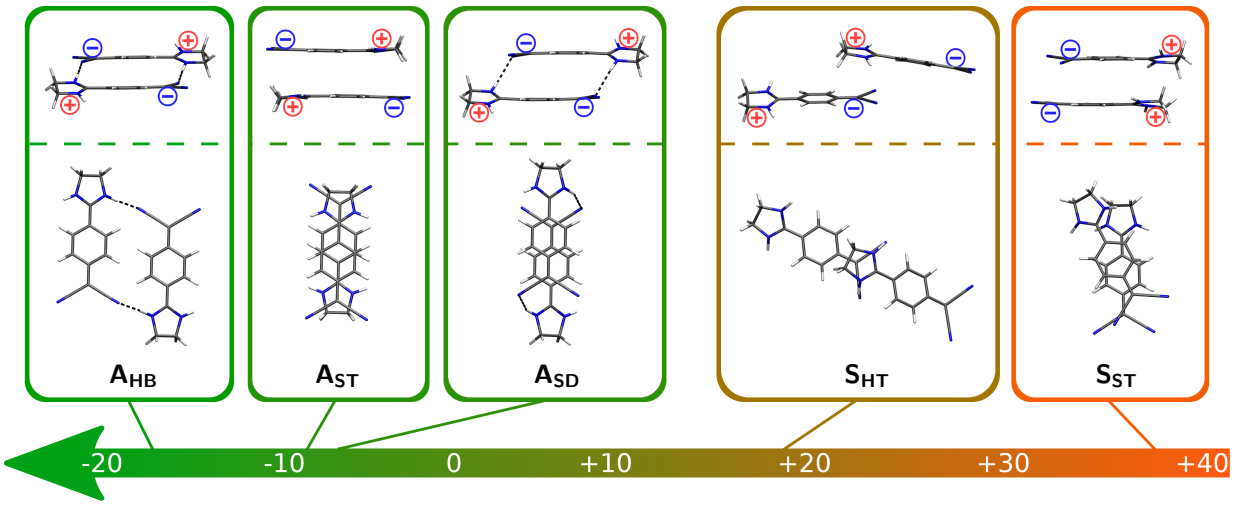

Figure 3: Total dipole moment canceling (*anti*-) and accumulating (*syn*-) dimer conformations analyzed in this study using the example of **1**. Two viewpoints are used for every structure separated by a dashed line. Positive and negative symbols indicate charge distributions in the monomers. A free enthalpy scale relative to two infinitely separated monomers is displayed with an arrow pointing in the direction of increasing stability. $\mathbf{A_{HB}}$: hydrogen-bonded *anti*-dimer, $\mathbf{A_{ST}}$: *anti*-dimer with monomers stacked directly on top of each other, $\mathbf{A_{SD}}$: *anti*-dimer with monomers stacked in a slightly displaced manner, $\mathbf{S_{HT}}$: *syn*-dimer with monomers stacked in a head-to-tail fashion, $\mathbf{S_{ST}}$: *syn*-dimer with monomers stacked on top of each other.

In agreement with our experimental findings, **1Me$_2$** and **2Me$_2$** do not form stable dimers due to the absence of hydrogen bonds and lack of efficient π-stacking sterically inhibited by the two methyl groups. In ACN all other *anti*-dimer conformations, except for **2Me**-A_{ST}, are stable with respect to dissociation with A_{HB} being most stable in all cases. In contrast to A_{HB}, conformation A_{ST} exhibits a stronger variation in stability with respect to the different systems. Notably, compound **2Me**-A_{ST} is significantly destabilized. This can be attributed to the distorted planarity of the singly-methylated monomers resulting in deteriorated π-stacking. In comparison, this effect is much less pronounced in **1Me**-A_{ST} that still possesses polarized hydrogen atoms at the ethylene bridge pointing toward the neighboring dicyano moieties (Figure S10). Interestingly, in DMSO (Table S3) we observe quite a different trend. Here, conformation A_{ST} is usually the most stable one (with the exception of **2Me** where all dimers are unstable). The general destabilization of the aggregates in DMSO is in agreement with our experimental finding that polar additives seem to break up DADQ aggregates.
Clearly, DADQs exhibit complex aggregation behavior already at the dimer level. In addition, our calculations predict complexes up to the size of hexamers that are still stable at room temperature (Table S9). Especially arrangements in which *anti*-conformations are stacked on top of each other show a significant stabilization (Figure S11).

H- and J-like properties of DADQ aggregates. To rationalize the photophysical properties of DADQ aggregates, we employed the DFT/MRCI[53] approach, which is particularly useful for the treatment of molecular aggregates.[54] In Kasha's exciton model[19] H- and J-aggregates are distinguished using the Coulomb coupling of the monomer transition dipole moments, $\boldsymbol{\mu}$:

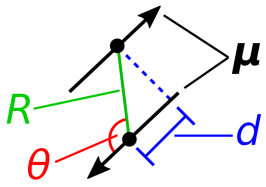

Figure 4: Structural parameters describing the relative orientation of two transition dipole moments (black arrows) which in turn define H- and J-aggregates according to equation (1).

$$J_{\mathrm{Coul}} \approx -\frac{\mu^2(1-3\cos^2(\theta))}{4\pi\varepsilon R^3} \qquad (1)$$

where R is the intermolecular distance between the centers of mass, θ is the angle between $\boldsymbol{\mu}$ and $\mathbf{R}$, and ε is the permittivity of the medium. We furthermore consider the displacement coordinate d as the projected distance between centers of mass (Figure 4). J_{Coul} is zero at $\theta = 54.7\,^\circ$ $(\arccos(1/\sqrt{3}))$. The negative sign deviates from Kasha's original model and originates from the antiparallel orientation of the transition dipole moments in the *anti*-dimers. In this framework, H- and J-aggregates correspond to negative and positive values of J_{Coul}.[55] Application of equation (1) to stable DADQ dimers predicts H-like features for conformations A-$_{HB}$ and A-$_{ST}$ and J-like features for A-$_{SD}$.
However, to our surprise, DFT/MRCI calculations predict a bright high-energy (S_2) state for all stable DADQs, including conformation A_{SD} (Table S12). Table 2 compares calculated and experimental spectral data for the monomers and *anti*-dimers of **1**, **1Me**, **2**, and **2Me** (see Table S10 for *syn*-dimers). The computed differences between the compounds are in good agreement with experiment. The deviations in

Table 2: Calculated absorption wavelengths in nm for the monomers and all *anti*-dimers of compounds **1**, **1Me**, **2**, and **2Me** obtained at the SMD/BHLYP/def2-TZVP(-f)/MRCI level in comparison to experimental values. Monomers are compared directly, while dimers are compared using energetic shifts with respect to the monomer signal. Experimental and metastable dimer shifts (see text) are given in eV as well for better comparability.

	1	**1Me**	**2**	**2Me**
$\lambda_{\mathrm{exc,mon}}$ (exp.)	355	344	392	366
$\lambda_{\mathrm{exc,mon}}$ (calc.)	375	355	420	399
A_{HB}	–6	–4	–12	–8
A_{ST}	+1	+11	+20	+13
A_{SD}	–1	+3	–6	+2
exp. (nm)	+55	+50	+48	+57
exp. (eV)	–0.47	–0.46	–0.35	–0.47
metastable dimer (nm)	+41	+34	+37	+47
metastable dimer (eV)	–0.33	–0.31	–0.24	–0.33

absolute values are all within the range of 0.1–0.2 eV and may be explained by a slight inaccuracy in the description of the partial charge-transfer character of the monomer, which is a well-known shortcoming of DFT/MRCI.[45] Repition of all excited-state calculations at the ωB97X-D3 level of TD-DFT showed overall qualitative agreement (Tables S11 and S13 and Figures S15 and S16) confirming our results.

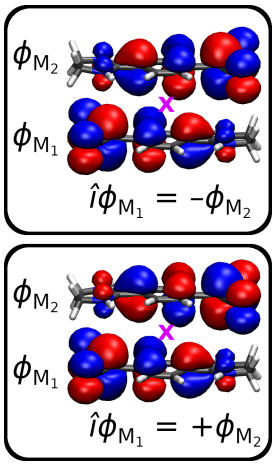

Figure 5: Illustration of an in-phase (bottom) and an out-of-phase (top) combination of two monomer MOs with respect to inversion operator $\hat{i}$ using the example of **1**-A_{ST}. The center of inversion is indicated by a purple cross. Plots were generated with ORBKIT,[56] isovalue = 0.02 a_0^{-3}.

The discrepancy between J_{Coul} and the ordering of the bright and dark state predicted by DFT/MRCI implies that long-range Coulomb coupling is insufficient for an accurate description of DADQ aggregates. In recent years, Spano and co-workers[38] have established that short-range wavefunction overlap between monomers in close proximity may result in charge-transfer mediated exciton coupling, J_{CT},

$$J_{\mathrm{CT}} \propto -t_{\mathrm{e}} t_{\mathrm{h}}. \tag{2}$$

J_{CT} exhibits a significantly different spatial behavior in comparison to J_{Coul} since the electron- and hole-transfer integrals, t_{e} and t_{h}, depend on the nodal structures of the molecular orbitals (MOs) involved. t_{e} and t_{h} are related to the splitting of the two monomer LUMOs, $\phi^{\mathrm{L}}_{\mathrm{M}_1}$ and $\phi^{\mathrm{L}}_{\mathrm{M}_2}$ and HOMOs, $\phi^{\mathrm{H}}_{\mathrm{M}_1}$ and $\phi^{\mathrm{H}}_{\mathrm{M}_2}$, upon dimer formation.[57] The sign of the integrals is essential in determining H- or J-like behavior and depends on the symmetry and phase of the MOs. Since DADQ *anti*-dimers display inversion symmetry (**1** and **2**: C_{2h}, **1Me** and **2Me**: C_i), we may conveniently define the phase using the inversion operator, $\hat{i}$ (Figure 5):

$$\hat{i}\phi_{\mathrm{M}_1} = +\phi_{\mathrm{M}_2} \text{ (in-phase)}$$
$$\hat{i}\phi_{\mathrm{M}_1} = -\phi_{\mathrm{M}_2} \text{ (out-of-phase)}$$

If ψ^{LUMO} corresponds to an in-phase (symmetric or *gerade*) and $\psi^{\mathrm{LUMO+1}}$ to an out-of-phase (antisymmetric or *ungerade*) linearly combined dimer MO, t_{e} has a negative sign because the interaction is stabilizing. The same argument applies to the phases of $\psi^{\mathrm{HOMO-1}}$ and ψ^{HOMO} for t_{h}.[34] Applying this scheme to the stable DADQ *anti*-dimers gives positive signs for J_{CT} in every case, indicating H-like properties. The subtle coaction of J_{CT} and J_{Coul} can be evaluated within the essential states model (ESM)[32,55] and can explain the computed energetic shifts of conformations A_{HB}, A_{ST}, and A_{SD} (Table 2). For instance, a vanishing total coupling $(J_{\mathrm{CT}} + J_{\mathrm{Coul}})$ may result in a dimer absorption band coinciding with the monomer band, which is the case in **1**-A_{ST}. Within this framework stable DADQ dimers can be referred to as integrated HJ-aggregates.

Unraveling absorption and fluorescence properties. The data presented in Table 2 clearly confirm that the experimental observations cannot be explained by stable dimers. Another explanation could be higher aggregates. As DFT/MRCI becomes prohibitively resource-demanding for large molecules, we have computed excited states for various trimers and tetramers of **1** at the ωB97X-D3 level of TD-DFT (Table S14). This is justified as we have seen qualitative agreement to DFT/MRCI at the dimer level. However, none of the examined oligomers yield the desired red-shift, even if we take into account that TD-DFT consistently overestimates excitation energies with respect to both the experiment and DFT/MRCI.

Since J-aggregates typically produce red-shifted absorption signals, we assumed that there might be a hidden mechanism involving H- to J-aggregation, as for example observed in various perylene derivatives.[42,43] Hence, we performed a relaxed PES scan along the displacement coordinate d (Figure 4) in a π-stacked *anti*-dimer of **1** (Figure 6) and **2** (Figure S14). The dimers essentially switch between Kasha J-

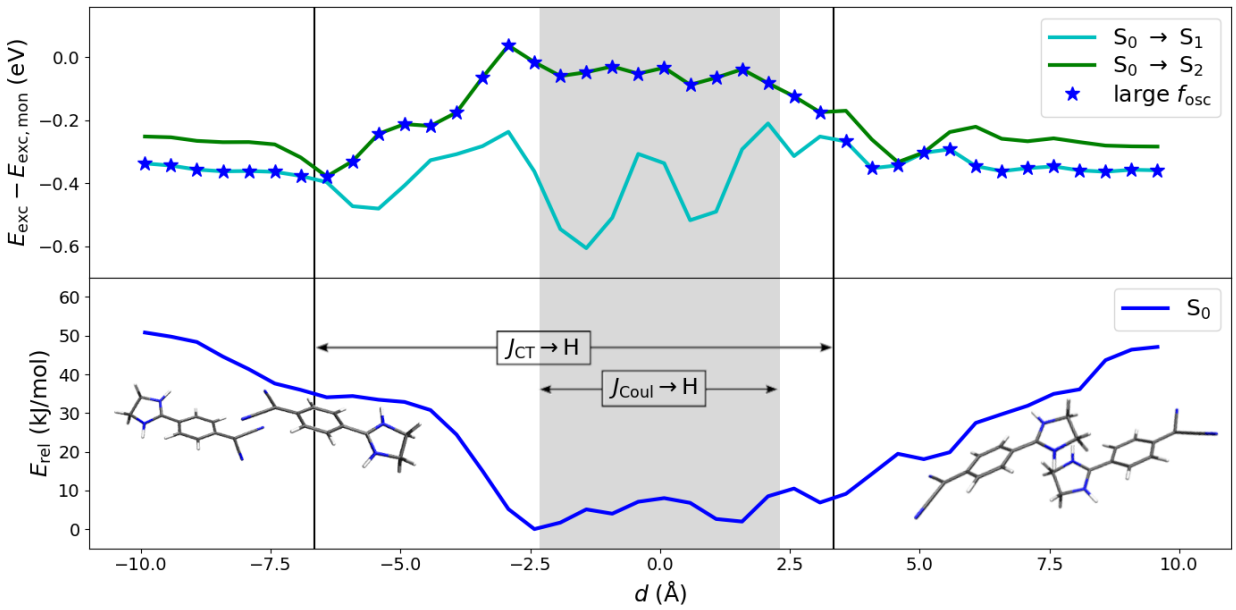

Figure 6: Displacement of two π-stacked *anti*-dimers of **1** along d (*cf.* Figure 4) with a fixed interplanar distance of 3.56 Å. Top: SMD/BHLYP/MRCI calculated excitation energy shifts relative to the monomer (3.31 eV, 375 nm). Darkblue stars indicate the bright state. Bottom: ground-state PES with the minimum of the curve set to zero obtained at the SMD/ωB97X-D3 level. Structures **1**-A_{ST} and **1**-A_{SD} are located at 1.2 Å and –2.4 Å, respectively. The transition state discussed in the text is located at around 4.1 Å. The grey shaded area and the two vertical lines encompass the H-aggregate zones according to the definitions of J_{Coul} and J_{CT}, respectively.

and H-aggregate behavior according to equation (1) when d is 2.32 Å (grey shaded area in Figure 6). A transition red-shifted by roughly 40 nm (–0.3 eV, Table 2) with a bright low-energy state is obtained when the two monomers are pushed –5.6 Å in the direction of separated diamino moities or 3.4 Å in the other direction. These displaced complexes are subsequently referred to as "metastable dimers". As noted earlier, the deviation from Kasha's model is due to the interplay of J_{Coul} and J_{CT}. While stable dimer conformations show positive signs for J_{CT}, metastable dimers display negative signs. This follows from Figure 7 which compares the symmetry of the frontier MOs of **1**-A_{SD} with that of a metastable dimer and assigns signs for t_e and t_h.

Furthermore, owing to the inversion symmetry of the *anti*-dimers, the intensity of the electronic excitations is governed by Laporte's rule, which states that electronic transitions are only allowed between states of different inversion symmetry. For displacements between –5.6 Å and +3.4 Å the dimer HOMO and LUMO have the same inversion symmetry, a_u, rendering a HOMO → LUMO transition forbidden (Figure 7 left). In contrast, for metastable dimers the phases of the LUMO and the LUMO+1 are interchanged and a HOMO → LUMO transition becomes symmetry allowed (Figure 7 right). This gives rise to a bright S_1 state and J-like properties. The formation of antiparallel displaced, metastable dimers may, hence, explain the red-shifted absorption band. Additionally, this exemplifies a rare case of a nonfluorescent J-aggregate.

Slip-stacked or displaced dimers similar to our proposed structures are known in literature, for example, for anthracenes.[58]

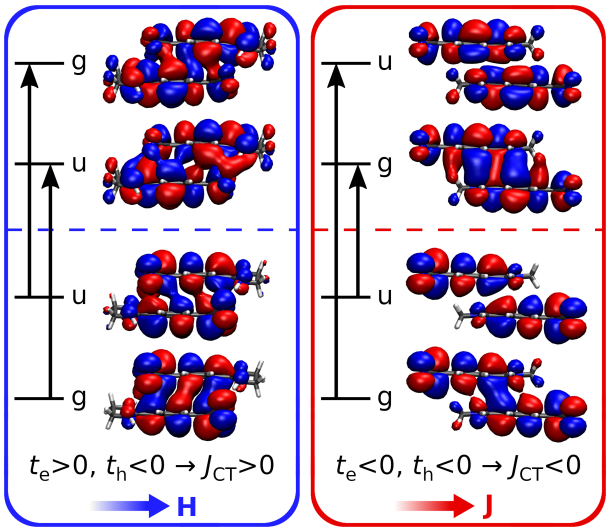

Figure 7: Frontier MOs of **1**-A_{SD} (blue box) and of a metastable dimer of **1** (red box). Black arrows indicate allowed orbital transitions. HOMO and LUMO are separated by a dashed line. MO inversion symmetry is either *gerade* (g) or *ungerade* (u) resulting in an allowed HOMO → LUMO transition and J-like features on the right and a forbidden HOMO → LUMO transition and H-like properties on the left. Plots were generated with ORBKIT,[56] isovalue = 0.01 a_0^{-3}.

To study the possibility of encountering metastable dimers in solution, we computed transition states on the ground-state PES of **1** and **1Me** for approaching diamino groups and analyzed the shape of the PES of **1** (Figure 6 bottom).

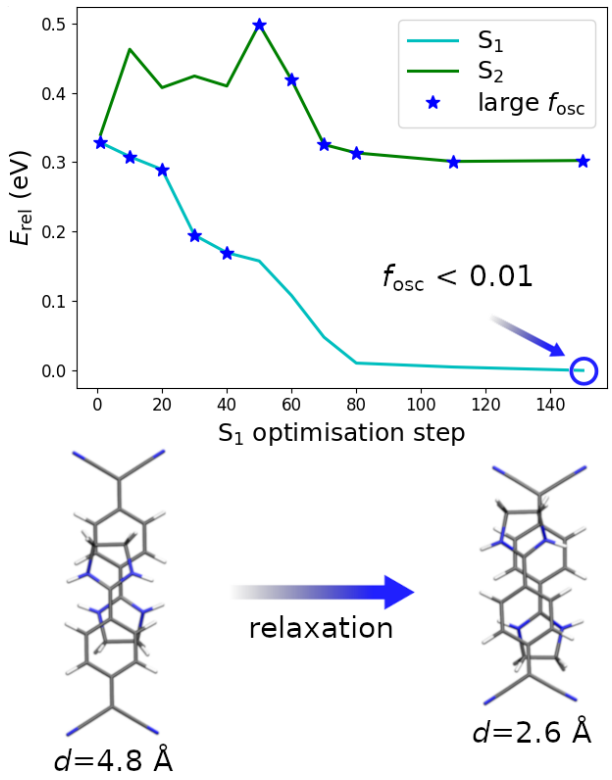

Figure 8: Changes in the S_1 and S_2 excited state energies upon relaxation of a displaced dimer structure of **1** at $d = 4.8$ Å in state S_1. Darkblue stars indicate the bright state. After optimization, the S_1 contains practically no oscillator strength.

At d = 4.1 Å, being slightly beyond the distance at which J_{CT} changes its sign, a barrier of 16.3 kJ/mol for **1** and 16.9 kJ/mol for **1Me** is found, which should be accessible at room temperature. While the overall PES is repulsive, we note that at the same time it is quite shallow with multiple local minima. The PES presumably allows relatively long lifetimes for metastable dimers making them detectable in steady-state absorption measurements. To test this idea, semi-empirical ab-initio molecular dynamics (AIMD) simulations using Grimme's GFN2-xTB[47] code were conducted on **1**-A_{ST} (section 8 in the Supporting Information). However, owing to the missing explicit description of the solvent environment, after 75 ps the dimer starts losing vibrational energy to rotational motion due to the flying ice cube effect,[59] which eventually leads to dissociation. Nevertheless, until dissociation occurs, almost 20% of conformations correspond to structures similar to the metastable dimers (Figure S17 and S18). In addition, our simulation clearly shows that motion along displacement coordinate d is one of the predominant modes in the dimer supporting our proposed model.
Finally, to rationalize fluorescence quenching of the dimer absorption band in the excitation emission matrices (Figure 2), an excited-state optimization of a metastable dimer of **1** at d = 4.8 Å (Figure 8) was performed. Apparently, the structure relaxes back along the displacement coordinate yielding a conformation similar to the stable *anti*-dimer A_{ST} with d = 2.6 Å. The S_1 completely loses its oscillator strength owing to the same symmetry reasons addressed above, which effectively traps the dimer in a dark state unable to decay radiatively.

Conclusion

The intriguing photophysical properties of diaminodicyanoquinones, being a relatively new class of fluorescent dyes, have yet to be explored in full. In this study, we investigated the aggregation behavior and spectroscopic features of a series of non-, singly-, and doubly-methylated DADQ compounds in solution. Using a combined approach of theory and experiment we revealed the vast and complex conformational landscape of DADQs. DFT/MRCI calculations suggest that stable DADQ dimers can be identified as integrated HJ-aggregates. However, the optical properties of DADQs in solution, namely the red-shifted absorption band and its insignificant emission rate, cannot be explained directly by any theory for H- and J-aggregation alone. By combining the extended theory of HJ-aggregates due to Spano and co-workers with relaxed excited-state PES scans, we propose that the unusual optical features of DADQs originate from metastable, antiparallel displaced dimers. In addition to representing a rare case of nonfluorescent J-aggregates, this showcases an unprecedented kind of aggregation-induced optical effect. These results will have implications for the photophysics of dye aggregates and aggregation-induced spectroscopic changes since DADQs are likely not the only system whose optical properties arise from metastable species, especially if large dipole moments play a role in the aggregation process.

Acknowledgement

The North-German Supercomputing Alliance (Norddeutscher Verbund für Hoch- und Höchstleistungsrechnen) and the computing facilities of Freie Universität Berlin (Zentrale Einrichtung für Datenverarbeitung) are acknowledged for providing computational resources. The authors thank the collaborative research center SFB 765 and the research grant PA 1360/16-1 of the Deutsche Forschungsgemeinschaft for financial support.

Competing Interests

The authors declare no competing interests.

References

[1] F. Würthner, "Dipole–Dipole Interaction Driven Self-Assembly of Merocyanine Dyes: From Dimers to Nanoscale Objects and Supramolecular Materials", *Acc. Chem. Res.* **2016**, *49*, 868–876.

[2] T. E. Kaiser, H. Wang, V. Stepanenko, F. Würthner, "Supramolecular Construction of Fluorescent J-Aggregates Based on Hydrogen-Bonded Perylene Dyes", *Angew. Chem. Int. Ed.* **2007**, *46*, 5541–5544.

[3] X. Zhang, H. Dong, W. Hu, "Organic Semiconductor Single Crystals for Electronics and Photonics", *Adv. Mater.* **2018**, *30*, 1801048.

[4] J.-L. Bredas, S. R. Marder, *The WSPC Reference on Organic Electronics: Organic Semiconductors*, *Vol. 1*, World Scientific, **2016**.

[5] O. Ostroverkhova, "Organic Optoelectronic Materials: Mechanisms and Applications", *Chem. Rev.* **2016**, *116*, 13279–13412.

[6] L. Zang, Y. Che, J. S. Moore, "One-Dimensional Self-Assembly of Planar π-Conjugated Molecules: Adaptable Building Blocks for Organic Nanodevices", *Acc. Chem. Res.* **2008**, *41*, 1596–1608.

[7] S. Reineke, M. Thomschke, B. Lüssem, K. Leo, "White organic light-emitting diodes: Status and perspective", *Rev. Mod. Phys.* **2013**, *85*, 1245–1293.

[8] N. Venkatramaiah, G. D. Kumar, Y. Chandrasekaran, R. Ganduri, S. Patil, "Efficient Blue and Yellow Organic Light-Emitting Diodes Enabled by Aggregation-Induced Emission", *ACS Appl. Mater. Interfaces* **2018**, *10*, 3838–3847.

[9] W. Qin, Z. Yang, Y. Jiang, J. W. Y. Lam, G. Liang, H. S. Kwok, B. Z. Tang, "Construction of Efficient Deep Blue Aggregation-Induced Emission Luminogen from Triphenylethene for Nondoped Organic Light-Emitting Diodes", *Chem. Mater.* **2015**, *27*, 3892–3901.

[10] J.-R. Gong, L.-J. Wan, S.-B. Lei, C.-L. Bai, X.-H. Zhang, S.-T. Lee, "Direct Evidence of Molecular Aggregation and Degradation Mechanism of Organic Light-Emitting Diodes under Joule Heating: an STM and Photoluminescence Study", *J. Phys. Chem. B* **2005**, *109*, 1675–1682.

[11] W. Li, W. Li, L. Gan, M. Li, N. Zheng, C. Ning, D. Chen, Y.-C. Wu, S.-J. Su, "J-Aggregation Enhances the Electroluminescence Performance of a Sky-Blue Thermally Activated Delayed-Fluorescence Emitter in Nondoped Organic Light-Emitting Diodes", *ACS Appl. Mater. Interfaces* **2020**, *12*, 2717–2723.

[12] R. W. Boys, *Nonlinear Optics*, 4th ed., Academic Press, **2020**.

[13] Y. Duan, C. Ju, G. Yang, E. Fron, E. Coutino-Gonzalez, S. Semin, C. Fan, R. S. Balok, J. Cremers, P. Tinnemans, Y. Feng, Y. Li, J. Hofkens, A. E. Rowan, T. Rasing, J. Xu, "Aggregation Induced Enhancement of Linear and Nonlinear Optical Emission from a Hexaphenylene Derivative", *Adv. Funct. Mater.* **2016**, *26*, 8968–8977.

[14] J. Xiong, X. Li, C. Yuan, S. Semin, Z. Yao, J. Xu, T. Rasing, X.-H. Bu, "Wavelength dependent nonlinear optical response of tetraphenylethene aggregation-induced emission luminogens", *Mat. Chem. Front.* **2018**, *2*, 2263–2271.

[15] F. Würthner, S. Yao, T. Debaerdemaeker, R. Wortmann, "Dimerization of Merocyanine Dyes. Structural and Energetic Characterization of Dipolar Dye Aggregates and Implications for Nonlinear Optical Materials", *J. Am. Chem. Soc.* **2002**, *124*, 9431–9447.

[16] S. S. Liow, H. Zhou, S. Sugiarto, S. Guo, M. L. S. Chalasani, N. K. Verma, J. Xu, X. J. Loh, "Highly Efficient Supramolecular Aggregation-Induced Emission-Active Pseudorotaxane Luminogen for Functional Bioimaging", *Biomacromolecules* **2017**, *18*, 886–897.

[17] D. Liu, M. Chen, K. Li, Z. Li, J. Huang, J. Wang, Z. Jiang, Z. Zhang, T. Xie, G. R. Newkome, P. Wang, "Giant Truncated Metallo-Tetrahedron with Unexpected Supramolecular Aggregation Induced Emission Enhancement", *J. Am. Chem. Soc.* **2020**, *142*, 7987–7994.

[18] Y.-M. Zhang, W. Zhu, X.-J. Huang, W.-J. Qu, J.-X. He, H. Fang, H. Yao, T.-B. Wei, Q. Lin, "Supramolecular Aggregation-Induced Emission Gels Based on Pillar[5]arene for Ultrasensitive Detection and Separation of Multianalytes", *ACS Sustainable Chem. Eng.* **2018**, *6*, 16597–16606.

[19] E. G. McRae, M. Kasha, "Enhancement of Phosphorescence Ability upon Aggregation of Dye Molecules", *J. Chem. Phys.* **1958**, *28*, 721–722.

[20] M. Kasha, "Energy Transfer Mechanisms and the Molecular Exciton Model for Molecular Aggregates", *Radiat. Res.* **1963**, *20*, 55.

[21] A. S. Davydov, *Theory of Molecular Excitons*, Springer US, Boston, MA, **1971**.

[22] E. E. Jelley, "Spectral Absorption and Fluorescence of Dyes in the Molecular State", *Nature* **1936**, *138*, 1009–1010.

[23] M. Kasha, "Characterization of electronic transitions in complex molecules", *Discuss. Faraday Soc.* **1950**, *9*, 14–19.

[24] S. Kirstein, S. Daehne, "J-aggregates of amphiphilic cyanine dyes: Self-organization of artificial light harvesting complexes", *Int. J. Photoenergy* **2006**, *2006*, 1–21.

[25] Takeyuki Kawaguchi, Kaoru Iwata, "Merocyanine J aggregates: Formation and structural change on chemical and thermal treatments", *Thin Solid Films* **1990**, *191*, 173–191.

[26] A. Liess, A. Lv, A. Arjona-Esteban, D. Bialas, A.-M. Krause, V. Stepanenko, M. Stolte, F. Würthner, "Exciton Coupling of Merocyanine Dyes from H- to J-type in the Solid State by Crystal Engineering", *Nano Lett.* **2017**, *17*, 1719–1726.

[27] H. von Berlepsch, C. Böttcher, L. Dähne, "Structure of J-Aggregates of Pseudoisocyanine Dye in Aqueous Solution", *J. Phys. Chem. B* **2000**, *104*, 8792–8799.

[28] F. Würthner, T. E. Kaiser, C. R. Saha-Möller, "J-Aggregates: From Serendipitous Discovery to Supramolecular Engineering of Functional Dye Materials", *Angew. Chem. Int. Ed.* **2011**, *50*, 3376–3410.

[29] J. L. Bricks, Y. L. Slominskii, I. D. Panas, A. P. Demchenko, "Fluorescent J-aggregates of cyanine dyes: basic research and applications review", *Methods Appl. Fluoresc.* **2017**, *6*, 012001.

[30] M. Bayda, F. Dumoulin, G. L. Hug, J. Koput, R. Gorniak, A. Wojcik, "Fluorescent H-aggregates of an asymmetrically substituted mono-amino Zn(II) phthalocyanine", *Dalton Trans.* **2017**, *46*, 1914–1926.

[31] E. A. Margulies, L. E. Shoer, S. W. Eaton, M. R. Wasielewski, "Excimer formation in cofacial and slip-stacked perylene-3,4:9,10-bis(dicarboximide) dimers on a redox-inactive triptycene scaffold", *Phys. Chem. Chem. Phys.* **2014**, *16*, 23735–23742.

[32] C. Zheng, C. Zhong, C. J. Collison, F. C. Spano, "Non-Kasha Behavior in Quadrupolar Dye Aggregates: The Red-Shifted H-Aggregate", *J. Phys. Chem. C* **2019**, *123*, 3203–3215.

[33] F. C. Spano, "Analysis of the UV/Vis and CD Spectral Line Shapes of Carotenoid Assemblies: Spectral Signatures of Chiral H -Aggregates", *J. Am. Chem. Soc.* **2009**, *131*, 4267–4278.

[34] N. J. Hestand, F. C. Spano, "Expanded Theory of H- and J-Molecular Aggregates: The Effects of Vibronic Coupling and Intermolecular Charge Transfer", *Chem. Rev.* **2018**, *118*, 7069–7163.

[35] A. Liess, A. Arjona-Esteban, A. Kudzus, J. Albert, A. Krause, A. Lv, M. Stolte, K. Meerholz, F. Würthner, "Ultranarrow Bandwidth Organic Photodiodes by Exchange Narrowing in Merocyanine H- and J-Aggregate Excitonic Systems", *Adv. Funct. Mater.* **2019**, *29*, 1805058.

[36] T. Eder, J. Vogelsang, S. Bange, K. Remmerssen, D. Schmitz, S. Jester, T. J. Keller, S. Höger, J. M. Lupton, "Interplay Between J- and H-Type Coupling in Aggregates of π-Conjugated Polymers: A Single-Molecule Perspective", *Angew. Chem. Int. Ed.* **2019**, *58*, 18898–18902.

[37] F. C. Spano, C. Silva, "H- and J-Aggregate Behavior in Polymeric Semiconductors", *Annu. Rev. Phys. Chem.* **2014**, *65*, 477–500.

[38] H. Yamagata, F. C. Spano, "Interplay between intrachain and interchain interactions in semiconducting polymer assemblies: The HJ-aggregate model", *J. Chem. Phys.* **2012**, *136*, 184901.

[39] H. Yamagata, D. S. Maxwell, J. Fan, K. R. Kittilstved, A. L. Briseno, M. D. Barnes, F. C. Spano, "HJ-Aggregate Behavior of Crystalline 7,8,15,16-Tetraazaterrylene: Introducing a New Design Paradigm for Organic Materials", *J. Phys. Chem. C* **2014**, *118*, 28842–28854.

[40] M. Szablewski, P. R. Thomas, A. Thornton, D. Bloor, G. H. Cross, J. M. Cole, J. A. K. Howard, M. Malagoli, F. Meyers, J.-L. Brédas, W. Wenseleers, E. Goovaerts, "Highly Dipolar, Optically Nonlinear Adducts of Tetracyano- p -quinodimethane: Synthesis, Physical Characterization, and Theoretical Aspects", *J. Am. Chem. Soc.* **1997**, *119*, 3144–3154.

[41] P. Rietsch, F. Witte, S. Sobottka, G. Germer, A. Becker, A. Güttler, B. Sarkar, B. Paulus, U. Resch–Genger, S. Eigler, "Diaminodicyanoquinones: Fluorescent Dyes with High Dipole Moments and Electron-Acceptor Properties", *Angew. Chem. Int. Ed.* **2019**, *58*, 8235–8239.

[42] A. Sarbu, L. Biniek, J.-M. Guenet, P. J. Mésini, M. Brinkmann, "Reversible J- to H-aggregate transformation in thin films of a perylenebisimide organogelator", *J. Mater. Chem. C* **2015**, *3*, 1235–1242.

[43] J. Lambrecht, C. Isenberg, C. Bruhn, T. P. I. Saragi, "Self-Assembled π-Conjugated Organic Wires with Unique Properties", *ChemistrySelect* **2017**, *2*, 3572–3576.

[44] S. Grimme, M. Waletzke, "A combination of Kohn–Sham density functional theory and multi-reference configuration interaction methods", *J. Chem. Phys.* **1999**, *111*, 5645–5655.

[45] I. Lyskov, M. Kleinschmidt, C. M. Marian, "Redesign of the DFT/MRCI Hamiltonian", *J. Chem. Phys.* **2016**, *144*, 034104.

[46] W. R. Hertler, H. D. Hartzler, D. S. Acker, R. E. Benson, "Substituted Quinodimethans. III. Displacement Reactions of 7,7,8,8-Tetracyanoquinodimethan", *J. Am. Chem. Soc.* **1962**, *84*, 3387–3393.

[47] S. Grimme, C. Bannwarth, P. Shushkov, "A Robust and Accurate Tight-Binding Quantum Chemical Method for Structures, Vibrational Frequencies, and Noncovalent Interactions of Large Molecular Systems Parametrized for All spd-Block Elements (Z = 1–86)", *J. Chem. Theory Comput.* **2017**, *13*, 1989–2009.

[48] S. Grimme, J. G. Brandenburg, C. Bannwarth, A. Hansen, "Consistent structures and interactions by density functional theory with small atomic orbital basis sets", *J. Chem. Phys.* **2015**, *143*, 054107.

[49] J.-D. Chai, M. Head-Gordon, "Systematic optimization of long-range corrected hybrid density functionals", *J. Chem. Phys.* **2008**, *128*, 084106.

[50] F. Eckert, A. Klamt, "Fast solvent screening via quantum chemistry: COSMO-RS approach", *AIChE J.* **2002**, *48*, 369–385.

[51] K. Kitaura, E. Ikeo, T. Asada, T. Nakano, M. Uebayasi, "Fragment molecular orbital method: an approximate computational method for large molecules", *Chem. Phys. Lett.* **1999**, *313*, 701–706.

[52] K. Kitaura, K. Morokuma, "A new energy decomposition scheme for molecular interactions within the Hartree-Fock approximation", *Int. J. Quantum Chem.* **1976**, *10*, 325–340.

[53] M. Kleinschmidt, C. M. Marian, M. Waletzke, S. Grimme, "Parallel multireference configuration interaction calculations on mini-β-carotenes and β-carotene", *J. Chem. Phys.* **2009**, *130*, 044708.

[54] C. M. Marian, A. Heil, M. Kleinschmidt, "The DFT/MRCI method", *WIREs Comput. Mol. Sci.* **2019**, *9:e1394*.

[55] C. Zhong, D. Bialas, F. C. Spano, "Unusual Non-Kasha Photophysical Behavior of Aggregates of Push–Pull Donor–Acceptor Chromophores", *J. Phys. Chem. C* **2020**, *124*, 2146–2159.

[56] G. Hermann, V. Pohl, J. C. Tremblay, B. Paulus, H.-C. Hege, A. Schild, "ORBKIT: A Modular Python Toolbox for Cross-Platform Postprocessing of Quantum Chemical Wavefunction Data", *J. Comput. Chem.* **2016**, *37*, 1511–1520.

[57] H. Yamagata, C. M. Pochas, F. C. Spano, "Designing J- and H-Aggregates through Wave Function Overlap Engineering: Applications to Poly(3-hexylthiophene)", *J. Phys. Chem. B* **2012**, *116*, 14494–14503.

[58] Y. Gao, H. Liu, S. Zhang, Q. Gu, Y. Shen, Y. Ge, B. Yang, "Excimer formation and evolution of excited state properties in discrete dimeric stacking of an anthracene derivative: a computational investigation", *Phys. Chem. Chem. Phys.* **2018**, *20*, 12129–12137.

[59] G. Bussi, D. Donadio, M. Parrinello, "Canonical sampling through velocity rescaling", *J. Chem. Phys.* **2007**, *126*, 014101.

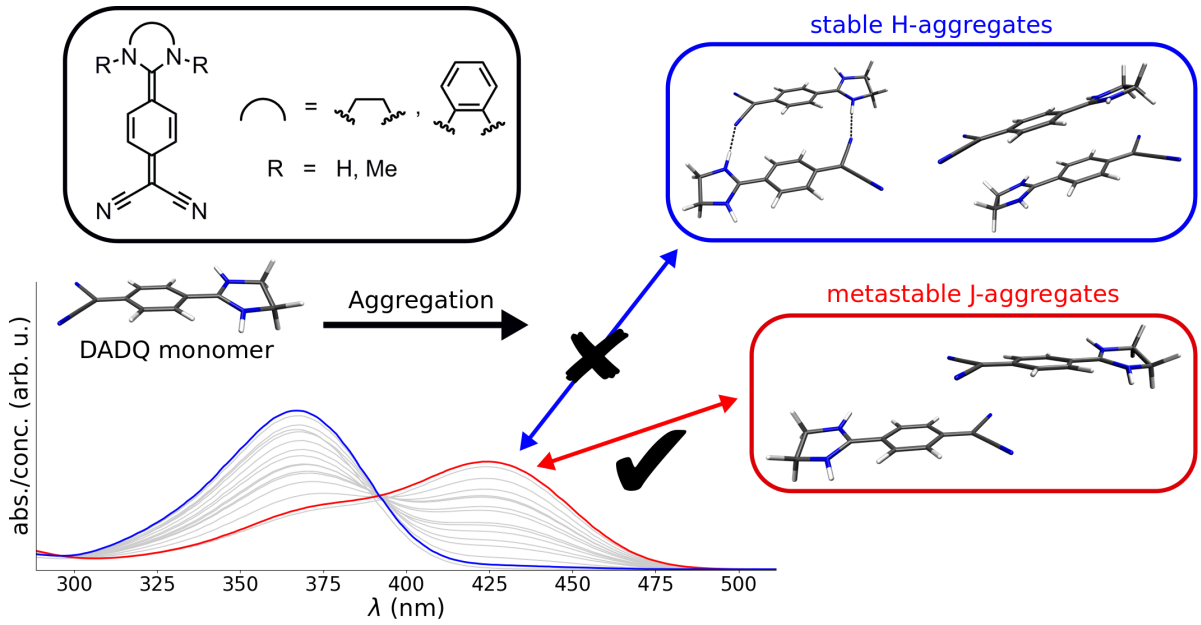

For Table of Contents Only: Unusual photophysical properties not in line with the common theories of H- and J-aggregation are observed for a series of diaminodicyanoquinone derivatives. To rationalize our experimental results, we employ advanced quantum-chemical methods and propose an unprecedented mechanism on the basis of metastable dimers in the electronic ground state, which have broad implications for the photophysics of dye aggregates.

Keywords: ab-initio calculations, aggregation, molecular modeling, noncovalent interactions, photophysics

Supporting Information: Fluorescence quenching in J-aggregates through the formation of unusual metastable dimers

Felix Witte,[1]* Philipp Rietsch,[2] Shreya Sinha,[3] Alexander Krappe,[2] Jan-O. Joswig,[1] Jan P. Götze,[1] Nithiya Nirmalananthan-Budau,[3] Ute Resch-Genger,[3] Siegfried Eigler,[2] and Beate Paulus[1]

[1] *F. Witte, J.-O. Joswig, J. P. Götze, Prof. Dr. B. Paulus*
Institute of Chemistry and Biochemistry
Freie Universität Berlin
Arnimallee 22, 14195 Berlin, Germany
E-mail: jf.witte@fu-berlin.de

[2] *P. Rietsch, A. Krappe, Prof. Dr. S. Eigler*
Institute of Chemistry and Biochemistry
Freie Universität Berlin
Takustr. 3, 14195 Berlin, Germany

[3] *S. Sinha, N. Nirmalananthan-Budau, U. Resch-Genger*
Division Biophotonics
Federal Institute for Material Research and Testing (BAM)
Richard-Willstätter-Straße 11, 12489 Berlin, Germany

Contents

1 General information

All reagents were purchased from commercial sources and used without further purification. Dry solvents were purchased from Acros Organics. ALUGRAM Xtra SIL G/UV254 plates by Macherey-Nagel were used for thin-layer chromatography. Isolation of products by chromatography was performed with silica from Macherey-Nagel Silica 60 M, 0.04–0.063 mm). NMR spectra were recorded on a JOEL ECX 400 (^{1}H 400 MHz, ^{13}C 101 MHz), JEOL Eclipse+ 500 (^{1}H 500 MHz, ^{13}C 126 MHz) and BRUKER AVANCE 700 (^{1}H 700 MHz, ^{13}C 176 MHz) spectrometer at 25 °C. The chemical shifts δ are calibrated on the respective solvent peak as internal standard. All shifts are reported in ppm and NMR multiplicities are abbreviated as s (singlet), d (duplet), t (triplet), m (multiplet). Coupling constants J are reported in Hz. UV/Vis spectra were recorded on a Cary 50 Bio photospectrometer (Varian). Fluorescence spectra were recorded on a LS 50 B luminescence spectrometer from PerkinElmer. UV/Vis and Fluorescence spectra were measured in quartz glass cuvettes with 1 cm path length. IR Spectra were recorded on a FT/IR 4100 spectrometer from JASCO. Elemental analysis were performed on an VARIO EL from Elementar.

2 Synthetic procedures and spectral characterization

2-(4-(cyano(pyrrolidin-1-yl)methylene)cyclohexa-2,5-dien-1-ylidene)malononitrile (PTCNQ) and compounds **1**, **2**, and **2Me$_2$** were synthesized as reported previously.[1]

2.1 2-(4-(imidazolidin-2-ylidene)cyclohexa-2,5-dien-1-ylidene)malononitrile (1)

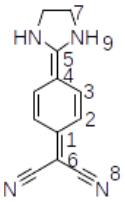

Ethylenediamine (26.6 mg, 0.44 mmol, 1 eq.) was added to a 40 °C warm solution of PTCNQ (110 mg, 0.44 mmol, 1 eq.) in acetonitrile (10 mL). The solution turned deep green immediately and to yellow in the next minutes. The solution was stirred at 70 °C for 4 hours and then cooled to room temperature. The precipitate was filtered off and washed with cooled acetonitrile (3x 5 mL) to yield the product as a yellow fine-grain powder (73.4 mg, 0.35 mmol, 79%).

^{1}H NMR (500 MHz, DMSO-d$_6$, RT): δ (ppm) = 9.76 (s, 2H, 9), 7.57 (d, ^3J = 5.0 Hz, 2H, 2), 6.82 (d, ^3J = 5.0 Hz, 2H, 2), 3.87 (bs, 4H, 7).
^{13}C NMR (125 MHz, DMSO-d$_6$, RT): δ (ppm) = 164.73 (1C, 6), 150.53 (1C, 5), 129.48 (1C, 1), 124.40 (2C, 2), 117.90 (2C, 3), 108.73 (2C, 8), 44.36 (1C, 4), 35.42 (2C, 7).
FT-IR (ATR) $\tilde{\nu}$ (cm^{-1}): 3084 (w), 3022 (vw), 3009 (vw), 2183 (s), 2144 (vs), 1594 (s), 1580 (s), 1507 (s), 1332 (s), 1282 (s), 1236 (w), 1199 (m), 952 (w), 873 (s), 747 (m).
UV/Vis (DMSO) λ_{max} nm (ε [Lmol^{-1} cm^{-1}]): 405 (22800).
UV/Vis (ACN) λ_{max} nm (ε [Lmol^{-1} cm^{-1}]): 357 (4000), 409 (4000).
UV/Vis (DMF) λ_{max} nm (ε [Lmol^{-1} cm^{-1}]): 363 (13000), 410 (18000).
UV/Vis (Methanol) λ_{max} nm (ε [Lmol^{-1} cm^{-1}]): 395 (36875).
MS (EI): m/z = 210.1 (100)[MH]$^{\cdot+}$; 209.1 (50); 182.1 (40); 181.1 (100); 155.1 (15); 141.0 (15); 114 (15).
EA: $C_{12}H_{10}N_4$; calc.: C, 68.56; N, 26.65; H, 4.79 meas.: C, 68.22; N, 25.76; H, 5.03.

2.2 2-(4-(1-Methylimidazolidin-2-yliden)cyclohexa-2,5-dien-1-yliden)malononitrile (1Me)

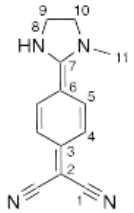

N-Methylethylendiamin (63 mg, 0.074 mL, 0.81 mmol, 1 eq.) was added to a 40 °C warm solution of PTCNQ (200 mg, 0.81 mmol, 1 eq.) in 25 mL acetonitrile. The solution turned green after addition and a yellow solid precipitated after approximately 30 minutes. The solution was stirred at 70 °C for 4 hours and then cooled to room temperature. The precipitate was filtered off and washed with cooled acetonitrile (3x 10 mL) to yield the product as a green powder (141.7 mg, 0.63 mmol, 78%).

^{1}H NMR (700 MHz, DMSO-d$_6$, RT): δ (ppm) = 9.59 (s, 1H, 8), 7.36 (d,^3J = 8.5 Hz, 2H, 4), 6.85 (d, ^3J = 8.5 Hz, 2H, 5), 3.98 (t, ^3J = 9.8 Hz, 2H, 9), 3.80 (t, ^3J = 9.8 Hz, 2H, 10), 3.14 (s, 3H, 11).
^{13}C NMR (176 MHz, DMSO-d$_6$, RT): δ (ppm) = 165.66 (1C, 2), 148.99 (1C, 7), 129.68 (1C, 3), 123.36 (2C, 4), 117.46 (2C, 5), 108.63 (2C, 1), 52.60 (1C, 6), 41.83 (1C, 9), 35.05 (1C, 10), 33.59 (1C, 11).

FT-IR (ATR) $\tilde{\nu}$ (cm^{-1}):3164 (w), 2177 (s), 2147 (s), 1570 (s), 1501 (s), 1378 (m), 1330 (s), 1300 (m), 1286 (m), 1190 (s), 944 (m), 836 (s).
UV/Vis (DMSO) λ_{max} nm (ε [$Lmol^{-1}$ cm^{-1}]):390 (29000).
UV/Vis (ACN) λ_{max} nm (ε [$Lmol^{-1}$ cm^{-1}]): 391 (21200).
UV/Vis (DMF) λ_{max} nm (ε [$Lmol^{-1}$ cm^{-1}]): 351 (17700).
UV/Vis (Methanol) λ_{max} nm (ε [$Lmol^{-1}$ cm^{-1}]): 380 (24600).
UV/Vis (THF) λ_{max} nm (ε [$Lmol^{-1}$ cm^{-1}]): 425 (18800).
MS (ESI): m/z = 471.20 (25)[2 M-Na]$^+$, 263.07 (32) [M-K]$^+$, 247.09 (82) [M-Na]$^+$, 225.11 (35) [M]$^+$.
EA*: $C_{13}H_{12}N_4$; calc.: C, 69.62; N, 24.98; H, 5.39; meas.: C, 67.50; N, 23.85; H, 5.207.
*Small amounts of acetonitrile and water may be responsible for the deviations of calculated and measured values.

2.3 2-(4-(1,3-Dimethylimidazolidin-2-yliden)cyclohexa-2,5-dien-1-yliden)malononitrile ($1Me_2$)

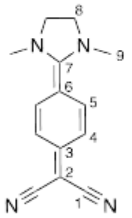

N,N'-Dimethylethylendiamin (71 mg, 0.087 mL, 0.81 mmol, 1 eq.) was added to a 40 °C warm solution of PTCNQ (200 mg, 0.81 mmol, 1 eq.) in 25 mL acetonitrile. The solution was stirred at 70 °C for 4 hours and then cooled to room temperature. The precipitate was filtered off and washed with cooled acetonitrile (3x 10 mL) to yield the product as a yellow powder (75.7 mg, 0.32 mmol, 39%).

^{1}H NMR (700 MHz, DMSO-d_6, RT): δ (ppm) = 7.19 (d, ^3J = 8.7 Hz, 2H, 4), 6.89 (d, ^3J = 8.7 Hz, 2H, 5), 3.90 (s, 4H, 8), 2.96 (s, 6H, 9).
^{13}C NMR (176 MHz, DMSO-d_6, RT): δ (ppm) = 166.35 (1C, 2), 148.35 (1C, 7), 130.01 (1C, 3), 124.03 (2C, 4), 118.03 (2C, 5), 107.79 (1C, 1), 50.21 (1C, 6), 35.45 (2C, 8), 32.95 (2C, 9).
FT-IR (ATR) $\tilde{\nu}$ (cm^{-1}):2932 (w), 2171 (s), 2132 (s), 1595 (s), 1499 (m), 1370 (m), 1324 (m), 1297 (m), 936 (m), 827 (s).
UV/Vis (DMSO) λ_{max} nm (ε [$Lmol^{-1}$ cm^{-1}]): 381 (23500).
UV/Vis (ACN) λ_{max} nm (ε [$Lmol^{-1}$ cm^{-1}]): 377 (22800).
UV/Vis (DMF) λ_{max} nm (ε [$Lmol^{-1}$ cm^{-1}]): 385 (25000).
UV/Vis (Methanol) λ_{max} nm (ε [$Lmol^{-1}$ cm^{-1}]): 368 (23900).
UV/Vis (THF) λ_{max} nm (ε [$Lmol^{-1}$ cm^{-1}]): 416 (4300).
MS (EI): 239.12 (100) [MH]$^+$, 238.12 (27) [M]$^{\cdot+}$, 180.98 (58), 166.02 (25), 68.99 (30).
EA*: $C_{14}H_{14}N_4$; calc.: C, 70.57; N, 23.51; H, 5.92; meas.: C, 70.61; N, 22.16; H, 6.021.
*Small amounts of acetonitrile and water may be responsible for the deviations of calculated and measured values.

2.4 2-(4-(1,3-dihydro-2*H*-benzo[*d*]imidazol-2-ylidene)cyclohexa-2,5-dien-1-ylidene)malononitrile (2)

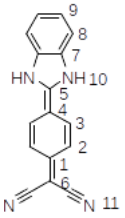

Under argon atmosphere, *ortho*-Phenylendiamine (70.0 mg, 0.64 mmol, 1 eq.), dissolved in acetonitrile (15 mL), was added to a 40 °C warm solution of PTCNQ (160.0 mg, 0.64 mmol, 1 eq.) in acetonitrile (20 mL). The solution turned red after 20 hours at 70 °. After cooling to room temperature, the solution stood for 4 days in the fridge. Filtration then yielded a fine grain greenish powder which was washed with cooled acetonitrile (3x 5 mL). The product was recrystallized from acetonitrile to yield fine yellow crystals (70.2 mg, 0.27 mmol, 43%).

^{1}H NMR (700 MHz, DMSO-d_6, RT): δ (ppm) = 14.35 (bs, 2H, 10), 7.86 (d, ^3J = 8.7 Hz, 2H, 2), 7.69 (q, ^3J = 8.7 Hz, 2H, 9), 7.47 (q, ^3J = 8.6 Hz, 2H, 8), 6.95 (d, ^3J = 8.7 Hz, 2H, 3).
^{13}C NMR (176 MHz, DMSO-d_6, RT): δ (ppm) = 150.27 (1C, 6), 149.31 (1C, 5), 132.26 (1C, 1), 128.54, 126.54 (1C, 2), 125.48 (2C, 8), 123.51 (2C, 7), 118.49 (2C, 3), 113.47 (2C, 9), 79.63 (1C, 4).
FT-IR (ATR) $\tilde{\nu}$ (cm^{-1}):2952 (w), 2877 (w), 2849 (w), 2761 (w), 2190 (s), 2140 (s), 1637 (w), 1612 (m), 1503 (m), 1459 (m), 1387 (m), 1336 (m), 1230 (m), 1201 (m), 819 (s), 742 (s).
UV/Vis (DMSO) λ_{max} nm (ε [$Lmol^{-1}$ cm^{-1}]): 392 (42200).
UV/Vis (ACN) λ_{max} nm (ε [$Lmol^{-1}$ cm^{-1}]): 385 (86800).

UV/Vis (DMF) λ_{max} nm (ε [Lmol^{-1} cm^{-1}]): 391 (56500).
UV/Vis (Methanol) λ_{max} nm (ε [Lmol^{-1} cm^{-1}]): 424 (20000).
UV/Vis (THF) λ_{max} nm (ε [Lmol^{-1} cm^{-1}]): 388 (7000).
MS (EI): m/z = 259.10 (15), 258.09 $[MH]^{\cdot+}$ (100), 257.10 (5), 232 (5)
EA: $C_{16}H_{10}N_4$; calc.: C, 74.40; N, 21.69; H, 3.90; meas.: C, 74.31; N, 21.78; H, 4.07.

2.5 2-(4-(1-Methyl-1,3-dihydro-2*H*-benzo[*d*]imidazol-2-yliden)cyclohexa-2,5-dien-1-yliden)malononitrile (2Me)

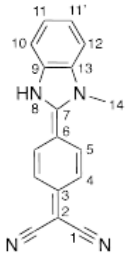

N-Methylphenylen-1,2-diamin (147 mg, 0.137 mL,1.21 mmol, 1 eq.) was added to a 40 °C warm solution of PTCNQ (300 mg, 1.21 mmol, 1 eq.) in acetonitrile. The solution was stirred at 70 °C for 24 hours and then cooled to room temperature. The precipitate was filtered off and washed with cooled acetonitrile (3x 5 mL) to yield the product as a green powder (58 mg, 0.23 mmol, 19%).

^{1}H NMR (500 MHz, DMSO-d_6, RT): δ (ppm) = 7.93 (m, 1H, 12), 7.73 (m, 1H, 10), 7.63 (d, ^3J = 8.7 Hz, 2H, 11), 7.56 (m, 2, 5), 6.97 (d, ^3J = 8.7 Hz, 2H, 4), 4.03 (s, 3H, 14).
^{13}C NMR (176 MHz, DMSO-d_6, RT): δ (ppm) = 151.32 (1C, 2), 148.65 (1C, 7), 133.97 (1C, 3), 130.70 (2C, 5), 126.31 (1C, 13), 125.61 (2C, 11), 123.77 (1C, 9), 118.34 (2C, 4), 113.85 (1C, 10), 113.11 (1C, 12), 109.17 (2C, 1), 34.04 (1C, 6), 33.49 (1C, 14).
FT-IR (ATR) $\tilde{\nu}$ (cm^{-1}):3045 (w), 2931 (w), 2875 (w), 2172 (s), 2127 (s), 1591 (s), 1566 (s), 1512 (m), 1494 (m), 1385 (s), 1319 (s), 1188 (s), 821 (s), 738 (s).
UV/Vis (DMSO) λ_{max} nm (ε [Lmol^{-1} cm^{-1}]): 373 (19750).
UV/Vis (ACN) λ_{max} nm (ε [Lmol^{-1} cm^{-1}]): 368 (7350).
UV/Vis (DMF) λ_{max} nm (ε [Lmol^{-1} cm^{-1}]): 374 (32700).
UV/Vis (Methanol) λ_{max} nm (ε [Lmol^{-1} cm^{-1}]): 375 (12200).
UV/Vis (THF) λ_{max} nm (ε [Lmol^{-1} cm^{-1}]): 303 (5650).
MS (EI): m/z = 273.11 (12) $[M]^+$, 272.10 (70) $[M]^{\cdot+}$, 271.10 (100) $[M]^{\cdot}$, 149.06 (25).
EA*: $C_{17}H_{12}N_4$; calc.: C, 74.98; N, 20.58; H, 4.44; meas.: C, 71.68; N, 20.58; H, 5.486.
*Small amounts of acetonitrile and water may be responsible for the deviations of calculated and measured values.

2.6 2-(4-(1,3-Dimethyl-1,3-dihydro-2*H*-benzo[*d*]imidazol-2-yliden)cyclohexa-2,5-dien-1-yliden)malononitrile ($2Me_2$)

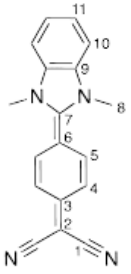

N,N'-Dimethyl-1,2-phenylendiamine (54 mg, 43.5 μL,0.4 mmol, 1 eq.) was added to a 40 °C warm solution of PTCNQ (300 mg, 1.21 mmol, 1 eq.) in acetonitrile. The solution was stirred at 70 °C for 20 hours and then cooled to room temperature. The precipitate was filtered off and washed with cooled acetonitrile (3x 5 mL) to yield the product as a green powder (28.3 mg, 0.10 mmol, 25%).

^{1}H NMR (700 MHz, DMSO-d_6, RT): δ (ppm) = 8.01 (dd, J = 6.0, 3.0 Hz, 2H, 11), 7.67 (dd, J = 6.0, 2.9 Hz, 2H, 10), 7.49 (d, J = 8.5 Hz, 2H, 5), 6.98 (d, J = 8.2 Hz, 2H, 4), 3.92 (s, 6H, 8).
^{13}C NMR (176 MHz, DMSO-d_6, RT): δ (ppm) = 151.54 (1C, 2), 147.79 (1C, 7), 131.82 (1C, 3), 131.00 (2C, 5), 126.04 (2C, 9), 123.46 (2C, 11), 117.68 (2C, 4), 112.90 (1C, 10), 109.51 (2C, 1), 106.52 (2C, 6), 32.92 (2C, 8).
FT-IR (ATR) $\tilde{\nu}$ (cm^{-1}):2166 (s), 2124 (s), 1598 (s), 1552 (m), 1508 (m), 1471 (s), 1422 (m), 1320 (s), 1195 (s), 1231 (m), 1164 (m), 1028 (m), 828 (s), 810 (m), 737 (s).
UV/Vis (DMSO) λ_{max} nm (ε [Lmol^{-1} cm^{-1}]): 410 (20950).
UV/Vis (ACN) λ_{max} nm (ε [Lmol^{-1} cm^{-1}]): 409 (22200).
UV/Vis (DMF) λ_{max} nm (ε [Lmol^{-1} cm^{-1}]): 415 (24100).

UV/Vis (Methanol) λ_{max} nm (ε [Lmol^{-1} cm^{-1}]):396 (16500).
UV/Vis (THF) λ_{max} nm (ε [Lmol^{-1} cm^{-1}]): 454 (11600).
MS (ESI): m/z = 881.34 (23) [3 M-Na]$^+$, 611.20 (26) [2 M-K]$^+$, 595.22 (55) [2 M-Na]$^+$, 325.08 (90) [M-K]$^+$, 309.10 (100) [M-Na]$^+$, 287.12 (55) [MH]$^+$.
EA*: $C_{18}H_{14}N_4$; C, 75.50; N, 19.57; H, 4.93; meas.: C, 71.13; N, 17.76; H, 5.11.
*Small amounts of acetonitrile and water may be responsible for the deviations of calculated and measured values.

3 UV/Vis titration experiments

Table S1: Fluorescence quantum yields (QY) in % and excited state lifetimes (τ) in ns of all compounds in solvents of increasing polarity as determined by the normalized Dimroth-Reichardt Parameter E_T^N.[2] Notably large quantum yields are highlighted in bold blue.

		1*		**1Me***		**1Me$_2$**		**2***		**2Me**		**2Me$_2$**	
E_T^N	solvent	QY	τ	QY	τ	QY	τ	QY	τ	QY	τ	QY	τ
0.207	THF	7	<0.2	<1	0.3	<1	0.3	**73**	2.4	3	1.6	<1	<0.2
0.386	DMF	7	2.1	4	2.1	3	2.77	**72**	1.8	**90**	2.1	3	0.5
0.444	DMSO	10	0.8	<1	1.1	<1	1.4	**92**	1.8	4	1.8	<1	0.5
0.460	ACN	7	<0.2	<1	0.5	<1	<0.2	**71**	6.3	**79**	2.2	<1	1.1
0.762	MeOH	<1	<0.2	<1	<0.2	<1	<0.2	35	0.4	16	0.5	<1	<0.2

* QY of **1**, **1Me**, and **2** were taken from ref.[1]

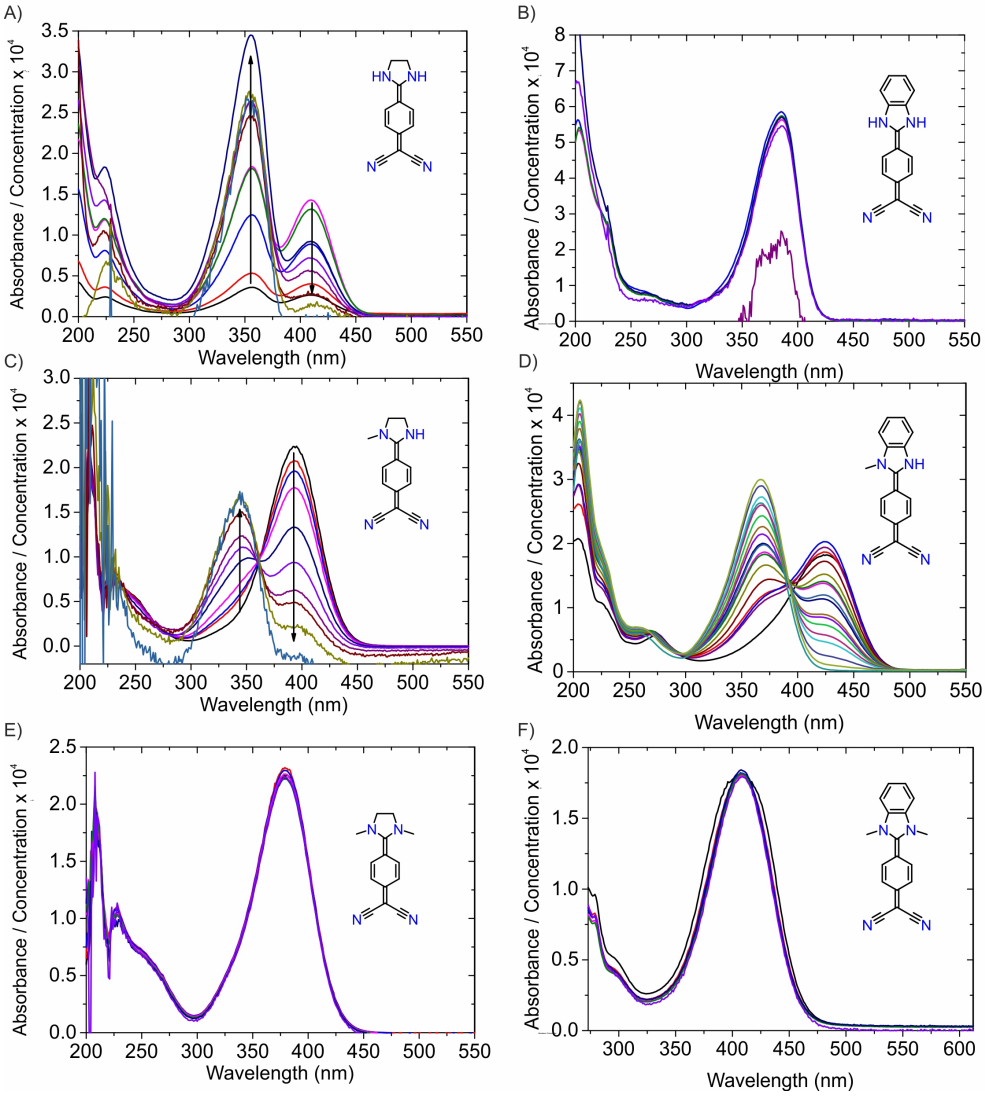

Figure S1: Wavelength-dependence of the concentration-normalized absorbance (absorbance spectra divided by dye concentration) of all compounds in acetonitrile. Concentrations range from $1x10^{-4}$M to $5x10^{-6}$M, in case of **2** (B) to $5x10^{-8}$M (purple graph).

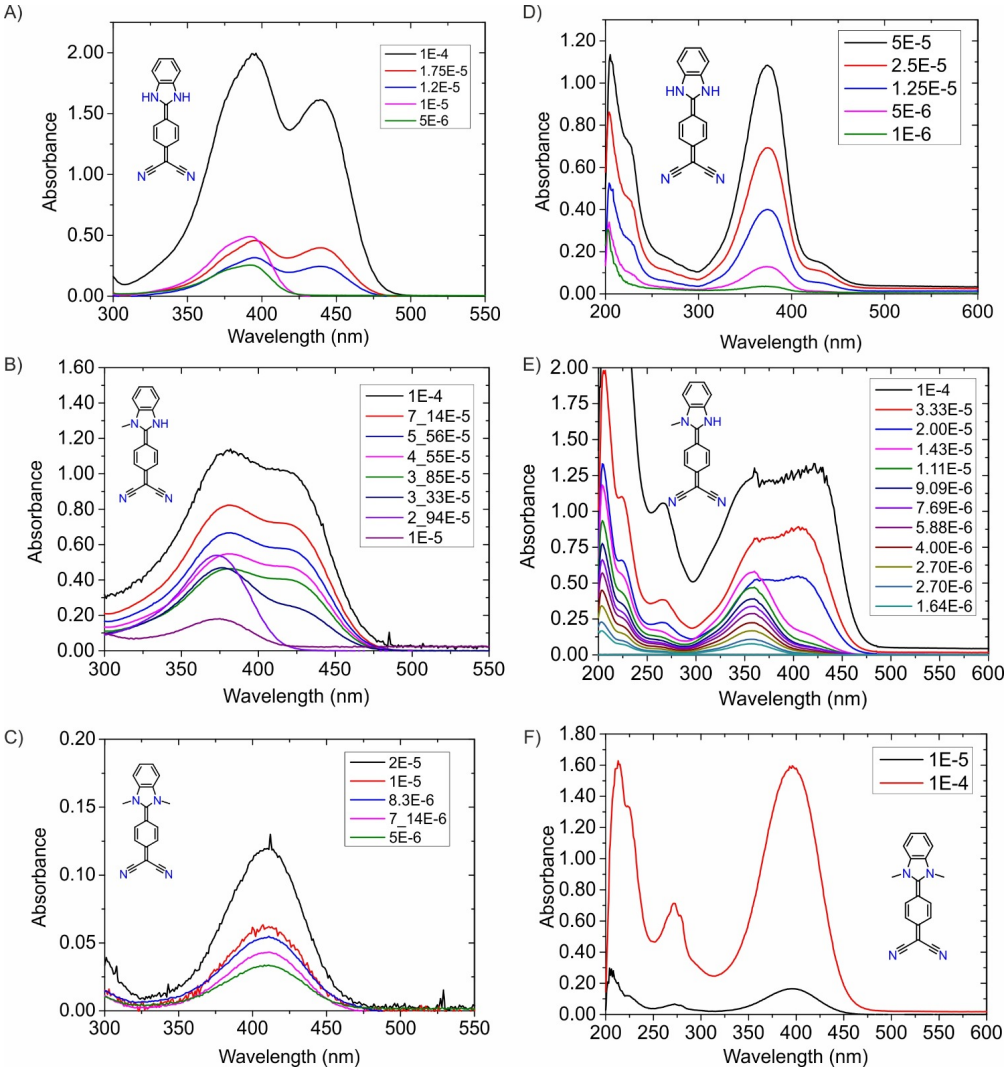

Figure S2: Absorption spectra of **2**, **2Me**, and **2Me$_2$** in DMSO (A-C) and MeOH (D-F) at different concentrations. Concentrations are given in the insets.

3.1 Temperature dependence

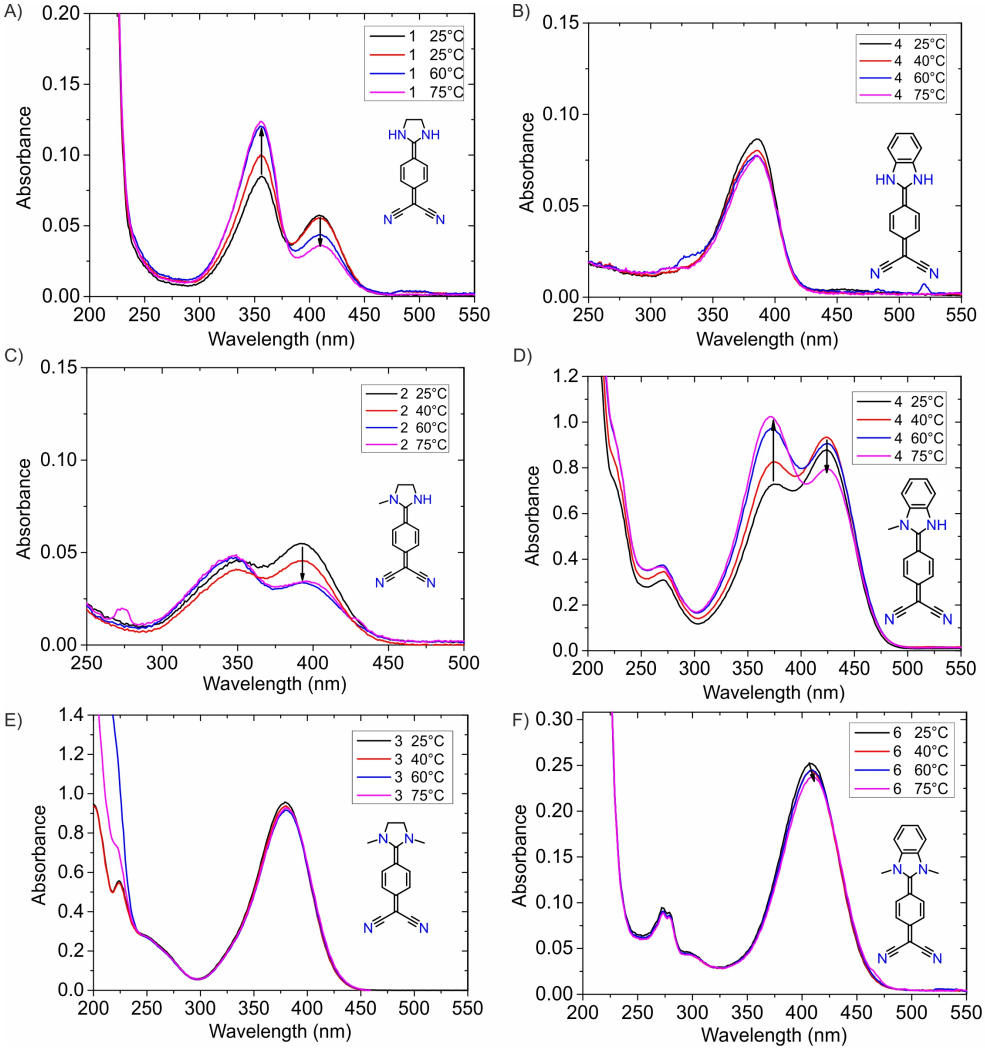

Figure S3: Temperature dependent absorption measurements of all compounds in solutions of acetonitrile with concentrations of $1x10^{-5}$M. Temperatures are given in the insets.

3.2 Effect of polar additives

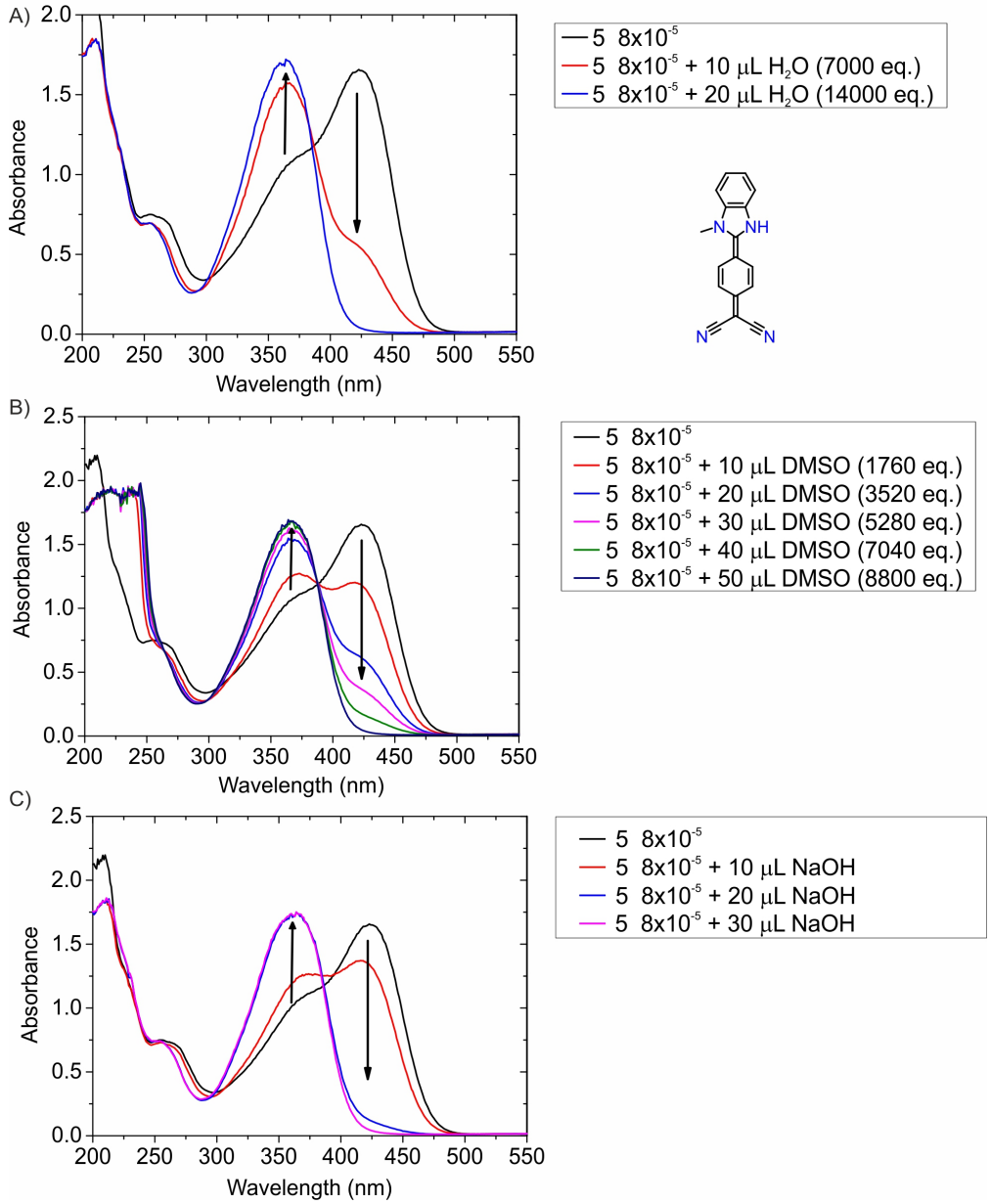

Figure S4: Absorption spectra of **2Me** in ACN with a starting concentration of $8x10^{-5}$M and increasing amounts of (polar) additives: A) H_2O. B) DMSO. C) Aqueous NaOH ($1x10^{-4}$M). Equivalents are given with respect to solute concentration.

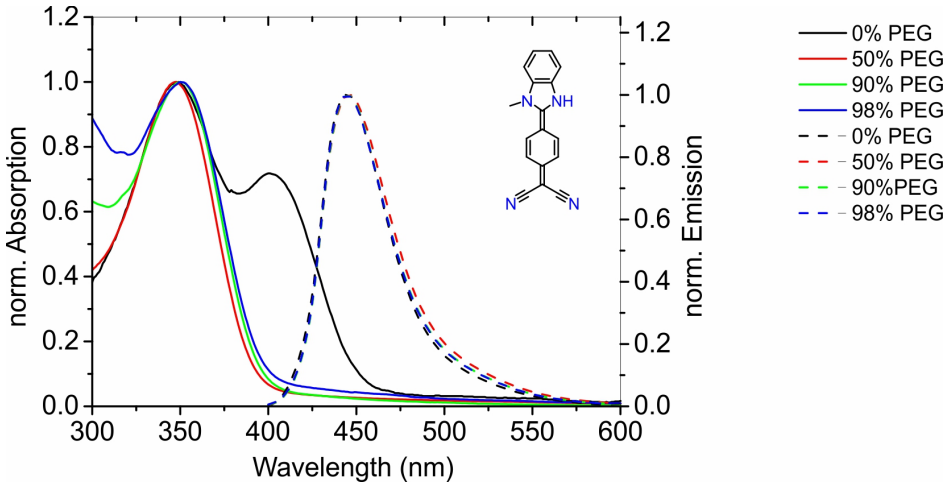

Figure S5: Normalized absorption (solid) and normalized emission (dashed) spectra (excitation at 366 nm) of **2Me** in pure acetonitrile (black) and mixtures of acetonitrile with polyethylenglycol: 50 % PEG (red), 90 % (green) and 98 % (blue). While the red-shifted absorption band disappears, the emission spectra are unaffected by the addition of PEG. The change in the absorption spectra is accompanied by a change in colour as observed in Fig. 1 in the main text.

Table S2: Measured densities ρ and dynamic viscosities η of the ACN/PEG mixture

ACN/PEG	ρ (20 °C) [g m L^{-1}]	η [m Pa s]
100/0	0.7843	0.3720
50/50	0.9710	4.1152
10/90	1.0966	54.3671
2/98	1.1153	99.9220

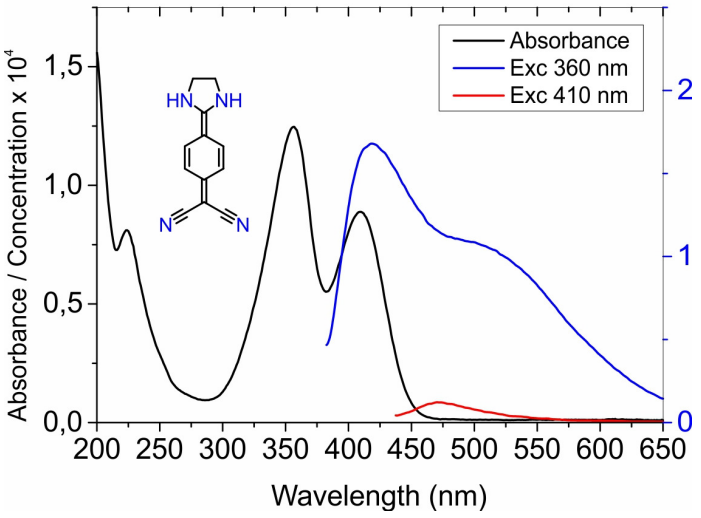

Figure S6: Absorption spectra of compound **1** in ACN at a concentration of 2·10^{-5} M (black line) and emission spectra recorded after exicitation at 360 nm (blue line) and 410 nm (red line). The emission after excitation at 410 nm, i.e., the red-shifted absorption band, is negligibly low compared to the emission after excitation of the blue shifted absorption band (360 nm).

4 Excitation emission matrices

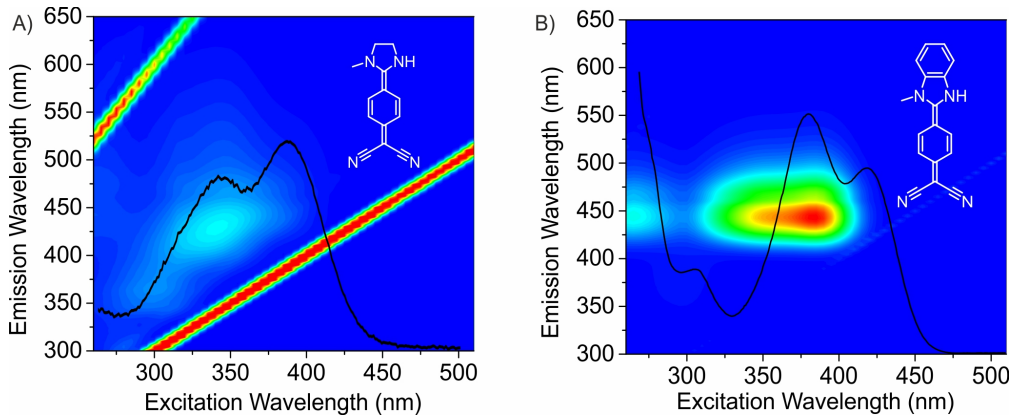

Figure S7: Excitation emission matrices (EEM) of **1Me** and **2Me** in ACN. The overlayed black spectra are the respective absorption spectra at the same concentration A) $5x10^{-6}$ M and B) $2x10^{-5}$ M.

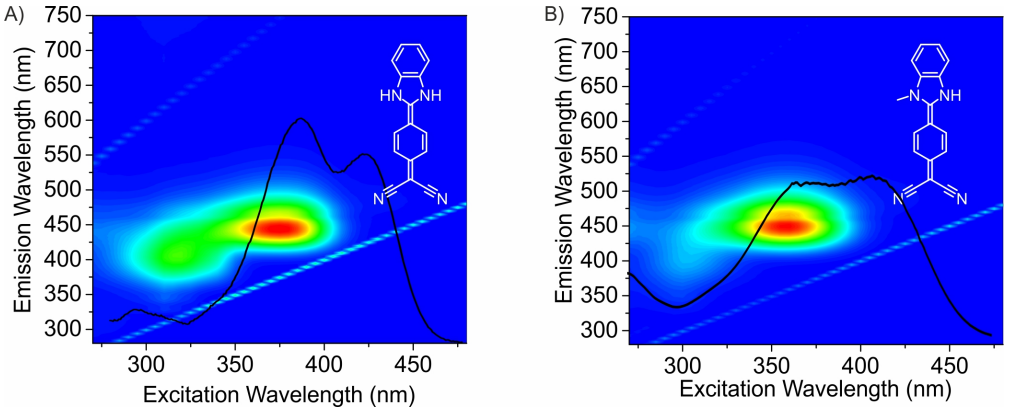

Figure S8: Excitation emission matrices (EEM) of **2** and **2Me** in methanol. The overlayed black spectra are the respective absorption spectra at the same concentration A) $5x10^{-6}$ M and B) $2x10^{-5}$ M.

5 Computational Details

The conformational landscape of DADQ aggregates was investigated by metadynamics simulations based on the GFN2-xTB method and CREST.[3,4] The dimers shown in Figure 2 of the main text and all other oligomers displayed further down below were chosen after visual inspection. All structure optimizations were performed using the Turbomole program package[5] employing the PBEh-3c[6] composite method in combination with the COSMO[7] solvent model. Stationary points were confirmed to be minima on the PES by normal mode analyses showing no imaginary frequencies. Vacuum single point electronic energies E were calculated at the ωB97X-D3/def2-QZVP[8–10] level of DFT utilizing the ORCA program package (version 4.2.0).[11] Solvation effects δG_{solv} were estimated within the COSMO-RS[12] framework with the COSMOtherm program suite[13] using its BP_TZVPD_FINE_19 parametrization. Free association enthalpies were computed according to

$$\Delta G_{\mathrm{a}} = \Delta E + \Delta H_{\mathrm{vib}} - T\Delta S_{\mathrm{vib}}^{\mathrm{RRHO}} + \Delta\delta G_{\mathrm{solv}}.$$

ΔH_{vib} and $\Delta S_{\mathrm{vib}}^{\mathrm{RRHO}}$ are extracted from normal mode analyses using, in addition, Grimme's rigid-rotor harmonic-oscillator (RRHO) correction to account for the anharmonicity of low-lying frequencies that often lead to inaccuracies in the calculation of binding energies,[14] $\Delta\delta G_{\mathrm{solv}}$ additionally contains a correction ΔG_{conc} of $+7.92$ kJ/mol taking into account the 1 M reference concentration in solution.[15] A lower-level combination of Grimme's semi-empirical GFN2-xTB program for optimizations and normal mode analyses and ωB97X-D3/def2-TZVP single point calculations was employed for higher aggregates up to hexamers.

The ground-state PES of **1** (Figure 6 in the main text) was scanned at the SMD/ωB97X-D3/def2-TZVP level by fixing the carbon atoms between the amino groups and cyano moities at every step to their cartesian position and optimizing every other coordinate of the dimer at a fixed intermolecular distance of 3.56 Å. Transition state searches were performed with Turbomole's *woelfling* module. Metastable dimer species were optimized with a much shorter displacement step (*dqmax=0.005*) than all other structures (*dqmax=0.05*). Electronic energies to estimate transition state barriers were computed at the ωB97X-D3/def2-QZVP level using the SMD[16] solvent model with $\varepsilon = 37.5$[17] for ACN since the COSMO-RS approach is much better suited for comparing relative energies of conformers rather than estimating transition state barriers.[18]

FMO-EDA[19,20] calculations were performed at the ωB97X-D3(BJ)/def2-TZVP level (*wB97X-D* and *idcver=3* keywords) with the GAMESS program package.[21] Note that due to differences in implementation, the dispersive correction used for energies and EDA calculations is not the same, but should yield comparable results. We refer to the respective program manuals for details.

To obtain insight into the photochemical behavior of DADQ aggregates, we employed the DFT/MRCI[22] approach, which is particularly useful for the treatment of molecular aggregates and especially our DADQs, as single-reference TD-DFT calculations may yield unreliable results due to the inadequate description of double excitations.[23] However, as we do not intend to base our results solely on a single method, we have additionally employed TD-DFT calculations to support the DFT/MRCI results.

Excited states were computed at the SMD/BHLYP/MRCI/def2-TZVP(-f)[16,22,24] level using the stand-alone DFT/MRCI program[25] interfaced with ORCA employing the R2016 Hamiltonian and $\varepsilon = 37.5$ and 46.8 for ACN and DMSO, respectively.[17] A reference space of 16 electrons and 14 orbitals with a default cut-off of 1.0 Hartree, which was carefully checked to not cut between degenerate orbitals, was chosen and all single and double excitations were incorporated. The reference space was refined once, i.e., two DFT/MRCI calculations were performed in succession. Initial testing found that a second refinement of the reference space did not yield any significant change in excitation energies, oscillator strengths, or transition dipole moments. Excited state PES scans (e.g., Figure 6 in the main text) were conducted with the smaller def2-SVP basis set. All of these excited state calculations, including the PES scans, were repeated at the ωB97X-D3/def2-TZVP level of TD-DFT to support the DFT/MRCI results. Furthermore, trimer and tetramer conformations were computed at the ωB97X-D3/def2-SVP level of TD-DFT to assess whether they may be responsible for the red-shifted absorption band (Table S14).

To study fluorescence quencing, an excited-state optimization of a ground-state optimized displaced ($d = 4.8$ Å) metastable dimer was performed at the IEFPCM/ωB97XD/def2-SVP[26,27] level of TD-DFT using the state-specific approach[28] of the Gaussian (Version 16) program package.[29]

6 Additional DADQ aggregation properties

Table S3: Free enthalpies of association in kJ/mol for the formation of a dimer conformation from two monomers in DMSO at 298.15 K.

	A_{HB}	A_{ST}	A_{SD}	S_{HT}	S_{ST}
1	+0.5	–8.0	+14.1	+35.3	+50.5
1Me	+5.7	+0.3	+13.9	+23.8	+60.3
1Me$_2$	+16.0	—	+8.0	—	—
2	+2.7	–4.1	+1.4	+18.2	+34.8
2Me	+3.9	+31.2	+18.8	+19.1	+48.8
2Me$_2$	+18.8	—	+23.1	—	—

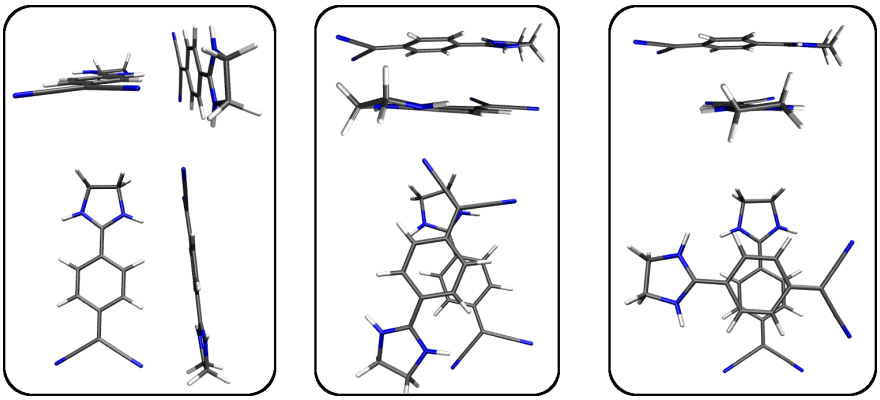

Figure S9: Other investigated dimer conformations of **1**. Two viewpoints (top and side) are shown. These conformations did not provoke any interest as they were either too high in free enthalpy (middle, right) or are simply intermediates between other conformations (left).

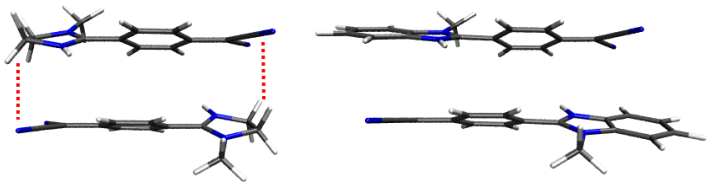

Figure S10: Side view of **1Me** and **2Me** to illustrate the difference in intermolecular interaction. **1Me** possesses slightly polarized terminal hydrogen atoms that may interact with the dicyano moiety in its vicinity (red dashed lines), which is not possible for **2Me**.

Table S4: Electronic, thermal, and solvation effect contributions to ΔG_{a} of all dimers in ACN normalized to a monomer and in kJ/mol

	ΔE	ΔG^{RRHO}	ΔG_{solv}	$\Delta G_{\mathrm{a}}^{\mathrm{tot}}$
		1		
A_{HB}	-88.2	32.6	46.8	-8.9
A_{ST}	-74.5	30.8	35.5	-8.2
A_{SD}	-90.1	32.2	53.9	-4.0
S_{HT}	-23.6	30.1	4.9	11.4
S_{ST}	-1.1	31.7	-10.8	19.9
		1Me		
A_{HB}	-90.5	31.8	50.6	-8.1
A_{ST}	-82.6	30.8	47.8	-3.9
A_{SD}	-63.1	31.9	60.9	29.7
S_{HT}	-30.1	30.7	10.0	10.6
S_{ST}	1.1	32.7	-8.1	25.7
		1Me$_2$		
A_{HB}	-57.7	29.5	34.4	6.1
A_{SD}	-80.1	32.7	49.2	1.8
		2		
A_{HB}	-96.6	35.5	51.0	-10.1
A_{ST}	-70.1	33.1	29.6	-7.5
A_{SD}	-87.1	32.0	52.4	-2.6
S_{HT}	-28.0	30.8	5.9	8.6
S_{ST}	-14.3	33.0	-6.7	12.0
		2Me		
A_{HB}	-100.2	34.8	54.6	-10.8
A_{ST}	-45.1	32.0	26.0	12.9
A_{SD}	-99.4	32.8	60.9	-5.7
S_{HT}	-32.4	30.6	9.6	7.9
S_{ST}	-14.7	33.9	-0.7	18.5
		2Me$_2$		
A_{HB}	-57.4	32.6	32.1	7.4
A_{SD}	-59.7	31.3	36.0	7.6

Table S5: Electronic, thermal, and solvation effect contributions to ΔG_{a} of all dimers in DMSO normalized to a monomer and in kJ/mol

	ΔE	ΔG^{RRHO}	ΔG_{solv}	$\Delta G_{\mathrm{a}}^{\mathrm{tot}}$
		1		
A_{HB}	-88.2	32.6	55.9	0.2
A_{ST}	-74.5	30.8	39.7	-4.0
A_{SD}	-90.1	32.2	64.9	7.0
S_{HT}	-16.7	30.4	3.9	17.6
S_{ST}	-1.1	31.7	-5.4	25.3
		1Me		
A_{HB}	-90.5	31.8	61.5	2.8
A_{ST}	-82.6	30.8	51.9	0.1
A_{SD}	-97.4	31.9	72.4	6.9
S_{HT}	-30.1	30.7	20.6	21.1
S_{ST}	1.1	32.7	-3.7	30.1
		1Me$_2$		
A_{HB}	-57.7	29.5	36.2	8.0
A_{SD}	-80.1	32.7	51.4	4.0
		2		
A_{HB}	-96.6	35.5	62.4	1.4
A_{ST}	-70.1	33.1	35.0	-2.1
A_{SD}	-87.1	32.0	65.3	10.3
S_{HT}	-28.0	30.8	29.5	32.2
S_{ST}	-14.3	33.0	-1.3	17.4
		2Me		
A_{HB}	-100.2	34.8	67.3	1.9
A_{ST}	-72.2	32.6	49.1	9.4
A_{SD}	-99.4	32.8	74.1	7.5
S_{HT}	-32.4	30.6	23.7	21.9
S_{ST}	-14.7	33.9	5.2	24.4
		2Me$_2$		
A_{HB}	-57.4	32.6	34.1	9.4
A_{SD}	-46.0	32.3	25.2	11.5

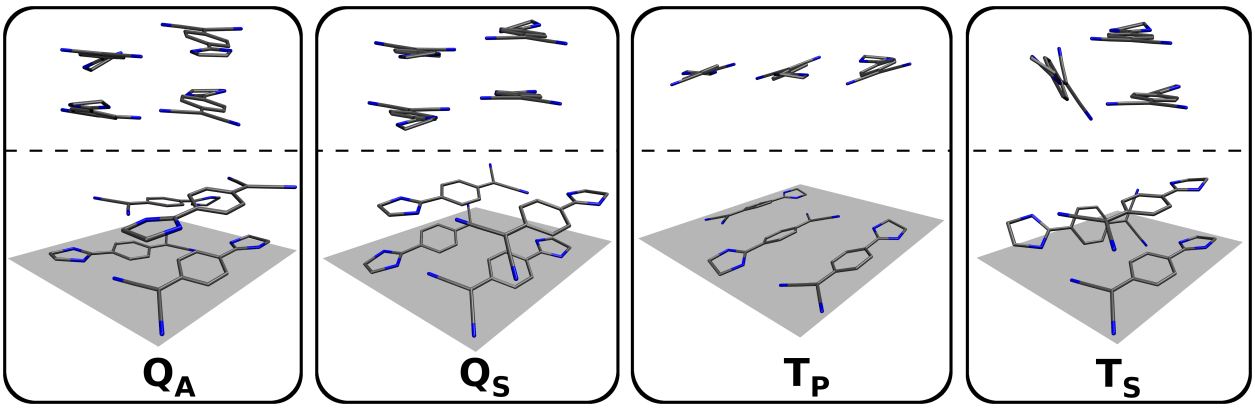

Figure S11: Selected trimer and tetramer conformations using the example of **1**. Two viewpoints are used for every structure separated by a dashed line. $\mathbf{Q_A}$: tetramer (or quadruplex) purely consisting of *anti*-dimer sub-units, $\mathbf{Q_S}$: tetramer (or quadruplex) containing *syn*-dimer sub-units, $\mathbf{T_P}$: trimer in planar structure, $\mathbf{T_S}$: trimer containing a *syn*-dimer sub-unit. Hydrogen atoms are omitted for clarity. While Q_A is always the most stable conformation, the stability of all other structures varies and depends on the DADQ compound.

6.1 Extension to trimers and tetramers

Apart from dimers, we have investigated DADQ trimers and tetramers, which are still somewhat feasible at an accurate level of computation. Figure S11 displays a few selected trimer and tetramer conformations of **1**. Table S6 summarizes the relative stabilities of the most stable conformation in each aggregate up to the tetramer for all molecules.

Table S6: Normalized free enthalpies of association in kJ/mol for the formation of *the most stable* conformation of a dimer (D), a trimer (T), and a tetramer (Q – quadruplex) in ACN at 298.15 K.

	D	T	Q
1	–8.9	–10.1	–19.9
1Me	–8.1	–4.6	–13.1
1Me$_2$	+1.8	—	—
2	–10.1	–13.0	–24.6
2Me	–10.8	–11.4	–18.8
2Me$_2$	+7.4	—	—

While there are seemingly endless possibilities to form such structures in solution, usually the tetramer Q_A (see caption of Figure S11 for designations) is the most stable conformation for all cases even in DMSO (excluding **1Me$_2$** and **2Me$_2$**). For example, the association of two **2**-A_{HB} dimers to form **2**-Q_A is accompanied by a remarkable gain in free enthalpy of roughly 60 kJ/mol in ACN. This large increase in stability is due to the local interaction of canceling dipole moments and is perhaps best illustrated using the example of **1**. It is observed that **1**-Q_S, which is a tetramer containing two *syn*-dimer sub-units, is almost 40 kJ/mol less stable than **1**-Q_A, which purely consists of *anti*-dimers (Table S7).
In contrast, stabilization of trimers is usually less pronounced in ACN and virtually non-existent in DMSO (Table S8) due to the lack of vanishing dipole moments. While **1** and **2** can be found in planar, hydrogen-bonded T_P structures owing to a free unmethylated amine group, **1Me** and **2Me** have to resort to trimeric conformations like T_S. Electrostatic interactions in the latter are somewhat inhibited causing a third monomer to mainly interact with the other two dispersively. This is supported by an EDA calculation, which yields around 74% for the electrostatic component of the stabilising interaction in **1**-T_P and circa 57% for **1**-T_S.
In general, **1Me** and **2Me** seem to form rather well-defined aggregates such as the dimer conformation A_{HB} or the tetramer conformation Q_A, while **1** and **2** may form aggregates of much greater complexity. For example, the latter two may extend the trimer conformation T_P with a fourth molecule to form a nearly planar tetramer purely facilitated through hydrogen-bonding. Figure S12 illustrates the expansive landscape of conformations

Table S7: Normalized free enthalpies of association in kJ/mol for the formation of trimer (T) and tetramer (Q) conformations in ACN at 298.15 K. See text for designations.

	Q_A	Q_S	T_P	T_S
1	–19.9	–10.1	–10.1	–6.0
1Me	–13.1	—	—	–4.6
2	–24.6	—	–12.5	–13.0
2Me	–18.8	—	—	–11.4

Table S8: Normalized free enthalpies of association in kJ/mol for the formation of trimer (T) and tetramer (Q) conformations in DMSO at 298.15 K. See text for designations.

	Q_A	Q_S	T_P	T_S
1	–6.9	+1.0	+2.0	+4.6
1Me	–1.4	—	—	6.8
2	–5.8	—	+2.6	+0.3
2Me	–4.8	—	—	+2.2

from dimers to tetramers for **2**.
Less accurate, but much more time- and resource-efficient semi-empirical calculations make it possible to obtain some information about aggregates beyond tetramers (Figure S13 and Table S9). It can be observed that even pentamers and hexamers may still be stable structures. While we are confident that most of the DADQ aggregation features are well covered by our dimer analyses, the properties of higher aggregates eventually leading up to the solid state are comparably difficult to address both experimentally and theoretically and will be the subject of further investigations in the future.

Table S9: Normalized free enthalpies of association in kJ/mol for the formation of dimers (D), trimers (T), tetramers (Q), pentamers (P), and hexamers (H) conformations in ACN at 298.15 K using lower-level calculations (see computational details).

	D	T	Q	P	H
1	–7.0	–7.7	–11.1	–12.6	–12.2
1Me	–4.1	–1.6	–12.7	–6.2	–10.1
$1Me_2$	–1.4	+4.2	+17.2	+12.2	+14.5
2	–12.9	–14.4	–21.1	–22.2	–22.8
2Me	–12.1	–8.7	–16.3	–17.2	–18.0
$2Me_2$	+12.2	+7.5	+3.8	+16.0	+19.1

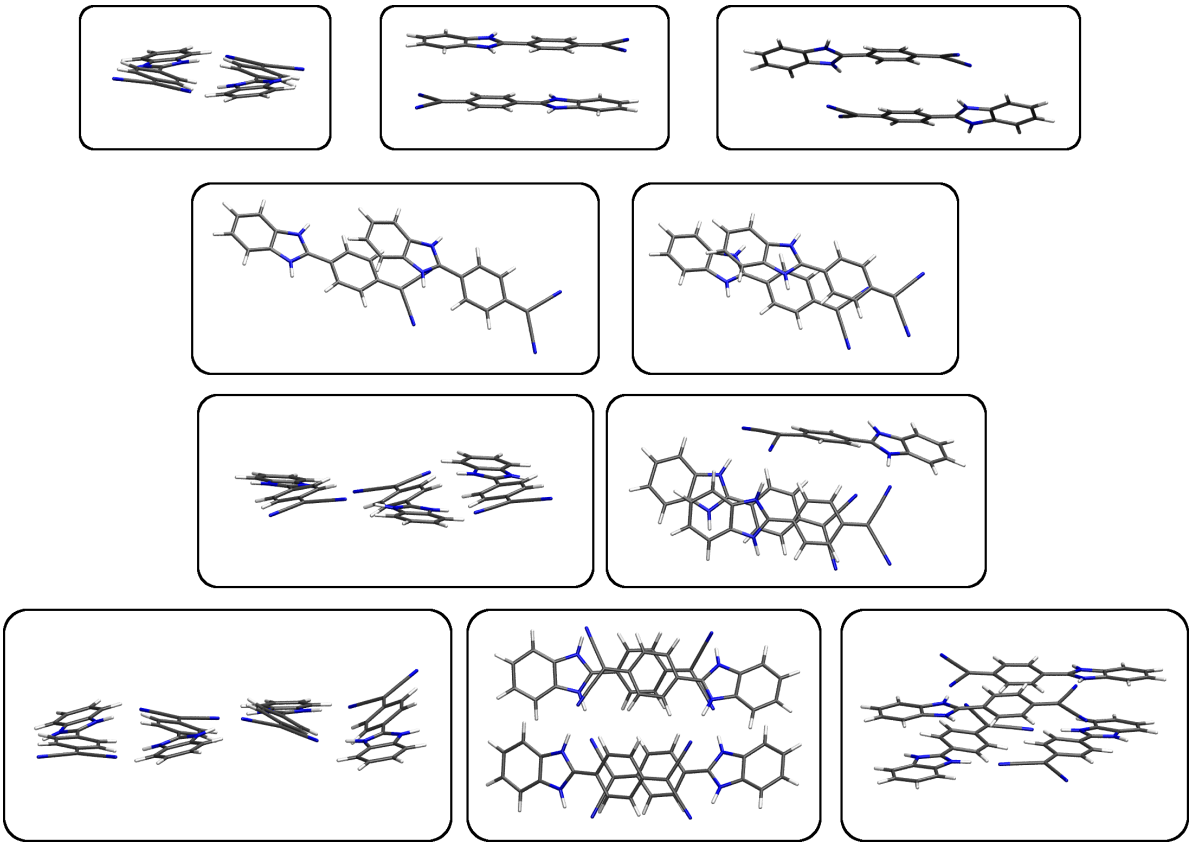

Figure S12: Conformational landscape of **2**. Two top rows: dimers, middle: trimers, bottom: tetramers

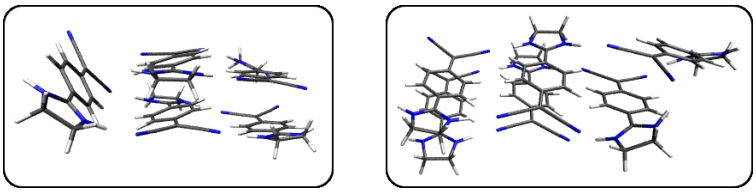

Figure S13: A pentamer (left) and a hexamer (right) of **1**.

7 Excited state calculations

Table S10: Comparison of experimental and calculated energetic shifts in nm relative to the computed monomer excitation wavelengths of compounds **1**, **1Me**, **2**, and **2Me** in the *syn* conformations computed at the SMD/BHLYP/def2-TZVP(-f)/MRCI level. The experimental red-shifts and those obtained by the transient dimer species (see text) are given in eV as well for better comparability.

	1	**1Me**	**2**	**2Me**
$\lambda_{\mathrm{exc,mon}}$ (calc.)	375	355	420	399
$\lambda_{\mathrm{exc,mon}}$ (exp.)	355	344	392	366
S_{HT}	+14	+15	+13	+7
S_{ST}	+17	+31	+17	+28
exp.	+55	+50	+48	+57
exp. (eV)	–0.47	–0.46	–0.35	–0.47
transient	+41	+34	+37	+47
transient (eV)	–0.33	–0.31	–0.24	–0.33

Table S11: Comparison of experimental and calculated values and energetic shifts in nm relative to the computed monomer excitation wavelengths of compounds **1**, **1Me**, **2**, and **2Me** in all stable *anti* conformations computed at the SMD/ωB97X-D3/def2-TZVP level of TD-DFT. The experimental red-shifts and those obtained by the transient dimer species (see main text) are given in eV as well for better comparability. Note that there is a systematic overestimation of the excitation energies with respect to experiment and DFT/MRCI (*cf.* table 2 in the main text).

	1	**1Me**	**2**	**2Me**
$\lambda_{\mathrm{exc,mon}}$ (exp.)	355	344	392	366
$\lambda_{\mathrm{exc,mon}}$ (calc.)	327	314	352	334
A_{HB}	–23	–20	–29	–22
A_{ST}	–15	–8	–7	–6
A_{SD}	–15	–12	–23	–13
exp.	+55	+50	+48	+57
exp. (eV)	–0.47	–0.46	–0.35	–0.47
transient	+7	+5	+1	+11
transient (eV)	–0.08	–0.06	–0.01	–0.12

Table S12: Detailed DFT/MRCI results for **1**, **1Me**, **2**, and **2Me**: Excitation wavelength is given in nm, transition dipole moments M_{trans} in Debye, orbital contributions in %. f_{osc} is the oscillator strenght in length formalism. HOMO and LUMO are abbreviated as H and L, respectively. The S_2 state is only analysed for the dimeric species. Oscillator strengths of zero are always due to the symmetry of the orbitals involved in the transition (see main text). Experimental values are given in the headings for comparison.

1: $\lambda_{\mathrm{ex}} = 355, 410$ nm

	S_1				S_2			
	λ_{ex}	f_{osc}	M_{trans}	orbital contributions	λ_{ex}	f_{osc}	M_{trans}	orbital contributions
Mon	375	0.93	8.62	H → L (89)				
A_{HB}	387	0.00	0.00	H → L (46), H-1 → L+1 (40)	369	1.55	11.03	H-1 → L (44), H → L+1 (42)
A_{ST}	413	0.00	0.06	H → L (80), H-1 → L+1 (7)	376	1.43	10.71	H-1 → L (67), H → L+1 (17)
A_{SD}	418	0.00	0.03	H → L (79), H-1 → L+1 (8)	374	1.02	9.04	H → L+1 (85), H-1 → L (1)
metastable	413	1.81	12.59	H → L (58), H-1 → L+1 (28)	400	0.00	0.08	H-1 → L (55), H → L+1 (30)

1Me: $\lambda_{\mathrm{ex}} = 344, 394$ nm

	S_1				S_2			
	λ_{ex}	f_{osc}	M_{trans}	orbital contributions	λ_{ex}	f_{osc}	M_{trans}	orbital contributions
Mon	355	0.87	8.10	H → L (89)				
A_{HB}	364	0.00	0.03	H → L (47), H-1 → L+1 (40)	351	1.48	10.50	H-1 → L (44), H → L+1 (43)
A_{ST}	400	0.00	0.03	H → L (77), H-1 → L+1 (10)	366	1.50	10.84	H-1 → L (50), H → L+1 (36)
A_{SD}	387	0.00	0.04	H → L (71), H-1 → L+1 (15)	358	1.25	9.76	H → L+1 (78), H-1 → L (9)

2: $\lambda_{\mathrm{ex}} = 392, 440$ nm

	S_1				S_2			
	λ_{ex}	f_{osc}	M_{trans}	orbital contributions	λ_{ex}	f_{osc}	M_{trans}	orbital contributions
Mon	420	1.33	10.93	H → L (86)				
A_{HB}	428	0.00	0.04	H → L (48), H-1 → L+1 (36)	408	2.31	14.17	H-1 → L (43), H → L+1 (41)
A_{ST}	478	0.00	0.05	H → L (74), H-1 → L+1 (10)	440	1.38	11.36	H-1 → L (84)
A_{SD}	466	0.00	0.09	H → L (72), H-1 → L+1 (11)	414	1.55	11.67	H → L+1 (80), H-1 → L (3)
metastable	459	2.60	15.93	H → L (45), H-1 → L+1 (39)	447	0.00	0.04	H-1 → L (42), H → L+1 (41)

2Me: $\lambda_{\mathrm{ex}} = 366, 423$ nm

	S_1				S_2			
	λ_{ex}	f_{osc}	M_{trans}	orbital contributions	λ_{ex}	f_{osc}	M_{trans}	orbital contributions
Mon	399	1.17	9.96	H → L (85)				
A_{HB}	407	0.00	0.08	H → L (45), H-1 → L+1 (36)	391	2.14	13.33	H → L+1 (43), H-1 → L (40)
A_{ST}	449	0.00	0.03	H → L (64), H-1 → L+1 (19)	412	1.86	12.83	H-1 → L (72), H → L+1 (11)
A_{SD}	427	0.00	0.06	H → L (68), H-1 → L+1 (13)	401	1.71	12.08	H → L+1 (76), H-1 → L (6)

Table S13: Detailed TD-ωB97X-D3/def2-TZVP results for **1**, **1Me**, **2**, and **2Me**: Excitation wavelength is given in nm, f_{osc} is the oscillator strenght in length formalism. The S_2 state is only shown for the dimeric species. Oscillator strengths of zero are always due to the symmetry of the orbitals involved in the transition (see main text).

1: $\lambda_{\mathrm{ex}} = 355, 410$ nm

	S_1		S_2	
	λ_{ex}	f_{osc}	λ_{ex}	f_{osc}
Mon	327	0.84		
A_{HB}	321	0.00	304	1.45
A_{ST}	343	0.00	312	1.39
A_{SD}	349	0.00	312	1.00
metastable	334	1.89	324	0.00

1Me: $\lambda_{\mathrm{ex}} = 344, 394$ nm

	S_1		S_2	
	λ_{ex}	f_{osc}	λ_{ex}	f_{osc}
Mon	314	0.78		
A_{HB}	309	0.00	294	1.37
A_{ST}	334	0.00	306	1.34
A_{SD}	329	0.00	302	1.20

2: $\lambda_{\mathrm{ex}} = 392, 440$ nm

	S_1		S_2	
	λ_{ex}	f_{osc}	λ_{ex}	f_{osc}
Mon	352	1.24		
A_{HB}	340	0.00	323	2.27
A_{ST}	379	0.00	345	1.54
A_{SD}	367	0.00	329	2.09
metastable	353	2.81	343	0.00

2Me: $\lambda_{\mathrm{ex}} = 366, 423$ nm

	S_1		S_2	
	λ_{ex}	f_{osc}	λ_{ex}	f_{osc}
Mon	334	1.12		
A_{HB}	327	0.00	312	2.12
A_{ST}	359	0.00	328	1.90
A_{SD}	344	0.00	321	1.88

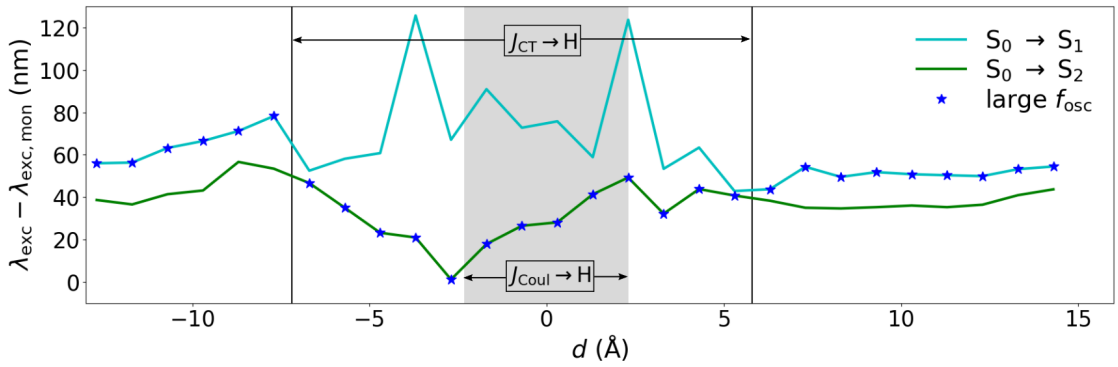

Figure S14: SMD/BHLYP/def2-SVP/MRCI excitation wavelength shift of the first two excited singlet states with respect to the computed monomer excitation wavelength (420 nm) of **2**. Darkblue Stars indicate the bright state. The grey shaded area and the two vertical lines encompass the H-aggregate zones according to the definitions of J_{Coul} and J_{CT}, respectively.

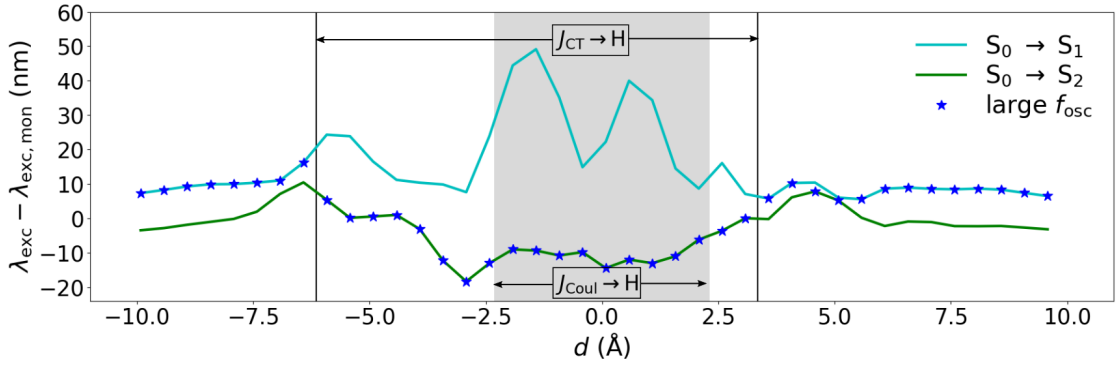

Figure S15: SMD/TD-ωB97X-D3/def2-TZVP excitation wavelength shift of the first two excited singlet states with respect to the computed monomer excitation wavelength (327 nm) of **1**. Darkblue Stars indicate the bright state. The grey shaded area and the two vertical lines encompass the H-aggregate zones according to the definitions of J_{Coul} and J_{CT}, respectively.

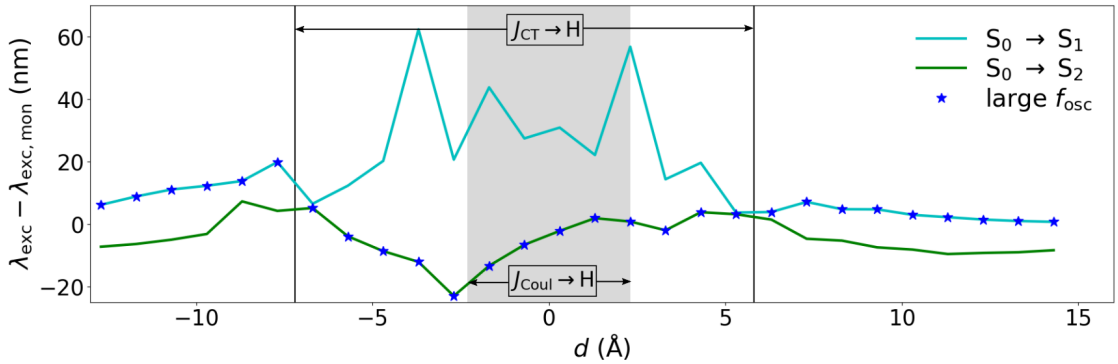

Figure S16: SMD/TD-ωB97X-D3/def2-TZVP excitation wavelength shift of the first two excited singlet states with respect to the computed monomer excitation wavelength (352 nm) of **2**. Darkblue Stars indicate the bright state. The grey shaded area and the two vertical lines encompass the H-aggregate zones according to the definitions of J_{Coul} and J_{CT}, respectively.

Table S14: Excitation wavelengths of the bright states and energetic shifts in nm relative to the computed monomer excitation wavelengths computed at the SMD/ωB97X-D3/def2-TZVP level of the investigated trimers and tetramers of **1**. Oscillator strengths are given in parentheses.

	Q_A	Q_S	T_P	T_S
$\lambda_{\mathrm{exc,mon}}$	308 (0.49) / 296 (1.64)	302 (2.16)	318 (0.27) / 297 (1.76)	326 (0.27) / 300 (1.31)
$\lambda_{\mathrm{exc}} - \lambda_{\mathrm{exc,mon}}$	-19 / -31	-25	-9 / -30	-1 / -27

8 AIMD simulations

Ab-initio molecular dynamics simulations were conducted using the GFN2-xTB[3] code to assess the possibility of encountering metastable dimers of **1**-A_{ST}. No explicit solvent molecules were used. Instead, the GBSA solvent model as implemented in the program was used for acetonitrile. The run lasted 75 ps before the dimer dissociated due to the energy being drained into rotational motion. This effect is an artifact of the algorithm and is known as "flying ice cube".[30] Nevertheless, conformational changes seemed sufficiently fast to warrant a conclusive analysis of the simulation. More accurate simulations employing more sophisticated methods and large explicit solvent cavities could not be achieved for useful time scales.
A time step of 0.5 fs in combination with the Berendsen thermostat[31] set to 293 K was used. Structures were written out every 10 steps, or 5 fs. The obtained trajectory was aligned by a translational and rotational fit with the positions of one mononmer in the starting frame as reference. Subsequently, the root-mean-square deviation (RMSD) of atomic positions throughout the simulation was calculated with the same reference. Density-based density-peaks clustering was used to cluster the RMSD time-series where as a result 4 clusters were selected (density-cutoff $\rho = 100$, distance-cutoff $\delta = 0.02$, Figure S17).[32]

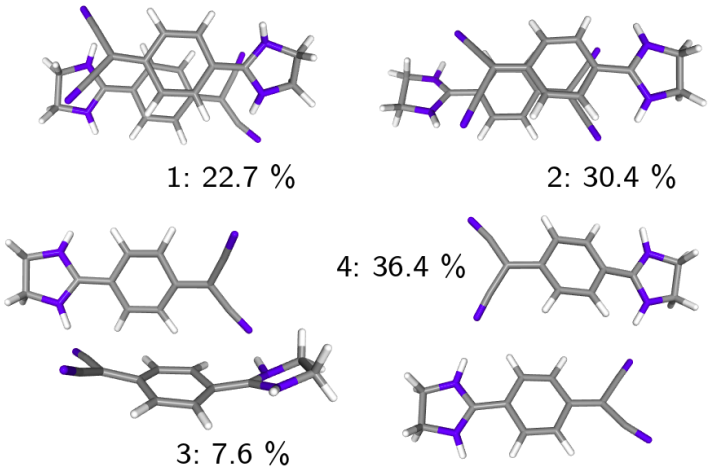

Figure S17: Representative snapshots for identified dimer orientations extracted by density-peaks clustering. A label indicates the relative population among all identified dimer states.

Among the identified dimers are stacked anti-parallel structures resembling **1**-A_{ST} or **1**-A_{SD} with varying degrees of shifting along longitudinal displacement coordinate d (clusters 1 and 2) besides flat hydrogen-bonded dimers comparable to **1**-A_{HB} (clusters 3 and 4). The stacked dimers show projected COM distances as illustrated in Figure S18. About 20% of the structures show a distance below –3 Å resembling a metastable dimer.

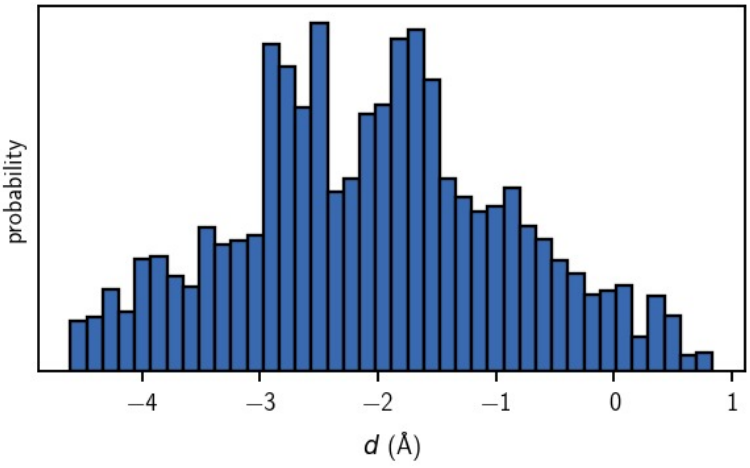

Figure S18: Histogram of the COM distance between the two monomers considering only stacked dimers.

9 Coordinates of molecular structures of all dimers

All SCF energies are given in Hartree at the ωB97X-D3/def2-QZVP level of DFT. All structures represent minima on their respective potential energy surface.

1-A_{HB}

Energy = -1361.609308247
N -0.4419774 6.2691284 -1.0838224
C -0.3392279 5.1836179 -0.6875822
C -0.2022421 3.8743497 -0.2089482
C -1.3629116 3.2217170 0.2037037
N -2.3162466 2.6541797 0.5457166
C 1.0710999 3.2079446 -0.1829668
C 2.2333690 3.8242835 -0.6857251
C 3.4461297 3.1752048 -0.6800136
C 3.5650984 1.8754402 -0.1750025
C 2.4197921 1.2584803 0.3402284
C 1.2075303 1.9073226 0.3408284
H 0.3501867 1.4011020 0.7664876
H 2.4752331 0.2673304 0.7712552
C 4.8365826 1.1871852 -0.1904647
N 6.0094171 1.7904014 -0.3025170
C 7.1087788 0.8452254 -0.1537600
C 6.3828057 -0.5043747 -0.2574091
N 4.9855800 -0.1183644 -0.1053420
H 4.2257986 -0.7917182 -0.2276542
H 4.3020150 3.6844810 -1.1050643
H 2.1816161 4.8225066 -1.1010479
N 1.0239380 -5.7430700 1.2159484
C 0.9211788 -4.6580688 0.8183254
C 0.7841821 -3.3493385 0.3382256
C 1.9450111 -2.6969864 -0.0745291
N 2.8984864 -2.1298008 -0.4167138
C -0.4892269 -2.6831163 0.3114184
C -0.6255849 -1.3825750 -0.2126066
C -1.8378264 -0.7337367 -0.2122332
C -2.9832388 -1.3506519 0.3028424
C -2.8644554 -2.6505386 0.8076363
C -1.6516865 -3.2995999 0.8135926
H -1.6001281 -4.2980652 1.2283582
H -3.7205511 -3.1598648 1.2321986
C -4.2546241 -0.6622657 0.3184991
N -5.4274758 -1.2654466 0.4308546
C -6.5267800 -0.3203176 0.2811298
C -5.8008704 1.0293061 0.3846917
N -4.4036201 0.6432777 0.2329361
H -3.6438327 1.3165956 0.3554097
H -1.8931329 0.2573936 -0.6433261
H 0.2318030 -0.8764527 -0.6382795
H -5.5502756 -2.2520891 0.2701673
H 6.1323012 2.7770513 -0.1420130
H 6.5341690 -0.9777620 -1.2281828
H 6.6845083 -1.2040399 0.5189095
H 7.8545994 0.9829399 -0.9331865
H 7.5891878 0.9808029 0.8157233
H -7.2730197 -0.4576942 1.0601929

H -7.0065557 -0.4561435 -0.6886079
H -5.9523614 1.5028921 1.3553690
H -6.1024090 1.7289488 -0.3917284

1-A_{ST}

Energy = -1361.606643984
N -4.4208466 3.2737398 4.4908444
C -4.3919811 2.1339412 4.7093142
C -4.3544076 0.7576927 4.9618547
C -5.5224841 0.1752417 5.4673716
N -6.4910362 -0.3134416 5.8806521
C -3.1696037 -0.0150459 4.7327432
C -1.9895274 0.5768481 4.2405899
C -0.8499230 -0.1630062 4.0404429
C -0.8171121 -1.5355588 4.3142615
C -1.9913818 -2.1344094 4.7863165
C -3.1335276 -1.3998598 4.9909010
H -4.0177589 -1.9060308 5.3563833
H -1.9668407 1.6355286 4.0166552
H 0.0250426 0.3547326 3.6689180
H -2.0331741 -3.1955294 4.9960114
C 0.3925578 -2.3020206 4.1382841
N 1.5248748 -1.8316847 3.6486372
H 1.6635944 -0.8815165 3.3517598
C 2.6072076 -2.8017933 3.7160182
H 3.0592189 -2.9450560 2.7370301
H 3.3794272 -2.4596459 4.4048338
C 1.8864036 -4.0621348 4.2269816
H 2.3255444 -4.4444621 5.1467634
H 1.8737967 -4.8659302 3.4923991
N 0.5393705 -3.5704839 4.4726157
H -0.1749171 -4.1313347 4.9033294
N 0.8422862 -6.3840748 1.2302190
C 0.8126150 -5.2436745 1.0150960
C 0.7739573 -3.8667769 0.7663248
C 1.9421054 -3.2817337 0.2639769
N 2.9107295 -2.7909258 -0.1465860
C -0.4118061 -3.0958641 0.9964405
C -1.5905290 -3.6894301 1.4899032
C -2.7309862 -2.9511995 1.6912122
C -2.7662134 -1.5787791 1.4170838
C -1.5932903 -0.9783075 0.9436235
C -0.4502538 -1.7111518 0.7380867
H 0.4325337 -1.2038412 0.3707051
H -1.6112276 -4.7479935 1.7146099
H -3.6044944 -3.4698967 2.0648636
H -1.5534778 0.0825760 0.7324471
C -3.9768664 -0.8139897 1.5937614
N -4.1229000 0.4565681 1.2672590
H -3.4066658 1.0207457 0.8443149
C -5.4727636 0.9445160 1.5043577
H -5.4667190 1.7511469 2.2357721
H -5.9084730 1.3217671 0.5807278
C -6.1921440 -0.3162783 2.0166914
H -6.6384709 -0.1745823 2.9986374

H -6.9688281 -0.6559147 1.3317660
N -5.1108226 -1.2879891 2.0760201
H -5.2506865 -2.2401553 2.3658934

1-A_{SD}

Energy = -1361.606006042
N -4.6102486 3.2517135 4.2882318
C -4.5009345 2.1398434 4.6115369
C -4.4071074 0.7993613 4.9876119
C -5.5918111 0.2098796 5.4469956
N -6.5755804 -0.2734646 5.8281064
C -3.2093749 0.0365122 4.7969301
C -2.0288932 0.6306692 4.3086800
C -0.8906608 -0.1090277 4.1009492
C -0.8709880 -1.4839117 4.3642952
C -2.0336893 -2.0829844 4.8632010
C -3.1678754 -1.3417637 5.0849373
H -4.0477457 -1.8393050 5.4717403
H -2.0155745 1.6857062 4.0671576
H -0.0205926 0.3844096 3.6865317
H -2.0498582 -3.1393312 5.0996254
C 0.2972407 -2.2733569 4.0760730
N 1.5293095 -1.8029807 3.9977242
H 1.7922305 -0.9029069 4.3657892
C 2.4992726 -2.8732744 3.8069629
H 3.2151666 -2.6240919 3.0272411
H 3.0431355 -3.0536457 4.7348929
C 1.5944090 -4.0545046 3.4301031
H 1.8639400 -4.9718133 3.9480847
H 1.6000610 -4.2480535 2.3563915
N 0.2800606 -3.5774936 3.8444596
H -0.5674098 -4.0478203 3.5506755
N -2.2703862 -4.2003750 2.0760284
C -2.3824016 -3.0885510 1.7534613
C -2.4793600 -1.7481895 1.3778734
C -1.2961616 -1.1555703 0.9184420
N -0.3140937 -0.6690239 0.5371827
C -3.6785488 -0.9879031 1.5692510
C -4.8571468 -1.5839608 2.0598343
C -5.9961376 -0.8460909 2.2698439
C -6.0187793 0.5286944 2.0060488
C -4.8583912 1.1293097 1.5035823
C -3.7233904 0.3899973 1.2798499
H -2.8454517 0.8888384 0.8903620
H -4.8680586 -2.6388468 2.3021292
H -6.8642652 -1.3408671 2.6867078
H -4.8444905 2.1854961 1.2662631
C -7.1864064 1.3169660 2.2996496
N -7.1691679 2.6216930 2.5287342
H -6.3203853 3.0932898 2.8163744
C -8.4809690 3.0979342 2.9520650
H -8.4784045 3.2947417 4.0251242
H -8.7559882 4.0131633 2.4332758
C -9.3871455 1.9142248 2.5860547
H -10.0947305 1.6648617 3.3732906

H -9.9407473 2.0918826 1.6634012
N -8.4172555 0.8453973 2.3874640
H -8.6820831 -0.0560524 2.0241705

1-S_{HT}

Energy = -1361.595580613
N 1.8343759 4.5563480 0.2042101
C 1.7878796 3.7963928 1.0800732
C 1.7230120 2.8771618 2.1348707
C 2.8883888 2.6952511 2.8902855
N 3.8499571 2.5392687 3.5210697
C 0.5202849 2.1571937 2.4284594
C -0.6517994 2.3382228 1.6641990
C -1.8054096 1.6494041 1.9497193
C -1.8570223 0.7345699 3.0096489
C -0.6980877 0.5441886 3.7735945
C 0.4555727 1.2355192 3.4947670
H 1.3247009 1.0655915 4.1171200
H -0.6947648 -0.1354066 4.6166289
C -3.0672822 0.0104844 3.3060796
N -4.2662579 0.3229402 2.8438336
C -5.3025706 -0.5179086 3.4296674
C -4.4759920 -1.6351113 4.0805367
N -3.1368984 -1.0599643 4.0777101
H -2.3276480 -1.5968289 4.3444144
H -2.6683122 1.8142991 1.3166637
H -0.6529629 3.0275228 0.8296549
N -7.2485709 -2.4481058 5.9053096
C -8.1497684 -2.2354677 5.2050587
C -9.2448340 -1.9878484 4.3682853
C -9.0428485 -1.0928704 3.3102125
N -8.8762169 -0.3528822 2.4316691
C -10.5101004 -2.6238845 4.5830959
C -11.6115291 -2.3764110 3.7370437
C -12.8250722 -2.9849796 3.9465087
C -13.0100096 -3.8809192 5.0076751
C -11.9221450 -4.1369158 5.8525469
C -10.7090354 -3.5253244 5.6498667
H -9.8981786 -3.7436594 6.3328312
H -12.0223813 -4.8045120 6.6991627
C -14.2826541 -4.5219140 5.2236115
N -14.4735684 -5.5810470 5.9914900
C -15.8429770 -6.0712267 5.8973418
C -16.5505139 -4.9028884 5.1978823
N -15.4245988 -4.1343096 4.6821815
H -15.5498466 -3.2286746 4.2596311
H -13.6293795 -2.7722950 3.2533573
H -11.5091281 -1.6991972 2.8988840
H -15.8717629 -6.9847390 5.3024522
H -16.2533993 -6.2831917 6.8816522
H -17.2056764 -5.2285312 4.3935317
H -17.1283982 -4.2953177 5.8951081
H -13.7202266 -6.1706438 6.3066559
H -5.9858292 -0.8853382 2.6678918
H -5.8736753 0.0510576 4.1645024

H -4.4889001 -2.5532495 3.4921772
H -4.8095925 -1.8621585 5.0894989
H -4.4779867 1.2197786 2.4374639

1-S_{ST}

Energy = -1361.600664080
N 4.0876123 3.6049562 -2.5602314
C 3.9251343 3.0445597 -1.5571816
C 3.7214288 2.3871760 -0.3380758
C 4.8660890 1.9717001 0.3531373
N 5.8120723 1.6340421 0.9341239
C 2.4107355 2.0851726 0.1388832
C 1.2586393 2.4475678 -0.5895103
C 0.0018683 2.1260426 -0.1433282
C -0.1858536 1.4347096 1.0606031
C 0.9553595 1.0855431 1.8005438
C 2.2121490 1.4037450 1.3594156
H 3.0644329 1.1053384 1.9556606
H 0.8683320 0.5647706 2.7457200
C -1.4977872 1.0685958 1.5094831
N -2.6378368 1.4645774 0.9500539
C -3.7855272 1.0790671 1.7619423
C -3.1779535 0.0286613 2.6986951
N -1.7541691 0.2825635 2.5415067
H -1.0543836 -0.2660683 3.0123158
H -0.8414063 2.3990732 -0.7653465
H 1.3576845 2.9657654 -1.5344451
N 4.2138860 -2.0479865 1.4834133
C 3.6753374 -1.6709841 0.5273092
C 3.0126847 -1.2262506 -0.6234436
C 3.8079184 -0.7116409 -1.6565544
N 4.4620870 -0.3095086 -2.5257866
C 1.5913733 -1.2766628 -0.7282432
C 0.9172113 -0.7464627 -1.8492875
C -0.4501010 -0.7706426 -1.9378373
C -1.2324176 -1.3403278 -0.9222613
C -0.5720098 -1.8997864 0.1817848
C 0.7949658 -1.8615037 0.2818520
H 1.2640477 -2.2859403 1.1599716
H -1.1302951 -2.3528653 0.9918843
C -2.6656666 -1.3361428 -1.0032424
N -3.4739507 -2.0428976 -0.2200888
C -4.8594210 -1.9453979 -0.6664180
C -4.8049207 -0.7409889 -1.6140569
N -3.3749564 -0.6173789 -1.8555258
H -2.9879663 0.1314527 -2.4057911
H -0.9107621 -0.3496009 -2.8229077
H 1.4828828 -0.2912507 -2.6515227
H -3.1501949 -2.8547627 0.2811102
H -5.1511015 -2.8596394 -1.1843286
H -5.5347526 -1.7922146 0.1720633
H -5.3485580 -0.9092197 -2.5405526
H -5.1886908 0.1701201 -1.1518124
H -3.4174595 -0.9896912 2.3896001
H -3.4889620 0.1577991 3.7325626

H -4.5907228 0.6794891 1.1492399
H -4.1683087 1.9421412 2.3079047
H -2.6815061 2.2670003 0.3432810

1Me-A_{HB}

Energy = -1440.049649916
N -0.5360340 6.0251403 -1.2883374
C -0.3922143 4.9846046 -0.7949718
C -0.2043467 3.7307754 -0.2006718
C -1.3236559 3.1207072 0.3614771
N -2.2470400 2.5955426 0.8313914
C 1.0826513 3.0845942 -0.1914399
C 2.1983906 3.6673510 -0.8201819
C 3.4296806 3.0509858 -0.8107411
C 3.6091719 1.8176037 -0.1770068
C 2.5048337 1.2218768 0.4405803
C 1.2757102 1.8417026 0.4405767
H 0.4504307 1.3545659 0.9444636
H 2.6104148 0.2726991 0.9497486
C 4.8891107 1.1306318 -0.1970695
N 6.0754808 1.7001990 -0.0745577
C 7.1405190 0.7161560 -0.2567774
C 6.3787056 -0.6161044 -0.2757349
N 4.9954928 -0.1729581 -0.3467231
H 4.2106777 -0.8011879 -0.5339500
H 4.2480740 3.5260573 -1.3357796
H 2.0985368 4.6149050 -1.3339459
N 1.1363206 -5.4778294 1.4310394
C 0.9861749 -4.4434705 0.9267157
C 0.7910510 -3.1970300 0.3192663
C 1.9051440 -2.5911707 -0.2578348
N 2.8242789 -2.0696811 -0.7401109
C -0.4973546 -2.5537772 0.3118929
C -0.6976635 -1.3184240 -0.3325456
C -1.9281387 -0.7015312 -0.3311636
C -3.0270104 -1.2928537 0.3002840
C -2.8402099 -2.5184627 0.9469543
C -1.6073856 -3.1318007 0.9550299
H -1.5017087 -4.0731252 1.4789593
H -3.6537582 -2.9892921 1.4831155
C -4.3085148 -0.6089455 0.3201870
N -5.4943291 -1.1826663 0.2122294
C -6.5604160 -0.1988618 0.3896560
C -5.8017638 1.1352570 0.3843303
N -4.4171769 0.6962047 0.4541618
H -3.6324985 1.3285774 0.6278182
H -2.0392857 0.2417264 -0.8501066
H 0.1231183 -0.8350778 -0.8473912
C -5.8019307 -2.5579064 -0.0954263
C 6.3841255 3.0706714 0.2527025
H 6.6323796 -1.2263591 -1.1397229
H 6.5472973 -1.2065215 0.6254844
H 7.6746378 0.9111681 -1.1882172
H 7.8517683 0.7802542 0.5654085
H -7.0864565 -0.3824829 1.3279986

H -7.2781557 -0.2757651 -0.4257472
H -6.0522505 1.7579192 1.2403521
H -5.9765574 1.7114969 -0.5248430
H -6.6326621 -2.5820924 -0.7987592
H -6.0896631 -3.1129628 0.7979165
H -4.9509648 -3.0465383 -0.5613733
H 5.5310878 3.5554265 0.7189287
H 6.6792749 3.6363131 -0.6315225
H 7.2100696 3.0839513 0.9619571

1Me-A_{ST}

Energy = -1440.044051886
N -6.9659971 4.9388729 6.3981302
C -6.9993568 3.7896392 6.2375239
C -7.0362156 2.4054170 6.0330796
C -8.2872602 1.7860068 6.1179641
N -9.3221480 1.2650866 6.1998505
C -5.8408989 1.6479898 5.7922268
C -4.5645944 2.2345602 5.8996775
C -3.4219668 1.4992025 5.6961023
C -3.4837967 0.1398461 5.3626370
C -4.7481445 -0.4437514 5.2221047
C -5.8920932 0.2861696 5.4405908
H -6.8489918 -0.2052234 5.3198795
H -4.4695010 3.2783793 6.1703767
H -2.4662646 1.9907593 5.8295724
H -4.8534346 -1.4693655 4.8981361
C -2.2598223 -0.5918962 5.1221470
N -1.1596604 -0.0150390 4.6660100
H -1.0986431 0.9559510 4.4120582
C -0.0239432 -0.9213015 4.6792049
C -0.7274439 -2.2686413 4.8377783
N -2.0499137 -1.8819891 5.3285905
C -2.9261863 -2.8560570 5.9322978
N -2.4441533 -3.8472344 1.1370501
C -2.4058046 -2.6973171 1.2916107
C -2.3628160 -1.3122234 1.4889459
C -1.1091876 -0.6987202 1.3983604
N -0.0719498 -0.1834028 1.3111044
C -3.5547566 -0.5488673 1.7277097
C -4.8335750 -1.1305899 1.6232276
C -5.9729652 -0.3898062 1.8253233
C -5.9050715 0.9702758 2.1543454
C -4.6382433 1.5493441 2.2917124
C -3.4975455 0.8140742 2.0743705
H -2.5384600 1.3018101 2.1923365
H -4.9334403 -2.1748380 1.3558229
H -6.9308851 -0.8776806 1.6942954
H -4.5286375 2.5756486 2.6121555
C -7.1255357 1.7081287 2.3933933
N -7.3296775 2.9982834 2.1821665
C -6.4510534 3.9647307 1.5698894
C -8.6495538 3.3933791 2.6730254
C -9.3590354 2.0500182 2.8390601
N -8.2277778 1.1381513 2.8530536

H -8.2923254 0.1690022 3.1130299
H -5.8893220 4.5306795 2.3142498
H -7.0542934 4.6628310 0.9931233
H -5.7576755 3.4790064 0.8890080
H -2.3213617 -3.5557583 6.5054591
H -3.4843306 -3.4190482 5.1829525
H -3.6230076 -2.3778599 6.6150370
H -0.2325647 -2.9182180 5.5568261
H -0.8255234 -2.8088676 3.8926485
H 0.6328475 -0.6960198 5.5214883
H 0.5445938 -0.8465254 3.7570106
H -9.1423255 4.0416440 1.9512404
H -8.5476545 3.9382433 3.6150328
H -10.0190414 1.8240233 1.9994885
H -9.9256134 1.9818677 3.7628970

1Me-A_{SD}

Energy = -1440.047042174
N -4.7066699 2.8697647 5.5322972
C -4.6834473 1.7259754 5.3365553
C -4.6588552 0.3461170 5.0992188
C -5.9026025 -0.2774923 5.0212563
N -6.9569229 -0.7653428 4.9521067
C -3.4308561 -0.3549899 4.8539074
C -2.1916709 0.3107972 4.8950705
C -1.0149014 -0.3534938 4.6445143
C -1.0098859 -1.7242169 4.3644943
C -2.2359019 -2.3979321 4.3220640
C -3.4143022 -1.7308278 4.5586385
H -4.3446956 -2.2797691 4.4898311
H -2.1536994 1.3692748 5.1183371
H -0.0840210 0.1975520 4.6900198
H -2.2793854 -3.4448899 4.0524012
C 0.2347891 -2.3856617 4.0388839
N 1.2071621 -1.7806749 3.3736101
H 1.0313958 -0.9423161 2.8295740
C 2.2887859 -2.6987461 3.0499776
C 1.9024651 -3.9480393 3.8522559
N 0.5644132 -3.6270351 4.3448457
C -0.0919021 -4.5134537 5.2770169
N -2.1693063 -3.3281015 0.7876077
C -2.1873122 -2.1844502 0.9846231
C -2.2064796 -0.8047350 1.2230903
C -0.9608612 -0.1850818 1.3017727
N 0.0942976 0.3007804 1.3716581
C -3.4318680 -0.0992948 1.4688293
C -4.6734270 -0.7606551 1.4286032
C -5.8475423 -0.0922161 1.6806543
C -5.8472543 1.2783417 1.9613664
C -4.6188904 1.9478702 2.0020788
C -3.4432209 1.2766728 1.7638500
H -2.5108243 1.8223251 1.8314357
H -4.7153857 -1.8189736 1.2052958
H -6.7804239 -0.6399379 1.6360389
H -4.5714242 2.9946135 2.2718966

C -7.0886764 1.9434879 2.2915391
N -7.4155822 3.1862706 1.9886824
C -6.7606409 4.0711668 1.0540652
C -8.7522077 3.5092533 2.4840159
C -9.1373273 2.2619335 3.2898126
N -8.0604345 1.3406348 2.9596688
H -7.8858509 0.4996102 3.4996327
H -6.2543476 4.8852986 1.5717272
H -7.5094958 4.4978824 0.3878740
H -6.0392675 3.5286317 0.4501502
H 0.6558801 -4.9407967 5.9439794
H -0.5968830 -5.3271961 4.7574404
H -0.8146719 -3.9720372 5.8803054
H 2.5667057 -4.1177629 4.7012613
H 1.8840099 -4.8537220 3.2472583
H 3.2537424 -2.2924751 3.3460390
H 2.3107145 -2.8896830 1.9770580
H -9.4183093 3.6773949 1.6361222
H -8.7318346 4.4162432 3.0869300
H -10.1054316 1.8584477 3.0003560
H -9.1515392 2.4539100 4.3627436

1Me-S_{HT}

Energy = -1440.036021237
N 2.2606658 2.3948539 -1.2190872
C 2.0680019 1.8790164 -0.1970126
C 1.8231714 1.2550306 1.0315823
C 2.9185568 1.0796657 1.8849387
N 3.8211224 0.9305820 2.5998402
C 0.5075969 0.8114735 1.3982729
C -0.5943206 0.9884623 0.5378705
C -1.8561141 0.5679821 0.8906177
C -2.0834961 -0.0629576 2.1184409
C -0.9954589 -0.2588780 2.9769202
C 0.2630179 0.1759513 2.6322497
H 1.0738597 0.0215658 3.3324924
H -1.1375623 -0.7331630 3.9402258
C -3.3891559 -0.5721859 2.4861060
N -4.5517492 -0.0003269 2.2411014
C -5.6517883 -0.8085450 2.7655237
C -4.9473271 -2.0686104 3.2860391
N -3.5446354 -1.7123250 3.1376956
H -2.8068962 -2.3947581 3.2060226
H -2.6628604 0.7015747 0.1815444
H -0.4572417 1.4579424 -0.4278353
N -7.5937744 -2.2627132 5.4673598
C -8.4933970 -2.2940004 4.7334260
C -9.5800786 -2.3280578 3.8527626
C -9.4148090 -1.6723311 2.6273259
N -9.2737288 -1.1307994 1.6098119
C -10.8049390 -2.9955468 4.1944304
C -11.9136804 -2.9888939 3.3246654
C -13.0916866 -3.6152210 3.6610360
C -13.2175191 -4.3046277 4.8723428
C -12.1232264 -4.3237518 5.7438800

C -10.9516209 -3.6800827 5.4173664
H -10.1343616 -3.7029742 6.1270770
H -12.1937959 -4.8140797 6.7063096
C -14.4817729 -4.9187802 5.2270189
N -14.6424840 -6.0641500 5.8587997
C -16.0623617 -6.3656593 6.0373405
C -16.7570008 -5.0961331 5.5288346
N -15.6474155 -4.3633138 4.9362842
H -15.7242499 -3.3908850 4.6838878
H -13.9160608 -3.5888722 2.9590431
H -11.8511877 -2.4804552 2.3708343
H -16.3177719 -7.2453727 5.4444109
H -16.2820762 -6.5806671 7.0820381
H -17.5300145 -5.3056671 4.7927680
H -17.1974278 -4.5154425 6.3389056
H -6.3803320 -1.0184196 1.9828876
H -6.1538236 -0.2569278 3.5619794
H -5.1740502 -2.9473382 2.6830626
H -5.1941891 -2.2843359 4.3229843
C -13.6518331 -7.0845097 6.1127786
H -12.7412060 -6.8871300 5.5547627
H -14.0474672 -8.0472364 5.7912672
H -13.4159904 -7.1444004 7.1745291
C -4.8011336 1.3491483 1.7910718
H -3.8935210 1.9438464 1.8323180
H -5.5394560 1.8092598 2.4469334
H -5.1882325 1.3567708 0.7726772

1Me-S_{ST}

Energy = -1440.039500568
N 4.6568379 3.1393828 -2.2507509
C 4.3747561 2.7589940 -1.1913031
C 4.0317868 2.3262920 0.0957051
C 5.0777504 2.2013181 1.0173461
N 5.9451208 2.1065174 1.7830450
C 2.6764242 2.0470001 0.4588600
C 1.6351807 2.0941106 -0.4894624
C 0.3377028 1.8188396 -0.1397375
C -0.0032541 1.4760135 1.1765835
C 1.0211402 1.4505027 2.1330256
C 2.3208980 1.7249358 1.7841744
H 3.0796795 1.7008751 2.5553121
H 0.8036621 1.2542877 3.1739291
C -1.3750525 1.1694895 1.4944342
N -2.3973160 1.6826166 0.8081831
C -3.6717405 1.3619070 1.4325303
C -3.2698346 0.2808281 2.4384290
N -1.8109424 0.3576587 2.4405287
C -1.0549283 -0.5593325 3.2618602
H -0.4158152 1.8286762 -0.9165565
H 1.8577801 2.3192319 -1.5244990
N 4.2304808 -1.4658724 1.1354083
C 3.6313433 -1.2778597 0.1598139
C 2.8999620 -1.0649023 -1.0151641
C 3.6148888 -0.6407012 -2.1419604

N 4.1979417 -0.3099590 -3.0891236
C 1.4807607 -1.2161151 -1.0484950
C 0.7299474 -0.9005232 -2.2011391
C -0.6409505 -0.9813621 -2.2117658
C -1.3462691 -1.4107919 -1.0785956
C -0.6050180 -1.7960010 0.0474529
C 0.7629224 -1.6905895 0.0695115
H 1.2935692 -1.9693283 0.9709607
H -1.1098114 -2.1655732 0.9316308
C -2.7860782 -1.5073872 -1.0516113
N -3.4266355 -2.4293260 -0.3443223
C -4.8694684 -2.3549472 -0.5190161
C -5.0189406 -1.1608631 -1.4723588
N -3.6413633 -0.7135502 -1.6705909
C -3.3769923 0.5243061 -2.3640075
H -1.1631314 -0.7380609 -3.1275735
H 1.2347072 -0.5691841 -3.0994814
H -2.9703170 -3.2638007 -0.0128773
H -5.2468379 -3.2785506 -0.9532474
H -5.3694110 -2.1958165 0.4354635
H -5.4693508 -1.4331564 -2.4270318
H -5.6094817 -0.3525210 -1.0400977
H -3.5753634 -0.7208038 2.1259505
H -3.6692421 0.4586529 3.4355831
H -4.3975156 1.0086124 0.7022845
H -4.0857235 2.2435374 1.9211062
H -2.2838352 2.5400687 0.2911328
H -0.0873922 -0.7748739 2.8182276
H -1.6089754 -1.4932548 3.3446181
H -0.9081800 -0.1601720 4.2650900
H -4.1489911 1.2460545 -2.1011900
H -3.3909731 0.3853741 -3.4447952
H -2.4153203 0.9335564 -2.0698166

$\mathbf{1Me_2\text{-}A_{HB}}$

Energy = -1518.481167024
N -0.0765891 6.4884801 -1.4770264
C -0.0218816 5.3568996 -1.2223501
C 0.0532873 3.9943205 -0.9148594
C -1.1536204 3.3152410 -0.7204831
N -2.1455008 2.7321326 -0.5597769
C 1.3154765 3.3117208 -0.8129886
C 2.5356673 3.9773732 -1.0393728
C 3.7410087 3.3181646 -0.9398577
C 3.7874540 1.9574423 -0.6254961
C 2.5858781 1.2812551 -0.4000453
C 1.3826048 1.9446669 -0.4831248
H 0.4697849 1.3963389 -0.2878616
H 2.5969908 0.2313753 -0.1313949
C 5.0562380 1.2512821 -0.5299039
N 6.0817116 1.6585911 0.1965679
C 7.2315431 0.7803014 0.0109397
C 6.6299887 -0.3947761 -0.7625978
N 5.3225517 0.1191937 -1.1541782
C 4.5030229 -0.5858464 -2.1099854

C 6.1449567 2.7874884 1.0912720
H 5.1462938 3.1432950 1.3272516
H 6.7202988 3.6047248 0.6554810
H 6.6266506 2.4785488 2.0177791
H 4.6543362 3.8663176 -1.1355258
H 2.5397730 5.0278278 -1.3014789
N 0.6932111 -5.9158705 1.6459672
C 0.6294981 -4.7973075 1.3408969
C 0.5438515 -3.4504520 0.9726376
C 1.7434110 -2.7858852 0.6993865
N 2.7294606 -2.2149634 0.4726051
C -0.7208463 -2.7701690 0.8873329
C -0.8015359 -1.4210077 0.4927050
C -2.0074151 -0.7601411 0.4255459
C -3.1987835 -1.4227272 0.7316269
C -3.1393511 -2.7664098 1.1104003
C -1.9308178 -3.4217352 1.1948038
H -1.9241870 -4.4579682 1.5082169
H -4.0440045 -3.3029554 1.3682776
C -4.4721187 -0.7227262 0.6524790
N -5.5241726 -1.1657187 -0.0124821
C -6.6691165 -0.2820504 0.1774444
C -6.0430539 0.9277753 0.8744748
N -4.7175730 0.4366785 1.2335083
C -3.8623199 1.1870067 2.1211766
C -5.6178880 -2.3336519 -0.8528736
H -6.1347219 -2.0669449 -1.7735876
H -6.1744335 -3.1310054 -0.3597194
H -4.6278889 -2.6988333 -1.1099542
H -2.0294156 0.2752580 0.1057723
H 0.1022552 -0.8862160 0.2293103
H -3.0759189 0.5510694 2.5176352
H -4.4583367 1.5555481 2.9545939
H -3.4094508 2.0316234 1.6027527
H 5.1317997 -0.9164749 -2.9352121
H 3.7340736 0.0704465 -2.5075217
H 4.0289053 -1.4525991 -1.6505671
H -6.5880398 1.2263373 1.7684207
H -5.9555056 1.7957326 0.2183678
H -7.4270693 -0.7766281 0.7874360
H -7.1124607 -0.0297923 -0.7845037
H 7.2104158 -0.6582843 -1.6451404
H 6.5112732 -1.2893315 -0.1484149
H 8.0129946 1.2988291 -0.5473649
H 7.6375304 0.4837749 0.9767239

$1Me_2\text{-}A_{SD}$

Energy = -1518.486353351
N -8.3479444 5.5193354 7.4680938
C -8.4059864 4.4732893 6.9678084
C -8.4645416 3.2115326 6.3657155
C -9.7183693 2.7725762 5.9298471
N -10.7579564 2.3929831 5.5765975
C -7.2932039 2.3939752 6.2187238
C -6.0449363 2.7965785 6.7321251

C -4.9267508 2.0070656 6.5954517
C -4.9909872 0.7727887 5.9385164
C -6.2253061 0.3625150 5.4246378
C -7.3444641 1.1494240 5.5625493
H -8.2817591 0.7956239 5.1541259
H -5.9531562 3.7373203 7.2597606
H -3.9980078 2.3461547 7.0360551
H -6.3107811 -0.5693940 4.8803473
C -3.8095657 -0.0604638 5.8083449
N -2.6083901 0.3845563 5.4738904
C -2.2205126 1.7120259 5.0670262
C -1.6114587 -0.6720326 5.6152565
C -2.4816316 -1.9213495 5.6855760
N -3.7889265 -1.3674347 6.0229982
C -4.8482569 -2.2120045 6.5180717
N -3.6014561 -3.6424146 0.4431481
C -3.5448409 -2.5892244 0.9283815
C -3.4878612 -1.3190417 1.5127186
C -2.2332131 -0.8692927 1.9350022
N -1.1927372 -0.4814261 2.2764989
C -4.6612092 -0.5031285 1.6529186
C -5.9092294 -0.9150882 1.1462997
C -7.0291571 -0.1266902 1.2748040
C -6.9670868 1.1154328 1.9170193
C -5.7332489 1.5345493 2.4249536
C -4.6122115 0.7488989 2.2948715
H -3.6754745 1.1096645 2.6985755
H -5.9993290 -1.8620926 0.6297356
H -7.9575573 -0.4729990 0.8391567
H -5.6494603 2.4726999 2.9586631
C -8.1501525 1.9475677 2.0394078
N -8.1732253 3.2521554 1.8112617
C -7.1161047 4.0926857 1.3048105
C -9.4808892 3.8077903 2.1441284
C -10.3487931 2.5579322 2.2327186
N -9.3499480 1.5041483 2.3804882
C -9.7359187 0.1796535 2.7982871
H -6.6405743 4.6638163 2.1031191
H -7.5394629 4.7925563 0.5865216
H -6.3629778 3.4976908 0.7962836
H -4.4274678 -2.9203487 7.2294986
H -5.3229291 -2.7738467 5.7125976
H -5.6018253 -1.6217416 7.0314260
H -2.1559900 -2.6215679 6.4522439
H -2.5344391 -2.4512351 4.7309215
H -1.0292602 -0.5126485 6.5259905
H -0.9401300 -0.6748436 4.7601742
H -9.8094625 4.4972667 1.3690166
H -9.4271496 4.3503999 3.0915161
H -10.9358761 2.3876500 1.3271357
H -11.0151997 2.5690746 3.0916504
H -1.7170944 2.2445079 5.8749024
H -3.0873568 2.2877340 4.7551864
H -1.5364622 1.6326505 4.2235534
H -8.8683834 -0.3923610 3.1150254
H -10.2383922 -0.3601111 1.9946912
H -10.4201900 0.2651514 3.6409278

2-A_{HB}

Energy = -1665.828220464
N -2.7462028 2.2596892 -0.3833424
C -1.7984631 2.9125365 -0.2324144
C -0.6392073 3.6604964 -0.0423220
C -0.7938070 5.0277389 0.2209316
N -0.9129596 6.1612671 0.4359036
C 0.6535496 3.0310352 -0.0612524
C 0.8001844 1.6705004 -0.3944434
C 2.0297621 1.0567488 -0.3776436
C 3.1845144 1.7689642 -0.0321120
C 3.0550090 3.1289068 0.2754133
C 1.8246367 3.7439011 0.2596857
H 1.7670196 4.7929561 0.5199746
H 3.9171753 3.7185538 0.5615131
C 4.4661523 1.1155931 0.0127101
N 4.6761385 -0.1959835 0.1295753
C 6.0305406 -0.4487700 0.1422010
C 6.7493165 -1.6309652 0.2461927
C 8.1287838 -1.5199925 0.2289299
C 8.7653830 -0.2769863 0.1122733
C 8.0470608 0.9020028 0.0094465
C 6.6652479 0.7870666 0.0285696
N 5.6564141 1.7226874 -0.0491018
H 5.7889827 2.7123533 -0.1973651
H 8.5388339 1.8607574 -0.0802039
H 9.8460251 -0.2374483 0.1035452
H 8.7309303 -2.4149747 0.3065125
H 6.2585985 -2.5904614 0.3356619
H 3.9475238 -0.9133482 0.2759914
H 2.0897786 0.0152550 -0.6659650
H -0.0633906 1.0875221 -0.6889367
N 0.9195439 -6.1332839 -0.2638303
C 0.8000531 -4.9998820 -0.0482913
C 0.6452178 -3.6327931 0.2156887
C 1.8042005 -2.8846216 0.4068880
N 2.7516614 -2.2316797 0.5589883
C -0.6476178 -3.0036291 0.2348781
C -1.8189629 -3.7169581 -0.0842061
C -3.0494031 -3.1021431 -0.0995562
C -3.1788776 -1.7418031 0.2064356
C -2.0238974 -1.0292707 0.5505009
C -0.7942324 -1.6427423 0.5668661
H 0.0695557 -1.0592444 0.8596024
H -2.0835873 0.0126051 0.8375423
C -4.4604057 -1.0882234 0.1614435
N -5.6508700 -1.6952033 0.2196907
C -6.6594580 -0.7590464 0.1433199
C -8.0413076 -0.8735796 0.1599621
C -8.7591176 0.3058958 0.0597415
C -8.1220940 1.5491061 -0.0518933
C -6.7424791 1.6597628 -0.0667972
C -6.0242268 0.4769452 0.0343822
N -4.6699319 0.2237807 0.0481155

H -3.9410755 0.9415369 -0.0953260
H -6.2514642 2.6194128 -0.1524558
H -8.7238257 2.4445581 -0.1273541
H -9.8398491 0.2665946 0.0665870
H -8.5334808 -1.8325530 0.2458432
H -5.7838766 -2.6854127 0.3638589
H -3.9116551 -3.6924737 -0.3839884
H -1.7615349 -4.7663098 -0.3432764

2-A_{ST}

Energy = -1665.823730518
N -6.6343463 5.2138048 5.4517987
C -6.6281864 4.0622724 5.5916506
C -6.5984293 2.6719243 5.7600777
C -7.7284585 2.0696873 6.3280157
N -8.6555370 1.5585568 6.8022480
C -5.4499561 1.9041390 5.3938406
C -4.3104671 2.5095186 4.8221472
C -3.2129489 1.7697180 4.4616269
C -3.1774422 0.3810009 4.6516269
C -4.3047272 -0.2287559 5.2204314
C -5.4055777 0.5060383 5.5813352
H -6.2527780 -0.0089108 6.0156060
H -4.2919874 3.5787750 4.6554261
H -2.3746281 2.2962719 4.0232658
H -4.3377679 -1.2979625 5.3874815
C -2.0295615 -0.3886196 4.2759022
N -0.9009882 0.0832447 3.7336206
H -0.7285689 1.0539443 3.5224292
C 0.0051156 -0.9397104 3.5465482
C -0.6243245 -2.0979900 3.9955520
N -1.8750117 -1.7090787 4.4276780
H -2.5627013 -2.3245565 4.8336983
N -1.9309027 -4.2558541 1.2152407
C -1.9364817 -3.1062010 1.0606327
C -1.9649997 -1.7180182 0.8746964
C -0.8382840 -1.1251272 0.2905436
N 0.0855399 -0.6216264 -0.1979788
C -3.1096455 -0.9433258 1.2383015
C -4.2494292 -1.5399268 1.8183657
C -5.3435651 -0.7934837 2.1753528
C -5.3749466 0.5936477 1.9736959
C -4.2468767 1.1950454 1.3974689
C -3.1495390 0.4534064 1.0397635
H -2.3017876 0.9618733 0.5987516
H -4.2705476 -2.6075723 1.9952269
H -6.1812994 -1.3127174 2.6232841
H -4.2114166 2.2623768 1.2191921
C -6.5193737 1.3699766 2.3461378
N -6.6571613 2.6942455 2.2131807
H -5.9542781 3.3085938 1.8324098
C -7.9087540 3.0908523 2.6356170
C -8.5569191 1.9329043 3.0580640
N -7.6601990 0.9026104 2.8663135
H -7.8495886 -0.0699684 3.0528867

C 1.2924083 -0.9577912 3.0366511
C 1.9235411 -2.1897404 3.0011629
C 1.2909891 -3.3539109 3.4532033
C 0.0018306 -3.3324446 3.9581211
H -0.4900000 -4.2315142 4.3012822
H 1.7775631 -0.0595649 2.6821201
H 2.9305872 -2.2544714 2.6122415
H 1.8219835 -4.2948061 3.4045628
C -8.5211453 4.3317458 2.6858497
C -9.8159885 4.3599860 3.1755200
C -10.4676795 3.1960035 3.5997453
C -9.8503441 1.9575308 3.5518107
H -10.3502499 1.0591515 3.8848890
H -8.0146618 5.2305976 2.3641365
H -10.3364979 5.3062567 3.2337566
H -11.4788121 3.2660684 3.9770834

2-A_{SD}

Energy = -1665.820686209
N -6.2224683 4.7023387 4.4755463
C -6.2353716 3.5685404 4.7300355
C -6.2682396 2.1946527 4.9861714
C -7.5360787 1.6222569 5.1518845
N -8.5863665 1.1447171 5.2759943
C -5.0833418 1.3900314 4.9400441
C -3.8085016 1.9644629 4.7666707
C -2.6803943 1.1868017 4.6784064
C -2.7588712 -0.2098843 4.7633728
C -4.0214391 -0.7881168 4.9515706
C -5.1488564 -0.0128558 5.0458644
H -6.1042249 -0.5019026 5.1815689
H -3.7051850 3.0387241 4.6828810
H -1.7315492 1.6844132 4.5214076
H -4.1366459 -1.8615766 5.0345132
C -1.5889958 -1.0259714 4.6267208
N -0.3203264 -0.6061520 4.6473416
H -0.0351374 0.3483190 4.8063620
C 0.5365751 -1.6663269 4.4464805
C -0.2705507 -2.7935207 4.3098710
N -1.5688834 -2.3503629 4.4376174
H -2.3865750 -2.9353317 4.3438972
N -3.3167394 -4.2102381 2.1442712
C -3.3047028 -3.0780208 1.8828051
C -3.2745212 -1.7054541 1.6195730
C -2.0081334 -1.1318724 1.4470622
N -0.9588086 -0.6539254 1.3167451
C -4.4610212 -0.9034018 1.6669529
C -5.7334230 -1.4814015 1.8465177
C -6.8636302 -0.7070643 1.9349844
C -6.7899943 0.6894522 1.8439403
C -5.5299582 1.2714903 1.6510298
C -4.4001588 0.4994444 1.5565623
H -3.4466566 0.9909133 1.4162141
H -5.8329105 -2.5556494 1.9352214
H -7.8103655 -1.2064869 2.0986340

H -5.4195527 2.3450738 1.5629648
C -7.9638311 1.5001250 1.9784245
N -7.9919156 2.8230155 2.1769138
H -7.1774897 3.4108867 2.2803919
C -9.2935807 3.2581856 2.3004387
C -10.0937734 2.1277524 2.1501719
N -9.2300015 1.0738451 1.9463176
H -9.5088093 0.1194837 1.7754537
C 0.2609859 -4.0530456 4.0848808
C 1.6415013 -4.1358578 4.0113536
C 2.4541015 -3.0046965 4.1573509
C 1.9181512 -1.7465212 4.3771670
H 2.5459260 -0.8731763 4.4874688
H -0.3683847 -4.9249888 3.9715476
H 2.1034171 -5.0980132 3.8372239
H 3.5279842 -3.1160615 4.0955624
C -11.4761832 2.1995625 2.2119357
C -12.0205631 3.4525581 2.4403003
C -11.2150799 4.5868455 2.6006142
C -9.8337621 4.5126166 2.5331315
H -9.2104249 5.3874648 2.6567209
H -12.0983673 1.3237601 2.0899323
H -13.0953793 3.5571644 2.4977785
H -11.6830971 5.5448096 2.7813393

2-S_{HT}

Energy = -1665.809602873
N -3.3589988 2.5871210 -0.6049024
C -2.3863312 3.1926286 -0.4195468
C -1.2112063 3.9216022 -0.1962177
C -1.3430180 5.3099199 -0.0672563
N -1.4452409 6.4607942 0.0416862
C 0.0629730 3.2791375 -0.0997274
C 0.1934837 1.8793174 -0.2188681
C 1.4163134 1.2641380 -0.1228689
C 2.5862121 2.0056846 0.0980300
C 2.4670514 3.3983624 0.2154909
C 1.2457033 4.0166761 0.1196265
H 1.2023777 5.0937868 0.2164923
H 3.3348701 4.0231734 0.3851591
C 3.8616707 1.3604297 0.2039490
N 4.0938890 0.0464181 0.1137190
C 5.4389766 -0.2118263 0.2681223
C 6.1654171 -1.3918729 0.2568014
C 7.5320389 -1.2769437 0.4492073
C 8.1454475 -0.0332835 0.6452241
C 7.4163232 1.1440347 0.6551541
C 6.0491891 1.0253106 0.4621726
N 5.0380640 1.9608840 0.4139640
H 5.1661561 2.9557655 0.5224412
H 7.8889695 2.1047791 0.8055379
H 9.2158152 0.0091133 0.7930102
H 8.1409169 -2.1705688 0.4480442
H 5.6906291 -2.3515183 0.1062091
H 3.3856647 -0.6546411 -0.0438683

H 1.4463572 0.1864907 -0.2233321
H -0.6820241 1.2659442 -0.3882119
N -16.5918670 8.6555116 -1.9241511
C -15.6892545 9.3518121 -1.7081259
C -14.5922135 10.1836520 -1.4477766
C -14.8502607 11.5556954 -1.3281014
N -15.0557996 12.6931562 -1.2271019
C -13.2698217 9.6561761 -1.3097507
C -13.0103505 8.2735559 -1.4245478
C -11.7406304 7.7698035 -1.2915488
C -10.6486014 8.6120650 -1.0353317
C -10.8961107 9.9879971 -0.9196713
C -12.1644292 10.4950873 -1.0523511
H -12.3062246 11.5636286 -0.9556365
H -10.0932108 10.6875747 -0.7239590
C -9.3234130 8.0845996 -0.8953052
N -8.9663834 6.7996063 -0.9975145
C -7.6083615 6.6650725 -0.8032686
C -6.7737002 5.5588549 -0.8093179
C -5.4307051 5.7983758 -0.5712938
C -4.9428952 7.0899596 -0.3367317
C -5.7800825 8.1927246 -0.3321214
C -7.1232286 7.9500232 -0.5706612
N -8.2153575 8.7878779 -0.6374410
H -8.1845078 9.7877480 -0.5065514
H -5.4045421 9.1905267 -0.1521312
H -3.8859058 7.2292073 -0.1550505
H -4.7422242 4.9641884 -0.5671551
H -7.1517620 4.5621572 -0.9901853
H -9.6000535 6.0387511 -1.1915832
H -11.6113657 6.6993230 -1.3901829
H -13.8213588 7.5841936 -1.6206364

2-S_{ST}

Energy = -1665.821415525
N -3.2939944 2.5678611 -0.8295765
C -2.3359354 3.1657566 -0.5656919
C -1.1679163 3.8802762 -0.2645988
C -1.2949462 5.2693934 -0.1270339
N -1.3922848 6.4208598 -0.0286248
C 0.0841361 3.2234747 -0.1031597
C 0.2102332 1.8231903 -0.2559558
C 1.4221440 1.1950733 -0.1321344
C 2.5909605 1.9165104 0.1632568
C 2.4720163 3.3052662 0.3399249
C 1.2629060 3.9381871 0.2098132
H 1.2212603 5.0102811 0.3512374
H 3.3375156 3.9148717 0.5681626
C 3.8544521 1.2580416 0.2819688
N 4.1078122 -0.0281648 0.0068820
C 5.4355225 -0.3150126 0.2447589
C 6.1659822 -1.4872558 0.1392327
C 7.5046897 -1.4152086 0.4888127
C 8.0871792 -0.2189301 0.9239541
C 7.3533035 0.9512022 1.0272855

C 6.0152936 0.8740003 0.6793703
N 5.0045328 1.8112685 0.6867704
H 5.1126449 2.7737543 0.9675192
H 7.8011193 1.8742466 1.3681160
H 9.1359386 -0.2081435 1.1874419
H 8.1145254 -2.3058768 0.4243161
H 5.7155003 -2.4112602 -0.1959097
H 3.4331871 -0.6798957 -0.3636649
H 1.4472089 0.1199549 -0.2621102
H -0.6632086 1.2240983 -0.4776086
N -6.0684736 3.1473572 1.7957494
C -5.1547623 3.8042385 2.0780320
C -4.0569730 4.5995138 2.4325020
C -4.2702673 5.9835728 2.4754666
N -4.4500270 7.1291138 2.5185354
C -2.7805403 4.0301627 2.7252713
C -2.5628334 2.6373980 2.6655367
C -1.3242435 2.0988086 2.8983101
C -0.2283838 2.9139614 3.2182492
C -0.4427008 4.2970262 3.3103887
C -1.6792440 4.8387401 3.0770142
H -1.7944169 5.9127173 3.1344570
H 0.3676280 4.9740747 3.5499477
C 1.0773629 2.3614595 3.3901200
N 1.4296962 1.0835094 3.1994851
C 2.7783692 0.9192903 3.4293212
C 3.6079423 -0.1882610 3.3462605
C 4.9439327 0.0143442 3.6502477
C 5.4285758 1.2726934 4.0255643
C 4.5989908 2.3791904 4.1006380
C 3.2634757 2.1742511 3.7908558
N 2.1811247 3.0266288 3.7542343
H 2.2086000 4.0061596 3.9926713
H 4.9745477 3.3521810 4.3859234
H 6.4790971 1.3851314 4.2554016
H 5.6295492 -0.8201285 3.5937049
H 3.2326430 -1.1613479 3.0608285
H 0.7964664 0.3519706 2.9159818
H -1.2190710 1.0236462 2.8244235
H -3.3774068 1.9745405 2.4058942

2Me-A_{HB}

Energy = -1744.271789856
N -0.6033831 6.0922074 -1.2022245
C -0.4583905 5.0376851 -0.7408307
C -0.2693187 3.7667336 -0.1833214
C -1.3917806 3.1234888 0.3292087
N -2.3147582 2.5634849 0.7576709
C 1.0221125 3.1296518 -0.1695218
C 2.1427431 3.7305377 -0.7708653
C 3.3758636 3.1179900 -0.7648886
C 3.5554146 1.8718223 -0.1539665
C 2.4452543 1.2623235 0.4435516
C 1.2139469 1.8751637 0.4393697
H 0.3871037 1.3750442 0.9276786

H 2.5476927 0.3075277 0.9427998
C 4.8264763 1.1834222 -0.1718320
N 6.0482497 1.7250514 -0.0608448
C 6.9899032 0.7154590 -0.1407909
C 6.2850820 -0.4770435 -0.2829508
C 6.9300514 -1.7017257 -0.3848551
C 8.3122753 -1.6780379 -0.3370974
C 9.0222195 -0.4782054 -0.1929495
C 8.3767043 0.7420265 -0.0928158
H 8.9341272 1.6629210 0.0114362
H 10.1028027 -0.5058340 -0.1621297
H 8.8593922 -2.6077298 -0.4135849
H 6.3808484 -2.6266176 -0.4959414
N 4.9545493 -0.1376249 -0.2994202
H 4.1757020 -0.8009479 -0.4518854
C 6.3756151 3.1120924 0.2074634
H 5.5547359 3.5922323 0.7310161
H 6.5876759 3.6488511 -0.7143989
H 7.2518428 3.1459890 0.8493903
H 4.1938786 3.6060758 -1.2777006
H 2.0448300 4.6876465 -1.2667752
N 1.1809503 -5.5678052 1.3468211
C 1.0375254 -4.5141126 0.8830474
C 0.8504501 -3.2441660 0.3226740
C 1.9740438 -2.6027099 -0.1897229
N 2.8974779 -2.0438512 -0.6186118
C -0.4404913 -2.6062437 0.3045192
C -0.6292661 -1.3519040 -0.3055763
C -1.8601141 -0.7382921 -0.3146814
C -2.9729124 -1.3470732 0.2785529
C -2.7964043 -2.5928341 0.8910681
C -1.5636156 -3.2059922 0.9024109
H -1.4680222 -4.1627199 1.3994909
H -3.6168303 -3.0801798 1.4008260
C -4.2441030 -0.6587549 0.2898921
N -5.4649336 -1.2004220 0.1702266
C -6.4072390 -0.1911225 0.2452177
C -5.7036845 1.0014008 0.3937387
C -6.3496030 2.2256664 0.4930978
C -7.7314835 2.2018030 0.4359244
C -8.4401649 1.0019829 0.2852041
C -7.7937367 -0.2179164 0.1876896
H -8.3500279 -1.1389155 0.0783595
H -9.5205375 1.0294694 0.2473951
H -8.2793123 3.1311999 0.5103297
H -5.8014668 3.1506148 0.6092815
N -4.3731414 0.6620647 0.4186970
H -3.5948531 1.3248851 0.5761797
C -5.7898438 -2.5871993 -0.1025082
H -6.6607764 -2.6204408 -0.7516106
H -6.0092050 -3.1251954 0.8169405
H -4.9644752 -3.0664703 -0.6197490
H -1.9600175 0.2164132 -0.8146090
H 0.1997291 -0.8524104 -0.7908382

2Me-A_{ST}

Energy = -1744.260370506
N -8.0466849 5.0457515 6.1320991
C -8.0306340 3.8864615 6.1670467
C -7.9945826 2.4865396 6.2023505
C -9.1801068 1.8203260 6.5327298
N -10.1514840 1.2499728 6.8129212
C -6.7970602 1.7615784 5.9057166
C -5.5615292 2.4158820 5.7225898
C -4.4102899 1.7114045 5.4721849
C -4.4176043 0.3114252 5.3688477
C -5.6505350 -0.3425926 5.4977727
C -6.8006681 0.3576695 5.7714129
H -7.7263286 -0.1952827 5.8765389
H -5.5016282 3.4931588 5.8090418
H -3.4836816 2.2660361 5.3921684
H -5.7330506 -1.4101229 5.3527877
C -3.1859113 -0.3907421 5.1253158
N -2.1188538 0.1558713 4.5301935
H -2.1213018 1.0707537 4.1047729
C -1.0899645 -0.7532112 4.4610964
C -1.5732999 -1.9164526 5.0502129
N -2.8675176 -1.6494863 5.4665128
C -3.6444906 -2.5708653 6.2741275
N -2.3575321 -3.3620078 1.4274080
C -2.3729606 -2.2027937 1.3893440
C -2.4070387 -0.8029609 1.3500635
C -1.2214986 -0.1392870 1.0144091
N -0.2509455 0.4300633 0.7294170
C -3.6027338 -0.0745784 1.6456298
C -4.8399845 -0.7248868 1.8314873
C -5.9890725 -0.0162279 2.0803103
C -5.9777075 1.3840465 2.1794507
C -4.7429741 2.0341788 2.0477987
C -3.5951347 1.3297347 1.7756634
H -2.6678362 1.8795346 1.6685443
H -4.9030966 -1.8023091 1.7486522
H -6.9172402 -0.5679077 2.1626289
H -4.6571294 3.1018894 2.1894698
C -7.2072120 2.0904254 2.4217351
N -7.5223848 3.3491785 2.0774608
C -6.7431495 4.2661255 1.2669445
C -8.8158400 3.6206022 2.4934578
C -9.3019865 2.4601232 3.0857141
N -8.2754536 1.5482448 3.0187714
H -8.2752373 0.6345304 3.4466918
C 0.1960048 -0.6677661 3.9519997
C 0.9754193 -1.8064539 4.0512994
C 0.4893895 -2.9803761 4.6395733
C -0.7944296 -3.0592961 5.1505196
H -1.1621200 -3.9723166 5.5981594
H 0.5666621 0.2360451 3.4905592
H 1.9854531 -1.7892655 3.6651737
H 1.1322130 -3.8482045 4.6954469
C -9.5920914 4.7650142 2.3900810
C -10.8761642 4.6904426 2.9011055

C -11.3650065 3.5192348 3.4924590
C -10.5881937 2.3790489 3.5949258
H -10.9610117 1.4772418 4.0585608
H -9.2224144 5.6759779 1.9398517
H -11.5170669 5.5595327 2.8424884
H -12.3751973 3.5053375 3.8783376
H -6.1069542 4.8973248 1.8836701
H -7.4259043 4.8972518 0.7053615
H -6.1373056 3.7138816 0.5549786
H -2.9602094 -3.2003373 6.8357391
H -4.2771392 -3.2033316 5.6550544
H -4.2537869 -2.0223891 6.9860326

2Me-A_{SD}

Energy = -1744.266136660
N -4.6449591 2.5940803 5.6089002
C -4.6568995 1.4558290 5.3833882
C -4.6781160 0.0825016 5.1069537
C -5.9438211 -0.4849201 4.9838360
N -7.0204003 -0.9128709 4.8685956
C -3.4734715 -0.6546707 4.8525531
C -2.2147926 -0.0272999 4.9005257
C -1.0597598 -0.7228845 4.6379570
C -1.0974736 -2.0892293 4.3347279
C -2.3436906 -2.7262121 4.2893804
C -3.4999611 -2.0267093 4.5410768
H -4.4464165 -2.5474816 4.4722467
H -2.1437252 1.0261789 5.1383497
H -0.1126105 -0.2008701 4.6910937
H -2.4205863 -3.7682759 4.0081888
C 0.1243986 -2.7743271 3.9973197
N 1.1150968 -2.2222236 3.2898042
H 1.0260607 -1.3237527 2.8134173
C 2.1343108 -3.1303827 3.1240912
C 1.7266166 -4.2889582 3.7806804
N 0.4799480 -4.0247807 4.3204014
C -0.2384918 -4.9417351 5.1836948
N -2.2354070 -3.5451941 0.7003852
C -2.2121879 -2.4083734 0.9319330
C -2.1792960 -1.0365364 1.2145737
C -0.9096686 -0.4783624 1.3383851
N 0.1690409 -0.0558871 1.4540052
C -3.3780761 -0.2911409 1.4725003
C -4.6416559 -0.9085491 1.4238317
C -5.7907218 -0.2054275 1.6925212
C -5.7418457 1.1588556 2.0033550
C -4.4906632 1.7863577 2.0472872
C -3.3405661 1.0795465 1.7887757
H -2.3900964 1.5929823 1.8570867
H -4.7214035 -1.9602503 1.1809558
H -6.7418447 -0.7201161 1.6389957
H -4.4047427 2.8262190 2.3337112
C -6.9560982 1.8502949 2.3539306
N -7.3011663 3.1084743 2.0497256
C -6.5790805 4.0293880 1.1935992

C -8.5425724 3.3773651 2.5993332
C -8.9585582 2.2138859 3.2418356
N -7.9490112 1.2982879 3.0586162
H -7.8689490 0.3914629 3.5195302
C 3.3523291 -3.0523064 2.4657687
C 4.1465697 -4.1852858 2.4982845
C 3.7400099 -5.3489219 3.1637237
C 2.5217143 -5.4250038 3.8169880
H 2.2123469 -6.3296461 4.3223884
H 3.6663719 -2.1533366 1.9536615
H 5.1052473 -4.1719225 1.9980764
H 4.3925255 -6.2112221 3.1646443
C -9.3263478 4.5216749 2.5830567
C -10.5421514 4.4485393 3.2413154
C -10.9570728 3.2797954 3.8924195
C -10.1740960 2.1385794 3.9049744
H -10.4946348 1.2356685 4.4059986
H -9.0104343 5.4302747 2.0889274
H -11.1860119 5.3171990 3.2556490
H -11.9132498 3.2690082 4.3974490
H -5.9880882 4.7272172 1.7827009
H -7.2942491 4.5853007 0.5930432
H -5.9289683 3.4760505 0.5230373
H 0.4778368 -5.4800143 5.7987917
H -0.8155219 -5.6551113 4.5994472
H -0.9014705 -4.3866749 5.8400583

2Me-S_{HT}

Energy = -1744.252759375
N 18.2839280 1.3582675 -3.5592668
C 17.7648382 0.8230721 -2.6696014
C 17.1297363 0.1802128 -1.6001862
C 17.9512385 -0.4696776 -0.6711555
N 18.6246986 -1.0115089 0.1036136
C 15.7020950 0.1845271 -1.4635298
C 14.8737825 0.8291455 -2.4044682
C 13.5053250 0.8388369 -2.2704795
C 12.8845942 0.2007616 -1.1888291
C 13.6964506 -0.4565828 -0.2540544
C 15.0645475 -0.4597344 -0.3833047
H 15.6540720 -0.9652818 0.3707746
H 13.2567141 -0.9489960 0.6046714
C 11.4512401 0.1566520 -1.0453413
N 10.5659373 1.1173624 -1.3385725
C 9.2912465 0.6521748 -1.0651423
C 9.4321040 -0.6379374 -0.5619958
C 8.3392869 -1.3987893 -0.1760419
C 7.0957439 -0.8088477 -0.3178786
C 6.9514321 0.4890310 -0.8249912
C 8.0453632 1.2458311 -1.2079976
H 7.9242370 2.2448059 -1.6039271
H 5.9601481 0.9085889 -0.9272885
H 6.2136033 -1.3629484 -0.0274689
H 8.4532469 -2.4002279 0.2151791
N 10.7820412 -0.8977609 -0.5685338

H 11.2112092 -1.7833822 -0.3420384
C 10.8536778 2.4736215 -1.7649244
H 10.7899982 2.5637112 -2.8469089
H 11.8447603 2.7635225 -1.4299970
H 10.1311832 3.1438869 -1.3071125
H 12.9165484 1.3179578 -3.0413610
H 15.3110179 1.3232460 -3.2625522
N 3.8134984 -1.6465894 1.2947592
C 3.2002121 -1.3404951 0.3575835
C 2.4566383 -0.9744489 -0.7704057
C 3.1707756 -0.4531660 -1.8560949
N 3.7585930 -0.0187743 -2.7579363
C 1.0307790 -1.1220823 -0.8083909
C 0.2827937 -0.7635861 -1.9487141
C -1.0839257 -0.9045242 -1.9819945
C -1.7826564 -1.4231761 -0.8830605
C -1.0519458 -1.7759334 0.2589713
C 0.3144399 -1.6278734 0.2952326
H 0.8384121 -1.8995782 1.2026175
H -1.5538190 -2.1351769 1.1476245
C -3.2189975 -1.5290102 -0.9342753
N -3.9905967 -2.4832124 -0.3989399
C -5.3166975 -2.1913653 -0.6673449
C -5.3277110 -1.0203565 -1.4199257
C -6.5077867 -0.4457827 -1.8666827
C -7.6794594 -1.0984517 -1.5258482
C -7.6704595 -2.2782328 -0.7705160
C -6.4899734 -2.8480680 -0.3255429
H -6.4929358 -3.7556328 0.2623678
H -8.6097498 -2.7547532 -0.5255784
H -8.6256481 -0.6871661 -1.8497759
H -6.5121554 0.4647230 -2.4496088
N -4.0106239 -0.6516472 -1.5591417
H -3.6809977 0.2034539 -1.9834327
C -3.5500535 -3.6971950 0.2617056
H -4.2271430 -4.5046923 -0.0032016
H -3.5467637 -3.5733248 1.3421790
H -2.5549699 -3.9637723 -0.0807901
H -1.6104907 -0.6338342 -2.8891560
H 0.7842820 -0.3746953 -2.8256923

2Me-S_{ST}

Energy = -1744.261031304
N 4.9739045 3.6369185 -2.0420270
C 4.6557075 3.1570749 -1.0348210
C 4.2735752 2.5998951 0.1924339
C 5.2933771 2.3719422 1.1246161
N 6.1370591 2.1862295 1.8998775
C 2.9108179 2.2838697 0.4843045
C 1.8900307 2.4593045 -0.4716252
C 0.5837826 2.1429814 -0.1947149
C 0.2109540 1.6401231 1.0612773
C 1.2226490 1.4657344 2.0205363
C 2.5277298 1.7794774 1.7446711
H 3.2710234 1.6306254 2.5166333

H 0.9860222 1.1034503 3.0136176
C -1.1229169 1.2070057 1.3612721
N -2.2833761 1.6197187 0.8229912
C -3.3223065 0.8824668 1.3672421
C -2.7573310 0.0113483 2.2940232
C -3.5229603 -0.8917281 3.0148939
C -4.8858182 -0.8831386 2.7676866
C -5.4578434 -0.0002093 1.8451831
C -4.6885136 0.9017292 1.1292824
H -5.1425846 1.5772129 0.4170533
H -6.5260180 -0.0276344 1.6793138
H -5.5224721 -1.5756600 3.3009574
H -3.0798283 -1.5668386 3.7339344
N -1.4064683 0.2593833 2.2652779
H -0.7069580 -0.2685401 2.7644916
C -2.4850873 2.7269760 -0.0904841
H -2.4408337 2.3999733 -1.1280338
H -1.7359394 3.4941322 0.0802899
H -3.4613742 3.1637697 0.1001093
H -0.1383865 2.2440002 -0.9915086
H 2.1364099 2.8168940 -1.4625942
N 3.9139087 -1.6125536 1.2385399
C 3.2839610 -1.2878218 0.3203512
C 2.5196586 -0.9103569 -0.7912816
C 3.1942992 -0.2722005 -1.8412355
N 3.7402170 0.2392666 -2.7275285
C 1.1133919 -1.1288769 -0.8421046
C 0.3372260 -0.6876363 -1.9377442
C -1.0206488 -0.8683356 -1.9731195
C -1.7029188 -1.5159012 -0.9265396
C -0.9347987 -1.9822260 0.1531954
C 0.4241694 -1.7927285 0.1954120
H 0.9682053 -2.1537413 1.0588818
H -1.4009365 -2.4672084 0.9988502
C -3.1358090 -1.6100205 -0.9696501
N -3.9398440 -2.4990345 -0.3662286
C -5.2586762 -2.1848857 -0.6509159
C -5.2386965 -1.0747025 -1.4878538
C -6.4017631 -0.4797202 -1.9487139
C -7.5929921 -1.0509692 -1.5341565
C -7.6158730 -2.1724991 -0.6967500
C -6.4494581 -2.7614979 -0.2379607
H -6.4791939 -3.6189283 0.4200572
H -8.5681786 -2.5865038 -0.3950829
H -8.5279160 -0.6194303 -1.8642878
H -6.3814004 0.3873730 -2.5943404
N -3.9118318 -0.7580564 -1.6575224
H -3.5626794 0.0193474 -2.1964959
C -3.5478104 -3.6800982 0.3774293
H -4.3125693 -4.4406437 0.2488072
H -3.4451491 -3.4599906 1.4383514
H -2.6148926 -4.0757489 -0.0122346
H -1.5545213 -0.5236254 -2.8505047
H 0.8142127 -0.1880000 -2.7706740

$2Me_2$-A_{HB}

Energy = -1822.701938228
N -0.0595495 6.5009381 -1.4453040
C -0.0121369 5.3667178 -1.2024580
C 0.0575396 4.0001817 -0.9091305
C -1.1508945 3.3231137 -0.7180328
N -2.1434222 2.7408461 -0.5590870
C 1.3166096 3.3143710 -0.8113317
C 2.5394228 3.9805292 -1.0239710
C 3.7425975 3.3189513 -0.9276617
C 3.7879848 1.9543429 -0.6219045
C 2.5815830 1.2785283 -0.4089071
C 1.3804090 1.9429297 -0.4977063
H 0.4657642 1.3931694 -0.3160271
H 2.5876164 0.2279413 -0.1432813
C 5.0495474 1.2505442 -0.5239350
N 6.1130627 1.6504538 0.1853409
C 7.1209103 0.7199317 0.0423978
C 6.6200761 -0.2851952 -0.7782190
C 7.3775858 -1.3970837 -1.1186977
C 8.6591461 -1.4540353 -0.6004464
C 9.1640476 -0.4408467 0.2254476
C 8.4064854 0.6667916 0.5624500
H 8.8048083 1.4476141 1.1957791
H 10.1717517 -0.5263469 0.6081581
H 9.2862748 -2.3024185 -0.8375929
H 6.9918594 -2.1849518 -1.7510907
N 5.3372667 0.0872900 -1.1205828
C 4.5032673 -0.6450183 -2.0559756
C 6.2003024 2.8154499 1.0445847
H 5.2043302 3.1355702 1.3334839
H 6.7122627 3.6306627 0.5384975
H 6.7492899 2.5490188 1.9439718
H 4.6559519 3.8677570 -1.1201358
H 2.5468451 5.0333474 -1.2756664
N 0.6837840 -5.9218291 1.6146446
C 0.6254570 -4.8006162 1.3194149
C 0.5431008 -3.4497491 0.9633701
C 1.7434609 -2.7836465 0.6977820
N 2.7299168 -2.2112677 0.4773792
C -0.7197998 -2.7689677 0.8803140
C -0.7992388 -1.4150275 0.5006222
C -2.0045580 -0.7555365 0.4290097
C -3.1996466 -1.4203866 0.7242767
C -3.1389913 -2.7685058 1.0936822
C -1.9315724 -3.4241240 1.1742926
H -1.9265627 -4.4631637 1.4778335
H -4.0428146 -3.3077126 1.3484495
C -4.4671165 -0.7245782 0.6467211
N -5.5566899 -1.1590106 0.0004405
C -6.5641290 -0.2288716 0.1479488
C -6.0361027 0.8120913 0.9043658
C -6.7872934 1.9321309 1.2318905
C -8.0905343 1.9594769 0.7682434
C -8.6225909 0.9104168 0.0067403
C -7.8712184 -0.2050939 -0.3178201

H -8.2899131 -1.0136936 -0.9011642
H -9.6466091 0.9737495 -0.3348889
H -8.7138763 2.8126357 0.9981350
H -6.3812339 2.7478039 1.8143658
N -4.7369198 0.4613177 1.2059079
C -3.8663786 1.2371878 2.0701593
C -5.6718500 -2.3588155 -0.8059575
H -6.2543653 -2.1307657 -1.6947786
H -6.1621966 -3.1531588 -0.2478847
H -4.6860873 -2.6889459 -1.1176799
H -2.0235946 0.2806467 0.1117826
H 0.1056908 -0.8766166 0.2494736
H -3.1171474 0.5881189 2.5127387
H -4.4625720 1.6686182 2.8700054
H -3.3769540 2.0272155 1.5052641
H 5.1314268 -1.0355234 -2.8524257
H 3.7702162 0.0248356 -2.4945206
H 3.9943709 -1.4621846 -1.5502501

$2Me_2$-A_{SD}

Energy = -1822.701444040
N -4.2469347 -0.5534517 5.7562753
C -4.3415644 -1.4527394 5.0279234
C -4.4429335 -2.5387558 4.1531457
C -5.7270136 -2.9178289 3.7529928
N -6.7891518 -3.2639682 3.4349631
C -3.2816812 -3.2283473 3.6727355
C -1.9943373 -2.9408882 4.1669908
C -0.8883345 -3.6323600 3.7324792
C -1.0052653 -4.6488163 2.7762662
C -2.2783830 -4.9258510 2.2590739
C -3.3825364 -4.2354885 2.6931422
H -4.3433981 -4.4618217 2.2495507
H -1.8632675 -2.1754352 4.9212839
H 0.0734852 -3.4006281 4.1717585
H -2.4028442 -5.6654081 1.4787321
C 0.1444976 -5.4074343 2.3434655
N 1.3470166 -4.9075768 2.0243479
C 1.7285223 -3.5098520 1.9702259
C 2.1830694 -5.9428757 1.6627883
C 1.4345509 -7.1109228 1.7558267
N 0.1806320 -6.7413716 2.1950756
C -0.8604002 -7.6881880 2.5458298
N -2.9840438 -3.6665007 -1.1574765
C -2.8869817 -2.7689569 -0.4272543
C -2.7832708 -1.6851348 0.4500010
C -1.4982696 -1.3102697 0.8513243
N -0.4348187 -0.9683378 1.1694730
C -3.9431089 -0.9948687 0.9322418
C -5.2305068 -1.2768216 0.4348090
C -6.3359159 -0.5873751 0.8736335
C -6.2188038 0.4215677 1.8379870
C -4.9452336 0.6946494 2.3564123
C -3.8414665 0.0068213 1.9173627
H -2.8805398 0.2295475 2.3626341

H -5.3619329 -2.0367283 -0.3250066
H -7.2974028 -0.8150801 0.4317022
H -4.8198391 1.4278065 3.1425633
C -7.3693255 1.1739079 2.2791932
N -7.4065947 2.5055372 2.4474945
C -6.3657007 3.4583739 2.1130433
C -8.6618196 2.8677955 2.8893485
C -9.4099929 1.6981831 2.9626773
N -8.5724933 0.6687680 2.5881279
C -8.9538522 -0.7297151 2.6212866
C 3.5098628 -5.9551036 1.2575449
C 4.0512343 -7.1905465 0.9469176
C 3.2968421 -8.3668883 1.0387478
C 1.9734652 -8.3508226 1.4442683
H 1.3950973 -9.2623809 1.5067159
H 4.0991198 -5.0509872 1.1887261
H 5.0823405 -7.2488146 0.6263292
H 3.7589567 -9.3109602 0.7847706
C -9.2021119 4.1024624 3.2187625
C -10.5266316 4.1117676 3.6206183
C -11.2809276 2.9339673 3.6917771
C -10.7380297 1.7036680 3.3639287
H -11.3272033 0.7984026 3.4171022
H -8.6239919 5.0151499 3.1721885
H -10.9898124 5.0516710 3.8879640
H -12.3130800 2.9869392 4.0098358
H -5.7883356 3.7314929 2.9933717
H -6.8285985 4.3495722 1.6972761
H -5.7054433 3.0343447 1.3631087
H -0.3978894 -8.5718806 2.9777732
H -1.4372089 -7.9767828 1.6701216
H -1.5212160 -7.2509017 3.2875652
H 2.3699008 -3.3559544 1.1060558
H 2.2674579 -3.2234831 2.8712494
H 0.8485987 -2.8839234 1.8579775
H -8.0748616 -1.3567668 2.7344697
H -9.4845238 -1.0053757 1.7120900
H -9.6030550 -0.8943847 3.4775926

References

[1] P. Rietsch, F. Witte, S. Sobottka, G. Germer, A. Becker, A. Güttler, B. Sarkar, B. Paulus, U. Resch–Genger, S. Eigler, *Angew. Chem. Int. Ed.* **2019**, *58*, 8235–8239.

[2] C. Reichardt, *Chem. Rev.* **1994**, *94*, 2319–2358.

[3] S. Grimme, C. Bannwarth, P. Shushkov, *J. Chem. Theory Comput.* **2017**, *13*, 1989–2009.

[4] P. Pracht, F. Bohle, S. Grimme, *Phys. Chem. Chem. Phys.* **2020**, *22*, 7169–7192.

[5] R. Ahlrichs, M. Bär, M. Häser, H. Horn, C. Kölmel, *Chem. Phys. Lett.* **1989**, *162*, 165–169.

[6] S. Grimme, J. G. Brandenburg, C. Bannwarth, A. Hansen, *J. Chem. Phys.* **2015**, *143*, 054107.

[7] A Klamt, G Schüürmann, *J. Chem. Soc. Perkin Trans. 2* **1993**, 799–805.

[8] J.-D. Chai, M. Head-Gordon, *J. Chem. Phys.* **2008**, *128*, 084106.

[9] S. Grimme, J. Antony, S. Ehrlich, H. Krieg, *J. Chem. Phys.* **2010**, *132*, 154104.

[10] F. Weigend, R. Ahlrichs, *Phys. Chem. Chem. Phys.* **2005**, *7*, 3297.

[11] F. Neese, *Wiley Interdiscip. Rev. Comp. Mol. Sci.* **2018**, *8*, e1327.

[12] F. Eckert, A. Klamt, *AIChE J.* **2002**, *48*, 369–385.

[13] COSMOtherm Program Suite COSMOlogic GmbH & Co KG.

[14] S. Grimme, *Chem. Eur. J.* **2012**, *18*, 9955–9964.

[15] C. P. Kelly, C. J. Cramer, D. G. Truhlar, *J. Phys. Chem. B* **2007**, *111*, 408–422.

[16] A. V. Marenich, C. J. Cramer, D. G. Truhlar, *J. Phys. Chem. B* **2009**, *113*, 6378–6396.

[17] *Handbook of Organic Solvent Properties*, Elsevier, **1996**.

[18] Q. Liu, L. Zhang, L. Liu, J. Du, Q. Meng, R. Gani, *Chem. Eng. Sci.* **2019**, *202*, 300–317.

[19] K. Kitaura, E. Ikeo, T. Asada, T. Nakano, M. Uebayasi, *Chem. Phys. Lett.* **1999**, *313*, 701–706.

[20] K. Kitaura, K. Morokuma, *Int. J. Quantum Chem.* **1976**, *10*, 325–340.

[21] M. W. Schmidt, K. K. Baldridge, J. A. Boatz, S. T. Elbert, M. S. Gordon, J. H. Jensen, S. Koseki, N. Matsunaga, K. A. Nguyen, S. Su, T. L. Windus, M. Dupuis, J. A. Montgomery, *J. Comput. Chem.* **1993**, *14*, 1347–1363.

[22] I. Lyskov, M. Kleinschmidt, C. M. Marian, *J. Chem. Phys.* **2016**, *144*, 034104.

[23] B. G. Levine, C. Ko, J. Quenneville, T. J. Martínez, *Mol. Phys.* **2006**, *104*, 1039–1051.

[24] A. D. Becke, *J. Chem. Phys.* **1993**, *98*, 1372–1377.

[25] M. Kleinschmidt, C. M. Marian, M. Waletzke, S. Grimme, *J. Chem. Phys.* **2009**, *130*, 044708.

[26] S. Miertus, J. Tomasi, *Chem. Phys.* **1982**, *65*, 239–245.

[27] J. L. Pascual-ahuir, E. Silla, I. Tuñon, *J. Comput. Chem.* **1994**, *15*, 1127–1138.

[28] R. Improta, G. Scalmani, M. J. Frisch, V. Barone, *J. Chem. Phys.* **2007**, *127*, 074504.

[29] M. J. Frisch, G. W. Trucks, H. B. Schlegel, G. E. Scuseria, M. A. Robb, J. R. Cheeseman, G. Scalmani, V. Barone, G. A. Petersson, H. Nakatsuji, X. Li, M. Caricato, A. V. Marenich, J. Bloino, B. G. Janesko, R. Gomperts, B. Mennucci, H. P. Hratchian, J. V. Ortiz, A. F. Izmaylov, J. L. Sonnenberg, D. Williams-Young, F. Ding, F. Lipparini, F. Egidi, J. Goings, B. Peng, A. Petrone, T. Henderson, D. Ranasinghe, V. G. Zakrzewski, J. Gao, N. Rega, G. Zheng, W. Liang, M. Hada, M. Ehara, K. Toyota, R. Fukuda, J. Hasegawa, M. Ishida, T. Nakajima, Y. Honda, O. Kitao, H. Nakai, T. Vreven, K. Throssell, J. Montgomery, J. A., J. E. Peralta, F. Ogliaro, M. J. Bearpark, J. J. Heyd, E. N. Brothers, K. N. Kudin, V. N. Staroverov, T. A. Keith, R. Kobayashi, J. Normand, K. Raghavachari, A. P. Rendell, J. C. Burant, S. S. Iyengar, J. Tomasi, M. Cossi, J. M. Millam, M. Klene, C. Adamo, R. Cammi, J. W. Ochterski, R. L. Martin, K. Morokuma, O. Farkas, J. B. Foresman, D. J. Fox, Gaussian16 Revision A.03, Wallingford, CT, **2016**.

[30] G. Bussi, D. Donadio, M. Parrinello, *J. Chem. Phys.* **2007**, *126*, 014101.

[31] H. J. C. Berendsen, J. P. M. Postma, W. F. van Gunsteren, A. DiNola, J. R. Haak, *J. Chem. Phys.* **1984**, *81*, 3684–3690.

[32] A. Rodriguez, A. Laio, *Science* **2014**, *344*, 1492–1496.

4.3 Paper A3

"Aggregation-induced emission leading to two distinct emissive species in the solid-state structure of high-dipole organic chromophores"

F. Witte, P. Rietsch, N. Nirmalananthan-Budau, J. P. Götze, U. Resch-Genger, S. Eigler, B. Paulus
manuscript in preparation for submission to Phys. Chem. Chem. Phys.

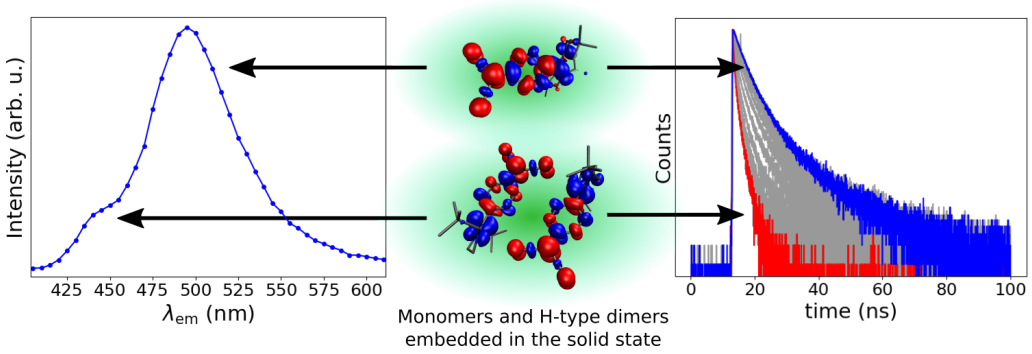

Figure 4.3: Graphical abstract of paper **A3**.

Contributions

The project was conceived by Felix Witte and Philipp Rietsch. F.W. designed and performed all quantum-chemical calculations and wrote the manuscript. Nithiya Nirmalananthan-Budau performed lifetime measurements of compounds 2 and 3. P.R. prepared and conducted all remaining experimental work. All authors contributed to the final version of the manuscript.

Aggregation-induced emission leading to two distinct emissive species in the solid-state structure of high-dipole organic chromophores

Felix Witte,[1]* Philipp Rietsch,[2] Nithiya Nirmalananthan-Budau,[3] Jan P. Götze,[1] Siegfried Eigler,[2] and Beate Paulus[1]

Abstract: The concept of aggregation-induced emission represents a means to rationalise photoluminescence of usually nonfluorescent excimers in solid-state materials. In this publication, we study the photophysical properties of selected diaminodicyanoquinone (DADQ) derivatives in the solid state using a combined approach of experiment and theory. DADQs are a class of high-dipole organic chromophores promising for applications in non-linear optics and light-harvesting devices. Among the compounds investigated, we find both aggregation-induced emission and aggregation-caused quenching effects rationalised by calculated energy transfer rates. Analysis of fluorescence spectra and lifetime measurements provide the curious result that (at least) two emissive species seem to contribute to the photophysical properties of DADQs. The main emission peak is notably broadened in the long-wavelength limit and exhibits a blue-shifted shoulder. We employ high-level quantum-chemical methods to validate a molecular approach to a solid-state problem and show that the complex emission features of DADQs can be attributed to a combination of H-type aggregates, monomers, and crystal structure defects.

Introduction

Understanding the mechanisms and intricacies related to the optical properties of solid-state materials opens the door towards applications in optoelectronic devices,[1,2] photosensors,[3–5] and bioimaging[6–8] and is therefore of broad interest for chemists, physicists, and material scientists alike. Notably, significant advances have been made in the field of luminescent organic solid-state materials.[9–15] One major drawback encountered in solid-state structures is so-called aggregation-caused quenching (ACQ) of emission promoted by close molecular packing within a crystal often leading to severe reduction of fluorescence quantum yields (QYs).[16–18] Probably the most prominent quenching mechanism in organic crystals involves energy transfer mediated through π-π-stacking in excimers. Quenching mechanisms include Förster resonance energy transfer (FRET) and the short-range Dexter process.[19,20] While the former depends on the potentially far-reaching ($>$10 Å) interaction of molecular (transition) dipoles, decaying with an R^{-6} dependence, the latter is determined by wavefunction overlap which decays much quicker with an exponential dependence on distance. Without the need for resource-demanding high-level quantum-chemical methods, Radhakrishnan and co-workers have developed and successfully applied a model based on the relative orientation and assembly of isolated diaminodicyanoquinones (DADQs) in the solid state to estimate Förster[19] and Dexter[20] energy transfer rates and rationalise fluorescence QY trends.[21]

In contrast to ACQ, solid-state materials may also experience QY enhancement due to close molecular packing. In 2001, Luo et al.[22,23] introduced the concept of aggregation-induced emission (AIE) presenting a silole compound which for the first time showed improved QYs upon aggregation in solution. This sparked a rapid increase in interest in this topic and many systems were introduced exploiting the AIE idea.[24–26] Approaches to enhance emission in the solid state include the design of materials based on J-aggregates[27] and embedded or isolated dimers, which may show diminished non-radiative decay rates due to the rigidity of their microscopic environment.

In this account, we examine the optical properties of selected solid-state DADQ derivatives. DADQs are a class of organic compounds promising for application in non-linear optics and light-harvesting devices due to their large dipole moments, redox activity, and fluorescence properties. We study four C_2 symmetric DADQ derivatives using a combination of fluorescence experiments and state-of-the-art quantum-chemical approaches. Due to an interplay of AIE and ACQ effects, a reverse trend between fluorescence QYs in solution and in the solid state is observed with respect to the substituents. We show that this can be related to the degree of π-π-stacking within the crystals which is furthermore supported by energy

[1] *F. Witte, J. P. Götze, Prof. Dr. B. Paulus*
Institute of Chemistry and Biochemistry
Freie Universität Berlin
Arnimallee 22, 14195 Berlin, Germany
E-mail: jf.witte@fu-berlin.de

[2] *P. Rietsch, Prof. Dr. S. Eigler*
Institute of Chemistry and Biochemistry
Freie Universität Berlin
Takustr. 3, 14195 Berlin, Germany

[3] *N. Nirmalananthan-Budau*
Division Biophotonics
Federal Institute for Material Research and Testing (BAM)
Richard-Willstätter-Straße 11, 12489 Berlin, Germany

transfer rates computed according to the ideas of Radhakrishnan and co-workers.[28]

We present an unexpected correlation between fluorescence lifetimes and emission wavelengths in solid-state DADQs. Lifetimes increase with increasing emission wavelength in a way that is incompatible with a two-state system and thus hint at the existence of (at least) one more emissive species. In one case, this results in a blue-shifted shoulder of the main emission peak. Additionally, fluorescence intensities are still detectable close to 100 nm beyond the main peak in the long-wavelength region.

We show that instead of computing the optical properties of entire crystal structures, which would necessitate resource-draining evaluation of Green's functions or Bethe-Salpeter equations, a molecular approach based on monomers and dimers embedded in the crystal is sufficient for a proper theoretical analysis. Our protocol is based on a combination of QM/MM (quantum-mechanics/molecular-mechanics) calculations and DFT/MRCI[29–31] (density functional theory/multireference configuration interaction). Finally, we reveal that the main emission peak can be attributed to monomers, while short-wavelength emission associated with much shorter lifetimes are caused by H-type dimers. Lastly, our calculations suggest that long lifetimes measured at the low-energy end of the spectra can be explained by crystal defects.

Results and Discussion

Synthesis. The synthesis of compounds **1**-**4** is illustrated in Scheme 1. The DADQs differ in their amino substituent: **1** for neopentyl, **2** for methyl, and **3** for para-methylbenzoate. Compound **4** is defined by a benzene instead of an ethyl bridge between the nitrogen atoms of the diamino group. All substances were prepared according to literature by coupling 7-pyrrolidino-7,8,8-tricyanoquinomethane (PTCNQ) and the respective diamine.[32,33]

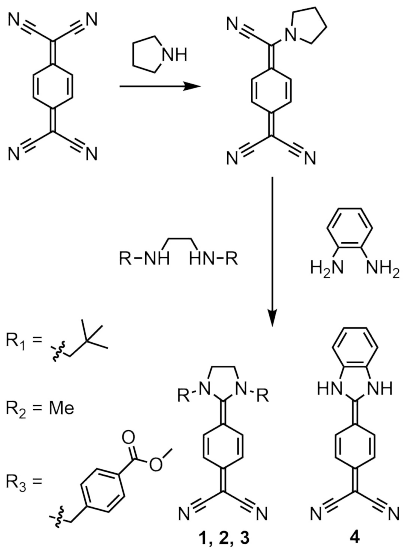

Scheme 1: Synthetic route to DADQ derivatives starting from TCNQ by reaction with pyrrolidine and subsequent reaction with the respective primary or secondary diamine. i) 0.8 eq. pyrrolidine, 70 °C, 4 hours. ii) 1 eq. of the respective diamine, 70 °C, 2–20 hours. Detailed protocols, yields and characterisation of the compounds can be found in the Supporting Information.

QY measurements in solution and in the solid state. Figure 1 depicts excerpts of the crystal structures either obtained from X-ray diffraction measurements (**1**-**3**) or from a quantum-chemical solid-state optimisation (**4**) (see sections 3 and 5 in the ESI for details). QYs in solution (ACN) and in the solid state are given below the figures. In solution, compound **4** is the only molecule showing relevant fluorescence QY (92%). The QY differences in solution are related to energetic barriers of intramolecular rotation around the dihedral angles near the dicyano and the amino moities, as we have shown in an earlier publication.[32] Especially rotation of the dicyano moiety provides a mechanism of fluorescence deactivation. In the solid-state, this rotational mode is obviously immobilised and cannot contribute to emission quenching ($\Delta E_{\mathrm{rot}} \approx 700$ kJ/mol, Figure S6).

Solid-state fluorescence QYs range from 18% in **1** to less than 1% in **4**. The QY trend observed in the solid state can be explained by the degree of π-π-stacking in the crystal structure. The shortest distances between the centres of mass (COM) are not extremely far apart for **1** (5.9 Å) and **4** (4.1 Å). However, while there is practically no effective overlap between the π-systems in **1** (8.3 Å), molecules in the crystal structure of **4** are efficiently stacked (4.1 Å). As we will see later, this can be related to energy transfer rates in the spirit of Förster and Dexter modes (Figure 4 down below).[21]

Dependence of lifetime and emission wavelength. Lifetimes τ for selected emission wavelengths λ_{em} for compounds **1**, **2**, and **3** are given in Table 1. A detailed spectroscopic analysis of compound **1** is illustrated in Figure 2 (Figures S3 and S4 for **2** and **3**, respectively). As can be seen in Figure 2a, there is a strong dependence of τ and λ_{em}, which is in correlation with the respective emission spectrum (Figure 2b) and is depicted in Figure 2c. From Fermi's golden rule it can be shown that in a two-level system there should be a linear relationship between τ^{-1} and $\lambda_{\mathrm{em}}^{-2}$.[34]

$$k \propto \tau^{-1} \propto \omega^3 M^2 \propto \omega^2 f_{\mathrm{osc}} \propto \lambda_{\mathrm{em}}^{-2} \qquad (1)$$

with radiative rate constant k, vertical excitation energy ω, transition dipole moment M, and oscillator strength f_{osc}. This relationship is not recovered in our measurements (Figure 2d). Assuming that the peak splitting in the emission spectrum of compound **1** is not caused by vibronic coupling, we tentatively conclude, that the observed emission properties arise from at least two emissive species. These could either be two different emitting states of the same structure, two different structural motifs in the same emissive electronic state, or two different structures in two different states. While the emission spectrum of compound **1** shows a clear high-energy shoulder, the spectra of compounds **2** and **3** do not unambiguously display a second signal. In their case,

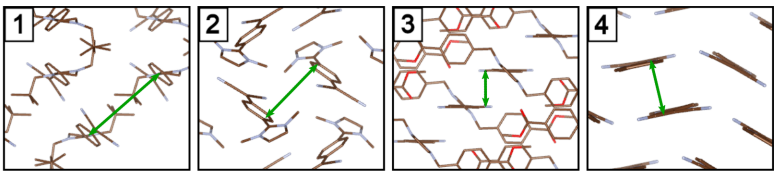

	1	2	3	4
QY (solution)	<1%	<1%	<1%	92%
QY (solid)	18%	10%	6%	<1%
π-π-stacking distance	8.3Å	6.1Å	4.2Å	4.1Å
closest COM distance	5.9Å	5.9Å	4.2Å	4.1Å

Figure 1: Crystal structure excerpts, QYs in the solid state and in solution (ACN), and selected distances of compounds **1**-**4**. Note that compound **4** was obtained by periodic DFT calculation at the PBE-D3(BJ) level (section 5.2 ESI). The increasing degree of π-π-overlap from **1** to **4** can be appreciated from the decreasing π-π-stacking distance (depicted in green). Hydrogen atoms were omitted for clarity.

Table 1: Solid-state lifetimes in ns of compounds **1**-**3** measured at different emission wavelengths given in nm in parentheses

1	0.86 (435)	3.60 (495)	4.31 (555)
2	1.20 (410)	2.13 (470)	3.44 (530)
3	0.46 (460)	0.60 (480)	3.95 (500)

the τ^{-1} against $\lambda_{\mathrm{em}}^{-2}$ plots reveal a similar behaviour as for **1**. We note that this is less clear in the case of compound **2**, which we attribute to the absence of true H-type aggregates in the solid-state structure, which will be discussed further down below.

The main emission peak of **1** has a significantly longer lifetime than the high-energy (short wavelength) transition indicating a smaller oscillator strength according to equation (1). However, their intensities in the emission spectrum are reversed. This may be caused by a larger degree of non-radiative quenching for the high-energy signal. The largest portion of the QY is, hence, unsurprisingly, due to the main peak. A Gaussian curve fit inside the experimental emission spectrum of **1** estimates a contribution of 3% to the overall QY from the high-energy shoulder (Figure S5). Further down below, we will show that these observations can be rationalised by the different optical properties obtained by treating isolated monomers and dimers embedded in the crystal structure. In the following we will apply a combination of energy transfer rate calculations, periodic quantum-chemical methods, and the DFT/MRCI approach to examine the electronic and optical properties of DADQs in the solid state and investigate what may be the origin of the two emitting species.

Energy transfer rates. To elucidate the differences in solid-state fluorescence QYs of compounds **1**-**4**, we calculated energy transfer rates in close relation to long-range Förster and short-range Dexter coupling modes (visualised in Figure 3). As proposed by Radhakrishnan and co-workers,[21] Förster rates, k_{F}, are determined by the relative orientation and distance of the transition dipole moments of two monomers by

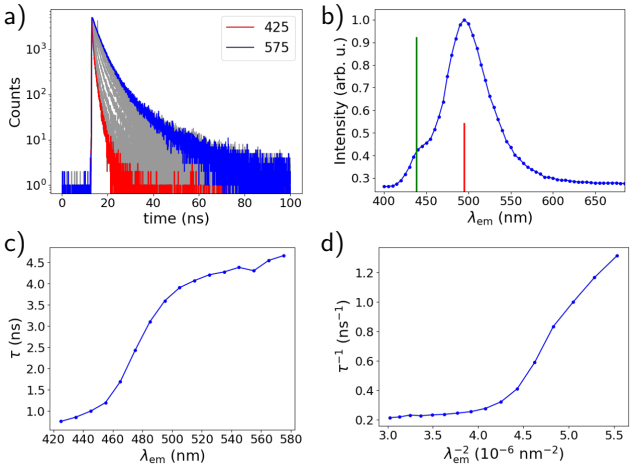

Figure 2: Fluorescence properties of **1**: a) lifetime decay measurements at various emission wavelengths ranging from 425 nm to 575 nm, b) emission spectrum measured after excitation at 375 nm with computed vertical transition insets obtained from DFT/MRCI calculations for an H-type dimer (green) and a monomer (red) scaled according to oscillator strengths, c) lifetime plotted against emission wavelength, d) reciprocal lifetime plotted against reciprocal squared emission wavelength.

$$k_{\mathrm{F}} \propto \frac{[3\cos(\alpha_1)\cos(\alpha_2) + \cos(\alpha_1 + \alpha_2)]^2}{R^6} \qquad (2)$$

where R connects the centres of mass of the molecules and α_1 and α_2 are the angles between R and the respective transition dipole. In contrast, Dexter energy transfer rates, k_{D}, depend on the relative orientation and distance of the molecular planes describing the quinone systems and fall off much quicker (exponential versus polynomial decay) since the short-range transfer rate depends on the wavefunction overlap of the two monomers:

$$k_{\mathrm{D}} \propto \cos(\theta)\cos(\phi)e^{-r'} = \cos(\theta)\cos(\phi)e^{-r\cos(\theta)} \qquad (3)$$

where r and r' refer to centre of plane distance and the perpendicular distance between the π-planes, respectively. θ defines the angle between the normal vector of the first plane and r, while ϕ describes the interplanar angle between the two π-systems.

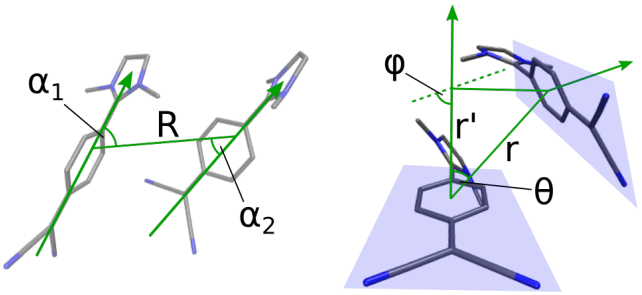

Figure 3: Illustration of the structural parameters determining k_F (left) and k_D (right). For the former, the arrows are aligned with the direction of the transition dipole moments. In the latter, the arrows point in the direction of the normal vectors of the molecules indicated by the blue planes.

While k_F links QYs to intermolecular (transition) dipole-dipole interaction, k_D can be interpreted as a relative measure to estimate energy transfer through π-π-stacking in the crystal. Figure 4 correlates relative values of k_F and k_D with the solid-state QYs of all compounds. Förster energy transfer is most important for compounds **1** and **2**, which show large intermolecular separation and π-π-stacking distances. In comparison, Dexter transfer is most prominent in compounds **3** and **4**, which display short π-π-stacking distances. The dimer motifs yielding the largest Förster and Dexter transfer rates are given in Figure S8 for all compounds.

Figure 4 furthermore reveals that k_F is unsuited to describe experimental differences with respect to compound **3**. It seems that regarding π-interactions becomes increasingly important for **3**, while it is not yet as essential in **1** and **2**. In general, while Dexter modes dominate the immediate environment of the monomers, most important for **3** and **4**, Förster interaction likely contributes as well especially at longer ranges due to the slower R^{-6} fall-off, which should be the main energy loss mechanism for compounds **1** and **2**. Details on how the values were obtained can be found in the ESI in section 5.1.

An important thing to note is that this analysis is based on the assumption that the optical properties of DADQs in the solid state can be reduced to the response of a monomer embedded in a crystal environment. In the following, we will refer to this idea as "molecular approach". In principle, it neglects the possibility of largely delocalised electronic transitions playing an important role in fluorescence experiments. Hence, in the next section, we will justify the molecular approach by analysing the solid-state properties of **1** and **2**, for which experimental data for crystal structures, QYs, and lifetimes are available.

The validity of a molecular approach to a solid-state problem. Periodic DFT calculations at the PBE-D3(BJ)[35–37] level were conducted to analyse the solid-state structure of compound **1** (see ESI for **2** and section 5.2 for computational details). A band gap of 2.31 eV at the PBE level and 3.20 eV using the HSE06[38] functional (Figure S10) are indicative of a semiconducting material. Calculations at the PBE level produce results in qualitative agreement with the HSE06 level. We note that the latter yields a band gap very similar to the experimentally measured absorption peak of the monomer in solution (3.02 eV in THF[32]). The band-structure and the density-of-states (DOS) plots shown in Figure 5a reveal a molecular, i.e., quite localised, picture of the solid-state electronic structure. The valence band (VB) and conduction band (CB) are energetically separated from the nearest occupied and virtual band by roughly 1.1 eV and 0.7 eV, respectively. A closer look at the VB and CB (Figure S11) shows four interacting bands originating from the four molecules comprising the unit cell. Furthermore, partial charge densities of the VB and CB depicted in Figure 5b can clearly be interpreted simply as the sum of the in-vacuo calculated highest occupied and lowest unoccupied molecular orbitals, respectively (Figure 5c). All in all, periodic electronic structure calculations present a solid basis for an approach based on small molecular clusters to examine the optical features of DADQs in the solid state.

Moreover, to obtain more insight and collect further arguments for (or against) a molecular approach we computed excited states employing the wB97X-D3[39] functional within the TD-DFT framework for a tetramer, i.e., the unit cell, and an octamer of compounds **1** and **2**, and an additional dodecamer of compound **2**. Various dimer conformations were computed for comparison. Larger clusters proved to be unfeasible at this level which prevented us from conducting convergence tests with respect to cluster size. The C-PCM[40] solvent model was utilised to mimic the dielectric properties of the crystal around the molecular clusters. The dielectric constant and refractive index necessary for the calculations were extracted from the dielectric tensor obtained at the periodic PBE level (section 5.2 in the ESI for details). Molecular structures (Figures S13 and S14), transition energies, and oscillator strengths (Tables S7–S12) are given in the Supporting Information.

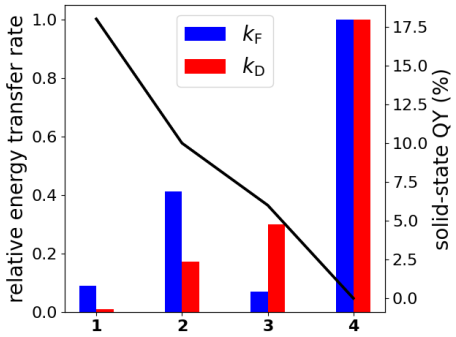

Figure 4: Relative Förster and Dexter energy transfer rates of compounds **1**-**4** (bars, **4** is set to 1.0) with additional indication of the solid-state QY (black line).

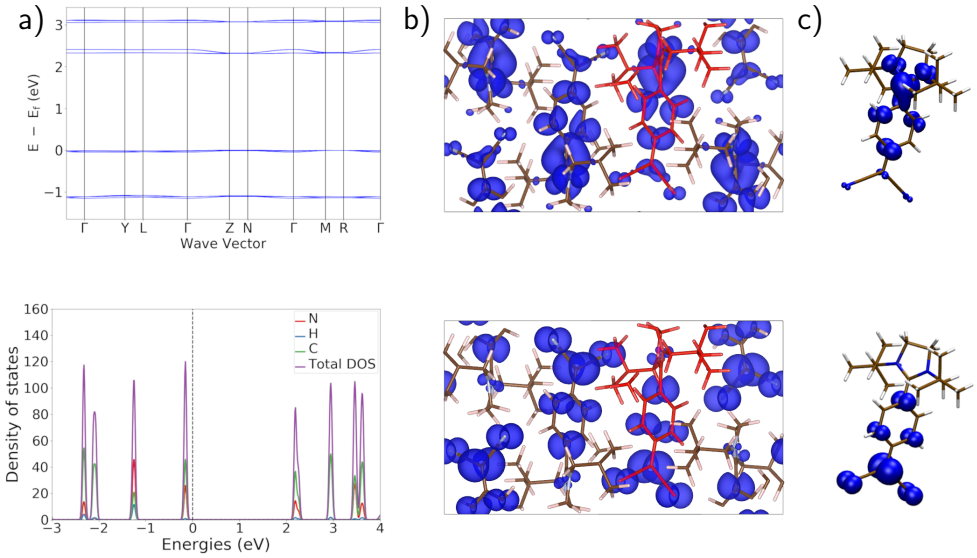

Figure 5: a) Bandstructure (top) and density-of-states (bottom) plots of **1**, b) partial charge densities of the conduction bands (top) and valence band (bottom) with indication of a monomer depicted in red for visual clarity, isovalue of 0.003 a_0^{-3}, and c) HOMO and LUMO density plots of a monomer of **1** calculated in-vacuo, isovalue of 0.003 a_0^{-3}. All plots were obtained from calculations employing the PBE functional.

Figure 6 depicts the difference densities for the excited states with the highest oscillator strengths of an octamer of **1** (S_5) and a dodecamer of **2** (S_{10}). In fact, all electronic transitions are fairly localised on either just a monomer or a dimer resembling an H-type aggregate. This provides a further argument in favour of a molecular approach. Note that in Figure 6 a transition localised on a monomer (dimer) still involves two (four) molecules, as both the octamer and the dodecamer consist of symmetrically equivalent sub-units. Hence, for clarity, only a part of the clusters is shown.

Certainly, one must be careful in assessing this approach as no experimental absorption data are available. More importantly, however, emission properties of these larger clusters are currently out of reach as this would necessitate excited-state optimisations requiring massive computational resources with the additional problem of modelling the solid-state environment. Still, our periodic DFT results in combination with localised excited states observed in molecular clusters provide sufficient evidence to justify a molecular approach based on monomers and dimers for the description of the electronic and optical properties of DADQs in the solid state. This comes with the major advantage that emission properties become feasible due to the manageable size of monomers and dimers. This will be exploited in the next part, where we will use a combination of the QM/MM method and DFT/MRCI to assess the absorption and emission properties of compounds **1** and **2**.

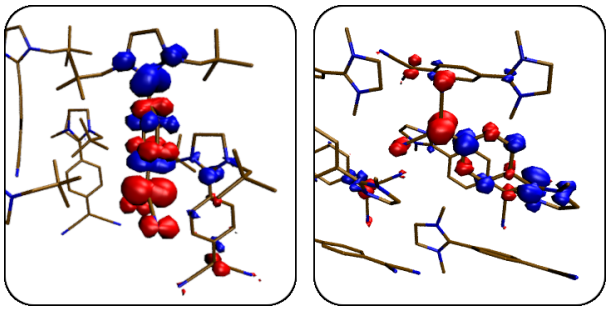

Figure 6: Difference densities of the excited states with the highest oscillator strengths in **1** (left, S_5 at 335 nm) and in **2** (right, S_{10} at 305 nm). Red and blue zones correspond to areas of electron depletion and accumulation, respectively. Hydrogen atoms were omitted for clarity. Isovalue=0.001 a_0^{-3}.

Rationalising solid-state fluorescence properties. In the previous section, we have established that it is sufficient to examine monomers and dimers of our DADQs embedded in their crystal structure to evaluate their photophysical solid-state properties. We calculated monomers and H- and J-like aggregated dimers embedded in the crystal structure of compound **1** and **2** (Figure 7 and Figure S19). Since compound **3** essentially only contains H-type aggregates (cf. Figure 1), J-aggregates are likely to play a subordinated role, if we assume that the mechanisms responsible for the emission properties are similar in all compounds. We employed the ONIOM[41] scheme to perform a QM/MM optimisation of ground- and excited states using the wB97XD functional for the high layer and the UFF (universal force field)[42] for the low layer. Note that the dispersion part of the functional differs from the one used earlier due to limitations of the employed quantum-chemical programme packages. Afterwards, the DFT/MRCI method in combination with the C-PCM model once again using the dielectric constant obtained from the periodic calculations was employed to compute absorption and emission peaks. A similar approach has been used recently for chalcone-based materials.[43] Due to the non-polarisable force field, state crossings with dark charge-transfer states pose

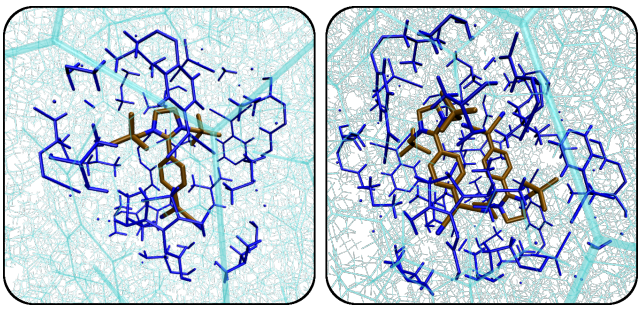

Figure 7: Monomer (left) and H-type dimer (right) of compound **1** embedded in their crystal environments. Hydrogens are omitted for the high layer for clarity. A part of the low layer (dark blue) was allowed to relax during the run. The static low layer is depicted in transparent cyan.

Table 2: Calculated absorption peaks, comparison of calculated and experimental emission wavelengths, emission oscillator strengths and lifetimes of compounds **1** and **2** for monomers (mon) and H-aggregates (H). Absorption and emission wavelengths are given in nm, lifetimes in ns.

			$\lambda_{abs}^{\text{calc.}}$	$\lambda_{em}^{\text{calc.}}$	$\lambda_{em}^{\text{exp.}}$	$f_{\text{osc,em}}$	$\tau_{\text{exp.}}$
1	mon	S_1	440	488	495	0.81	3.60
	H	S_1	404	466	438*	0.00	0.86
		S_2	387	432		1.38	
2	mon	S_1	412	463	463	0.73	2.13
	H	S_1	409	439	**	0.00	1.19
		S_2	392	419		1.38	

* extracted from Gaussian fit, ** not reliably extractable

a hypothetical problem. However, excited states in DADQ dimers are of local nature which can be deduced from the difference densities of the S_1 and S_2 states in the H-type dimer displaying the same nodal shape (Figure S20). Details about the DFT/MRCI excited state calculations can be found in section 5.2 of the ESI. As can be seen in Table 2, our protocol yields a nice agreement between calculated vertical transitions and experimental emission energies. For compound **1**, the main peak at 495 nm is energetically close to the S_1 of the monomer, while the shoulder at 438 nm is near the S_2 of the H-type dimer. Both emission energies differ by less than 7 nm (0.07 eV, vertical transition lines in Figure 2b above). J-aggregates can be assumed to only play a minor role for the emission spectrum, presumably in between the main peak and the high-energy (short wavelength) shoulder (Table S13). Figure 8 illustrates the mechanism and shows that excited-state and ground-state structures optimised in a crystal environment differ only very slightly, as expected. For compound **2**, the main peak is exactly reproduced by the calculation likely benefitting from fortuitous error cancellation, while the high-energy component of the spectrum cannot be extracted reliably.

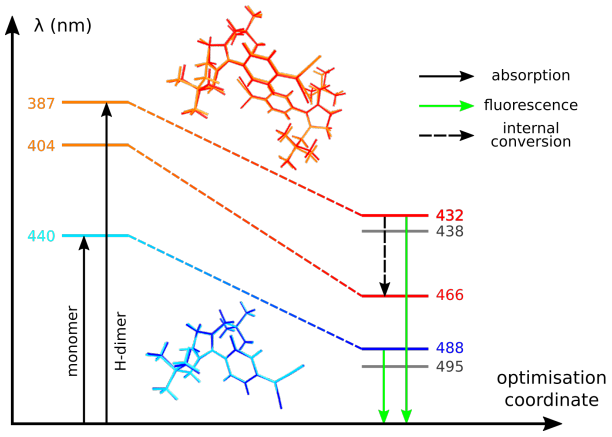

Figure 8: Excited-state optimisation of **1** in the solid-state: Ground- and excited-state optimised structures are overlaid. Monomer and H-dimer are represented by a cyan to blue and an orange to red colour change, respectively. Solid arrows refer to absorption and emission, while the dashed arrow indicates fluorescence quenching of the H-dimer due to internal conversion. Experimental emission wavelengths are depicted in grey.

As has been addressed earlier, there is a mismatch between emission intensities and fluorescence lifetimes, as shorter lifetimes indicate larger oscillator strengths (equation (1)) which, in turn, imply larger intensities. In Table 2, we can see that this discrepancy can now be explained by non-radiative fluorescence quenching through internal conversion of the high-energy S_2 of the H-type dimer to its dark S_1 which lies 34 nm (0.2 eV) lower in energy. Technically, emission from the high-lying S_2 violates Kasha's rule,[44] which states that emission originates from the lowest excited state (S_1). However, the two states are very close in energy enabling potentially multiple state crossings or conical intersections that allow for dynamical population exchange. Future analysis would therefore require quantum dynamics which is however not covered in this work.

Depending on the emitting system, the radiative decay pathway of the monomer can vary between quenched or unquenched. We assign the vast majority of the fluorescence QY to the monomers, as those exhibit the largest contribution to the emission according to Table 2. In conclusion, we attribute the general shape of the emission spectrum of **1** to monomers and H-type dimers embedded in the solid-state crystal structure.

One remaining issue is the low-energy (long wavelength) end of the emission spectrum. For compound **1**, the longest lifetimes are measured at around 570 nm, almost 80 nm (0.33 eV) red-shifted with respect to the monomer emission peak. This is noteworthy, as lifetime broadening should actually sharpen the signal rather than widening it. Monomers with higher conformational mobility in the crystal should produce larger Stokes shifts and may, thus, explain this observation. Such structural freedom may be achieved by defects in the solid-state structure. Rather large R-factors of the crystal structures (Table S4) support this claim. Hence, we repeated the computational procedure described above for monomers placed inside a defect. As there is no experimental data for the nature of possible defects available, we opted to simply use the cavity formed by the H-type dimer of **1** and put a

monomer inside of it. The resulting emission peak is located at 516 nm, red-shifted by 34 nm, making it a potential candidate for the observed long lifetimes near the low-energy end of the emission spectrum. In the most extreme case, without the rigid crystal environment, the monomer loses all of its oscillator strength while constantly increasing the Stokes shift upon relaxation on the S_1 (Figure 9). We can thus assume, that depending on the size of the defect cavity, the monomer may show small amounts of fluorescence at various emission energies beyond the main emission peak.

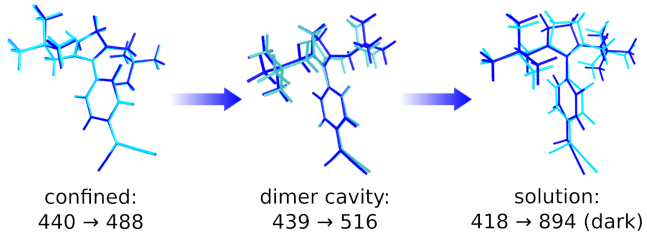

Figure 9: Absorption and emission wavelengths depending on the degree of conformational mobility of the monomer. Left: completely confined in the crystal, middle: encapsulated inside a dimer cavity, right: "free" inside a dielectric continuum with the same permittivity and refractive index as compound **1** as a solid. Ground- and excited-state optimised structures are overlaid in cyan and blue, respectively.

Conclusion

Using both experimental and computational approaches, we were able to explain the emergence of aggregation-induced emission in an organic crystal system. The solid-state optical properties of four DADQ derivatives were rationalised and the corresponding mechanisms supported by molecular models.

Differences in solid-state fluorescence QYs can be related to the efficiency of π-π-stacking interactions within the crystal which were quantified by energy transfer rate calculations according to Radhakrishnan and co-workers. While benzene-bridged, unsubstituted compound **4** experiences aggregation-caused quenching, dineopentyl-substituted derivative **1** is subject to an aggregation-induced emission effect. Furthermore, lifetime measurements at various emission wavelengths reveal multiple emitting species in compounds **1**-**3**, which we attribute to H-type dimers and monomers, while J-aggregates only play a minor role for the optical properties. Our computational protocol based on QM/MM calculations and the DFT/MRCI method to evaluate the photophysical properties of DADQs in the solid state, may serve as a general approach to study optical problems in organic crystals.

In conclusion, our joint study was able to elucidate a wide range of effects occurring in organic crystals, likely not limited to the DADQ compounds studied here. The results may have implications for the design of organic light emitting compounds.

Acknowledgement

We thank Tim Küllmey for helpful discussions. The North-German Supercomputing Alliance (Norddeutscher Verbund für Hoch- und Höchstleistungsrechnen) and the computing facilities of Freie Universität Berlin (Zentrale Einrichtung für Datenverarbeitung) are acknowledged for providing computational resources. FW and JPG gratefully acknowledge the Deutsche Forschungsgemeinschaft for financial support through research grant PA 1360/16-1 and project No. 393271229, respectively.

Competing Interests

The authors declare no competing interests.

References

[1] M. M. Stylianakis, *Nanomaterials* **2020**, *10*, 520.
[2] X. Wang, Y. Cui, T. Li, M. Lei, J. Li, Z. Wei, *Adv. Opt. Mater.* **2019**, *7*, 1801274.
[3] T. L. Mako, J. M. Racicot, M. Levine, *Chem. Rev.* **2019**, *119*, 322–477.
[4] R. D. Jansen-van Vuuren, A. Armin, A. K. Pandey, P. L. Burn, P. Meredith, *Adv. Mater.* **2016**, *28*, 4766–4802.
[5] D. Yang, D. Ma, *Adv. Opt. Mater.* **2019**, *7*, 1800522.
[6] H.-B. Cheng, Y. Li, B. Z. Tang, J. Yoon, *Chem. Soc. Rev.* **2020**, *49*, 21–31.
[7] Q. Qi, C. Li, X. Liu, S. Jiang, Z. Xu, R. Lee, M. Zhu, B. Xu, W. Tian, *J. Am. Chem. Soc.* **2017**, *139*, 16036–16039.
[8] C.-B. Ma, Z.-T. Zhu, H.-X. Wang, X. Huang, X. Zhang, X. Qi, H.-L. Zhang, Y. Zhu, X. Deng, Y. Peng, Y. Han, H. Zhang, *Nanoscale* **2015**, *7*, 10162–10169.
[9] J. De, S. P. Gupta, S. Sudheendran Swayamprabha, D. K. Dubey, I. Bala, I. Sarkar, G. Dey, J.-H. Jou, S. Ghosh, S. K. Pal, *J. Phys. Chem. C* **2018**, *122*, 23659–23674.
[10] S. Feuillastre, M. Pauton, L. Gao, A. Desmarchelier, A. J. Riives, D. Prim, D. Tondelier, B. Geffroy, G. Muller, G. Clavier, G. Pieters, *J. Am. Chem. Soc.* **2016**, *138*, 3990–3993.
[11] I. Bala, N. Singh, R. A. K. Yadav, J. De, S. P. Gupta, D. P. Singh, D. K. Dubey, J.-H. Jou, R. Douali, S. K. Pal, *J. Mater. Chem. C* **2020**, *8*, 12485–12494.
[12] A. Adak, T. Panda, A. Raveendran, K. S. Bejoymohandas, K. S. Asha, A. P. Prakasham, B. Mukhopadhyay, M. K. Panda, *ACS Omega* **2018**, *3*, 5291–5300.
[13] R. Butkute, R. Lygaitis, V. Mimaite, D. Gudeika, D. Volyniuk, G. Sini, J. V. Grazulevicius, *Dyes Pigm.* **2017**, *146*, 425–437.
[14] S. Mukherjee, P. Thilagar, *Angew. Chem. Int. Ed.* **2019**, *58*, 7922–7932.
[15] P. Pallavi, V. Kumar, M. W. Hussain, A. Patra, *ACS Appl. Mater. Interfaces* **2018**, *10*, 44696–44705.

[16] Y. Huang, J. Xing, Q. Gong, L.-C. Chen, G. Liu, C. Yao, Z. Wang, H.-L. Zhang, Z. Chen, Q. Zhang, *Nat. Commun.* **2019**, *10*, 169.

[17] W. Z. Yuan, P. Lu, S. Chen, J. W. Y. Lam, Z. Wang, Y. Liu, H. S. Kwok, Y. Ma, B. Z. Tang, *Adv. Mater.* **2010**, *22*, 2159–2163.

[18] B. Andreiuk, A. Reisch, E. Bernhardt, A. S. Klymchenko, *Chem. Asian J.* **2019**, *14*, 836–846.

[19] T. Förster, *Ann. Physik* **1948**, *437*, 55–75.

[20] D. L. Dexter, *J. Chem. Phys.* **1953**, *21*, 836–850.

[21] P. Srujana, P. Sudhakar, T. P. Radhakrishnan, *J. Mater. Chem. C* **2018**, *6*, 9314–9329.

[22] J. Luo, Z. Xie, J. W. Y. Lam, L. Cheng, B. Z. Tang, H. Chen, C. Qiu, H. S. Kwok, X. Zhan, Y. Liu, D. Zhu, *Chem. Commun.* **2001**, 1740–1741.

[23] Y. Hong, J. W. Y. Lam, B. Z. Tang, *Chem. Soc. Rev.* **2011**, *40*, 5361.

[24] Y. Shen, H. Liu, S. Zhang, Y. Gao, B. Li, Y. Yan, Y. Hu, L. Zhao, B. Yang, *J. Mater. Chem. C* **2017**, *5*, 10061–10067.

[25] H. Liu, L. Yao, B. Li, X. Chen, Y. Gao, S. Zhang, W. Li, P. Lu, B. Yang, Y. Ma, *Chem. Commun.* **2016**, *52*, 7356–7359.

[26] H. Liu, D. Cong, B. Li, L. Ye, Y. Ge, X. Tang, Y. Shen, Y. Wen, J. Wang, C. Zhou, B. Yang, *Cryst. Growth Des.* **2017**, *17*, 2945–2949.

[27] F. Würthner, T. E. Kaiser, C. R. Saha-Möller, *Angew. Chem. Int. Ed.* **2011**, *50*, 3376–3410.

[28] P. Srujana, T. P. Radhakrishnan, *Chem. Eur. J.* **2018**, *24*, 1784–1788.

[29] I. Lyskov, M. Kleinschmidt, C. M. Marian, *J. Chem. Phys.* **2016**, *144*, 034104.

[30] M. Kleinschmidt, C. M. Marian, M. Waletzke, S. Grimme, *J. Chem. Phys.* **2009**, *130*, 044708.

[31] C. M. Marian, A. Heil, M. Kleinschmidt, *WIREs Comput. Mol. Sci.* **2019**, *9:e1394*.

[32] P. Rietsch, F. Witte, S. Sobottka, G. Germer, A. Becker, A. Güttler, B. Sarkar, B. Paulus, U. Resch–Genger, S. Eigler, *Angew. Chem. Int. Ed.* **2019**, *58*, 8235–8239.

[33] P. Sudhakar, T. P. Radhakrishnan, *J. Mater. Chem. C* **2019**, *7*, 7083–7089.

[34] D. Toptygin, *J. Fluoresc.* **2003**, *13*, 201–219.

[35] J. P. Perdew, K. Burke, M. Ernzerhof, *Phys. Rev. Lett.* **1996**, *77*, 3865–3868.

[36] S. Grimme, J. Antony, S. Ehrlich, H. Krieg, *J. Chem. Phys.* **2010**, *132*, 154104.

[37] S. Grimme, S. Ehrlich, L. Goerigk, *J. Comput. Chem.* **2011**, *32*, 1456–1465.

[38] J. Heyd, G. E. Scuseria, M. Ernzerhof, *J. Chem. Phys.* **2003**, *118*, 8207–8215.

[39] J.-D. Chai, M. Head-Gordon, *J. Chem. Phys.* **2008**, *128*, 084106.

[40] V. Barone, M. Cossi, *J. Phys. Chem. A* **1998**, *102*, 1995–2001.

[41] M. Svensson, S. Humbel, R. D. J. Froese, T. Matsubara, S. Sieber, K. Morokuma, *J. Phys. Chem.* **1996**, *100*, 19357–19363.

[42] A. K. Rappe, C. J. Casewit, K. S. Colwell, W. A. Goddard, W. M. Skiff, *J. Am. Chem. Soc.* **1992**, *114*, 10024–10035.

[43] M. Dommett, M. Rivera, M. T. H. Smith, R. Crespo-Otero, *J. Mater. Chem. C* **2020**, *8*, 2558–2568.

[44] M. Kasha, *Discuss. Faraday Soc.* **1950**, *9*, 14–19.

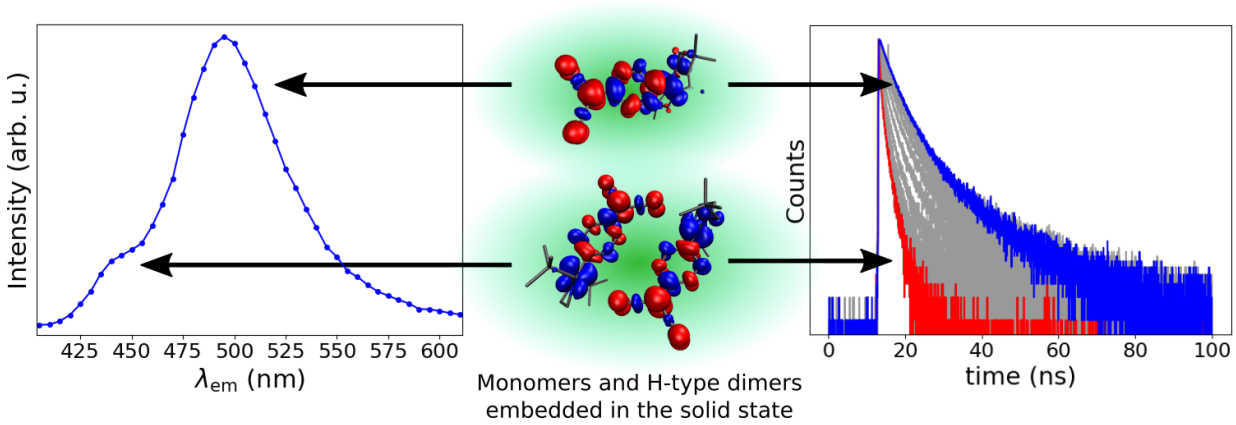

Fluorescence lifetime measurements reveal two emissive species in the solid-state structure of high-dipole chromophores unravelled by a combination of high-level quantum-chemical approaches.

Keywords: aggregation, fluorescence, molecular modelling, solid-state physics

Supporting Information:
Aggregation-induced emission leading to two distinct emissive species in the solid-state structure of high-dipole organic chromophores

Felix Witte,[1]* Philipp Rietsch,[2] Nithiya Nirmalananthan-Budau,[3] Jan P. Götze,[1] Siegfried Eigler,[2] and Beate Paulus[1]

[1] *F. Witte, J. P. Götze, Prof. Dr. B. Paulus*
Institute of Chemistry and Biochemistry
Freie Universität Berlin
Arnimallee 22, 14195 Berlin, Germany
E-mail: jf.witte@fu-berlin.de

[2] *P. Rietsch, Prof. Dr. S. Eigler*
Institute of Chemistry and Biochemistry
Freie Universität Berlin
Takustr. 3, 14195 Berlin, Germany

[3] *N. Nirmalananthan-Budau*
Division Biophotonics
Federal Institute for Material Research and Testing (BAM)
Richard-Willstätter-Straße 11, 12489 Berlin, Germany

Contents

1 General information

All reagents were purchased from commercial sources and used without further purification. Dry solvents were purchased from Acros Organics. ALUGRAM Xtra SIL G/UV^{254} plates by Macherey-Nagel were used for thin-layer chromatography. Isolation of products by chromatography was performed with silica from Macherey-Nagel Silica 60 M (0.04–0.063 mm). NMR spectra were recorded on a JOEL ECX 400 (^{1}H 400 MHz, ^{13}C 101 MHz), JEOL Eclipse+ 500 (^{1}H 500 MHz, ^{13}C 126 MHz) and BRUKER AVANCE 700 (1H 700 MHz, 13C 176 MHz) spectrometer at 25 °C. The chemical shifts δ are calibrated on the respective solvent peak as internal standard. All shifts are reported in ppm and NMR multiplicities are abbreviated as s (singlet), d (duplet), t (triplet), m (multiplet). Coupling constants J are reported in Hz. UV/Vis spectra were recorded on a Cary 50 Bio photospectrometer (Varian). Fluorescence spectra were recorded on a LS 50 B luminescence spectrometer from PerkinElmer. UV/Vis and Fluorescence spectra were measured in quartz glass cuvettes with 1 cm path length. IR Spectra were recorded on a FT/IR 4100 spectrometer from JASCO. Elemental analysis was performed on an VARIO EL from Elementar. Photoluminescence quantum yields (Φ_{fl}) were determined absolutely with an integrating sphere setup from Hamamatsu (Quantaurus-QY C11347-11). All Φ_{fl} measurements were performed at 25 °C using special 10 mm x 10 mm long neck quartz cuvettes from Hamamatsu. Values below 1% quantum yield are not reliable in the measurement setup and are therefore given as $< 1\%$.
The fluorescence lifetime (τ), the average time in which the fluorophore is in an excited state before it relaxes to the ground state, was recorded on a fluorometer FLS 920 (Edinburgh Instruments) equipped with a Hamamatsu R3809U-50 (range 200–850 nm, response width <25 ps), Multi-Channel Plate (MCP) detector, Czerny-Turner double monochromators and either a supercontinuum laser (Fianium SC400-2-PP) or a Edinburgh Instrument EPLED-330 (picosecond pulsed light emitting diode) for excitation at 375 nm, or a Edinburgh Instrument EPL-375 (picosecond pulsed diode laser) for excitation at 330 nm. All the measurements were performed at T = 298 K using 10 mm–10 mm quartz cuvettes from Hellma GmbH always filled with 2 mL of solvent or dye solution. Before each measurement, the instrument response function (IRF) was measured. The lifetime measurements were analysed with Edinburgh Instruments FAST Software and fitted with a reconvolution fit. All the lifetimes could be evaluated mono, bi- or tri-exponentially with a reduced χ^2 between 0.8 and 3.0.
The fluorescence spectra of the crystals in the solid-state and microscopic images were recorded with an Olympus FluoView FV1000 (Olympus GmbH, Hamburg, Germany). For UV excitation, a DPSS Cobolt Zouk® (355 nm; 10 mW), and for transmission imaging an additional multiline argon ion laser (30 mW, 488 nm) were used as excitation sources, which were reflected by a beamsplitter (BS 20/80) and focused onto the sample through an Olympus objective UPLSAPO 10X (numerical aperture N.A. 0.40). The emitted photons were recollected with the same objective and focused onto a PMT. Emission signals were detected in a wavelength range between 460 nm and 700 nm with spectral resolution of 5 nm and a step width of 2 nm. The spatial resolved fluorescence spectra are raw spectra, not specifically corrected for the wavelength-dependent spectral responsivity of the detection system of the microscope.

2 Synthetic procedures and spectral characterization

The synthesis of **1**, **2** and **4** was done according to literature.[1] For compound **3** the diamine **5** was synthesized as shown in **Fig. S1** and described in detail below via the imine intermediate which was not isolated. The numbers of the compounds were chosen for an easier understanding in the paper. The NMR spectra of **1**–**4** are given at the end of this document.

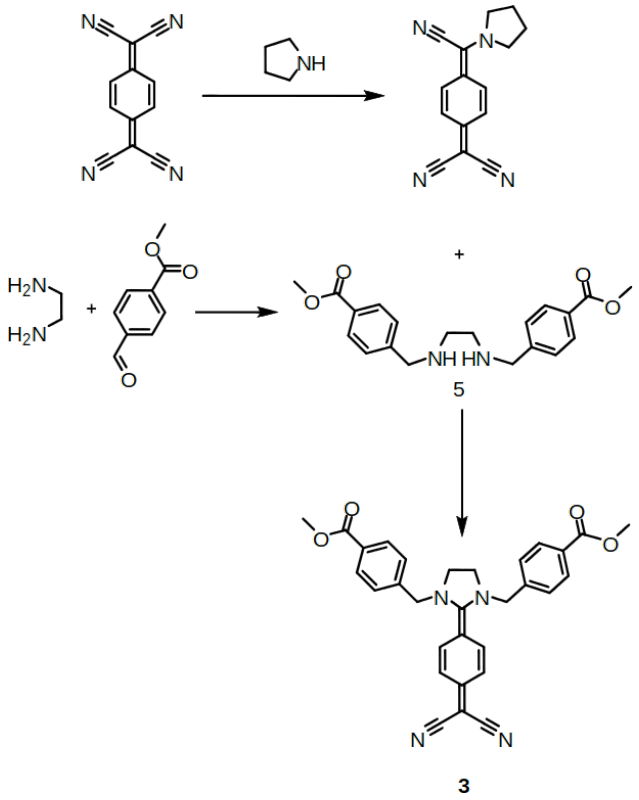

Figure S1: Synthetic route towards diaminodicyanoquinone derivative **3**.

2.1 2-(4-(1,3-dineopentylimidazolidin-2-ylidene)cyclohexa-2,5-dien-1-ylidene) malononitrile (1)

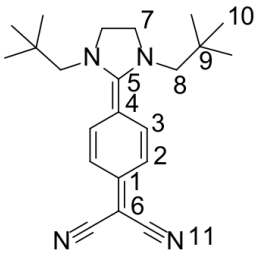

Compound **5** (95 mg, 0.47 mmol, 1 eq.), dissolved in acetonitrile (5 mL), was added to a 40 °C warm solution of Compound **6** (117.7 mg, 0.47 mmol, 1 eq.) in acetonitrile (7 mL). After 4 hours at 75 °C the solution was deep yellow and allowed to cool to room temperature over night. The precipitate, an yellow powder, was filtered off, washed with cooled acetonitrile (3x 3 mL) and recrystallized in acetonitrile to form neat orange crystals (113.9 mg, 0.32 mmol, 65.4%).

^{1}H NMR (500 MHz, DMSO-d_6, RT): δ (ppm) = 7.11 (d, 2H, ^{3}J = 10.0 Hz, 2), 6.86 (d, 2H, ^{3}J = 10.0 Hz, 3), 4.03 (s, 4H, 7), 3.11 (s, 4H, 8), 0.78 (s, 18H, 10)
^{13}C NMR (125 MHz, DMSO-d_6, RT): δ (ppm) = 168.87 (1C, 6), 146.96 (1C, 5), 129.73 (1C, 1), 124.57 (2C, 2), 118.08 (2C, 3), 109.05 (2C, 11), 87.58 1C, 4), 58.77 (2C, 8), 50.86 (2C, 7), 33.10 (2C, 9), 28.33 (6C, 10)
FT-IR (ATR) $\tilde{\nu}$ (cm^{-1}): 2975 (s), 2891 (m), 1648 (m), 1455 (w), 1418 (m), 1378 (m), 1318 (vw), 1085 (vs), 1045 (s), 879 (s)
UV/Vis (Ethanol) λ_{max} nm (ε [Lmol^{-1} cm^{-1}]): 363 (16218)
UV/Vis (Methanol) λ_{max} nm (ε [Lmol^{-1} cm^{-1}]): 354 (16800)
UV/Vis (THF) λ_{max} nm (ε [Lmol^{-1} cm^{-1}]): 334 (6250), 410 (22750)

UV/Vis (ACN) λ_{max} nm (ε [Lmol^{-1} cm^{-1}]): 362 (11500)
UV/Vis (DMSO) λ_{max} nm (ε [Lmol^{-1} cm^{-1}]):
UV/Vis (DMF) λ_{max} nm (ε [Lmol^{-1} cm^{-1}]): 366 (12000)
MS (EI): m/z = 389.21 (10) [M-K$^+$]; 373.24 (25) [M-Na$^+$]; 351.25 (100) [M$^+$] 281.18 (8), 211.10 (5)
EA: $C_{22}H_{30}N_4$; calc.: C, 75.39; N, 15.98; H, 8.63 meas.: C, 75.39; N, 16.04; H, 8.77

2.2 2-(4-(1,3-Dimethylimidazolidin-2-yliden)cyclohexa-2,5-dien-1-yliden)malononitrile (2)

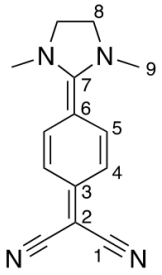

N,N'-Dimethylethylendiamin (71 mg, 0.087 mL, 0.81 mmol, 1 eq.) was added to a 40 °C warm solution of compound 6 (2-(4-(cyano(pyrrolidin-1-yl)methylene)cyclohexa-2,5-dien-1-ylidene)malononitrile) (200 mg, 0.81 mmol, 1 eq.) in 25 mL acetonitrile. The solution was stirred at 70 °C for 4 hours and then cooled to room temperature. The precipitate was filtered off and washed with cooled acetonitrile (3x 10 mL) to yield the product as a yellow powder (75.7 mg, 0.32 mmol, 39%).

^{1}H NMR (700 MHz, DMSO-d$_6$, RT): δ (ppm) = 7.19 (d, ^{3}J = 8.7 Hz, 2H, 4), 6.89 (d, ^{3}J = 8.7 Hz, 2H, 5), 3.90 (s, 4H, 8), 2.96 (s, 6H, 9).
^{13}C NMR (125 MHz, DMSO-d$_6$, RT): δ (ppm) = 166.35 (1C, 2), 148.35 (1C, 7), 130.01 (1C, 3), 124.03 (2C, 4), 118.03 (2C, 5), 107.79 (1C, 1), 50.21 (1C, 6), 35.45 (2C, 8), 32.95 (2C, 9).
FT-IR (ATR) $\tilde{\nu}$ (cm^{-1}): 2932 (w), 2171 (s), 2132 (s), 1595 (s), 1499 (m), 1370 (m), 1324 (m), 1297 (m), 936 (m), 827 (s)
UV/Vis (ACN) λ_{max} nm (ε [Lmol^{-1} cm^{-1}]): 377 (22800).
UV/Vis (DMF) λ_{max} nm (ε [Lmol^{-1} cm^{-1}]): 385 (25000).
UV/Vis (DMSO) λ_{max} nm (ε [Lmol^{-1} cm^{-1}]): 381 (23500).
UV/Vis (MeOH) λ_{max} nm (ε [Lmol^{-1} cm^{-1}]): 368 (23900).
UV/Vis (THF) λ_{max} nm (ε [Lmol^{-1} cm^{-1}]): 416 (4300).
MS (EI): m/z = 239.12 (100) [MH]$^+$; 238.12 (27) [M]$^{\cdot+}$, 180.98 (58), 166.02 (25), 68.99 (30).
EA: $C_{13}H_{12}N_4$; calc.: C, 70.57; N, 23.51; H, 5.92; meas.: C, 68.22; N, 25.76; H, 5.03.

2.3 Dimethyl 4,4'-((2-(4-(dicyanomethylene)cyclohexa-2,5-dien-1-ylidene)imidazolidine-1,3-diyl)bis(methylene))dibenzoate (3)

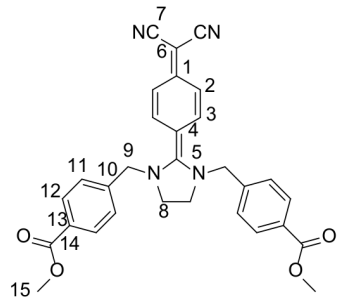

Under argon atmosphere, Dimethyl 4,4'-((ethane-1,2-diylbis(azanediyl))bis-(methylene))dibenzoate (300.00 mg, 1.21 mmol), dissolved in acetonitrile (15 mL), was added to a 40 °C warm solution of Compound 6 (430.65 mg; 1.21 mmol) in acetonitrile (20 mL). The solution turned yellow after 20 hours at 70 °C. After cooling to room temperature, the solution stood for 1 day in the fridge. Filtration then yielded fine yellow crystal needles which were washed with cooled acetonitrile (3x 5 mL) to yield compound **4** (403.86 mg; 0.79 mmol; 66.0%).

^{1}H NMR (500 MHz, DMSO-d$_6$, RT): δ (ppm) = 8.00 (d, ^{3}J = 8.5 Hz, 4H, 12), 7.50 (d, ^{3}J = 8.5 Hz, 4H, 11), 7.19 (d, ^{3}J = 9.0 Hz, 2H, 3), 6.84 (d, ^{3}J = 9.0 Hz, 2H, 2), 4.64 (t, ^{3}J = 20.0 Hz, 4H, 8), 3.88 (s, 4H, 9), 3.87 (s, 6H, 15)
^{13}C NMR (176 MHz, DMSO-d$_6$, RT): δ (ppm) = 169.19 (1C, 5), 166.48 (2C, 14), 148.78 (1C, 4), 141.37 (2C, 13), 140.55 (1C, 6); 130.30 (4C, 12), 129.89 (2C, 10), 129.36 (2C, 3), 128.40 (4C, 11), 118.51 (2C, 2), 107.75 (2C, 7), 51.83 (2C, 8), 52.85 (2C, 15), 48.58 (2C, 9)
FT-IR (ATR) $\tilde{\nu}$ (cm^{-1}): 3025 (vw), 2945 (w), 2841 (vw), 2361 (w), 2171 (s), 2129 (s), 1719 (s), 1596 (m), 1555 (s), 1491 (m), 1432 (m), 1375 (w), 1320 (m), 1267 (s), 1188 (m), 1107 (m), 1014 (m), 920 (m), 844 (m), 820 (m), 747 (m)
UV/Vis (Ethanol) λ_{max} nm (ε [Lmol^{-1} cm^{-1}]): 234 (4.35), 393 (4.24)

MS (EI): m/z = 1542.57 $[HNa\text{-}M_3]^+$ (8), 1035.38 [HNa-M2]+(50), 529.18 $[HNa\text{-}M_2]^+$ (100), 507.20 $[H\text{-}M]^+$ (20)
EA: $C_{30}H_{26}N_4O_4$; calc.: C, 71.13; N, 11.06; H, 5.17 meas.: C, 70.83; N, 11.28; H, 5.27

2.4 2-(4-(1,3-dihydro-2H-benzo[d]imidazol-2-ylidene)cyclohexa-2,5-dien-1-ylidene) malononitrile (4)

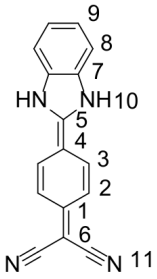

Under argon atmosphere, ortho-Phenylendiamine (70.0 mg, 0.64 mmol, 1 eq.), dissolved in acetonitrile (15 mL), was added to a 40 °C warm solution of Compound 6 (160.0 mg, 0.64 mmol, 1 eq.) in acetonitrile (20 mL). The solution turned red after 20 hours at 70 °C. After cooling to room temperature, the solution stood for 4 days in the fridge. Filtration then yielded a fine grain greenish powder which was washed with cooled acetonitrile (3x 5 mL). The product was recrystallized from acetonitrile to yield fine yellow crystals (70.2 mg, 0.27 mmol, 42.5%).

^{1}H NMR (700 MHz, DMSO-d_6, RT): δ (ppm) = 14.35 (bs, 2H, 10), 7.86 (d, ^{3}J = 8.7 Hz, 2H, 2), 7.69 (q, ^{3}J = 8.7 Hz, 2H, 9), 7.47 (q, ^{3}J = 8.6 Hz, 2H, 8), 6.95 (d, ^{3}J = 8.7 Hz, 2H, 3)
^{13}C NMR (176 MHz, DMSO-d_6, RT): δ (ppm) = 150.27 (1C, 6), 149.31 (1C, 5), 132.26 (1C, 1), 128.54, 126.54 (1C, 2), 125.48 (2C, 8), 123.51 (2C, 7), 118.49 (2C, 3), 113.47 (2C, 9), 79.63 (1C, 4)
FT-IR (ATR) $\tilde{\nu}$ (cm^{-1}): 2952 (w), 2877 (w), 2849 (w), 2761 (w), 2190 (s), 2140 (s), 1637 (w), 1612 (m), 1503 (m), 1459 (m), 1387 (m), 1336 (m), 1230 (m), 1201 (m), 819 (s), 742 (s)
UV/Vis (DMF) λ_{max} nm (ε [$Lmol^{-1}$ cm^{-1}]): 391 (56500)
UV/Vis (ACN) λ_{max} nm (ε [$Lmol^{-1}$ cm^{-1}]): 385 (86800)
UV/Vis (DMSO) λ_{max} nm (ε [$Lmol^{-1}$ cm^{-1}]): 392 (42200)
UV/Vis (THF) λ_{max} nm (ε [$Lmol^{-1}$ cm^{-1}]): 388 (7000)
UV/Vis (MeOH) λ_{max} nm (ε [$Lmol^{-1}$ cm^{-1}]): 424 (20000)
MS (EI): m/z = 259.10 (15), 258.09 $[MH]^{\cdot+}$ (100), 257.10 (5), 232 (5).
EA: $C_{16}H_{16}N_4$; calc.: C, 74.40; N, 21.69; H, 3.90; meas.: C, 74.31; N, 21.78; H, 4.07

2.5 Dimethyl 4,4'-((ethane-1,2-diylbis(azanediyl))bis(methylene))dibenzoate (5)

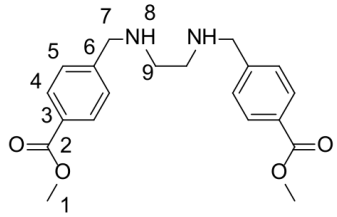

Ethane-1,2-diamine (1 g, 16.64 mmol) was added dropwise with stirring to a solution of methyl 4-formylbenzoate (6.28 g, 38.27 mmol) in 30 mL of dry methanol. The mixture was stirred for 4 days. After addition of 100 ml dry methanol, $NaBH_4$ (3.15 g; 83.19 mmol) was added and the mixture was stirred ON. Cooling in ice water precipitated a white solid which was filtered off and washed with cooled H2O (2x 50 mL), ethanol (2x 25 mL), and dried under vacuum.

^{1}H NMR (500 MHz, DMSO-d_6, RT): δ (ppm) = 7.90 (d, ^{3}J = 6.0 Hz, 4H, 4), 7.46 (d, ^{3}J = 6.0 Hz, 4H, 5), 3.80 (s, 6H, 1), 3.70 (s, 4H, 7), 2.58 (s, 4H, 9), 2.25 (bs, 2H, 8)
^{13}C NMR (176 MHz, DMSO-d_6, RT): δ (ppm) = 166.79 (2C, 2), 147.62 (4C, 3), 129.59 (4C, 4), 128.58 (2C, 5), 128.40 (2C, 3), 53.11 (2C, 9), 52.56 (2C, 1), 48.98 (2C, 7)
MS (EI): m/z = 379.16 $[Na\text{-}M]^+$ (25), 357.18 $[MH]^{\cdot+}$ (100), 326.37 (15), 192.10 (15), 149.06 (10)

2.6 2-(4-(cyano(pyrrolidin-1-yl)methylene)cyclohexa-2,5-dien-1-ylidene)malononitrile (6)

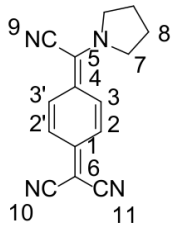

To a stirred warm solution of TCNQ (250.0 mg, 1.22 mmol, 1 eq.) in acetonitrile (20 mL), pyrrolidine (69.7 mg, 0.98 mmol, 0.8 eq.) was added in one shot. The solution turned green and then purple. After stirring for 4 hours at 70 °C the solution was cooled to room temperature and then stored in the fridge for 3 days. The precipitate was filtered and washed with cooled acetonitrile (3x 5 mL) to yield the product as fine purple crystal needles (232.4 mg, 0.93 mmol, 76.5%).

^{1}H NMR (400 MHz, DMSO-d_6, RT): δ (ppm) = 7.73 (dt, ^{4}J = 0.7Hz, ^{3}J = 7Hz, 2H, 3), 7.81 (dt, ^{4}J = 0.7Hz, ^{3}J = 7Hz, 2H, 2), 4.11 (bs, 4H, 7), 2.08 (m, 4H, 8)
^{13}C NMR (100 MHz, DMSO-d_6, RT): δ (ppm) = 153.95 (1C, 6), 137.76 (1C, 4), 134.32 (2C, 2), 120.11 (2C, 3), 118.92 (1C, 10), 116.78 (1C, 11), 113.09 (1C, 9), 57.40(1C, 6), 50.92 (2C, 7), 25.60 (2C, 8)
FT-IR (ATR) $\tilde{\nu}$ (cm^{-1}): 2190 (m), 2164 (s), 1611 (s), 1536 (m), 1474 (w), 1381 (s), 1341 (m), 1207, (s), 861 (s), 823 (s), 727 (m), 650 (s)
UV/Vis (ACN) λ_{max} nm (ε [Lmol^{-1} cm^{-1}]): 275 (6300), 480 (13000)
MS (EI): m/z = 249.1 (20); 248.0 (100)$[MH]^{\cdot+}$; 221.1 (15); 179.1 (17); 154.1 (20)
EA: $C_{15}H_{12}N_4$; calc.: C, 72.56; H, 4.87; N, 22.57, meas.: C, 72.74; N, 21.57; H, 4.89

3 Crystal structures

3.1 Data

Table S1: Crystal data and structure refinement for **1**

Identification code	NN_Neopentyl_Ethan
Empirical formula	$C_{22}H_{30}N_4$
Formula weight	350.5
Temperature/K	100(2)
Crystal system	monolinic
Space group	P21/c
a/Å	9.3411(2)
b/Å	19.6042(3)
c/Å	11.8719(2)
α	90
β	109.8547(7)
γ	90
Volume/Å^3	2044.81(6)
Z	4
ρ_{calc}g/cm^3	1.139
μ/mm^{-1}	0.068
F(000)	760
Crystal size/mm^3	0.560 x 0.480 x 0.180
Radiation	MoKα ($\lambda = 0.71073$)
2θ range for data collection/°	4.636 to 51.464
Index ranges	$-11 \leq h \leq 11$, $-23 \leq k \leq 23$, $-14 \leq l \leq 14$
Reflections collected	19722
Independent reflections	3889 [$R_{int} = 0.0310$, $R_{sigma} = 0.0228$]
Data/restraints/parameters	3889/0/242
Goodness-of-fit on F^2	1.037
Final R indexes [$I \geq 2\sigma$ (I)]	$R_1 = 0.0384$, $wR_2 = 0.0918$
Final R indexes [all data]	$R_1 = 0.0444$, $wR_2 = 0.0954$
Largest diff. peak/hole / e Å^{-3}	0.30/-0.21

Table S2: Crystal data and structure refinement for **2**

Identification code	NN_Methyl_Ethan
Empirical formula	$C_{28}H_{28}N_8$
Formula weight	476.58
Temperature/K	100(2)
Crystal system	monoclinic
Space group	P21/c
a/Å	9.1324(7)
b/Å	11.5952(8)
c/Å	11.7818(7)
α	90
β	98.419(2)
γ	90
Volume/Å^3	1234.15(15)
Z	2
ρ_{calc}g/cm^3	1.282
μ/mm^{-1}	0.08
F(000)	504
Crystal size/mm^3	0.13 x 0.12 x 0.12
Radiation	MoKα ($\lambda = 0.71073$)
2θ range for data collection/°	4.508 to 50.808
Index ranges	-11 $\leq$ h $\leq$ 11, -13 $\leq$ k $\leq$ 13, -13 $\leq$ l $\leq$ 14
Reflections collected	15361
Independent reflections	2259 [$R_{int} = 0.0723$, $R_{sigma} = 0.0411$]
Data/restraints/parameters	2259/0/165
Goodness-of-fit on F^2	1.055
Final R indexes [I$\geq 2\sigma$ (I)]	$R_1 = 0.0413$, $wR_2 = 0.0874$
Final R indexes [all data]	$R_1 = 0.0660$, $wR_2 = 0.0988$
Largest diff. peak/hole / e Å^{-3}	0.15/-0.31

Table S3: Crystal data and structure refinement for **3**

Identification code	PR111-sr-final
Empirical formula	C30H26N4O4
Formula weight	506.55
Temperature/K	100(2)
Crystal system	triclinic
Space group	P-1
a/Å	9.45250(10)
b/Å	11.1197(2)
c/Å	14.54330(10)
α	97.639(4)
β	108.409(4)
γ	106.008(3)
Volume/Å^3	1352.99(5)
Z	2
ρ_{calc}g/cm^3	1.243
μ/mm^{-1}	0.683
F(000)	532
Crystal	size/mm3
Radiation	CuKα ($\lambda = 1.54178$)
2θ range for data collection/°	6.6 to 133.5
Index ranges	-9 $\leq$ h $\leq$ 11, -13 $\leq$ k $\leq$ 13, -17 $\leq$ l $\leq$ 17
Reflections collected	17026
Independent reflections	4780 [$R_{int} = 0.0662$, $R_{sigma} = 0.0558$]
Data/restraints/parameter s	4780/0/345
Goodness-of-fit on F^2	
Final R indexes [I$\geq 2\sigma$ (I)]	$R_1 = 0.0495$, $wR_2 = 0.1144$
Final R indexes [all data]	$R_1 = 0.0678$, $wR_2 = 0.1237$
Largest diff. peak/hole / e Å^{-3}	0.17/-0.26

Table S4: R-factors of crystal structures

	1	**2**	**3**
R-factor	3.84	4.13	4.95

3.2 Unit cells

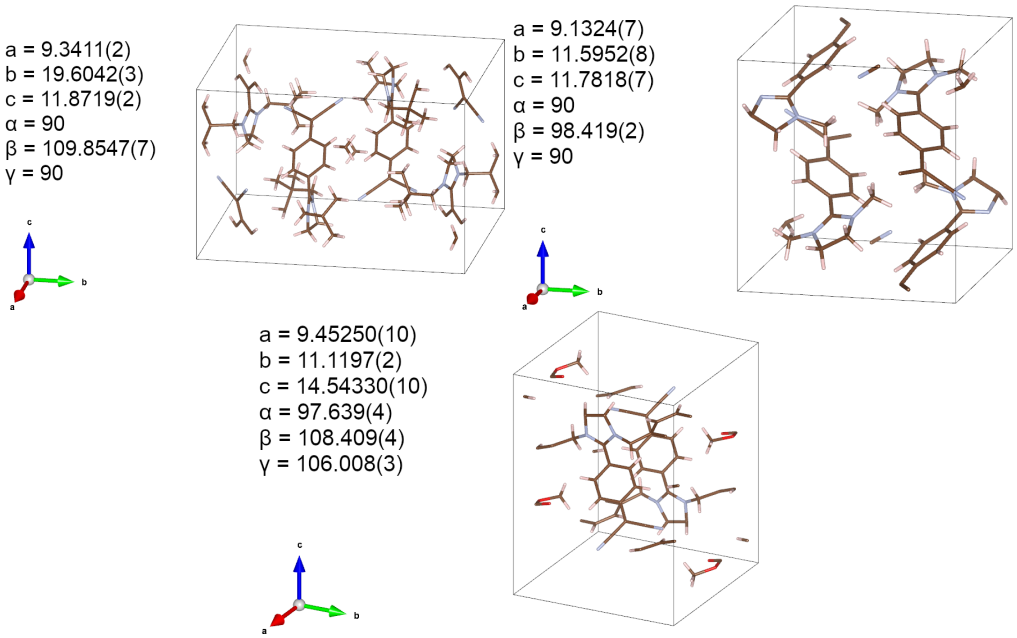

Figure S2: Unit cell with parameters of compound **1** (top left), **2** (top right), and **3** (bottom).

4 Emission properties

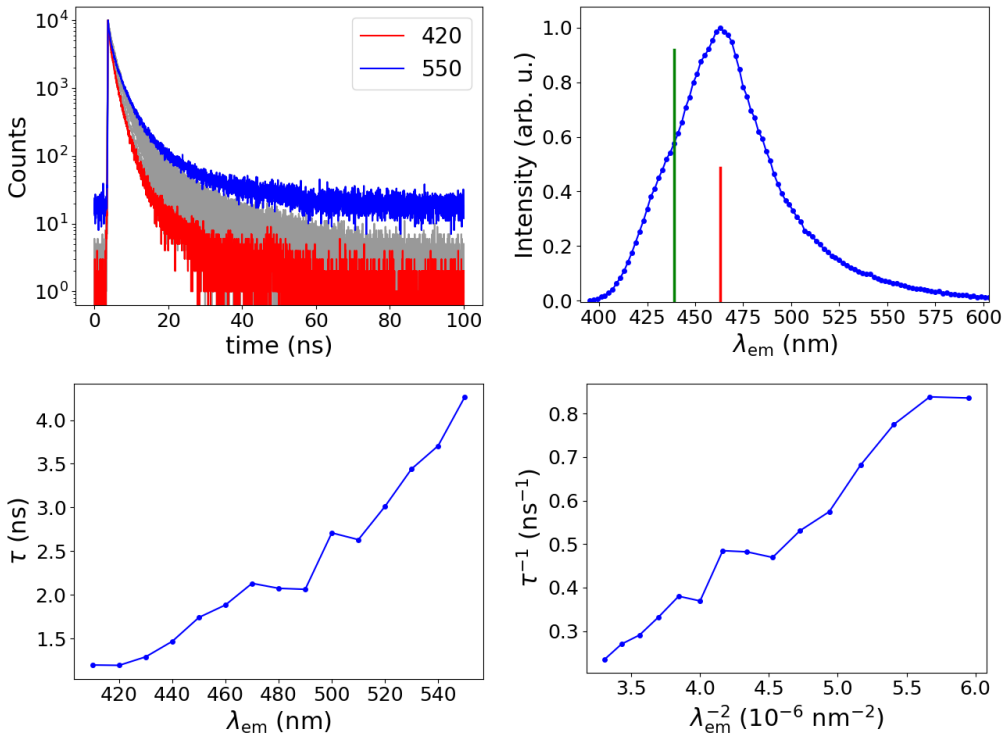

Figure S3: Emission properties of compound **2**: lifetime measurements (top left), solid-state emission spectrum with computed vertical transition lines obtained at the BHLYP/def2-SVP/MRCI level (top right), lifetime-emission wavelength dependence (bottom left), reciprocal lifetime to reciprocal squared emission wavelength dependence (bottom right).

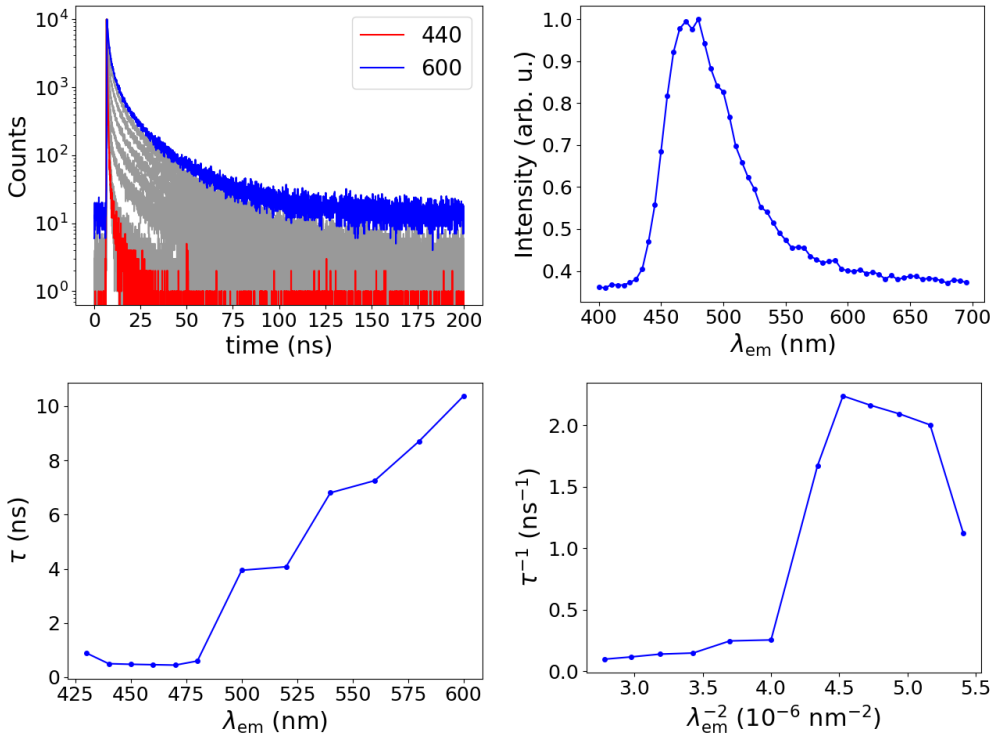

Figure S4: Emission properties of compound **3**: lifetime measurements (top left), solid-state emission spectrum (top right), lifetime-emission wavelength dependence (bottom left), reciprocal lifetime to reciprocal squared emission wavelength dependence (bottom right).

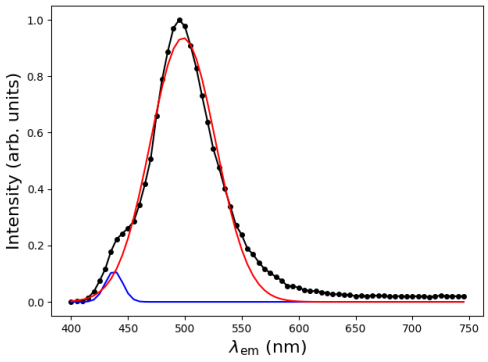

Figure S5: Gaussian fit of the emission specturm of compound **1** to estimate the emission energy of the high-energy (low-wavelength) shoulder (ca. 438 nm), ratio of the integrals: ca. 32:1 (red:blue).

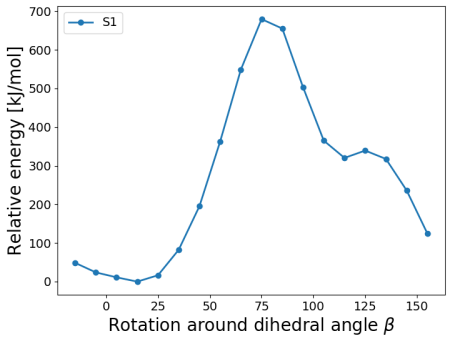

Figure S6: Lowest singlet excited state potential energy surface for the rotation of the dicyano group (dihedral angle β) of a monomer in the crystal structure of **2** estimated from an ONIOM(PBE/def2-SVP/UFF) calculation.

5 Computational Details

5.1 Förster and Dexter energy transfer rates

From the optimised solid-state structure (for optimisation procedure see below) of each compound, one molecule in the centre of a large supercell surrounded by a sphere of molecules with a radius of 10 Å was chosen to evaluate both Förster and Dexter transfer rates for each dimer that included the central structure. The total transfer rates are simply the sum of all individual contributions. As proposed Radhakrishnan and co-workers,[radhakrishnan] for Dexter rates, only neighbouring molecules of the central structure were considered for which $r\sin(\theta) < 10$ Å and $r' > 2.5$ Å (10 Å is approximately the length of one DADQ moiety, for designations, see main text). The centre of the π-plane was chosen to coincide with the centre of the benzene ring. For compound **4**, both benzene rings were regarded since the excitation is delocalised over the entire system.[1] For compound **3**, the benzene rings of the benzoate moieties were not regarded since the excited state is localised on the DADQ moiety (**Fig. S7**). **Table S5** summarises absolute values obained for k_{F} and k_{D} in comparison to solid-state QYs. **Fig. S8** illustrates the dimers that yielded the largest contribution to the transfer rates.

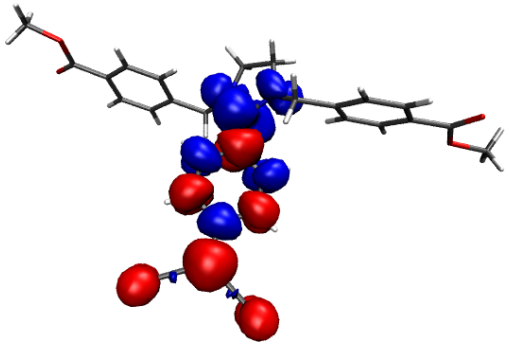

Figure S7: S_1 difference density of compound **3** obtained at the ωB97X-D3/def2-SVP[2,3] level of DFT, isovalue = 0.001 a_0^{-3}.

Table S5: Solid-state QYs and Förster and Dexter energy transfer rates of all compounds.

	solid-state QY	$k_{\mathrm{F}}/10^{-4}$	$k_{\mathrm{D}}/10^{-3}$
1	18	0.828	2.48
2	10	3.75	36.6
3	6	0.637	63.0
4	<1	9.06	210

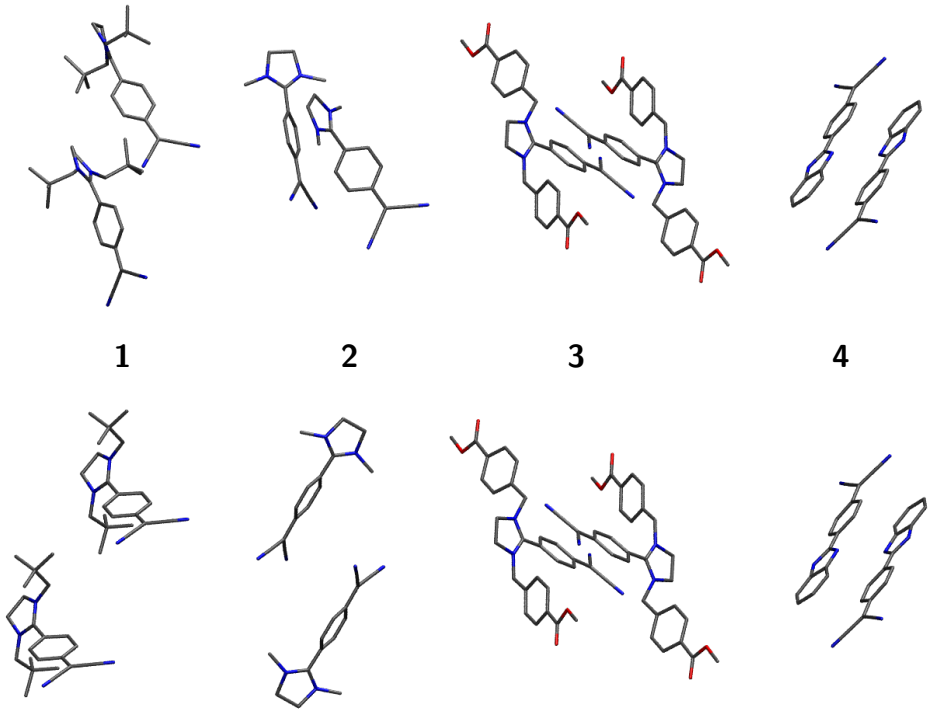

Figure S8: Structural motifs contributing most to k_{F} (top) and k_{D} (bottom) for each compound.

5.2 Calculation of excited states

5.2.1 Periodic calculations

For compounds **1**–**3**, the crystal structures were used as a starting point for subsequent calculations. For compound **4**, we used the crystal structure of a cyclohexyl-bridged derivative of our DADQs, obtained from an earlier publication[1] as a starting structure and manipulated the cyclohexyl unit by hand (Fig. S9). Periodic density

Figure S9: Unit cell and parameters of compound **4** after hand-manipulation of a the solid-state structure of a cyclohexyl-bridged DADQ derivative and subsequent solid-state optimisation (for details see down below).

functional theory (DFT) calculations at the PBE-D3(BJ)[4–6] level using VASP[7–9] were employed to optimise the solid state structures of compounds **1**, **2** and **4**. Plane-wave basis sets with an energy cutoff of 421 eV was used in combination with projector-augmented wave potentials.[10] The convergence threshold for the SCF cycles were set to 10^{-4} eV employing the blocked Davidson algorithm. Internal and external lattice parameters were relaxed using the conjugate-gradient algorithm with a force convergence parameter of 10^{-3} eV/Å^2 on a 6x6x6 k-grid constructed using the Monkhorst-Pack scheme.[11] For the bandstructure calculations, the k-grid was refined to 8x8x8 k-points and the energy cutoff was increased to 520 eV. For density-of-states (DOS) plots and partial charge densities (Figure 5 in main text), the k-grid was furthermore increased to 10x10x10. Partial charge densities were produced for the four lowest-lying unoccupied and four highest-lying occupied bands. Dielectric tensors were computed at the same energy cutoff on a 6x6x6 k-grid again. According to literature,[12] the eigenvalues of the dielectric tensor l_i can be used to calculate an effective static (zero frequency) dielectric constant,

$$\varepsilon = \frac{3l_1l_2l_3}{l_1l_2 + l_1l_3 + l_2l_3},$$

and the refractive index n is obtained as the square root of the average of the eigenvalues of the dielectric tensor,

$$n = \sqrt{(l_1 + l_2 + l_3)/3} \quad (1)$$

The obtained values for ε and n are summarised in **Table S6**. Furthermore, DOS plots were generated employing

Table S6: Dielectric tensor and refractive index obtained from periodic PBE calculations

	ε	n
1	3.247	1.823
2	3.582	1.946

the HSE06 functional[13] to compare to the PBE results (Figure 5 in main text). Due to the large unit cell sizes (224 atoms for **1**, 128 atoms for **2**), calculations were performed on a smaller 2x2x2 k-grid, the energy cutoff of 520 eV was however retained.

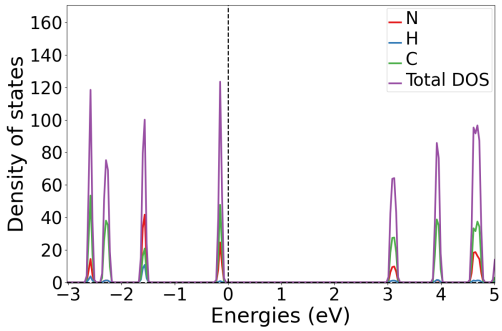

Figure S10: DOS plot of compound **1** obtained at the HSE06 level of DFT.

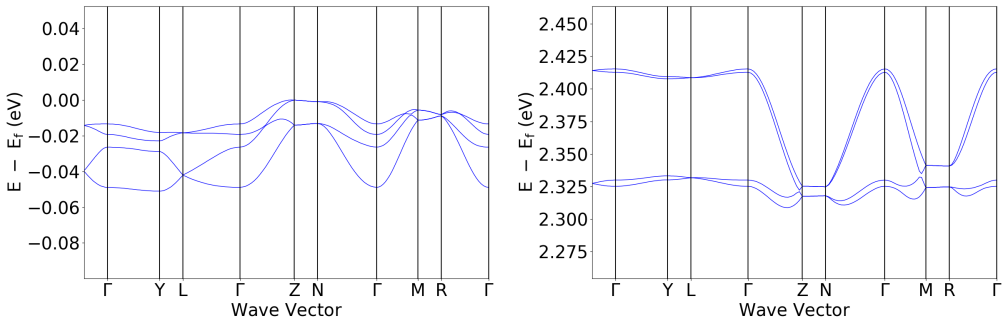

Figure S11: VB and CB of compound **1** obtained at the PBE level.

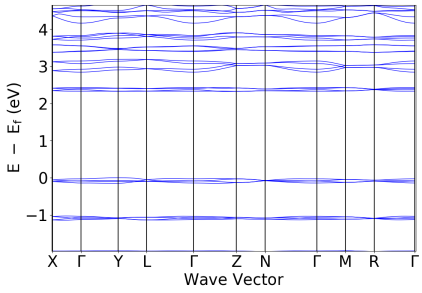

(a) Bandstructure of compound **2** obtained at the PBE level.

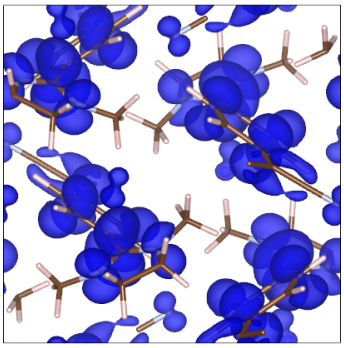

(b) LUMO charge density of compound **2** obtained at the PBE level, isovalue=0.003a_0^{-3}.

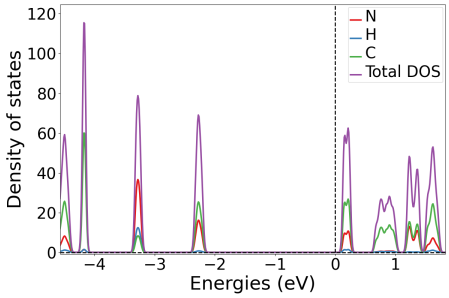

(c) DOS plot of compound **2** obtained at the PBE level.

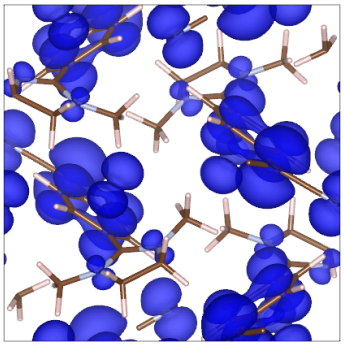

(d) HOMO charge density of compound **2** obtained at the PBE level, isovalue=0.003a_0^{-3}.

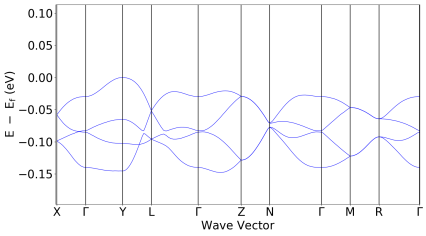

(e) VB of compound **2** obtained at the PBE level.

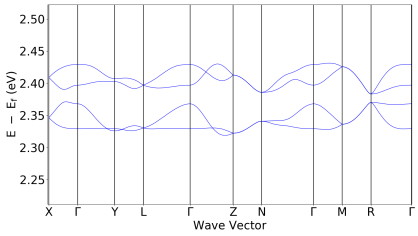

(f) CB of compound **2** obtained at the PBE level.

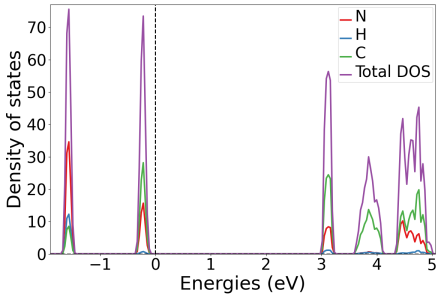

(g) DOS plot of compound **2** obtained at the HSE06 level.

Figure S12: Solid-state results for compound **2**.

5.2.2 TD-DFT calculations for oligomers

Time-dependent DFT (TD-DFT) calculations were performed at the ωB97X-D3/def2-SVP[2,3] level for various dimers, the unit cell tetramers, and an octamer of compounds **1** and **2** to estimate the locality of the electronic transitions in the solid state. For compound **2**, a dodecamer could also be calculated. As an approximation to the solid-state environment, the effective dielectric constant and refractive index obtained in the periodic calculations (**Table S6**) were used for the evaluation of the excited states. All structures are depicted in **Fig. S13** and **Fig. S14**. **Tables S7** to **S12** summarise all computed excited states with their transition energies and oscillator strengths. Figures S15 to S17 depict a selected few difference densities of the transitions with the highest oscillator strengths. Especially in the octamers and the dodecamer it can be observed that all transitions are fairly localised on either a monomer or a dimer with small contributions from anything else.

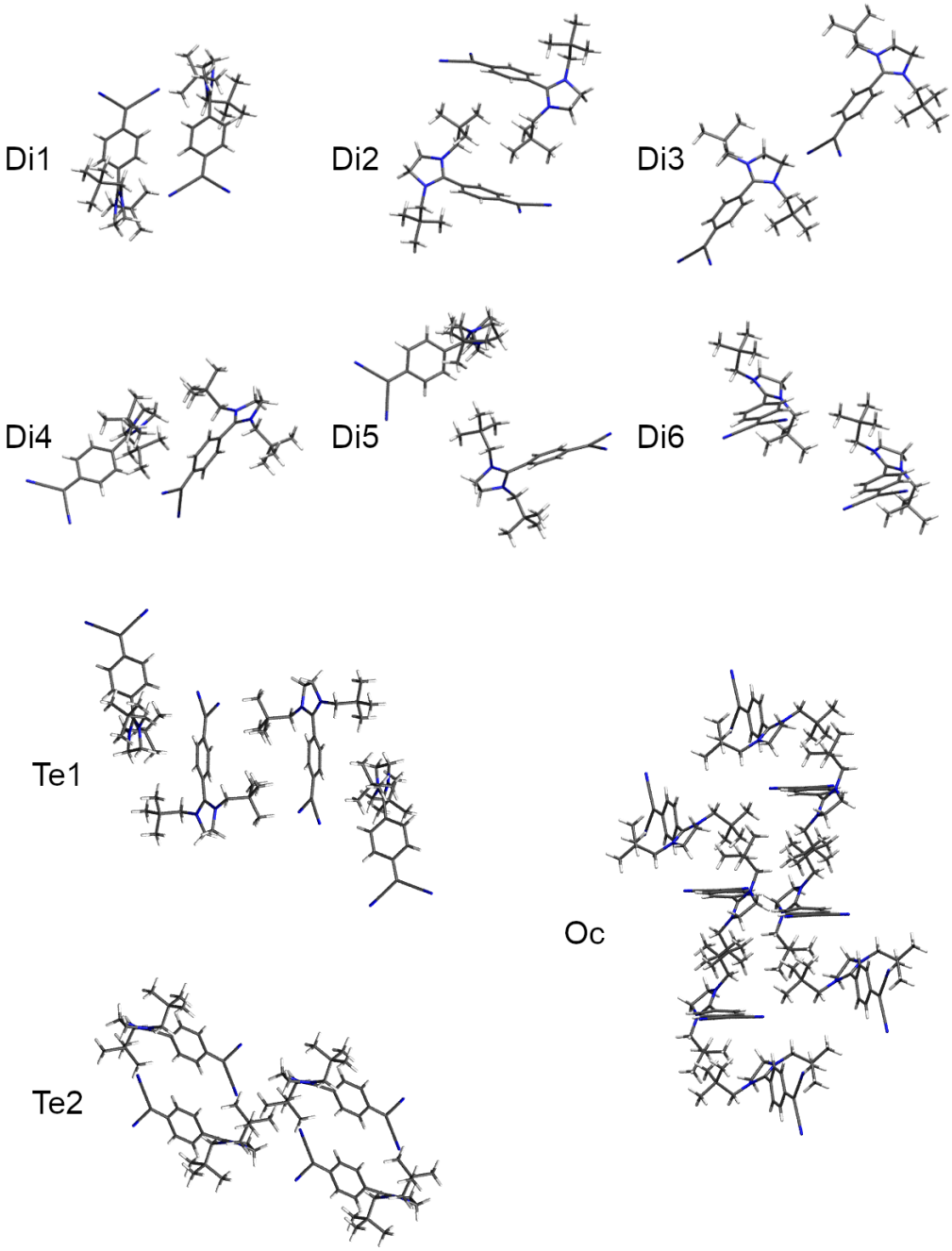

Figure S13: Oligomer structures of compound **1** used for TD-DFT evaluation.

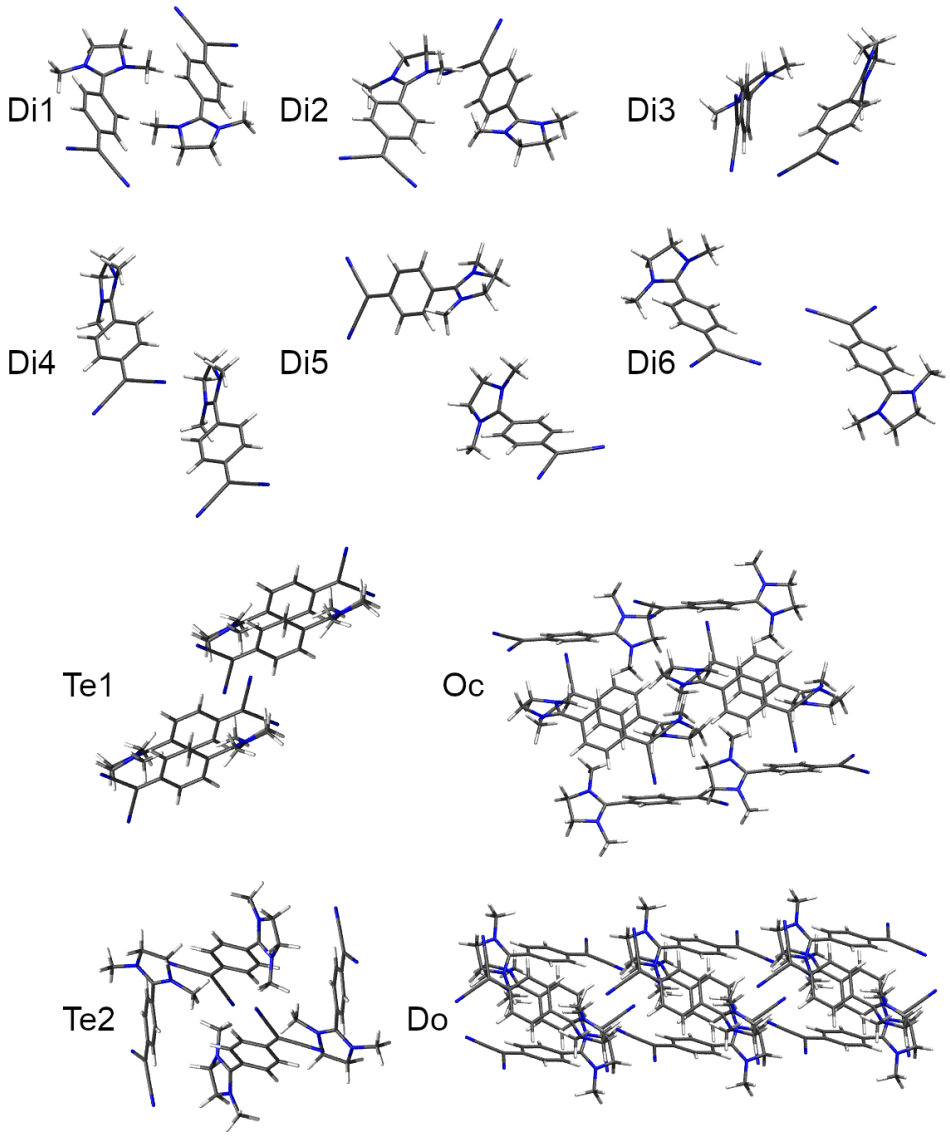

Figure S14: Oligomer structures of compound **2** used for excited-state calculations at the TD-DFT level.

Compound **1**:

Table S7: Excited state wavelengths in nm and oscillator strenghts of various dimers of compound **1** obtained at the ωB97X-D3/def2-SVP level of TD-DFT.

Structure	excited state	λ_{abs}	f_{osc}	Structure	excited state	λ_{abs}	f_{osc}
Di1	S_1	325.9	0.00	Di4	S_1	347.2	0.27
	S_2	312.5	1.16		S_2	346.1	1.02
Di2	S_1	332.7	0.00	Di5	S_1	335.8	0.02
	S_2	325.8	1.20		S_2	334.7	1.28
Di3	S_1	332.5	1.53	Di6	S_1	346.3	0.00
	S_2	325.6	0.02		S_2	341.2	1.24

Table S8: Excited state wavelengths in nm and oscillator strenghts of two tetramers of compound **1** obtained at the ωB97X-D3/def2-SVP level of TD-DFT.

Structure	excited state	λ_{abs}	f_{osc}	Structure	excited state	λ_{abs}	f_{osc}
Te1	S_1	332.9	0.00	Te2	S_1	321.5	0.00
	S_2	337.6	1.07		S_2	318.3	0.00
	S_3	334.3	0.00		S_3	310.7	2.81
	S_4	327.9	1.41		S_4	303.9	0.00

Table S9: Excited state wavelengths in nm and oscillator strenghts of an octamer of compound **1** obtained at the ωB97X-D3/def2-SVP level of TD-DFT.

Structure	excited state	λ_{abs}	f_{osc}
Oc	S_1	344.4	0.01
	S_2	344.3	0.00
	S_3	337.7	0.04
	S_4	338.0	0.00
	S_5	334.5	2.92
	S_6	334.8	0.02
	S_7	326.7	0.00
	S_8	314.0	1.40

Compound **2**:

Table S10: Excited state wavelengths in nm and oscillator strenghts of various dimers of compound **2** obtained at the ωB97X-D3/def2-SVP level of TD-DFT.

Structure	excited state	λ_{abs}	f_{osc}	Structure	excited state	λ_{abs}	f_{osc}
Di1	S_1	338.2	0.00	Di4	S_1	343.0	1.43
	S_2	325.4	1.27		S_2	335.1	0.10
Di2	S_1	340.2	0.14	Di5	S_1	350.5	1.37
	S_2	332.9	1.18		S_2	347.0	0.12
Di3	S_1	358.3	0.13	Di6	S_1	351.3	0.16
	S_2	351.3	1.15		S_2	350.9	1.27

Table S11: Excited state wavelengths in nm and oscillator strenghts of two tetramers of compound **2** obtained at the ωB97X-D3/def2-SVP level of TD-DFT.

Structure	excited state	λ_{abs}	f_{osc}	Structure	excited state	λ_{abs}	f_{osc}
Te1	S_1	339.5	0.00	Te2	S_1	332.2	0.00
	S_2	339.7	0.35		S_2	327.6	0.10
	S_3	339.6	0.00		S_3	320.9	2.66
	S_4	323.3	1.89		S_4	314.9	0.00

Table S12: Excited state wavelengths in nm and oscillator strenghts of an octamer and a dodecamer of compound **2** obtained at the ωB97X-D3/def2-SVP level of TD-DFT.

Structure	excited state	λ_{abs}	f_{osc}	Structure	excited state	λ_{abs}	f_{osc}
Oc	S_1	333.6	0.00	Do	S_1	320.7	0.00
	S_2	334.3	0.24		S_2	321.5	0.27
	S_3	332.7	0.00		S_3	318.0	0.00
	S_4	328.4	0.34		S_4	316.7	0.00
	S_5	328.3	0.18		S_5	317.2	0.53
	S_6	328.9	0.99		S_6	317.7	1.43
	S_7	317.3	3.12		S_7	311.8	0.54
	S_8	311.9	0.00		S_8	309.9	0.00
	—	—	—		S_9	308.0	0.00
	—	—	—		S_{10}	305.4	6.72

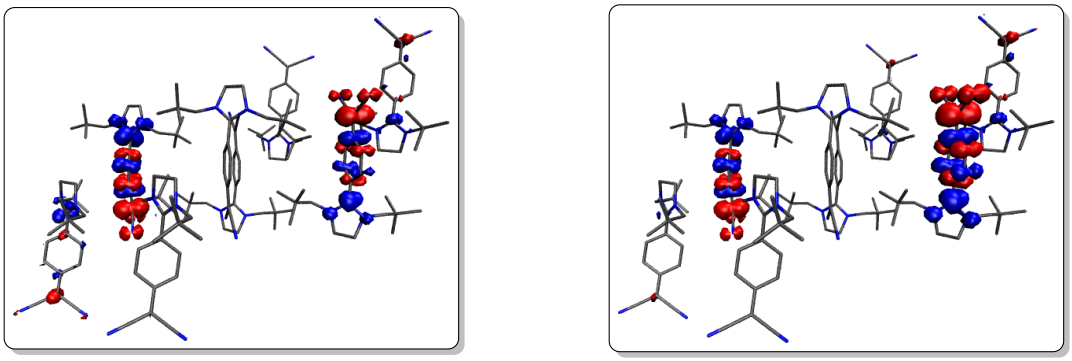

Figure S15: S_5 (left) and S_8 (right) difference densities of an octamer of compound **1**, isovalue = 0.001 a_0^{-3}. Blue and red zones correspond to areas of electron enhancement and electron depletion.

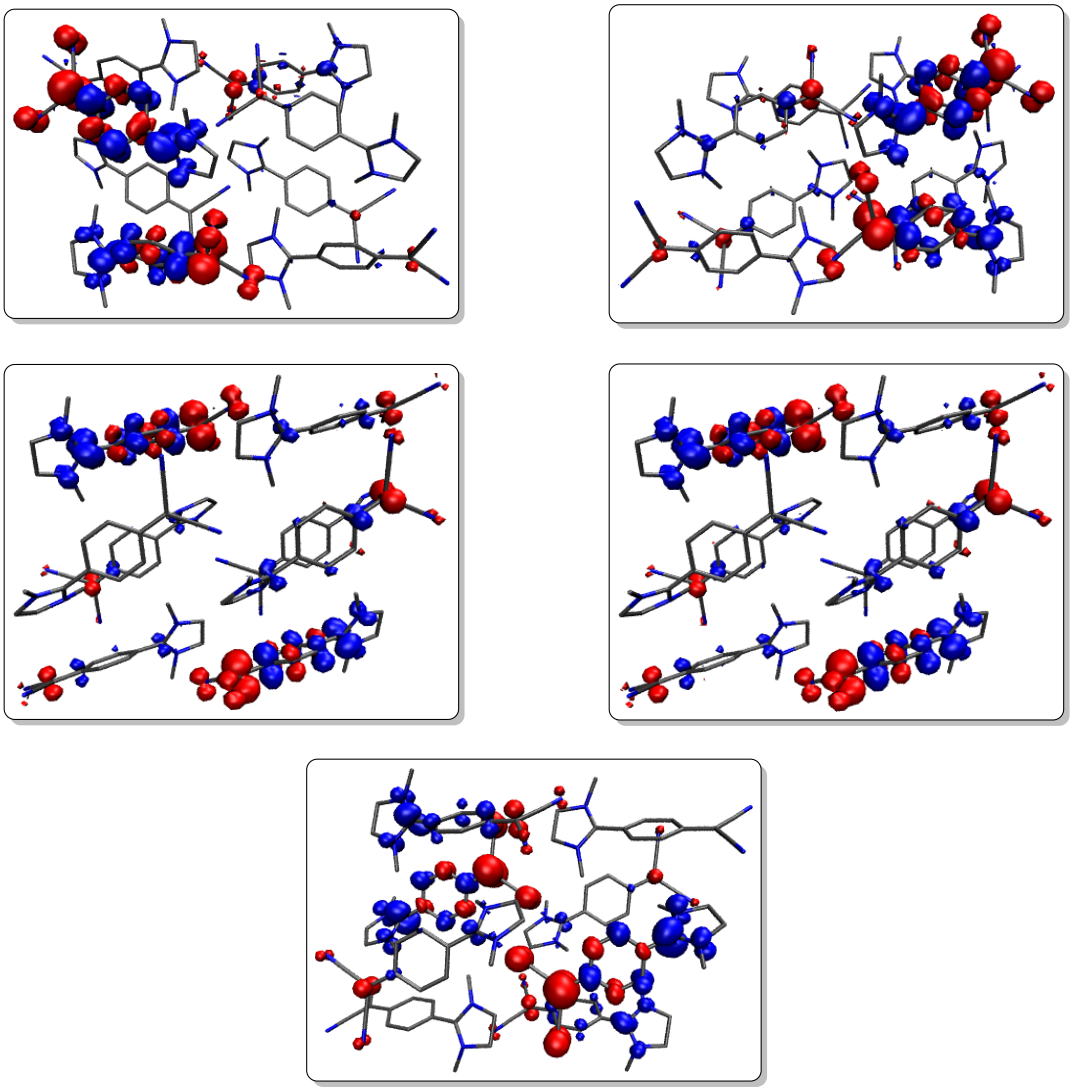

Figure S16: From top left to bottom right: S_2, S_4, S_5, S_6, and S_7 difference densities of an octamer of compound **2**, isovalue = 0.001 a_0^{-3}. Blue and red zones correspond to areas of electron enhancement and electron depletion. Note that the S_7 difference density is just comprised of two nodal structures localised on H-type dimers. However, it appears much more delocalised due to the inversion centre in the middle of the cluster which is somewhat difficult to discern in a static picture.

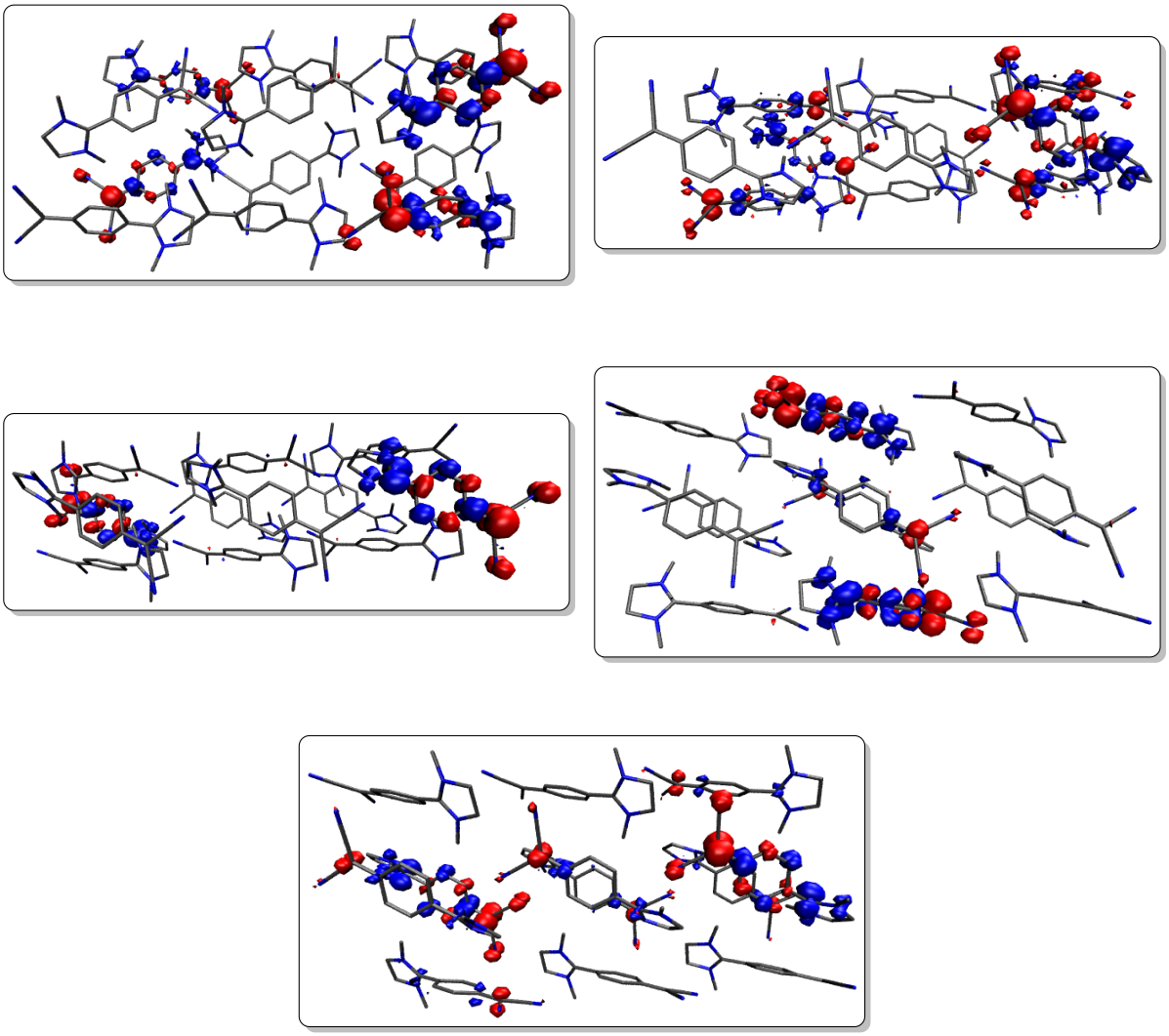

Figure S17: From top left to bottom right: S_2, S_4, S_5, S_6, and S_7 difference densities of an dodecamer of compound **2**, isovalue = 0.001 a_0^{-3}. Blue and red zones correspond to areas of electron enhancement and electron depletion.

5.2.3 QM/MM and DFT/MRCI calculations of monomers and dimers

In the next step, a 6x4x6 supercell of compound **1** and a 6x4x4 supercell of compound **2** (**Fig. S18**) were generated to mimic the crystal environment in a subsequent QM/MM optimisation of monomers and dimers (**Fig. S19**) embedded in their crystal structures. Gaussian's[14] ONIOM[15] scheme was utilised using the ωB97XD functional for the high layer and the universal force field (UFF) for the low layer. All atoms within 5 Å of the high layer atoms were allowed to relax during the run.

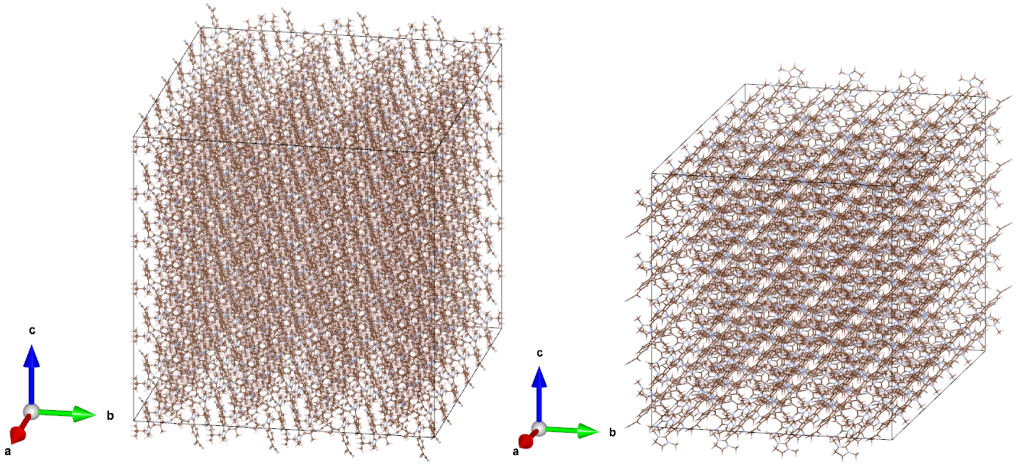

Figure S18: 6x4x6 supercell of compound **1** (left), 6x4x4 supercell of compound **2**.

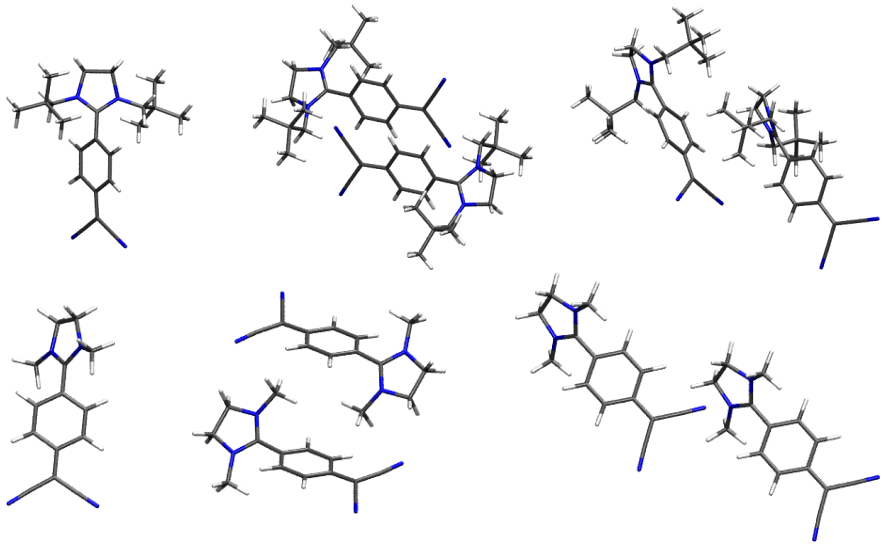

Figure S19: Structures examined in a QM/MM + DFT/MRCI study of compound **1** (top) and **2** (bottom).

First, a ground-state optimisation was performed succeeded by an excited-state optimisation of the state with the highest oscillator strength, which is the S_1 for monomers and J-aggregates, and the S_2 for H-aggregates. Afterwards, the trajectory of the excited-state optimisation is used to assess the PES of the bright state employing the DFT/MRCI[16–18] together with the C-PCM model[19] once again using the dielectric constant obtained from the periodic calculations. The minima of the S_0 and S_1 (or S_2 for H-dimers) then define the Stokes shift of the compounds and the emission peaks can be compared to experiment. **Table S13** summarises all excited states prior to and after optimisations with their transition energies and oscillator strengths. For the DFT/MRCI calculations, a reference space of 16 electrons and 14 orbitals with a default cut-off of 1.0 Hartree, which was carefully checked to not cut between degenerate orbitals, was chosen and all single and double excitations were incorporated. The reference space was refined once, i.e., two DFT/MRCI calculations were performed in succession. Initial testing found that a second refinement of the reference space did not yield any significant change in excitation energies or oscillator strengths.

Table S13: Absorption and emission wavelengths in nm, oscillator strengths, and lifetimes in ns of a monomer (mon), an H-type and a J-type dimer of compounds **1** and **2**

			λ_{abs} (calc.)	f_{osc} (abs)	λ_{em} (calc.)	λ_{em} (exp.)	f_{osc} (em)	τ (exp.)
1	mon	S_1	440	0.84	488	495	0.81	3.60 at 495 nm
	H-dimer	S_1	404	0.00	466	438*	0.00	0.86 at 435 nm
		S_2	387	1.22	432		1.38	
	J-dimer	S_1	444	0.87	507		0.82	
		S_2	430	0.77	439		0.75	
2	mon	S_1	412	0.81	463	463	0.73	1.35 at 460 nm
	H-dimer	S_1	409	0.00	439	— **	0.00	1.18 at 425 nm
		S_2	392	1.35	419		1.38	
	J-dimer	S_1	400	1.70	436		1.29	
		S_2	391	0.02	420		0.33	

* estimated from Gaussian fit, ** could not be estimated reliably

J-aggregate S_1 and S_2 difference densities (**Fig. S21**) are significantly localised on the monomer units, with the degree of localisation increasing during the excited-state optimisation. As a result, both the S_1 and the S_2 show non-negligible oscillator strengths especially for compound **1**. The usually smaller oscillator strength of the S_2 may be an alternative explanation for the high-energy shoulder encountered in the experimental emission spectra. However, for compound **2**, if we assume a large contribution from J-aggregates to the emission properties, we should expect a third intense band in between the main peak and the high-energy shoulder, which we do not observe, although this may be somewhat difficult to evaluate due to the dominating main emission peak. For compound **1**, we do see an agreement between experimental and calculated emission energies. However, J-type dimers should produce shorter lifetimes for the main peak due to the larger oscillator strength of the S_1. Furthermore, the localisation of the difference densities onto the monomer units indicates small intermolecular coupling in comparison to H-type dimers which show completey delocalised difference densities (**Fig. S20**). Due to the small intermolecular coupling and since they do not seem to significantly contribute to the emission properties, the term "J-aggregate" should in this context probably be taken with a grain of salt. In conclusion, J-type aggregation may play a minor hypothetical role, possibly for the spectral area in between main peak and high-energy shoulder and in polarising monomers. In general, however, monomers and H-aggregates determine the overall emission properties of DADQs in the solid state.

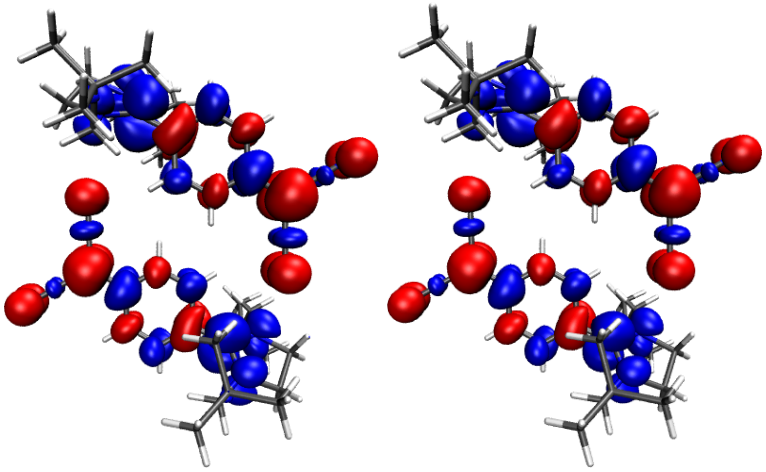

Figure S20: S_1 (left) and S_2 (right) difference densities of compound **1** in an H-type conformation, isovalue = 0.001 a_0^{-3}. Blue and red zones correspond to areas of electron enhancement and electron depletion.

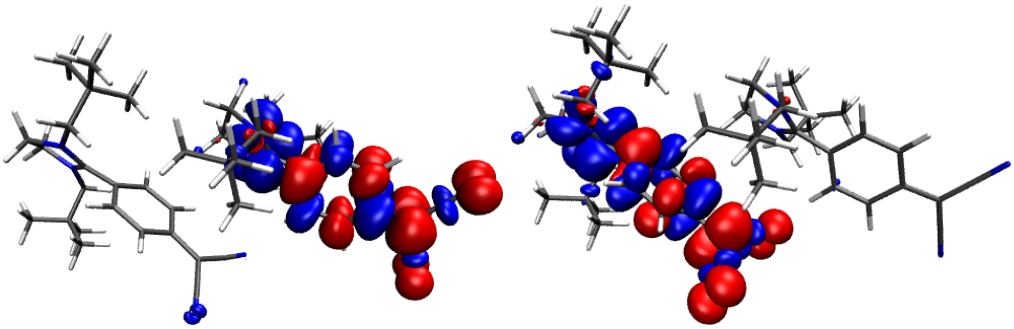

Figure S21: S_1 (left) and S_2 (right) difference densities of compound **1** in a J-type conformation, isovalue = 0.001 a_0^{-3}. Blue and red zones correspond to areas of electron enhancement and electron depletion.

6 Coordinates of molecular structures of all dimers

The cartesian coordinates of the monomers, H-dimers, and J-dimers of compounds **1** and **2** in ground and excited states will be provided in a separate file.

References

[1] P. Rietsch, F. Witte, S. Sobottka, G. Germer, A. Becker, A. Güttler, B. Sarkar, B. Paulus, U. Resch–Genger, S. Eigler, *Angew. Chem. Int. Ed.* **2019**, *58*, 8235–8239.

[2] J.-D. Chai, M. Head-Gordon, *J. Chem. Phys.* **2008**, *128*, 084106.

[3] F. Weigend, R. Ahlrichs, *Phys. Chem. Chem. Phys.* **2005**, *7*, 3297.

[4] J. P. Perdew, K. Burke, M. Ernzerhof, *Phys. Rev. Lett.* **1996**, *77*, 3865–3868.

[5] S. Grimme, J. Antony, S. Ehrlich, H. Krieg, *J. Chem. Phys.* **2010**, *132*, 154104.

[6] S. Grimme, S. Ehrlich, L. Goerigk, *J. Comput. Chem.* **2011**, *32*, 1456–1465.

[7] G. Kresse, J. Hafner, *Phys. Rev. B* **1993**, *47*, 558–561.

[8] G. Kresse, J. Furthmüller, *Comput. Mater. Sci.* **1996**, *6*, 15–50.

[9] G. Kresse, J. Furthmüller, *Phys. Rev. B* **1996**, *54*, 11169–11186.

[10] P. E. Blöchl, *Phys. Rev. B* **1994**, *50*, 17953–17979.

[11] H. J. Monkhorst, J. D. Pack, *Phys. Rev. B* **1976**, *13*, 5188–5192.

[12] I. Petousis, W. Chen, G. Hautier, T. Graf, T. D. Schladt, K. A. Persson, F. B. Prinz, *Phys. Rev. B* **2016**, *93*, 115151.

[13] J. Heyd, G. E. Scuseria, M. Ernzerhof, *J. Chem. Phys.* **2003**, *118*, 8207–8215.

[14] M. J. Frisch, G. W. Trucks, H. B. Schlegel, G. E. Scuseria, M. A. Robb, J. R. Cheeseman, G. Scalmani, V. Barone, G. A. Petersson, H. Nakatsuji, X. Li, M. Caricato, A. V. Marenich, J. Bloino, B. G. Janesko, R. Gomperts, B. Mennucci, H. P. Hratchian, J. V. Ortiz, A. F. Izmaylov, J. L. Sonnenberg, D. Williams-Young, F. Ding, F. Lipparini, F. Egidi, J. Goings, B. Peng, A. Petrone, T. Henderson, D. Ranasinghe, V. G. Zakrzewski, J. Gao, N. Rega, G. Zheng, W. Liang, M. Hada, M. Ehara, K. Toyota, R. Fukuda, J. Hasegawa, M. Ishida, T. Nakajima, Y. Honda, O. Kitao, H. Nakai, T. Vreven, K. Throssell, J. Montgomery, J. A., J. E. Peralta, F. Ogliaro, M. J. Bearpark, J. J. Heyd, E. N. Brothers, K. N. Kudin, V. N. Staroverov, T. A. Keith, R. Kobayashi, J. Normand, K. Raghavachari, A. P. Rendell, J. C. Burant, S. S. Iyengar, J. Tomasi, M. Cossi, J. M. Millam, M. Klene, C. Adamo, R. Cammi, J. W. Ochterski, R. L. Martin, K. Morokuma, O. Farkas, J. B. Foresman, D. J. Fox, Gaussian16 Revision A.03, Wallingford, CT, **2016**.

[15] M. Svensson, S. Humbel, R. D. J. Froese, T. Matsubara, S. Sieber, K. Morokuma, *J. Phys. Chem.* **1996**, *100*, 19357–19363.

[16] C. M. Marian, A. Heil, M. Kleinschmidt, *WIREs Comput. Mol. Sci.* **2019**, *9:e1394*.

[17] I. Lyskov, M. Kleinschmidt, C. M. Marian, *J. Chem. Phys.* **2016**, *144*, 034104.

[18] M. Kleinschmidt, C. M. Marian, M. Waletzke, S. Grimme, *J. Chem. Phys.* **2009**, *130*, 044708.

[19] V. Barone, M. Cossi, *J. Phys. Chem. A* **1998**, *102*, 1995–2001.

4.4 Paper B1

"Switchable synchronisation of pirouetting motions in a redox-active [3]rotaxane"

H. V. Schröder, A. Mekic, H. Hupatz, S. Sobottka, F. Witte, L. H. Urner, M. Gaedke, K. Pagel, B. Sarkar, B. Paulus, C. A. Schalley
Nanoscale **2018**, 10, 21425–21433.
DOI: 10.1039/c8nr05534c
URL: https://doi.org/10.1039/C8NR05534C

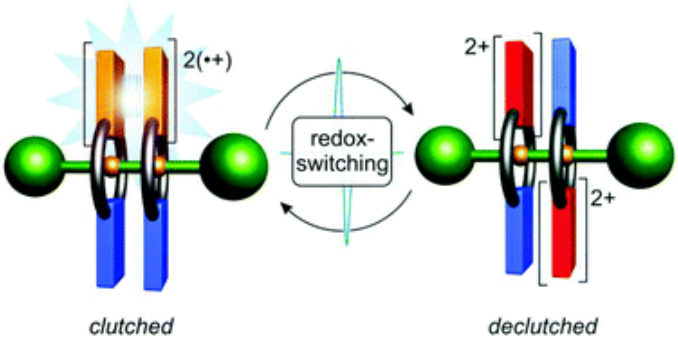

Figure 4.4: Graphical abstract of paper **B1**.

Contributions

Hendrik Schröder and Henrik Hupatz conceived the project. H.S. wrote the manuscript with help from Christoph Schalley. All computational work was carried out by Felix Witte. Synthetic work was conducted by H.S. and Amel Mekic. Marius Gaedke helped with the synthesis of the axle molecule. CV experiments were performed by A.M. and H.S. Nuclear magnetic resonance (NMR), and variable-temperature-NMR (VT-NMR) experiments were furthermore conducted by H.S. H.H. performed isothermal calorimetry (ITC) measurements. H.S. and Sebastian Sobottka carried out electron paramagnetic resonance (EPR), and UV/Vis-near-infrared (NIR) experiments and evaluated the data with help from Biprajit Sarkar. Leonhard H. Urner and H.S. conducted ion mobility-mass spectrometry (IM-MS) measurements and calculated collision cross sections (CCS) and evaluated the data with help from Kevin Pagel. All authors contributed to the final version of the manuscript.

Nanoscale

PAPER

View Article Online
View Journal | View Issue

Published on 24 October 2018. Downloaded by Freie Universitaet Berlin on 11/30/2020 6:21:37 PM.

Check for updates

Cite this: *Nanoscale*, 2018, **10**, 21425

Switchable synchronisation of pirouetting motions in a redox-active [3]rotaxane†

Hendrik V. Schröder, [a] Amel Mekic,[a] Henrik Hupatz,[a] Sebastian Sobottka,[b] Felix Witte,[a] Leonhard H. Urner,[a] Marius Gaedke,[a] Kevin Pagel,[a,c] Biprajit Sarkar, [b] Beate Paulus[a] and Christoph A. Schalley *[a]

Received 9th July 2018,
Accepted 23rd October 2018

DOI: 10.1039/c8nr05534c

rsc.li/nanoscale

In this study, the crown/ammonium [3]rotaxane **R2** is reported which allows a switchable synchronisation of wheel pirouetting motions. The rotaxane is composed of a dumbbell-shaped axle molecule with two mechanically interlocked macrocycles which are decorated with a redox-active tetrathiafulvalene (TTF) unit. Electrochemical, spectroscopic, and electron paramagnetic resonance experiments reveal that rotaxane **R2** can be reversibly switched between four stable oxidation states (**R2**, $\mathbf{R2}^{\bullet+}$, $\mathbf{R2}^{2(\bullet+)}$, and $\mathbf{R2}^{4+}$). The oxidations enable non-covalent, cofacial interactions between the TTF units in each state—including a stabilised mixed-valence $(TTF_2)^{\bullet+}$ and a radical-cation $(TTF^{\bullet+})_2$ dimer interaction—which dictate a *syn* (**R2**, $\mathbf{R2}^{\bullet+}$, and $\mathbf{R2}^{2(\bullet+)}$) or *anti* ($\mathbf{R2}^{4+}$) ground state co-conformation of the wheels in the rotaxane. Furthermore, the strength of these wheel–wheel interactions varies with the oxidation state, and thus electrochemical switching allows a controllable synchronisation of the wheels' pirouetting motions. DFT calculations explore the potential energy surface of the counter-rotation of the two interacting wheels in all oxidation states. The controlled coupling of pirouetting motions in rotaxanes can lead to novel molecular gearing systems which transmit rotational motion by switchable non-covalent interactions.

Introduction

A great contemporary challenge in nanoscience is the construction of molecular machines and motors which can produce repetitive motion fuelled by external stimuli such as energy or concentration gradients.[1] Generation and control of rotational motion is one of the most worthwhile goals. Nature's biomachinery elegantly fulfils this task as seen for the unidirectional rotation in ATP synthase or the flagella-based motility of bacteria.[2] In the last two decades, directional rotation was also realised in artificial systems[3] including Feringa's light-driven rotary motors[4] based on overcrowded alkenes. However, a further step towards applicable artificial molecular machinery is a multi-component approach in which a molecular motor (active component) is coupled with a passive component to transmit rotational motion to the surrounding environment.[5]

Pioneering work on correlated rotational motion has been reported by Iwamura and Mislow who studied the dynamics of molecular bevel gears.[6] These gears consist of covalently linked and tightly intermeshed triptycene groups. Based on the idea of sterically correlated rotors, the coupling of rotation has been further investigated in more sophisticated gearing systems.[7] Moreover, it is desirable that molecular gears are also susceptible to external stimuli, and thus the transmission of rotational motion can be switched on and off or regulated in a controlled manner.[8] Examples of molecular gears have been reported in which the steric rotor correlation can be influenced by ions,[9] ligands,[10] or light and thermal stimuli.[11] Additionally, stimuli-controlled transmission of rotational motion has been achieved in gears based on organometallic carousel compounds such as metallocenes[12] or double-decker porphyrins.[13]

The operation of such controllable gearing systems is reminiscent of the working principle of macroscopic clutches, common mechanical devices which can be found, for example, in motor vehicles. Transmission of rotation is realised by a connection between two rotating shafts. A disengagement (declutching) of the shafts leads to desynchronisation of rotation rates, and thus to an interruption of power transmission. Although the technomimetic comparison of mole-

[a]*Institut für Chemie und Biochemie, Freie Universität Berlin, Takustraße 3, 14195 Berlin, Germany. E-mail: c.schalley@fu-berlin.de*
[b]*Institut für Chemie und Biochemie, Freie Universität Berlin, Fabeckstraße 34/36, 14195 Berlin, Germany*
[c]*Fritz Haber Institute of the Max Planck Society, Department of Molecular Physics, Faradayweg 4-6, 14195 Berlin, Germany*

†Electronic supplementary information (ESI) available: General experimental methods, synthetic procedures, rotaxane characterization, EPR, UV/VIS-NIR, ITC, CV and DS, IM-MS, VT-NMR, and computational details. See DOI: 10.1039/c8nr05534c

Published on 24 October 2018. Downloaded by Freie Universitaet Berlin on 11/30/2020 6:21:37 PM.

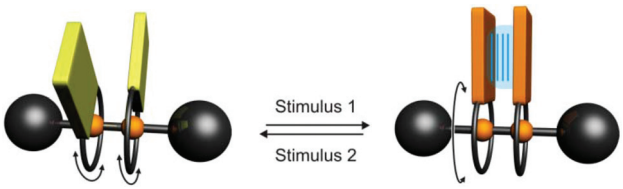

Fig. 1 Representation of a stimuli-responsive [3]rotaxane which allows a switchable synchronisation of macrocycle pirouetting motions.

cular machines at the nanoscale with macroscopic machines certainly has its limitations,[14] this approach has been frequently used by groups in the field as it provides an easy-to-understand description of the overall function of these molecular devices.

Here, we present a novel type of [3]rotaxane which allows the switchable synchronisation of pirouetting motions of two macrocycles (Fig. 1). Our molecular system is based on the symmetric [3]rotaxane **R2** (Fig. 2). Two macrocycles are threaded on a dumbbell-shaped axle molecule. A synchronisation or, in other words, a coupling of the wheel's pirouetting motions can be achieved by switchable non-covalent interactions between the wheels. In this study, we show by a combination of experimental and theoretical methods two major outcomes: (i) **R2** can be operated as a rotational switch in which the wheels adopt a *syn* or *anti* ground-state co-conformation. (ii) The wheel–wheel interactions, and thus the synchronisation of their pirouetting motions, can be adjusted by electrochemical switching.

Results and discussion

Design considerations and synthesis

In contrast to the well-studied wheel translation, for example in molecular shuttles,[15] the use of the pirouetting motion in rotaxanes to drive a molecular machine remains challenging.[1b,16] One reason is the high structural flexibility of most rotaxane architectures, which makes motion transmission by steric correlation difficult. However, a [3]rotaxane with two wheels is ideally suited to realise a coupling of wheel pirouetting motions. The wheels are spatially fixed in close contact by mechanical interlocking but can still freely rotate around the axle. The well-known crown/ammonium rotaxane motif was chosen due to its straightforward structural modifiability and high-yielding supramolecular synthesis.[17] Stoddart and co-workers showed that axles with a trismethylene group between two ammonium binding sites provide a suitable spacing (~3.4 Å) for π–π interactions between crown ether macrocycles.[18]

The key building block in rotaxane **R2** is the switching unit implemented in the wheels, which controls their non-covalent interactions. The organosulfur compound tetrathiafulvalene[19] (TTF) is suitable, because TTF can undergo two reversible one-electron oxidations to yield a stable radical-cation ($TTF^{\bullet+}$) and dication (TTF^{2+}).[20] Similar to viologen radical cations,[21] TTF radical cations have an outstanding ability to form long-bonded dimers with cofacial arrangements: the mixed-valence dimer $(TTF_2)^{\bullet+}$ and the radical-cation dimer $(TTF^{\bullet+})_2$.[22] These weakly-associated species are usually not stable in solution under ambient conditions.[23] However, TTF dimers have been lately observed in carefully designed supramolecular complexes with confined environments including capsules,[24] clips,[25] or mechanically interlocked architectures such as rotaxanes[26] or catenanes.[27]

In our previous work involving TTF-decorated crown/ammonium (pseudo)rotaxanes, we directly implemented the TTF unit in a [24]crown-8 wheel (**TTFC8**).[28] Coulomb repulsion between the oxidised wheel **TTFC8** and the charged ammonium axles was used as the basis for redox-switchable shuttles. However, this design leads to the major drawbacks for the concept of synchronised wheel pirouetting: (i) the sulfur atoms in the wheel drastically lower the binding constant to dialkyl ammonium axles due to weaker hydrogen bonding.[29] (ii) The spatial proximity of TTF and the axle causes charge repulsion between the oxidised TTF and the ammonium station.[28b] (iii) Unsubstituted TTF forms only weak dimers. To circumvent these difficulties, an extended

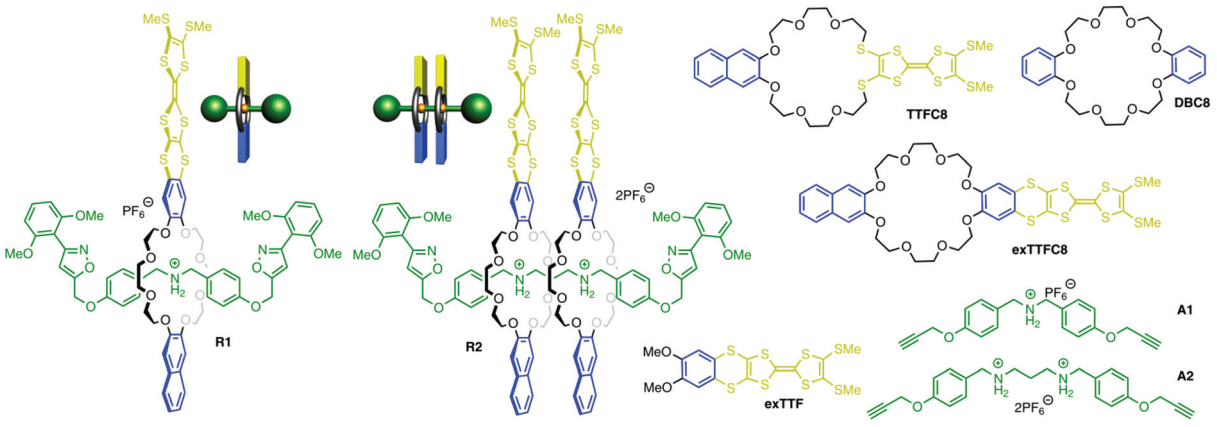

Fig. 2 Chemical structures of [3]rotaxane **R2** and other compounds investigated in this report.

 This journal is © The Royal Society of Chemistry 2018

Published on 24 October 2018. Downloaded by Freie Universitaet Berlin on 11/30/2020 6:21:37 PM.

macrocycle (**exTTFC8**) with a 1,2-dimercaptobenzene spacer between the TTF and the crown ether wheel was designed and synthesised (ESI, section 1.2†). In a very recent report, we showed that a TTF fused to a veratrole molecule (**exTTF**) features an enhanced dimer stability in comparison to unsubstituted TTF.[30]

A prerequisite for efficient rotaxane capping synthesis is a sufficiently strong template effect in the pseudorotaxane precursor complexes. Isothermal titration calorimetry (ITC) with monovalent axle **A1** and wheels **exTTFC8**, **TTFC8** and dibenzo-24-crown-8 (**DBC8**) showed mainly enthalpy-driven binding for all three pseudo[2]rotaxanes (ESI, section 4 and Table S1†). Compared to **TTFC8** ($K_a = (3.8 \pm 0.4) \times 10^3$ M^{-1} in $ClCH_2CH_2Cl/CH_3CN$ = 10 : 1), a 13-fold increase of the binding constant is observed for **exTTFC8** ($K_a = (50 \pm 5) \times 10^3$ M^{-1}). Furthermore, similar ΔH and ΔS values of **exTTFC8** as compared to those of **DBC8** corroborate our previous assumption of a stronger binding due to the separation of the crown binding site and TTF unit.

A capping strategy introduced by Takata and co-workers using a catalyst-free click reaction with a nitrile oxide stopper[31] was employed for the synthesis of [3]rotaxane **R2** (see section 1.3 in the ESI† for details). Besides the target compound **R2**, the structurally similar [2]rotaxane **R1** bearing one wheel was synthesised. Since all intramolecular wheel–wheel interactions can be excluded, **R1** serves as an ideal control compound to identify the effects in **R2** that emerge from its divalent nature. Experimental evidence obtained by ^1H, ^{13}C, and 2D NMR, high-resolution mass spectrometry, and infrared multiphoton dissociation experiments is consistent with the mechanically interlocked structures of both rotaxanes **R1** and **R2** (Fig. S1–7, ESI†).

Electrochemical switching

Two major questions arise for the switching of [3]rotaxane **R2**: (i) what is the wheels' ground state co-conformation (GSCC) in each oxidation state (Fig. 3a)? (ii) How strong are the TTF-induced wheel–wheel interactions, and thus the coupling between the wheels in each state (Fig. 3b)?

Regarding the first question, both macrocycles can pirouette around the axle and many different rotamers are potentially accessible. Only in a *syn* or *anti* co-conformation of the wheels, however, favorable cofacial stacking between the TTF and/or the naphthalene units is possible.[32] Spectroscopic evidence for intramolecular TTF dimer interactions—for example mixed-valence or radical-cation interactions—would thus imply a *syn* GSCC of the wheels.

Initially, the electrochemical properties of rotaxanes **R1** and **R2** were probed by cyclic voltammetry (CV) experiments in CH_3CN (Fig. 4). [2]Rotaxane **R1** shows two reversible one-electron oxidations with half-wave potentials of $E^1_{1/2}$ = 0.16 V and

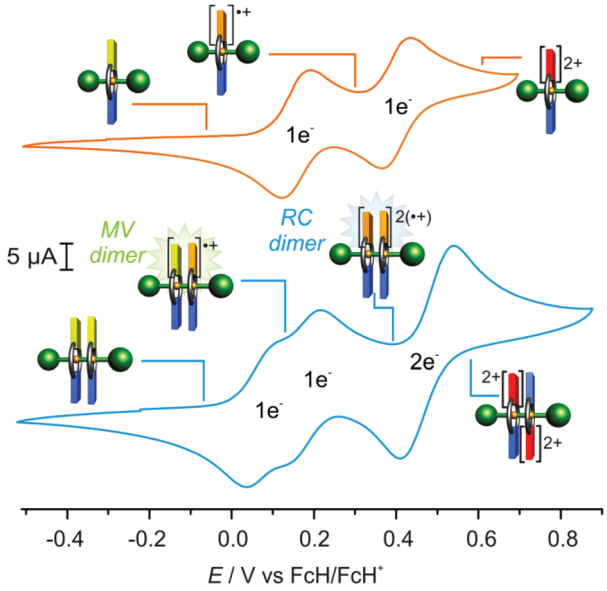

Fig. 4 Cyclic voltammograms (CH_3CN, 298 K, 1.0 mM, 100 mV s^{-1}) of rotaxanes **R1** (orange) and **R2** (blue) with *n*-Bu_4NPF_6 (0.1 M) as the electrolyte.

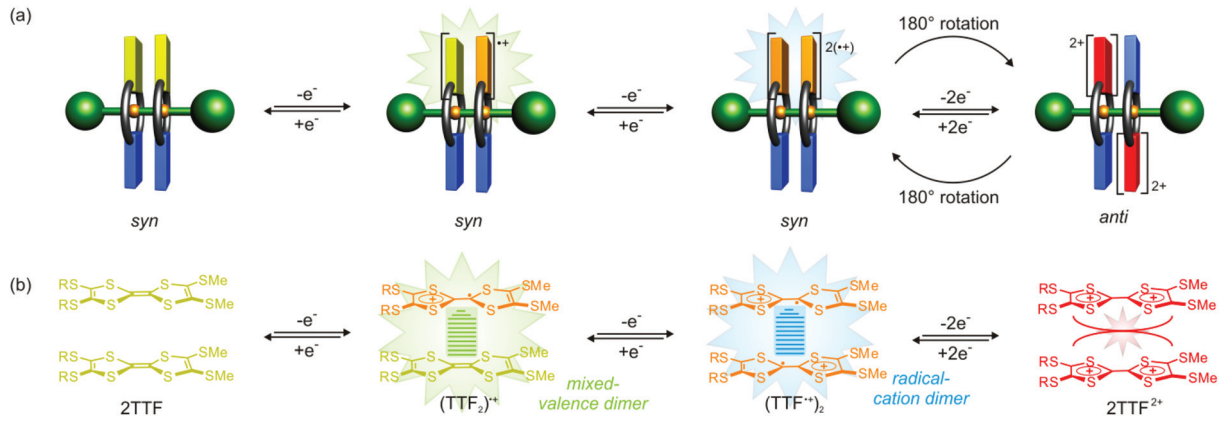

Fig. 3 (a) Graphical illustrations of [3]rotaxane **R2** in all oxidation states to illustrate the expected interconversion between the *syn* and *anti* ground state co-conformations of the wheels. (b) Cofacial TTF-TTF dimer interactions during successive oxidation of the two TTF molecules in **R2**.

Published on 24 October 2018. Downloaded by Freie Universitaet Berlin on 11/30/2020 6:21:37 PM.

$E^2_{1/2}$ = 0.40 V against the ferrocene/ferrocenium couple which we assign to the two oxidations of the TTF unit. The potentials are very similar to those of monomer **exTTF** (0.16 and 0.39 V).[30] This demonstrates that the positively charged ammonium axle has only a negligible effect on the TTF oxidation in **R1**. Additionally, no significant peak potential differences were observed for measurements of **R1** and **exTTFC8** in CH_2Cl_2 as a solvent of low dielectric constant (ESI, Fig. S12†). Thus, the charge–charge distance increase caused by the 1,2-dimercaptobenzene spacer sufficiently decreases the Coulomb repulsion between the oxidised TTF and charged axle.

[3]Rotaxane **R2** shows characteristic differences as compared to its monovalent analogue **R1**: three reversible oxidation processes are observed, two one-electron and a two-electron process with half-wave potentials of $E^1_{1/2}$ = 0.08 V, $E^2_{1/2}$ = 0.19 V, and $E^3_{1/2}$ = 0.48 V, respectively. The splitting of the first oxidation into two one-electron waves is indicative of an intramolecular mixed-valence interaction ($(TTF_2)^{\bullet+}$).[33] Based on the peak-to-peak separation, the comproportionation equilibrium of $\mathbf{R2}^{\bullet+}$ can be determined (K_c = 73) which clearly indicates a thermodynamically stable $\mathbf{R2}^{\bullet+}$ state.[33a,34] The third wave, corresponding to the $\mathbf{R2}^{2(\bullet+)} \rightarrow \mathbf{R2}^{4+}$ transition, is anodically shifted (+0.08 V) in contrast to the $\mathbf{R1}^{\bullet+} \rightarrow \mathbf{R1}^{2+}$ oxidation. This potential difference cannot merely be attributed to charge repulsion, as the system is flexible enough to elude the repulsion between the TTF^{2+} units by wheel pirouetting.[33c] Hence, the shift is assumed to be a consequence of an intramolecular stabilising interaction in the $\mathbf{R2}^{2(\bullet+)}$ state, most likely the radical-cation dimer $(TTF^{\bullet+})_2$, which has to be overcome by the additional potential.

In order to gain more detailed insight here, the CV data of **R2** were evaluated by electrochemical digital simulations (DS), a powerful tool to establish chemical–electrochemical mechanisms and to estimate the thermodynamic and kinetic parameters of equilibrium reactions (ESI, section 5†).[35] Our simulations indicate the states $\mathbf{R2}^{\bullet+}$ and $\mathbf{R2}^{2(\bullet+)}$ to be significantly stabilised by attractive wheel–wheel interactions. The estimated stabilisation energies in the four different states provide the following wheel–wheel interaction ranking: $\mathbf{R2}^{\bullet+}$ (mixed-valence dimer) > $\mathbf{R2}^{2(\bullet+)}$ (radical-cation dimer) > **R2** ≫ $\mathbf{R2}^{4+}$. This follows the order of the previously reported dimerisation energies of TTF monomers.[22,30] Notably, $\mathbf{R2}^{4+}$ displays a significantly smaller attractive interaction than neutral **R2** implying that the repulsive forces between the wheels affect the $\mathbf{R2}^{4+}$ state. Here, charge repulsion between the two TTF^{2+} units leads to an opening of the cofacial TTF dimer and subsequently to a change in the wheel's co-conformation.[27,33b] An *anti* GSCC is reasonable as it increases the charge–charge distance and simultaneously enables cofacial interactions between the electron-poor TTF^{2+} and the electron-rich naphthalene units.

The paramagnetic properties of **R1** and **R2** in their different oxidation states were investigated by continuous wave electron paramagnetic resonance (CW EPR) titration experiments (Fig. 5a). CH_3CN solutions of **R1** and **R2** were chemically oxidised by stepwise addition of $Fe(ClO_4)_3$ as a one-electron oxidant. A test reaction using Zn dust for back reduction

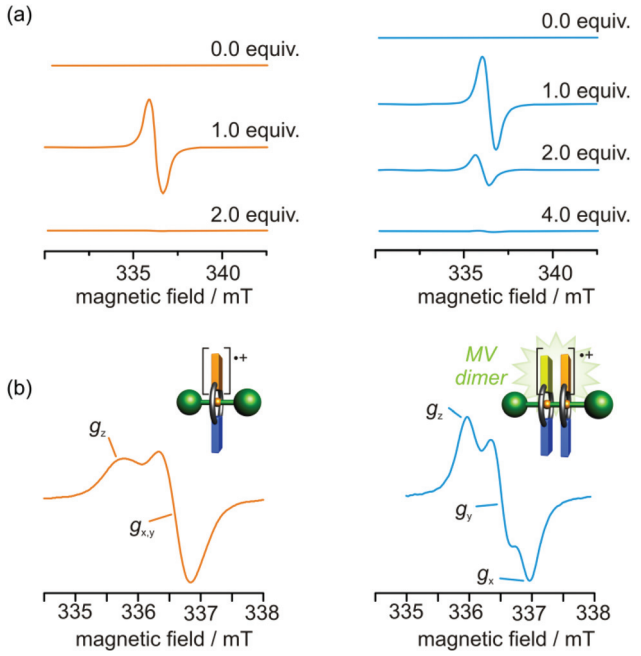

Fig. 5 (a) CW EPR spectra (CH_3CN, 298 K, 0.1 mM) of [2]rotaxane **R1** (orange) and [3]rotaxane **R2** (blue) upon titration with the oxidant $Fe(ClO_4)_3$. (b) EPR spectra (163 K, 0.1 mM) of frozen CH_2Cl_2 solutions of $\mathbf{R1}^{\bullet+}$ and $\mathbf{R2}^{\bullet+}$.

demonstrates the reversibility of this chemical oxidation (ESI, Fig. S9b†).[28a,30] After each addition of the oxidant, an EPR spectrum was recorded. For **R1**, addition of 1.0 equiv. of the oxidant leads to a signal with g = 2.010 which corresponds to the radical-cationic species $\mathbf{R1}^{\bullet+}$.[23] Further oxidation results in a decrease of intensity in accordance with an $\mathbf{R1}^{2+}$ singlet state. The same protocol was applied for [3]rotaxane **R2**. A maximum of intensity for the paramagnetic $\mathbf{R2}^{\bullet+}$ state (g = 2.010) is reached after the addition of 1.0 equiv. of the oxidant. The signal intensity decreases with further oxidation which indicates radical-paring and is thus indicative of the formation of a diamagnetic radical-cation dimer ($(TTF^{\bullet+})_2$) in rotaxane $\mathbf{R2}^{2(\bullet+)}$.[22,27,36] However, a weak signal is still present after adding 2.0 equiv. which may be explained by charge disproportionation or equilibria between the EPR-silent radical–cation dimer and alternative EPR-active co-conformations of $\mathbf{R2}^{2(\bullet+)}$.[27,37] Further oxidation leads to a virtual absence of any signal intensity which is, again, in accordance with the diamagnetic $\mathbf{R2}^{4+}$ state.

In solution, molecular tumbling of paramagnetic molecules often averages out the anisotropy of the g-factor which gives a more detailed view on the coupling to the electrostatic field of the spatial environment. In frozen solution, however, the g factor anisotropy can become visible.[38] Therefore, additional EPR experiments of $\mathbf{R1}^{\bullet+}$ and $\mathbf{R2}^{\bullet+}$ were performed in CH_2Cl_2 at room temperature and in frozen solutions (Fig. 5b). The radical species were prepared by prior chemical oxidation with $Fe(ClO_4)_3$. At room temperature, rotaxanes $\mathbf{R1}^{\bullet+}$ and $\mathbf{R2}^{\bullet+}$ show isotropic signals at g values of 2.009 and 2.008, respectively. In

 This journal is © The Royal Society of Chemistry 2018

Published on 24 October 2018. Downloaded by Freie Universitaet Berlin on 11/30/2020 6:21:37 PM.

frozen solution (163 K), however, $\mathbf{R1}^{\bullet+}$ exhibits *g*-anisotropy and shows an EPR spectrum of axial symmetry with *g*-values g_z = 2.012 and g_{xy} = 2.008. Going from $\mathbf{R1}^{\bullet+}$ to $\mathbf{R2}^{\bullet+}$, an EPR spectrum of rhombic symmetry with three *g*-values of 2.011, 2.008 and 2.005 is observed. This indicates that the radical in $\mathbf{R2}^{\bullet+}$ experiences environmental effects different from those in $\mathbf{R1}^{\bullet+}$ in agreement with the mixed-valence interaction in $\mathbf{R2}^{\bullet+}$.

The presence of a radical-cation dimer in $\mathbf{R2}^{2(\bullet+)}$ was further verified by UV/Vis-NIR spectroscopy in CH_3CN. Fig. 6a depicts the photometric titrations of rotaxanes **R1** and **R2** by the oxidant $Fe(ClO_4)_3$. After the addition of 1.0 equiv. of oxidant, $\mathbf{R2}^{\bullet+}$ displays characteristic $TTF^{\bullet+}$ bands (450, 870 nm) accompanied by a broad low intensity charge-resonance band (>1300 nm) of the mixed-valence dimer $(TTF_2)^{\bullet+}$.[30,37,39] The low-energy band disappears in the course of further oxidation. The addition of 2.0 equiv. results in the formation of the radical-cation dimer interaction ($(TTF^{\bullet+})_2$) as clearly seen from the emergent shoulder[33c] between 1000 and 1500 nm and the blue shift (ESI, Fig. S9a†) of the $TTF^{\bullet+}$ bands at 430 nm and 820 nm. This Davydov blue shift is diagnostic of cofacially stacked radical-cation dimers[40] and is not observed in the oxidation of **R1**. This is an additional strong piece of evidence for a *syn* GSCC in $\mathbf{R2}^{2(\bullet+)}$. A typical TTF^{2+} band at 660 nm is observed for the fully oxidised rotaxane $\mathbf{R2}^{4+}$. The differences in absorption for each state can also be easily identified with the naked eye (Fig. 6b). Including the sextuply (including the two ammonium ions of the axle) charged $\mathbf{R2}^{4+}$ state, all chemically generated oxidation states of **R2** showed remarkable stability in CH_3CN towards moisture and air for several months as indicated by the persistent colors of the solutions.

Co-conformation of non-switched R2

To reveal the co-conformation and wheel–wheel interactions of **R2** before electrochemical switching, further ITC investigations of the pseudo[3]rotaxane formation with divalent axle **A2** and **exTTFC8** were conducted and compared with the binding data obtained for the TTF-free control **A2**⊂(**DBC8**)$_2$ (ESI, section 4 and Table S1†). Not unexpectedly, **A2**⊂(**DBC8**)$_2$ displays similar binding enthalpies for both wheels (ΔH_1 = (−35.6 ± 1.3) kJ mol^{-1}; ΔH_2 = (−31.1 ± 4.9) kJ mol^{-1}). Consequently, non-cooperative binding occurs here. In marked contrast, the second crown ether in **A2**⊂(**exTTFC8**)$_2$ binds significantly stronger than the first (ΔH_1 = (−32.6 ± 1.0) kJ mol^{-1}; ΔH_2 = (−45.4 ± 4.3) kJ mol^{-1}). This clearly points to positive cooperativity, which can easily be traced back to the attractive π-interactions between the two cofacial **exTTFC8** wheels. The TTF and naphthalene units are thus crucial for the wheel–wheel interactions in **A2**⊂(**exTTFC8**)$_2$.[41] However, the more fixed conformation leads to a strong entropic penalty of the second binding event which decreases K_2 in comparison with K_1. In accordance with the ITC results, the ^{1}H NMR spectrum of **R2** shows significant high-field shifts of the wheels' naphthalene signals ($\Delta\delta$ = −0.24 ppm) in comparison with **R1** (Fig. S8, ESI†). We attribute these shifts to a shielding effect caused by the intramolecular π-interactions between the two wheels in **R2**.[18b]

Since no crystals suitable for X-ray diffraction could be obtained, ion mobility mass spectrometry (IM-MS) was applied to investigate the conformation and underpin the assumption of a *syn* GSCC of the wheels in the **R2** state (see section 6 and Table S2 in the ESI† for details). IM-MS has proven to be highly valuable to unravel the conformations of mechanically interlocked molecules.[18a,28c,42] The mass spectrum obtained from **R2** shows one signal (*m*/*z* = 1217) that corresponds to the $[\mathbf{R2} - 2PF_6]^{2+}$ ion (Fig. S15a, ESI†). IM-MS analysis revealed only one narrow and Gaussian-shaped arrival time distribution for the $[\mathbf{R2} - 2PF_6]^{2+}$ ion indicating the presence of one energetically preferred conformer (ESI, Fig. S15b†). The experimental collision cross section (CCS) of 410 Å^2 matches with the theoretical CCS calculated from a force-field-optimised structure in which the wheels adopt a *syn* GSCC (412 A^2). Theoretical CCS values calculated for other possible wheel co-conformations were instead not consistent with the experimental CCS, which underlines the assumption that the *syn* GSCC is the most relevant conformation (ESI, Table S2†). Although the structure of **R2** in the gas phase is not necessarily identical to that in solution, such a *syn* GSCC is in good agreement with the ITC data and NMR results.

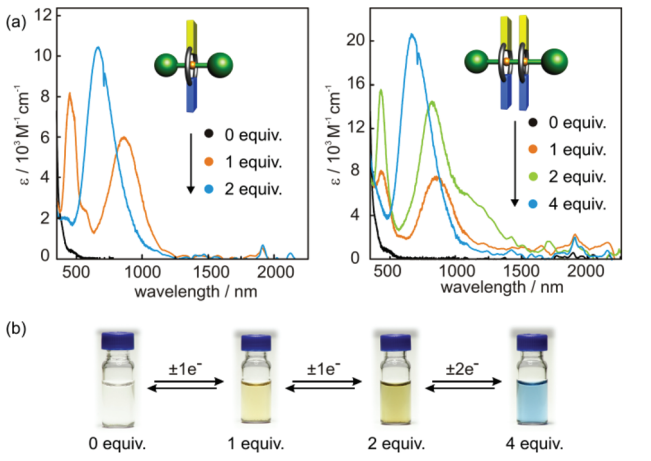

Fig. 6 (a) UV/Vis-NIR spectra (CH_3CN, 298 K, 2.5 × 10^{-5} M) of rotaxanes **R1** (left) and **R2** (right) upon titration with the oxidant $Fe(ClO_4)_3$. (b) Photographs of **R2** solutions (CH_3CN, 10^{-4} M) in all four stable oxidation states.

DFT calculations

Theoretical calculations were employed to gain further insight into the energetics and conformational aspects of **R2**. After structural relaxation of each co-conformation (*syn* and *anti*) in each of its four charge states, *i.e.* 8 structures in total, single point calculations at the PBE0-D3(BJ)/def2-TZVP level of DFT were performed to estimate co-conformational stabilities and oxidation potentials (for full computational details, see the ESI†). Additionally, the valence electronic structure of **R2** is investigated. We have shown previously that this level of theory sufficiently describes the conformational and electronic properties of our redox-active compounds.[30] Fig. 7 depicts the

Published on 24 October 2018. Downloaded by Freie Universitaet Berlin on 11/30/2020 6:21:37 PM.

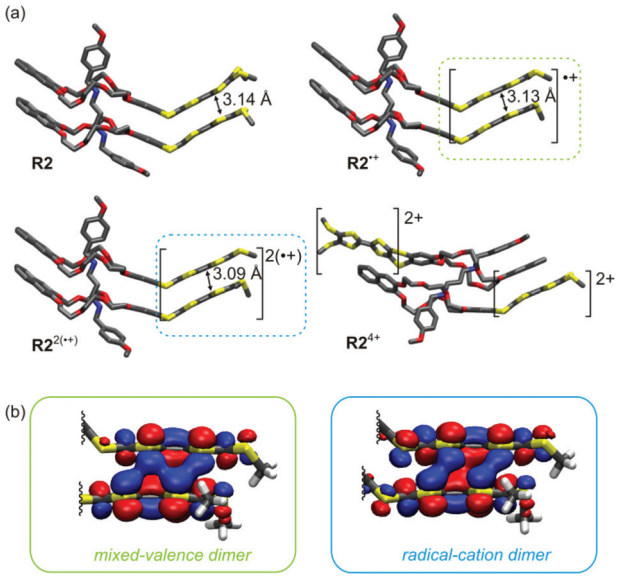

Fig. 7 (a) Calculated structures of the GSCC of a stopper-less pseudorotaxane analogue of **R2** in its four oxidation states. (b) Bonding orbitals of the TTF_2 complex in the mixed-valence and radical-cation dimer states.

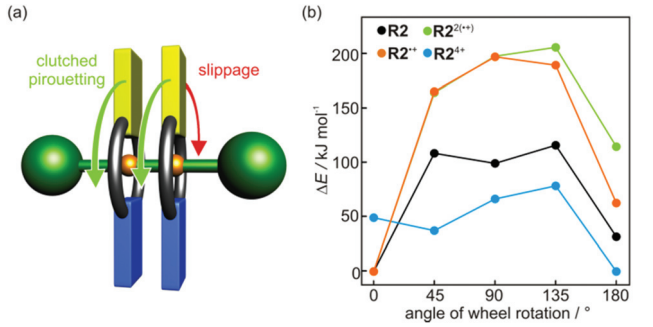

Fig. 8 (a) Schematic representation of the two rotational wheel motions in **R2** relative to the axle molecule. (b) DFT results of relaxed angular PES scans for counter-rotation of the wheels (slippage) in all stable oxidation states of **R2**.

most stable co-conformation of a computer-time-reducing, stopper-less pseudorotaxane analogue of **R2** in each state. In agreement with the experimental findings, the calculations suggest a *syn* GSCC for **R2**, $\mathbf{R2}^{\bullet+}$, and $\mathbf{R2}^{2(\bullet+)}$ whereas the *anti* co-conformation is lower in energy for $\mathbf{R2}^{4+}$. This is further supported by structural changes: during the first two oxidation processes in *syn*-**R2**, the interplanar distance between the TTF units decreases from 3.14 Å to 3.09 Å while the distance between the stacked naphthalene moieties remains rather constant around 3.32 Å. However, the last oxidation results in a significant increase of the TTF–TTF distance (from 3.09 Å to 3.17 Å) and a notable decrease of the naphthalene dimer separation (from 3.32 Å to 3.16 Å) due to the unfavourable electrostatic interaction of the two TTF^{2+} units. In contrast to *syn*-**R2**, the interplanar distances in *anti*-**R2** are only slightly altered upon oxidation (going from 3.31 Å in *anti*-**R2** to 3.27 Å in *anti*-$\mathbf{R2}^{4+}$).

Analysis of the molecular orbitals reveals that the valence electronic structure of $\mathbf{R2}^{\bullet+}$ and $\mathbf{R2}^{2(\bullet+)}$ is dominated by the mixed-valence and radical-cation dimer interactions, respectively, as visualised in Fig. 7b. The shape of the valence orbitals suggests multi-centered bonding[43] between the TTF units leading to attractive non-covalent interactions. Computed energies for the oxidative processes decently agree with experimental trends (Table S3, ESI†). Two contributions were considered: the pure electronic energy difference between two oxidation states and the difference arising from the rearrangement of a *syn* to an *anti* co-conformation or *vice versa*. For the second oxidative transition ($\mathbf{R2}^{\bullet+}/\mathbf{R2}^{2(\bullet+)}$) no rearrangement is expected and, hence, the mere electronic contribution reproduces the experiment very well.

Rotational motions

As illustrated in Fig. 8a, two rotational motions can be assumed for the wheels of **R2:** (i) a concerted pirouetting of the clutched macrocycles around the dialkyl ammonium thread (green arrow) or (ii) an independent counter-rotation of both wheels reminiscent of a slippage motion (red arrow).

The degree of concertedness of the wheel pirouetting increases with the strength of attractive wheel–wheel interactions in the different oxidation states as the most relevant parameter. However, in order to draw conclusions about the rotation from the interaction energies—that are thermodynamic values—it is necessary to know that there are no other barriers hampering the rotation of the wheels around the axle. In other words, only when the crown ethers are generally free to rotate, the TTF/TTF or TTF/naphthalene interactions will determine how much concerted, clutched motion occurs and how important gear slippage becomes.

Variable-temperature NMR (VT-NMR) experiments with **R2** result in only one set of signals for a C_{2v} symmetric species indicating a fast rotamer interconversion at room temperature. Upon gradual cooling to 203 K (400 MHz), the ^{1}H signals strongly broaden, but no decoalescence was observed. This is in accordance with other crown ether complexes, which show fast rotation with low barriers that is not detectable by standard VT-NMR techniques.[44] Consequently, the wheels in **R2** undergo a fast and random pirouetting motion even at temperatures significantly lower than room temperature. Unfortunately, the presence of paramagnetic species in the $\mathbf{R2}^{\bullet+}$, $\mathbf{R2}^{2(\bullet+)}$, and $\mathbf{R2}^{4+}$ states prevents reliable VT-NMR measurements for these states. Nevertheless, it is reasonable to assume that the rotation of the wheels is still fast in these states.

Quantum mechanical methods are a commonly-used tool[7] to approach the potential energy surface (PES) of molecular gears and rotors and to calculate energy barriers for different motions. Restricted optimisations and subsequent single-point calculations at the PBE0 level were performed for **R2** in steps of 45° for the dihedral angle between the two TTF units (Fig. S18, ESI†). Estimated barriers for counter-rotation of the wheels were obtained which are in the order of *ca.* 200 kJ mol^{-1} for $\mathbf{R2}^{\bullet+}$ and

 This journal is © The Royal Society of Chemistry 2018

Published on 24 October 2018. Downloaded by Freie Universitaet Berlin on 11/30/2020 6:21:37 PM.

$\mathbf{R2}^{2(\bullet+)}$ (Fig. 8b). These two oxidation states are thus much more strongly clutched in their *syn* co-conformation in comparison to **R2** and $\mathbf{R2}^{4+}$, for which these barriers are notably lower in energy. While non-switched **R2** shows a medium barrier height of approximately 100 kJ mol^{-1}, *syn*-$\mathbf{R2}^{4+}$ is not even predicted to be a local minimum structure. The latter readily falls into an intermediate structure at around 45° which in turn converts into the *anti* co-conformation with a barrier of ~40 kJ mol^{-1}. This can be attributed to the increasing Coulomb repulsion between the TTF^{2+} units. A clear differentiation between $\mathbf{R2}^{\bullet+}$ and $\mathbf{R2}^{2(\bullet+)}$ is rather difficult as their rotational motion is governed by a similar degree of non-covalent interactions. Although absolute values for rotational barriers may suffer from errors inherent in the applied DFT approach, their relative trends should be reliable. In spite of this, the calculations clearly indicate that a co-conformational change is accomplished in the last oxidative process when going from $\mathbf{R2}^{2(\bullet+)}$ to $\mathbf{R2}^{4+}$, which is in agreement with our experimental findings.

Overall, the experimental and computational results indicate stronger wheel–wheel interactions—and, thus, a higher barrier of wheel slippage—for the $\mathbf{R2}^{\bullet+}$ and $\mathbf{R2}^{2(\bullet+)}$ states than for the **R2** and $\mathbf{R2}^{4+}$ states. This clearly confirms the function as a switchable system with different motion coupling efficiencies in the four oxidation states. Although the wheels of the [3]rotaxane cannot be fully disengaged, the coupling can be adjusted by electrochemical switching.

Conclusions

In summary, the synthesis and electrochemical switching of a crown/ammonium [3]rotaxane **R2** consisting of a dumbbell-shaped axle with two tetrathiafulvalene-decorated wheels has been reported. The rotaxane can be switched between four stable oxidation states including two states featuring mixed-valence $(TTF_2)^{\bullet+}$ or radical-cation $(TTF^{\bullet+})_2$ dimer interactions. Each state shows a specific wheel ground state co-conformation and wheel–wheel interactions of different strengths. Quantum chemical calculations reveal that the barrier for gear slippage, which is identical to the counter-rotation of both wheels, can be adjusted by electrochemical switching. To the best of our knowledge, this is the first example of a gear-type system which operates with wheel pirouetting motions in a rotaxane. The switchable synchronisation of pirouetting motions equates with the working principle of a controllable gearing system. As a next step, ordered arrays of these rotaxanes on surfaces or in solid state materials could be investigated regarding their optoelectronic and conformational properties in external fields. A concerted behaviour of such multi-dimensional arrays may lead to macroscopic effects which are highly interesting for functional devices.

Conflicts of interest

There are no conflicts to declare.

Acknowledgements

This research was funded by the Deutsche Forschungsgemeinschaft (CRC 765). We thank Max Bartetzko and Mathias Ellwanger for NMR measurements, Fabian Klautzsch for help with the ITC, Jongcheol Seo for help with IM-MS, and Constantin Stuckhardt for help with synthesis.

Notes and references

1 (*a*) V. Balzani, A. Credi, F. M. Raymo and J. F. Stoddart, *Angew. Chem., Int. Ed.*, 2000, **39**, 3348; (*b*) S. Erbas-Cakmak, D. A. Leigh, C. T. McTernan and A. L. Nussbaumer, *Chem. Rev.*, 2015, **115**, 10081.
2 (*a*) D. Stock, *Science*, 1999, **286**, 1700; (*b*) H. Terashima, S. Kojima and M. Homma, *Int. Rev. Cell Mol. Biol.*, 2008, **270**, 39.
3 S. Kassem, T. van Leeuwen, A. S. Lubbe, M. R. Wilson, B. L. Feringa and D. A. Leigh, *Chem. Soc. Rev.*, 2017, **46**, 2592.
4 N. Koumura, R. W. Zijlstra, R. A. van Delden, N. Harada and B. L. Feringa, *Nature*, 1999, **401**, 152.
5 (*a*) P. Stacko, J. C. M. Kistemaker, T. van Leeuwen, M. C. Chang, E. Otten and B. L. Feringa, *Science*, 2017, **356**, 964; (*b*) M. Baroncini and A. Credi, *Science*, 2017, **356**, 906.
6 H. Iwamura and K. Mislow, *Acc. Chem. Res.*, 1988, **21**, 175.
7 G. S. Kottas, L. I. Clarke, D. Horinek and J. Michl, *Chem. Rev.*, 2005, **105**, 1281.
8 (*a*) W. R. Browne and B. L. Feringa, *Nat. Nanotechnol.*, 2006, **1**, 25; (*b*) B. L. Feringa, *Angew. Chem., Int. Ed.*, 2017, **56**, 11060.
9 W. Setaka, T. Nirengi, C. Kabuto and M. Kira, *J. Am. Chem. Soc.*, 2008, **130**, 15762.
10 K. Sanada, H. Ube and M. Shionoya, *J. Am. Chem. Soc.*, 2016, **138**, 2945.
11 H. Ube, Y. Yasuda, H. Sato and M. Shionoya, *Nat. Commun.*, 2017, **8**, 14296.
12 (*a*) J. D. Crowley, I. M. Steele and B. Bosnich, *Chem. – Eur. J.*, 2006, **12**, 8935; (*b*) A. Iordache, M. Oltean, A. Milet, F. Thomas, B. Baptiste, E. Saint-Aman and C. Bucher, *J. Am. Chem. Soc.*, 2012, **134**, 2653.
13 S. Ogi, T. Ikeda, R. Wakabayashi, S. Shinkai and M. Takeuchi, *Chem. – Eur. J.*, 2010, **16**, 8285.
14 J. Schummer, *Found. Chem.*, 2006, **8**, 53.
15 (*a*) P. L. Anelli, N. Spencer and J. F. Stoddart, *J. Am. Chem. Soc.*, 1991, **113**, 5131; (*b*) A. Altieri, F. G. Gatti, E. R. Kay, D. A. Leigh, D. Martel, F. Paolucci, A. M. Slawin and J. K. Wong, *J. Am. Chem. Soc.*, 2003, **125**, 8644; (*c*) F. Coutrot and E. Busseron, *Chem. – Eur. J.*, 2008, **14**, 4784.
16 (*a*) E. A. Neal and S. M. Goldup, *Chem. Commun.*, 2014, **50**, 5128; (*b*) C. A. Schalley, K. Beizai and F. Vögtle, *Acc. Chem. Res.*, 2001, **34**, 465.
17 (*a*) P. R. Ashton, P. J. Campbell, P. T. Glink, D. Philp, N. Spencer, J. F. Stoddart, E. J. T. Chrystal, S. Menzer, D. J. Williams and P. A. Tasker, *Angew. Chem., Int. Ed. Engl.*,

Published on 24 October 2018. Downloaded by Freie Universitaet Berlin on 11/30/2020 6:21:37 PM.

1995, **34**, 1865; (*b*) N. Yamaguchi and H. W. Gibson, *Angew. Chem., Int. Ed.*, 1999, **38**, 143; (*c*) T. J. Hubin and D. H. Busch, *Coord. Chem. Rev.*, 2000, **200–202**, 5; (*d*) X. Fu, Q. Zhang, S. J. Rao, D. H. Qu and H. Tian, *Chem. Sci.*, 2016, **7**, 1696; (*e*) S. J. Rao, Q. Zhang, J. Mei, X. H. Ye, C. Gao, Q. C. Wang, D. H. Qu and H. Tian, *Chem. Sci.*, 2017, **8**, 6777.

18 (*a*) M. E. Belowich, C. Valente, R. A. Smaldone, D. C. Friedman, J. Thiel, L. Cronin and J. F. Stoddart, *J. Am. Chem. Soc.*, 2012, **134**, 5243; (*b*) A. J. Avestro, D. M. Gardner, N. A. Vermeulen, E. A. Wilson, S. T. Schneebeli, A. C. Whalley, M. E. Belowich, R. Carmieli, M. R. Wasielewski and J. F. Stoddart, *Angew. Chem., Int. Ed.*, 2014, **53**, 4442.

19 (*a*) M. B. Nielsen, C. Lomholt and J. Becher, *Chem. Soc. Rev.*, 2000, **29**, 153; (*b*) C. P. Collier, G. Mattersteig, E. W. Wong, Y. Luo, K. Beverly, J. Sampaio, F. M. Raymo, J. F. Stoddart and J. R. Heath, *Science*, 2000, **289**, 1172; (*c*) J. L. Segura and N. Martín, *Angew. Chem., Int. Ed.*, 2001, **40**, 1372; (*d*) J. O. Jeppesen, M. B. Nielsen and J. Becher, *Chem. Rev.*, 2004, **104**, 5115; (*e*) D. Canevet, M. Sallé, G. Zhang, D. Zhang and D. Zhu, *Chem. Commun.*, 2009, 2245.

20 (*a*) D. L. Coffen and P. E. Garrett, *Tetrahedron Lett.*, 1969, **10**, 2043; (*b*) S. Hünig, G. Kießlich, H. Quast and D. Scheutzow, *Liebigs Ann. Chem.*, 1973, 310.

21 Q. Zhang, D. H. Qu, Q. C. Wang and H. Tian, *Angew. Chem., Int. Ed.*, 2015, **54**, 15789.

22 S. V. Rosokha and J. K. Kochi, *J. Am. Chem. Soc.*, 2007, **129**, 828.

23 V. Khodorkovsky, L. Shapiro, P. Krief, A. Shames, G. Mabon, A. Gorgues and M. Giffard, *Chem. Commun.*, 2001, 2736.

24 (*a*) A. Y. Ziganshina, Y. H. Ko, W. S. Jeon and K. Kim, *Chem. Commun.*, 2004, 806; (*b*) M. Yoshizawa, K. Kumazawa and M. Fujita, *J. Am. Chem. Soc.*, 2005, **127**, 13456.

25 P. T. Chiang, N. C. Chen, C. C. Lai and S. H. Chiu, *Chem. – Eur. J.*, 2008, **14**, 6546.

26 I. Aprahamian, J. C. Olsen, A. Trabolsi and J. F. Stoddart, *Chem. – Eur. J.*, 2008, **14**, 3889.

27 J. M. Spruell, A. Coskun, D. C. Friedman, R. S. Forgan, A. A. Sarjeant, A. Trabolsi, A. C. Fahrenbach, G. Barin, W. F. Paxton, S. K. Dey, M. A. Olson, D. Benitez, E. Tkatchouk, M. T. Colvin, R. Carmielli, S. T. Caldwell, G. M. Rosair, S. G. Hewage, F. Duclairoir, J. L. Seymour, A. M. Slawin, W. A. Goddard III, M. R. Wasielewski, G. Cooke and J. F. Stoddart, *Nat. Chem.*, 2010, **2**, 870.

28 (*a*) H. V. Schröder, H. Hupatz, A. J. Achazi, S. Sobottka, B. Sarkar, B. Paulus and C. A. Schalley, *Chem. – Eur. J.*, 2017, **23**, 2960; (*b*) H. V. Schröder, S. Sobottka, M. Nössler, H. Hupatz, M. Gaedke, B. Sarkar and C. A. Schalley, *Chem. Sci.*, 2017, **8**, 6300; (*c*) H. V. Schröder, J. M. Wollschläger and C. A. Schalley, *Chem. Commun.*, 2017, **53**, 9218.

29 H. Nagai, Y. Suzaki and K. Osakada, *Eur. J. Inorg. Chem.*, 2014, **2014**, 4376.

30 H. V. Schröder, F. Witte, M. Gaedke, S. Sobottka, L. Suntrup, H. Hupatz, A. Valkonen, B. Paulus, K. Rissanen, B. Sarkar and C. A. Schalley, *Org. Biomol. Chem.*, 2018, **16**, 2741.

31 T. Matsumura, F. Ishiwari, Y. Koyama and T. Takata, *Org. Lett.*, 2010, **12**, 3828.

32 (*a*) C. A. Hunter and J. K. M. Sanders, *J. Am. Chem. Soc.*, 1990, **112**, 5525; (*b*) C. R. Martinez and B. L. Iverson, *Chem. Sci.*, 2012, **3**, 2191.

33 (*a*) D. L. Sun, S. V. Rosokha, S. V. Lindeman and J. K. Kochi, *J. Am. Chem. Soc.*, 2003, **125**, 15950; (*b*) V. A. Azov, R. Gómez and J. Stelten, *Tetrahedron*, 2008, **64**, 1909; (*c*) M. Hasegawa, K. Daigoku, K. Hashimoto, H. Nishikawa and M. Iyoda, *Bull. Chem. Soc. Jpn.*, 2012, **85**, 51.

34 (*a*) K. D. Demadis, C. M. Hartshorn and T. J. Meyer, *Chem. Rev.*, 2001, **101**, 2655; (*b*) M. B. Robin and P. Day, *Adv. Inorg. Chem. Radiochem.*, 1968, **10**, 247.

35 (*a*) Y. Wang, S. Mendoza and A. E. Kaifer, *Inorg. Chem.*, 1998, **37**, 317; (*b*) W. S. Jeon, K. Moon, S. H. Park, H. Chun, Y. H. Ko, J. Y. Lee, E. S. Lee, S. Samal, N. Selvapalam, M. V. Rekharsky, V. Sindelar, D. Sobransingh, Y. Inoue, A. E. Kaifer and K. Kim, *J. Am. Chem. Soc.*, 2005, **127**, 12984.

36 J. M. Lu, S. V. Rosokha and J. K. Kochi, *J. Am. Chem. Soc.*, 2003, **125**, 12161.

37 A. Coskun, J. M. Spruell, G. Barin, A. C. Fahrenbach, R. S. Forgan, M. T. Colvin, R. Carmieli, D. Benitez, E. Tkatchouk, D. C. Friedman, A. A. Sarjeant, M. R. Wasielewski, W. A. Goddard III and J. F. Stoddart, *J. Am. Chem. Soc.*, 2011, **133**, 4538.

38 (*a*) F. A. Walker, H. Boi Hanh, W. R. Scheidt and S. R. Osvath, *J. Am. Chem. Soc.*, 1986, **108**, 5288; (*b*) C. Gouverd, F. Biaso, L. Cataldo, T. Berclaz, M. Geoffroy, E. Levillain, N. Avarvari, M. Fourmigué, F. X. Sauvage and C. Wartelle, *Phys. Chem. Chem. Phys.*, 2005, **7**, 85.

39 (*a*) G. Barin, A. Coskun, D. C. Friedman, M. A. Olson, M. T. Colvin, R. Carmielli, S. K. Dey, O. A. Bozdemir, M. R. Wasielewski and J. F. Stoddart, *Chem. – Eur. J.*, 2011, **17**, 213; (*b*) M. Hasegawa, J.-I. Takano, H. Enozawa, Y. Kuwatani and M. Iyoda, *Tetrahedron Lett.*, 2004, **45**, 4109.

40 (*a*) M. Iyoda, K. Hara, Y. Kuwatani and S. Nagase, *Org. Lett.*, 2000, **2**, 2217; (*b*) M. Iyoda, M. Hasegawa and Y. Miyake, *Chem. Rev.*, 2004, **104**, 5085; (*c*) M. Hasegawa, K. Nakamura, S. Tokunaga, Y. Baba, R. Shiba, T. Shirahata, Y. Mazaki and Y. Misaki, *Chem. – Eur. J.*, 2016, **22**, 10090.

41 (*a*) M. Lohse, K. Nowosinski, N. L. Traulsen, A. J. Achazi, L. K. S. von Krbek, B. Paulus, C. A. Schalley and S. Hecht, *Chem. Commun.*, 2015, **51**, 9777; (*b*) K. Nowosinski, L. K. S. von Krbek, N. L. Traulsen and C. A. Schalley, *Org. Lett.*, 2015, **17**, 5076; (*c*) L. K. S. von Krbek, A. J. Achazi, S. Schoder, M. Gaedke, T. Biberger, B. Paulus and C. A. Schalley, *Chem. – Eur. J.*, 2017, **23**, 2877.

42 E. Hanozin, B. Mignolet, D. Morsa, D. Sluysmans, A. S. Duwez, J. F. Stoddart, F. Remacle and E. De Pauw, *ACS Nano*, 2017, **11**, 10253.

 This journal is © The Royal Society of Chemistry 2018

43 (*a*) M. Capdevila-Cortada and J. J. Novoa, *Chem. – Eur. J.*, 2012, **18**, 5335; (*b*) M. Fumanal, M. Capdevila-Cortada and J. J. Novoa, *Phys. Chem. Chem. Phys.*, 2017, **19**, 3807.
44 (*a*) J. Dale and P. O. Kristiansen, *J. Chem. Soc. D*, 1971, 670; (*b*) D. K. Frantz, A. Linden, K. K. Baldridge and J. S. Siegel, *J. Am. Chem. Soc.*, 2012, **134**, 1528; (*c*) C. I. Ratcliffe, J. A. Ripmeester, G. W. Buchanan and J. K. Denike, *J. Am. Chem. Soc.*, 1992, **114**, 3294; (*d*) V. N. Vukotic, K. J. Harris, K. Zhu, R. W. Schurko and S. J. Loeb, *Nat. Chem.*, 2012, **4**, 456.

Published on 24 October 2018. Downloaded by Freie Universitaet Berlin on 11/30/2020 6:21:37 PM.

Electronic Supplementary Material (ESI) for Nanoscale.
This journal is © The Royal Society of Chemistry 2018

Electronic Supplementary Information (ESI†)

Switchable synchronisation of pirouetting motions in a redox active [3]rotaxane

Hendrik V. Schröder,[a] Amel Mekic,[a] Henrik Hupatz,[a] Sebastian Sobottka,[b] Felix Witte,[a] Leonhard H. Urner,[a] Marius Gaedke,[a] Kevin Pagel,[ac] Biprajit Sarkar,[b] Beate Paulus[a] and Christoph A. Schalley[a]*

[a] Institut für Chemie und Biochemie, Freie Universität Berlin
Takustraße 3, 14195 Berlin, Germany.
[b] Institut für Chemie und Biochemie, Freie Universität Berlin
Fabeckstraße 34/36, 14195 Berlin, Germany.
[c] Fritz Haber Institute of the Max Planck Society, Department of Molecular Physics,
Faradayweg 4-6, Berlin, 14195 Berlin, Germany.
*Corresponding author e-mail: c.schalley@fu-berlin.de

Table of contents

1. Experimental and synthetic details

1.1. General methods

All reagents and solvents were obtained from commercial sources and used without further purification. Dry solvents were purchased from Acros Organics. Monomer **exTTF**,[S1] ditosylate **A**,[S2] bis(4-(prop-2-yn-1-yloxy)benzyl)-ammonium hexafluorophosphate,[S3] 4-(prop-2-yn-1-yloxy)benzaldehyde[S4] and 2,6-dimethoxybenzonitrile oxide (**S1**)[S5] were synthesised according to literature procedures. Thin-layer chromatography was performed on silica gel-coated plates with fluorescent indicator F254 (Merck). For column chromatography, silica gel (0.04–0.063 mm, Merck) was used. ^{1}H and ^{13}C NMR experiments were performed on a JEOL ECX 400, JEOL ECP 500 or a Bruker AVANCE 700 MHz instrument. VT NMR experiments were performed on a JEOL ECS 400 MHz spectrometer. Solvent residue signals were used as the internal standard. All shifts are reported in ppm and NMR multiplicities are abbreviated as s (singlet), d (doublet), t (triplet), m (multiplet) and br (broad). Coupling constants *J* are reported in Hertz. Solvents and impurities are marked with an asterisk. High-resolution ESI mass spectra were measured on an Agilent 6210 ESI-TOF instrument (Agilent Technologies). Infrared multiphoton dissociation (IRMPD) experiments were performed on an Ionspec QFT-7 ESI-FTICR mass spectrometer from Varian Inc. equipped with a Micromass/Waters Z-spray electrospray ion source. IR laser pulses of 1000 ms width and 15–25 % laser intensity were applied to initiate fragmentation. HPLC grade solvents were used with a flow rate of 2–4 µL/min. Melting points were determined on a SMP 30 (Stuart) instrument. Melting points are uncorrected. EPR spectra at X-band frequency (ca. 9.5 GHz) were obtained with a Magnettech MS-5000 benchtop EPR spectrometer equipped with a rectangular TE 102 cavity and TC HO4 temperature controller. The measurements were carried out in synthetic quarz glass tubes. Dry and freshly distilled solvents (CH_2Cl_2 and CH_3CN) were used. Sample preparation and measurements were performed under nitrogen. UV/Vis spectra were recorded on a Varian Cary 50 Bio Photospectrometer equipped with a xenon lamp or on an Avantes spectrometer with a light source (AvaLight-DH-S-Bal), a UV/Vis detector (AvaSpec-ULS2048), and a NIR detector (AvaSpec-NIR256-TEC). Solvents with HPLC grade and Suprasil glass cuvettes with a path-length of 1 cm were used. Cyclic voltammetry was performed on an Autolab PGSTAT302N potentiostat using a three-electrode configuration: a freshly polished glassy carbon working electrode, a platinum wire counter electrode and a silver wire pseudoreference electrode. All measurements were conducted twice and with a broad range of different scan rates (25–1000 mV s^{-1}) to ensure electrochemical reversibility of the processes. The decamethylferrocene/ decamethylferrocenium couple was used as internal reference and the determined potentials are given against the ferrocene/ferrocenium (Fc/Fc^{+}) couple. Dry and argon purged solvents were used.

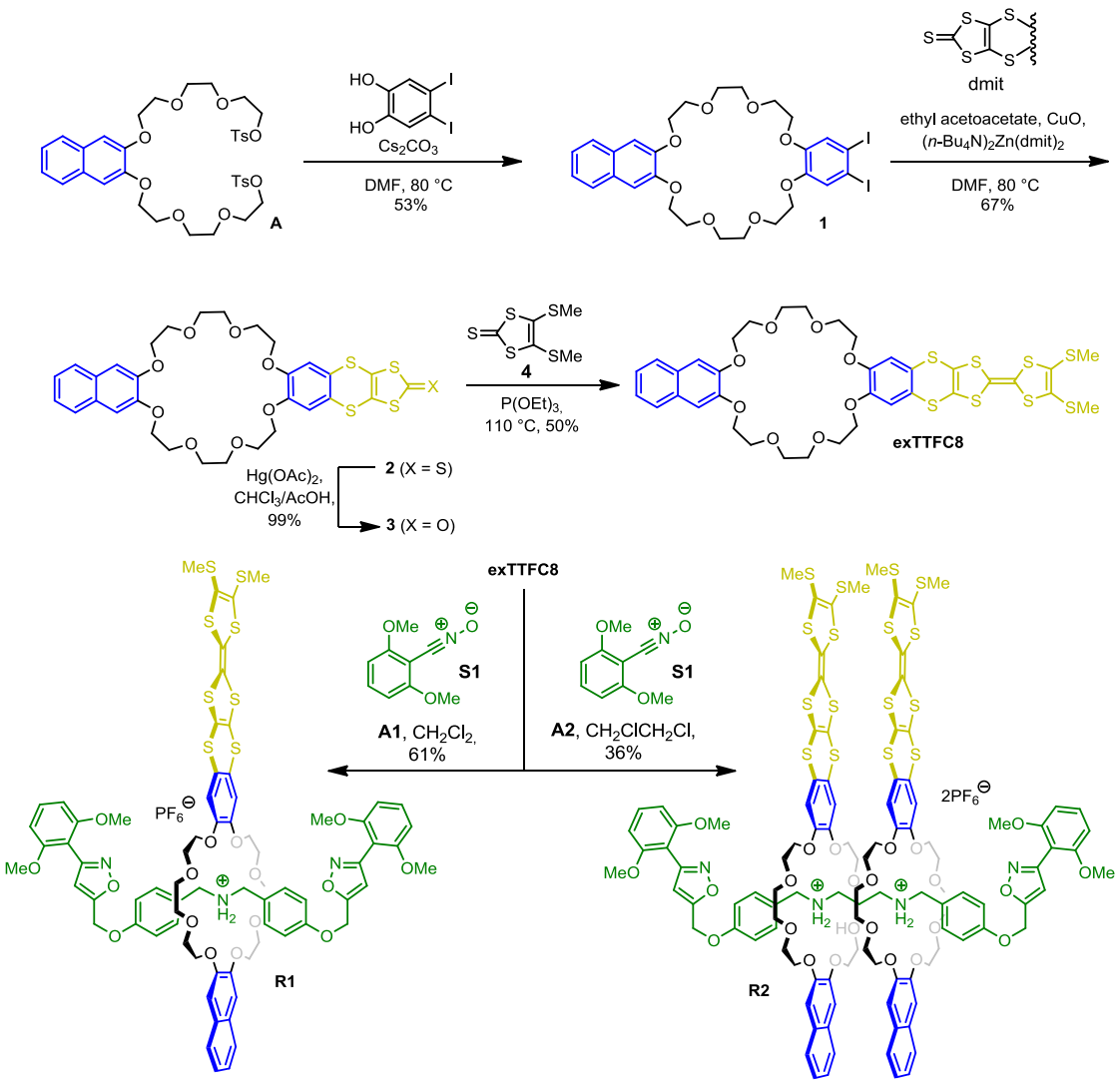

Scheme S1 General synthesis route to macrocycle **exTTFC8** and rotaxanes **R2** and **R3**.

1.2. Synthesis of macrocycle exTTFC8

Diiodide 1

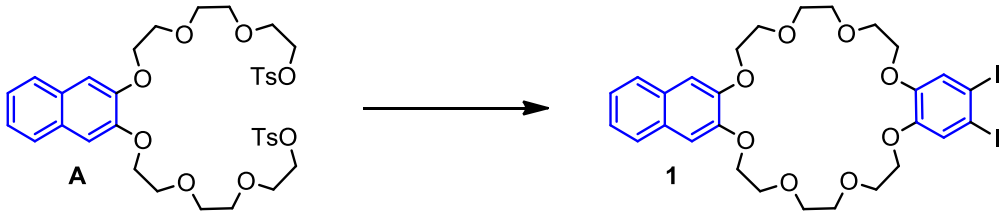

A solution of 4,5-diiodobenzene-1,2-diol (494 mg, 1.36 mmol) in dimethylformamide (DMF, 20 mL) was slowly added to a dispersion of Cs_2CO_3 (1.77 g, 5.44 mmol) in DMF (100 mL)

under argon atmosphere. Afterwards, the mixture was heated to 80 °C and a solution of ditosylate **A** (1.000 g, 1.36 mmol) in DMF (150 mL) was added dropwise over 2 h. The reaction was kept at 80 °C for another 2 d, before it was cooled down to room temperature. The solvent was removed *in vacuo* and the residue was dissolved in CH_2Cl_2. After filtering, the filtrate was concentrated *in vacuo* and purified by column chromatography (SiO_2, ethyl acetate/pentane = 3:1). The desired product (540 mg, 0.72 mmol, 53%) was obtained as a white solid. R_f ~ 0.4 in ethyl acetate/pentane = 3:1; m.p. 142 °C; ^{1}H NMR (500 MHz, $CDCl_3$, 298 K): δ = 7.64 (AA'XX' spin system , $^3J_{AA'XX'}$ = 6.1 Hz , 2H, H_{Ar}), 7.32 (AA'XX' spin system, $^3J_{AA'XX'}$ = 6.1 Hz , 2H, H_{Ar}), 7.22 (s, 2H, H_{Ar}), 7.09 (s, 2H, H_{Ar}), 4.27–4.22 (m, 4H, OCH_2), 4.09 – 4.06 (m, 4H, OCH_2), 4.00–3.97 (m, 4H, OCH_2), 3.91–3.85 (m, 8H, OCH_2), 3.83–3.81 (m, 2H, OCH_2) ppm; ^{13}C NMR (126 MHz, $CDCl_3$, 298 K): δ = 149.6, 149.1, 129.4, 126.5, 124.4, 124.1, 108.1, 96.6, 71.6, 71.6, 69.9, 69.8, 69.8, 69.3 ppm; ESI-HRMS: *m/z* calcd for $C_{28}H_{32}O_8I_2$: 788.9818 $[M+K]^+$, found: 788.9850.

Thioketone 2

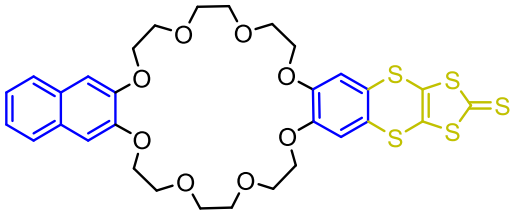

Diiodide **1** (360 mg, 0.48 mmol), $(NEt_4)_2[Zn(dmit)_2]$ (dmit = 1,3-dithiole-2-thione-4,5-dithiolate, 226 mg, 0.24 mmol), Cu_2O (7.2 mg, 0.01 mmol) and ethyl acetoacetate (13 µL, 0.10 mmol) were suspended in DMF (5 mL) and heated to 80 °C overnight. Afterwards, the reaction mixture was cooled down to room temperature and CH_2Cl_2 (20 mL) was added. The resulting mixture was washed with water (4x10 mL) and brine (10 mL) and dried over $MgSO_4$. The crude product was purified by column chromatography (SiO_2, CH_2Cl_2 → CH_2Cl_2/MeOH = 50:1) and the desired product (223 mg, 0.32 mmol, 67%) was obtained as a yellow solid. R_f = 0.4 in CH_2Cl_2/MeOH = 50:1; m.p. >189°C decomposition; ^{1}H NMR (700 MHz, $CDCl_3$. 298 K): δ = 7.64 (AA'XX' spin system, $^3J_{AA'XX'}$ = 6.2 Hz, 2H, HAr), 7.32 (AA'XX' spin system, $^3J_{AA'XX'}$ = 6.2 Hz, 2H, H_{Ar}), 7.09 (s, 2H, H_{Ar}), 6.91 (s, 2H, H_{Ar}), 4.27–4.24 (m, 4H, OCH_2), 4.13–4.10 (m, 4H, OCH_2), 4.01–3.97 (m, 4H, OCH_2), 3.93–3.90 (m, 4H, OCH_2), 3.89–3.86 (m, 4H, OCH_2), 3.84–3.81 (m, 4H, OCH_2) ppm; ^{13}C-NMR (176 MHz, $CDCl_3$, 298 K): δ = 212.8, 149.5, 149.0, 131.9, 129.4, 126.4, 125.7, 124.4, 114.0, 107.9, 71.6, 71.5, 69.9, 69.9, 69.7, 69.3 ppm; ESI-HRMS: *m/z* calcd for $C_{31}H_{32}O_8S_5$: 715.0593 $[M+K]^+$, found: 715.0598.

Ketone 3

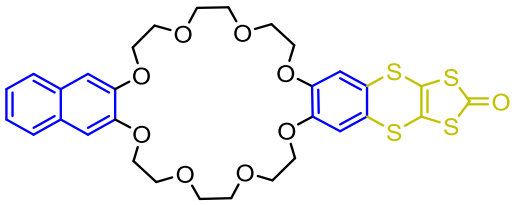

Thione **2** (150 mg, 0.22 mmol) and mercury(II) acetate (210 mg, 0.66 mmol) were dispersed in a mixture of $CHCl_3$ (7 mL) and acetic acid (2 mL) and stirred for 2 days at room temperature. Afterwards, the mixture was filtered through a celite pad, diluted with $CHCl_3$ and washed with saturated aqueous $NaHCO_3$ solution (50 mL) and brine (50 mL). The organic phase was dried over $MgSO_4$ and purified by column chromatography (SiO_2, CH_2Cl_2/Me_2CO = 1:1) to give the desired product (146 mg, 0.22 mmol, 99%) as an off-white solid. R_f = 0.30 in CH_2Cl_2/Me_2CO = 1:1; m. p. 174 °C; ^{1}H NMR (700 MHz, $CDCl_3$, 298 K): δ = 7.64 (m, 2H, H_{Ar}), 7.31 (m, 2H, H_{Ar}), 7.09 (s, 2H, H_{Ar}), 6.92 (s, 2H, H_{Ar}), 4.27–4.24 (m, 4H, OCH_2), 4.13–4.10 (m, 4H, OCH_2), 4.00–3.97 (m, 4H, OCH_2), 3.92–3.90 (m, 4H, OCH_2), 3.88–3.86 (m, 4H, OCH_2), 3.82 (m, 4H, OCH_2) ppm; ^{13}C NMR (176 MHz, $CDCl_3$, 298 K): δ = 191.82, 150.16, 149.62, 129.87, 126.77, 126.34, 124.69, 122.51, 114.48, 108.42, 71.83, 71.80, 70.26, 70.22, 70.11, 69.51 ppm; ESI-HRMS: *m/z* calcd for $C_{31}H_{32}O_9S_4$: 699.0821 $[M+Na]^+$, found: 699.0822.

Macrocycle exTTFC8

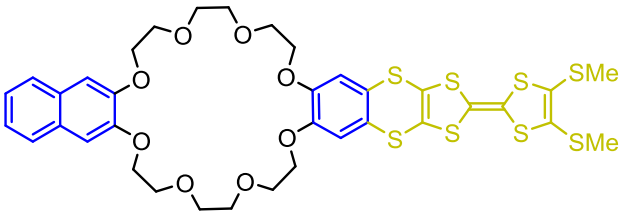

Ketone **3** (105 mg, 155 µmol) and 4,5-bis(methylthio)-1,3-dithiol-2-thione (35.1 mg, 155 µmol) were dissolved in $P(OEt)_3$ (40 mL) and the mixture was heated to 110 °C under argon atmosphere for 3 h. After cooling to room temperature, all volatiles were removed *in vacuo* and the residue was purified by column chromatography (SiO_2, CH_2Cl_2 → CH_2Cl_2/Me_2CO = 20:1). The desired product was obtained as a yellow solid (66.0 mg, 77.2 µmol, 50%). R_f = 0.30 in CH_2Cl_2/MeOH = 100:1; m.p. >189 °C decomposition;^{1}H NMR (700 MHz, CD_2Cl_2): δ = 7.65 (m, 2 H, H_{Ar}), 7.31 (m, 2H, H_{Ar}), 7.12 (s, 2H, H_{Ar}), 6.91 (s, 2H, H_{Ar}), 4.21 (m, 4H, OCH_2), 4.11 (m, 4H, OCH_2), 3.94 (m, 4H, OCH_2), 3.84 (m, 4H, OCH_2), 3.80 (m, 4H, OCH_2), 3.77 (m,

4H, OCH_2), 2.42 (s, 6H, SCH_3) ppm; ^{13}C NMR (176 MHz, CD_2Cl_2): δ = 149.76, 149.63, 129.88, 128.07, 126.97, 126.77, 124.68, 123.96, 116.72, 114.61, 113.33, 108.43, 71.81, 71.76, 70.22, 70.22, 70.13, 69.50, 54.00, 19.64 ppm; ESI-HRMS: *m/z* calcd for $C_{36}H_{38}O_8S_8$: 892.9969 $[M+K]^+$, found: 892.9995.

1.3. Synthesis of rotaxanes R1 and R2

N^1,N^3-bis(4-(prop-2-yn-1-yloxy)benzyl)propane-1,3-diaminium dihexafluorophosphate (A2)

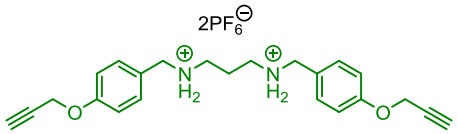

1,3-Diaminopropane (340 µL, 4.0 mmol) and 4-(prop-2-yn-1-yloxy)benzaldehyde (1.28 g, 8.0 mmol) were dissolved in dry EtOH (80 mL) under argon atmosphere and heated to reflux for 6 hours. Afterwards, the mixture was cooled to room temperature and $NaBH_4$ (1.51 g, 40 mmol) was carefully added. The reaction was stirred overnight. Superfluous $NaBH_4$ was quenched by slow addition of a small volume of saturated aqueous $NaHCO_3$ solution. After no gas evolution was observed anymore, all volatiles were removed *in vacuo*. The residue was dissolved in CH_2Cl_2 (50 mL), washed with saturated aqueous $NaHCO_3$ solution (50 mL) and brine (3x50 mL) and dried over $MgSO_4$. After solvent evaporation, the crude product was purified by column chromatograph (SiO_2, CH_2Cl_2 → CH_2Cl_2/MeOH/NEt_3 = 100:10:1). The resulting diamine was transferred to the corresponding hydrochloride by addition of conc. HCl in MeOH (5 mL, 1:1). After drying *in vacuo*, the desired hydrochloride (820 mg, 1.88 mmol) was obtained as a white solid. For the synthesis of the hexafluorophophate salt, part of the hydrochloride (200 mg, 0.46 mmol) and NH_4PF_6 (1.50 g, 9.2 mmol) were dissolved in CH_3CN/water (50 mL, 5:1) and the mixture was stirred for four hours at room temperature. After removing all solvents under reduced pressure, the residue was dissolved in ethyl acetate (100 mL) and washed with water (3x100 mL). Drying over $MgSO_4$ and concentration *in vacuo* yielded the desired product (180 mg, 0.28 mmol, 28% overall yield) as white powder. m.p. 198 °C (decomposition); ^1H NMR (400 MHz, CD_3CN, 298 K): δ = 7.48–7.34 (m, 4H, H_{Ar}), 7.05 (m, 4H, H_{Ar}), 4.77 (d, ^3J = 2.4 Hz, 4H, CH_2), 4.13 (s, 4H, CH_2), 3.15–3.00 (m, 4H, CH_2), 2.84 (t, ^3J = 2.4, 2H, CCH), 2.02 (t, ^3J = 7.8 Hz, 2H, CH_2) ppm; ^{13}C NMR (101 MHz, CD_3CN, 298 K): δ = 159.5, 132.8, 124.0, 116.3, 79.4, 77.2, 56.6, 52.3, 45.5, 23.3 ppm; ESI-HRMS: *m/z* calcd for $C_{23}H_{28}N_2O_2$: 363.2067 $[M-H-2PF_6]^+$, found: 363.2084.

[2]Rotaxane R1

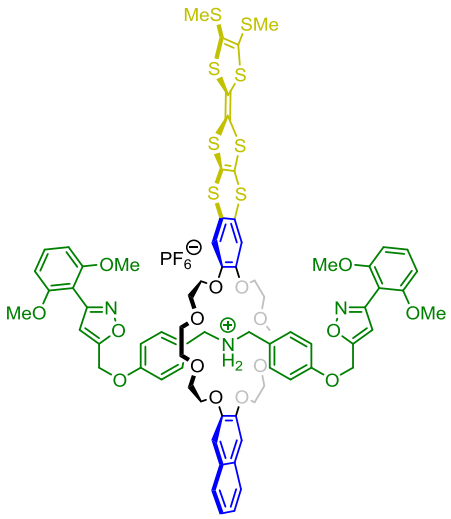

Bis(4-(prop-2-yn-1-yloxy)benzyl)ammonium hexafluorophosphate (4.4 mg, 9.8 µmol) and macrocycle **exTTFC8** (10 mg, 11.7 µmol) were suspended in CH_2Cl_2 (0.5 mL). The mixture was sonicated until the solids were fully dissolved. Afterwards, 2,6-dimethoxybenzonitrile oxide (4.2 mg, 23.4 µmol) was added and the reaction was stirred overnight at 30 °C. The mixture was directly subjected to column chromatography (SiO_2, CH_2Cl_2/MeOH = 250:1). The desired rotaxane **R1** was obtained as an orange solid (10 mg, 6.0 µmol, 61%). R_f = 0.20 in CH_2Cl_2/MeOH = 100:1; ^{1}H NMR (700 MHz, CD_2Cl_2, 298 K): δ = 7.66 (m, 2H, H_{Ar}), 7.44 (s, 2H, NH2), 7.39 (t, ^3J = 8.4 Hz, 2H, H_{Ar}), 7.35 (m, 2H, H_{Ar}), 7.27–7.25 (m, 4H, H_{Ar}), 6.99 (s, 2H, H_{Ar}), 6.83 (s, 2H, H_{Ar}), 6.76– 6.73 (m, 4H, H_{Ar}), 6.67 (d, ^3J = 8.4 Hz, 4H, H_{Ar}), 6.40 (s, 2H, H_{isox}), 4.86–4.81 (m, 4H, OCH_2), 4.62–4.58 (m, 4H, CH_2), 4.18–4.15 (m, 4H, OCH_2), 4.11–4.09 (m, 4H, OCH_2), 3.88–3.86 (m, 4H, OCH_2), 3.82–3.80 (m, 4H, OCH_2), 3.77 (s, 12H, OMe), 3.67–3.64 (m, 4H, OCH_2), 3.60–3.58 (m, 4H, OCH_2), 2.41 (s, 6H, SMe) ppm; ^{13}C NMR (176 MHz, CD_2Cl_2): δ = 166.3, 159.2, 159.1, 157.7, 148.4, 147.8, 131.9, 131.2, 129.7, 128.1, 127.5, 126.9, 125.4, 125.2, 123.8, 117.4, 115.3, 113.2, 112.8, 108.4, 107.4, 107.3, 104.7, 71.6, 71.3, 70.8, 70.7, 69.0, 68.8, 61.3, 56.5, 52.5, 19.6 ppm; ESI-HRMS: *m/z* calcd for $[C_{74}H_{76}N_3O_{16}S_8]^+$: 1518.2991 $[M\text{-}PF_6]^+$, found: 1518.3005.

[3]Rotaxane R2

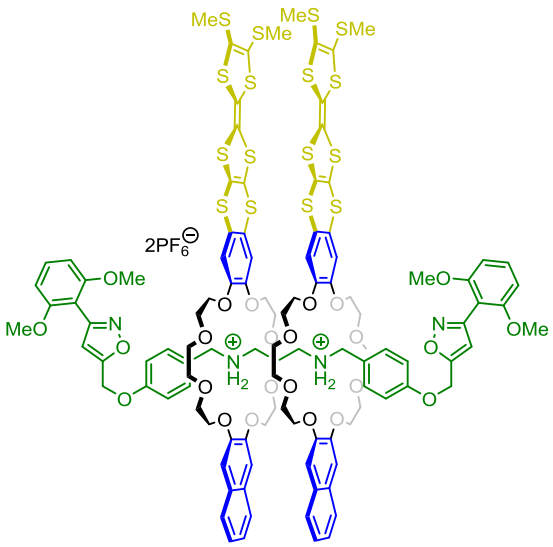

N^1,N^3-Bis(4-(prop-2-yn-1-yloxy)benzyl)propane-1,3-diaminium dihexafluorophosphate (3.3 mg, 5.0 µmol) and macrocycle **exTTFC8** (10 mg, 12.0 µmol) were suspended in 1,2-dichloroethane (1.8 mL). The mixture was sonicated until all solids were completely dissolved. Afterwards, stopper **S1** (2.7 mg, 15.0 µmol) was added and the reaction was stirred for 2 days at room temperature. The mixture was directly subjected to column chromatography (SiO_2, CH_2Cl_2/MeOH = 50:1). The desired product was obtained as an orange solid (5.0 mg, 1.8 µmol, 36%). R_f = 0.5 in SiO_2, CH_2Cl_2/MeOH = 25:1; m.p. >209°C decomposition; ^{1}H NMR (700 MHz, CD_2Cl_2/CD_3CN = 9:1, 298 K): δ = 7.36 (m, 6H, H_{Ar}), 7.11 (m, 8H, NH_2 and H_{Ar}), 7.05 (m, 4H, H_{Ar}), 6.87 (s, 4H, H_{Ar}), 6.72 (s, 4H, H_{Ar}), 6.65 (m, 4H, H_{Ar}), 6.58 (m, 4H, H_{Ar}), 6.32 (s, 2H, $H_{isox.}$), 4.66 (s, 4H, CH_2), 4.37 (m, 4H, $C\underline{H_2}NH_2$), 4.02 (m, 12H, OCH_2), 3.80 (m, 24H, OCH_2), 3.73 (s, 12H, OCH_3), 3.68 (m, 12H, OCH_2), 3.52 (m, 4H, $NH_2C\underline{H_2}CH_2$), 2.38 (s, 12H, SCH_3), 2.02 (m, 2H, $CH_2C\underline{H_2}CH_2$) ppm; ^{13}C NMR (176 MHz, CD_2Cl_2/CD_3CN = 9:1, 298 K): δ = 166.1, 159.1, 158.9, 157.5, 148.0, 147.4, 131.8, 131.2, 129.3, 127.7, 127.5, 126.5, 125.2, 124.1, 123.5, 116.9, 115.2, 113.3, 112.1, 108.8, 107.1, 107.1, 104.5, 71.2, 70.9, 70.6, 70.5, 68.7, 68.5, 61.0, 56.3, 54.0, 45.5, 30.0, 23.0, 19.3 ppm; ESI-HRMS: *m/z* calcd for $C_{113}H_{122}N_4O_{24}S_{16}P_2F_{12}$: 1215.1985 $[M-2PF_6]^{2+}$, found: 1215.1987.

2. Rotaxane characterisation

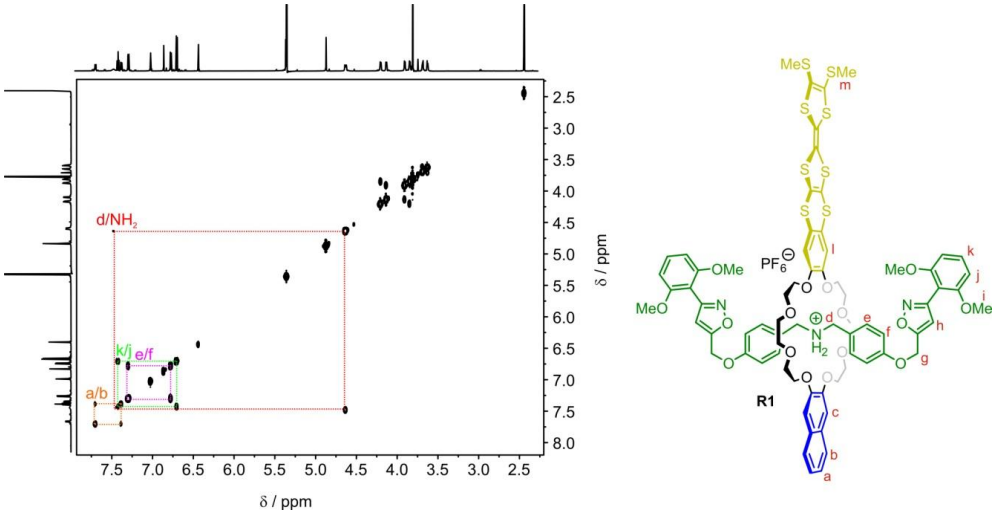

Fig. S1 ^{1}H,^{1}H COSY (700 MHz, CD_2Cl_2, 298 K) of [2]rotaxane **R1** with selected cross peaks confirming the depicted structure.

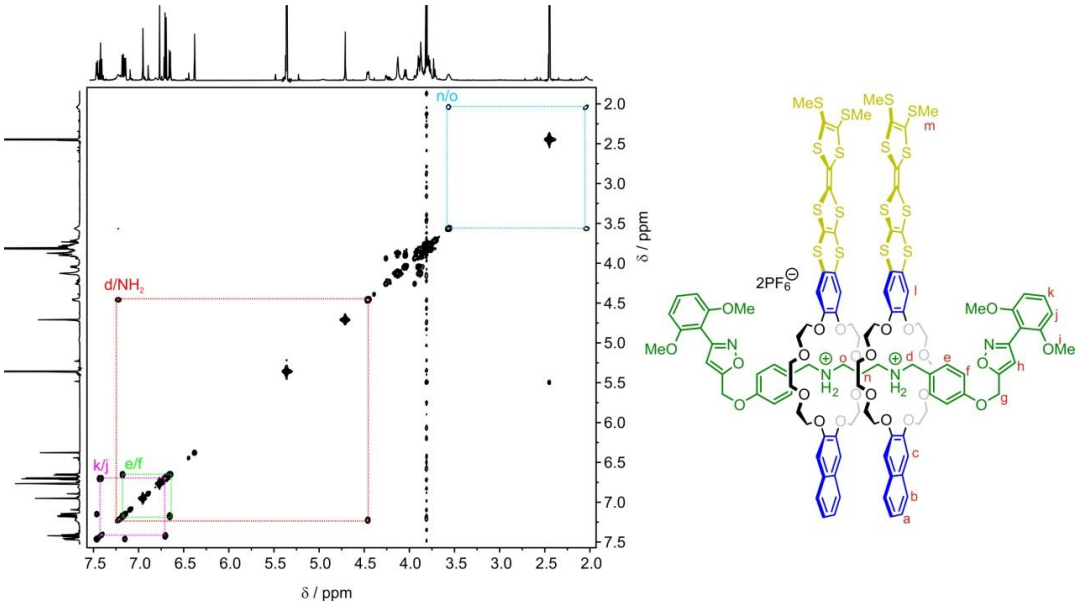

Fig. S2 ^{1}H,^{1}H COSY, (700 MHz, CD_2Cl_2, 298 K) of [3]rotaxane **R2** with selected cross peaks confirming the depicted structure.

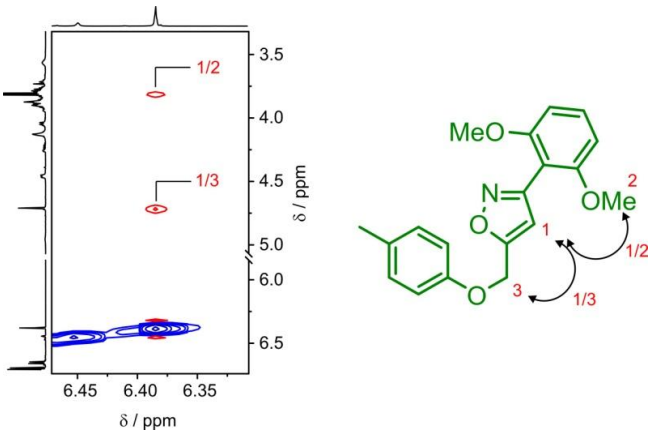

Fig. S3 Partial ^{1}H,^{1}H NOESY, (700 MHz, CD_2Cl_2, 298 K) of [3]rotaxane **R2** showing the cross peaks of the isoxazole signal arising by its spatial coupling with neighbouring protons.

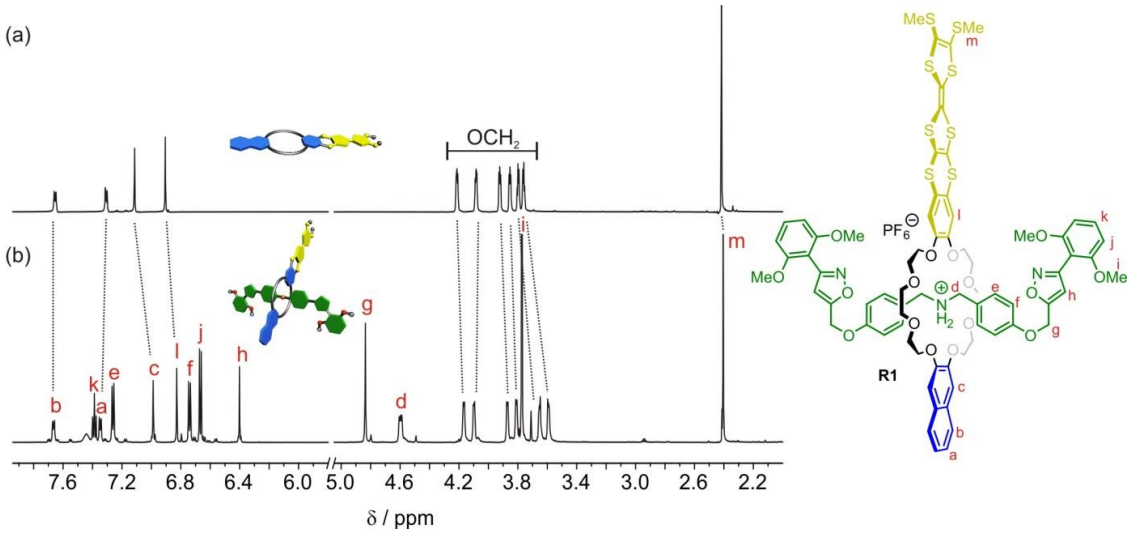

Fig. S4 Stacked ^{1}H NMR spectra (700 MHz, CD_2Cl_2, 298 K) of (a) macrocycle **exTTFC8** and (b) [2]rotaxane **R1** with characteristic signal shifts which can be addressed to a successful rotaxane formation.[S6]

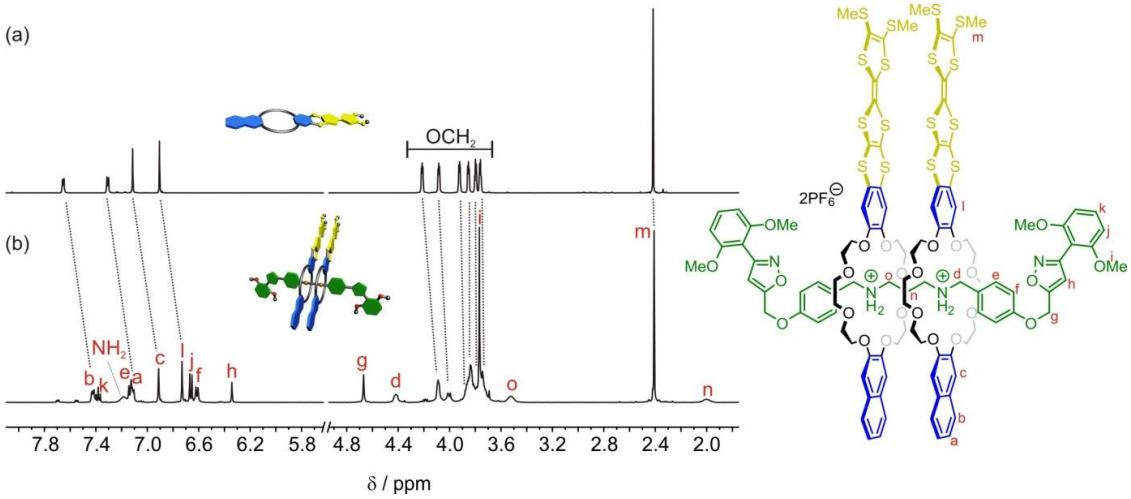

Fig. S5 Stacked ^{1}H NMR spectra (700 MHz, CD_2Cl_2, 298 K) of (a) macrocycle **exTTFC8**, (b) [2]rotaxane **R2** with characteristic signal shifts which can be addressed to a successful rotaxane formation.[S6]

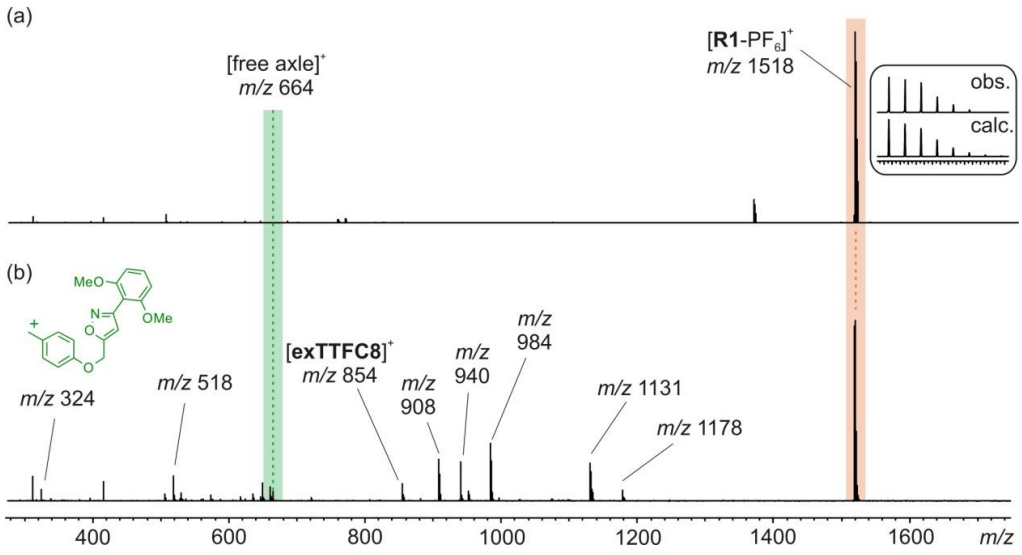

Fig. S6 ESI-FTICR spectra (MeOH, 50 µM, positive mode) of [2]rotaxane **R1**: (a) mass spectrum with base peak *m/z* 1518 (orange area) corresponding to [**R1**-PF_6]$^+$ and (b) mass spectrum after MS/MS IRMPD experiment with selected fragments. The signals *m/z* 854 and *m/z* 324 correspond to the oxidised macrocycle [**exTTFC8**]$^+$ and an axle fragment which results from CN bond breaking in the axle molecule, respectively. The green area indicates the channel for the *m/z* value for the axle without wheel, which is not observed in significant amounts. The fragments between *m/z* 908–1178 are also present in the fragmentation of **R2** and result from different fragmentation channels where an axle piece attacks the wheel. The signal *m/z* 1178, for example, can be addressed to a wheel (*m/z* 854) and the axle fragment (*m/z* 324). This fragmentation pathway speaks in favor of a mechanically interlocked structure as shown previously.[S6]

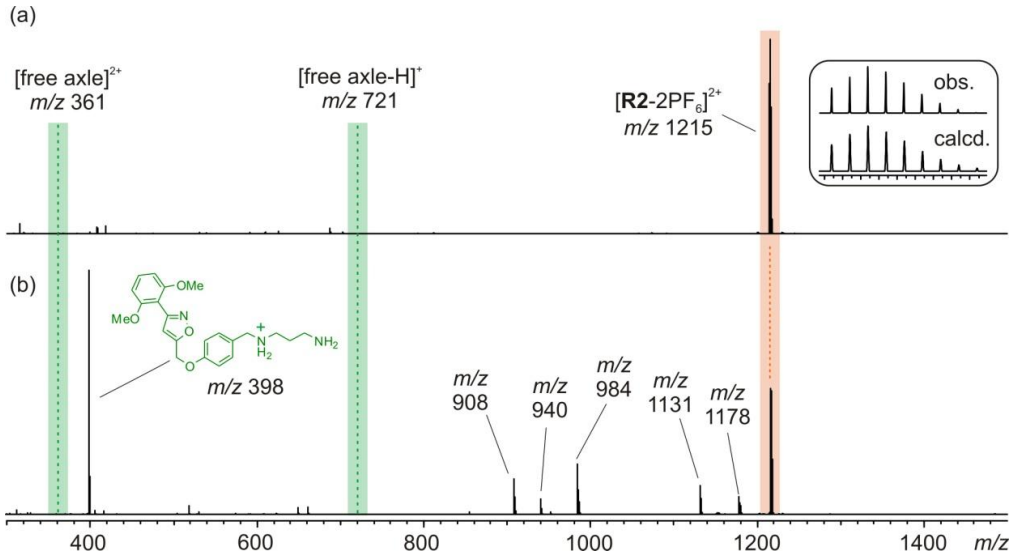

Fig. S7 ESI-FTICR spectra (MeOH, 50 µM, positive mode) of [2]rotaxane **R2**: (a) mass spectrum with base peak *m/z* 1215 (orange area) corresponding to [**R2**-2PF$_6$]$^{2+}$ and (b) mass spectrum after MS/MS IRMPD experiment with selected fragments. The signal *m/z* 398 corresponds to an axle fragment derived by CN bond breaking in the axle molecule. The green area indicates the channel for the *m/z* values for the axle without wheels, which is not observed. The fragments between *m/z* 908–1178 are also present in the fragmentation of **R1** and result from different fragmentation channels where an axle piece attacks the wheel. The signal *m/z* 1178, for example, can be addressed to a wheel (*m/z* 854) and the opposite axle fragment (*m/z* 324). This fragmentation pathway speaks in favor of a mechanically interlocked structure as shown previously.[S6]

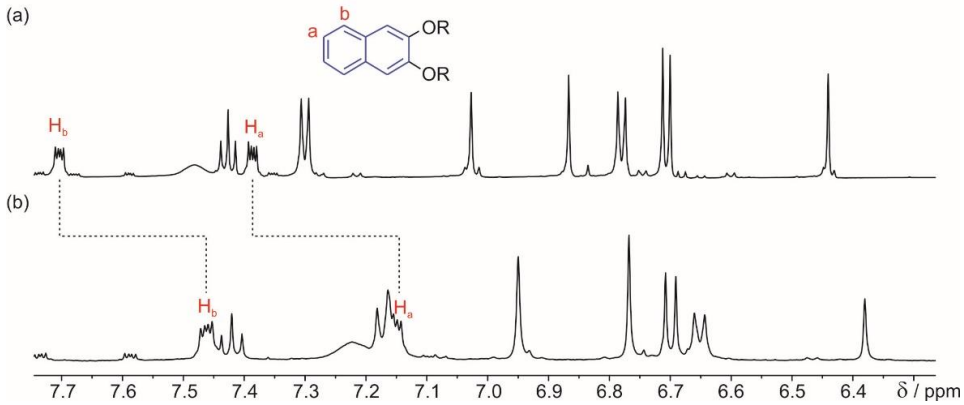

Fig. S8 Comparison of ^{1}H NMR spectra (700 MHz, CD_2Cl_2, 298 K) of (a) [2]rotaxane **R1** and (b) [3]rotaxane **R2** with characteristic signal shifts. For [3]rotaxane **R2**, both naphthalene signals $H_{a/b}$ are significantly shifted by $\Delta\delta$ = -0.24 ppm to higher field. As both rotaxanes are structurally similar, we attribute the quite pronounced upfield shifts of the naphthalene signals H_a and H_b to intramolecular π-stacking interactions between the two wheels in **R2**.

3. UV/Vis-NIR spectroscopy

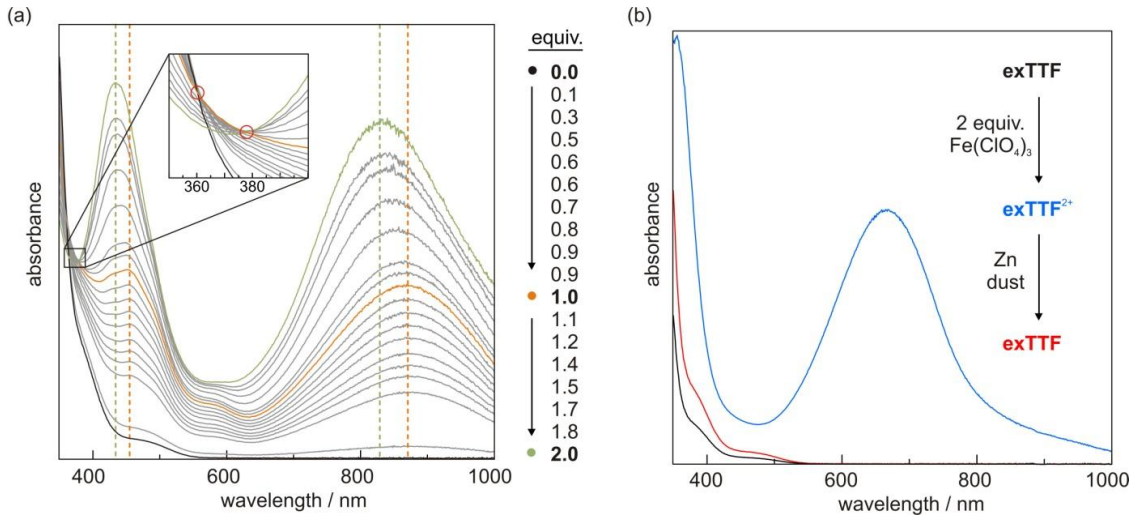

Fig. S9 (a) Photometric UV/Vis titration of **R2** (0.15 mM, CH_3CN, 298 K) by stepwise addition of two equivalents $Fe(ClO_4)_3$. The colored lines corresponds to the UV/Vis spectra of the **R2** (black), **R2**$^{\bullet+}$ (orange) and **R2**$^{2(\bullet+)}$ (green) oxidation state. The dotted lines mark the wavelength of maximum absorbance of the characteristic TTF$^{\bullet+}$ bands. The blue shift going from **R2**$^{\bullet+}$ to **R2**$^{2(\bullet+)}$ is known as "Davydov blue shift" which is characteristic for cofacial TTF radical-cation dimers.[S7] This is additionally supported by two isosbestic points (inset) which are in accordance to two separate transitions **R2**/**R2**$^{\bullet+}$ and **R2**$^{\bullet+}$/**R2**$^{2(\bullet+)}$. (b) UV/Vis spectra of redox-active building block **exTTF** (5 x 10^{-5} M, CH_3CN/CH_2Cl_2 (2:1), 298 K): before oxidation (black), after addition of two equivalents $Fe(ClO_4)_3$ (blue), and (iii) after back reduction by addition of excess Zn dust (red).

4. Isothermal titration calorimetry

ITC titrations were carried out in mixtures of dry 1,2-dichloroethane and acetonitrile (10:1) at 298 K on a TAM III microcalorimeter (Waters GmbH, TA Instruments, Eschborn, Germany). In a typical experiment, a solution of macrocycle (800 µL, 1 mM) was placed in the sample cell and a solution of the ammonium salt (250 µL, 8 mM) was put into a syringe. Titrations consisted of 32 consecutive injections of 8 µL, each with a 15 min interval between injections. Heats of dilution were determined by titration of ammonium salt solutions into the sample cell containing blank solvent and were subtracted from each data set. The heat flow generated in the sample cell is measured as a differential signal between sample and reference cell. Hence, an exothermic event results in a positive and an endothermic in a negative heat flow. The data were analysed using the instrument's internal software package

and fitted with a 1:1 or 1:2 binding model. Each titration was conducted three times and the measured values for *K*, Δ*G* and Δ*H* were averaged.

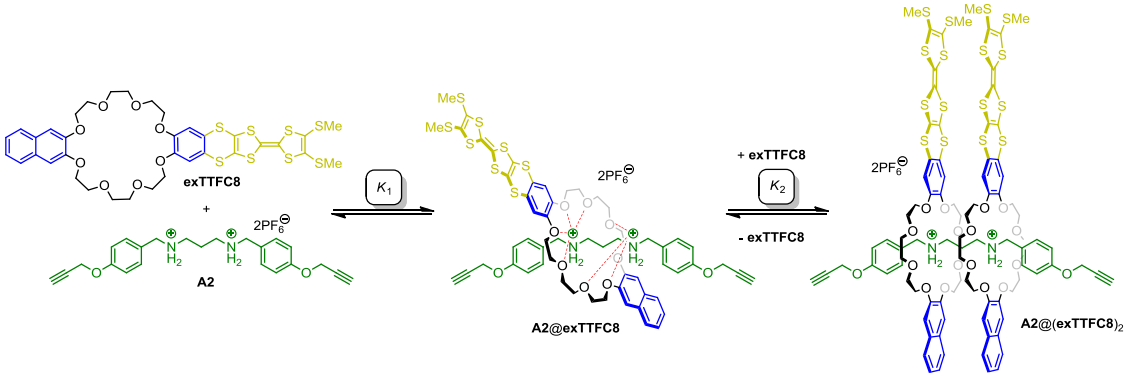

Fig. S10 Schematic representation of the two binding steps (with association constants K_1 and K_2) in the divalent pseudo[3]rotaxane **A2**@(**exTTFC8**)$_2$.

The trends in thermodynamic parameters in the pseudo[3]rotaxanes **A2**@(**exTTFC8**)$_2$ and **A2**@(**DBC8**)$_2$ can be explained by different effects. Considering statistics, a ratio between the binding constants of the monovalent (e.g. **A1**@**exTTFC8**) and divalent complex (e.g. **A2**@(**exTTFC8**)$_2$) of $K = K_1/2 = 2K_2$ is expected if no communication between the two binding sites occurs (non-cooperative binding). However, the ammonium binding station in the divalent axle **A2** is assumed to bind weaker to the wheel than the monovalent one due to the absence of a second polarisable benzylic methylene group. The observation that K_1 is roughly two times *K* is explained in Figure S10. We assume that the first wheel partially binds to both binding stations. Thus, the second ammonium station site is blocked for the second binding event and a lower K_2 value can thus easily be rationalised by the competition between the first and the second macrocycle for the second station. The high enthalpic gain of the second binding event, in case of **exTTFC8** macrocycle, can be attributed to rather strong attractive wheel-wheel interactions. On the other hand, this comes together with the high entropic penalty, as the conformation of the two crown ether macrocycles for additional wheel-wheel interactions is very rigid.

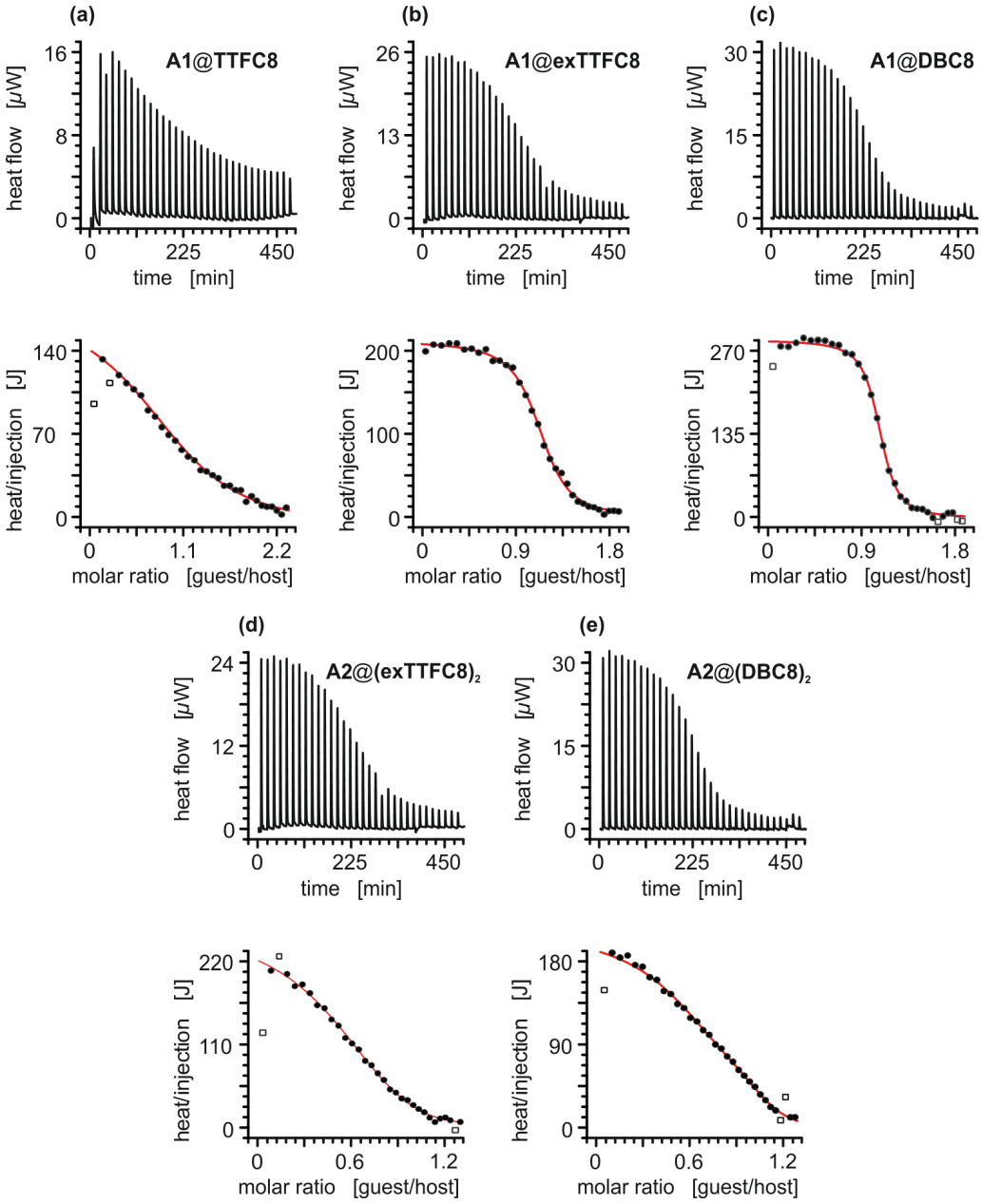

Fig. S11 Titration plots (heat flow versus time and heat/volume versus guest/host ratio) obtained from ITC experiments at 298 K in 1,2-dichloroethane/acetonitrile 10:1 (v/v). Concentrations: (a) host: 0.96 mM, guest: 7.7 mM; (b) host: 1.03 mM, guest: 6.0 mM; (c) host: 1.22 mM, guest: 7.6 mM; (d) host: 0.87 mM, guest: 3.2 mM; (e) host: 0.87 mM, guest: 3.3 mM; Points marked with a non-filled square were not included in the fitting process.

Table S1. Thermodynamic binding data of pseudo[2]- and [3]rotaxane formation between axles (**A1** and **A2**) and macrocycles (**exTTFC8**, **TTFC8**, and **DBC8**) obtained from ITC experiments in 1,2-dichloroethane/acetonitrile (10:1) at 298 K.

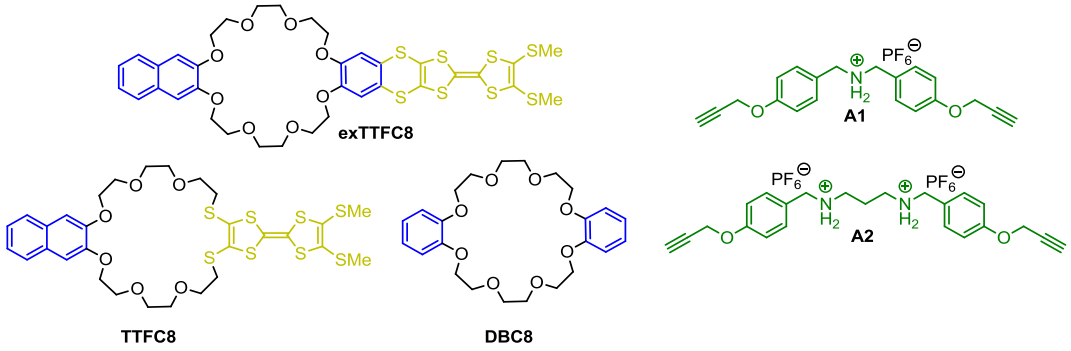

		K_n / 10^3 M^{-1}	ΔG / kJ mol^{-1}	ΔH / kJ mol^{-1}	$T\Delta S$ / kJ mol^{-1}
A1⊂exTTFC8	K_1	50 ± 5	-26.8 ± 0.2	-36.8 ± 1.2	-10.0 ± 1.4
A1⊂TTFC8	K_1	3.8 ± 0.4	-20.4 ± 0.3	-23.3 ± 0.4	-2.8 ± 0.7
A1⊂DBC8	K_1	90 ± 9	-28.3 ± 0.2	-35.7 ± 1.8	-8.0 ± 2.0
A2⊂(exTTFC8)$_2$	K_1	99 ± 30	-28.5 ± 0.7	-32.6 ± 1.0	-4.1 ± 1.7
	K_2	2.4 ± 0.6	-19.3 ± 0.5	-45.4 ± 4.3	-26.1 ± 4.8
A2⊂(DBC8)$_2$	K_1	180 ± 40	-30.0 ± 0.5	-35.6 ± 1.3	-5.6 ± 1.8
	K_2	2.7 ± 0.6	-19.5 ± 0.5	-31.1 ± 4.9	-11.7 ± 5.4

5. Cyclic voltammetry and digital simulations

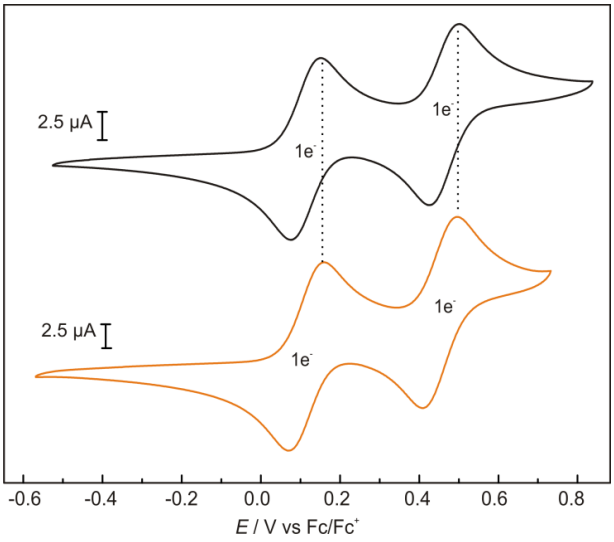

Fig. S12 Cyclic voltammograms (CH_2Cl_2, 298 K, 1 mM, 100 mV s^{-1}) of macrocycle **exTTFC8** (top) and [2]rotaxane **R1** (bottom). The potential were referenced against the ferrocene/ferrocenium (Fc/Fc^+) couple as described earlier.[S8] No significant difference in half-wave potentials is observed for the CH_2Cl_2 measurement which indicates that the charge repulsion between oxidised macrocycle and ammonium axle in **R1** does not play a significant role.

Digital simulations. The cyclic voltammogram of **R2** was simulated with the DigiElch Professional software (ElchSoft GbR) using the Butler-Volmer equation. The surface area of the working electrode was set to 0.14 cm^2 and the starting concentration of **R2** was set to 1 mM. The charge-transfer coefficients α were at the initial value of 0.5 and the heterogeneous rate constants k_s were estimated by the peak separation and set between 0.001 and 0.01 $cm^2\ s^{-1}$. The diffusion coefficient was roughly estimated by fitting the experimental electrochemical data and set to $1x10^{-10}\ m^2\ s^{-1}$.

The electrochemical reaction mechanism of **R2** can be described by an eight-member square scheme as depicted in Scheme 1. In each oxidation state, the electrochemical equilibrium is coupled with a reversible interaction (C1–C4) between the two wheels in **R2**. The wheel-wheel interactions (ΔG) result in an intramolecular binding constant K_{Cm} (m = 1–4). On the left side of the square scheme, the species marked with an asterisk ((**R2**$^{n+}$)*; n = 0, 1, 2, or 4) are representing an unbound situation in which wheel-wheel interaction are absent. The left side (**R2**$^{n+}$) displays the bound situation in which wheel-wheel interactions—such as attractive dispersion interactions or charge repulsion—are present. If all K_{Cm} values would be negligible ($\Delta G \approx 0$), the intramolecular equilibrium is mainly on the side of the non-

interacting species (**R2**$^{n+}$)*. This would be true, for example, if both wheels are widely separated by a long spacer and cannot form any type of interaction. Consequently, the potentials should be similar to those of monovalent [2]rotaxane **R1** (E1*–E3*) where all intramolecular wheel-wheel interaction can be fully excluded. If the K_{Cm} values are significant, however, the **R2**$^{n+}$ states are more populated which results in an altered voltammetric response (E1–E3).

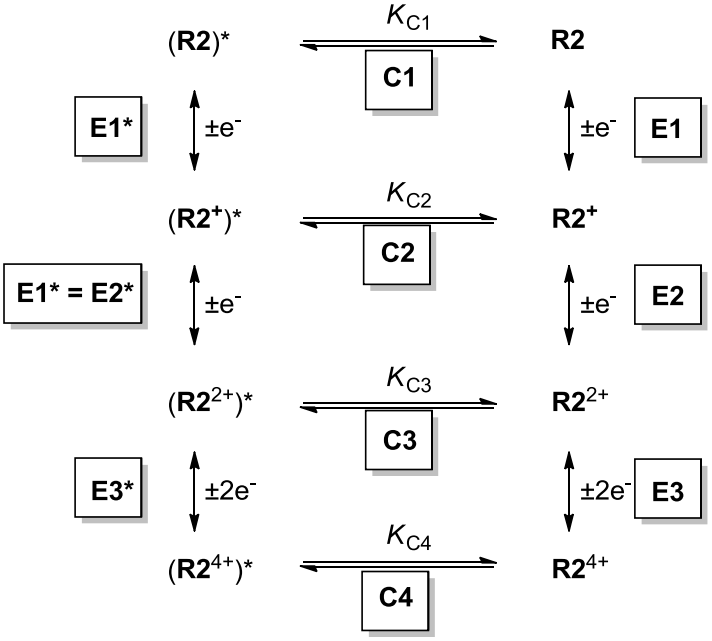

Scheme S2 Square scheme of the electrochemical reaction mechanism of **R2**

The experimental data were fitted according the following equilibria:

(**R2**)*		⇌	**R2**		(C1)
(**R2**$^{\bullet+}$)*		⇌	**R2**$^{\bullet+}$	MV Dimer	(C2)
(**R2**$^{2(\bullet+)}$)*		⇌	**R2**$^{2(\bullet+)}$	RC Dimer	(C3)
(**R2**$^{4+}$)*		⇌	**R2**$^{4+}$		(C4)
(**R2**$^{\bullet+}$)*	+e$^-$	⇌	(**R2**)*	(0.16 V)	(E1*)
(**R2**$^{2+}$)*	+e$^-$	⇌	(**R2**$^{\bullet+}$)*	(0.16 V)	(E2*)
(**R2**$^{4+}$)*	+2e$^-$	⇌	(**R2**$^{2(\bullet+)}$)*	(0.40 V)	(E3*)
R2$^{\bullet+}$	+e$^-$	⇌	**R2**	(0.08 V)	(E1)
R2$^{2(\bullet+)}$	+e$^-$	⇌	**R2**$^{\bullet+}$	(0.19 V)	(E1)
R2^{4+}	+2e$^-$	⇌	**R2**$^{2(\bullet+)}$	(0.48 V)	(E1)

The fitting and simulation process is based on several assumptions (see above) and involves a large number of fitting parameters. It is therefore important to emphasise that the computational model only gives a qualitative picture of the K_{Cm} values (wheel-wheel interactions) in the present situation.[S9] The applied model results in the following qualitative order of binding constants:

$$K_{C2}\ (\mathbf{R2}^{\bullet+}) > K_{C3}\ (\mathbf{R2}^{2(\bullet+)}) > K_{C1}\ (\mathbf{R2}) >> K_{C4}\ (\mathbf{R2}^{4+})$$

Furthermore, the model provides a rough estimate of the constant's relations:

$$K_{C1} \approx K_{C2}/18 \approx K_{C3}/4 \approx K_{C4}/0.01$$

In Figure S12, the effect of varying the absolute value of a binding constant on the simulated cyclic voltammogram is demonstrated using K_{C2} as example. A value of K_{C2} = 10 leads to a voltammetric response obviously different from the experimental one. By going to higher K_{C2} values, the model provides a good simulation at K_{C2} ≈ 1000. However, a further increase does not significantly influence the simulated cyclic voltammogram. This demonstrates that the present computational model, based on the proposed mechanism, can reproduce the experimental data, but is insufficient to determine reliable quantitative thermodynamic and kinetic values.

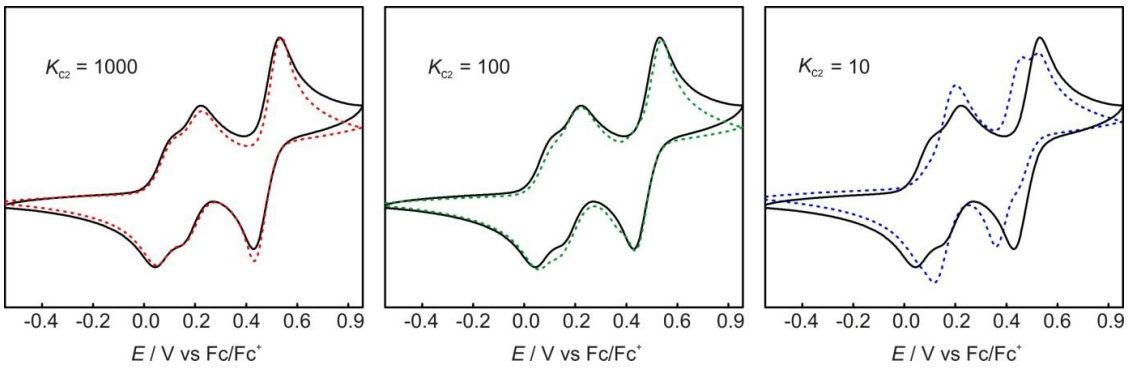

Fig. S13 Experimental cyclic voltammogram of **R2** (black trace, 100 mV s^{-1}, CH_3CN, 1 mM, 298 K) with *n*-Bu_4NPF_6 (0.1 M) as the electrolyte and simulated cyclic voltammograms with different values of the intramolecular binding constant K_{C2}.

6. IM-MS

Instrumentation and CCS determination. Ion mobility analysis was carried out by means of a home-built drift tube ion mobility-mass spectrometry (IM-MS) instrument (Fig. S14).[S10] Briefly, ions are generated by a nanoelectrospray ionisation (nESI) source (positive ion mode) and transferred into an ion funnel from which the ions are pulsed into the drift tube region (length = 80.55 cm). Guided by a weak electric field the ions traverse the drift tubes, which are filled with a neutral buffer gas (helium, 4.18 mbar, 23.4 °C). The time required for the ions to pass the drift tube region depends on their mobility, which in turn is dictated by the molecules' overall shape and charge. Compact molecules undergo fewer collisions with the buffer gas and traverse the drift tube region faster than more extended structures of same mass-to-charge ratio (*m/z*). The ions become subsequently guided by a second ion funnel into high vacuum where the ions are selected according to their *m/z* by means of a quadrupole mass analyser. The arrival time distributions (ATDs) of the ions are recorded by measuring the time that ions of a specific *m/z* need to traverse the drift region. The time which corresponds to the intensity maximum of the ATD was taken as the drift time (t_D). The t_D values were determined for different drift voltages (V_D) and plotted against $1/V_D$. The data were fitted to a linear function (Fig. S15b). As described previously, the slope of the linear fit was used to calculate the mobility of the ion from which finally the collision cross section (CCS) could be determined by using the Mason-Schamp equation.[S11,12]

Calculations. The calculated CCS values of model conformers of [3]rotaxane **R2** without PF_6^- counter ions (**A**–**H**) were obtained by the projection approximation (PA) method.[S13] For the conformer search, we structurally optimised different wheel coconformations (**C**–**H**) using the semi-empirical PM3 method as implemented in the ORCA 3.0.3 program package (Fig. S16).[S14,15] The conformers **A** and **B**—which were further optimised by the MMFF94 force field as implemented in the Avogadro[S15,16] 1.1.1 software—are representing a *syn* coconformation in which the stopper groups are either tightly wrapped around the stacked wheels (**A**) or off-standing (**B**).

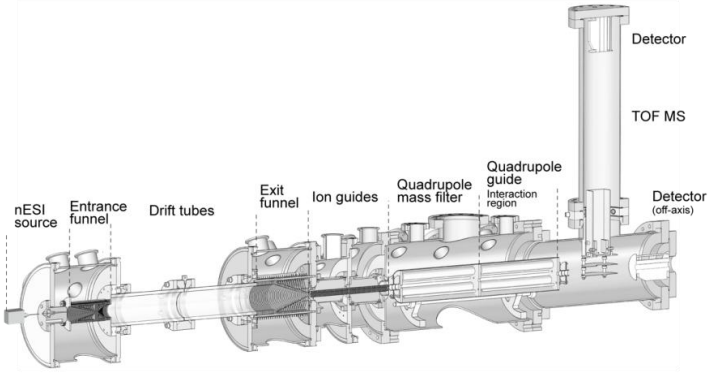

Fig. S14 Instrumental setup of the drift tube ion mobility mass spectrometer.[S10]

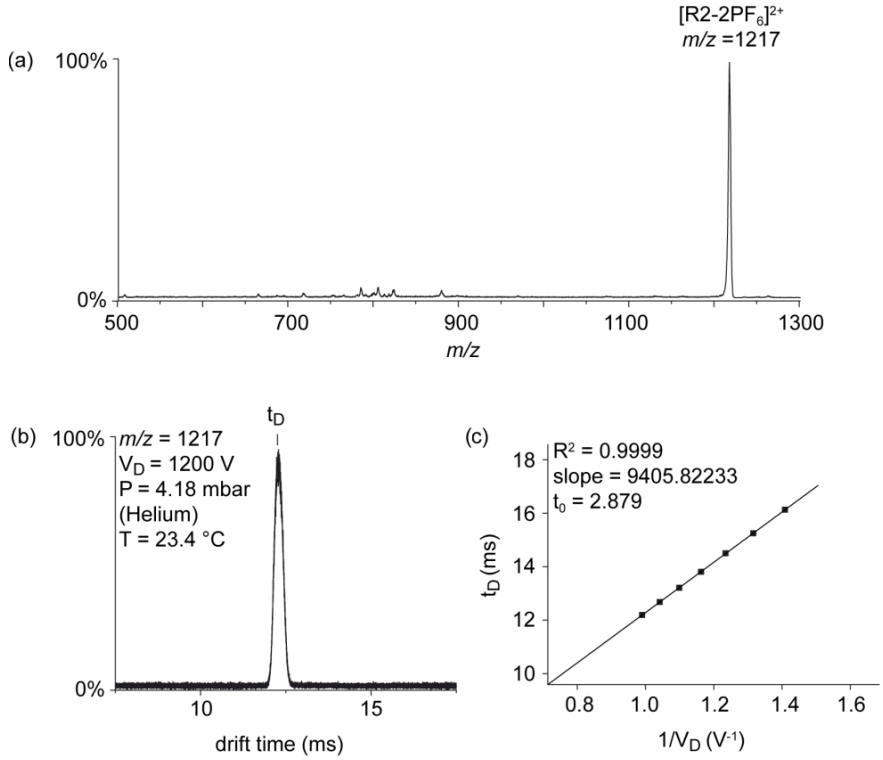

Fig. S15 Overview of IM-MS data: (a) nESI(+)-MS spectrum of **R2** sprayed from CH_2Cl_2, (b) Representative ATD obtained from the [**R2**-2PF_6]$^{2+}$ ion (*m/z* = 1217), (c) Drift time (t_D) values that were determined for the [**R2**-2PF_6]$^{2+}$ ion population at different drift voltages (V_D) and plotted against 1/V_D. The offset (t_0 - interception with the y-axis) is the time required for the ions to travel from the exit of the drift tubes to the detector.

Table S2 Comparison of experimental CCS of [**R2**-2PF_6]$^{2+}$ (*m/z* 1217) to theoretical CCS values of optimised conformer structures (**A**–**H**) depicted in Figure S15.

ion	**CCS_{exp}** / Å^2	**Conformer**	**CCS_{calcd}** / Å^2	**Deviation** / %
[**R2**-2PF_6]$^{2+}$	410	A	412.2	0.5
		B	464.2	13.2
		C	472.2	15.2
		D	472.4	15.2
		E	472.6	15.3
		F	477.7	16.5
		G	491.0	19.8
		H	498.2	21.5

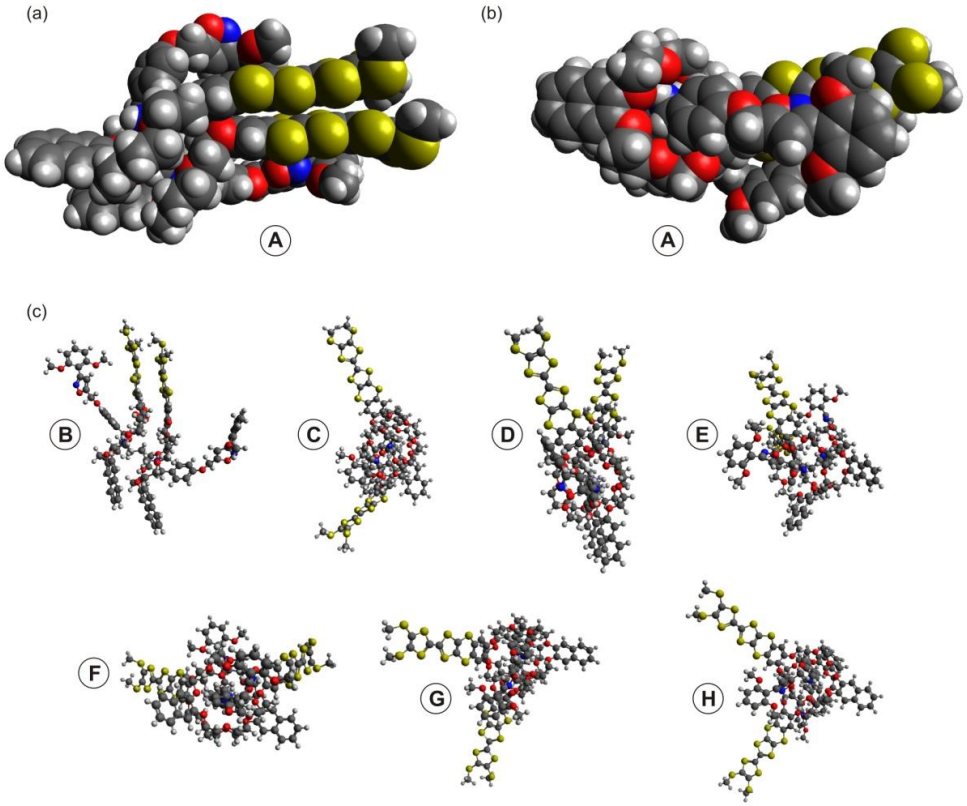

Fig. S16 PM3 (**C**–**H**) or force-field-optimised (**A** and **B**) conformers of [3]rotaxane **R2** without PF_6^- counter ions. (a) Side-view and (b) top-view of conformer **A** with *syn* coconformation of the wheels. The molecules are depicted as Van der Waals sphere models. (c) Ball and stick models of conformers **B**–**H**.

7. VT-NMR

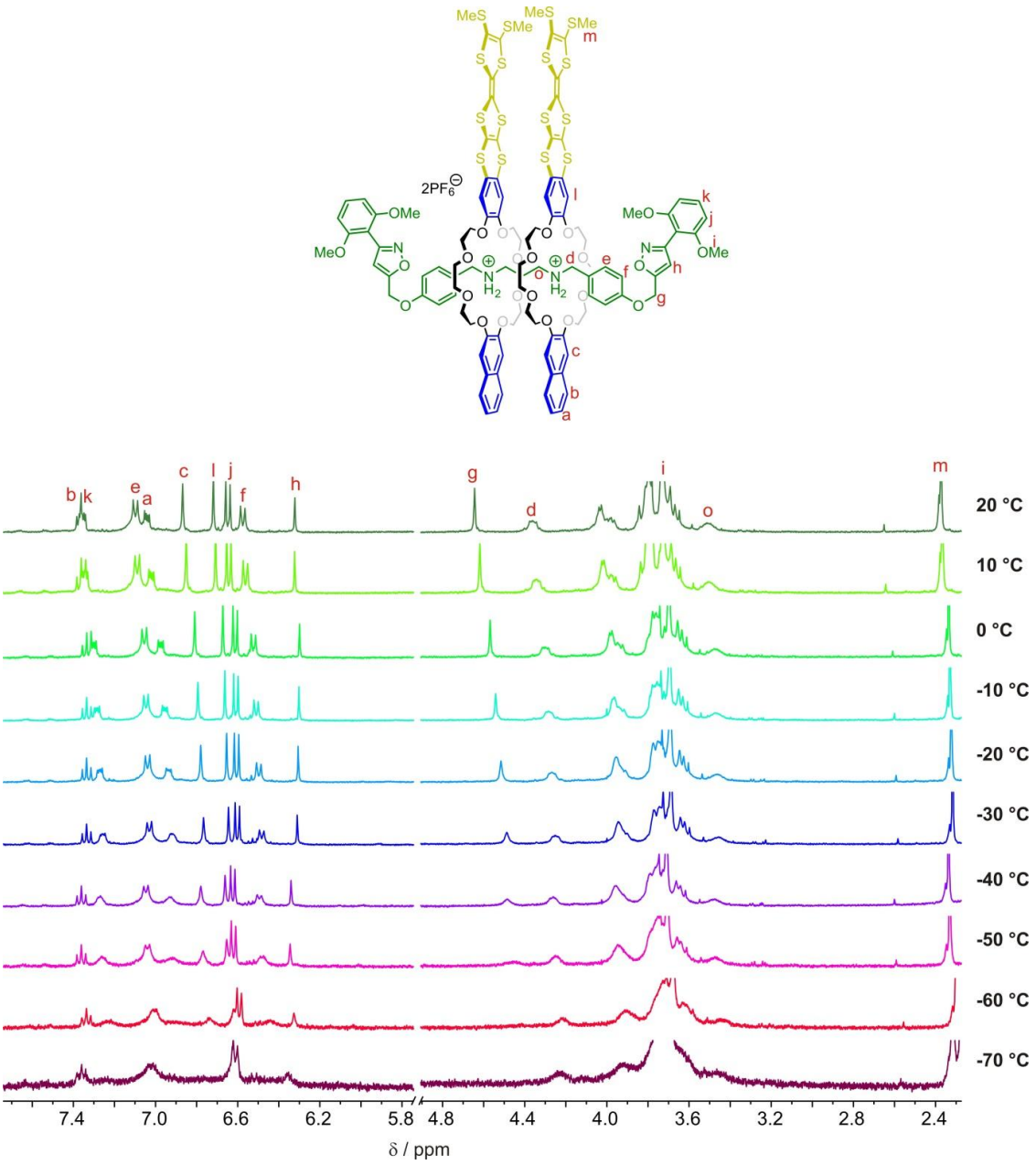

Fig. S17 ^{1}H NMR spectra (400 MHz, CD_2Cl_2/CD_3CN = 9:1, 1.0 mM) of **R2** with gradual cooling from 20 to -70 °C. No signal decoalescence was observed which indicates a fast rotamer interconversion and, thus, a low barrier for the pirouetting motion of the clutched wheels of **R2**.

8. Computational details

Structural ground-state aspects of *syn* and *anti* R2. All calculations were performed using the program package Turbomole (Version 7.0.1).[S18] Structure optimisations were carried out at the TPSS-D3(BJ)/def2-SVP[S19-22] level of DFT employing the RI*J*-approximation[S23,24] together with its multipole acceleration extension (MARIJ)[S25] and regarding implicit solvent effects with COSMO[S26] (ε = 36.64 for MeCN). We used a computer-time-reducing, stopper-less pseudorotaxane analogue. During the first two oxidation processes in *syn* **R2**, the interplanar distance between the TTF units decreases from 3.14 Å to 3.09 Å while the distance between the stacked naphthalene moieties remains rather constant around 3.32 Å. However, the last oxidation in *syn* **R2** results in a significant increase of the TTF-TTF distance (from 3.09 Å to 3.17 Å) and a notable decrease of the naphthalene dimer separation (from 3.32 Å to 3.16 Å). This corresponds to an influence being exerted by the naphthalene moieties on the electronic structure of *syn* **R2** upon the last oxidation process and relates to the unfavorable molecular structure of *syn* **R2**$^{4+}$ in comparison to *anti* **R2**$^{4+}$. In contrast to *syn* **R2**, the interplanar distances in *anti* **R2** are only slightly altered upon oxidation (going from 3.31 Å in *anti* **R2** to 3.27 Å in *anti* **R2**$^{4+}$). Furthermore, *anti* **R2** displays a triply π-stacked system at one side, while the other is a somewhat distorted TTF-naphthalene dimer (see Fig. 7).

Electronic structure and energetic aspects. Single point calculations at the relaxed geometries were performed at the PBE0-D3(BJ)/def2-TZVP[S27] level using COSMO (ε = 36.64 for MeCN). The molecular orbitals obtained at this level of theory suggest that in each oxidation state the valence electronic structure of *syn* **R2** is dominated by the TTF dimer (see Fig. 6 for *syn* **R2**$^{\bullet+}$ and *syn* **R2**$^{2(\bullet+)}$). In *anti* **R2** on the other hand, the single TTF units both participate in the valence electronic structure, albeit without the non-covalent interactions between the moieties. Table S3 compares the calculated ionisation potentials to the experimentally determined values by CV. Since the CV measurement is considerably slower than the intramolecular rearrangements that constitute the switching from *syn* **R2** to *anti* **R2**, the energy of the rearrangement process between the two conformers is taken into account for the first (**R2/R2**$^{\bullet+}$) and third (**R2**$^{2(\bullet+)}$**/R2**$^{4+}$) oxidation process. As seen in Table S3, no rearrangement needs to be considered for the second oxidation process (**R2**$^{\bullet+}$/ **R2**$^{2(\bullet+)}$). An overall decent agreement between experiment and theory is observed, especially in the case of the second oxidative process, which does not require any consideration about intramolecular rearrangements. The other processes do display small deviations from experimental values. This might be in parts due to the somewhat superficial treatment of the rearrangement energy and, moreover, due to inherent inaccuracies of the method.

Table S3 Calculated and experimental ionisation potentials (in eV) of **R2**. $\mathbf{IP_0}$ denotes the ionisation potential computed via $\mathbf{IP_0} = E(N) - E(N\text{-}1)$, where E is the ground state energy of the structurally relaxed compound. $\mathbf{IP_{rearr}}$ regards the rearrangement between *syn* **R2** and *anti* **R2** via $\mathbf{IP_{rearr}} = \mathbf{IP_0} + \Delta E_{syn/anti}$, where $\Delta E_{syn/anti}$ denotes the ground state energetic difference between the relaxed *syn* and *anti* structure. Experimental values are obtained by referencing the CV data to the Fc/Fc^+ couple according to $\mathbf{IP_{exp}} = (-(E_{1/2})/V - 4.80)$ eV, where $E_{1/2}$ is the half-wave potential of the oxidation peak.

Oxidation	$\mathbf{IP_0}$	$\mathbf{IP_{rearr}}$	$\mathbf{IP_{exp}}$
$\mathbf{R2/R2^{\bullet+}}$	4.43	4.76	4.88
$\mathbf{R2^{\bullet+}/R2^{2(\bullet+)}}$	4.98	4.98*	4.99
$\mathbf{R2^{2(\bullet+)}/R2^{4+}}$	6.13	5.62	5.29

[a] No rotation occurs.

Rotational motion. In order to mimic the gear slippage motion of **R2** in its four oxidation states, one of the macrocycles was displaced against the other in steps of 45° (Fig. S18). At every position a restricted optimisation was performed by fixing the coordinates of the central C-C bond in each TTF unit to obtain an intermediate structure on the way between *syn* **R2** and *anti* **R2**. The method employed for the optimisation was the semi-empirical HF-3c approach recently proposed by Grimme,[S28] as conventional methods (e.g., TPSS-D3(BJ)) failed to converge the structures. The potential energy curves depicted in Fig. 7b were received at the PBE0-D3(BJ)/def2-TZVP level using COSMO[S26] (ε = 36.64 for MeCN).

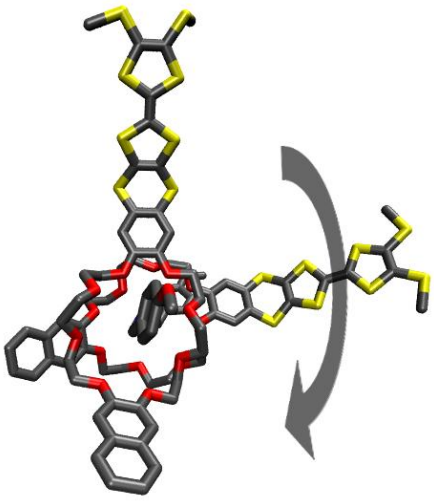

Fig. S18 Example for an intermediate structure between syn and *anti* **R2** (90°). The arrow indicates the rotational motion accomplished by displacing one macrocycle against the other. A computer-time-reducing, stopper-less pseudorotaxane analogue is used.

9. ^{1}H and ^{13}C NMR spectra

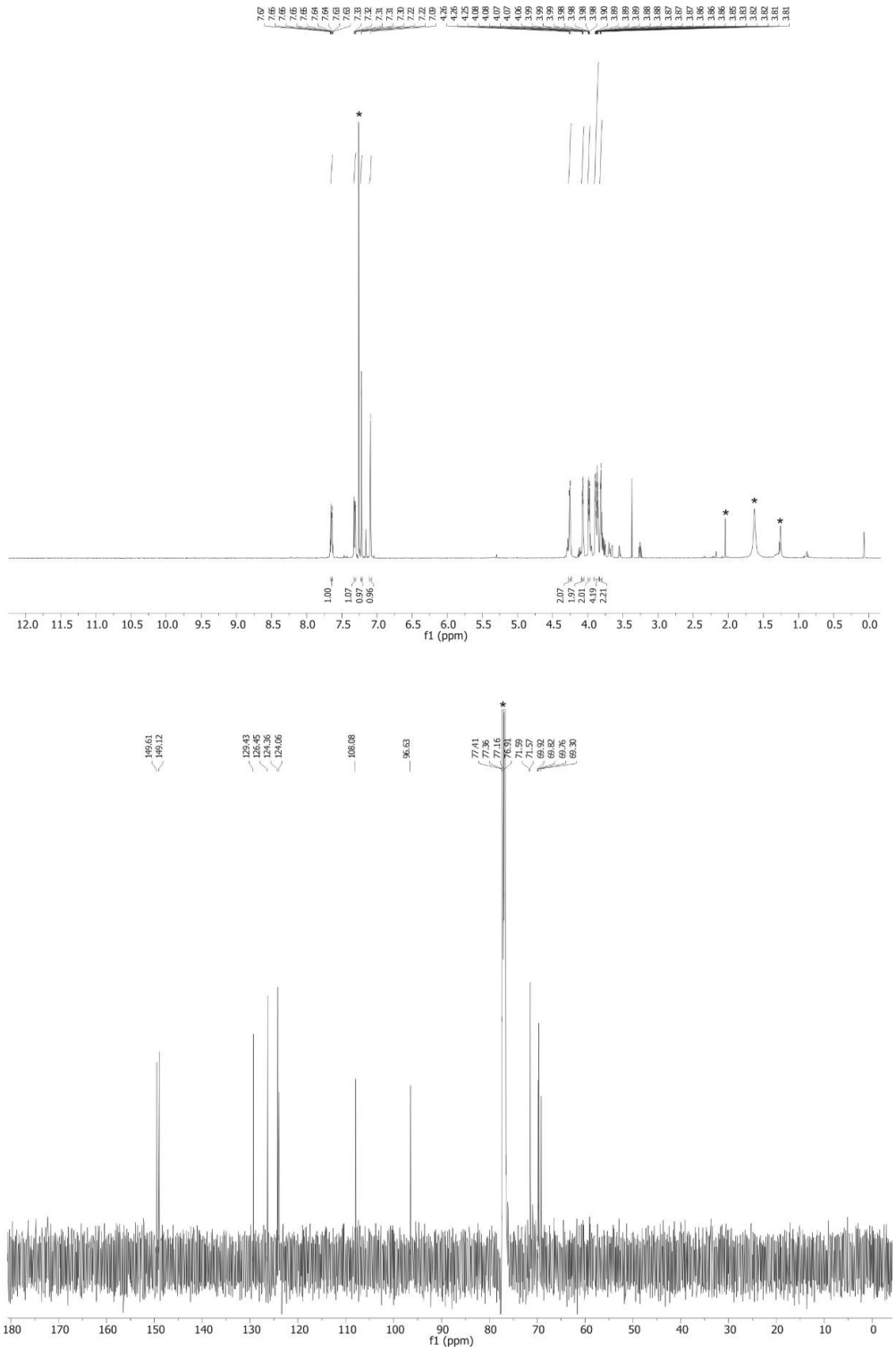

Fig. S19 ^{1}H and ^{13}C NMR spectrum (500/126 MHz, $CDCl_3$, 298 K) of diodide **1**.

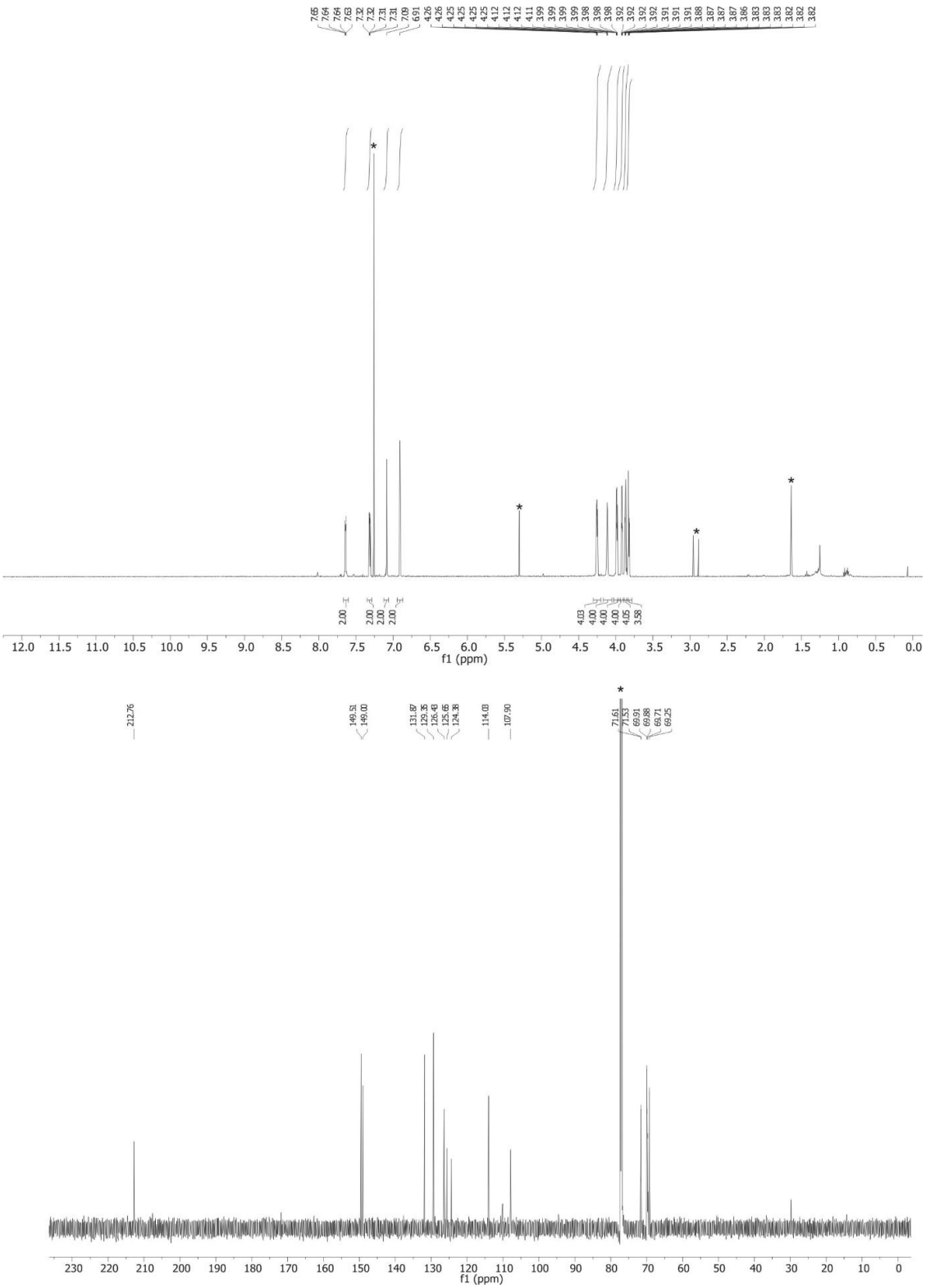

Fig. S20 ^{1}H and ^{13}C NMR spectrum (700/176 MHz, $CDCl_3$ 298 K) of thione **2**.

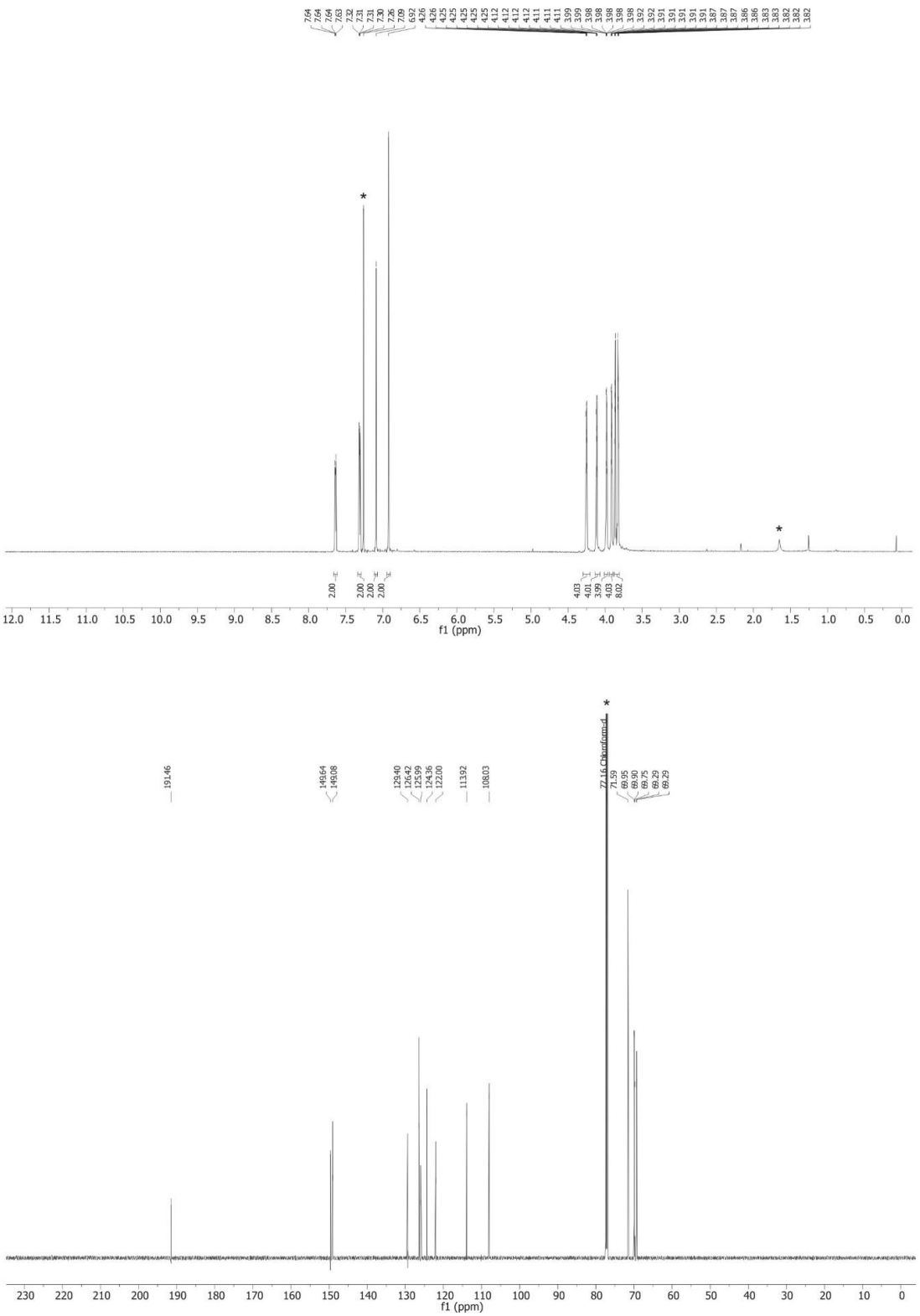

Fig. S21 ^{1}H and ^{13}C NMR spectrum (700/176 MHz, $CDCl_3$ 298 K) of ketone **3**.

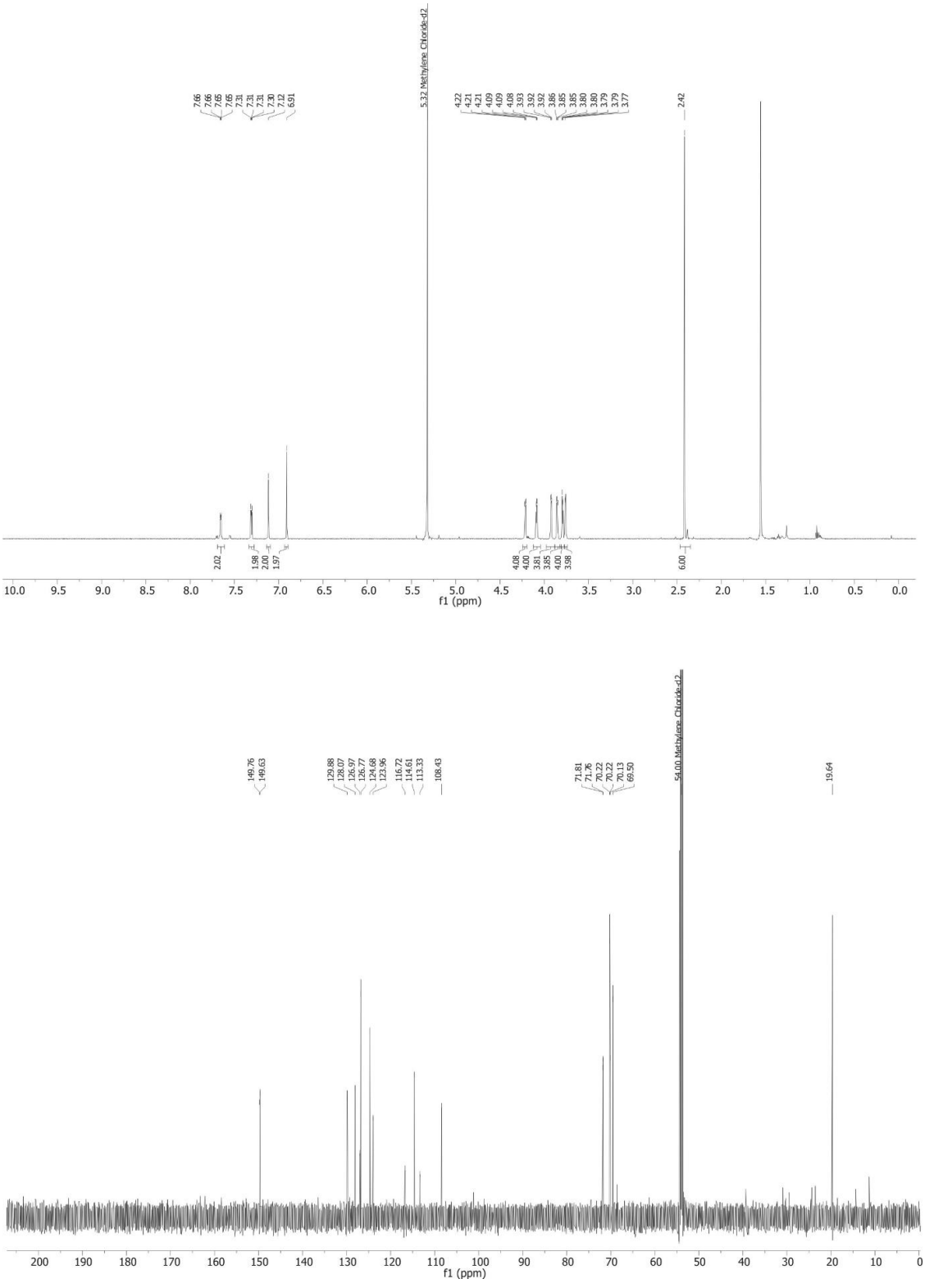

Fig. S22 ^{1}H and ^{13}C NMR spectrum (700/176 MHz, CD_2Cl_2, 298 K) of **exTTFC8**.

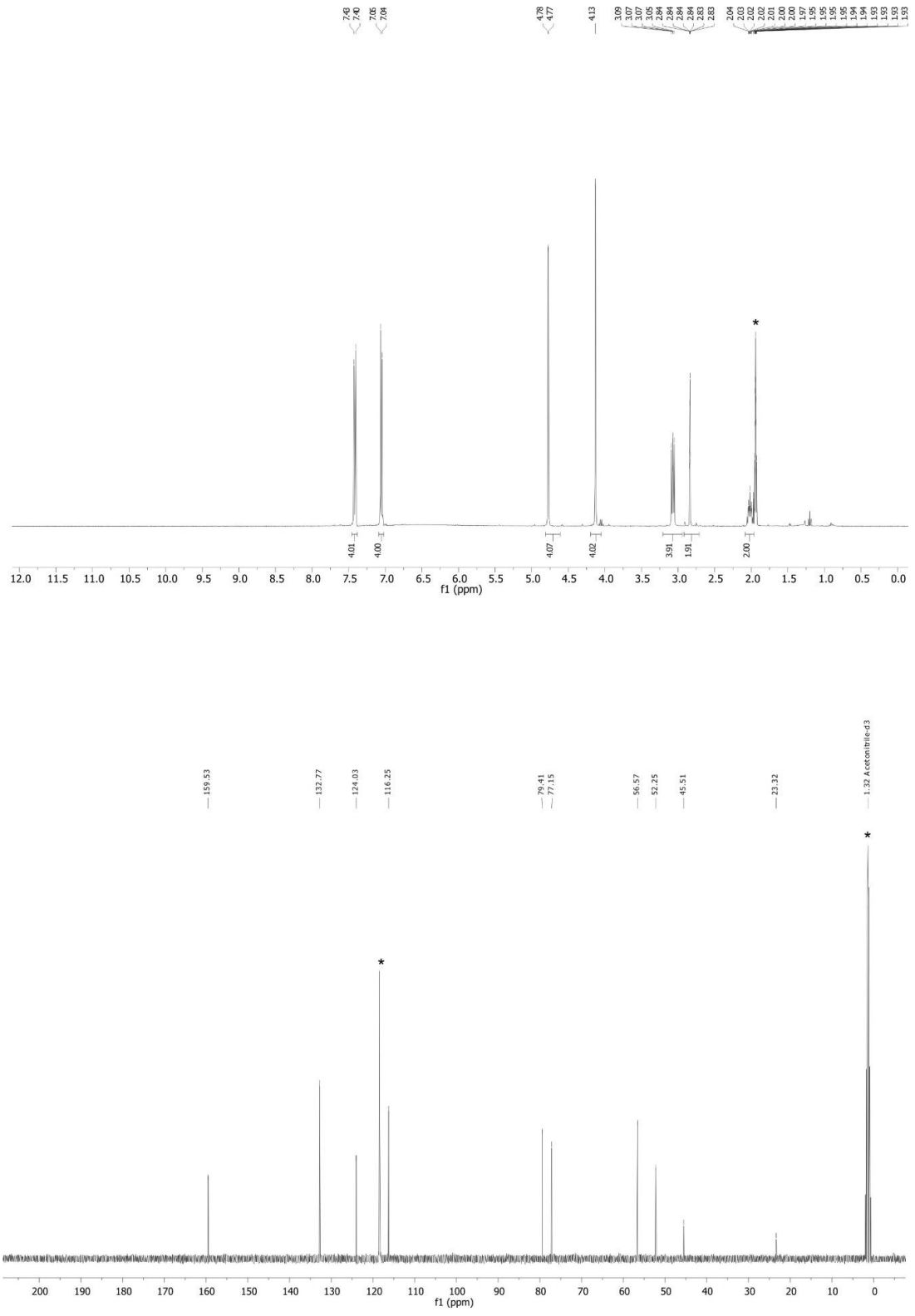

Fig. S23 ^{1}H and ^{13}C NMR spectrum (400/101 MHz, CD_2Cl_2, 298 K) of axle **A2**.

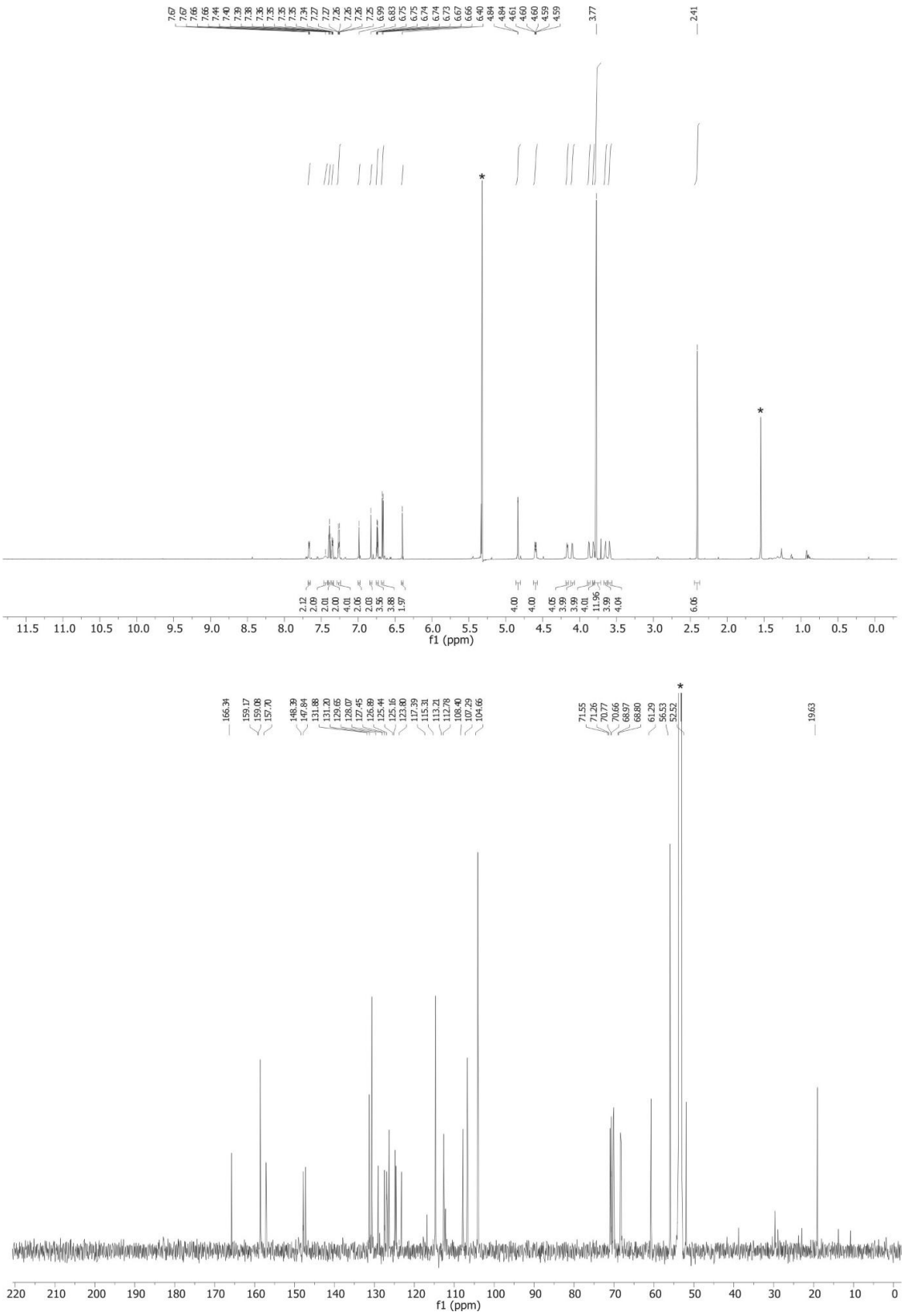

Fig. S24 ^{1}H and ^{13}C NMR spectrum (700/176 MHz, CD_2Cl_2, 298 K) of [2]rotaxane **R1**.

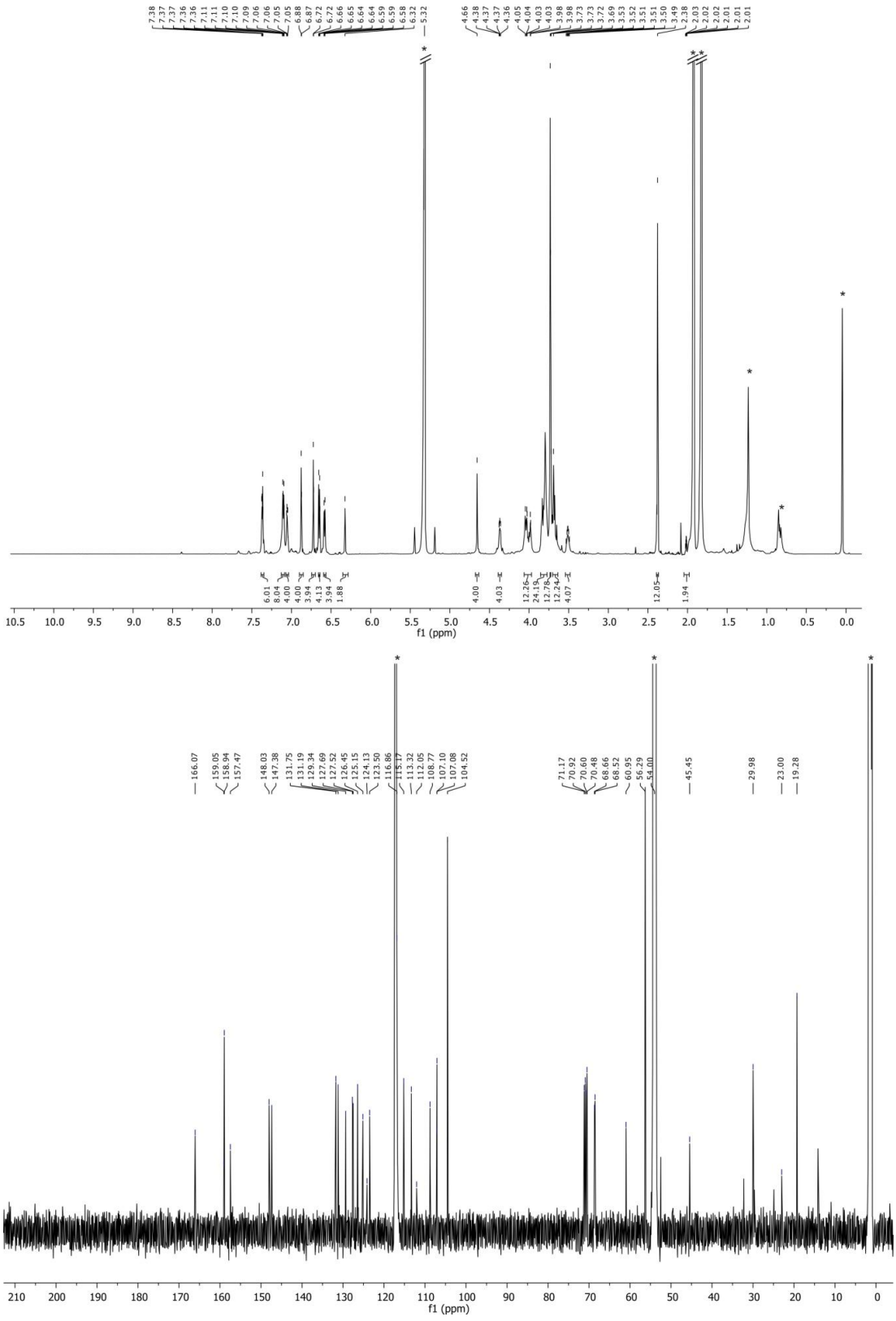

Fig. S25 ^{1}H and ^{13}C NMR spectrum (700/176 MHz, CD_2Cl_2/CD_3CN = 9:1, 298 K) of [3]rotaxane **R2**.

10. Supporting information references

S1 H. V. Schröder, F. Witte, M. Gaedke, S. Sobottka, L. Suntrup, H. Hupatz, A. Valkonen, B. Paulus, K. Rissanen, B. Sarkar and C. A. Schalley, *Org. Biomol. Chem.,* 2018*,* **16***,* 2741.

S2 J. D. Badjic, C. M. Ronconi, J. F. Stoddart, V. Balzani, S. Silvi and A. Credi, *J. Am. Chem. Soc.*, 2006, **128**, 1489.

S3 Z.-J. Zhang, H.-Y. Zhang, H. Wang and Y. Liu, *Angew. Chem. Int. Ed.*, 2011, **50**, 10834.

S4 M. Pal, K. Parasuraman and K. R. Yeleswarapu, *Org. Lett.*, 2003, **5**, 349.

S5 T. Matsumura, F. Ishiwari, Y. Koyama and T. Takata, *Org. Lett.*, 2010, **12**, 3828.

S6 H. V. Schröder, S. Sobottka, M. Nößler, H. Hupatz, M. Gaedke, B. Sarkar and C. A. Schalley, *Chem. Sci.*, 2017, **8**, 6300.

S7 J.-M. Lü, S. V. Rosokha and J. K. Kochi, *J. Am. Chem. Soc.*, 2003, **125**, 12161.

S8 J. R. Aranzaes, M.-C. Daniel, D. Astruc, *Can. J. Chem.*, 2006, **84**, 288.

S9 A. E. Kaifer and M. Gómez-Kaifer, *Supramolecular Electrochemistry*; Wiley, Weinheim, Germany, 1999.

S10 S. Warnke, C. Baldauf, M. T. Bowers, K. Pagel and G. von Helden, *J. Am. Chem. Soc.*, 2014, **136**, 10308.

S11 H. E. Revercomb and E. A. Mason, *Anal. Chem.*, 1975, **47**, 970.

S12 E. A. Mason and E. W. McDaniel, *Transport properties of ions in gases*, Wiley, New York, 1988, 145–159.

S13 G. von Helden, M. T. Hsu, N. Gotts and M. T. Bowers, *J. Phys. Chem.*, 1993, **97**, 8182.

S14 F. Neese, *WIREs Comput. Mol. Sci.*, 2012, **2**, 73.

S15 J. J. P. Stewart, *J. Comput. Chem.*, 1989, **10**, 209.

S16 M. D. Hanwell, D. E. Curtis, D. C. Lonie, T. Vandermeersch, E. Zurek and G. R. Hutchison, *J. Cheminform.*, 2012, **4**, 17.

S17 T. A. Halgren, *J. Comput. Chem.*, 1996, **17**, 490.

S18 TURBOMOLE V7.0 2015, a development of University of Karlsruhe and Forschungszentrum Karlsruhe GmbH, 1989-2007, TURBOMOLE GmbH, since 2007; available from http://www.turbomole.com.

S19 J. Tao, J. P. Perdew, V. N. Staroverov and G. E. Scuseria, *Phys. Rev. Lett.*, 2003, 91.

S20 S. Grimme, J. Antony, S. Ehrlich and H. Krieg, *J. Chem. Phys.*, 2010, **132**, 154104.

S21 S. Grimme, S. Ehrlich and L. Goerigk, *J. Comput. Chem.*, 2011, **32**, 1456.

S22 F. Weigend and R. Ahlrichs, *Phys. Chem. Chem. Phys.*, 2005, **7**, 3297.

S23 K. Eichkorn, O. Treutler, H. Ohm, M. Häser and R. Ahlrichs, *Chem. Phys. Lett.*, 1995, **240**, 283.

S24 F. Weigend, *Phys. Chem. Chem. Phys.*, 2006, **8**, 1057.

S25 M.Sierka, A. Hogekamp and R. Ahlrichs*, J. Chem. Phys.*, 2003, **118**, 9136.

S26 A. Klamt and G. Schüürmann, *J. Chem. Soc. Perkin Trans. 2*, 1993, 799.

S27 J. P. Perdew, M. Ernzerhof and K. Burke, *J. Chem. Phys.*, 1996, **105**, 9982.

S28 R. Sure and S. Grimme, *J. Comput. Chem.*, 2013, **34**, 1672.

4.5 Paper B2

"Chiroptical inversion of a planar chiral redox-switchable rotaxane"

M. Gaedke, F. Witte, J. Anhäuser, H. Hupatz, H. V. Schröder, A. Valkonen, K. Rissanen, A. Lützen, B. Paulus, C. A. Schalley
Chem. Sci. **2019**, 10, 10003–10009.
DOI: 10.1039/C9SC03694F
URL: https://doi.org/10.1039/C9SC03694F

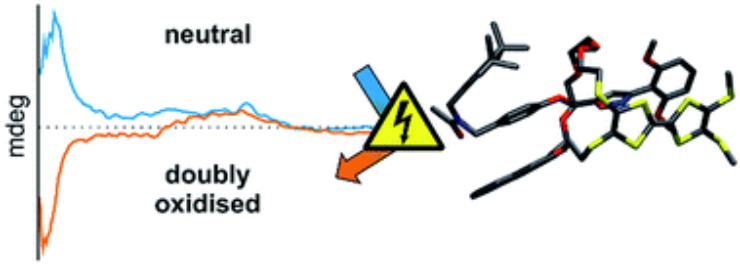

Figure 4.5: Graphical abstract of paper **B2**.

Contributions

The project was conceived by Marius Gaedke with help from Henrik Hupatz and Hendrik Schröder. M.G. furthermore carried out all synthetic work and NMR, UV/Vis, CV, MS, and circular dichroism (CD) experiments and wrote the manuscript. All computational work was conducted by Felix Witte. Jana Anhäuser performed chiral high performance liquid chromatography experiments. H.H. conducted ITC measurements. H.S. helped with synthetic work and data analysis. Arto Valkonen measured and interpreted X-ray diffraction data. All authors contributed to the final version of the manuscript.

Chemical Science

ROYAL SOCIETY OF CHEMISTRY

EDGE ARTICLE

View Article Online
View Journal | View Issue

Check for updates

Cite this: *Chem. Sci.*, 2019, **10**, 10003

All publication charges for this article have been paid for by the Royal Society of Chemistry

Received 26th July 2019
Accepted 4th September 2019

DOI: 10.1039/c9sc03694f

rsc.li/chemical-science

Chiroptical inversion of a planar chiral redox-switchable rotaxane†

Marius Gaedke,[a] Felix Witte,[a] Jana Anhäuser,[b] Henrik Hupatz,[a] Hendrik V. Schröder,[a] Arto Valkonen,[c] Kari Rissanen,[c] Arne Lützen,[b] Beate Paulus[a] and Christoph A. Schalley *[a]

A tetrathiafulvalene (TTF)-containing crown ether macrocycle with C_s symmetry was designed to implement planar chirality into a redox-active [2]rotaxane. The directionality of the macrocycle atom sequence together with the non-symmetric axle renders the corresponding [2]rotaxane mechanically planar chiral. Enantiomeric separation of the [2]rotaxane was achieved by chiral HPLC. The electrochemical properties – caused by the reversible oxidation of the TTF – are similar to a non-chiral control. Reversible inversion of the main band in the ECD spectra for the individual enantiomers was observed after oxidation. Experimental evidence, conformational analysis and DFT calculations of the neutral and doubly oxidised species indicate that mainly electronic effects of the oxidation are responsible for the chiroptical switching. This is the first electrochemically switchable rotaxane with a reversible inversion of the main ECD band.

Introduction

Evidenced by the homochirality in our biosphere,[1–3] chirality is a fundamental principle, which governs the molecular recognition and activity of virtually all biomolecules. Therefore, gaining control over the preferred isomer of a molecule or an assembly by carefully designing a molecular system is a worthwhile endeavour.

The term "chiroptical switch" has been used by Canary to refer to molecules, which are capable of "changes in their interaction with polarized light".[4] Potential applications are information processing, data storage and sensing. In this context, the ground breaking work of Feringa and co-workers[5–7] on overcrowded alkenes, which act as light triggered chiroptical switches was awarded with the Nobel Prize in chemistry 2016 "for the design and synthesis of molecular machines"[8] and underlines the general interest in this topic.

Mechanically interlocked molecules (MIMs)[9–12] consist of parts that can move relative to each other guided by intramolecular forces. Therefore, we envisioned them to be ideal candidates for chiroptical switches in which co-conformational or even configurational changes in the MIM occur.

An achiral wheel with directionality in its atom sequence forms a chiral [2]rotaxane, when threaded onto a directional

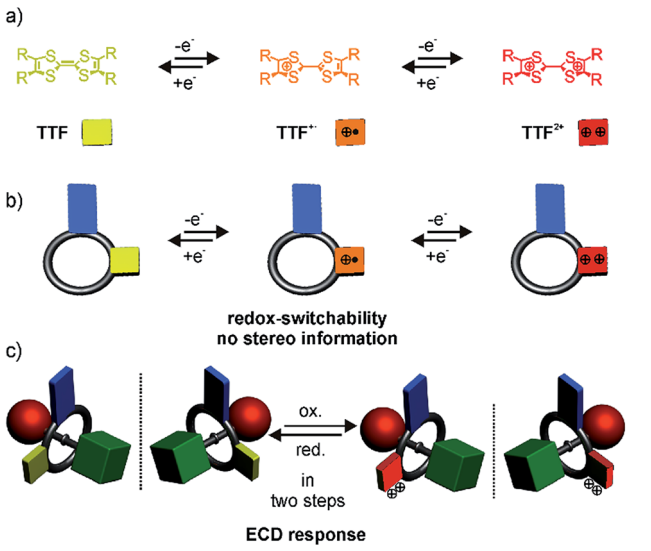

Scheme 1 (a) Reversible one-electron oxidations of the TTF moiety, (b) reversible oxidation of a directional crown ether wheel bearing a TTF unit, (c) chiroptical switching of the planar chiral [2]rotaxane enantiomers.

[a]*Institut für Chemie und Biochemie, Freie Universität Berlin, Takustr. 3, 14195 Berlin, Germany. E-mail: c.schalley@schalley-lab.de*

[b]*Kekulé-Institut für Organische Chemie und Biochemie, Universität Bonn, Gerhard-Domagk-Str. 1, 53121 Bonn, Germany*

[c]*University of Jyvaskyla, Department of Chemistry, P.O. Box 35, 40014 Jyväskylä, Finland*

† Electronic supplementary information (ESI) available: Synthetic procedures including full characterisation of new compounds, electrochemical data, crystallographic data and mass spectrometry data. CCDC 1910670. For ESI and crystallographic data in CIF or other electronic format see DOI: 10.1039/c9sc03694f

Open Access Article. Published on 04 September 2019. Downloaded on 11/30/2020 6:22:50 PM. This article is licensed under a Creative Commons Attribution-NonCommercial 3.0 Unported Licence.

Open Access Article. Published on 04 September 2019. Downloaded on 11/30/2020 6:22:50 PM.
This article is licensed under a Creative Commons Attribution-NonCommercial 3.0 Unported Licence.

axle (Scheme 1). In 1997, Vögtle *et al.* reported on the first resolution of a racemate of such mechanically planar chiral rotaxanes.[13] Chiral rotaxanes may be chiral from inclusion of classical stereogenic elements or by virtue of being mechanically planar chiral. Since then, several examples followed,[14–25] in which the mechanically interlocked structure was used to induce directionality in polymers,[26–28] for sensing,[29–31] and to act as an enantioselective catalyst.[32] Today, sophisticated synthetic protocols allow an efficient enantioselective synthesis. For example, Goldup and co-workers[33,34] described elegant protocols to synthesise planar chiral enantiopure [2]rotaxanes using readily available chiral auxiliaries. However, switchable planar chiral rotaxanes remain rare. So far, the modulation of chirality relies on heat,[21] the choice of solvent, anion exchange,[35] or pH.[36]

Recently, we described redox-switchable rotaxanes, in which the wheels are decorated with tetrathiafulvalenes (TTF).[37–41] TTF can be reversibly oxidised to the $TTF^{\bullet+}$ and TTF^{2+} states (Scheme 1). Large-amplitude motion and co-conformational changes in (oligo)rotaxanes were triggered by redox chemistry.[38,42–50] Apart from rotaxanes, TTF derivatives with covalently bound chiral substituents exhibited a chiroptical response to a change of their redox-state.[51–57] Hence, our switchable rotaxanes display ideal optoelectronic properties since they are air stable in their neutral and oxidised form and show a clear-cut optical output,[37] which is even visible by the naked eye.

In this paper, we report the synthesis, characterisation and optical resolution of a new mechanically planar chiral tristable [2]rotaxane based on the 24-crown-8/secondary ammonium binding motif.[58] The rotaxane consists of the directional wheel **dTTFC8** (Scheme 2), which is derived from a C_{2v}-symmetric TTF-decorated crown ether **TTFC8** (Scheme 2) published by our group recently.[38] ECD measurements show reversible chiroptical switching, which can be explained mainly by electronic changes. The measurements are supported by quantum chemical calculations, which were also used to determine the absolute configuration. To the best of our knowledge, this is the first example of a chiroptical switch with a complete sign reversal of the main band in the ECD spectra based on electronic changes in a mechanically bound assembly.

Results and discussion

Synthesis and characterisation

The prerequisite for rotaxane formation is a sufficiently high binding constant between the crown ether and the ammonium axle. ITC experiments revealed an association constant of $K_a = (3.6 \pm 0.3)\ 10^5\ M^{-1}$ and a 1 : 1 stoichiometry for pseudorotaxane formation from **dTTFC8** and axle **A1** (Scheme 2). The binding constant is very similar to that of our previous non-directional TTF-decorated wheel **TTFC8** ($K_a = (4.4 \pm 0.4)\ 10^5\ M^{-1}$, for thermodynamic parameters see ESI,† Section 4),[38] which indicates the positional change of the TTF unit not to significantly affect the binding properties of the wheel.

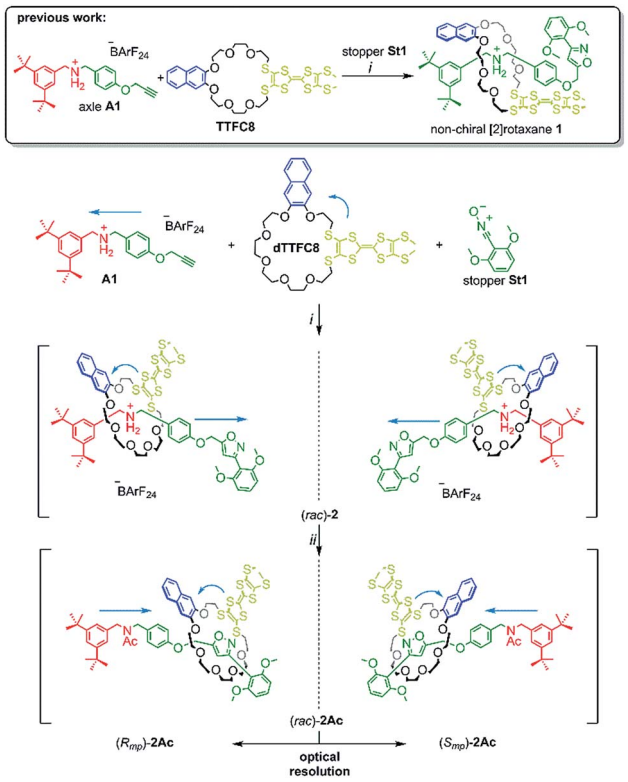

Scheme 2 Synthesis of rotaxanes (*rac*)-**2** and (*rac*)-**2Ac**. Conditions and reagents: (i) DCM, 35 °C, 12 h (73%); (ii) Ac_2O, NEt_3, ACN, 12 h, r.t. (95%).

As for the non-chiral [2]rotaxane **1**, rotaxane formation was achieved with nitrile-oxide stopper **St1** using a catalyst-free end-capping protocol established by Takata and co-workers[59] yielding a racemic mixture of rotaxane (*rac*)-**2** (73%). The non-ionic version (*rac*)-**2Ac** (95%) was obtained through *N*-acylation with Ac_2O[60] (Scheme 2). The ^1H NMR spectra of (*rac*)-**2** and (*rac*)-**2Ac** (Fig. 1) reveal a diastereotopic splitting of the macrocycle's methylene protons as well as of the axle methylene protons H_h.[37,38] The splitting of both macrocycle and axle protons is characteristic for the formation of a chiral, yet racemic [2]rotaxane. Isoxazole formation during stopper attachment leads to a strong downfield shift of 3.88 ppm for proton H_i.

In (*rac*)-**2**, the *S*-methyl protons on **dTTFC8** split into two singlets of the same intensity. Comparable rotaxanes also showed this behaviour on the same position.[27,28] HR-ESI mass and tandem MS experiments support the interlocked architecture (Fig. S1†).

For non-ionic (*rac*)-**2Ac**, the shift of H_i ($\Delta\delta = +0.28$ ppm) and H_h ($\Delta\delta = +0.76$ ppm) relative to (*rac*)-**2** suggests that the wheel translates towards the isoxazole moiety in the absence of attractive interactions with the ammonium ion. Two sets of signals are observed due to the *cis–trans* isomerism of the amide bond in (*rac*)-**2Ac**. Variable temperature NMR experiments (Fig. S3†) in DMSO-d_6 reveal the same barrier ($\Delta G^{\ddagger} = 74 \pm 2$ kJ mol^{-1}) for amide *cis–trans* isomerisation as observed for a similar acetylated rotaxane.[41]

This journal is © The Royal Society of Chemistry 2019

Open Access Article. Published on 04 September 2019. Downloaded on 11/30/2020 6:22:50 PM.
This article is licensed under a Creative Commons Attribution-NonCommercial 3.0 Unported Licence.

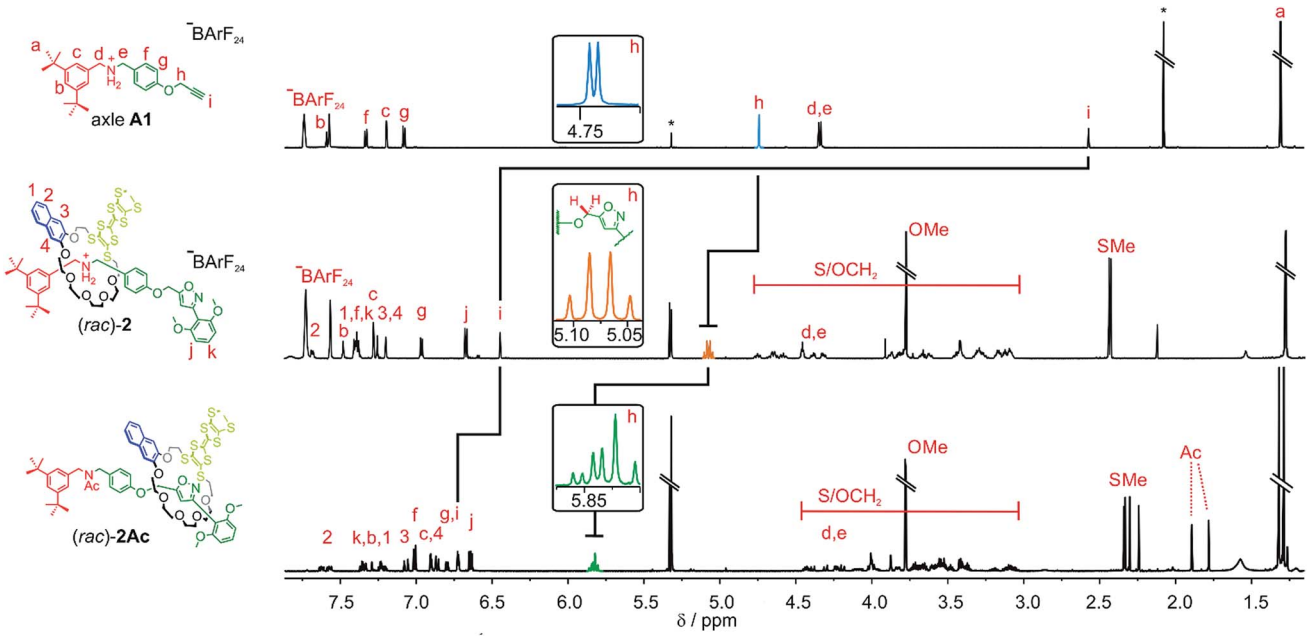

Fig. 1 Comparison of the shifts and splitting in the partial ^{1}H NMR spectra of the methylene groups on the axle **A1** (top), rotaxane (*rac*)-**2** (middle) and acetylated rotaxane (*rac*)-**2Ac** (bottom) (700 MHz, 298 K, CD_2Cl_2).

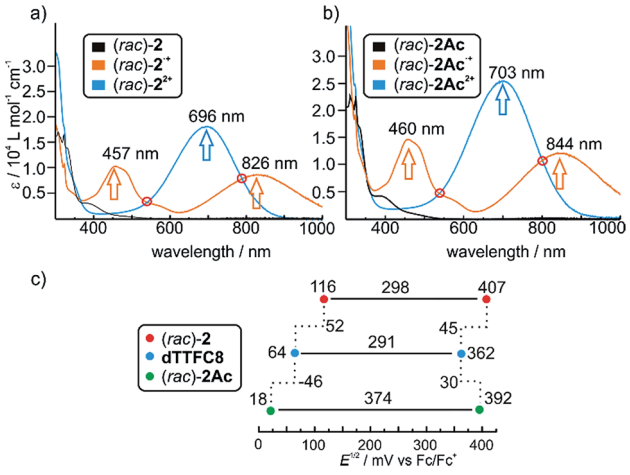

Fig. 2 UV/Vis spectra of (a) ionic (*rac*)-**2** and (b) non-ionic (*rac*)-**2Ac** in different oxidation states. Isosbestic points indicating a clean transition from $TTF^{\bullet+}$ to TTF^{2+} are highlighted with red circles. Spectra were obtained with 25 μM solutions in CH_2Cl_2 using bulk $Fe(ClO_4)_3$ as the oxidant; (c) correlation diagram of half-wave potentials obtained by cyclic voltammetry for the first and second redox process of (*rac*)-**2**, **dTTFC8** and (*rac*)-**2Ac** (each 1 mM) in CH_2Cl_2 referenced against $Fe(Cp)_2^{0/+}$ with NBu_4PF_6 (0.1 M) as the electrolyte.

Optoelectronic properties

Photometric titrations of (*rac*)-**2** and (*rac*)-**2Ac** with $Fe(ClO_4)_3$ (Fig. 2a and b) show similar bands for the three redox states (TTF, $TTF^{\bullet+}$ and TTF^{2+})[61–63] of both rotaxanes with distinct isosbestic points. These findings are consistent with structurally related rotaxanes featuring a non-directional TTF-decorated wheel.[38]

Cyclovoltammetric (CV) experiments were conducted with **dTTFC8**, (*rac*)-**2** and (*rac*)-**2Ac** in dichloromethane (Fig. 2c). The potentials for (*rac*)-**2** (116 mV and 407 mV) are considerably higher for both oxidation steps as compared to **dTTFC8** (64 mV and 362 mV). Both oxidations are thus energetically disfavoured because of the charge repulsion between the TTF cation radical as well as the TTF dication and the ammonium station. In case of (*rac*)-**2Ac** (18 mV and 392 mV) the first oxidation is more easily accomplished in comparison to the free macrocycle and the second oxidation is disfavoured. We attribute this behaviour to a stabilising interaction with the isoxazole moiety on the axle for the first oxidation.

For the second oxidation, the limited accessibility of the TTF^{2+} by counterions caused by the steric demand of the axle needs to be taken into account. Again these trends were already observed for the non-directional macrocycle and rotaxanes thereof.[38] The reversibility of the redox-waves of (*rac*)-**2** and (*rac*)-**2Ac** strongly indicated that the interlocked structures remain intact during the redox switching, however it is reasonable to assume conformational changes to occur due to charge repulsion and charge stabilisation. The data does not show any significant change in the electrochemical properties by introducing directionality into the TTF decorated wheel.

Enantiomer separation on chiral HPLC and CD spectroscopy

The two enantiomers of (*rac*)-**2Ac** could be separated using HPLC with a CHIRALPAK® IA stationary phase. The optical purity was determined (>99% ee; Fig. 3a) and mirror-image CD spectra were obtained for the neutral enantiomers with bands at 242 nm and 325 nm (Fig. 3b). We assigned the absolute configuration based on the computational results (see below).

Open Access Article. Published on 04 September 2019. Downloaded on 11/30/2020 6:22:50 PM.
This article is licensed under a Creative Commons Attribution-NonCommercial 3.0 Unported Licence.

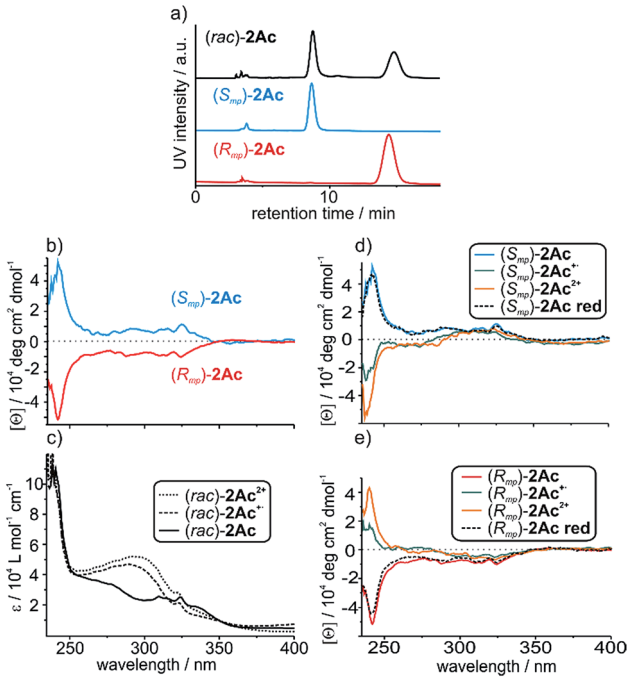

Fig. 3 (a) Traces of analytical chiral HPLC. The chromatographic resolution of (*rac*)-**2Ac** was realised by chiral phase HPLC on a CHIRALPAK® IA column using methyl *tert*-butylether/CH_2Cl_2 80 : 20 (v/v) as the eluent. (b) CD spectra of the individual neutral enantiomers and (c) partial UV/Vis spectra of the neutral, singly and doubly oxidized (*rac*)-**2Ac**. (d and e) CD spectra of the individual enantiomers in their three oxidation states and after reduction to the neutral state. Spectra were taken from 160 μM solutions in CH_2Cl_2 using bulk $Fe(ClO_4)_3$ as the oxidant and Zn dust as the reductant.

The oxidised species $\mathbf{2Ac}^{\bullet+}$ and $\mathbf{2Ac}^{2+}$ show bands at the same wavelengths. While no sign inversion occurs at 325 nm, the band at 242 nm exhibits a sign inversion during the first and a significant intensity increase during the second oxidation step. To exclude decomposition to be responsible for the switching, $\mathbf{2Ac}^{2+}$ was reduced back to the neutral state using Zn dust and then showed the initial CD spectrum again (Fig. 3d and e dashed lines). Surprisingly, no other CD signals are observed at a higher wavelength, although the change in UV/Vis absorption is most pronounced at 460 nm and 844 nm for the radical cation and at 703 nm for the dication (Fig. 2b). The reason for the sign change remains ambiguous. In fact, conformational changes were observed to induce transitions in CD spectra of non-interlocked TTF derivatives with centrochiral elements earlier.[53,64] Other examples show varying intensities[54] or shifts of the maxima[56] upon oxidation of the TTF attached.

Nevertheless, no TTF derivative is reported that shows a sign reversal in the maximum of an ECD spectrum without a shift in the wavelength. Apart from TTF derivatives, chiroptical switching *via* a redox process can be achieved with catechol,[65] viologen,[66] and tetraarylethylene[67] building blocks. Intense switching with a sign reversal was also observed for a viologen-type dicationic helquat.[68] Chiral inversion can also be achieved with metal ion complexation[69,70] acid–base-[71] and photoswitching.[6,68,72]

Computational results

To investigate whether the redox-induced sign inversion at 242 nm in the ECD spectra of (R_{mp})-**2Ac** is due to a change in its electronic properties or to a (co-)conformational change, density functional theory (DFT) calculations were performed at the TPSS-D3(BJ)[73–75] and ωB97X-D3 (ref. 76) levels. Conformational analyses reveal the structure depicted in Fig. 4 (left) to be the most stable one for (R_{mp})-**2Ac**. It is at least 18 kJ mol^{-1} more favourable than any other possible conformation found by theory (see Table S2†). For (R_{mp})-$\mathbf{2Ac}^{2+}$, there are two conformations relatively close in electronic energy: Conformer **A** (Fig. 4 middle) and **B** (Fig. 4 right) with a flipped naphthalene unit, *ca.* 9 kJ mol^{-1} more stable than **A**. This conformational change is explained by the oxidation of (R_{mp})-**2Ac** occuring fairly localised at the TTF unit.[77] The emerging charge of the oxidised TTF moiety is then stabilised by the naphthalene that moves into close proximity of the TTF^{2+}. Additionally, an atoms-in-molecules (AIM) analysis suggests that the electrostatic attraction between the naphthalene and TTF moieties outweighs all other non-covalent interactions for (R_{mp})-$\mathbf{2Ac}^{2+}$, while the maximisation of non-covalent interactions (C–H···π and π–π-stacking) is the most important factor in the neutral state (see ESI† for details).

The simulated CD spectra in Fig. 4 were obtained using simplified time-dependent DFT[78] at the ωB97X-D3 level. The spectrum of (R_{mp})-**2Ac** shows a deviation of around 40–50 nm, while that of (R_{mp})-$\mathbf{2Ac}^{2+}$ is off by less than 20 nm compared to experiment. The experimentally detected sign inversion at 242 nm is reproduced well by the calculations. The conformational change of (R_{mp})-**2Ac** upon oxidation, however, hardly influences the shape of the CD spectra as both conformations yield very similar CD spectra in the region between 230 and 400 nm. Therefore, we exclude the conformational change as the prime origin of the sign inversion.

To rationalise the optical behaviour of (R_{mp})-**2Ac** and (R_{mp})-$\mathbf{2Ac}^{2+}$, we examined its valence electronic structure, which is, as expected, dominated by orbitals localised at the TTF moiety (see Fig. S20†). Analysing the electronic transitions in the spectral region between 230 and 400 nm reveals that practically every excitation involves the TTF unit to some extent. While many transitions are of local nature, *i.e.*, between orbitals in close proximity, quite a few display a charge-transfer-like behaviour (insets Fig. 4 and S21†). For neutral (R_{mp})-**2Ac**, the vast majority of these transitions can be described by advancing an electron from an orbital centred at the TTF core, usually the HOMO, into an orbital located in another part of the rotaxane (*e.g.* the dimethoxy-phenyl moiety). For (R_{mp})-$\mathbf{2Ac}^{2+}$, the corresponding transitions progress from some orbital in the molecule into an orbital localised at the TTF moiety, usually the LUMO or LUMO+1. This induces differently oriented magnetic dipole transition moments leading to different signs in the CD spectrum. Hence, we conclude that the sign inversion in the CD spectra upon oxidation can be exclusively attributed to the change of the electronic structure.

This journal is © The Royal Society of Chemistry 2019

Open Access Article. Published on 04 September 2019. Downloaded on 11/30/2020 6:22:50 PM.
This article is licensed under a Creative Commons Attribution-NonCommercial 3.0 Unported Licence.

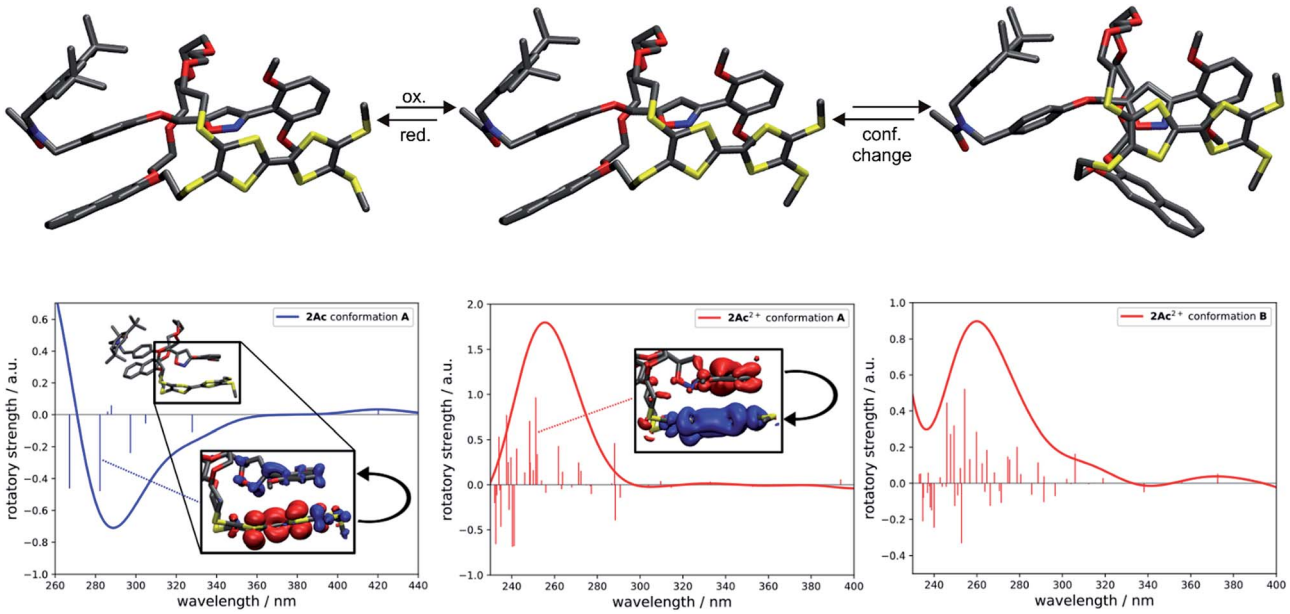

Fig. 4 Structural and spectral comparison of the most stable conformation of (R_{mp})-**2Ac** and the two most stable conformations, **A** and **B**, of (R_{mp})-**2Ac**$^{2+}$. Oxidation induces a flip of the naphthalene moiety in **A** towards the TTF unit yielding conformation **B**. The difference in electronic energy between **A** and **B** is around 9 kJ mol^{-1}. All structures were obtained at the TPSS-D3(BJ) level. Corresponding simulated CD spectra with excited state difference densities of selected transitions (insets) visualising the change in electronic structure upon photoexcitation of (R_{mp})-**2Ac** (left) and (R_{mp})-**2Ac**$^{2+}$ (middle). The difference in the CD spectra due to the conformational change of (R_{mp})-**2Ac**$^{2+}$ is negligible in the region of interest. The spectra were obtained at the ωB97X-D3 level using sTD-DFT. Gaussian line broadening with $\sigma = 20$ nm was applied. Insets: blue and red zones correspond to areas of electron enhancement and electron depletion, respectively. Isovalue = 0.001 a_0^{-3}.

Conclusions

In conclusion, electrochemically switchable crown ether/ammonium [2]rotaxanes bearing a directional wheel are reported. The wheel features a redox-switchable TTF unit. The directionality had no observable impact on the electrochemical and optical properties of the racemic mixtures determined by UV/Vis spectroscopy and CV measurements. Instead, the pure enantiomers of the acetylated non-ionic derivatives display a redox-induced reversible inversion of the sign in the ECD spectrum without a change of absolute configuration. The mechanism and the absolute configuration of this chiroptical switch has been examined by computational methods. While co-conformational changes have hardly any impact on the ECD spectra, the changes in electronic structure induced by oxidation play a pivotal role. These results underline the impact of the mechanical bond, which allows the construction of intriguing switchable chemical assemblies with unexpected properties. This is the first in class example of a redox-controlled chiroptical switch with a complete sign reversal based on a mechanically planar chiral rotaxane. In the future, these properties could be employed in materials science to construct novel optoelectronic building blocks.

Conflicts of interest

There are no conflicts to declare.

Acknowledgements

We thank the Deutsche Forschungsgemeinschaft (CRC 765) and Academy of Finland (KR proj. no. 309399, AV proj. no. 314343) for funding. We are grateful to the Alexander von Humboldt-Foundation for support of KR (AvH research award). JA thanks the Studienstiftung des deutschen Volkes for a doctoral scholarship. Furthermore, we thank Dr Lucia Volbach for help with the chiral separation and Dr Rakesh Puttreddy for help with the crystallisation.

Notes and references

1 R. Breslow and Z. L. Cheng, *Proc. Natl. Acad. Sci. U. S. A.*, 2009, **106**, 9144–9146.
2 F. Jafarpour, T. Biancalani and N. Goldenfeld, *Phys. Rev. E*, 2017, **95**, 032407.
3 D. G. Blackmond, *Cold Spring Harbor Perspect. Biol.*, 2010, **2**, a002147.
4 J. W. Canary, *Chem. Soc. Rev.*, 2009, **38**, 747–756.
5 N. Koumura, R. W. Zijlstra, R. A. van Delden, N. Harada and B. L. Feringa, *Nature*, 1999, **401**, 152–155.
6 B. L. Feringa, R. A. van Delden, N. Koumura and E. M. Geertsema, *Chem. Rev.*, 2000, **100**, 1789–1816.
7 B. L. Feringa, R. A. van Delden and M. K. J. ter Wiel, *Pure Appl. Chem.*, 2003, **75**, 563–575.
8 B. L. Feringa, *Angew. Chem., Int. Ed.*, 2017, **56**, 11060–11078.
9 J. F. Stoddart, *Angew. Chem., Int. Ed.*, 2017, **56**, 11094–11125.

Open Access Article. Published on 04 September 2019. Downloaded on 11/30/2020 6:22:50 PM. This article is licensed under a Creative Commons Attribution-NonCommercial 3.0 Unported Licence.

10 E. A. Neal and S. M. Goldup, *Chem. Commun.*, 2014, **50**, 5128–5142.
11 J. F. Stoddart, *Chem. Soc. Rev.*, 2009, **38**, 1802–1820.
12 J. E. Lewis, M. Galli and S. M. Goldup, *Chem. Commun.*, 2016, **53**, 298–312.
13 C. Yamamoto, Y. Okamoto, T. Schmidt, R. Jäger and F. Vögtle, *J. Am. Chem. Soc.*, 1997, **119**, 10547–10548.
14 E. M. G. Jamieson, F. Modicom and S. M. Goldup, *Chem. Soc. Rev.*, 2018, **47**, 5266–5311.
15 N. H. Evans, *Chem.–Eur. J.*, 2018, **24**, 3101–3112.
16 P. E. Glen, J. A. T. O'Neill and A.-L. Lee, *Tetrahedron*, 2013, **69**, 57–68.
17 N. Kameta, K. Hiratani and Y. Nagawa, *Chem. Commun.*, 2004, 466–467.
18 J. Niemeyer and N. Pairault, *Synlett*, 2018, **29**, 689–698.
19 Y. Makita, N. Kihara, N. Nakakoji, T. Takata, S. Inagaki, C. Yamamoto and Y. Okamoto, *Chem. Lett.*, 2007, **36**, 162–163.
20 Y. Tachibana, N. Kihara, Y. Ohga and T. Takata, *Chem. Lett.*, 2000, **29**, 806–807.
21 Y. Mochizuki, K. Ikeyatsu, Y. Mutoh, S. Hosoya and S. Saito, *Org. Lett.*, 2017, **19**, 4347–4350.
22 M. Asakawa, G. Brancato, M. Fanti, D. A. Leigh, T. Shimizu, A. M. Z. Slawin, J. K. Y. Wong, F. Zerbetto and S. Zhang, *J. Am. Chem. Soc.*, 2002, **124**, 2939–2950.
23 T. Ogoshi, D. Yamafuji, T. Aoki, K. Kitajima, T. A. Yamagishi, Y. Hayashi and S. Kawauchi, *Chem.–Eur. J.*, 2012, **18**, 7493–7500.
24 G. Bottari, D. A. Leigh and E. M. Pérez, *J. Am. Chem. Soc.*, 2003, **125**, 13360–13361.
25 P. R. Ashton, J. A. Bravo, F. M. Raymo, J. F. Stoddart, A. J. P. White and D. J. Williams, *Eur. J. Org. Chem.*, 1999, 899–908.
26 Y.-G. Lee, Y. Koyama, M. Yonekawa and T. Takata, *Macromolecules*, 2010, **43**, 4070–4080.
27 S. Suzuki, F. Ishiwari, K. Nakazono and T. Takata, *Chem. Commun.*, 2012, **48**, 6478–6480.
28 F. Ishiwari, K. Nakazono, Y. Koyama and T. Takata, *Angew. Chem., Int. Ed.*, 2017, **56**, 14858–14862.
29 N. Kameta, Y. Nagawa, M. Karikomi and K. Hiratani, *Chem. Commun.*, 2006, 3714–3716.
30 J. Y. C. Lim, I. Marques, V. Felix and P. D. Beer, *Angew. Chem., Int. Ed.*, 2018, **57**, 584–588.
31 K. Hirose, M. Ukimi, S. Ueda, C. Onoda, R. Kano, K. Tsuda, Y. Hinohara and Y. Tobe, *Symmetry*, 2018, **10**, 20.
32 Y. Tachibana, N. Kihara and T. Takata, *J. Am. Chem. Soc.*, 2004, **126**, 3438–3439.
33 R. J. Bordoli and S. M. Goldup, *J. Am. Chem. Soc.*, 2014, **136**, 4817–4820.
34 M. A. Jinks, A. de Juan, M. Denis, C. J. Fletcher, M. Galli, E. M. G. Jamieson, F. Modicom, Z. Zhang and S. M. Goldup, *Angew. Chem., Int. Ed.*, 2018, **57**, 14806–14810.
35 S. Corra, C. de Vet, J. Groppi, M. La Rosa, S. Silvi, M. Baroncini and A. Credi, *J. Am. Chem. Soc.*, 2019, **141**, 9129–9133.
36 C. E. Gell, T. A. McArdle-Ismaguilov and N. H. Evans, *Chem. Commun.*, 2019, **55**, 1576–1579.
37 H. V. Schröder, H. Hupatz, A. J. Achazi, S. Sobottka, B. Sarkar, B. Paulus and C. A. Schalley, *Chem.–Eur. J.*, 2017, **23**, 2960–2967.
38 H. V. Schröder, S. Sobottka, M. Nößler, H. Hupatz, M. Gaedke, B. Sarkar and C. A. Schalley, *Chem. Sci.*, 2017, **8**, 6300–6306.
39 H. V. Schröder, J. M. Wollschläger and C. A. Schalley, *Chem. Commun.*, 2017, **53**, 9218–9221.
40 H. V. Schröder, A. Mekic, H. Hupatz, S. Sobottka, F. Witte, L. H. Urner, M. Gaedke, K. Pagel, B. Sarkar, B. Paulus and C. A. Schalley, *Nanoscale*, 2018, **10**, 21425–21433.
41 H. V. Schröder, F. Stein, J. M. Wollschläger, S. Sobottka, M. Gaedke, B. Sarkar and C. A. Schalley, *Angew. Chem., Int. Ed.*, 2019, **58**, 3496–3500.
42 H. V. Schröder and C. A. Schalley, *Beilstein J. Org. Chem.*, 2018, **14**, 2163–2185.
43 A. Coskun, M. Banaszak, R. D. Astumian, J. F. Stoddart and B. A. Grzybowski, *Chem. Soc. Rev.*, 2012, **41**, 19–30.
44 S. Erbas-Cakmak, D. A. Leigh, C. T. McTernan and A. L. Nussbaumer, *Chem. Rev.*, 2015, **115**, 10081–10206.
45 A. Jana, M. Ishida, J. S. Park, S. Bahring, J. O. Jeppesen and J. L. Sessler, *Chem. Rev.*, 2017, **117**, 2641–2710.
46 M. Fumanal, M. Capdevila-Cortada, J. S. Miller and J. J. Novoa, *J. Am. Chem. Soc.*, 2013, **135**, 13814–13826.
47 M. Yoshizawa, K. Kumazawa and M. Fujita, *J. Am. Chem. Soc.*, 2005, **127**, 13456–13457.
48 M. R. Bryce, *J. Mater. Chem.*, 2000, **10**, 589–598.
49 D. Canevet, M. Salle, G. Zhang, D. Zhang and D. Zhu, *Chem. Commun.*, 2009, 2245–2269.
50 J. L. Segura and N. Martín, *Angew. Chem., Int. Ed.*, 2001, **40**, 1372–1409.
51 A. Saad, F. Barriere, E. Levillain, N. Vanthuyne, O. Jeannin and M. Fourmigue, *Chem.–Eur. J.*, 2010, **16**, 8020–8028.
52 M. Hasegawa, J. Endo, S. Iwata, T. Shimasaki and Y. Mazaki, *Beilstein J. Org. Chem.*, 2015, **11**, 972–979.
53 F. Pop, S. Laroussi, T. Cauchy, C. J. Gomez-Garcia, J. D. Wallis and N. Avarvari, *Chirality*, 2013, **25**, 466–474.
54 E. Gomar-Nadal, J. Veciana, C. Rovira and D. B. Amabilino, *Adv. Mater.*, 2005, **17**, 2095–2098.
55 Y. Zhou, D. Zhang, L. Zhu, Z. Shuai and D. Zhu, *J. Org. Chem.*, 2006, **71**, 2123–2130.
56 T. Biet, A. Fihey, T. Cauchy, N. Vanthuyne, C. Roussel, J. Crassous and N. Avarvari, *Chem.–Eur. J.*, 2013, **19**, 13160–13167.
57 F. Riobe and N. Avarvari, *Chem. Commun.*, 2009, 3753–3755.
58 P. R. Ashton, P. J. Campbell, P. T. Glink, D. Philp, N. Spencer, J. F. Stoddart, E. J. T. Chrystal, S. Menzer, D. J. Williams and P. A. Tasker, *Angew. Chem., Int. Ed.*, 1995, **34**, 1865–1869.
59 T. Matsumura, F. Ishiwari, Y. Koyama and T. Takata, *Org. Lett.*, 2010, **12**, 3828–3831.
60 Y. Tachibana, H. Kawasaki, N. Kihara and T. Takata, *J. Org. Chem.*, 2006, **71**, 5093–5104.
61 S. V. Rosokha and J. K. Kochi, *J. Am. Chem. Soc.*, 2007, **129**, 828–838.
62 M. B. Kirketerp, L. A. Leal, D. Varsano, A. Rubio, T. J. Jorgensen, K. Kilsa, M. B. Nielsen and S. B. Nielsen, *Chem. Commun.*, 2011, **47**, 6900–6902.

 This journal is © The Royal Society of Chemistry 2019

Open Access Article. Published on 04 September 2019. Downloaded on 11/30/2020 6:22:50 PM.
This article is licensed under a Creative Commons Attribution-NonCommercial 3.0 Unported Licence.

63 V. Khodorkovsky, L. Shapiro, P. Krief, A. Shames, G. Mabon, A. Gorgues and M. Giffard, *Chem. Commun.*, 2001, 2736–2737.
64 T. Cauchy, F. Pop, J. Cuny and N. Avarvari, *Chimia*, 2018, **72**, 389–393.
65 M. Fukui, T. Mori, Y. Inoue and R. Rathore, *Org. Lett.*, 2007, **9**, 3977–3980.
66 J. Deng, N. Song, Q. Zhou and Z. Su, *Org. Lett.*, 2007, **9**, 5393–5396.
67 T. Mori and Y. Inoue, *J. Phys. Chem. A*, 2005, **109**, 2728–2740.
68 L. Pospisil, L. Bednarova, P. Stepanek, P. Slavicek, J. Vavra, M. Hromadova, H. Dlouha, J. Tarabek and F. Teply, *J. Am. Chem. Soc.*, 2014, **136**, 10826–10829.
69 E. Lee, H. Ju, I. H. Park, J. H. Jung, M. Ikeda, S. Kuwahara, Y. Habata and S. S. Lee, *J. Am. Chem. Soc.*, 2018, **140**, 9669–9677.
70 A. Homberg, E. Brun, F. Zinna, S. Pascal, M. Gorecki, L. Monnier, C. Besnard, G. Pescitelli, L. Di Bari and J. Lacour, *Chem. Sci.*, 2018, **9**, 7043–7052.
71 T.-Y. Tai, Y.-H. Liu, C.-C. Lai, S.-M. Peng and S.-H. Chiu, *Org. Lett.*, 2019, **21**, 5708–5712.
72 C. Petermayer and H. Dube, *J. Am. Chem. Soc.*, 2018, **140**, 13558–13561.
73 J. Tao, J. P. Perdew, V. N. Staroverov and G. E. Scuseria, *Phys. Rev. Lett.*, 2003, **91**, 146401.
74 S. Grimme, S. Ehrlich and L. Goerigk, *J. Comput. Chem.*, 2011, **32**, 1456–1465.
75 F. Weigend and R. Ahlrichs, *Phys. Chem. Chem. Phys.*, 2005, **7**, 3297–3305.
76 J. D. Chai and M. Head-Gordon, *J. Chem. Phys.*, 2008, **128**, 084106.
77 R. F. W. Bader, *Chem. Rev.*, 1991, **91**, 893–928.
78 H. J. C. Berendsen, J. P. M. Postma, W. F. van Gunsteren, A. DiNola and J. R. Haak, *J. Chem. Phys.*, 1984, **81**, 3684–3690.

Electronic Supplementary Material (ESI) for Chemical Science.
This journal is © The Royal Society of Chemistry 2019

Supporting Information

Chiroptical inversion of a planar chiral redox-switchable rotaxane

Marius Gaedke,[a] Felix Witte,[a] Jana Anhäuser,[b] Henrik Hupatz,[a] Hendrik V. Schröder,[a] Arto Valkonen,[c], Kari Rissanen,[c] Arne Lützen,[b] Beate Paulus[a] and Christoph A. Schalley*[a]

[a] Institut für Chemie und Biochemie, Organische Chemie, Freie Universität Berlin, Takustraße 3, 14195 Berlin, Germany.
[b] Kekulé-Institut für Organische Chemie und Biochemie, Universität Bonn, Gerhard-Domagk-Str. 1, 53121 Bonn, Germany.
[c] University of Jyvaskyla, Department of Chemistry, P.O. Box 35, 40014 Jyväskylä, Finland.
*Corresponding author e-mail: c.schalley@fu-berlin.de

Table of contents

1. Experimental details

1.1. General methods

All reagents and solvents were obtained from commercial sources and used without further purification. Dry solvents were purchased from Acros Organics or obtained from the M. BRAUN Solvent purification system SPS 800. 2-Hydroxyethyl 4-methylbenzenesulfonate **S4**,[1] 2-[(tetrahydropyran-2-yl)oxy]ethyl *p*-toluenesulfonate) **S5**,[2] 2,3-bis(2-cyanoethylthio)-6,7-bis(methylthio)tetrathiafulvalene **S12**,[3] axle **A1**,[4] and 2,6-dimethoxybenzonitrile oxide stopper **St1**[5] were synthesised according to literature procedures. Thin-layer chromatography was performed on silica gel-coated plates with fluorescent indicator F254 (Merck). For column chromatography, silica gel (0.04-0.063 mm, Merck) was used.

^{1}H and ^{13}C NMR experiments were performed on JEOL ECX 400, JEOL ECP 500, Bruker AVANCE 500 or Bruker AVANCE 700 instruments. Residual solvent signals were used as the internal standards. All shifts are reported in ppm and NMR multiplicities are abbreviated as s (singlet), d (doublet), t (triplet), m (multiplet) and br (broad). Coupling constants *J* are reported in Hertz. Compounds containing the tetrakis[3,5-bis(trifluoromethyl)phenyl]borate ($BArF_{24}^-$) anion show ^{13}C NMR spectra with ^{19}F, ^{10}B and ^{11}B couplings. These signals were denoted as one signal.

Melting points were determined on a SMP 30 (Stuart) instrument and are uncorrected.

High-resolution ESI mass spectra were measured on an Agilent 6210 ESI-TOF device. Tandem MS and infrared multiphoton dissociation (IRMPD) experiments were performed on a Varian Inc. Ionspec Q FT-7 equipped with a 7 T superconducting magnet and a Micromass Z-spray ESI source. HPLC grade solvents were used for sample preparation and the samples introduced into the ion source with a flow rate of 2-4 µL/min.

UV/Vis spectra were recorded with a Varian Cary 50 Bio spectrometer equipped with a xenon lamp. Solvents with HPLC grade and Suprasil glass cuvettes with a path-length of 1 cm were used.

ECD spectra were recorded on a JASCO-8-10 spectropolarimeter at 20°C. Solvents with HPLC grade and Suprasil glass cuvettes with a path-length of 2 mm were used. During the measurements, a constant flow of 3.2 L/min N_2 was provided. Each dataset is an average of three subsequent measurements.

CV measurements were carried out with an Autolab PGSTAT302N potentiostat in a 2 mL measuring cell in dichloromethane with 0.1 M n-Bu_4NPF_6 as the conducting salt. The working electrode was made of glassy carbon, the reference Ag electrode was etched with conc. aq. HCl. A Pt wire worked as a counter electrode. The cyclic voltammogram traces were recorded with 10, 25, 50, 100, 250, 500, 1000 and 2500 mV/s scan rates, to ensure that the observed

processes are reversible and diffusion-limited. For better comparability, only the 100 mV/s traces were plotted and compared in the discussion. In order to obtain the correct half-wave potentials, FeCp*/FeCp*$^{+}$ was used as the reference. These values were afterwards referenced to Fc/Fc^{+} as described in the literature.[6] The raw data was treated with Nova 1.5 by Metrohm and the plots were made with Origin *8* by OriginLab.

The chromatographic resolution was performed on a Shimadzu Prominence LC-20 HPLC system, equipped with two LC20-AT pumps, a DGU-20A3 solvent degasser, a diode array detector SPD-M20A (190-640 nm) and a fraction collector FRC-10A. For the analytical HPLC resolution, a Daicel CHIRALPAK® IA column (0.46 cm Ø, 25 cm) was used as the chiral stationary phase and *tert*-butyl methyl ether/CH_2Cl_2 (HPLC grade, 80:20 v/v) as the eluent with a flow rate of 1 mL/min. For the semi-preparative HPLC resolution, a CHIRALPAK® IA column (1 cm Ø, 25 cm) was used as the chiral stationary phase and *tert*-butyl methyl ether/dichloromethane (HPLC grade, 80:20 v/v) as the eluent with a flow rate of 4 mL/min.

1.2. Synthesis of dTTFC8

The directional wheel **dTTFC8** was synthesised starting from naphthalene-2,3-diol through consecutive substitution[7] with tetrahydropyranyl-protected mono- and pentaethylene glycol. After deprotection[8] to the diol and tosylation,[9] the corresponding diiodide was formed through a Finkelstein reaction.[4] In the last step, a CsOH•H_2O-mediated macrocyclisation[10] with the dicyanoethyl-protected TTF derivative[11] was carried out.

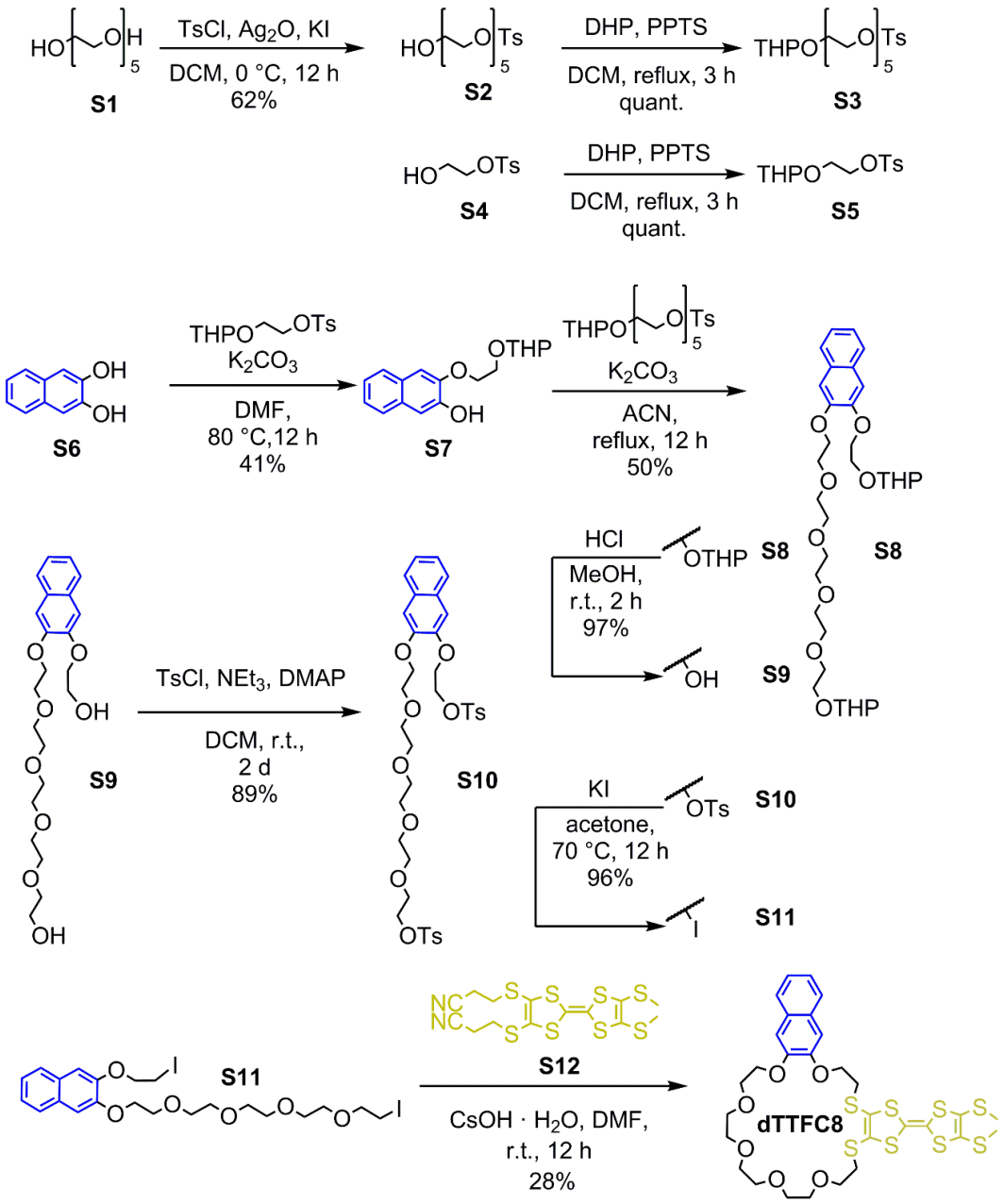

Scheme S1 Synthesis of wheel **dTTFC8** with a directional atom sequence.

14-Hydroxy-3,6,9,12-tetraoxatetradecyl 4-methylbenzenesulfonate[12]

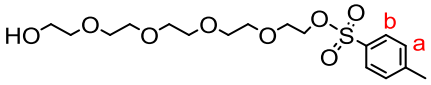

S2

4-Toluenesulfonyl chloride (444 mg, 2.3 mmol, 1.1 equiv.) was slowly added to a suspension of pentaethylene glycol **S1** (0.45 mL 1.9 mmol, 1.0 equiv.), KI (71.0 mg 0.42 mmol, 0.2 equiv.) and fresh Ag_2O (770 mg 3.3 mmol, 1.5 eq) in CH_2Cl_2 (21 mL) at 0 °C. The mixture was stirred overnight in a thawing ice bath. Afterwards, the mixture was filtered through a short celite pad and rinsed with EtOAc. After removal of the solvent, the crude product was purified by column chromatography (SiO_2, EtOAc/hexane = 2:1 → EtOAc, R_f ~ 0.3 in EtOAc) to isolate the desired product **S2** as a colourless oil in a 62% yield (466 mg, 1.2 mmol). **^{1}H NMR** (500 MHz, $CDCl_3$): δ = 2.42 (s, 3H, -C<u>H</u>$_3$), 2.69 (s, 1H, -O<u>H</u>), 3.47 – 3.70 (m, 18H, -OC<u>H</u>$_2$), 4.08 – 4.17 (m, 2H, TsO-C<u>H</u>$_2$-), 7.31 (d, J = 8.1 Hz, 2H, a), 7.76 (d, J = 8.1 Hz, 2H, b) ppm. **^{13}C NMR** (126 MHz, $CDCl_3$): δ = 21.7, 61.7, 68.7, 69.3, 70.3, 70.5, 70.6, 70.6, 70.6, 72.5, 128.0, 129.9, 133.0, 144.9 ppm. **ESI-HRMS**(ACN): *m/z* calcd. for $[C_{17}H_{28}O_8S]$: 415.1398 $[M+Na]^+$, found: 415.1394; calcd. for $[M+K]^+$:431.1137, found: 431.1130.

14-((Tetrahydro-2*H*-pyran-2-yl)oxy)-3,6,9,12-tetraoxatetradecyl 4-methylbenzenesulfonate[12]

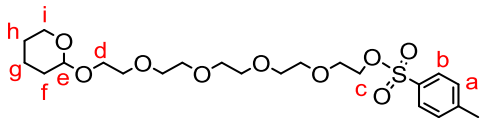

S3

A solution of monotosylate **S2** (1.00 g, 2.6 mmol, 1.0 equiv.), pyridinium tosylate (132 mg, 0.5 mmol, 0.2 equiv.) and 3,4-dihydro-*2H*-pyran (360 µL, 3.8 mmol, 97%, 1.5 equiv.) in CH_2Cl_2 (40 mL) was refluxed for 3 h. Afterwards, the mixture was poured into ice water, then extracted with CH_2Cl_2, washed with brine and dried with $MgSO_4$. After removal of the solvent, the crude product was purified by column chromatography (SiO_2, EtOAc, R_f ~ 0.6 in EtOAc) to isolate the desired product **S3** as a colourless oil in quantitative yield (1.26 g, 2.6 mmol). **^{1}H NMR** (500 MHz, $CDCl_3$): δ = 1.38 – 1.84 (m, 6H, f, g, h), 2.38 (s, 3H, -C<u>H</u>$_3$), 3.38 – 3.49 (m, 2H, d), 3.49 – 3.65 (m, 16H, O-CH_2), 3.73 – 3.86 (m, 2H, i), 4.04 – 4.13 (m, 2H, c), 4.56 (dd, J = 4.3, 2.9 Hz, 1H, e), 7.29 (d, J = 8.1 Hz, 2H, a), 7.73 (d, J = 8.1 Hz, 2H, b) ppm. **^{13}C NMR:** (126 MHz, $CDCl_3$) δ = 19.4, 19.7, 21.6, 25.4, 30.5, 30.6, 43.6, 62.1, 62.8, 66.6, 68.6, 69.2, 70.4, 70.5, 70.6, 94.5, 94.5, 98.8, 98.9, 127.9, 129.8, 132.9 ppm. **ESI-HRMS**(ACN): *m/z* calcd. for $[C_{22}H_{36}O_9S]$: 499.1972 $[M+Na]^+$, found: 499.1955; calcd. for $[M+K]^+$: 515.1712, found: 515.1694.

3-(2-((Tetrahydro-2*H*-pyran-2-yl)oxy)ethoxy)-2-naphthol[7]

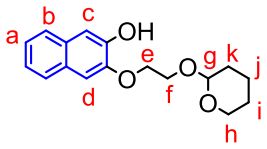

S7

A solution of protected monotosylate **S5** (96.0 mg, 0.32 mmol, 1.0 equiv.), naphthol **S6** (51.0 mg, 0.32 mmol, 1.0 equiv.) and K_2CO_3 (190 mg, 1.4 mmol, 4.3 eq) in dry DMF (20 mL) was stirred at 80 °C in an argon atmosphere for 12 h. Afterwards, residual K_2CO_3 was filtered off and the solvent was removed under reduced pressure. The crude product was then purified by column chromatography (SiO_2, CH_2Cl_2/MeOH = 100:1, R_f ~ 0.8 in CH_2Cl_2/MeOH = 50:1) to isolate the desired product **S7** as a colourless oil in a 41% yield (37.5 mg, 0.13 mmol). **^{1}H NMR** (500 MHz, $CDCl_3$): δ = 1.50 – 1.91 (m, 6H, j, k, l), 3.53 – 3.60 (m, 1H, h'), 3.89 – 3.97 (m, 2H, h'', f'), 4.07 – 4.16 (m, 1H,f''), 4.31 – 4.35 (m, 2H, e), 4.73 (dd, *J* = 4.6, 2.9 Hz, 1H, g), 7.20 (s, 1H, c), 7.27 (s, 1H, d), 7.28 – 7.34 (m, 2H, a, a'), 7.63 – 7.67 (m, 2H, b, b') ppm. **^{13}C NMR** (126 MHz, $CDCl_3$): δ = 19.7, 25.4, 30.7, 30.8, 62.8, 66.4, 69.5, 99.7, 109.0, 110.0, 123.5, 123.9, 124.6, 126.5, 126.7, 128.9, 130.4, 146.7, 147.0 ppm. **ESI-HRMS**(MeOH): *m/z* calcd. for $[C_{17}H_{20}O_4]$: 311.1254 $[M+Na]^+$, found: 311.1279; calcd for $[M+K]^+$ 327.0993, found: 327.1018.

2-(2-((3-((14-((Tetrahydro-2*H*-pyran-2-yl)oxy)-3,6,9,12-tetraoxatetradecyl)oxy)naphthalen-2-yl)oxy)ethoxy)tetrahydro-2*H*-pyran[7]

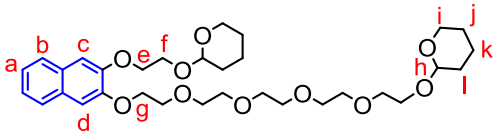

S8

A suspension of protected monotosylate **S3** (3.10 g, 6.44 mmol, 1 equiv.), monosubstituted naphthol **S7** (1.86 g, 6.44 mmol, 1 equiv.) and K_2CO_3 (3.80 g, 27.7 mmol, 4.3 equiv.) in dry ACN (100 mL) was refluxed under an argon atmosphere overnight. Afterwards K_2CO_3 was filtered off and the solvent was removed under reduced pressure. The crude product was then purified by column chromatography (SiO_2, EtOAc, R_f ~ 0.5 in EtOAc) to isolate the desired product **S8** as a colourless oil in a 50% yield (1.90 g, 3.21 mmol). **^{1}H NMR** (500 MHz, $CDCl_3$): δ = 1.44 – 1.90 (m, 12H, j, k, l), 3.45 – 3.61 (m, 4H, i), 3.61 – 3.91 (m, 15H, O-C$\underline{H}_2$), 3.91 – 3.96 (m, 2H, f), 3.96 – 4.02 (m, H, O-C$\underline{H}_2$), 4.11 – 4.16 (m, 1H, O-C$\underline{H}_2$), 4.17 – 4.23 (m, 1H, O-C$\underline{H}_2$), 4.25 – 4.33 (m, 4H, e, g), 4.59 – 4.63 (m, 1H, h), 4.73 – 4.78 (m, 1H, h'), 7.16 (s, 1H, d), 7.18 (s, 1H, c), 7.29 – 7.35 (m, 2H, a, a'), 7.63 – 7.67 (m, 2H, b, b') ppm. **^{13}C NMR** (126 MHz,

$CDCl_3$): δ = 19.4, 19.6, 19.9, 25.5, 25.6, 30.6, 30.7, 30.8, 62.2, 62.3, 65.7, 66.7, 68.3, 68. 6, 69.7, 70.6, 70.7, 70.7, 70.8, 71.1, 99.0, 108.7, 108.8, 124.3, 124.3, 124.5, 124.5, 126.4, 126.4, 126.5, 126.5, 129.4, 129.5, 129.6, 149.2, 149.3 ppm. **ESI-HRMS**(MeOH): *m/z* calcd. for $[C_{32}H_{48}O_{10}]$: 615.3140 $[M+Na]^+$, found: 615.3136; calcd for $[M+K]^+$: 631.2879, found: 631.2876.

14-((3-(2-Hydroxyethoxy)naphthalen-2-yl)oxy)-3,6,9,12-tetraoxatetradecan-1-ol[8]

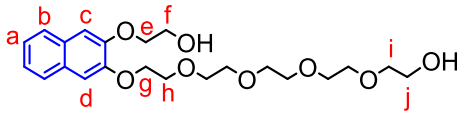

S9

A solution of diprotected glycol ether **S8** (1.90 g, 3.21 mmol) in MeOH (50 mL) was acidified with conc. HCl, until the solution reached pH = 1. After 2 h stirring at r.t. the solvent was removed under reduced pressure and the oily residue was stirred at 40 °C in oil pump vacuum for 5 h to obtain the desired product **S9** as a colourless oil in a 96% yield (1.31 g, 3.08 mmol). **^{1}H NMR** (500 MHz, $CDCl_3$): δ = 3.53 – 3.58 (m, 2H, j), 3.61 – 3.73 (m, 12H, O-C$\underline{H}_2$), 3.73 – 3.77 (m, 2H, i), 3.91 – 3.95 (m, 2H, h), 3.97 – 4.02 (m, 2H, f), 4.14 – 4.19 (m, 2H, e), 4.25 – 4.29 (m, 2H, g), 7.09 (s, 2H, d), 7.15 (s, 2H, c), 7.28 – 7.34 (m, 2H ,a, a'), 7.61 – 7.68 (m, 2H, b, b') ppm. **^{13}C NMR** (126 MHz, $CDCl_3$): δ = 60.9, 61.7, 68.2, 69.5, 70.3, 70.4, 70.6, 70.6, 70.7, 71.1, 72.7, 108.0, 108.1, 124.3, 124.5, 124.5, 126.4, 126.4, 129.2, 129.5, 148.7, 148.9 ppm. **ESI-HRMS**(ACN): *m/z* calcd. for $[C_{22}H_{32}O_8]$: 447.1989 $[M+Na]^+$, found: 447.1968; calcd for $[M+K]^+$: 463.1729, found: 463.1706.

2-((3-((14-(Tosyloxy)-3,6,9,12-tetraoxatetradecyl)oxy)naphthalen-2-yl)oxy)ethyl 4-methylbenzenesulfonate[9]

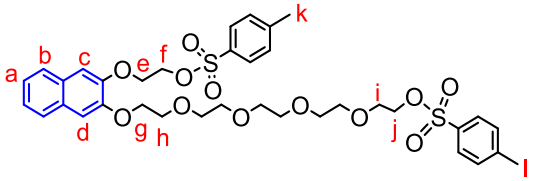

S10

A solution of 50 mg (0.12 mmol, 1.0 equiv.) diol **S9**, 100 µL (0.71 mmol, 6.0 eq) NEt_3, 0.1 mg (0.6 µmol, 0.5 mol%) DMAP and 135 mg (0.71 mmol, 6 eq) 4-toluenesulfonyl chloride in dry methylene chloride (25 mL) was left stirring at r.t. for 2 days. The reaction mixture was washed with saturated NH_4Cl aq. solution and dried with $MgSO_4$. The crude product was then purified by column chromatography (SiO_2, CH_2Cl_2 → EtOAc, R_f ~ 0.8 in EtOAc) to obtain the desired product **S10** as a colourless oil in 89% yield (77 mg, 0.11 mmol). **^{1}H NMR** (500 MHz, $CDCl_3$):

δ = 2.38 (s, 3H, l), 2.41 (s, 3H, k), 3.52 – 3.69 (m, 12H, O-CH_2), 3.75 – 3.78 (m, 2H, i), 3.91 – 3.95 (m, 2H, h), 4.11 – 4.15 (m, 2H, j), 4.22 – 4.26 (m, 2H, g), 4.27 – 4.32 (m, 2H, e), 4.41 – 4.47 (m, 2H, f), 7.04 (s, 1H, d), 7.14 (s, 1H, c), 7.27 – 7.36 (m, 6H, a, a', H-Ar-CCH_3), 7.58 – 7.67 (m, 2H, b, b'), 7.76 – 7.83 (m, 4H, H-Ar-CSO_3R) ppm. **^{13}C NMR** (126 MHz, $CDCl_3$): δ = 21.7, 21.7, 66.7, 68.2, 68.6, 68.7, 69.4, 69.6, 70.6, 70.6, 70.7, 70.8, 70.8, 71.0, 100.1, 108.9, 110.0, 110.0, 124.4, 124.7, 126.4, 126.5, 128.0, 128.1, 129.2, 129.9, 129.9, 129.9, 130.0, 133.0, 133.1, 144.9, 144.9, 145.0, 148.2, 149.1 ppm. **ESI-HRMS**(ACN): *m/z* calcd. for [$C_{36}H_{44}O_{12}S_2$]: 755.2166 [M+Na]$^+$, found: 755.2168; calcd for [M+K]$^+$: 771.1906, found: 771.1905.

1-Iodo-14-((3-(2-iodoethoxy)naphthalen-2-yl)oxy)-3,6,9,12-tetraoxatetradecane[4]

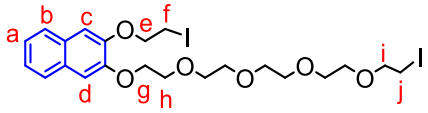

S11

A solution of 61.4 mg (83.8 µmol, 1.0 eq) ditosylate **S10** and 55.6 mg (335 mmol, 4.0 eq) KI in acetone (5 mL) was stirred at 70 °C overnight. When the reaction mixture turned yellow and a white precipitate formed, the solvent was removed under reduced pressure. The residue was dissolved in EtOAc and washed with brine. After drying with $MgSO_4$, the solvent was removed to isolate the desired product **S11** as a yellowish oil in a 96% yield (52 mg, 80.9 µmol). **^{1}H NMR** (500 MHz, $CDCl_3$): δ = 3.21 – 3.25 (m, 2H, j), 3.49 – 3.53 (m, 2H, f), 3.61 – 3.71 (m, 10H, O-CH_2), 3.71 – 3.74 (m, 2H, i), 3.78 – 3.82 (m, 2H, O-CH_2), 3.94 – 3.97 (m, 2H, h), 4.26 – 4.30 (m, 2H, g), 4.35 – 4.40 (m, 2H, e), 7.15 (s, 1H, d), 7.18 (s, 1H, c), 7.31 – 7.34 (m, 2H, a, a'), 7.64 – 7.67 (m, 2H, b, b') ppm. **^{13}C NMR** (126 MHz, $CDCl_3$): δ = 68.8, 69.7, 69.9, 70.3, 70.3, 70.7, 70.7, 70.8, 70.8, 71.1, 72.1, 72.1, 109.0, 109.9, 124.5, 124.7, 126.5, 126.5, 129.3, 129.8, 148.1, 149.1 ppm. **ESI-HRMS**(ACN): *m/z* calcd. for [$C_{22}H_{30}I_2O_6$]: 667.0024 [M+Na]$^+$, found: 666.9996; calcd. for [M+K]$^+$: 682.9763, found: 682.9730.

2-(4,5-Bis(methylthio)-1,3-dithiol-2-ylidene)-5,6,8,9,11,12,14,15,17,18,27,28-dodeca-hydro-[1,3]dithiolo[4,5-t]naphtho[2,3-b][1,4,7,10,13,16]hexaoxa[19,22]dithiacyclo-tetracosane[10]

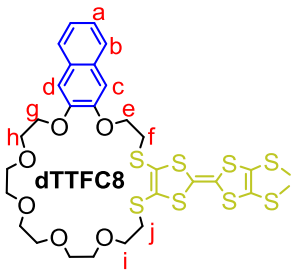

A solution of 74 mg (0.44 mmol, 2.0 equiv.) CsOH · H_2O in dry MeOH (2 mL) was added over 30 min to 104 mg (0.22 mmol, 1.0 equiv.) TTF precursor **S12** in dry DMF (5 mL). After the mixture turned dark red, it was added over 1 h to 143 mg (0.22 mmol, 1.0 equiv.) to diiodide **S11** in dry DMF (25 mL) and stirred at r.t. under argon overnight. Afterwards, the solvent was removed under reduced pressure and the residue was dissolved in CH_2Cl_2. The solution was washed with water and brine. After drying with $MgSO_4$, the crude product was purified by column chromatography (SiO_2, CH_2Cl_2, R_f ~ 0.5 in CH_2Cl_2/MeOH = 100:1) to isolate the desired product **dTTFC8** as an orange powder in a 28% yield (45.7 mg, 61 µmol). **M.p.** 79.3°C; **^{1}H NMR** (700 MHz, CD_2Cl_2): δ = 2.43 (s_{br}, 6H, S-CH_3), 3.02 (s_{br}, 4H, j), 3.30 (t, J = 6.5 Hz, 2H, f), 3.49 – 3.52 (m, 2H, O-C$\underline{H}_2$), 3.53 – 3.56 (m, 2H, O-C$\underline{H}_2$), 3.56 – 3.59 (m, 2H, O-C$\underline{H}_2$), 3.59 – 3.65 (m, 4H, i, O-C$\underline{H}_2$), 3.65 – 3.68 (m, 2H, O-C$\underline{H}_2$), 3.76 – 3.79 (m, 2H, O-C$\underline{H}_2$), 3.89 – 3.97 (m, 2H, h), 4.25 (m, 2H, O-C$\underline{H}_2$), 4.38 (s_{br}, 2H, e), 7.17 (s, 1H, c), 7.20 (s, 1H, d), 7.30 – 7.35 (m, 2H, a), 7.66 – 7.70 (m, 2H, b).ppm. **^{13}C NMR** (176 MHz, CD_2Cl_2): δ = 23.3, 29.9, 30.3, 32.5, 68.4, 69.5, 70.0, 71.0, 71.1, 71.2, 71.3, 71.7, 109.1, 109.8, 124.8, 124.9, 126.8, 126.9, 129.8, 130.2, 149.1, 149.7 ppm. **ESI-HRMS**(ACN): *m/z* calcd. for [$C_{30}H_{36}O_6S_8$]: 771.0170 $[M+Na]^+$, found: 771.0182; calcd. for $[M+K]^+$: 786.9909, found: 786.9916.

1.3. Synthesis of [2]rotaxane (*rac*)-2 and (*rac*)-2Ac

[2]Rotaxane (*rac*)-2

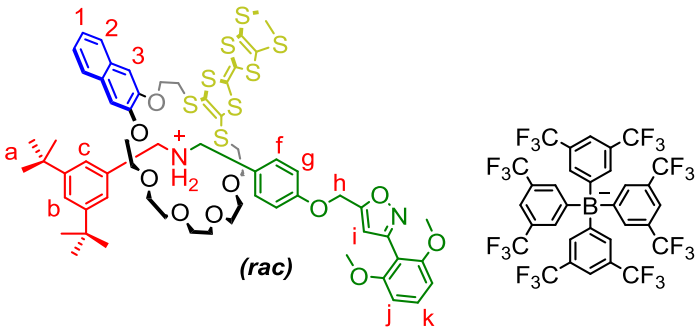

(*rac*)-**2**

Axle **A1** (74 mg, 60 µmol, 1.0 equiv.) and macrocycle **dTTFC8** (50 mg, 67 µmol, 1.1 equiv.) were dissolved in dry CH_2Cl_2 (200 µL) and stirred at r.t. for 10 min. Afterwards 2,6-dimethoxybenzonitrile oxide **St1** (14 mg, 78 µmol, 1.3 equiv.) was added and the mixture was stirred in a sealed tube under argon at 35 °C overnight. Then, the mixture was applied directly onto a preparative thin layer chromatography plate (SiO_2 2000 µm, CH_2Cl_2, R_f ~ 0.6 in CH_2Cl_2) to obtain the desired racemic product (*rac*)-**2** (129 mg, 60 µmol, 73 %) as a yellowish oil. **^{1}H NMR** (700 MHz, CD_2Cl_2): δ = 1.25 (s, 18H, a), 2.42 (s, 3H, -SMe), 2.43 (s, 3H, -SMe), 3.05 – 3.18 (m, 6H, O-C$\underline{H}_2$), 3.23 – 3.33 (m, 4H, O-C$\underline{H}_2$), 3.37 – 3.46 (m, 4H, O-C$\underline{H}_2$), 3.58 – 3.68 (m, 2H, O-C$\underline{H}_2$), 3.75 – 3.91 (m, 10H, O-C$\underline{H}_2$, -OMe), 4.28 – 4.40 (m, 2H, O-C$\underline{H}_2$), 4.43 – 4.46 (m, 2H, O-C$\underline{H}_2$), 4.53 – 4.77 (m, 4H, C$\underline{H}_2$-NH_2), 5.04 (d, *J* = 12.8 Hz, 1H, h), 5.08 (d, *J* = 13.0 Hz, 1H, h), 6.44 (s, 1H, i), 6.66 (d, *J* = 8.5 Hz, 2H, j), 6.95 (d, *J* = 8.7 Hz, 2H, g), 7.19 (s, 1H, 3), 7.24 (s, 1H, 3), 7.27 (d, *J* = 1.6 Hz, 2H, c), 7.35 – 7.41 (m, 5H, f, k, 1), 7.47 (t, *J* = 1.8 Hz, 1H, b), 7.55 (s_{br}, 4H, $BArF_{24}$), 7.66 – 7.69 (m, 2H, 2), 7.69 (s_{br}, 8H, $BArF_{24}$) 7.77 – 7.86 (m, 2H, NH_2) ppm. **^{13}C NMR** (176 MHz, CD_2Cl_2): δ = 19.6, 31.7, 35.4, 36.3, 37.3, 53.3, 56.5, 61.6, 68.7, 69.4, 70.5, 70.6, 71.0, 71.2, 71.2, 71.3, 71.5, 104.7, 107.3, 107.4, 109.1, 109.3, 109.6, 113.8, 115.6, 118.0, 118.1, 124.4, 124.7, 124.8, 125.0, 125.7, 126.0, 126.9 127.5, 127.8, 128.2, 128.2, 128.8, 129.4, 129.8, 129.9, 130.9, 132.0, 132.0, 135.4, 148.3, 148.4, 152.4, 157.8, 159.5, 162.3, 166.2 ppm. **ESI-HRMS**(MeOH): *m/z* calcd. for $[C_{64}H_{79}N_2O_{10}S_8]^+$: 1291.3495 $[M]^+$, found: 1291.3479.

[2]Rotaxane (*rac*)-2Ac

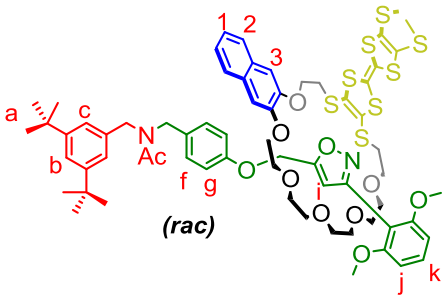

(*rac*)-**2Ac**

Rotaxane (*rac*)-**2** (14 mg, 6.5 µmol, 1.0 equiv.), NEt_3 (27 µL, 190 µmol, 30.0 equiv.) and Ac_2O (18 µL, 190 µmol, 30.0 equiv.) were dissolved in ACN (5 mL) and stirred at r.t. overnight. Then, the crude mixture was purified by preparative TLC (SiO_2 2000 µm, CH_2Cl_2/MeOH 50:1, R_f ~ 0.3 in CH_2Cl_2/MeOH = 50:1) to isolate the desired racemic product (*rac*)-**2Ac** as a yellowish oil in 95% yield (8.2 mg, 3.5 µmol). **^{1}H NMR** (700 MHz, CD_2Cl_2): δ = 1.29 (s, 9H, a), 1.32 (s, 9H, a), 1.78 (s, 1.5H, Ac), 1.90 (s, 1.5H, Ac), 2.24 (s, 1.5H, SMe), 2.30 (s, 1.5H, SMe), 2.33 (s, 1.5H, SMe), 2.34 (s, 1.5H, SMe), 3.02 – 3.15 (m, 3.6H, O-CH_2), 3.16 – 3.22 (m, 1.4H, O-CH_2), 3.34 – 3.44 (m, 4.5H, O-CH_2), 3.45 – 3.62 (m, 8H, O-CH_2), 3.64 – 3.74 (m, 5H, O-CH_2), 3.78 (d, *J* = 3.9 Hz, 6H, OMe), 3.81 – 3.83 (m, 0.7H, O-CH_2), 3.83 – 3.85 (m, 0.7H, O-CH_2), 3.95 – 4.04 (m, 4H, CH_2-N, O-CH_2), 4.05 – 4.13 (m, 2H, O-CH_2), 4.18 – 4.21 (m, 1H, CH_2-N), 4.22 – 4.26 (m, 1H, O-CH_2), 4.29 – 4.32 (m, 1H, CH_2-N), 4.37 – 4.40 (m, 1H, CH_2-N), 4.41 – 4.46 (m, 1H, CH_2-N), 5.80 – 5.87 (m, 2H, h), 6.64 (dd, *J* = 8.4, 5.6 Hz, 2H, j), 6.71 – 6.73 (m, 2H, g, i), 6.78 – 6.81 (m, 1H, g), 6.85 (s, 0.5H, 3), 6.87 (d, *J* = 1.8 Hz, 1H, c), 6.90 (s, 0.5H, 3), 6.91 (d, *J* = 1.8 Hz, 1H, c), 7.00 – 7.02 (m, 2H, f), 7.05 (*s*, 0.5H, 3), 7.07 (*s*, 0.5H, 3), 7.19 – 7.25 (m, 2H, 1), 7.29 (t, *J* = 1.9 Hz, 0.5H, b), 7.33 (t, *J* = 1.8 Hz, 0.5H, b), 7.35 (td, *J* = 8.4, 4.6 Hz, 1H, k), 7.55 – 7.59 (m, 1H, 2), 7.60 – 7.64 (m, 1H, 2) ppm. **^{13}C NMR** (176 MHz, CD_2Cl_2): δ = 19.2, 19.3, 19.3, 19.4, 21.8, 21.8, 30.3, 31.8, 32.5, 34.6, 35.2, 35.3, 35.5, 35.6, 46.59, 47.9, 48.8, 50.9, 51.3, 56.5, 56.5, 61.4, 61.4, 67.5, 67.5, 69.1, 69.2, 70.1, 70.2, 70.2, 70.5, 70.5, 71.2, 71.3, 71.3, 71.5, 71.5, 71.7, 71.7, 71.9, 104.5, 104.6, 107.1, 107.4, 107.5, 108.0, 108.1, 108.4, 108.4, 110.0, 110.1, 110.8, 115.2, 115.4, 121.0, 121.6, 121.8, 122.4, 123.9, 124.3, 124.6, 124.6, 124.6, 126.6, 126.7, 126.7, 126.7, 127.6, 127.7, 128.8, 129.0, 129.5, 129.6, 129.6, 129.9, 131.5, 131.5, 134.2, 134.5, 136.7, 137.3, 148.8, 148.9, 149.0, 149.1, 151.9, 157.4, 158.2, 158.3, 159.3, 168.9, 169.1, 171.1, 171.2 ppm. **ESI-HRMS**(MeOH): *m/z* calcd. for $[C_{66}H_{80}N_2O_{11}S_8]$: 1333.3606 $[M+H]^+$, found: 1333.3505; calcd. for $[M+Na]^+$: 1355.3425, found: 1355.3442; calcd. for $[M+K]^+$: 1371.3165, found: 1371.3185.

2. FTICR mass spectroscopy

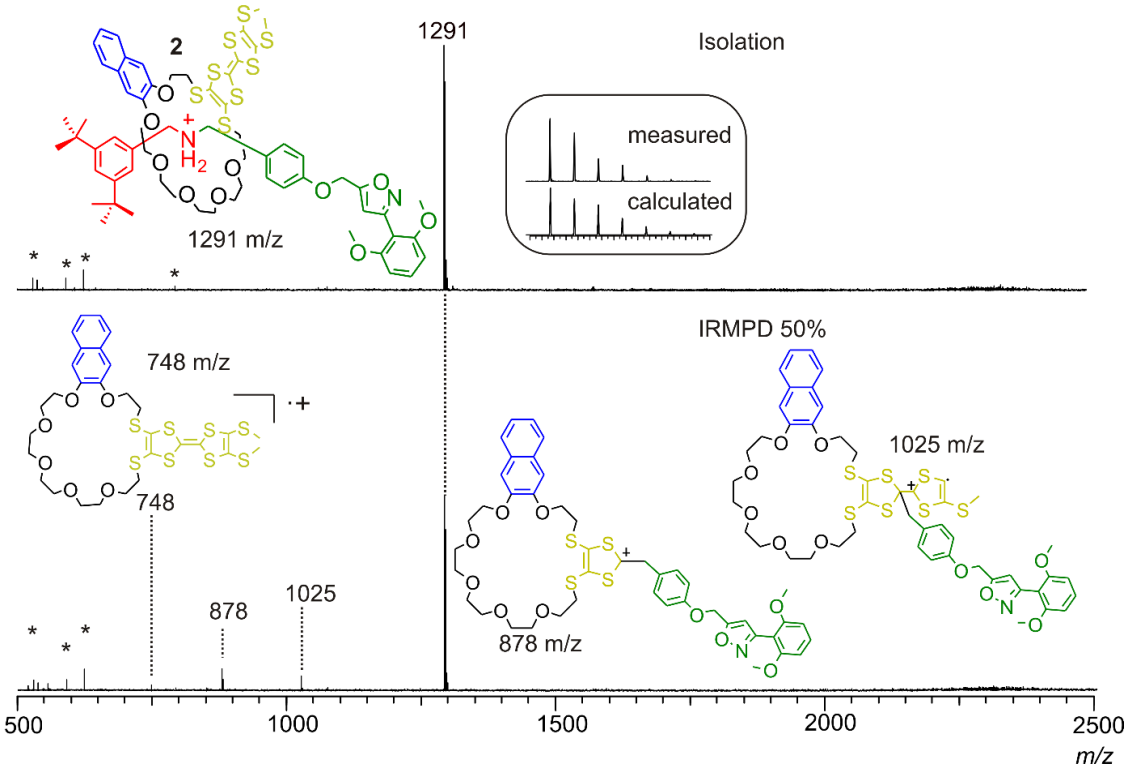

Fig. S1 ESI-FTICR infrared multiphoton dissociation (IRMPD) experiment with mass-selected rotaxane ions at *m/z* 1291 obtained from a MeOH solution (10 µM) of [2]rotaxane (*rac*)-**2**: (top) after mass-selection; (bottom) after fragmentation. The fragment peaks could be assigned to the free macrocycle as a radical cation (748 *m/z*) and two adducts, which arise from an attack of the TTF moiety on the benzylic position next to the nitrogen of the axle. These fragments are in line with the fragments obtained from rotaxanes of the non-directional **TTFC8** macrocycle.[4] As no free axle is observed as the fragmentation product, it can be concluded that the ionised and mass selected species are in fact mechanically interlocked. Electromagnetic stray radiation is marked with asterisks.

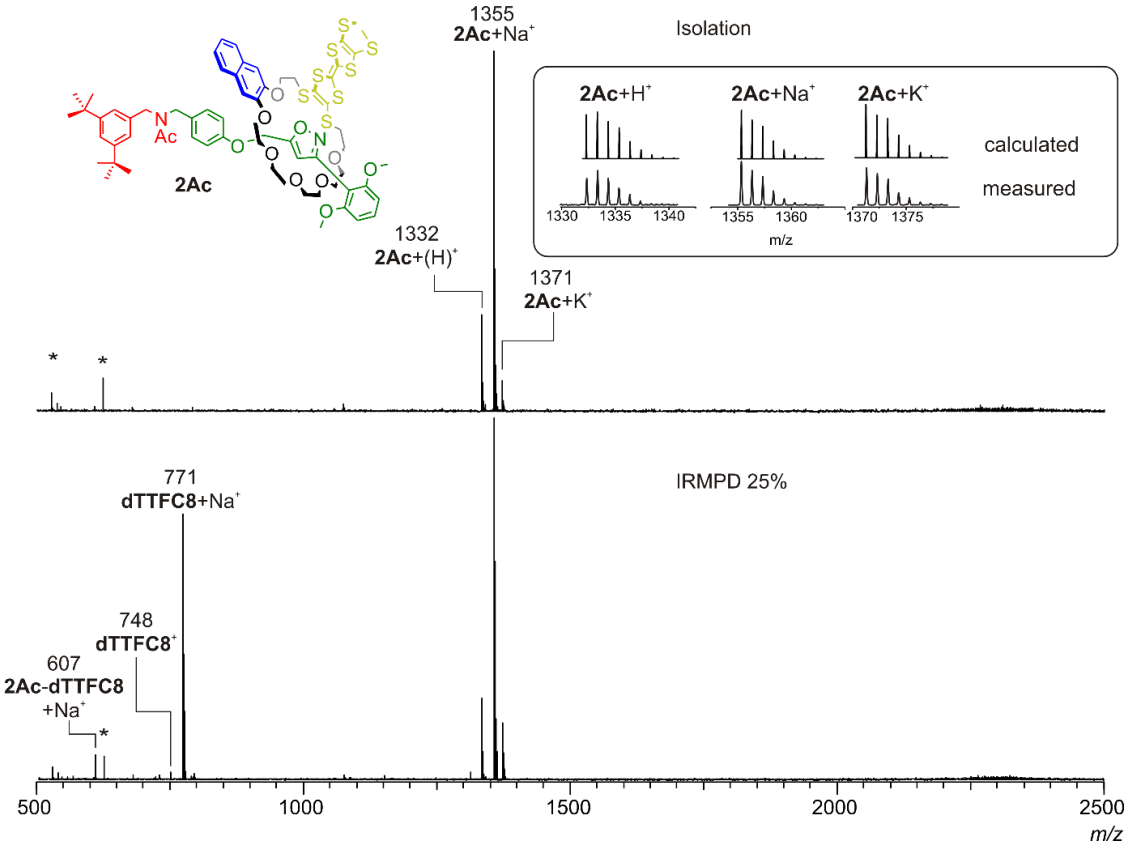

Fig. S2 ESI-FTICR infrared multiphoton dissociation (IRMPD) experiment with mass range-selected rotaxane ions obtained from a MeOH solution (10 µM) of [2]rotaxane (*rac*)-**2Ac**. The acetylated [2]rotaxane **2Ac** ions do not show the same fragmentation pattern as **2,** as no fragments from an intramolecular attack could be observed. Fragmentation proceeds by either losing the macrocycle (607 m/z) or fragmenting the axle leaving the charge on the macrocycle (748 and 771 m/z)

3. Variable Temperature NMR Spectroscopy

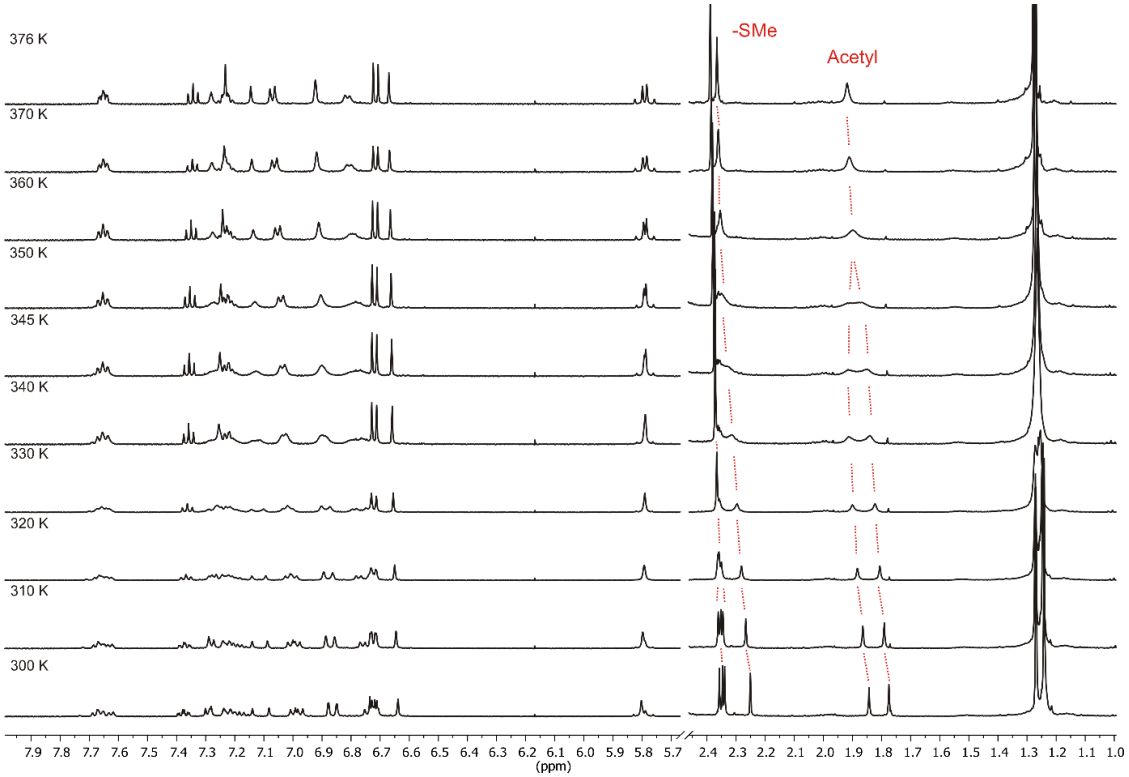

Fig. S3 Partial spectra of [2]rotaxane (*rac*)-**2Ac** in a VT ^{1}H NMR (500 MHz, DMSO-d6) experiment (gradual heating from 300 to 375 K), showing the coalescence of the acetyl groups and merging of the four singlets corresponding to SMe on the TTF into two singlets upon heating.

The free energy of activation ($\Delta G^{\ddagger}$) was calculated using the modified Eyring equation (eq. 1), where R is the ideal gas constant, T_c the coalescence temperature and $\Delta\nu$ the peak to peak separation between the signals for the two interconverting isomers in Hz.

$$\Delta G^{\ddagger} = R\,T_c\,(22.96 + \ln(T_c/\Delta\nu))\ \text{kJ mol}^{-1} \qquad \text{(eq. 1)}$$

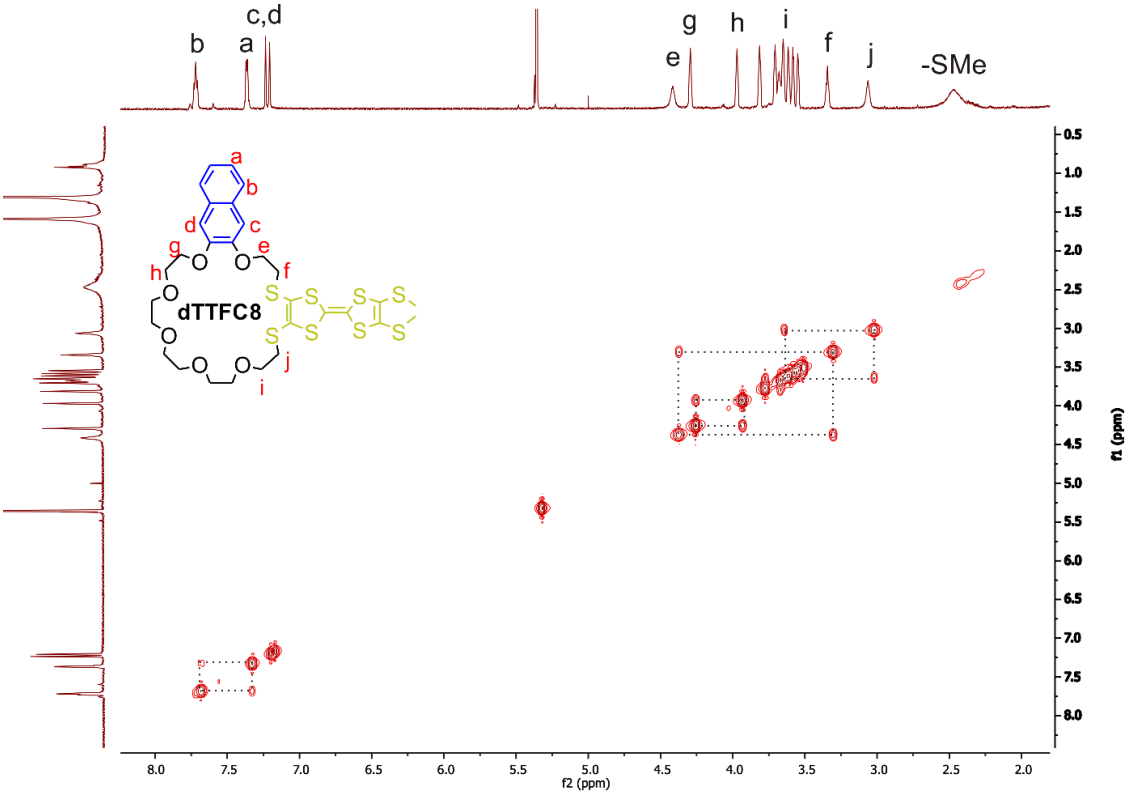

Fig. S4 COSY spectrum of **dTTFC8** in a (700 MHz, CD_2Cl_2).

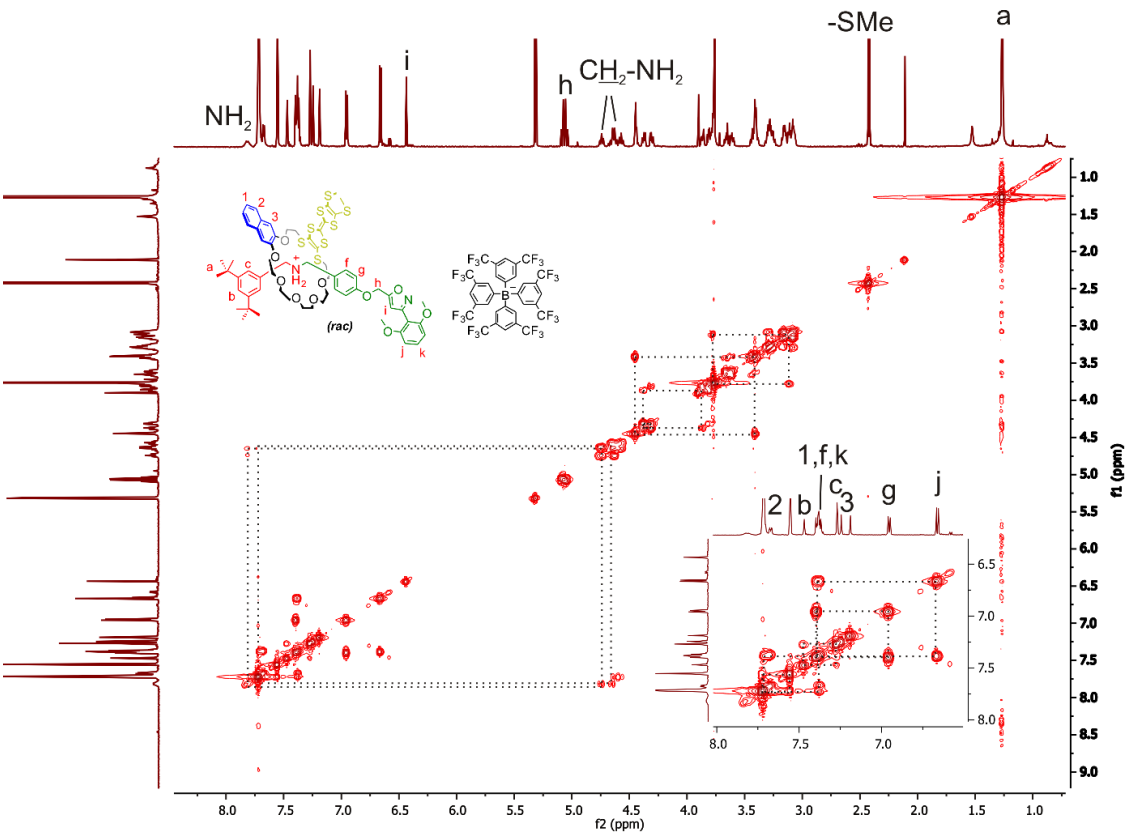

Fig. S5 COSY spectrum of (*rac*)-**2** in a (700 MHz, CD_2Cl_2).

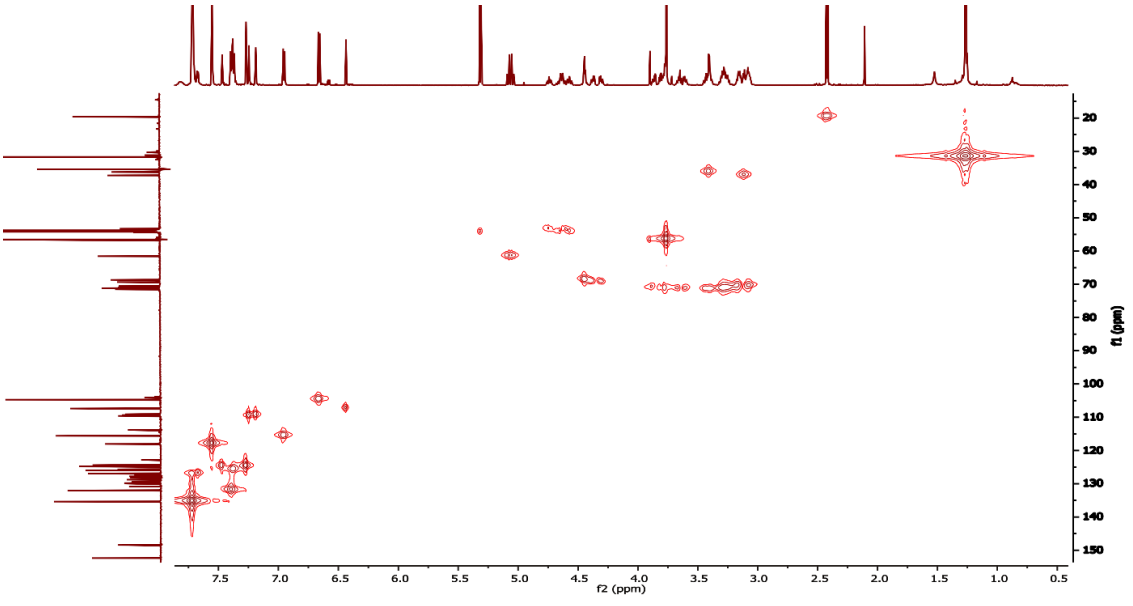

Fig. S6 HMQC spectrum of (*rac*)-**2** in a (700 MHz, CD_2Cl_2).

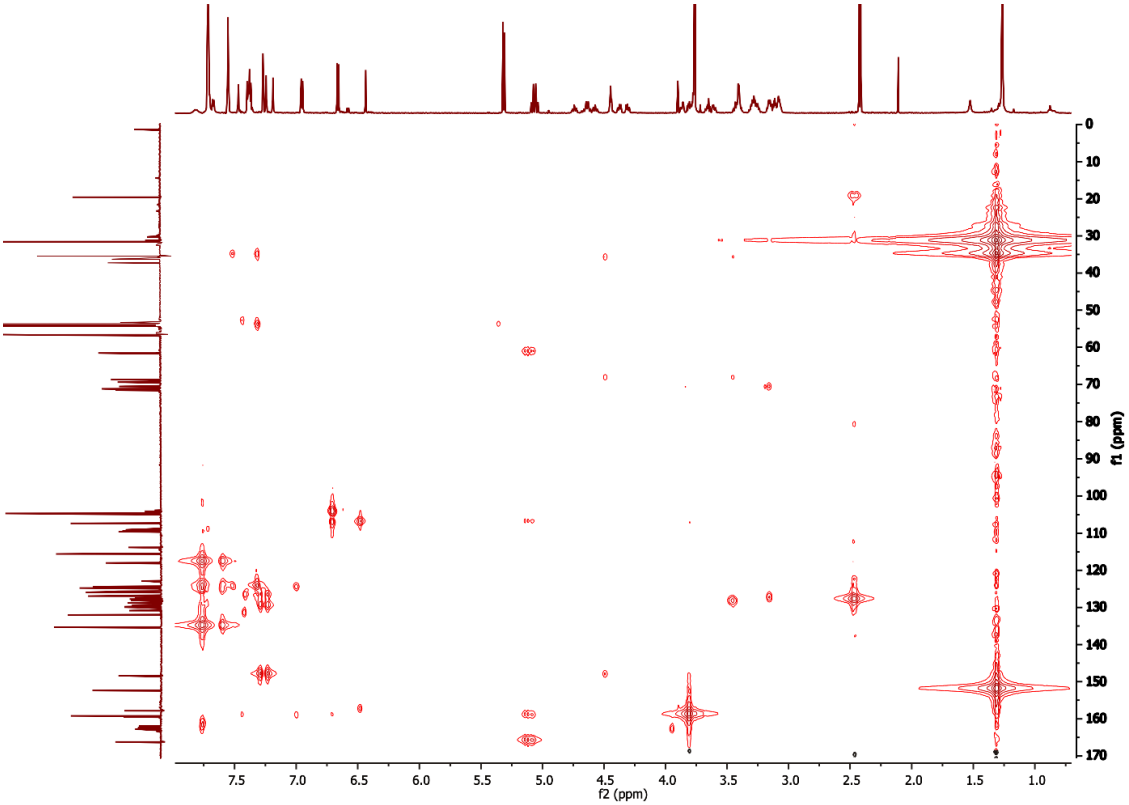

Fig. S7 HMBC spectrum of (*rac*)-**2** in a (700 MHz, CD_2Cl_2).

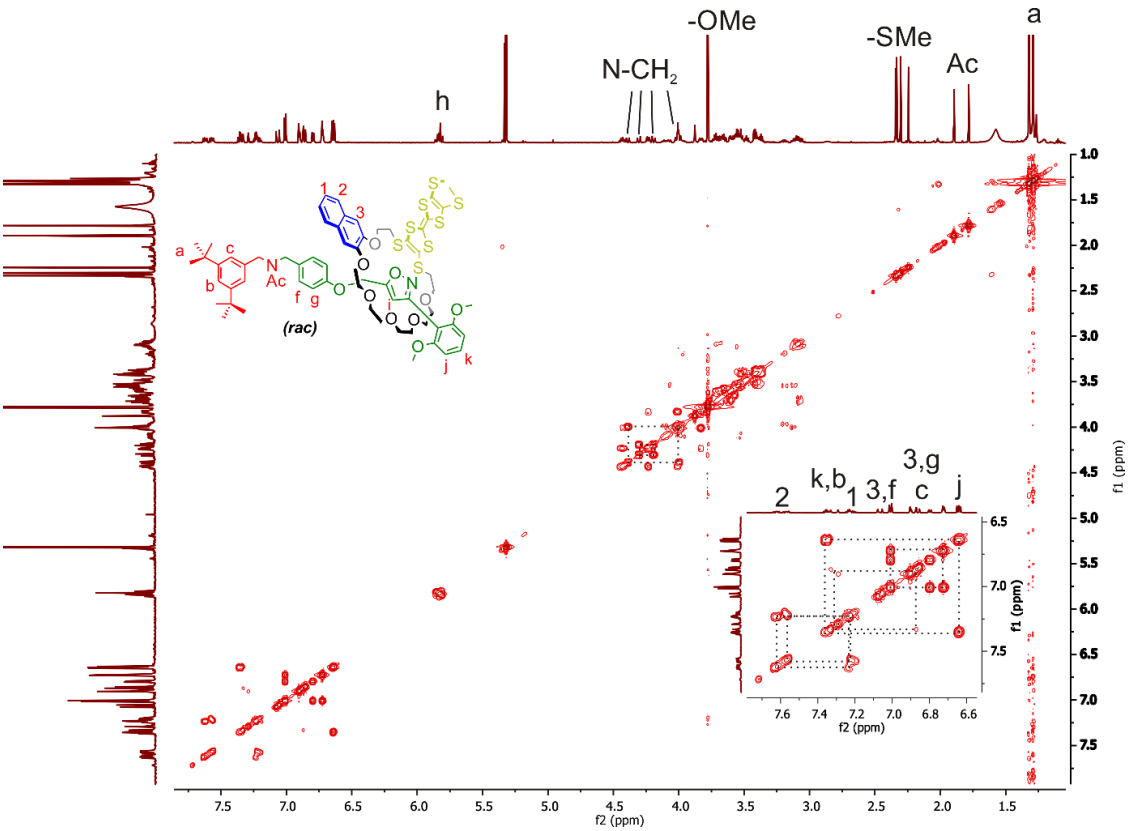

Fig. S8 COSY spectrum of (*rac*)-**2Ac** in a (700 MHz, CD_2Cl_2).

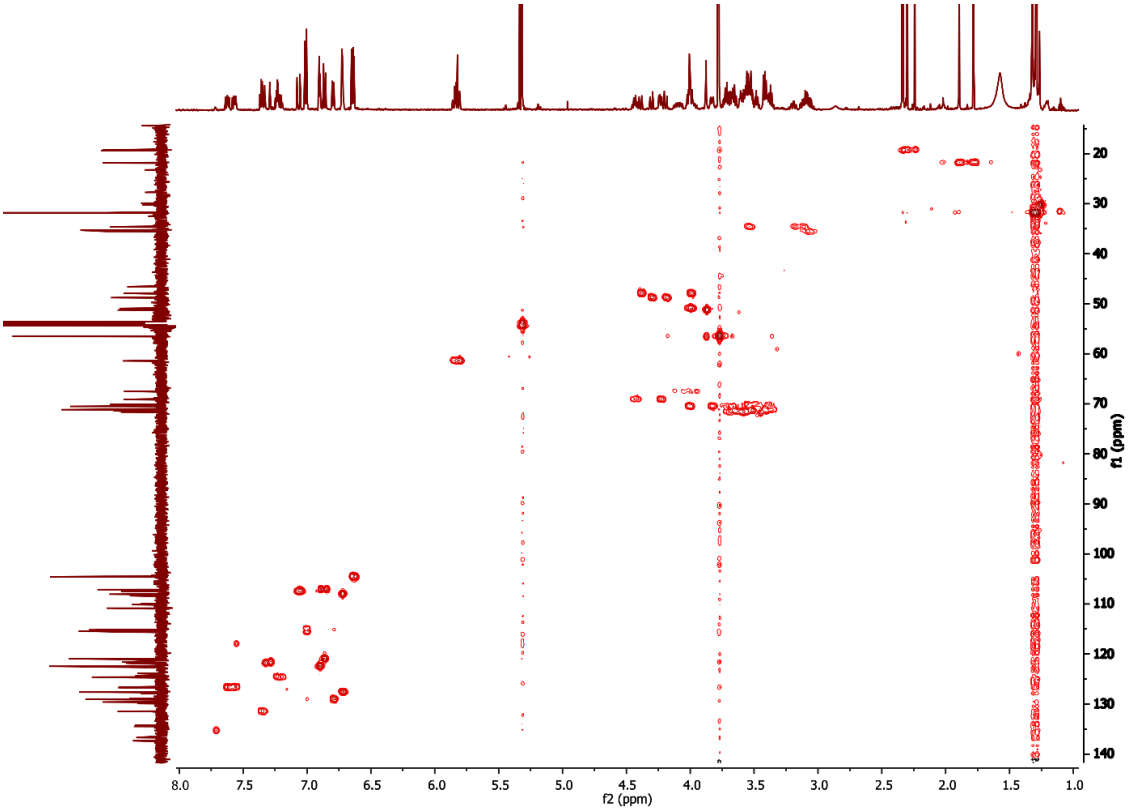

Fig. S9 HMQC spectrum of (*rac*)-**2Ac** in a (700 MHz, CD_2Cl_2).

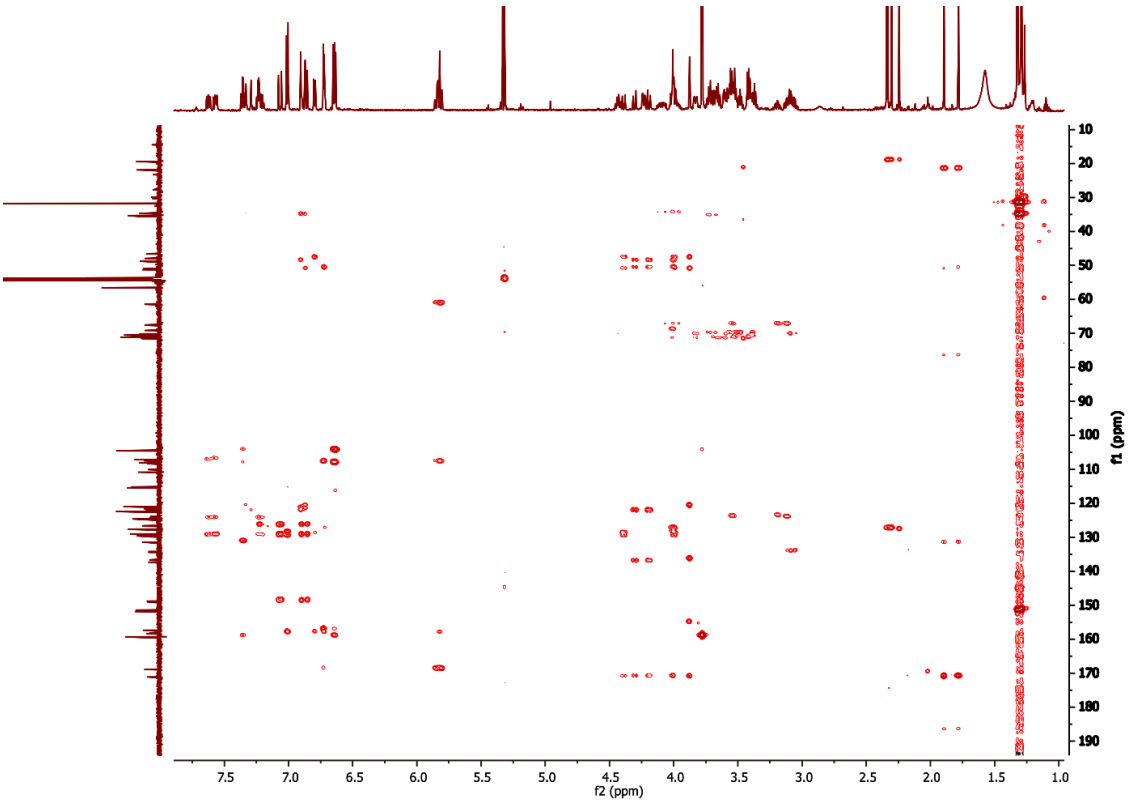

Fig. S10 HMBC spectrum of (*rac*)-**2Ac** in a (700 MHz, CD_2Cl_2).

4. Isothermal titration calorimetry

ITC experiments were carried out in dry 1,2-dichloroethane at 298 K on a TAM III microcalorimeter (Waters GmbH, TA Instruments, Eschborn, Germany). In a typical experiment, an 800 µL solution of crown ether was placed in the sample cell at a concentration of 1.1 mM, and 250 µL of a solution of the ammonium salt (8.0 mM) were put into the syringe. The titrations consisted of 32 consecutive injections of 8 µL each with a 15 min interval between injections. Heats of dilution were determined by titration of ammonium salt solutions into the sample cell containing blank solvent and were subtracted from each data set. The heat flow generated in the sample cell is measured as a differential signal between sample and reference cell. Hence, an exothermic event results in a positive and an endothermic in a negative heat flow. The data were analysed using the instrument's internal software package and fitted with a 1:1 binding model. Each titration was conducted three times and the measured values for *K* and Δ*H* were averaged.

Tab. S1: Thermodynamic data obtained from the ITC experiments.

	K_a /10^5 M^{-1}	ΔG / kJ mol^{-1}	ΔH / kJ mol^{-1}	$T\Delta S$ / kJ mol^{-1}
axle **A1⊂TTFC8**	4.4 ± 0,4	-32.2 ± 0.3	-46.2 ± 0.7	-14.0 ± 1.0
axle **A1⊂dTTFC8**	3.6 ± 0.3	-31.7 ± 0.2	-41.1 ± 1.1	-11.0 ± 1.3

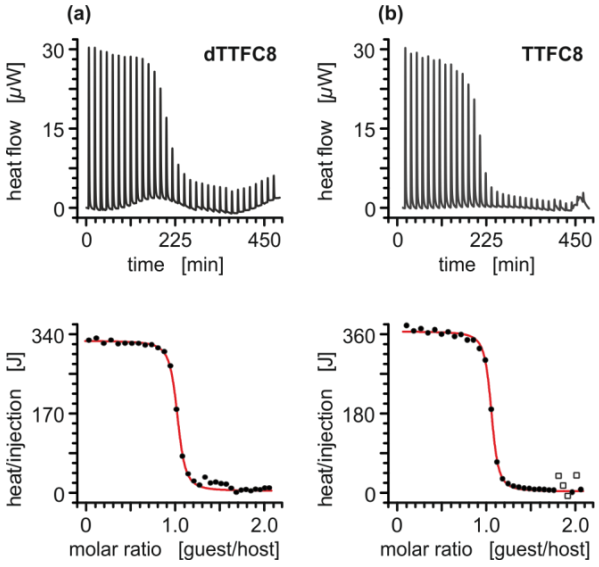

Figure S11. Titration plots (heat flow versus time and heat/volume versus guest/host ratio) obtained from ITC experiments at 298 K in 1,2-dichloroethane**: (a)** vial: **dTTFC8**, syringe: axle **A1**; **(b)** vial: **TTFC8**, syringe: axle **A1**; Points marked with non-filled squares were not considered in the fitting process.

5. Electrochemical measurements

Redox-potentials reported in this study were obtained by cyclic voltammetry. All measurements were at least conducted twice. Measurements were conducted in CH_2Cl_2 with 0.1 M electrolyte and 1 mM analyte concentration.

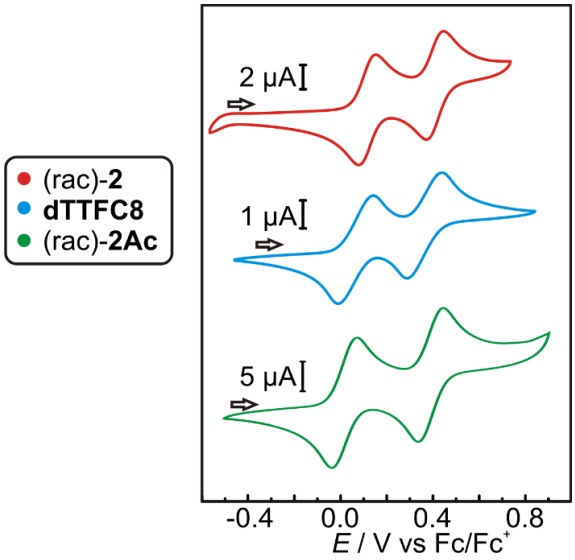

Fig. S12 Stacked cyclic voltammograms (CH_2Cl_2, n-Bu_4NPF_6, 298 K) of (*rac*)-**2**, **dTTFC8** and (*rac*)-**2Ac**

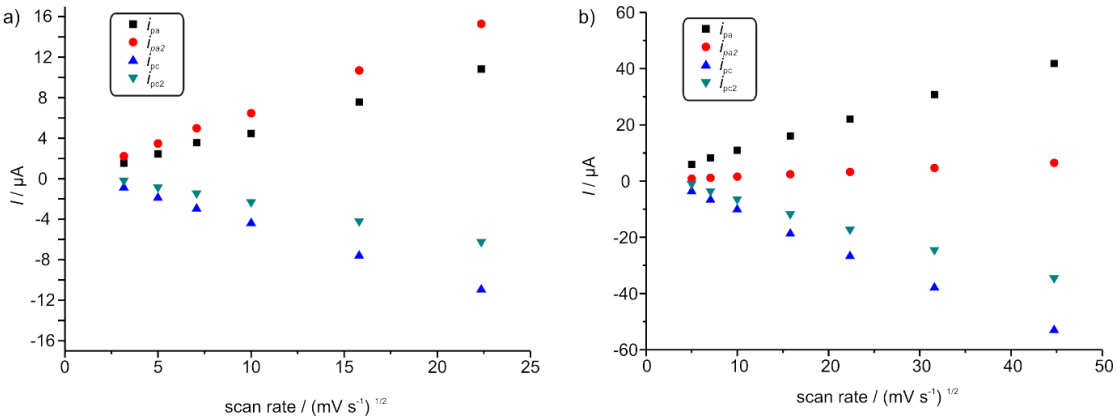

Fig. S13 Peak currents plotted against the square root of scan speed based on cyclic voltammograms of a) (*rac*)-**2** and b) (*rac*)-**2Ac** (CH_2Cl_2, with n-Bu_4NPF_6 as the electrolyte, 298 K). The peak currents can be approximated by linear functions, showing the reversibility of the redox process.

6. CD spectra

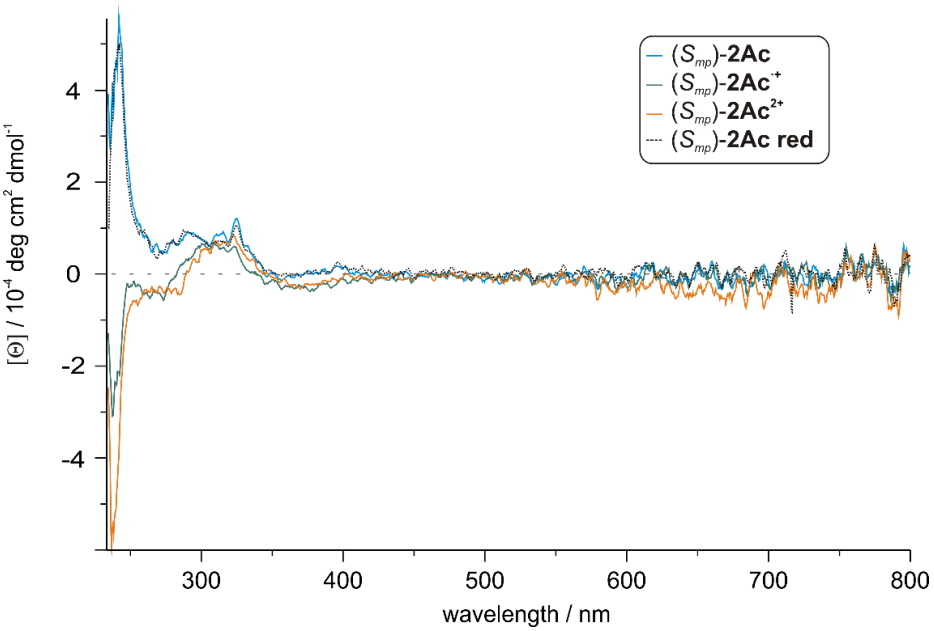

Fig. S14 CD spectra of (S_{mp})-**2Ac** (160 µM in CH_2Cl_2, 298 K, bulk $Fe(ClO_4)_3$ as the oxidant) in the TTF^0, $TTF^{\bullet+}$ and TTF^{2+} state and after reduction to the neutral form with Zn dust.

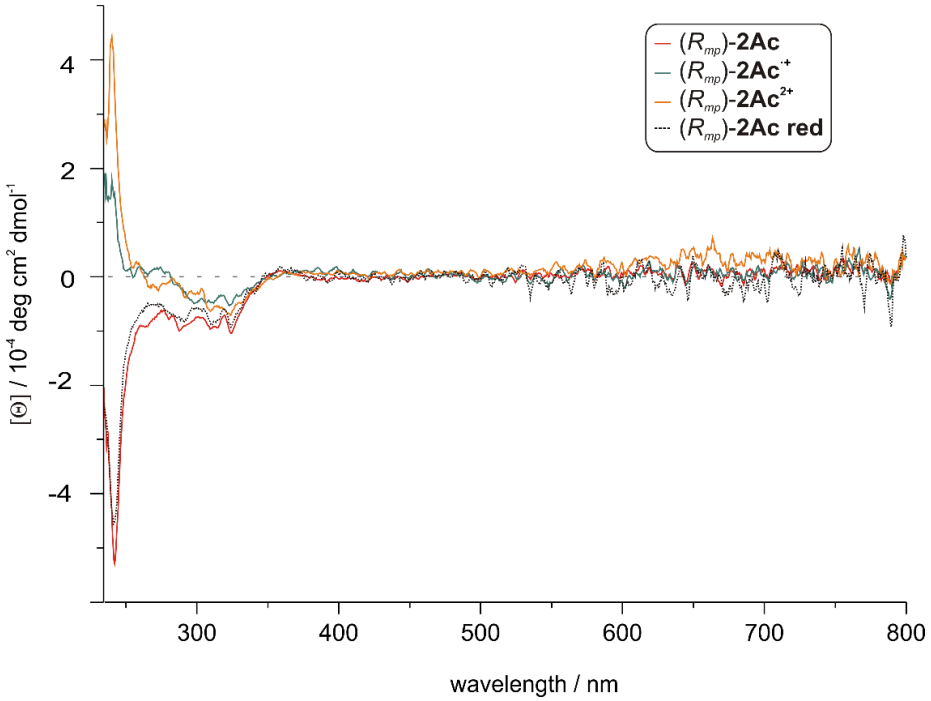

Fig. S15 CD spectra of (R_{mp})-**2Ac** (160 µM in CH_2Cl_2, 298 K, bulk $Fe(ClO_4)_3$ as oxidant) in the TTF^0, $TTF^{\bullet+}$ and TTF^{2+} state and after reduction to the neutral form with Zn dust.

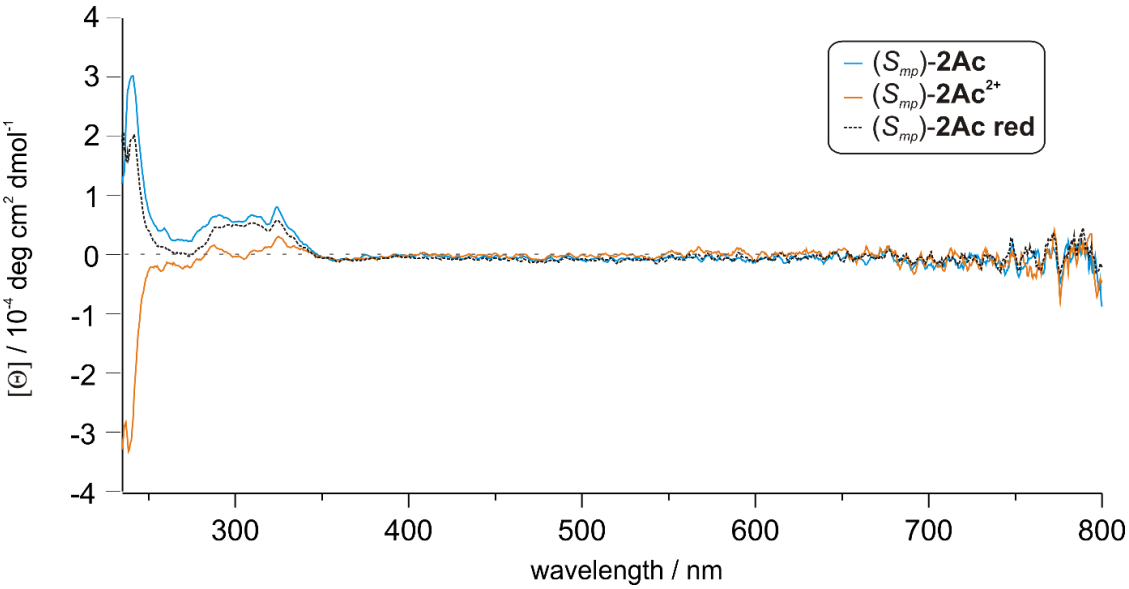

Fig. S16 CD spectra of (S_{mp})-**2Ac** (220 µM in ACN, 298 K, bulk $Fe(ClO_4)_3$ as the oxidant) in the TTF^0 and TTF^{2+} state and after reduction to the neutral form with Zn dust.

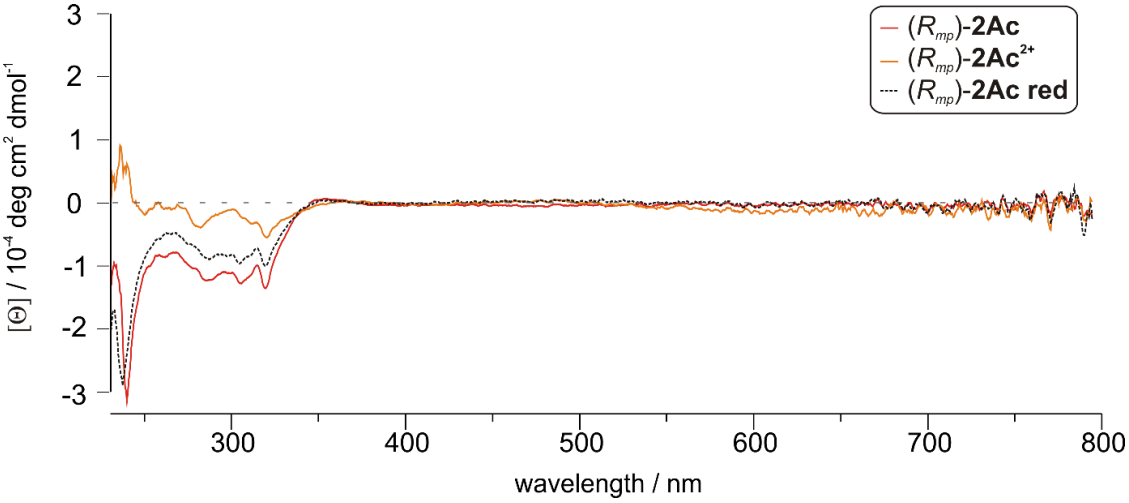

Fig. S17 CD spectra of (R_{mp})-**2Ac** (220 µM in ACN, 298 K, bulk $Fe(ClO_4)_3$ as oxidant) in the TTF^0 and TTF^{2+} state and after reduction to the neutral form with Zn dust.

7. Computational details

Conformational search. To study the influence of different conformations on the optical activity of *(*R_{mp}*)*-**2Ac**, we performed simulated annealing with the xTB (extended tight-binding) programme by Stefan Grimme.[13] This approach is based on DFTB (density functional tight binding)[14] and has been optimised for non-covalent interactions. GBSA (generalised Born accessible surface area)[15] was included as an implicit solvent model in the calculation. Using the Berendsen thermostat,[16] a maximum and minimum temperature of 1000 K and 300 K were chosen for annealing, respectively. The run time for each annealing step was 50 ps, the time step was 2 fs, and structures were dumped every 50 fs. Furthermore, the SHAKE algorithm[17] was applied to restrain hydrogen atoms from dissociating.

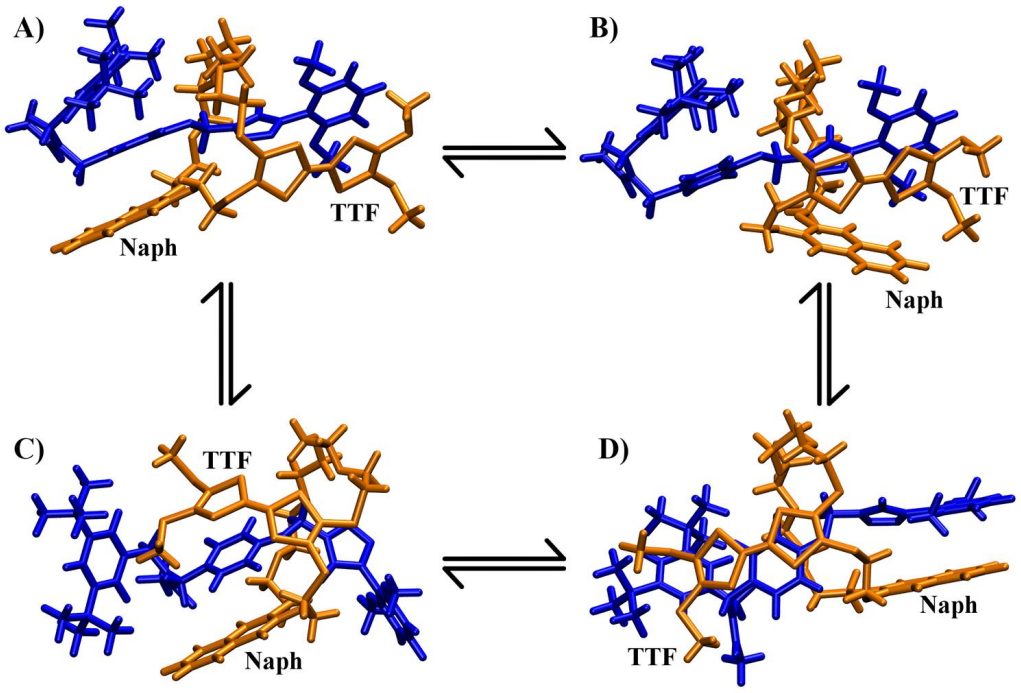

Fig. S18: The four most favourable conformations of (*R_{mp}*)-**2Ac**: **A**, **B**, **C**, and **D**. The conformations differ in the way the TTF core, the naphthalene unit, and the axle are positioned with respect to each other. Every conformation can be interconverted into another by flipping the TTF or the naphthalene unit or both.

Fig. S18 displays the four most stable conformations re-optimised at the RI*J*-TPSS-D3(BJ)/def2-SVP[18-22] level of density functional theory (DFT) with the programme package Turbomole (version 7.1)[23]. COSMO (ε = 8.9 for CH_2Cl_2)[24] was employed as the solvent model. Subsequent single-point calculations to assess the relative stabilities of the four conformations (see Table S2) were performed at the RI*J*COSX-ωB97X-D3/def2-TZVP[25, 26] level with CPCM[27]

as solvent model using ORCA (version 4.0.1)[28]. Finally, Grimme's sTD-DFT (simplified time-dependent DFT)[29] approach was used at the same level to connect electronic properties and optical activity, i.e. the ECD spectra (Fig. 4 in main text) of (R_{mp})-**2Ac**. The entire procedure was conducted for both (R_{mp})-**2Ac** and (R_{mp})-**2Ac^{2+}**.

Tab. S2: Relative electronic energies of all conformations in charge states 0 and 2+ calculated at the ωB97X-D3 level of DFT (values in kJ/mol)

charge state	conformer A	conformer B	conformer C	conformer D
0	0.0	30.4	43.9	17.9
2+	8.5	0.0	54.6	58.6

Calculations at other levels of theory (PBE0[30], CAM-B3LYP[31], and M06-2X[32]) confirm the relative stabilities of the four conformers. Moreover, the shapes of the simulated ECD spectra are considered reliable as they agree with each other regarding the signs of the CD bands. Nevertheless, a systematic red-shift in wavelengths of sometimes up to 50 nm compared to experiment is observed, which is however expected for different density functionals (see Fig. S19 for an illustrative example).

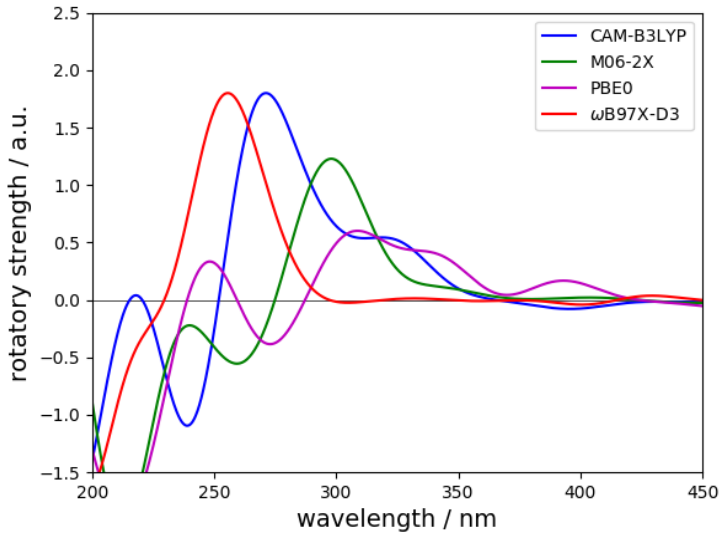

Fig. S19: ECD spectra of (R_{mp})-**2Ac**$^{2+}$ in conformation **A** computed at the sTD-DFT level with various functionals. Gaussian line broadening with σ = 20 nm was applied. Vertical transition lines are omitted for clarity. It can be observed that the general shapes of the spectra agree while the absolute positions of the signals vary in wavelengths to some extent.

Furthermore, it should be noted that (R_{mp})-**2Ac**$^{2+}$ in all four conformations displays non-negligible rotarory strengths for the TTF-centered transition at around 650-700 nm (not shown in Fig. S19) which is caused by an overestimation of the magnetic dipole transition moment

owing to a seemingly poor description of the TTF-TTF transition within the sTD-DFT framework.

Electronic structure and transitions.

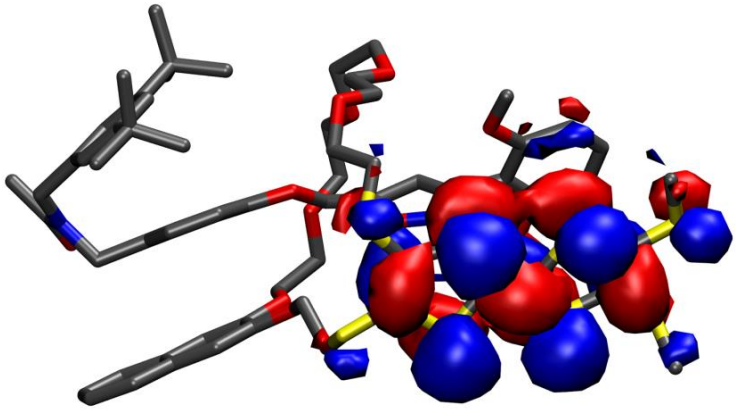

Fig. S20: HOMO of **2Ac** in conformation **A** (the same nodal shape can be observed for the LUMO of **2Ac**$^{2+}$), isovalue = 0.01 a_0^{-3}.

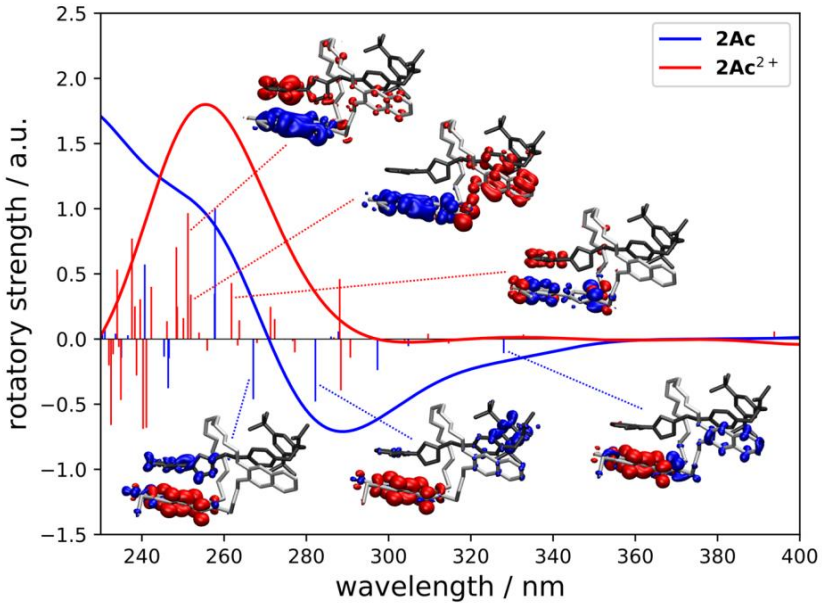

Fig. S21: Simulated ECD spectra of (R_{mp})-**2Ac** and (R_{mp})-**2Ac^{2+}** both in conformation **A** obtained at the ωB97X-D3/def2-TZVP level of sTD-DFT. Gaussian line broadening with σ = 20 nm was applied. Insets: Excited state difference densities of selected transitions to visualise the electron flow during these excitations. Blue and red zones correspond to areas of electron-enhancement and electron-depletion, respectively. Isovalue: 0.001 a_0^{-3}.

Intramolecular interactions. An atoms-in-molecules (AIM)[33] bonding analysis was performed for *(R_{mp})*-**2Ac** in all *four* conformations and charge state 0 and 2+. Fig. S22 shows *(R_{mp})*-**2Ac** in conformation **A** with its bond critical points as a representative example. An AIM analysis is useful for studying non-covalent interactions. C-H···π and π-π-stacking interactions can thus be easily identified within *(R_{mp})*-**2Ac**. Together with the results from our DFT calculations at the RI*J*COSX-ωB97X-D3/def2-TZVP level, we can deduce what is likely responsible for the conformational behaviour of *(R_{mp})*-**2Ac** and *(R_{mp})*-**2Ac**$^{2+}$. Important aspects are the energetic gain through π-π-stacking between the various (aromatic) units and the delocalisation of electron density near the TTF unit.

First, we will discuss the neutral molecule *(R_{mp})*-**2Ac**. Conformation **A** exhibits a large amount of intramolecular interactions especially through π-π-stacking of aromatic units. Furthermore, the TTF unit's proximity to the isoxazole core and the dimethoxy-phenyl moiety yield non-covalent interactions. In conformation **B**, many of the π-π-stacking interactions are lost as the naphthalene moiety attaches itself to the TTF unit, which makes this conformation around 30 kJ/mol less stable. The energetic gain in conformation **D** is based on the interaction

between the naphthalene, the isoxazole core, and the dimethoxy-phenyl unit and the stacking of the TTF unit and the phenyl spacer. However, the di-*tert*butyl-phenyl unit is not able to stack with any of the other aromatic units anymore, which results in a net loss of almost 18 kJ/mol with respect to conformation **A**. Finally, conformation **C** is the least stable structure (ca. 44 kJ/mol with respect to **A**) since effective π-π-stacking is neither achieved by the isoxazole unit nor by the dimethoxy-phenyl ring nor by the di-*tert*butyl-phenyl moiety. The energetic gain through non-covalent interactions is solely based on the arguably inefficient stacking between TTF core, phenyl spacer and naphthalene unit.

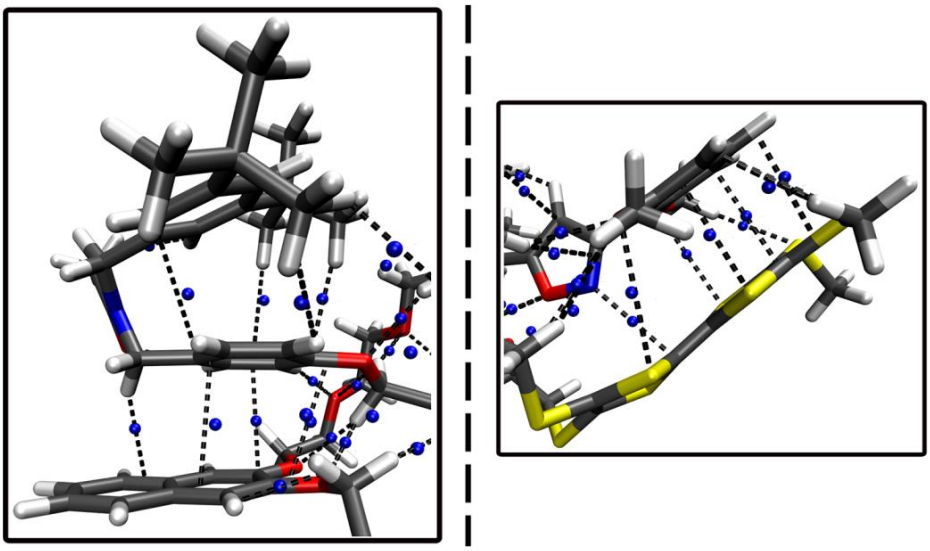

Fig. S22: Bond critical points (blue spheres) obtained at the ωB97X-D3/def2-TZVP level utilising the Multiwfn programme[34] near the naphthalene moiety (left) and the TTF unit (right) illustrating the non-covalent interactions within **2Ac** in conformation **A**.

For *(R_{mp})*-**2Ac**$^{2+}$ the picture is quite different. Now conformation **B** is the most stable structure since the charge, which is mostly localised on the TTF unit, can be delocalised over the TTF core, the naphthalene unit, the isoxazole ring, and the dimethoxy-phenyl moiety. Additionally, there is still the π-π-stacking interaction between the di-*tert*butyl-phenyl unit and the phenyl spacer contributing to its energetic stability. The charge delocalisation over four different units in the molecule is missing in conformation **A**, which makes it somewhat less stable than **B** (~ 9 kJ/mol). Similar arguments account for conformation **D**, which is – maybe somewhat surprisingly - by far the least stable structure now (over 58 kJ/mol), as the charge is not efficiently delocalised which seems to massively overcompensate any π-π-stacking interactions. In conformation **C**, the charge can be somewhat better delocalised than in **D**,

however, due to its lack of more efficient π-π-stacking interactions it is also somewhat less stable than **B** (ca. 55 kJ/mol).

8. Crystallographic data

General details. Single crystal X-ray data in the present study were collected at 170 K on a Bruker-Nonius KappaCCD diffractometer with APEX-II detector and graphite monochromatized Mo-Kα (λ = 0.71073 Å) radiation. The *COLLECT*[35] software was used for data collection (θ and ω scans) and *DENZO-SMN*[36] for the processing. Lorentzian polarization correction was applied on all data and absorption effects were corrected with multi-scan method (*SADABS*[37]). The structures were solved by intrinsic phasing methods (*SHELXT*[38]) and refined by full-matrix least squares on F^2 using *SHELXL*-2018/3.[39] The *SQUEEZE* module of *PLATON*[40, 41] was utilized in the structure refinement to remove the residual electron densities, which could not be reliably assigned and refined. Anisotropic displacement parameters were assigned to non-H atoms. Positional disorder in the structures was treated by gently restraining geometric and anisotropic displacement parameters. All hydrogen atoms were refined using riding models with U_{eq}(H) of 1.5U_{eq}(C) for terminal methyl groups and of 1.2U_{eq}(C) for other groups. The main details of crystal data collection and refinement parameters are presented below. CCDC 1910670 contains the supplementary crystallographic data for this paper. These data can be obtained free of charge via http://www.ccdc.cam.ac.uk/conts/retrieving.html (or from the CCDC, 12 Union Road, Cambridge CB2 1EZ, UK; Fax: +44 1223 336033; E-mail: deposit@ccdc.cam.ac.uk).

Structure of dTTFC8: Compound **dTTFC8** was crystallised as orange needles with vapour diffusion of Et_2O into CH_2Cl_2 solution of the compound. Crystal data and refinement parameters of **dTTFC8**: $C_{30}H_{36}O_6S_8$, M = 749.07, monoclinic, space group $P2_1/n$ (no. 14), a = 25.1361(6), b = 5.09490(10), c = 30.6018(9) Å, β = 109.649(2)°, V = 3690.8(2) Å^3, Z = 4, ρ_{calc} = 1.348 Mgm^{-3}, μ = 0.522 mm^{-1}, F_{000} = 1568, θ range = 1.82-26.37°, 14025 reflections collected of which 7554 unique (R_{int} = 0.1129), No. of reflections with $I>2\sigma(I)$ = 3856, which were used in all calculations, 409 parameters and 32 restraints, Goodness-of-fit (F^2) = 1.018. The final R indices [$I>2\sigma(I)$]: R1 = 0.0734 and wR2 = 0.1436. R indices (all data): R1 = 0.1606 and wR2 = 0.1770. Largest residual electron densities: 0.598 and -0.408 e.Å^{-3}.

Structure description for dTTFC8: Crystal structure solution of **dTTFC8** shows nicely that the substituted TTF is attached to the naphthalene crown ether macrocycle. There is a slight disorder in one oxygen atom of crown ether, which is divided over two spatial positions. The substituted TTF moiety exhibits typical bond distances for neutral TTF derivatives,[42-44] like

characteristically short C=C distance of 1.345(7) Å between the 1,3-dithiole rings and a distance range of 1.749(6) to 1.764(5) Å for C-S bonds. An Interesting geometric feature is the planarity of substituted TTF moiety with both 1,3-dithiole rings and all S atoms, as well lying in the same plane. The notably acute angle between the naphthalene and TTF planes (74.8°) can be attributed to the connecting ethylene bridge which avoids ecliptic and gauche conformations by maintaining an OCCS dihedral angle of 159.4°. In the crystal packing, the molecules are arranged in columnar stacks. Naphthalenes stack with naphthalenes with a plane-to-plane distance of 3.29 Å shifted sideways by 3.88 Å and TTFs on top of each other. Instead, TTFs stack with plane-to-plane distances of 3.47 Å, and a sideways slip of 3.73 Å, respectively.

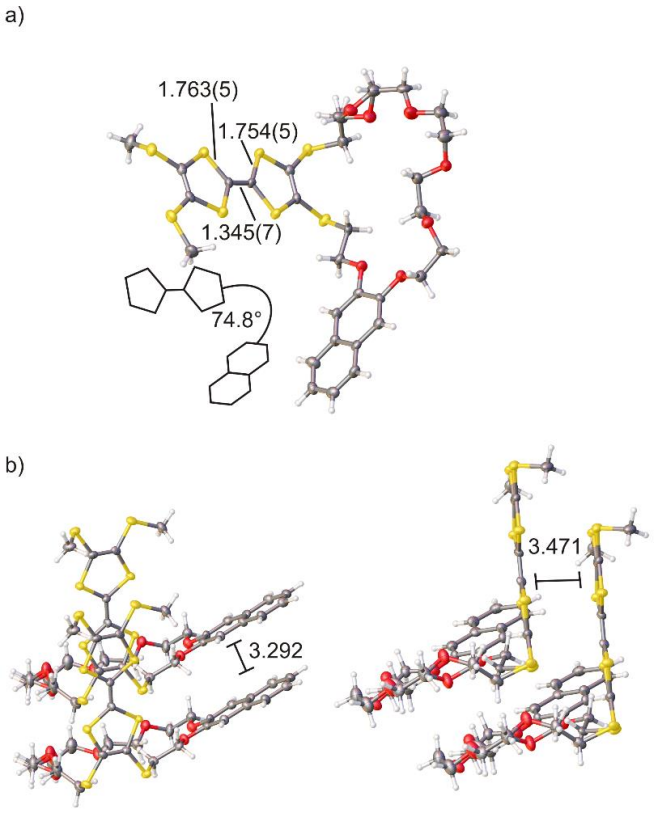

Figure S23: Solid-state structure of **dTTFC8**. (a) Top view with selected bond lengths (Å) and the angle between the naphthalene and the TTF plane. (b) Side view of two stacked **dTTFC8** molecules in the crystal with distances (Å) between molecule planes. Colour codes: S = yellow; O = red; C = grey; H = black (spheres).

9. ^{1}H, ^{13}C NMR

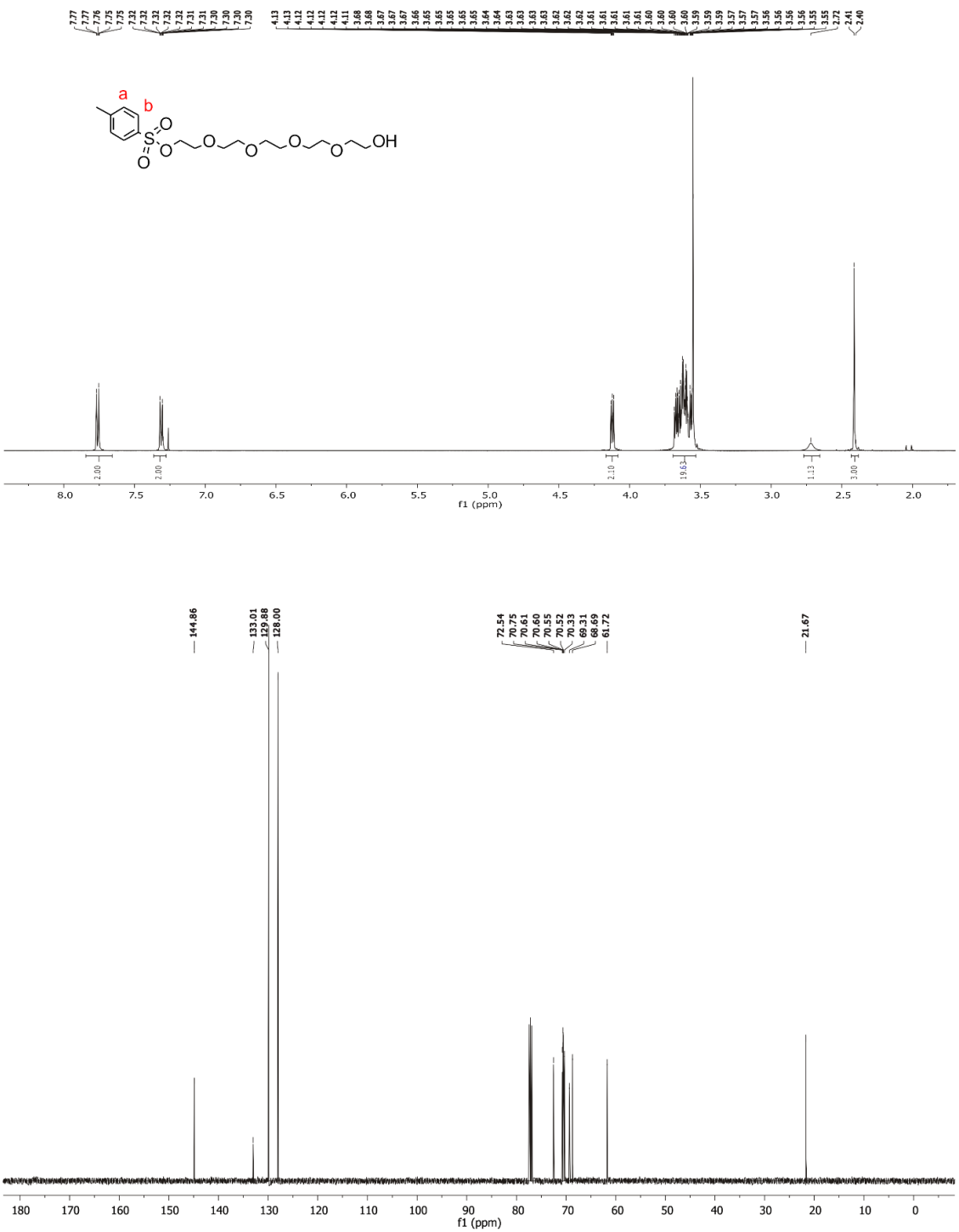

Fig. S24 ^{1}H (top) and ^{13}C (bottom) NMR spectrum (500/126 MHz, $CDCl_3$, 298 K) of **S2**.

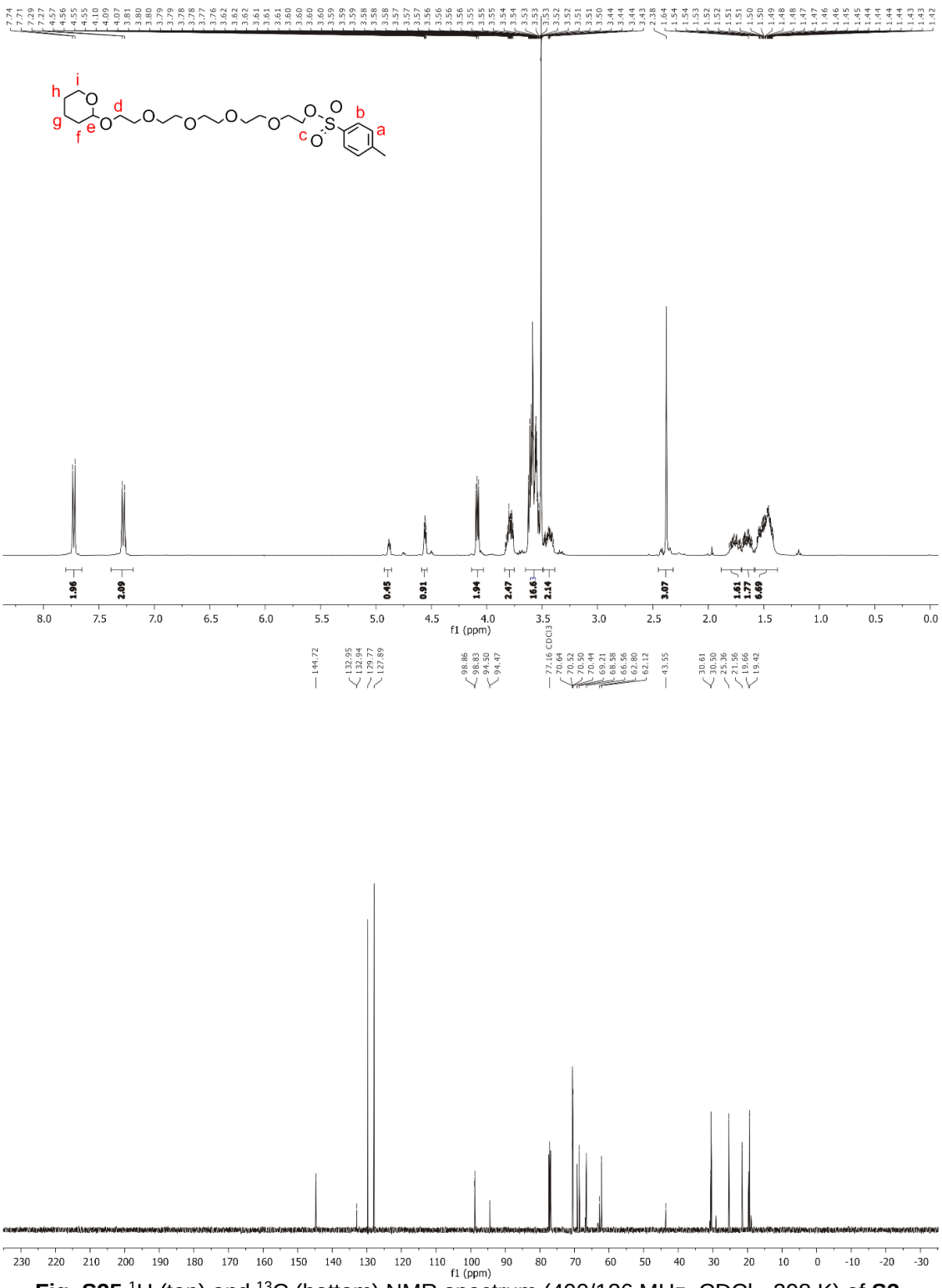

Fig. S25 ^{1}H (top) and ^{13}C (bottom) NMR spectrum (400/126 MHz, $CDCl_3$, 298 K) of **S3**.

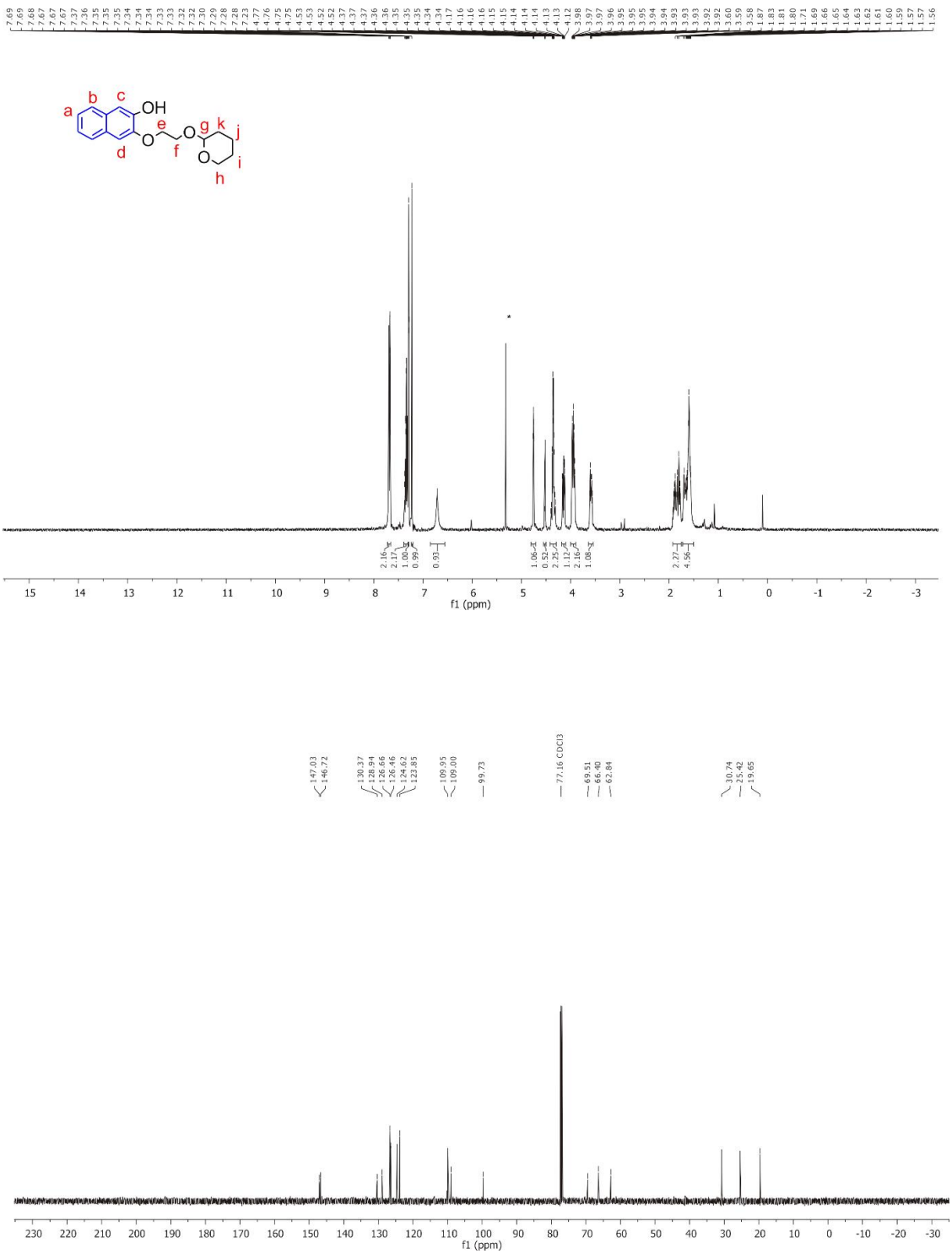

Fig. S26 ^{1}H (top) and ^{13}C (bottom) NMR spectrum (400/126 MHz, $CDCl_3$, 298 K) of **S7**.

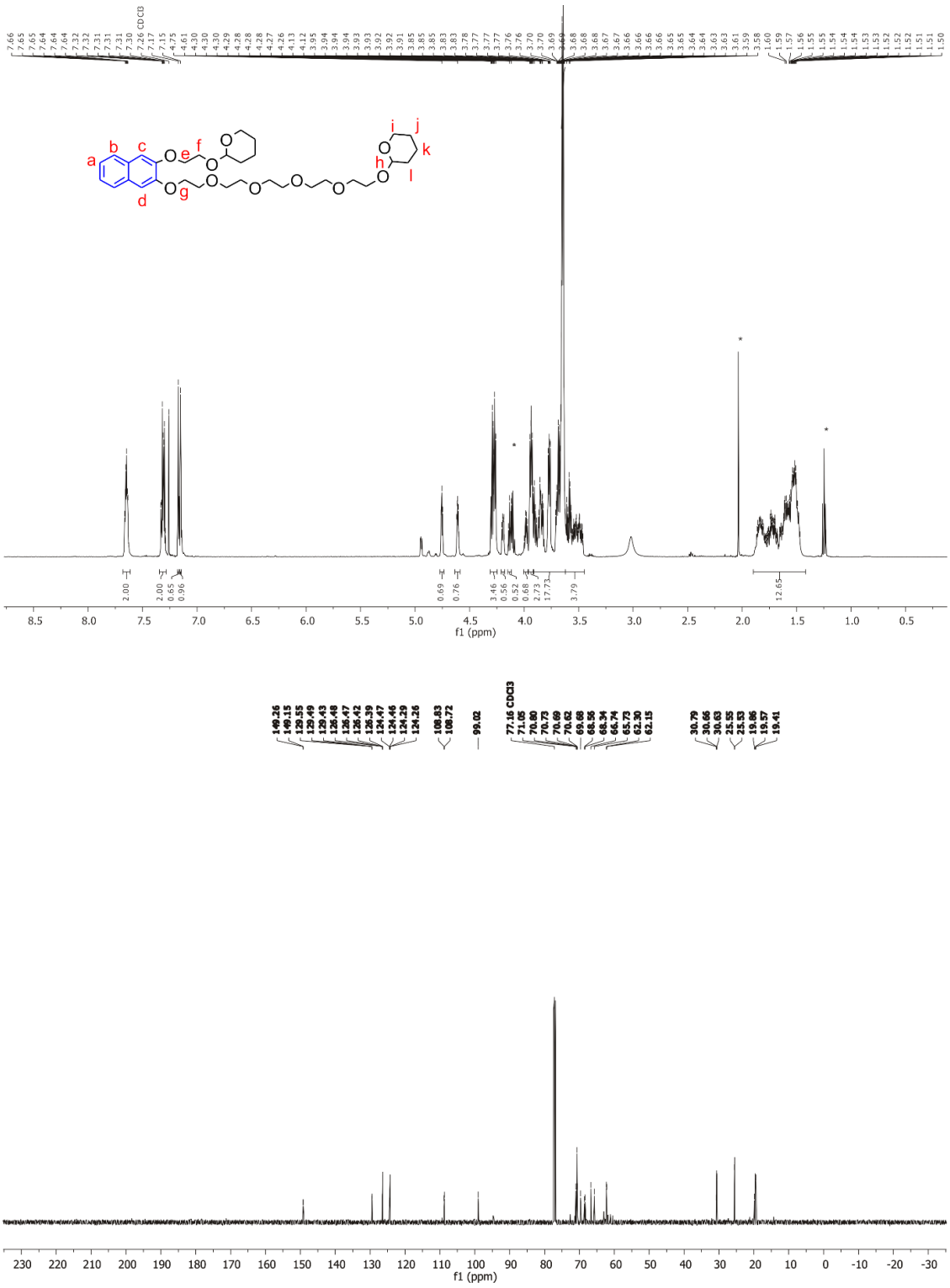

Fig. S27 ^{1}H (top) and ^{13}C (bottom) NMR spectrum (500/126 MHz, $CDCl_3$, 298 K) of **S8**.

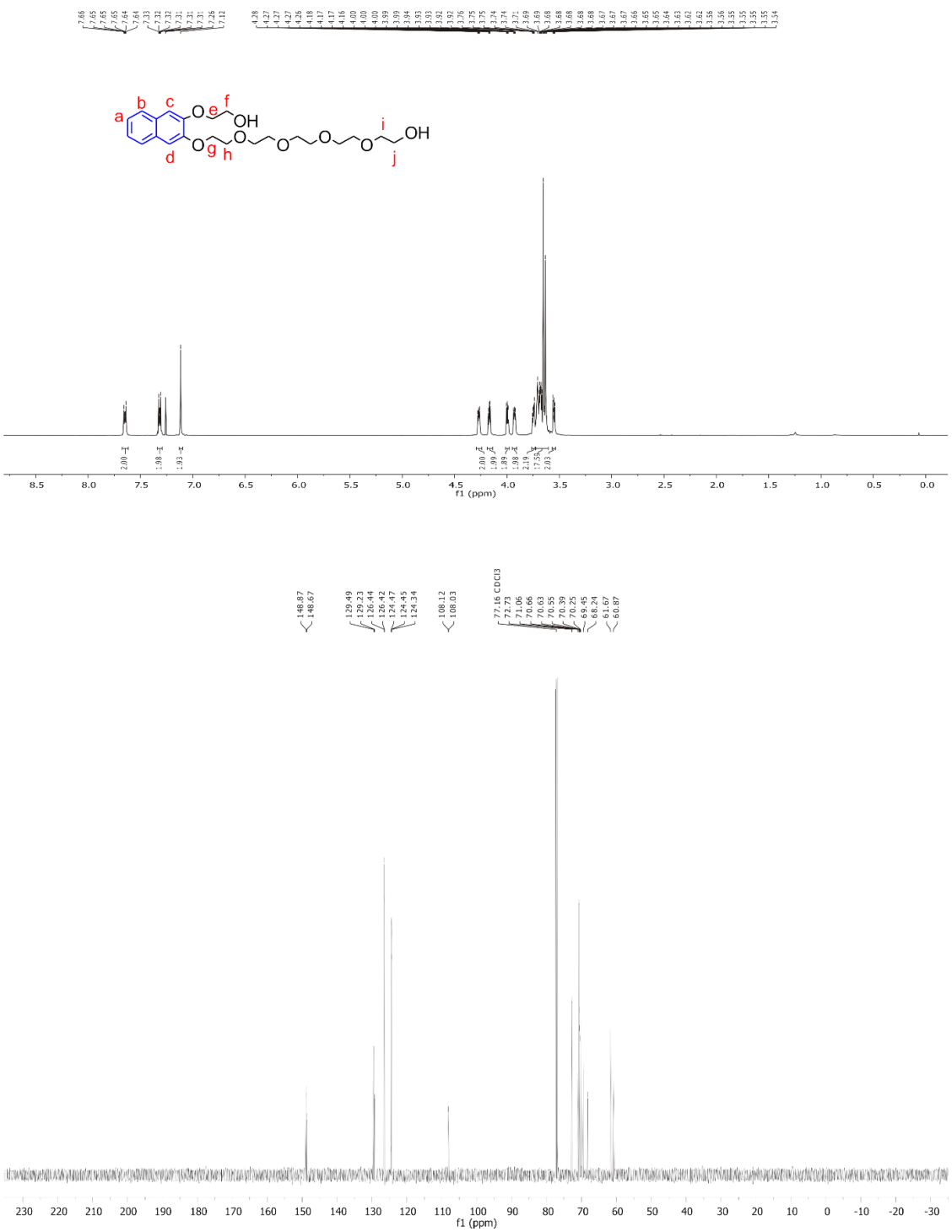

Fig. S28 ^{1}H (top) and ^{13}C (bottom) NMR spectrum (500/126 MHz, $CDCl_3$, 298 K) of **S9**.

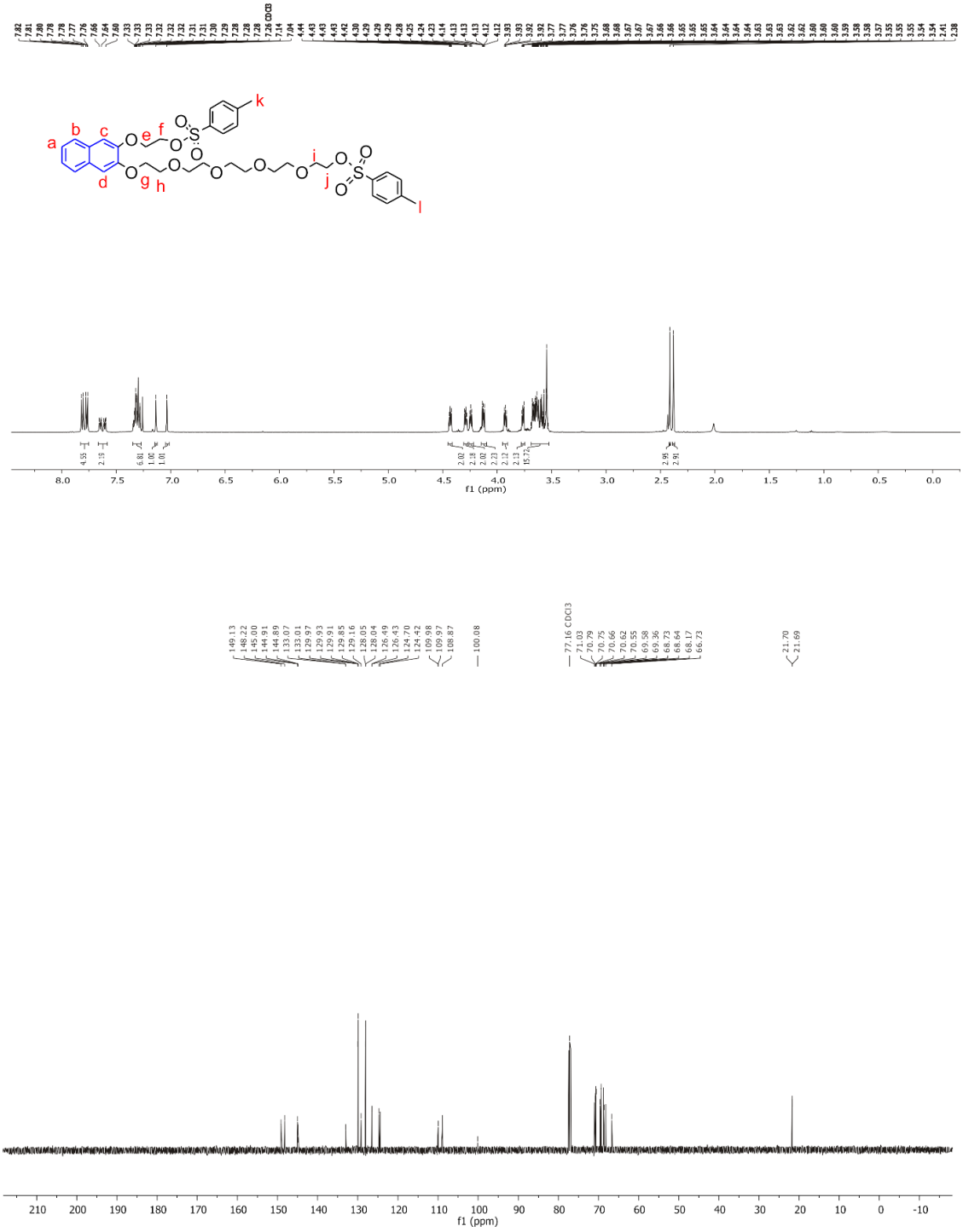

Fig. S29 ^{1}H (top) and ^{13}C (bottom) NMR spectrum (500/126 MHz, $CDCl_3$, 298 K) of **S10**.

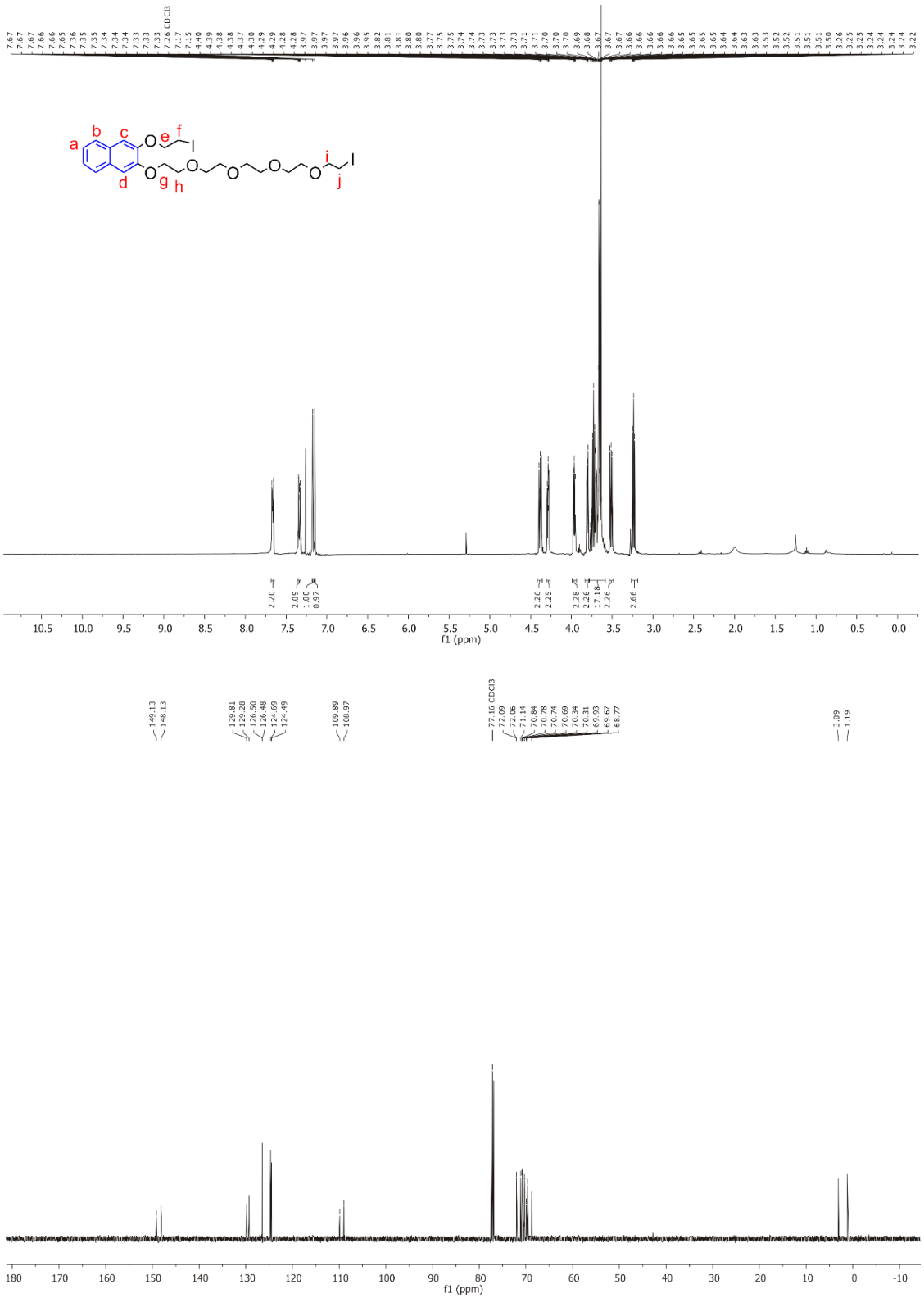

Fig. S30 ^{1}H (top) and ^{13}C (bottom) NMR spectrum (500/126 MHz, $CDCl_3$, 298 K) of **S11**.

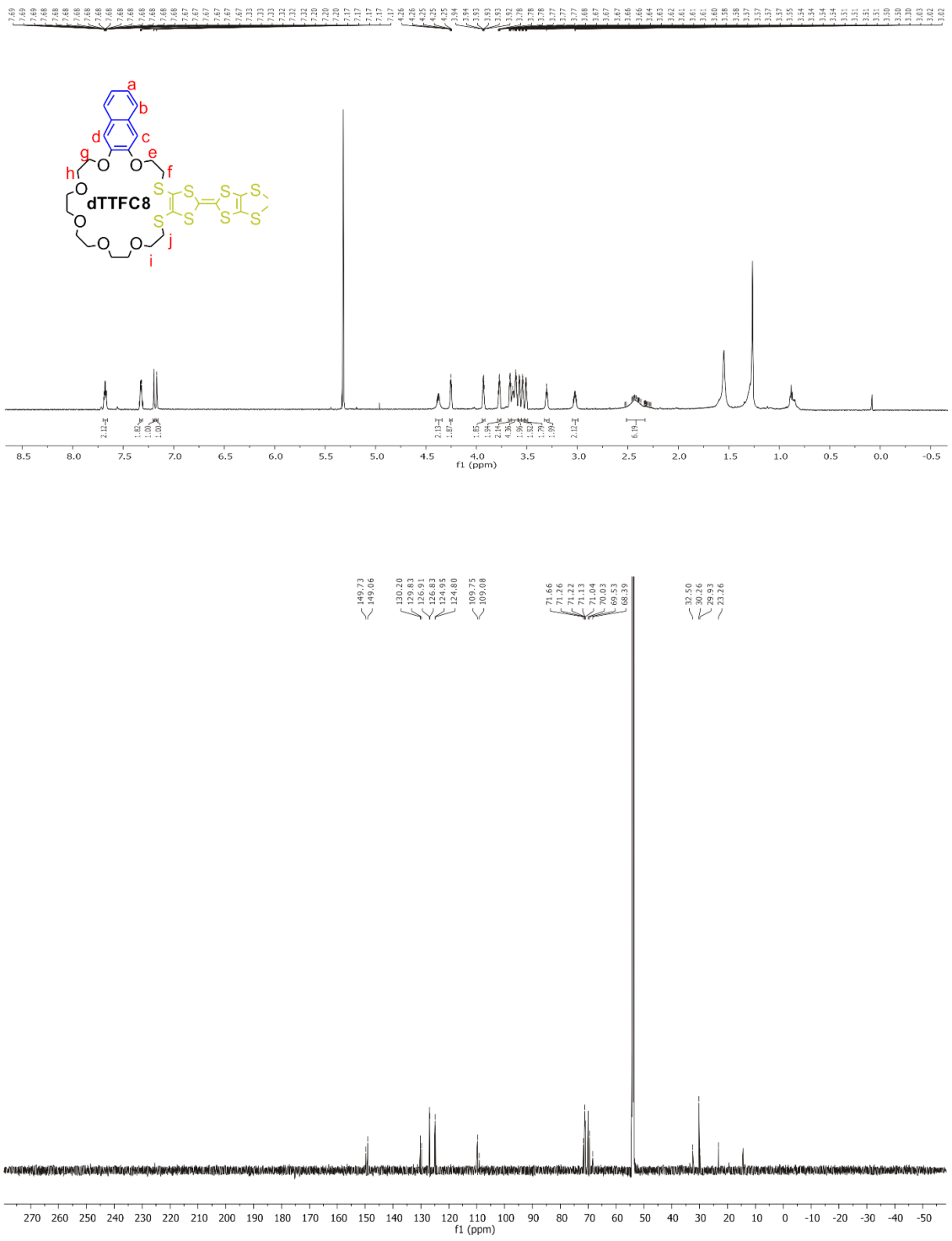

Fig. S31 ^{1}H (top) and ^{13}C (bottom) NMR spectrum (700/176 MHz, $CDCl_3$, 298 K) of **dTTFC8**.

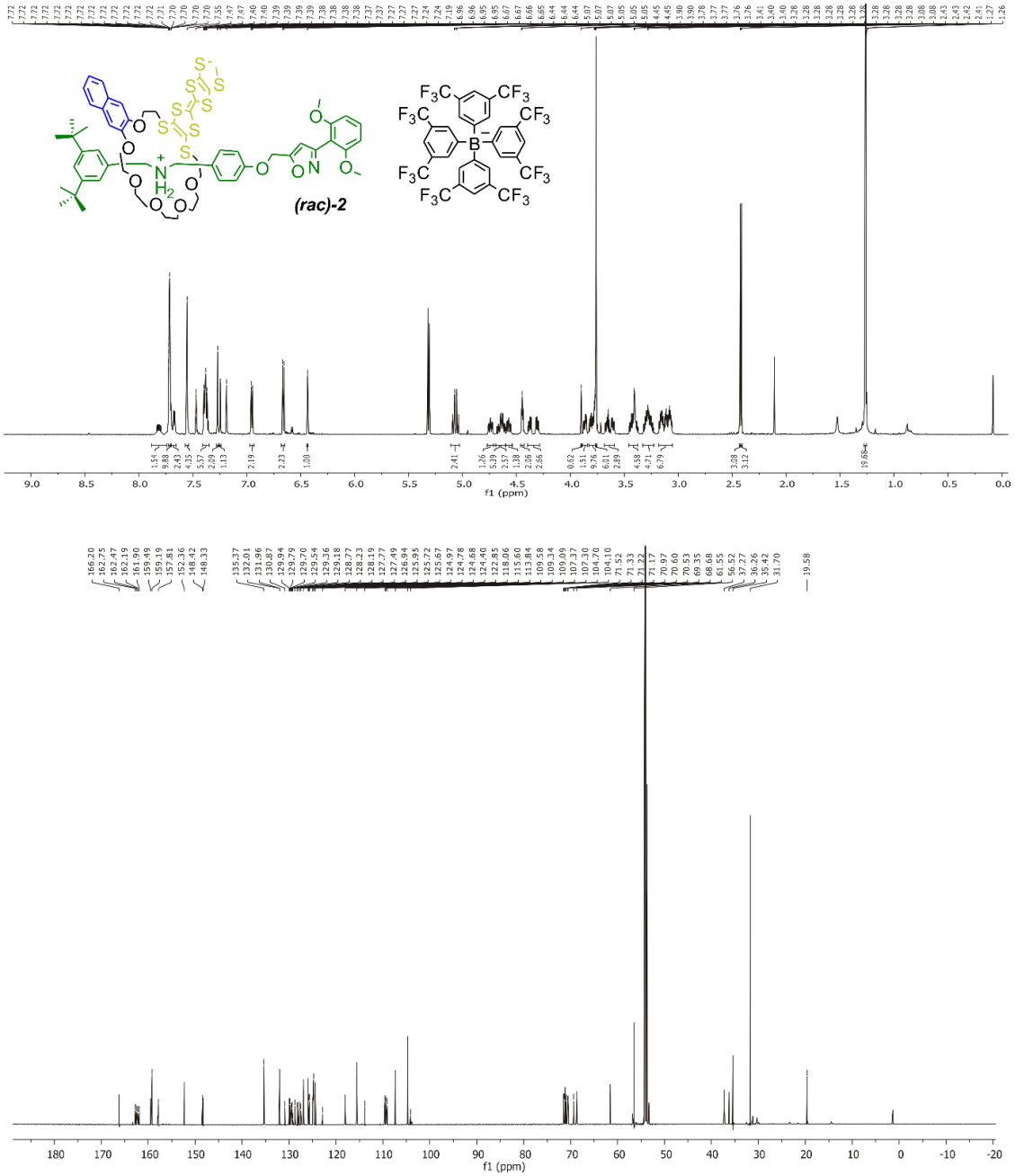

Fig. S32 ^{1}H (top) and ^{13}C (bottom) NMR spectrum (700/176 MHz, CD_2Cl_2, 298 K) of the racemic mixture of **2**.

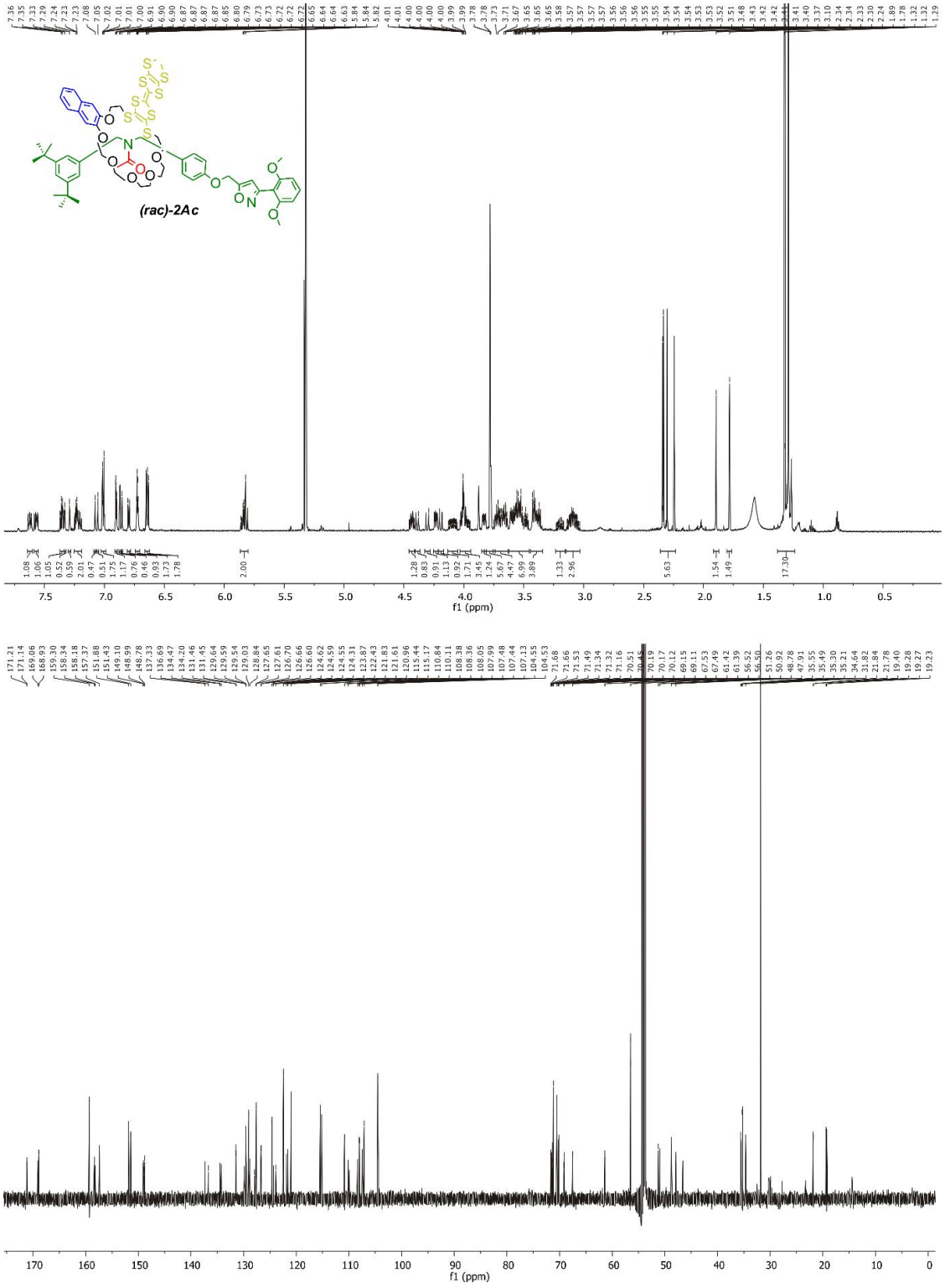

Fig. S33 ^{1}H (top) and ^{13}C (bottom) NMR spectrum (700/176 MHz, CD_2Cl_2, 298 K) of the racemic mixture of **2Ac**.

9. HR-MS

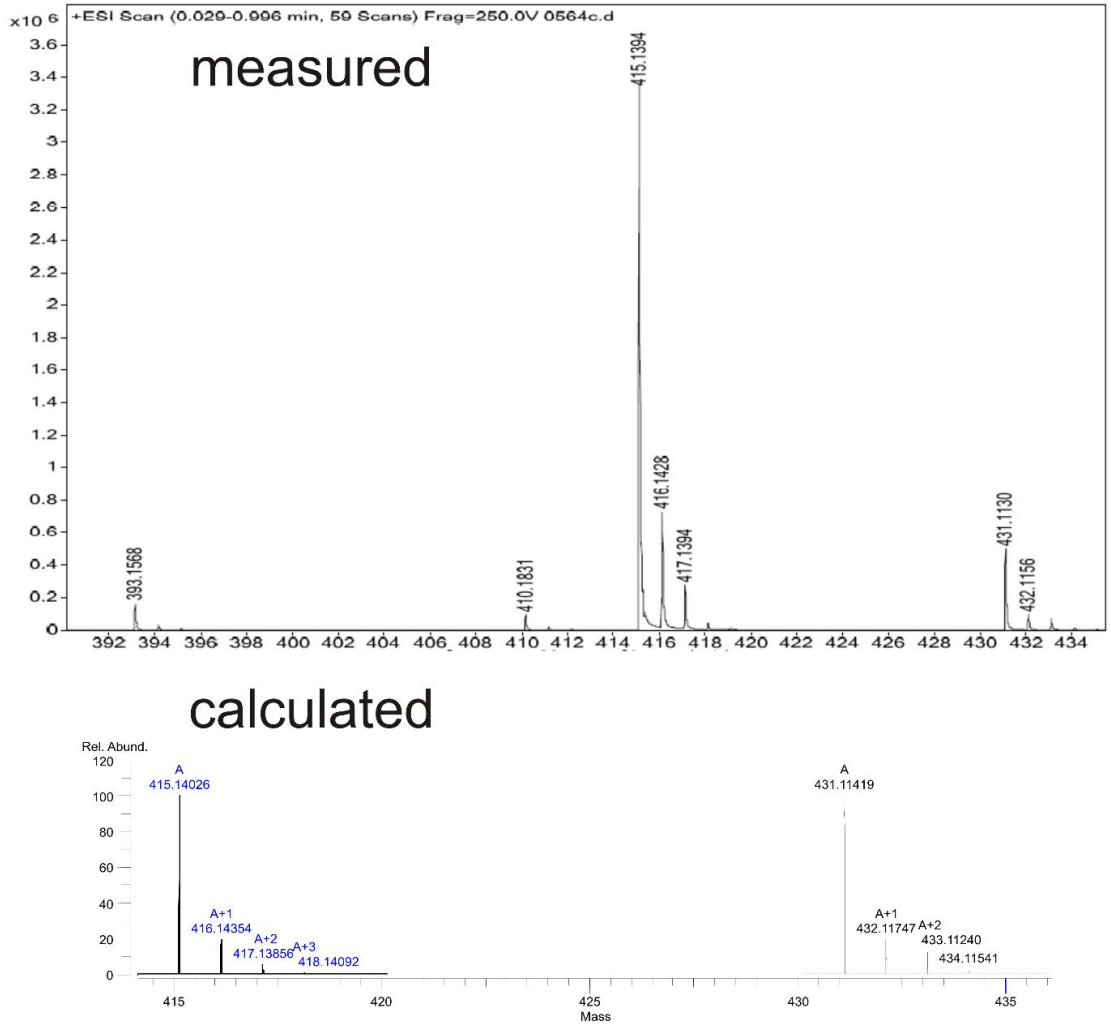

Fig. S34 HRMS ESI$^+$ (top) and calculated (bottom) of **S2**.

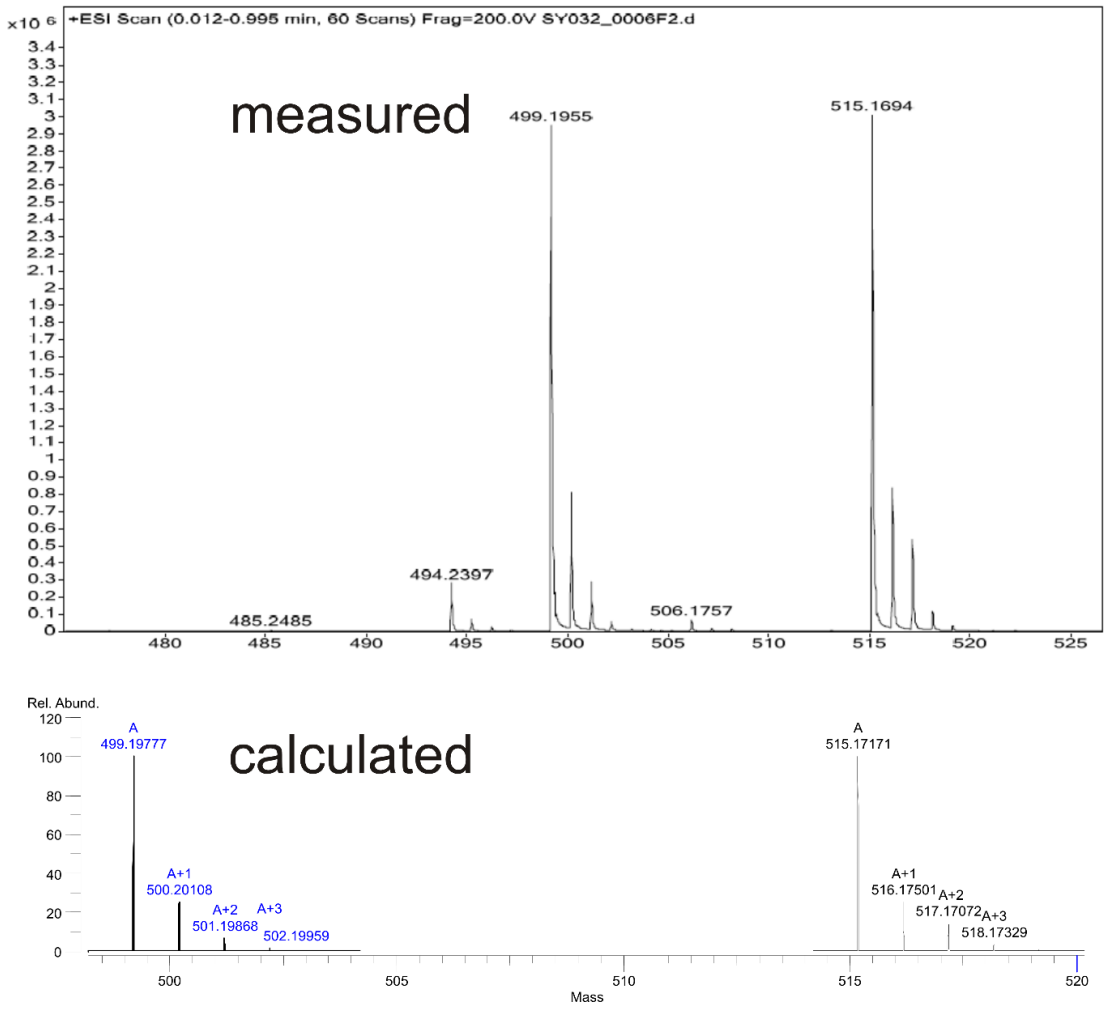

Fig. S35 HRMS ESI$^+$ (top) and calculated (bottom) of **S3**.

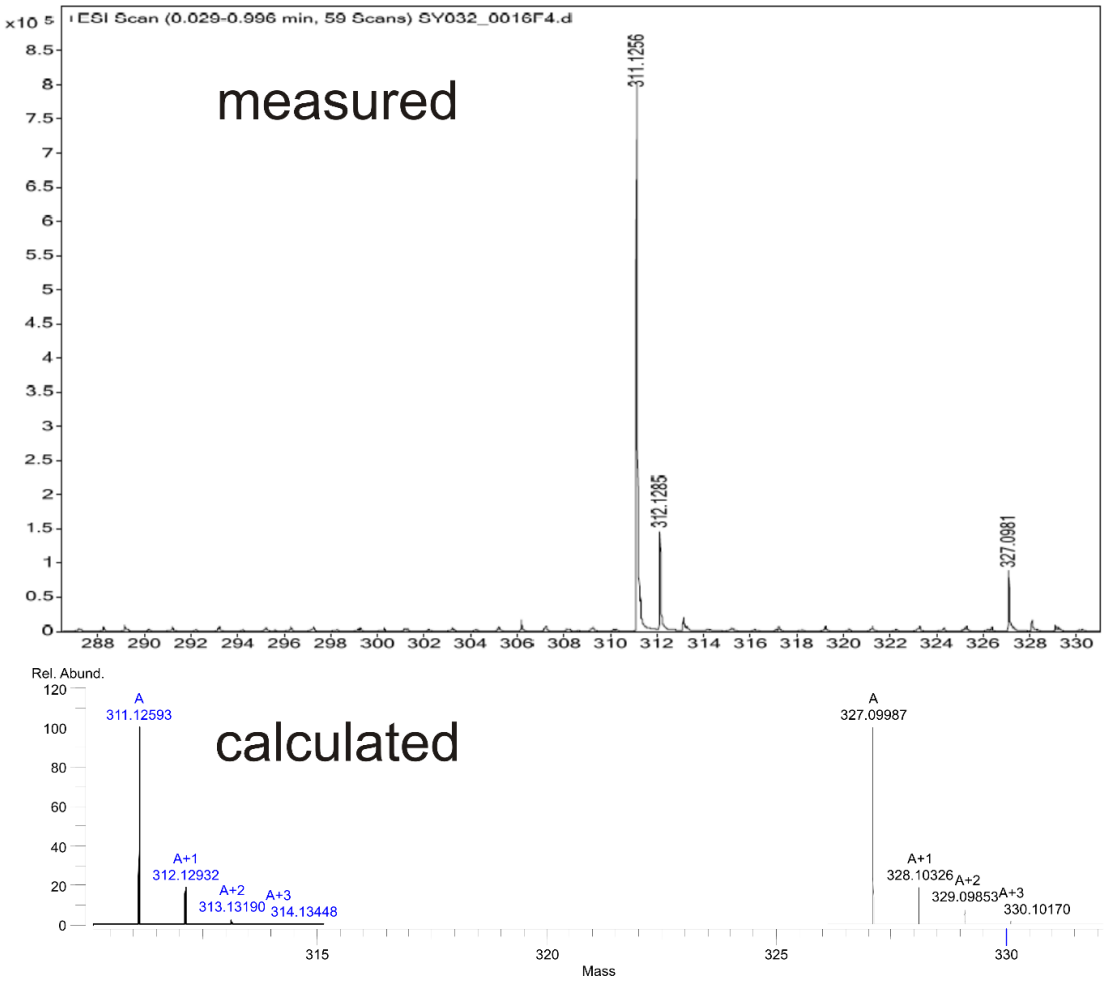

Fig. S36 HRMS ESI$^+$ (top) and calculated (bottom) of **S7**.

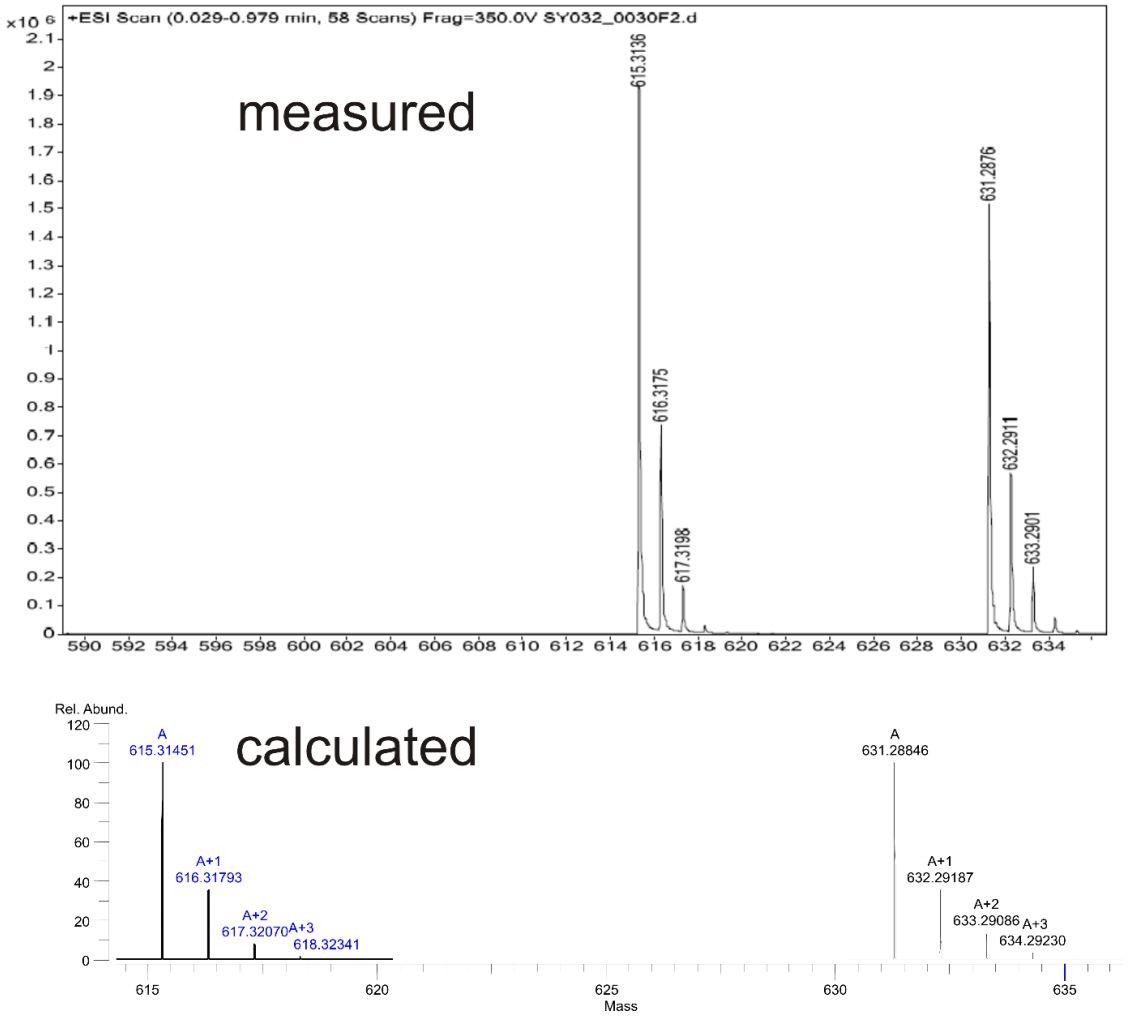

Fig. S37 HRMS ESI$^+$ (top) and calculated (bottom) of **S8**.

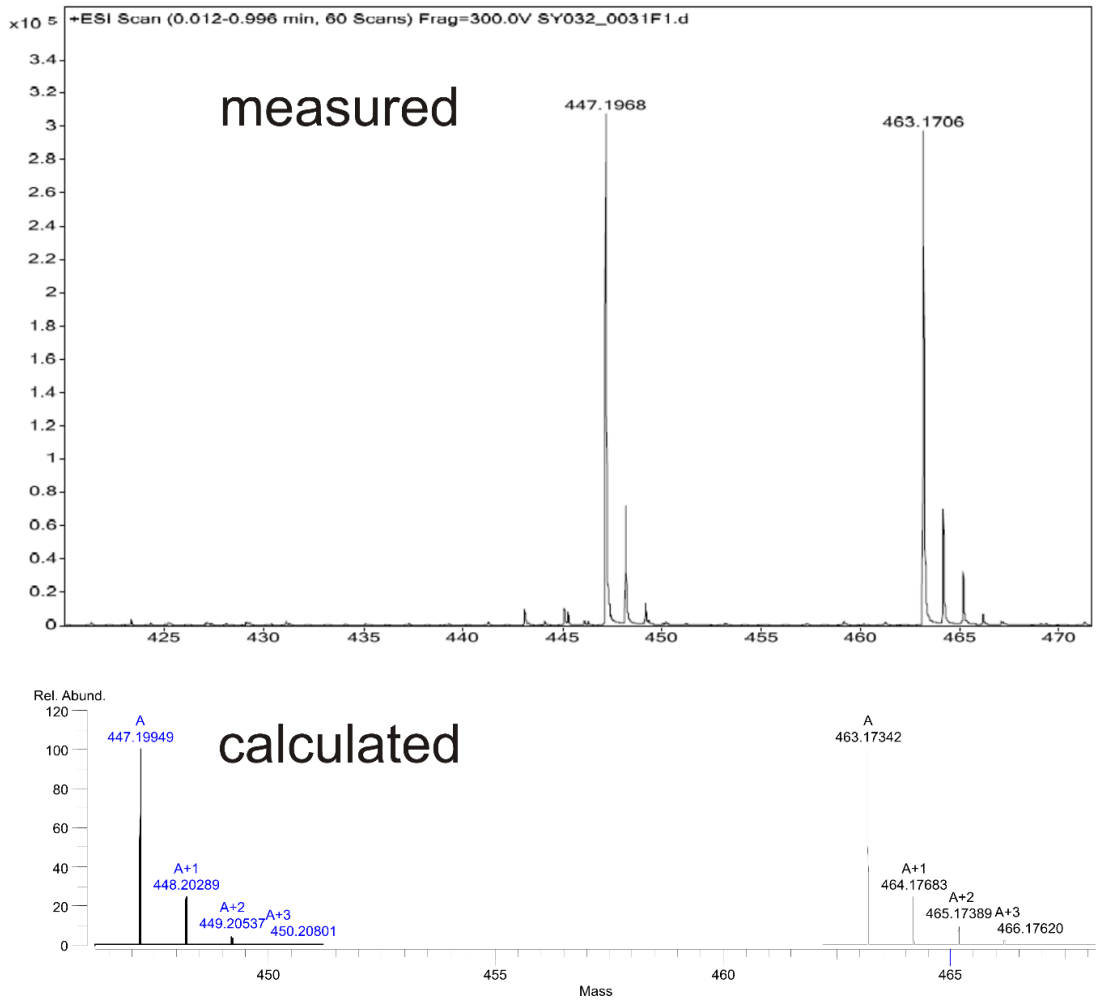

Fig. S38 HRMS ESI$^+$ (top) and calculated (bottom) of **S9**.

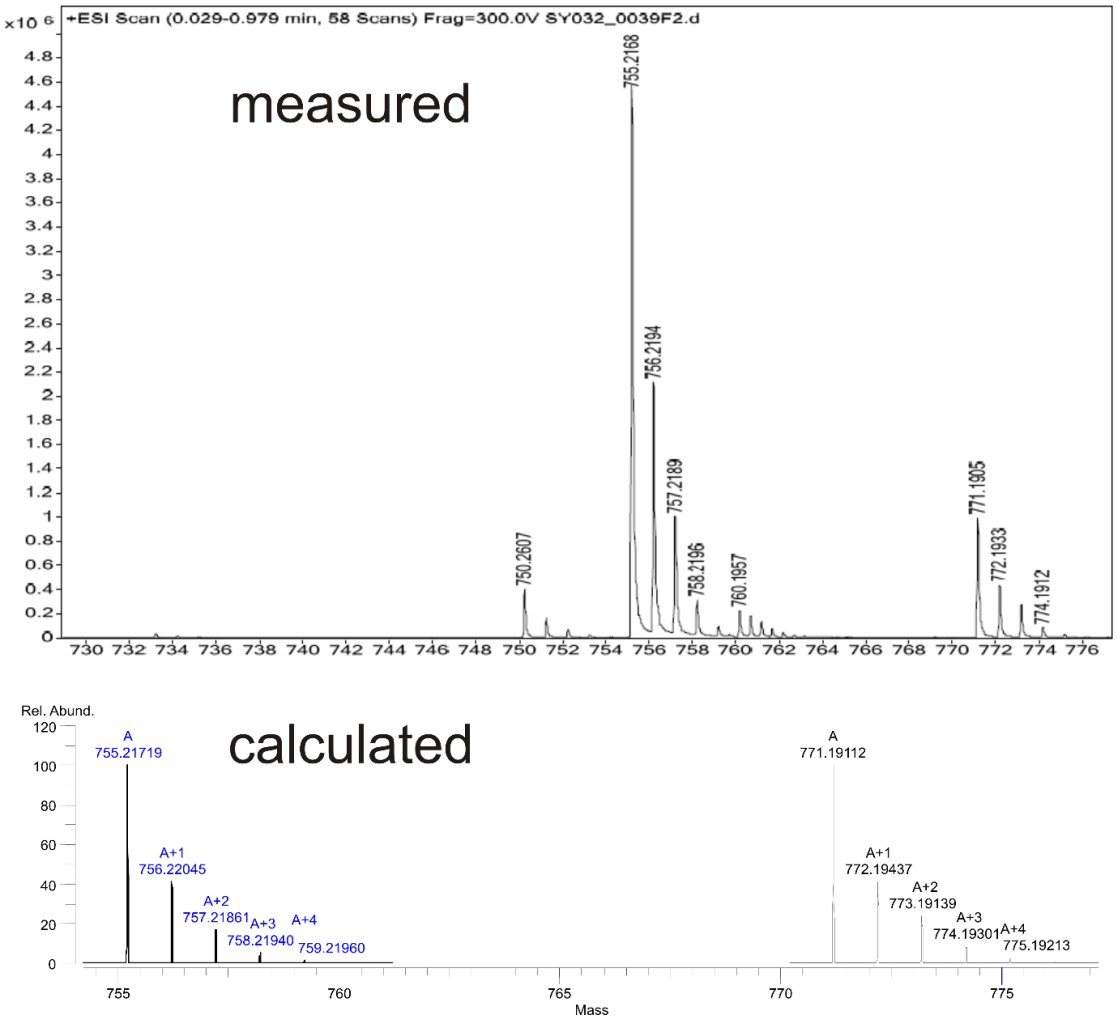

Fig. S39 HRMS ESI$^+$ (top) and calculated (bottom) of **S10**.

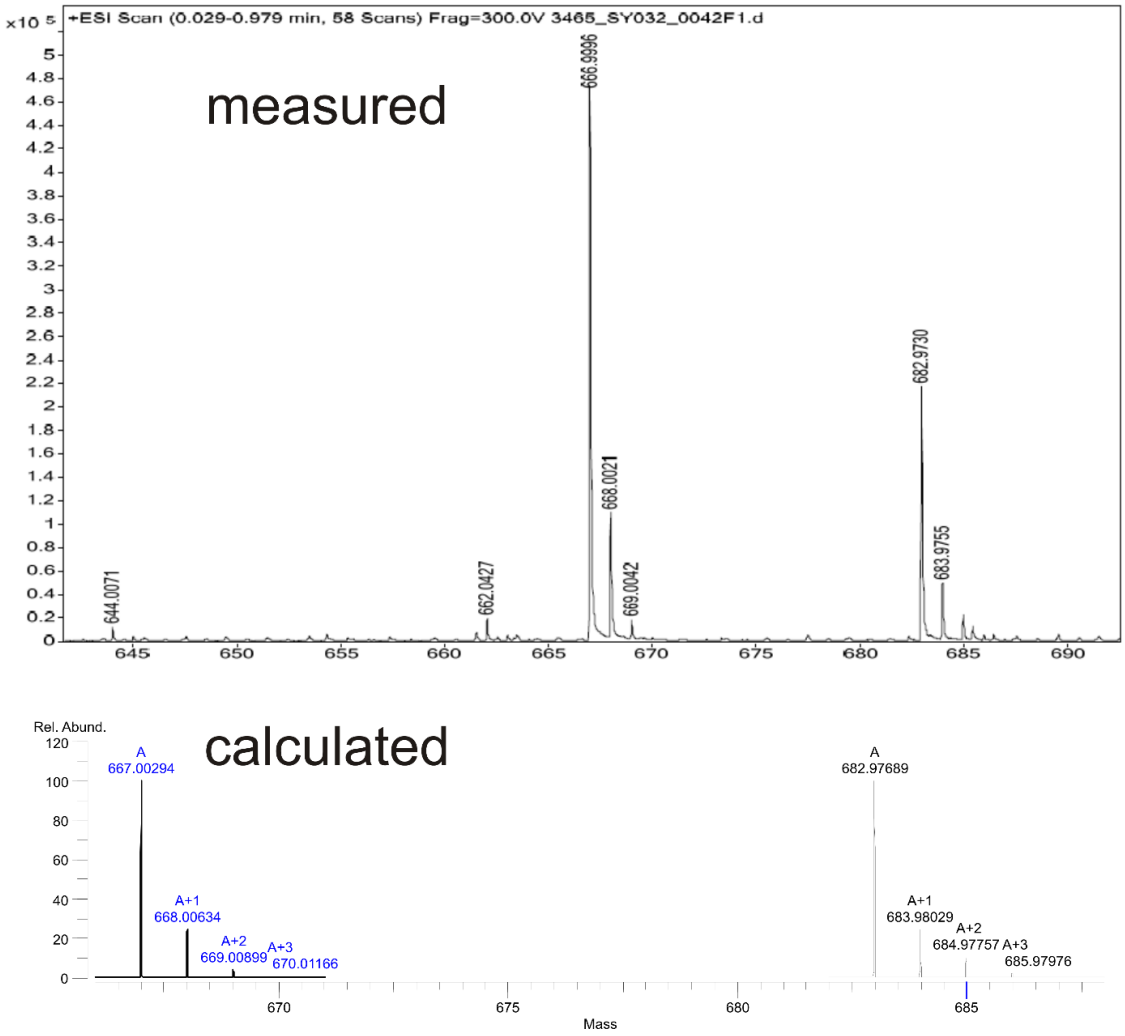

Fig. S40 HRMS ESI$^+$ (top) and calculated (bottom) of **S11**.

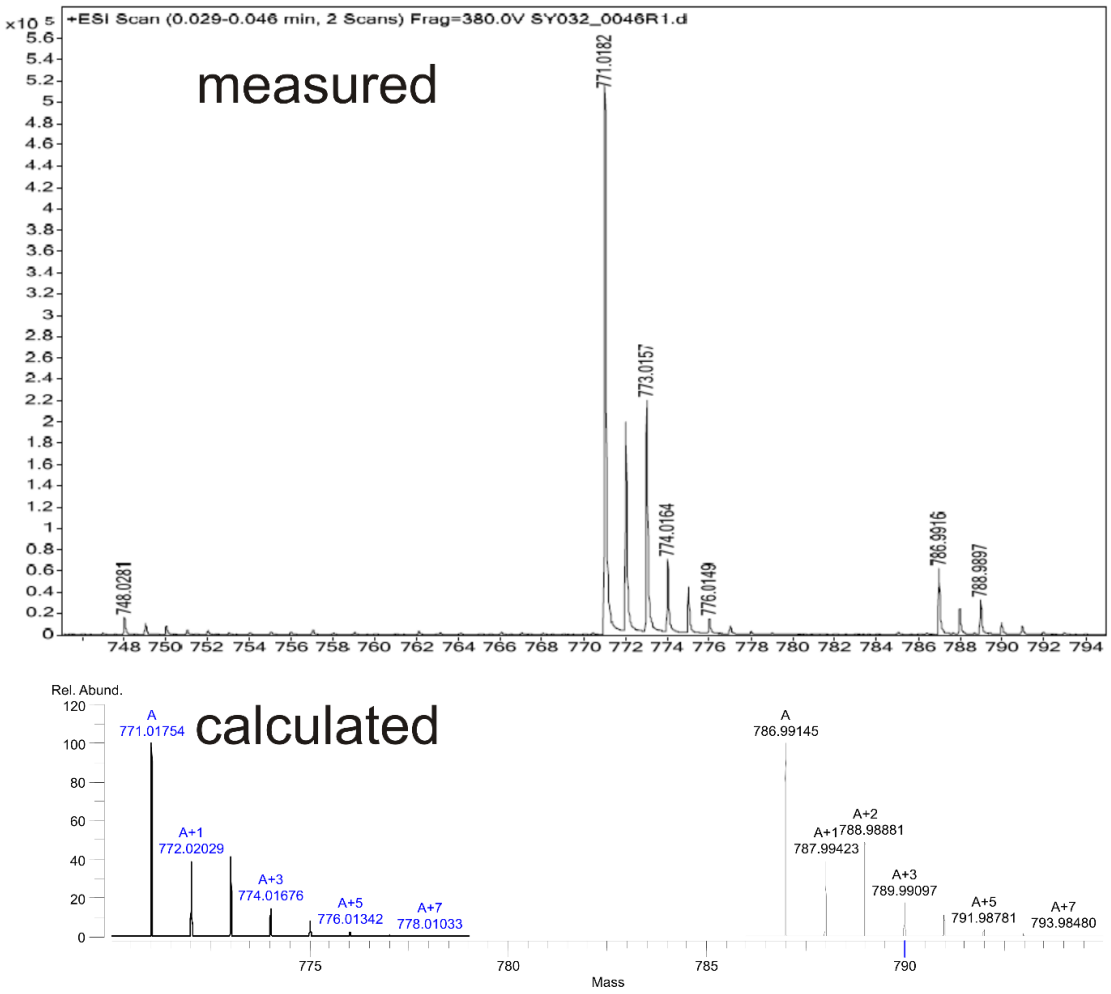

Fig. S41 HRMS ESI$^+$ (top) and calculated (bottom) of **dTTFC8**.

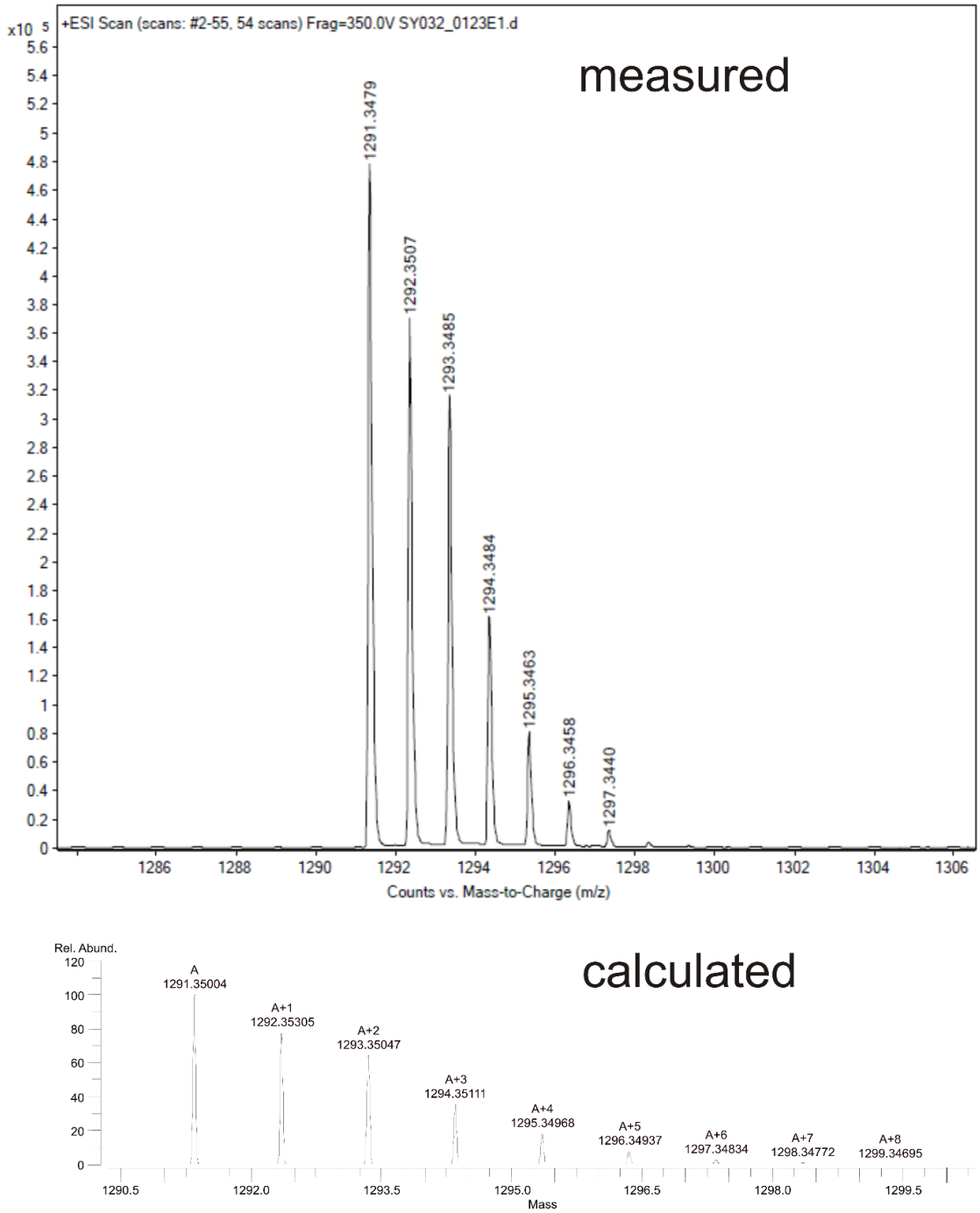

Fig. S42 HRMS ESI$^+$ (top) and calculated (bottom) of (*rac*)-**2**.

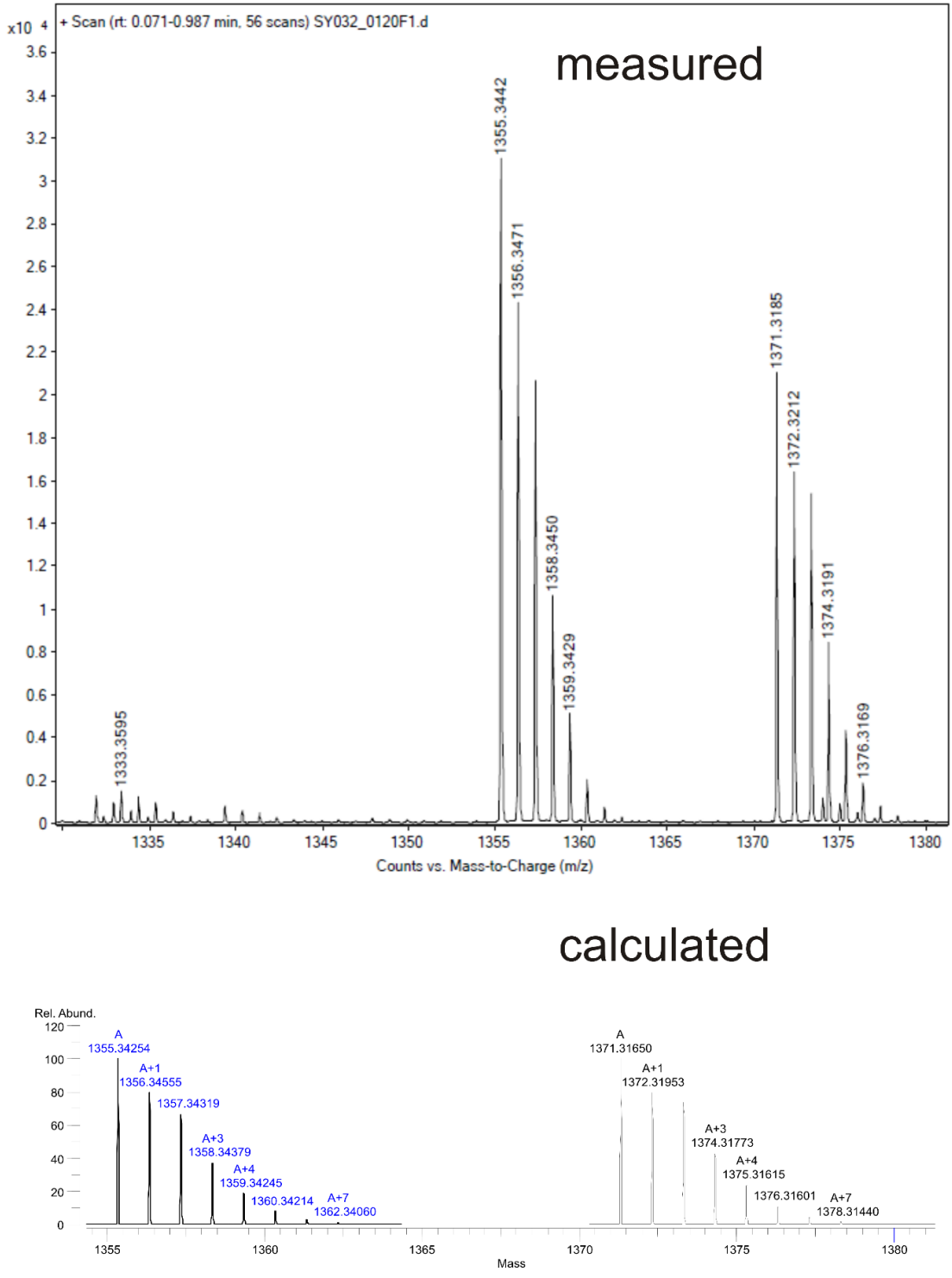

Fig. S43 HRMS ESI$^+$ (top) and calculated (bottom) of (*rac*)-**2Ac**.

11. References

1. M. Popr, S. Hybelbauerova and J. Jindrich, *Beilstein J. Org. Chem.*, 2014, **10**, 1390-1396.
2. W. Mamdouh, I. H. Uji, A. E. Dulcey, V. Percec, S. De Feyter and F. C. De Schryver, *Langmuir*, 2004, **20**, 7678-7685.
3. N. Svenstrup, K. M. Rasmussen, T. K. Hansen and J. Becher, *Synthesis*, 1994, **1994**, 809-812.
4. H. V. Schröder, S. Sobottka, M. Nößler, H. Hupatz, M. Gaedke, B. Sarkar and C. A. Schalley, *Chem. Sci.*, 2017, **8**, 6300-6306.
5. T. Matsumura, F. Ishiwari, Y. Koyama and T. Takata, *Org. Lett.*, 2010, **12**, 3828-3831.
6. J. R. Aranzaes, M.-C. Daniel and D. Astruc, *Can. J. Chem.*, 2006, **84**, 288-299.
7. X. Z. Zhu and C. F. Chen, *J. Am. Chem. Soc.*, 2005, **127**, 13158-13159.
8. K. Zimmermann, *Synth. Commun.*, 1995, **25**, 2959-2962.
9. S. Passemard, D. Staedler, L. Ucnova, G. S. Schneiter, P. Kong, L. Bonacina, L. Juillerat-Jeanneret and S. Gerber-Lemaire, *Bioorg. Med. Chem. Lett.*, 2013, **23**, 5006-5010.
10. J. Sly, P. Kasak, E. Gomar-Nadal, C. Rovira, L. Gorriz, P. Thordarson, D. B. Amabilino, A. E. Rowan and R. J. Nolte, *Chem. Commun.*, 2005, **10**, 1255-1257.
11. K. B. Simonsen, N. Svenstrup, J. Lau, O. Simonsen, P. Mørk, G. J. Kristensen and J. Becher, *Synthesis*, 1996, **1996**, 407-418.
12. F. A. Loiseau, K. K. Hii and A. M. Hill, *J. Org. Chem.*, 2004, **69**, 639-647.
13. S. Grimme, C. Bannwarth and P. Shushkov, *J. Chem. Theory. Comput.*, 2017, **13**, 1989-2009.
14. D. Porezag, T. Frauenheim, T. Köhler, G. Seifert and R. Kaschner, *Phys. Rev. B*, 1995, **51**, 12947-12957.
15. *Grimme et. al.*
16. H. J. C. Berendsen, J. P. M. Postma, W. F. van Gunsteren, A. DiNola and J. R. Haak, *J. Chem. Phys.*, 1984, **81**, 3684-3690.
17. J.-P. Ryckaert, G. Ciccotti and H. J. C. Berendsen, *J. Comput. Phys.*, 1977, **23**, 327-341.
18. K. Eichkorn, O. Treutler, H. Öhm, M. Häser and R. Ahlrichs, *Chem. Phys. Lett.*, 1995, **240**, 283-290.
19. J. Tao, J. P. Perdew, V. N. Staroverov and G. E. Scuseria, *Phys. Rev. Lett.*, 2003, **91**, 146401.
20. S. Grimme, J. Antony, S. Ehrlich and H. Krieg, *J. Chem. Phys.*, 2010, **132**, 154104.
21. S. Grimme, S. Ehrlich and L. Goerigk, *J. Comput. Chem.*, 2011, **32**, 1456-1465.
22. F. Weigend and R. Ahlrichs, *Phys. Chem. Chem. Phys.*, 2005, **7**, 3297-3305.
23. R. Ahlrichs, M. Bär, M. Häser, H. Horn and C. Kölmel, *Chem. Phys. Lett.*, 1989, **162**, 165-169.
24. A. Klamt and G. Schüürmann, *Perkin Trans. 2*, 1993, **5**, 799-805.
25. F. Neese, F. Wennmohs, A. Hansen and U. Becker, *Chem. Phys.*, 2009, **356**, 98-109.
26. J. D. Chai and M. Head-Gordon, *J. Chem. Phys.*, 2008, **128**, 084106.
27. V. Barone and M. Cossi, *J. Phys. Chem. A*, 1998, **102**, 1995-2001.
28. F. Neese, *Wiley Interdiscip. Rev.-Comput. Mol. Sci.*, 2012, **2**, 73-78.
29. C. Bannwarth and S. Grimme, *Comput. Theor. Chem.*, 2014, **1040-1041**, 45-53.
30. J. P. Perdew, M. Ernzerhof and K. Burke, *J. Chem. Phys.*, 1996, **105**, 9982-9985.
31. T. Yanai, D. P. Tew and N. C. Handy, *Chem. Phys. Lett.*, 2004, **393**, 51-57.
32. Y. Zhao and D. G. Truhlar, *Theor. Chem. Acc.*, 2007, **120**, 215-241.
33. R. F. W. Bader, *Chem. Rev.*, 1991, **91**, 893-928.
34. T. Lu and F. Chen, *J. Comput. Chem.*, 2012, **33**, 580-592.
35. COLLECT, Bruker AXS, Inc., Madison, Wisconsin, USA, 2008.
36. Z. O. a. W. Minor, *Methods Enzymol., vol. 276, Macromolecular Crystallography, Part A,* , Academic Press, New York, 1997.
37. G. M. Sheldrick, *SADABS*. University of Göttingen, Germany, **1996**.
38. G. M. Sheldrick, *Acta Crystallogr., Sect. A: Found. Adv.*, 2015, **71**, 3-8.
39. G. M. Sheldrick, *Acta Crystallogr., Sect. C: Struct. Chem.*, 2015, **71**, 3-8.
40. A. L. Spek, *Acta Crystallogr., Sect. C: Struct. Chem.*, 2015, **71**, 9-18.

41. A. L. Spek, *Acta Crystallogr., Sect. D: Biol. Crystallogr.*, 2009, **65**, 148-155.
42. J. Sun, X. Lu, J. Shao, X. Li, S. Zhang, B. Wang, J. Zhao, Y. Shao, R. Fang, Z. Wang, W. Yu and X. Shao, *Chem. Eur. J.*, 2013, **19**, 12517-12525.
43. H. Kobayashi, R. Kato, T. Mori, A. Kobayashi, Y. Sasaki, G. Saito, T. Enoki and H. Inokuchi, *Mol. Cryst. Liq. Cryst.*, 2011, **107**, 33-43.
44. P. R. Ashton, J. Becher, M. C. T. Fyfe, M. B. Nielsen, J. F. Stoddart, A. J. P. White and D. J. Williams, *Tetrahedron*, 2001, **57**, 947-956.

4.6 Paper B3

"Naphthocage: A Flexible yet Extremely Strong Binder for Singly Charged Organic Cations"

F. Jia, H. Hupatz, L.-P. Yang, H. V. Schröder, D.-H. Li, S. Xin, D. Lentz, F. Witte, X. Xie, B. Paulus, C. A. Schalley, W. Jiang
J. Am. Chem. Soc. **2019**, 141, 10, 4468–4473.
DOI: 10.1021/jacs.9b00445
URL: https://doi.org/10.1021/jacs.9b00445

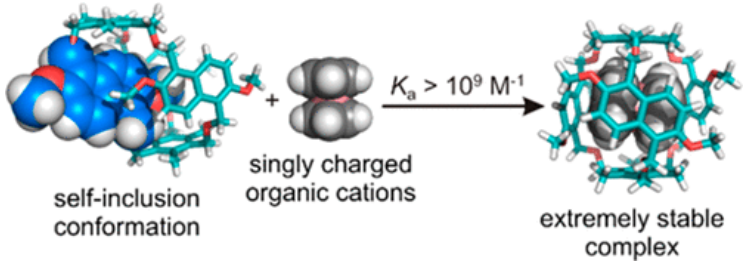

Figure 4.6: Graphical abstract of paper **B3**.

Contributions

The project was conceived by Fei Jia. Wei Jiang and F.J. wrote the manuscript. F.J. furthermore conducted all synthetic and characterisation work of the "naphthocage" and conducted host-guest complexation and redox-switching experiments. All computational work was carried out by Felix Witte. Dong-Hao Li and Liu-Pan Yang repeated the synthesis of the naphthocage. L.Y. and Henrik Hupatz performed ITC and competition experiments. Hendrik Schröder carried out CV measurements. Shan Xie and Xiaojiang Xie performed ion-selective electrode experiments. Dieter Lentz measured and refined the crystal structure of the naphthocage. All authors contributed to the final version of the manuscript.

5 Summary

I would like to begin this final section by pointing out that this thesis at its core is a homage to the remarkable efficiency of combining experimental and theoretical approaches to study complex problems and phenomena in chemistry. The thorough investigations summarised as part **A** of this work resulted from a fruitful cooperation with the work group of Prof. Dr. Siegfried Eigler, while the insights obtained in part **B** could be achieved by a successful collaboration with the work group of Prof. Dr. Christoph Schalley.
The overall goal of this thesis can be separated into two major aspects: provide valuable scientific insight into complex organic systems and develop powerful computational approaches for their analysis. All papers as a whole display the versatility and intriguing physico-chemical properties of photo- or redox-responsive organic (supra)molecules. We have encountered metastable J-type dimers, switchable ECD responses, and an extremely strong binding supramolecular host just to name a few. Our theoretical methods were crucial in understanding a selection of intricate and unexpected physical and chemical mechanisms. Our results furthermore provide a solid basis for the potential application of the studied (and similar) molecular systems as building blocks in novel nanotechnologies, such as optoelectronic devices or sensory materials.
While some theoretical methods, such as the DFT/MRCI approach, have repeatedly found successful application throughout this thesis, none of the developed computational protocols as a whole were used more than once. On the one hand, this was partially required by the nature of the molecules themselves and the different spectroscopic techniques used for their examination (CV, ECD, UV/Vis, etc.). On the other hand, this was done so quite deliberately to demonstrate the remarkable flexibility of quantum-mechanical approaches when applied to complex chemical problems. In the following, I will summarise and discuss the results of each project and consistently evaluate their individual significance in the greater context of this thesis.

Part **A** was focussed on a relatively new class of fluorescent dyes: diaminodicyanoquinones (DADQs). Despite first synthetic works in the 1960s,[245] DADQs have never been viewed as fluorescent dyes as their emission is usually very low[246] and only solid-state compounds with moderate fluorescence quantum yields (QYs) are known.[247] Their electron-acceptor properties and high-dipole moments, however, were already known[248,249] which prompted this research project since a combination of all of these features is very desirable for numerous photochemical applications. In paper **A1** we could show, that DADQs can indeed be tailored to produce notable QYs exceeding 90%.
Four different DADQ derivatives **1**–**4** have been investigated by comparing their absorption and emission spectra and QYs (**Fig. 5.1**). Special attention was paid to compound **4** defined by a benzene bridge connecting the two amino nitrogens. Depending on the solvent this molecule showed remarkable QYs ranging from 35% in polar protic methanol to 92% in polar aprotic DMSO. The other DADQs showed QYs of at most around 12% and usually below. All data point towards the importance of the benzene moiety which enlarges the delocalised π-system and the influence of substituents at the nitrogen atoms which twist the molecular ground-state structure. This is further underlined by three additional benzene-bridged DADQs synthesised in the course of the projects.
It is well known in literature that fluorescence deactivation pathways in single molecules often progress through internal rotations around dihedral angles.[250] This fact led us to examine the

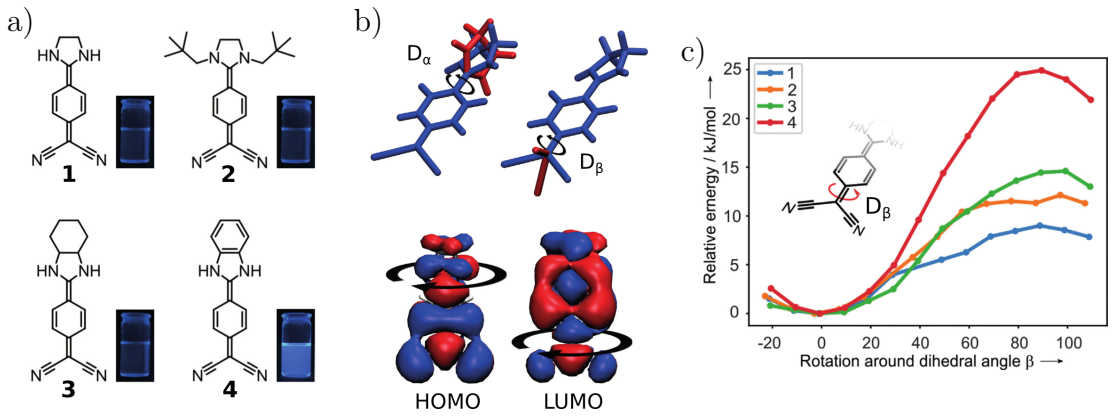

Figure 5.1: Paper **A1**: a) Compounds **1**–**4** together with vials depicting the differences in fluorescence QYs, b) dihedral angles important for fluorescence deactivation in DADQs and HOMO/LUMO orbitals indicating which angle is more flexible at which state (S_0 dominated by HOMO, S_1 dominated by LUMO), c) comparison of rotational barriers of compounds **1**–**4** around dihedral angle D_β rationalising the differences in QYs.

two dihedral angles D_α and D_β in the compounds theoretically. A TD-DFT calculation at the CAM-B3LYP[200] level yields a bright S_1 dominated by a simple HOMO → LUMO transition. Examining these orbitals is quite insightful as their nodal shapes already imply which dihedral angle will show a large or small rotational barrier in which state (**Fig. 5.1**b). This can be deduced from the basis function overlap of the π-orbitals centred at the central benzene unit with the diamino and dicyano groups. Assuming that the HOMO mainly determines the properties of the S_0 and the LUMO those of the S_1, we can infer that D_α will show a small rotational barrier in the S_0 and D_β in the S_1 as otherwise basis function overlap will be strongly impeded.
DFT/MRCI[213] based on BHLYP[123] generated KS orbitals was used in our calculations of the PESs which proved far superior over standard DFT or even long-range corrected approaches. It seems that a certain small but non-negligible multi-referential character determines the electronic properties of DADQs which lead to the failure of single-reference TD-DFT methods. The shapes of the PESs of the ground and lowest singlet excited states were obtained as expected from our reasoning above with large barriers of around 60–100 kJ/mol for D_α and D_β in the S_1 and S_0, respectively, and small barriers usually below 30 kJ/mol otherwise. We realised that the crucial dihedral angle is D_β representing the most likely fluorescence deactivation pathway, since at a 90° angle an intersystem crossing was imminent due to a vanishingly small singlet-triplet separation of well below 0.1 eV. Our theoretical results are in satisfactory agreement with experiment as compound **4**, by far displaying the largest QY, showed the highest rotational barrier with roughly 25 kJ/mol while compounds **1**–**3** showed barriers below 15 kJ/mol (**Fig. 5.1**c). It can be shown that in terms of rate constants, compound **4** is less likely to show fluorescence quenching through D_β by a factor of up to 480.
Paper **A1** may be viewed in the context of substitution-pattern controlled optical properties and represents the first step in a bottom-up-like approach to systematically increase the complexity of DADQs. Already in their simplest form as monomers, DADQs show promising physico-chemical features for potential application in optoelectronic devices. Consequently, the focus will now be shifted away from monomers to molecular aggregates in solution.

To understand the implications of paper **A2**, it is essential to have some knowledge about the theory of H- and J-aggregation. This has been done in detail in **section 3.4.2**. In short, H-aggregates show nonfluorescent blue-shifted absorption peaks with respect to the monomer signal, and J-aggregates show fluorescent red-shifted absorption bands. In paper **A2** we investigated a series of six different DADQ derivatives (**Fig. 5.2**a) and examined their photophysical properties with respect to aggregation in solution. We made the puzzling observation that aggregation-induced

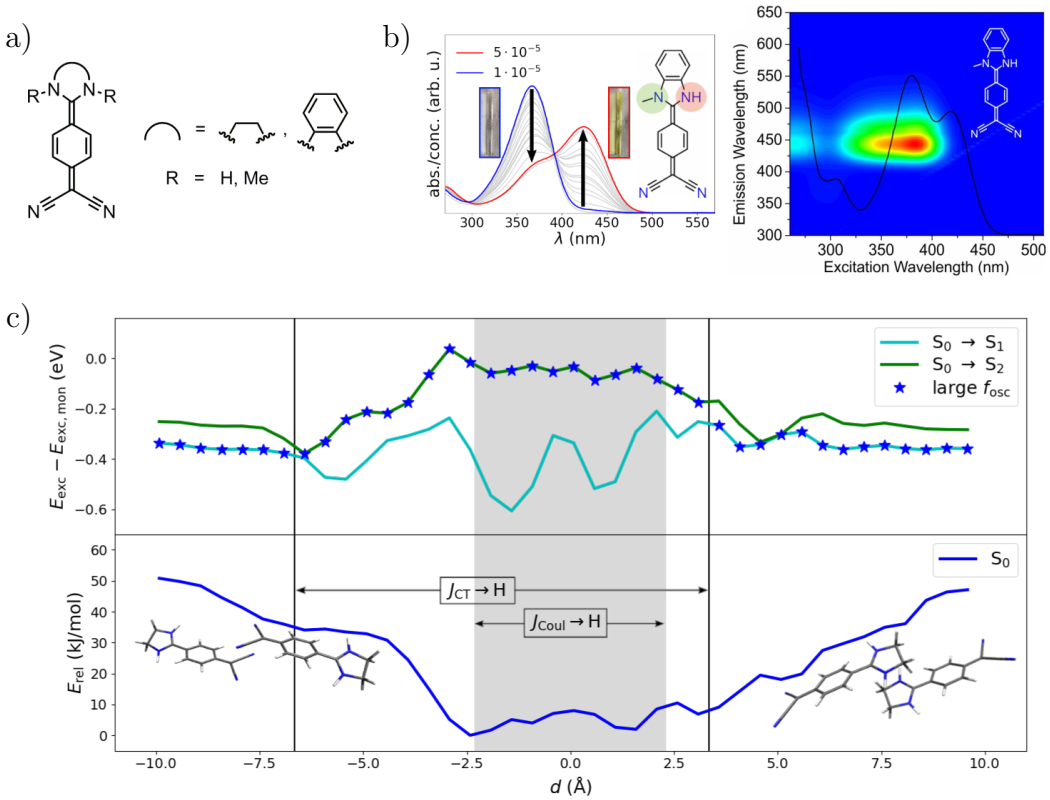

Figure 5.2: Paper **A2**: a) Six different compounds are defined through a diamino bridge and diamino-substituents, b) concentration-dependent absorption spectra and excitation-emission matrix using the example of a singly methyl-substituted benzene-bridged DADQ, c) S_0 PES for longitudinal displacement of two antiparallel π-stacked DADQs (bottom) and excitation energies referenced to that of the respective monomer of the two lowest excited states with stars indicating the bright state (top).

bands were red-shifted but nonfluorescent (**Fig. 5.2**b). Emission quenching to some extent through molecules in close proximity is in and of itself not impossible. However, virtually no emission at all was found in excitation-emission matrices for the aggregation band, while the monomer peak remained just as fluorescent as expected from the results of paper **A1**. It can be inferred that we have either found an example of so-called red-shifted H-aggregates or nonfluorescent J-aggregates. Importantly, none of these unusual systems can be described using the framework of Kasha's aggregate theory.

We have opted to first examine the conformational landscape of DADQs in solution to collect potential candidates for the aggregates responsible for the experimental observations. To this end, we employed metadynamics simulations using Grimme's GFN2-xTB code[152] and dispersion-corrected DFT methods at the PBEh-3c[251] and ωB97X-D3[205] levels. It was revealed that DADQ aggregation behaviour is remarkably complex and vast including series of possible stable oligomers

up to hexamers and possibly beyond. We opted to focus on stable dimers which could in general be identified by cancelling dipole moments of the individual monomers.
Once again, we employed the DFT/MRCI approach to study optical properties as it proved very useful in paper **A1**. Interestingly, all stable dimers showed a bright high-energy S_2 state, which is indicative of an H-aggregate, even though not all stable dimers could be classified as H-aggregates according to Kasha's theory. Invoking Spano's expanded HJ-aggregate theory in addition to Kasha's ideas, we could show that stable DADQ dimers show aspects of both H- and J-aggregates and can in part, hence, be identified as so-called integrated HJ-aggregates.
However, to our surprise none of the stable dimers were able to reproduce our experimental findings. Moreover, also no trimer or tetramer we tested showed the desired red-shift. The aggregation-induced band seems to originate from something more unusual. Prompted by H- to J-aggregation encountered in the literature,[20] we tried to find a similar mechanism using antiparallel π-stacked dimers. We varied the longitudinal displacement coordinate of the two monomers and analysed the shapes of the resulting PES in the S_0, S_1, and S_2 (**Fig. 5.2**c). It can be observed that after a certain threshold, the S_1 instead of the S_2 is populated or rather that the two states become almost degenerate. The resulting structures may be referred to as metastable, displaying red-shifted absorption peaks fitting nicely to experiment. Furthermore, the metastable dimers explain the virtually nonexistent emission of the aggregation band in a straight-forward manner. An excited-state optimisation along the S_1 reveals that the metastable structure relaxes back along the displacement coordinate to yield an H-type aggregate which possesses a dark S_1 rendering the molecule unable to show fluorescence. The slip-stack motion as a dominant molecular mode is additionally supported by *ab-initio* molecular dynamics simulations.
Paper **A2** provides a fascinating addition to the photophysical features of DADQs and is a prime example of the intriguing properties that can arise when supramolecular aggregation is studied, especially in the context of photo-responsive materials. Having addressed monomers and aggregates, the logical next step is to examine the solid state structure of DADQs. As we will see, it was in fact very expedient to have studied monomers and aggregates first.

The results of paper **A3** are especially important in the context of aggregation-induced emission (AIE) and aggregation-caused quenching (ACQ). Substitution-pattern control of solution and solid-state emission is observed for four different DADQ compounds (**Fig. 5.3**a). Compound **4**, which was already the protagonist of paper **A1**, shows remarkable QYs in solution but is completely quenched in the solid state, while compound **1**, which used to be compound **2** in paper **A1**, yields practically no emission in solution but shows moderate QY as a solid. In other words, there are both AIE as well as ACQ effects observable among DADQs.
These first experimental findings can be rationalised by Förster and Dexter energy transfer calculations (**section 3.4.2**) according to a scheme proposed by Radhakrishnan and co-workers based on the immediate interaction of monomers in close proximity in the crystal structure (**Fig. 5.3**b).[243,244] Especially the significance of the Dexter process increases in the series from compound **1**, where large intermolecular distances prevent notable fluorescence quenching, to compound **4**, where energy transfer is efficiently mediated by closely packed π-π-stacked dimers.
Furthermore, an interesting trend was found in fluorescence lifetime measurements of compounds **1**–**3** which revealed two different emissive states or structures in the solid (**Fig. 5.3**c). From Fermi's rule it can be shown that in a two-state system, a proportionality between reciprocal lifetime τ^{-1}

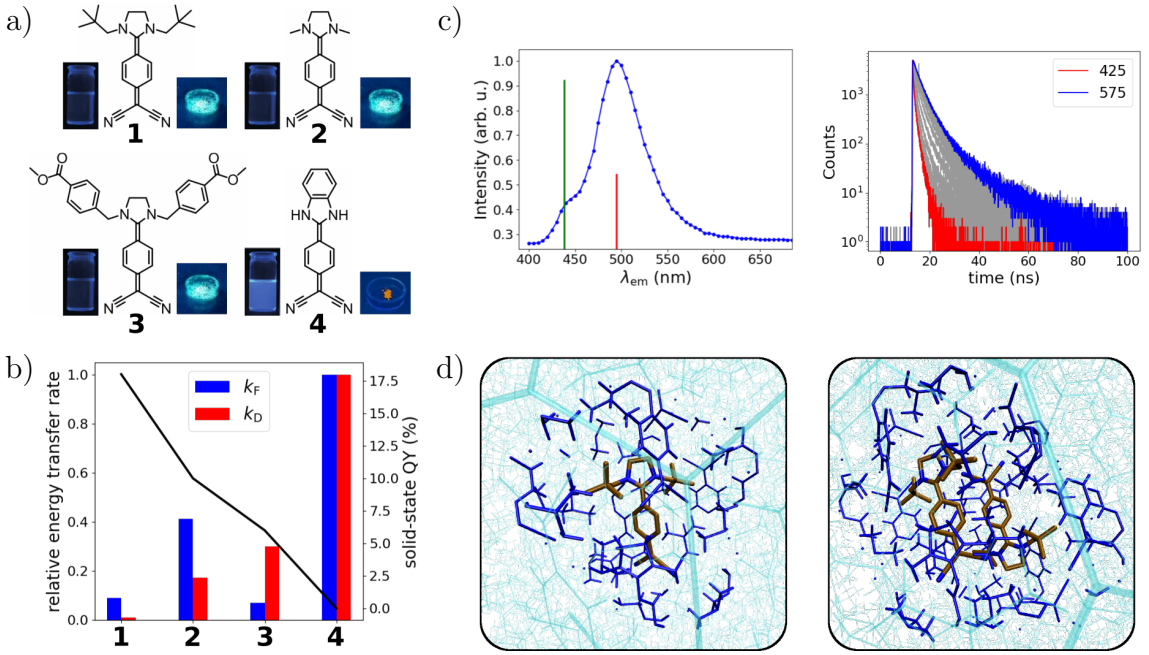

Figure 5.3: Paper **A3**: Compounds **1**–**4** with vials (solution) and petri dishes (solids) to indicate differences in fluorescence QYs, b) relative Förster (k_F) and Dexter (k_D) transfer rates in comparison to solid-state QYs (solid line), c) emission spectrum (left) with vertical transitions obtained from DFT/MRCI calculations for an H-type dimer (green) and a monomer (red) and fluorescence lifetime measurements (right) of compound **1**, d) illustration of monomer (left) and dimer (right) embedded in a large supercell extracted from the crystal structures in a QM/MM set-up, the molecules themselves and the atoms depicted in blue were allowed to relax during an excited-state optimisation.

and reciprocal squared emission wavelength λ^{-2} should be observed. This relationship is however not recovered in our experiments. Instead, a high-energy component in the emission spectrum of all compounds but **4** is observed, whose origin we wanted to find out.

We employed a combination of periodic calculations based on the PBE and HSE06[252] functionals and TD-DFT at the ωB97X-D3 level to investigate the solid-state structure of compounds **1** and **2**. Investigating the optical properties of solids can be extremely resource-demanding, if Green's function methods or the evaluation of the Bethe-Salpeter equation are necessary. Fortunately however, our calculations showed that the solid-state optical properties can in fact be decently described by examining monomers and dimers (**Fig. 5.3**d). We utilised a QM/MM ansatz in conjunction with TD-DFT excited-state optimisations to model monomers and dimers embedded in the inhomogeneous environment of the crystal. Final estimations of absorption and emission features were evaluated at the DFT/MRCI level using the C-PCM[253] solvent model for environmental effects. For the latter, we used the dielectric constant and refractive index computed at the periodic PBE level. In a way, we pretend here that the monomer or dimer under investigation is dissolved in its solid-state structure. This approach obviously excludes short-range explicit effects. Nevertheless, we obtained satisfying results in comparison to experiment.

It turned out that the main band of the emission spectrum can be identified as the monomer signal polarised by the crystal structure, while the high-energy (small wavelength) shoulder can be attributed to H-type aggregates. The oscillator strength associated with the transition in the H-dimers is larger than that of the monomers, which explains the difference in fluorescence life-

times. In contrast, the emission intensity of the dimer is much smaller than that of the monomer. This is attributed to fluorescence quenching, because the S_1 is a dark state in H-aggregates. Due to the rigid solid, the bright S_2 cannot or only barely internally convert into the S_1. Otherwise the high-energy shoulder would not exist at all. The two states likely form a conical intersection.
J-aggregates are potential candidates to explain the experimental observations as well. However, the high-energy S_2 possesses a smaller oscillator strength in J-aggregates which is in contrast to the experimentally determined lifetimes. Furthermore, from analysing the excited states in J-aggregates, we know that the intermolecular coupling between the monomers is extremely small. This can be inferred from completely localised difference densities, which are entirely delocalised over the whole dimer in H-aggregates.
Lastly, the emission spectrum of compound **1** shows non-negligible emission even over 100 nm away from the main peak. This is somewhat unexpected as lifetime broadening should actually sharpen the signal rather than spreading it. We proposed that crystal defects may be responsible for this observation. Our calculations confirm that a monomer which can relax a little more freely inside a defect cavity shows larger Stokes shifts and emission well beyond that of the main peak.
To finish part **A** of this thesis, I would like to note that paper **A3** completes a circle, so to speak, as it turned out that knowledge about the monomers and dimers of papers **A1** and **A2**, respectively, could be utilised for a proper analysis of the photophysics of solid-state DADQs. Closely tied to this is the important idea in systems chemistry that the single components of a large, complex system can act in concert to define its properties as a whole. This concept is perfectly embodied by the supramolecular structures of part **B**, which shows how the two parts are intertwined. While DADQs can be identified as photo-responsive organic systems defined by substitution-pattern controlled optical properties, in the following we will demonstrate the versatility of redox-responsive supramolecular frameworks and outline how quantum-chemical methods can be employed to rationalise their physico-chemical behaviour.

The Nobel Prize in Chemistry 2016 awarded for the design of molecular machines is proof of the general interest in the topic. Especially, rotaxanes are promising candidates for the synthesis of such architectures due to the structural flexibility of their individual components, namely axle and macrocycle. Paper **B1** presents and studies a redox-responsive [3]rotaxane **R2** consisting of two macrocycles each equipped with a TTF unit, which can either move "clutched" in concert or "declutched" on their own in a counterrotatory fashion (**Fig. 5.4**). In this way, the working mechanism of **R2** is reminiscent of a macroscopic friction clutch, in which the gears operate according to the noncovalent interactions governed by the coupling of the two TTF moieties. Other examples of molecular gears can be found in the literature based on interconnected triptycene groups or organometallic carousel compounds.[254–257]
The properties of the TTF_2 dimer have been discussed in the introduction of this thesis. In short, the charge of the molecule determines the interaction strength between the two monomers with the singly oxidised mixed-valence state being the most strongly bound, while the fully oxidised state drifts the monomers apart due to electrostatic repulsion. The second oxidised state, the radical-cation dimer, is also quite strongly bound in solution. As a consequence, **R2** can be reversibly switched between two ground-state co-conformations (GSCCs) *syn* and *anti* (**Fig. 5.4**b).

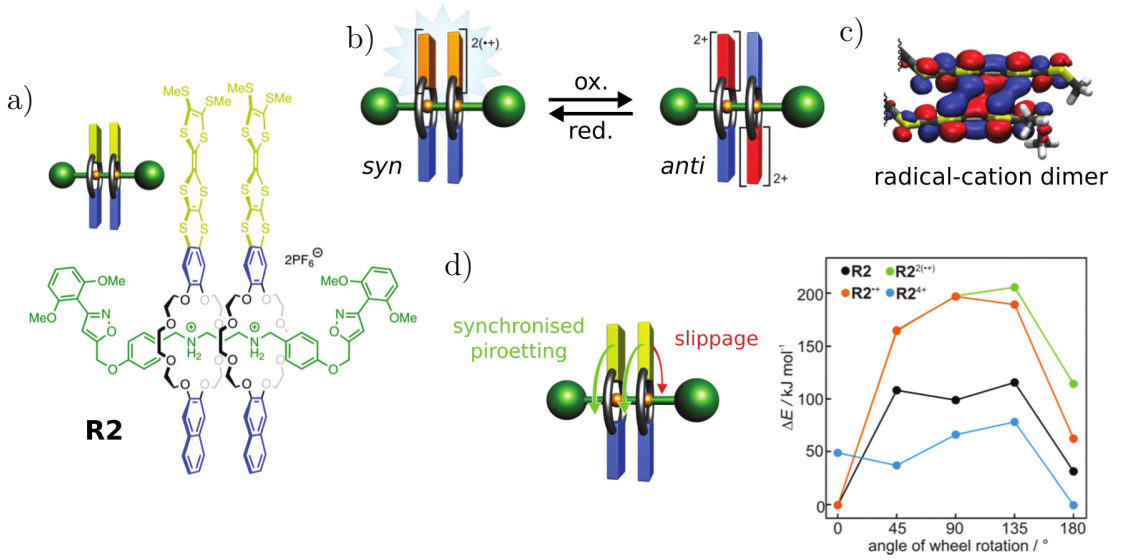

Figure 5.4: Paper **B1**: a) [3]rotaxane **R2** used in the project, b) two different GSCCs interconvertable through oxidation and reduction, c) delocalised HOMO of the radical-cation dimer illustrating the non-covalent interactions responsible for the coupling of the two macrocycles in **R2**, d) counterrotation scan ("slippage" motion) of the two macrocycles showing that the final oxidative process leads to an immediate decoupling of the macrocycles.

The molecular structure of the two co-conformations was investigated using a less resource-demanding stopper-less pseudorotaxane version of **R2** for the calculations. In agreement with experiment, **R2** is found most stable in the *syn* GSCC in charge states 0, 1+, and 2+, whereas the *anti* GSCC is lower in energy for $\mathbf{R2}^{4+}$. Furthermore, the interplanar distance of the two TTF units is smallest in $\mathbf{R2}^{2+}$ which is also illustrated by a complete delocalisation of the electronic structure (here represented by the HOMO) over the TTF_2 moiety (**Fig. 5.4**c).

While the stationary GSCCs are comparably easy to analyse experimentally, the microscopic motion of the macrocycles is extremely difficult to observe spectroscopically even with more sophisticated methods like variable-temperature NMR experiments as the rotational motion is always much faster than the NMR time scale. However, a computational approach can be applied in a straight-forward manner as examining the rotational motion "simply" boils down to scanning the PES depending on the charge of the molecules. Our model was based on Grimme's semi-empirical HF-3c scheme[258] for a rough first estimate of the shape of the relaxed PES. Afterwards, single point energies of structures on the PES were calculated at the PBE0-D3(BJ) level of DFT (**Fig. 5.4**d). Our computational model indeed confirmed what was suggested based on spectroscopic measurements. After the final oxidation which generates $\mathbf{R2}^{4+}$, the two macrocycles start repelling each other and the synchronised motion turns into a counterrotation. For all other charge states, the clutched *syn* co-conformation is the most stable one. It should be noted, that the values shown in **Fig. 5.4**d are upper bounds of the true rotational barriers as the PESs that we obtained are rough estimates. A more thorough investigation at this point was however deemed unnecessary and would have likely been very cumbersome due to a potentially extremely complex and shallow PES, if more than the five points shown were included.

Paper **B1** gives a unique example of a redox-switchable system which is able to convert electrical energy into a change of molecular motion. Furthermore, the importance of utilising quantum-

chemical methods was illustrated as the structural freedom of **R2** allowed for fast intramolecular interconversions of co-conformations which were not accessible by a multitude of spectroscopic techniques.

Similar to paper **B1**, paper **B2** utilises the redox-active TTF unit incorporated into a planar chiral [2]rotaxane. The chirality of the resulting supramolecule **2Ac** originates from the directionality of the macrocycle. **2Ac** is identified as a chiroptical switch showing a reversible sign inversion of its ECD response upon oxidation (**Fig. 5.5**a). In this context, Feringa and co-workers' seminal works on overcrowded alkenes acting as light and heat triggered chiroptical switches should be mentioned.[55,259,260] Mechanically interlocked planar chiral rotaxanes were first reported by Vögtle in 1997.[261]

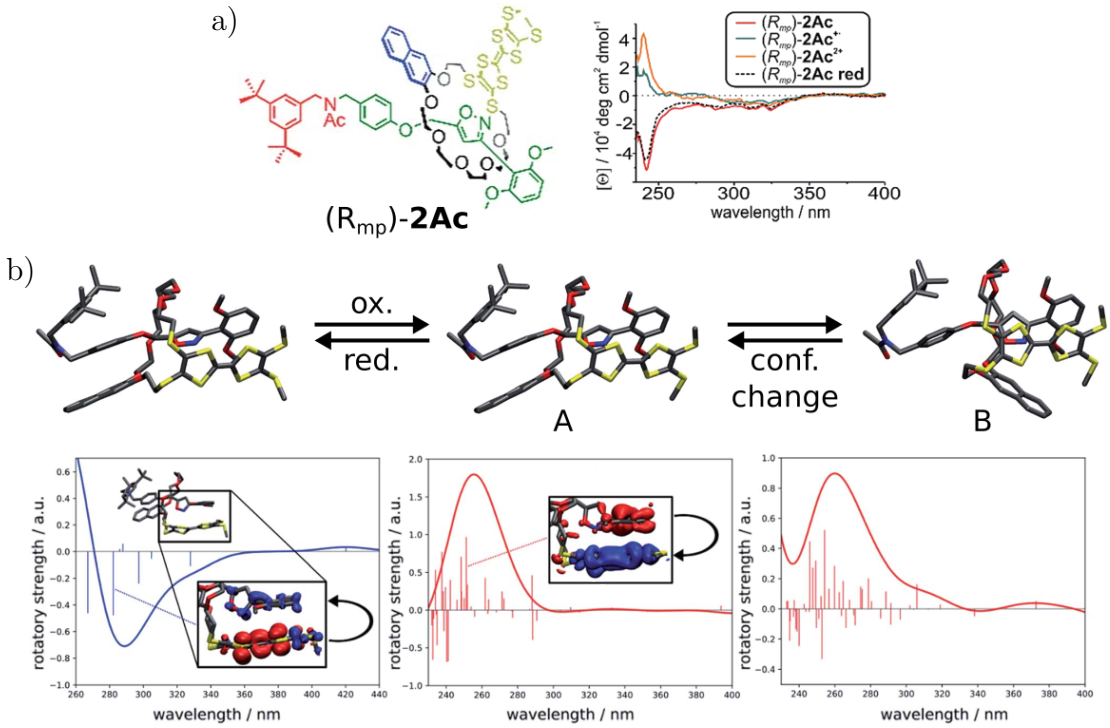

Figure 5.5: Paper **B2**: Redox-switchable chiroptical [2]rotaxane **2Ac** (left, shown in configuration R_{mp}) and its redox-dependent ECD spectra, b) change in conformation upon oxidation (top) and corresponding simulated ECD spectra (bottom) with difference densities to indicate the nature of two selected examples of excited states as insets.

The impact of the directionality of the macrocycle solely amounts to the ECD response, while absorption and electrochemical properties of the racemic mixture remained similar to those of analogous achiral rotaxanes.[63] Using standard spectroscopic techniques, the origin of the observed ECD sign inversion could not be unravelled. Instead a computational approach had to be employed.

We assumed that the chiroptical switching can either be explained by a change in conformation or a change in the electronic structure, likely governed by the properties of the TTF unit. To this end, we first conducted a sampling of the conformational landscape using Grimme's GFN2-xTB programme, re-optimised the most unique structures at the TPSS-D3(BJ) level and calculated sin-

gle point energies using the long-range corrected ωB97X-D3 DFA. And indeed, it turned out that an oxidation-induced conformational change (A → B) may take place owing to the localisation of the charge at the TTF unit (**Fig. 5.5**b). **2Ac**$^{2+}$ (irrespective of the absolute configuration) seems to be stabilised by a flip of the naphthalene moiety towards the electron-poor TTF^{2+} unit in comparison to neutral **2Ac**.
ECD spectra were simulated at the ωB97X-D3 level using the simplified TD-DFT ansatz, which was necessary due to the size of the molecule and the number of states that had to be calculated. We observed that the structural change to conformation B in fact reproduces the inverted ECD response. However, calculation of conformation A of **2Ac**$^{2+}$ resulted in a similar ECD spectrum also reproducing the ECD sign inversion. We realised that the oxidation itself irrespective of any conformational changes had to be responsible for the chiroptical properties of **2Ac**. In fact, our unexpected experimental finding can be explained in a surprisingly simple way. Analysing the electronic transitions in the spectral region of interest between 230 and 400 nm reveals that practically every excitation involves the TTF unit to some extent. While many transitions are localised, a fair amount exhibit charge-transfer behaviour. For neutral **2Ac**, these can be interpreted as advancing an electron *from the TTF core* into an orbital centred somewhere else in the molecule, e.g., on the isoxazole unit. For oxidised **2Ac**$^{2+}$, on the other hand, these transitions are reversed and charge is transferred *to the TTF core* (insets in **Fig. 5.5**b). Differently oriented magnetic transition dipole moments with more or less unchanged electronic transition dipole moments are the result which explain the ECD sign inversion.
Paper **B2** underlines the impact of the mechanical bond and supramolecular aggregation resulting in unexpected photophysical properties. The use of a comparably involved computational ansatz was necessary leading to a surprisingly straight-forward interpretation of the experimental results. This project furthermore serves as a didactically valuable example, as the complexity of the findings is effectively boiled down to fairly simple concepts like charge-transfer and one-electron transitions, that can be readily understood by undergraduate students.

Finally, paper **B3** revolves around a naphthalene-based molecular cage, naphthocage **NC**, with extremely high binding affinities towards singly charged organic compounds. Redox-switchable host-guest complexes (**Fig. 5.6**a) could be formed with the ferrocene/ferrocenium and cobaltocene/cobaltocenium couples with an association free enthalpy of roughly –60 kJ/mol for $CoCp_2^+$@**NC** obtained from ITC experiments. **NC** exhibits conformational flexibility and adapts a self-included structure with one naphthalene moiety sandwiched between the other two naphthalene walls of the system in the crystal structure (**Fig. 5.6**b). Host-guest complexes can form in two isomers, **NC-I** (D_3 symmetric) and **NC-II** (C_2 symmetric), differing in a rotated naphthalene unit (**Fig. 5.6**c). Furthermore, an ion-selective electrode for acetylcholine chloride made from **NC** displays a super-Nernstian response of 85 mV. Evidently, **NC** is an all-rounder with lots of desirable features for applications in electrochemical and stimuli-responsive materials or devices.
Our computational approach based on the TPSS-D3(BJ) and B3LYP-D3(BJ) levels of DFT addressed the conformational freedom of **NC** and the nature of its remarkable binding affinities. We showed that the self-inclusion complex adapted in the crystal structure remains the most stable conformation in solution. Due to a significant entropic penalty ($\Delta S \approx 177$ kJ/mol) when explicit solvent molecules are encapsulated, no host-guest complex forms, even though including three dichloromethane molecules induces an energetic stabilisation of roughly 86 kJ/mol.

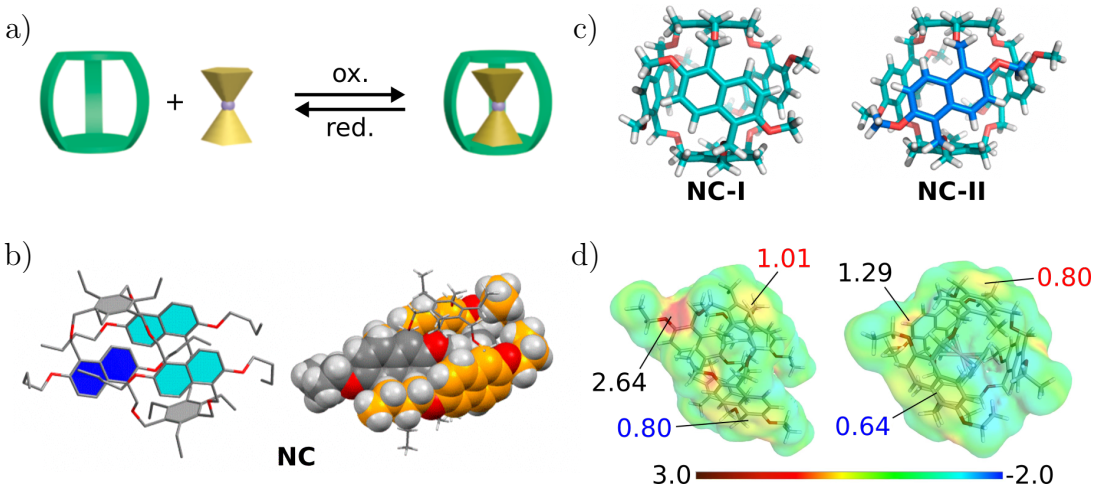

Figure 5.6: Paper **B3**: a) schematic representation of the redox-switchability of a $CoCp_2^+$@**NC** host-guest complex, b) self-included structure of **NC**, c) two different conformers of a shortened version of **NC** optimised with encapsulated $CoCp_2^+$ (not shown for visual clarity), d) σ-surfaces of **NC** and $CoCp_2^+$@**NC** obtained from a COSMO treatment of the structures with indication of screening charges at different zones (blue for naphthalene, red for benzene, black for the highest screening charge observed).

The association free enthalpy of $CoCp_2^+$@**NC** was computed to be around –64 kJ/mol, which is in good agreement with experiment and confirms the encapsulation of the organometallic complex. Side-on complexation would have been conceivable otherwise. The dominant isomer for the host-guest structure is the more symmetric **NC-I** around 9 kJ/mol more stable than the host-guest complex with **NC-II**. We found that the interaction between **NC** and $CoCp_2^+$ is mainly of electrostatic nature rather than caused by charge transfer. This can be observed from the valence electronic structure, which fails to show delocalisation over both host and guest in the occupied MOs. The electrostatic interaction was visualised by the screening charge surface (σ-surface) generated with COSMO, which illustrates the charge compensation effect of the charged guest on the polarised surface of **NC** (**Fig. 5.6**d).

In comparison to papers **B1** and **B2**, paper **B3** was focussed on thermodynamic properties rather than optical features. **NC** represents another intriguing example of a supramolecular system with tailorable qualities for potential application in sensory materials. Our computational model proved crucial in the description of more subtle effects regarding the conformational flexibility and electronic properties of **NC**.

6 Conclusion and outlook

All in all, the most significant difference between part **A** and part **B** is that papers **A1**–**A3** built up complexity along the way starting *at the bottom*, while papers **B1**–**B3** featured intricate supramolecular systems *at the top*, so to speak. With both parts combined in this thesis, I hope to offer an impression of the broad versatility of stimuli-responsive supramolecular materials and the tremendous capability and indispensability of quantum-chemical approaches to tackle complex problems.

Future research based on our studies may involve both experimental as well as theoretical perspectives. The presented systems are now equipped with an in-depth understanding of their thermodynamic and optical properties, which paves the way towards applications in novel optoelectronic technologies, such as organic light-emitting diodes, light-harvesting devices, or sensory materials. Obviously, this requires collaboration with experts from other branches of chemistry and materials science. Nonetheless, the groundwork for these kinds of projects has been laid by the results of this thesis.

From a theoretical point of view, one may extend the research by introducing more rigor into the calculations. While the applied DFT methods are certainly not inaccurate, some difficult-to-assess, systematic errors may always arise due to the nature of DFAs. A possible remedy is to employ systematically improved wavefunction-based methods. For example, Christian Ochsenfeld an co-workers developed a linear-scaling MP2 approach, which was used to calculate a DNA repair system with more than 2000 atoms.[262,263] Furthermore, in recent years, Frank Neese and co-workers have introduced linear-scaling coupled-cluster methods based on so-called pair natural orbitals.[264–266] The latest approximation is called domain-based local pair natural orbital (DLPNO). In 2013, the broad capability of this approach was impressively illustrated, when the protein Crambin with 644 atoms was treated at the DLPNO-CCSD(T) level.[267] In combination with complete basis set extrapolation schemes,[268–270] the electronic energy of large systems may be converged to a near perfect level.

Another aspect concerns the comparability of theoretical and experimental results. In most of the studies presented in this thesis, solvent effects are simulated by utilising implicit continuum solvation models. These methods assume a homogeneous environment around the solute. This approximation can become quite severe, especially in polar, protic solvents, where hydrogen bonding can directly affect not only the electronic but also the molecular structure of the solute. Whereas methods like the COSMO-RS approach are promising workarounds, there will always be quite a few limitations attached.[271] Especially the influence of solvent molecules on excited states is quite difficult to estimate. A more rigorous approach might be an extensive application of QM/MM schemes (*cf.* paper **A3**) in combination with *ab-initio* molecular dynamics (MD, *cf.* paper **A2**).[272] This methodology has been successfully applied numerous times in the literature.[273–275] Especially the treatment of the counterrotation PES in paper **B1** or the simulated ECD spectra in paper **B2** may profit from this. Unfortunately, for realistic chemical systems, high-level wavefunction based methods are usually too computationally expensive for long *ab-initio* MD simulation times. Consequently, low-level TDA or TD-DFT methods with rather small basis sets are employed, which requires separate validation of the results, e.g., by calculating selected points on a trajectory with a more accurate method.[276,277]

A possibility to reduce the cost of long simulation times has recently emerged with the advent of machine learning (ML) algorithms.[278] In principle, approaches like neural networks or kernel ridge regression can notably speed up large-scale calculations, not only limited to MD runs, by relying on a pre-computed data set.[279–281] In recent years, quite a few studies have utilised ML approaches to examine PESs and obtain long MD simulation times for large systems.[282–285] However, ML algorithms come with a rather significant drawback when it comes to analysing complex quantum-chemical phenomena. Due to the vastness of chemical space[286,287] the pre-computed data set, the so-called training set, is not necessarily well-suited to describe the system one is interested in. As a consequence, to set up a decent training set, resource-draining high-level quantum-chemical calculations have to be performed, anyway.
Nevertheless, there is a continuous emergence of efficiently approximated high-level quantum-chemical methods. In combination with access to high-performance computing clusters, the future looks bright for the field of computational chemistry, especially with respect to the accurate treatment of large and intricate supramolecular structures.

References

[1] A. D. Becke, *J. Chem. Phys.* **2014**, *140*, 18A301.

[2] K. Autumn, Y. A. Liang, S. T. Hsieh, W. Zesch, W. P. Chan, T. W. Kenny, R. Fearing, R. J. Full, *Nature* **2000**, *405*, 681–685.

[3] K. Autumn, M. Sitti, Y. A. Liang, A. M. Peattie, W. R. Hansen, S. Sponberg, T. W. Kenny, R. Fearing, J. N. Israelachvili, R. J. Full, *Proc. Natl. Acad. Sci.* **2002**, *99*, 12252–12256.

[4] B. Rozitis, E. MacLennan, J. P. Emery, *Nature* **2014**, *512*, 174–176.

[5] B. Heyne, *Photochem. Photobiol. Sci.* **2016**, *15*, 1103–1114.

[6] J. N. Israelachvili, *Intermolecular and Surface Forces*, Elsevier, **2011**.

[7] E. E. Jelley, *Nature* **1936**, *138*, 1009–1010.

[8] E. E. Jelley, *Nature* **1937**, *139*, 631–631.

[9] G. Scheibe, *Angew. Chem.* **1937**, *50*, 212–219.

[10] G. Scheibe, L. Kandler, H. Ecker, *Naturwissenschaften* **1937**, *25*, 75–75.

[11] S. Kirstein, S. Daehne, *Int. J. Photoenergy* **2006**, *2006*, 1–21.

[12] E. G. McRae, M. Kasha, *J. Chem. Phys.* **1958**, *28*, 721–722.

[13] M. Kasha, *Radiat. Res.* **1963**, *20*, 55.

[14] M. Kasha, *Discuss. Faraday Soc.* **1950**, *9*, 14–19.

[15] M. Bayda, F. Dumoulin, G. L. Hug, J. Koput, R. Gorniak, A. Wojcik, *Dalton Trans.* **2017**, *46*, 1914–1926.

[16] C. Zheng, C. Zhong, C. J. Collison, F. C. Spano, *J. Phys. Chem. C* **2019**, *123*, 3203–3215.

[17] E. A. Margulies, L. E. Shoer, S. W. Eaton, M. R. Wasielewski, *Phys. Chem. Chem. Phys.* **2014**, *16*, 23735–23742.

[18] F. C. Spano, *J. Am. Chem. Soc.* **2009**, *131*, 4267–4278.

[19] A. Liess, A. Arjona-Esteban, A. Kudzus, J. Albert, A. Krause, A. Lv, M. Stolte, K. Meerholz, F. Würthner, *Adv. Funct. Mater.* **2019**, *29*, 1805058.

[20] T. Eder, J. Vogelsang, S. Bange, K. Remmerssen, D. Schmitz, S. Jester, T. J. Keller, S. Höger, J. M. Lupton, *Angew. Chem. Int. Ed.* **2019**, *58*, 18898–18902.

[21] J. Liu, H. Lu, Y. Liu, J. Zhang, C. Li, X. Xu, Z. Bo, *ACS Appl. Mater. Interfaces* **2020**, *12*, 10746–10754.

[22] G. Zhang, J. Feng, X. Xu, W. Ma, Y. Li, Q. Peng, *Adv. Funct. Mater.* **2019**, *29*, 1906587.

[23] H. Wang, L. Chen, Y. Xiao, *J. Mater. Chem. C* **2017**, *5*, 12816–12824.

[24] Y. Wang, D. Fang, T. Fu, M. U. Ali, Y. Shi, Y. He, Z. Hu, C. Yan, Z. Mei, H. Meng, *Mat. Chem. Front.* **2020**, *4*, 3546–3555.

[25] P. Yu, Y. Zhen, H. Dong, W. Hu, *Chem* **2019**, *5*, 2814–2853.

[26] Y. Matsuo, H. Okada, Y. Kondo, I. Jeon, H. Wang, Y. Yu, T. Matsushita, M. Yanai, T. Ikuta, *ACS Appl. Mater. Interfaces* **2018**, *10*, 11810–11817.

[27] O. Ostroverkhova, *Chem. Rev.* **2016**, *116*, 13279–13412.

[28] M. Yu, R. Huang, J. Guo, Z. Zhao, B. Z. Tang, *PhotoniX* **2020**, *1*, 11.

[29] D. L. Dexter, *J. Chem. Phys.* **1953**, *21*, 836–850.

[30] T. Förster, *Ann. Physik* **1948**, *437*, 55–75.

[31] J. Luo, Z. Xie, J. W. Y. Lam, L. Cheng, B. Z. Tang, H. Chen, C. Qiu, H. S. Kwok, X. Zhan, Y. Liu, D. Zhu, *Chem. Commun.* **2001**, 1740–1741.

[32] Y. Hong, J. W. Y. Lam, B. Z. Tang, *Chem. Soc. Rev.* **2011**, *40*, 5361.

[33] Y. Shen, H. Liu, S. Zhang, Y. Gao, B. Li, Y. Yan, Y. Hu, L. Zhao, B. Yang, *J. Mater. Chem. C* **2017**, *5*, 10061–10067.

[34] H. Liu, L. Yao, B. Li, X. Chen, Y. Gao, S. Zhang, W. Li, P. Lu, B. Yang, Y. Ma, *Chem. Commun.* **2016**, *52*, 7356–7359.

[35] H. Liu, D. Cong, B. Li, L. Ye, Y. Ge, X. Tang, Y. Shen, Y. Wen, J. Wang, C. Zhou, B. Yang, *Cryst. Growth Des.* **2017**, *17*, 2945–2949.

[36] F. Würthner, T. E. Kaiser, C. R. Saha-Möller, *Angew. Chem. Int. Ed.* **2011**, *50*, 3376–3410.

[37] J.-M. Lehn, *Angew. Chem. Int. Ed.* **1988**, *27*, 89–112.

[38] J.-P. Sauvage, *Angew. Chem. Int. Ed.* **2017**, *56*, 11080–11093.

[39] J. F. Stoddart, *Angew. Chem. Int. Ed.* **2017**, *56*, 11094–11125.

[40] B. L. Feringa, *Angew. Chem. Int. Ed.* **2017**, *56*, 11060–11078.

[41] E. Wasserman, *J. Am. Chem. Soc.* **1960**, *82*, 4433–4434.

[42] D. J. Cram, J. M. Cram, *Science* **1974**, *183*, 803–809.

[43] J. Rebek Jr., *Chem. Commun.* **2000**, 637–643.

[44] C. Márquez, R. R. Hudgins, W. M. Nau, *J. Am. Chem. Soc.* **2004**, *126*, 5806–5816.

[45] C. Dietrich-Buchecker, J. Sauvage, J. Kintzinger, *Tetrahedron Lett.* **1983**, *24*, 5095–5098.

[46] A. Livoreil, C. O. Dietrich-Buchecker, J.-P. Sauvage, *J. Am. Chem. Soc.* **1994**, *116*, 9399–9400.

[47] J.-P. Collin, P. Gavinã, J.-P. Sauvage, *Chem. Commun.* **1996**, 2005–2006.

[48] B. Odell, M. V. Reddington, A. M. Z. Slawin, N. Spencer, J. F. Stoddart, D. J. Williams, *Angew. Chem. Int. Ed.* **1988**, *27*, 1547–1550.

[49] R. A. Bissell, E. Córdova, A. E. Kaifer, J. F. Stoddart, *Nature* **1994**, *369*, 133–137.

[50] R. Ballardini, V. Balzani, A. Credi, M. T. Gandolfi, S. J. Langford, S. Menzer, L. Prodi, J. F. Stoddart, M. Venturi, D. J. Williams, *Angew. Chem. Int. Ed.* **1996**, *35*, 978–981.

[51] Y. Liu, A. H. Flood, P. A. Bonvallet, S. A. Vignon, B. H. Northrop, H.-R. Tseng, J. O. Jeppesen, T. J. Huang, B. Brough, M. Baller, S. Magonov, S. D. Solares, W. A. Goddard, C.-M. Ho, J. F. Stoddart, *J. Am. Chem. Soc.* **2005**, *127*, 9745–9759.

[52] J. D. Badjić, V. Balzani, A. Credi, S. Silvi, J. F. Stoddart, *Science* **2004**, *303*, 1845–1849.

[53] K. Ariga, T. Kunitake, *Supramolecular Chemistry - Fundamentals and Applications*, Springer Berlin Heidelberg, **2006**.

[54] H. V. Schröder, F. Stein, J. M. Wollschläger, S. Sobottka, M. Gaedke, B. Sarkar, C. A. Schalley, *Angew. Chem. Int. Ed.* **2019**, *58*, 3496–3500.

[55] N Koumura, R. W. Zijlstra, R. A. van Delden, N Harada, B. L. Feringa, *Nature* **1999**, *401*, 152–155.

[56] R. Eelkema, M. M. Pollard, J. Vicario, N. Katsonis, B. S. Ramon, C. W. M. Bastiaansen, D. J. Broer, B. L. Feringa, *Nature* **2006**, *440*, 163–163.

[57] T. Kudernac, N. Ruangsupapichat, M. Parschau, B. Maciá, N. Katsonis, S. R. Harutyunyan, K.-H. Ernst, B. L. Feringa, *Nature* **2011**, *479*, 208–211.

[58] M. B. Nielsen, C. Lomholt, J. Becher, *Chem. Soc. Rev.* **2000**, *29*, 153–164.

[59] M. Riba-Moliner, A. Gómez-Rodríguez, D. B. Amabilino, J. Puigmartí-Luis, A. González-Campo, *Polymer* **2016**, *103*, 251–260.

[60] J. Tian, Y.-D. Ding, T.-Y. Zhou, K.-D. Zhang, X. Zhao, H. Wang, D.-W. Zhang, Y. Liu, Z.-T. Li, *Chem. Eur. J.* **2014**, *20*, 575–584.

[61] S. V. Bhosale, C. H. Jani, C. H. Lalander, S. J. Langford, I. Nerush, J. G. Shapter, D. Villamaina, E. Vauthey, *Chem. Commun.* **2011**, *47*, 8226.

[62] *Naphthalenediimide and its congeners: from molecules to materials*, (Ed.: G. D. Pantoş), Royal Society of Chemistry, London, **2017**.

[63] H. V. Schröder, S. Sobottka, M. Nößler, H. Hupatz, M. Gaedke, B. Sarkar, C. A. Schalley, *Chem. Sci.* **2017**, *8*, 6300–6306.

[64] Y. Qiu, S. Yi, A. E. Kaifer, *Org. Lett.* **2011**, *13*, 1770–1773.

[65] V. A. Azov, *Tetrahedron Lett.* **2016**, *57*, 5416–5425.

[66] M. Fumanal, M. Capdevila-Cortada, J. J. Novoa, *Phys. Chem. Chem. Phys.* **2017**, *19*, 3807–3819.

[67] M. Yoshizawa, K. Kumazawa, M. Fujita, *J. Am. Chem. Soc.* **2005**, *127*, 13456–13457.

[68] S. V. Rosokha, J. K. Kochi, *J. Am. Chem. Soc.* **2007**, *129*, 828–838.

[69] M. Hasegawa, K. Daigoku, K. Hashimoto, H. Nishikawa, M. Iyoda, *Bull. Chem. Soc. Jpn.* **2012**, *85*, 51–60.

[70] I. Garcia-Yoldi, J. S. Miller, J. J. Novoa, *J. Phys. Chem. A* **2009**, *113*, 484–492.

[71] M. Fumanal, M. Capdevila-Cortada, J. Ribas-Arino, J. J. Novoa, *J. Chem. Theory Comput.* **2015**, *11*, 2651–2660.

[72] A. Y. Ziganshina, Y. H. Ko, W. S. Jeon, K. Kim, *Chem. Commun.* **2004**, 806–807.

[73] V. Khodorkovsky, L. Shapiro, P. Krief, A. Shames, G. Mabon, A. Gorgues, M. Giffard, *Chem. Commun.* **2001**, 2736–2737.

[74] R. P. Feynman, R. B. Leighton, M. Sands, *The Feynman Lectures on Physics*, Addison-Wesley, **1964**.

[75] E. Schrödinger, *Ann. Physik* **1926**, *384*, 361–376.

[76] M. Born, R. Oppenheimer, *Ann. Physik* **1927**, *389*, 457–484.

[77] D. R. Yarkony, *Rev. Mod. Phys.* **1996**, *68*, 985–1013.

[78] W. Pauli, *Z. Phys.* **1925**, *31*, 765–783.

[79] J. C. Slater, *Phys. Rev.* **1930**, *35*, 210–211.

[80] J. C. Slater, *Phys. Rev.* **1951**, *81*, 385–390.

[81] D. R. Hartree, *Proc. Cambridge Phil. Soc.* **1928**, *24*, 89–110.

[82] V. Fock, *Z. Phys.* **1930**, *61*, 126–148.

[83] C. Froese, *Can. J. Phys.* **1963**, *41*, 1895–1910.

[84] R. A. Friesner, *J. Chem. Phys.* **1986**, *85*, 1462–1468.

[85] C. C. J. Roothaan, *Rev. Mod. Phys.* **1951**, *23*, 69–89.

[86] *Proc. R. Soc. Lond. A* **1951**, *205*, 541–552.

[87] A. Szabo, N. S. Ostlund, *Modern Quantum Chemistry: Introduction to Advanced Electronic Structure Theory*, Macmillan, **1982**.

[88] C. Møller, M. S. Plesset, *Phys. Rev.* **1934**, *46*, 618–622.

[89] H. J. Monkhorst, *Int. J. Quantum Chem. Symp.* **1977**, *12*, 421–432.

[90] P.-O. Löwdin in *Adv. Chem. Phys.* (Ed.: I. Prigogine), Wiley, **1958**, pp. 207–322.

[91] R. Buenker, S. Peyerimhoff, *Theoret. Chim. Acta* **1974**, *35*, 33–58.

[92] T. Helgaker, P. Jørgensen, J. Olsen, *Molecular Electronic-Structure Theory*, John Wiley & Sons, Ltd, Chichester, UK, **2000**.

[93] E. Besalú, R. Carbó-Dorca, *J. Math. Chem.* **2011**, *49*, 1769–1784.

[94] B. Silvi, M. Causà, R. Dovesi, C. Roetti, *Mol. Phys.* **1989**, *67*, 891–901.

[95] C. Kittel, *Introduction to Solid State Physics*, 8th ed., Wiley, **2004**.

[96] F. Bloch, *Z. Phys.* **1929**, *52*, 555–600.

[97] G. Kresse, J. Hafner, *Phys. Rev. B* **1993**, *47*, 558–561.

[98] G. Kresse, J. Furthmüller, *Comput. Mater. Sci.* **1996**, *6*, 15–50.

[99] G. Kresse, J. Furthmüller, *Phys. Rev. B* **1996**, *54*, 11169–11186.

[100] L. H. Thomas, *Math. Proc. Cambridge Philos. Soc.* **1927**, *23*, 542.

[101] E Fermi, *Z. Angew. Phys.* **1928**, *48*, 73–79.

[102] P. Hohenberg, W. Kohn, *Phys. Rev.* **1964**, *136*, B864–B871.

[103] W. Koch, M. C. Holthausen, *A Chemist's Guide to Density Functional Theory*, 2nd ed., 5, Wiley-VCH, Weinheim, **2008**.

[104] W. Kohn, L. J. Sham, *Phys. Rev.* **1965**, *140*, A1133–A1138.

[105] J. P. Perdew, K. Burke, M. Ernzerhof, *Phys. Rev. Lett.* **1996**, *77*, 3865–3868.

[106] F. Weigend, R. Ahlrichs, *Phys. Chem. Chem. Phys.* **2005**, *7*, 3297.

[107] J. P. Perdew, R. G. Parr, M. Levy, J. L. Balduz, *Phys. Rev. Lett.* **1982**, *49*, 1691–1694.

[108] A. Ruzsinszky, J. P. Perdew, G. I. Csonka, O. A. Vydrov, G. E. Scuseria, *J. Chem. Phys.* **2006**, *125*, 194112.

[109] K. Burke, *J. Chem. Phys.* **2012**, *136*, 150901.

[110] D. P. Chong, *Recent Advances in Density Functional Methods*, World Scientific, **1995**.

[111] S. F. Sousa, P. A. Fernandes, M. J. Ramos, *J. Phys. Chem. A* **2007**, *111*, 10439–10452.

[112] K. Burke, L. O. Wagner, *Int. J. Quantum Chem.* **2013**, *113*, 96–101.

[113] G. I. Csonka, A. Ruzsinszky, J. Tao, J. P. Perdew, *Int. J. Quantum Chem.* **2005**, *101*, 506–511.

[114] J. Tao, J. P. Perdew, V. N. Staroverov, G. E. Scuseria, *Phys. Rev. Lett.* **2003**, *91*, 146401.

[115] T. Risthaus, S. Grimme, *J. Chem. Theory Comput.* **2013**, *9*, 1580–1591.

[116] L. Goerigk, S. Grimme, *Phys. Chem. Chem. Phys.* **2011**, *13*, 6670.

[117] Y. Zhao, D. G. Truhlar, *J. Chem. Phys.* **2006**, *125*, 194101.

[118] N. Mardirossian, M. Head-Gordon, *J. Chem. Theory Comput.* **2016**, *12*, 4303–4325.

[119] Y. Zhao, D. G. Truhlar, *Chem. Phys. Lett.* **2011**, *502*, 1–13.

[120] L. Goerigk, *J. Phys. Chem. Lett.* **2015**, *6*, 3891–3896.

[121] M. Städele, J. A. Majewski, P. Vogl, A. Görling, *Phys. Rev. Lett.* **1997**, *79*, 2089–2092.

[122] S. Kümmel, J. P. Perdew, *Phys. Rev. B* **2003**, *68*, 035103.

[123] A. D. Becke, *J. Chem. Phys.* **1993**, *98*, 1372–1377.

[124] H. S. Yu, S. L. Li, D. G. Truhlar, *J. Chem. Phys.* **2016**, *145*, 130901.

[125] K. Eichkorn, O. Treutler, H. Öhm, M. Häser, R. Ahlrichs, *Chem. Phys. Lett.* **1995**, *240*, 283–290.

[126] F. Neese, F. Wennmohs, A. Hansen, U. Becker, *Chem. Phys.* **2009**, *356*, 98–109.

[127] Y. Zhao, D. G. Truhlar, *Theor. Chem. Acc.* **2008**, *120*, 215–241.

[128] A. D. Becke, *J. Chem. Phys.* **1993**, *98*, 5648–5652.

[129] J. P. Perdew, M. Ernzerhof, K. Burke, *J. Chem. Phys.* **1996**, *105*, 9982–9985.

[130] C. Adamo, V. Barone, *J. Chem. Phys.* **1999**, *110*, 6158–6170.

[131] R. Huenerbein, B. Schirmer, J. Moellmann, S. Grimme, *Phys. Chem. Chem. Phys.* **2010**, *12*, 6940.

[132] É. Brémond, M. Savarese, N. Q. Su, Á. J. Pérez-Jiménez, X. Xu, J. C. Sancho-García, C. Adamo, *J. Chem. Theory Comput.* **2016**, *12*, 459–465.

[133] S. Grimme, A. Hansen, J. G. Brandenburg, C. Bannwarth, *Chem. Rev.* **2016**, *116*, 5105–5154.

[134] J. Hermann, R. A. DiStasio, A. Tkatchenko, *Chem. Rev.* **2017**, *117*, 4714–4758.

[135] C. Mavroyannis, M. Stephen, *Mol. Phys.* **1962**, *5*, 629–638.

[136] M. Elstner, P. Hobza, T. Frauenheim, S. Suhai, E. Kaxiras, *J. Chem. Phys.* **2001**, *114*, 5149–5155.

[137] S. Grimme, J. Antony, S. Ehrlich, H. Krieg, *J. Chem. Phys.* **2010**, *132*, 154104.

[138] E. Caldeweyher, S. Ehlert, A. Hansen, H. Neugebauer, S. Spicher, C. Bannwarth, S. Grimme, *J. Chem. Phys.* **2019**, *150*, 154122.

[139] B. M. Axilrod, E. Teller, *J. Chem. Phys.* **1943**, *11*, 299–300.

[140] Y Muto, *Proc. Phys. Math. Soc. Japan* **1943**, *17*, 629.

[141] A Koide, *J. Phys. B* **1976**, *9*, 3173–3183.

[142] S. Grimme, S. Ehrlich, L. Goerigk, *J. Comput. Chem.* **2011**, *32*, 1456–1465.

[143] O. A. Vydrov, T. Van Voorhis, *J. Chem. Phys.* **2010**, *133*, 244103.

[144] M. Dion, H. Rydberg, E. Schröder, D. C. Langreth, B. I. Lundqvist, *Phys. Rev. Lett.* **2004**, *92*, 246401.

[145] A. Tkatchenko, M. Scheffler, *Phys. Rev. Lett.* **2009**, *102*, 073005.

[146] A. L. Mackay, *A Dictionary of Scientific Quotations*, CRC Press, London, **1994**.

[147] P. Pulay, *J. Comput. Chem.* **1982**, *3*, 556–560.

[148] J. Almlöf in *Lecture Notes in Quantum Chemistry II. Lecture Notes in Chemistry*, Springer Berlin Heidelberg, **1994**, pp. 1–90.

[149] F. Jensen, *Introduction to Computational Chemistry*, 3rd ed., Wiley, **2017**.

[150] S. Grimme, *J. Chem. Theory Comput.* **2019**, *15*, 2847–2862.

[151] M. Elstner, D. Porezag, G. Jungnickel, J. Elsner, M. Haugk, T. Frauenheim, S. Suhai, G. Seifert, *Phys. Rev. B* **1998**, *58*, 7260–7268.

[152] S. Grimme, C. Bannwarth, P. Shushkov, *J. Chem. Theory Comput.* **2017**, *13*, 1989–2009.

[153] C. Bannwarth, S. Ehlert, S. Grimme, *J. Chem. Theory Comput.* **2019**, *15*, 1652–1671.

[154] A. S. Christensen, T. Kubař, Q. Cui, M. Elstner, *Chem. Rev.* **2016**, *116*, 5301–5337.

[155] Y. Yang, H. Yu, D. York, Q. Cui, M. Elstner, *J. Phys. Chem. A* **2007**, *111*, 10861–10873.

[156] M. Gaus, Q. Cui, M. Elstner, *J. Chem. Theory Comput.* **2011**, *7*, 931–948.

[157] N. D. Mermin, *Phys. Rev.* **1965**, *137*, A1441–A1443.

[158] M. K. Beyer, *Angew. Chem.* **2013**, *125*, 3893–3893.

[159] S. Grimme, *Chem. Eur. J.* **2012**, *18*, 9955–9964.

[160] J.-D. Chai, M. Head-Gordon, *Phys. Chem. Chem. Phys.* **2008**, *10*, 6615.

[161] M. Karplus, *Angew. Chem. Int. Ed.* **2014**, *53*, 9992–10005.

[162] H. M. Senn, W. Thiel, *Angew. Chem. Int. Ed.* **2009**, *48*, 1198–1229.

[163] S. Shaik, S. Cohen, Y. Wang, H. Chen, D. Kumar, W. Thiel, *Chem. Rev.* **2010**, *110*, 949–1017.

[164] H. M. Senn, W. Thiel, *Curr. Opin. Chem. Biol.* **2007**, *11*, 182–187.

[165] C. J. Cramer, D. G. Truhlar, *Chem. Rev.* **1999**, *99*, 2161–2200.

[166] J. Tomasi, B. Mennucci, R. Cammi, *Chem. Rev.* **2005**, *105*, 2999–3094.

[167] A Klamt, G Schüürmann, *J. Chem. Soc. Perkin Trans. 2* **1993**, 799–805.

[168] F. Eckert, A. Klamt, *AIChE J.* **2002**, *48*, 369–385.

[169] A. Klamt, *Wiley Interdiscip. Rev. Comp. Mol. Sci.* **2018**, *8*, e1338.

[170] COSMOtherm Program Suite COSMOlogic GmbH & Co KG.

[171] M. W. Wong, M. J. Frisch, K. B. Wiberg, *J. Am. Chem. Soc.* **1991**, *113*, 4776–4782.

[172] M. W. Wong, K. B. Wiberg, M. J. Frisch, *J. Am. Chem. Soc.* **1992**, *114*, 523–529.

[173] C. J. Cramer, D. G. Truhlar, *Acc. Chem. Res.* **2008**, *41*, 760–768.

[174] A. V. Marenich, C. J. Cramer, D. G. Truhlar, *J. Phys. Chem. B* **2009**, *113*, 6378–6396.

[175] R. Sure, S. Grimme, *J. Chem. Theory Comput.* **2015**, *11*, 3785–3801.

[176] A. V. Marenich, C. J. Cramer, D. G. Truhlar, *J. Phys. Chem. B* **2009**, *113*, 4538–4543.

[177] T. Koopmans, *Physica* **1934**, *1*, 104–113.

[178] J. F. Janak, *Phys. Rev. B* **1978**, *18*, 7165–7168.

[179] J. A. Wheeler, *AmSci* **1986**, *74*, 366–375.

[180] E. Runge, E. K. U. Gross, *Phys. Rev. Lett.* **1984**, *52*, 997–1000.

[181] R. van Leeuwen, *Phys. Rev. Lett.* **1999**, *82*, 3863–3866.

[182] A. Dreuw, M. Head-Gordon, *Chem. Rev.* **2005**, *105*, 4009–4037.

[183] F. L. Pilar, *J. Chem. Educ.* **1984**, *61*, A248.

[184] E. Gross, W. Kohn in *Advances in Quantum Chemistry*, **1990**, pp. 255–291.

[185] P.-O. Löwdin, P. Mukherjee, *Chem. Phys. Lett.* **1972**, *14*, 1–7.

[186] H. Hettema, H. J. A. Jensen, P. Jo/rgensen, J. Olsen, *J. Chem. Phys.* **1992**, *97*, 1174–1190.

[187] L. Frediani, H. Ågren, L. Ferrighi, K. Ruud, *J. Chem. Phys.* **2005**, *123*, 144117.

[188] M. E. Casida in *Recent Advances in Density Functional Methods*, **1995**, pp. 155–192.

[189] R. Bauernschmitt, R. Ahlrichs, *Chem. Phys. Lett.* **1996**, *256*, 454–464.

[190] E. Fermi, *Nuclear Physics*, University of Chicago Press., **1950**.

[191] P. A. M. Dirac, *Proc. R. Soc. A* **1927**, *114*, 243–265.

[192] H. A. Bethe, E. E. Salpeter, *Quantum Mechanics of One- and Two-Electron Atoms*, Springer Berlin Heidelberg, **1957**.

[193] S. Hirata, M. Head-Gordon, *Chem. Phys. Lett.* **1999**, *314*, 291–299.

[194] S. Grimme, *J. Chem. Phys.* **2013**, *138*, 244104.

[195] K. Nishimoto, N. Mataga, *Z. Phys. Chem.* **1957**, *12*, 335–338.

[196] K. Ohno, *Theoret. Chim. Acta* **1964**, *2*, 219–227.

[197] G. Klopman, *J. Am. Chem. Soc.* **1964**, *86*, 4550–4557.

[198] C. Bannwarth, S. Grimme, *Comp. Theo. Chem.* **2014**, *1040-1041*, 45–53.

[199] A. Dreuw, M. Head-Gordon, *J. Am. Chem. Soc.* **2004**, *126*, 4007–4016.

[200] T. Yanai, D. P. Tew, N. C. Handy, *Chem. Phys. Lett.* **2004**, *393*, 51–57.

[201] F. Neese, *Wiley Interdiscip. Rev. Comp. Mol. Sci.* **2018**, *8*, e1327.

[202] G. Hermann, V. Pohl, J. C. Tremblay, B. Paulus, H.-C. Hege, A. Schild, *J. Comput. Chem.* **2016**, *37*, 1511–1520.

[203] A. Dreuw, J. L. Weisman, M. Head-Gordon, *J. Chem. Phys.* **2003**, *119*, 2943–2946.

[204] J.-D. Chai, M. Head-Gordon, *J. Chem. Phys.* **2008**, *128*, 084106.

[205] J.-D. Chai, M. Head-Gordon, *J. Chem. Phys.* **2008**, *128*, 084106.

[206] A. D. Laurent, D. Jacquemin, *Int. J. Quantum Chem.* **2013**, *113*, 2019–2039.

[207] Y. Shao, Y. Mei, D. Sundholm, V. R. I. Kaila, *J. Chem. Theory Comput.* **2020**, *16*, 587–600.

[208] S. Grimme, *J. Chem. Phys.* **2006**, *124*, 034108.

[209] A. Karton, A. Tarnopolsky, J.-F. Lamere, G. C. Schatz, J. M. L. Martin, *J. Phys. Chem. A* **2008**, *112*, 12868–12886.

[210] M. Alipour, *Theor. Chem. Acc.* **2016**, *135*, 67.

[211] L. Goerigk, J. Moellmann, S. Grimme, *Phys. Chem. Chem. Phys.* **2009**, *11*, 4611.

[212] S. Grimme, M. Waletzke, *J. Chem. Phys.* **1999**, *111*, 5645–5655.

[213] C. M. Marian, A. Heil, M. Kleinschmidt, *WIREs Comput. Mol. Sci.* **2019**, *9:e1394*.

[214] R. van Meer, O. V. Gritsenko, E. J. Baerends, *J. Chem. Theory Comput.* **2014**, *10*, 4432–4441.

[215] R. W. Wetmore, G. A. Segal, *Chem. Phys. Lett.* **1975**, *36*, 478–483.

[216] J.-M. Mewes, V. Jovanović, C. M. Marian, A. Dreuw, *Phys. Chem. Chem. Phys.* **2014**, *16*, 12393–12406.

[217] I. Lyskov, M. Kleinschmidt, C. M. Marian, *J. Chem. Phys.* **2016**, *144*, 034104.

[218] A. Heil, C. M. Marian, *J. Chem. Phys.* **2017**, *147*, 194104.

[219] A. Heil, M. Kleinschmidt, C. M. Marian, *J. Chem. Phys.* **2018**, *149*, 164106.

[220] J. M. Foster, S. F. Boys, *Rev. Mod. Phys.* **1960**, *32*, 300–302.

[221] J. Pipek, P. G. Mezey, *J. Chem. Phys.* **1989**, *90*, 4916–4926.

[222] A. T. Amos, G. G. Hall, *Proc. R. Soc. A* **1961**, *263*, 483–493.

[223] American College of Neuropsychopharmacology, *Advances in Biochemical Psychopharmacology, Vol. 25*, New York, Raven Press, **1980**, p. 3.

[224] H.-J. Kunze in *Springer Series on Atomic, Optical, and Plasma Physics*, **2009**, pp. 153–178.

[225] Z.-Q. You, J.-M. Mewes, A. Dreuw, J. M. Herbert, *J. Chem. Phys.* **2015**, *143*, 204104.

[226] R. A. Marcus, *J. Chem. Phys.* **1956**, *24*, 966–978.

[227] R. A. Marcus, *J. Chem. Phys.* **1956**, *24*, 979–989.

[228] I. S. Pekar, *Research in electron theory of crystals*, Oak Ridge, Tenn.: U. S. Atomic Energy Commission, **1963**.

[229] L. Rosenfeld, *Z. Angew. Phys.* **1929**, *52*, 161–174.

[230] C. Diedrich, S. Grimme, *J. Phys. Chem. A* **2003**, *107*, 2524–2539.

[231] H. H. Jaffe, A. L. Miller, *J. Chem. Educ.* **1966**, *43*, 469.

[232] A. S. Davydov, *Theory of Molecular Excitons*, Springer US, Boston, MA, **1971**.

[233] Takeyuki Kawaguchi, Kaoru Iwata, *Thin Solid Films* **1990**, *191*, 173–191.

[234] A. Liess, A. Lv, A. Arjona-Esteban, D. Bialas, A.-M. Krause, V. Stepanenko, M. Stolte, F. Würthner, *Nano Lett.* **2017**, *17*, 1719–1726.

[235] H. von Berlepsch, C. Böttcher, L. Dähne, *J. Phys. Chem. B* **2000**, *104*, 8792–8799.

[236] F. Würthner, T. E. Kaiser, C. R. Saha-Möller, *Angew. Chem. Int. Ed.* **2011**, *50*, 3376–3410.

[237] J. L. Bricks, Y. L. Slominskii, I. D. Panas, A. P. Demchenko, *Methods Appl. Fluoresc.* **2017**, *6*, 012001.

[238] N. J. Hestand, F. C. Spano, *Chem. Rev.* **2018**, *118*, 7069–7163.

[239] H. Yamagata, C. M. Pochas, F. C. Spano, *J. Phys. Chem. B* **2012**, *116*, 14494–14503.

[240] F. C. Spano, C. Silva, *Annu. Rev. Phys. Chem.* **2014**, *65*, 477–500.

[241] H. Yamagata, F. C. Spano, *J. Chem. Phys.* **2012**, *136*, 184901.

[242] H. Yamagata, D. S. Maxwell, J. Fan, K. R. Kittilstved, A. L. Briseno, M. D. Barnes, F. C. Spano, *J. Phys. Chem. C* **2014**, *118*, 28842–28854.

[243] P. Srujana, T. P. Radhakrishnan, *Chem. Eur. J.* **2018**, *24*, 1784–1788.

[244] P. Srujana, P. Sudhakar, T. P. Radhakrishnan, *J. Mater. Chem. C* **2018**, *6*, 9314–9329.

[245] W. R. Hertler, H. D. Hartzler, D. S. Acker, R. E. Benson, *J. Am. Chem. Soc.* **1962**, *84*, 3387–3393.

[246] M. Szablewski, M. A. Fox, F. B. Dias, H. Namih, E. W. Snedden, S. M. King, D. Dai, L.-O. Pålsson, *J. Phys. Chem. B* **2014**, *118*, 6815–6828.

[247] P. Srujana, T. Gera, T. P. Radhakrishnan, *J. Mater. Chem. C* **2016**, *4*, 6510–6515.

[248] M. Szablewski, P. R. Thomas, A. Thornton, D. Bloor, G. H. Cross, J. M. Cole, J. A. K. Howard, M. Malagoli, F. Meyers, J.-L. Brédas, W. Wenseleers, E. Goovaerts, *J. Am. Chem. Soc.* **1997**, *119*, 3144–3154.

[249] M. Ravi, D. N. Rao, S. Cohen, I. Agranat, T. P. Radhakrishnan, *J. Mater. Chem.* **1996**, *6*, 1853–1855.

[250] N. Scholz, A. Jadhav, M. Shreykar, T. Behnke, N. Nirmalananthan, U. Resch-Genger, N. Sekar, *J. Fluoresc.* **2017**, *27*, 1949–1956.

[251] S. Grimme, J. G. Brandenburg, C. Bannwarth, A. Hansen, *J. Chem. Phys.* **2015**, *143*, 054107.

[252] J. Heyd, G. E. Scuseria, M. Ernzerhof, *J. Chem. Phys.* **2003**, *118*, 8207–8215.

[253] V. Barone, M. Cossi, *J. Phys. Chem. A* **1998**, *102*, 1995–2001.

[254] H. Iwamura, K. Mislow, *Acc. Chem. Res.* **1988**, *21*, 175–182.

[255] J. D. Crowley, I. M. Steele, B. Bosnich, *Chem. Eur. J.* **2006**, *12*, 8935–8951.

[256] A. Iordache, M. Oltean, A. Milet, F. Thomas, B. Baptiste, E. Saint-Aman, C. Bucher, *J. Am. Chem. Soc.* **2012**, *134*, 2653–2671.

[257] S. Ogi, T. Ikeda, R. Wakabayashi, S. Shinkai, M. Takeuchi, *Chem. Eur. J.* **2010**, *16*, 8285–8290.

[258] R. Sure, S. Grimme, *J. Comput. Chem.* **2013**, *34*, 1672–1685.

[259] B. L. Feringa, R. A. van Delden, N. Koumura, E. M. Geertsema, *Chem. Rev.* **2000**, *100*, 1789–1816.

[260] B. L. Feringa, R. A. van Delden, M. K. J. ter Wiel, *Pure Appl. Chem.* **2003**, *75*, 563–575.

[261] C. Yamamoto, Y. Okamoto, T. Schmidt, R. Jäger, F. Vögtle, *J. Am. Chem. Soc.* **1997**, *119*, 10547–10548.

[262] B. Doser, D. S. Lambrecht, J. Kussmann, C. Ochsenfeld, *J. Chem. Phys.* **2009**, *130*, 064107.

[263] S. A. Maurer, D. S. Lambrecht, J. Kussmann, C. Ochsenfeld, *J. Chem. Phys.* **2013**, *138*, 014101.

[264] F. Neese, F. Wennmohs, A. Hansen, *J. Chem. Phys.* **2009**, *130*, 114108.

[265] F. Neese, A. Hansen, D. G. Liakos, *J. Chem. Phys.* **2009**, *131*, 064103.

[266] C. Riplinger, F. Neese, *J. Chem. Phys.* **2013**, *138*, 034106.

[267] C. Riplinger, B. Sandhoefer, A. Hansen, F. Neese, *J. Chem. Phys.* **2013**, *139*, 134101.

[268] D. W. Schwenke, *J. Chem. Phys.* **2005**, *122*, 014107.

[269] J. Friedrich, *J. Chem. Theory Comput.* **2015**, *11*, 3596–3609.

[270] A. Altun, F. Neese, G. Bistoni, *J. Chem. Theory Comput.* **2020**, *16*, 6142–6149.

[271] A. Klamt, F. Eckert, W. Arlt, *Annu. Rev. Chem. Biomol. Eng.* **2010**, *1*, 101–122.

[272] J. Rydzewski, W. Nowak in *Handbook of Computational Chemistry*, Springer Netherlands, Dordrecht, **2015**, pp. 1–25.

[273] B. M. Rode, T. S. Hofer, B. R. Randolf, C. F. Schwenk, D. Xenides, V. Vchirawongkwin, *Theor. Chem. Acc.* **2006**, *115*, 77–85.

[274] T. K. Woo, P. M. Margl, P. E. Blöchl, T. Ziegler, *J. Phys. Chem. B* **1997**, *101*, 7877–7880.

[275] R. A. Friesner, V. Guallar, *Annu. Rev. Phys. Chem.* **2005**, *56*, 389–427.

[276] I. Tavernelli, B. F. Curchod, U. Rothlisberger, *Chem. Phys.* **2011**, *391*, 101–109.

[277] B. F. E. Curchod, T. J. Martínez, *Chem. Rev.* **2018**, *118*, 3305–3336.

[278] J. Westermayr, P. Marquetand, *Mach. Learn.: Sci. Technol.* **2020**, *1*, 043001.

[279] P. O. Dral, *J. Phys. Chem. Lett.* **2020**, *11*, 2336–2347.

[280] R. Ramakrishnan, P. O. Dral, M. Rupp, O. A. von Lilienfeld, *J. Chem. Theory Comput.* **2015**, *11*, 2087–2096.

[281] K. T. Schütt, M. Gastegger, A. Tkatchenko, K.-R. Müller, R. J. Maurer, *Nat. Commun.* **2019**, *10*, 5024.

[282] F. Noé, A. Tkatchenko, K.-R. Müller, C. Clementi, *Annu. Rev. Phys. Chem.* **2020**, *71*, 361–390.

[283] J. Gebhardt, M. Kiesel, S. Riniker, N. Hansen, *J. Chem. Inf. Model.* **2020**, *60*, 5319–5330.

[284] M. Gastegger, J. Behler, P. Marquetand, *Chem. Sci.* **2017**, *8*, 6924–6935.

[285] Z. Li, J. R. Kermode, A. De Vita, *Phys. Rev. Lett.* **2015**, *114*, 096405.

[286] P. Kirkpatrick, C. Ellis, *Nature* **2004**, *432*, 823–823.

[287] O. A. von Lilienfeld, K.-R. Müller, A. Tkatchenko, *Nat. Rev. Chem.* **2020**, *4*, 347–358.